

**COMPUTATIONAL ASSESSMENT OF ZEOLITIC IMIDAZOLATE  
FRAMEWORKS FOR KINETIC GAS SEPARATIONS**

A Dissertation  
Presented to  
The Academic Faculty

by

Ross James Verploegh

In Partial Fulfillment  
of the Requirements for the Degree  
Doctor of Philosophy in Chemical Engineering in the  
School of Chemical & Biomolecular Engineering

Georgia Institute of Technology  
August 2017

**COPYRIGHT (C) 2017 BY ROSS JAMES VERPLOEGH**

**COMPUTATIONAL ASSESSMENT OF ZEOLITIC IMIDAZOLATE  
FRAMEWORKS FOR KINETIC GAS SEPARATIONS**

Approved by:

Dr. David S. Sholl, Advisor  
School of Chemical & Biomolecular  
Engineering  
*Georgia Institute of Technology*

Dr. Sankar Nair  
School of Chemical & Biomolecular  
Engineering  
*Georgia Institute of Technology*

Dr. Christopher W. Jones  
School of Chemical & Biomolecular  
Engineering  
*Georgia Institute of Technology*

Dr. Krista S. Walton  
School of Chemical & Biomolecular  
Engineering  
*Georgia Institute of Technology*

Dr. Thomas M. Orlando  
School of Chemistry & Biochemistry  
*Georgia Institute of Technology*

Date Approved: July 13th, 2017

*I did not believe that it was possible to study Brownian motion with such a precision.*

-From a letter from Albert Einstein to Jean Perrin (1909)

*To my mother, a chemical engineer, and my father, a computer science major. I am a true hybrid of both of you.*

-RJV



## ACKNOWLEDGEMENTS

The road to finishing my Ph.D. was long and arduous; there was nothing easy about it. It reminds me of a childhood book I much enjoyed called *Pilgrim's Progress* where the protagonist makes a journey “from this world, to that which is to come.” Along the way, the pilgrim is helped by many different people he meets along his journey and without them his journey would never have been possible. These are the people who made my Ph.D. possible.

I knew I wanted to do research with atomistic simulations when researching graduate schools and purposefully selected those that had excellent computational researchers. At that time, I did not truly know Dr. David Sholl, the mentor and advisor I would have for five years, but am thankful for my choice. David challenged me with difficult research problems and allowed me to discover the path forward on them, even if it took a little longer than expected. He is an excellent family man and leads his research group by example. When my original funding through Phillips 66 ended because of the sharp decline of oil, he provided stability to my research by finding other funding sources. I am truly grateful for the time I have spent learning from David and his encouragement throughout my Ph.D.

Throughout the last five years at Georgia Tech, I have had very productive research conversations with many talented professors. I had the pleasure of working with Dr. Sankar Nair closely on the Phillips 66 project. He was actually the first Georgia Tech professor I talked to when deciding on graduate schools; he served on my qualifying exam committee and would become one of my committee members. Over the last five years, I have worked at various stages with Dr. Krista Walton, Dr. Christopher Jones and Dr. Thomas Orlando. Their input as my committee members was truly valuable and helped shape my research at Tech.

There are four talented individuals with whom I have worked closely and had many conversations over coffee. I would first like to thank Dr. Krishna Jayachandrababu. He is a close friend and I will never forget our many musings about diffusion, politics, and comedians. I would like to thank Ying Wu, a visiting scholar from China, for being a great officemate and working with me through some difficult conceptual problems. I also learned a tremendous amount about atomistic simulations from Dr. Salah Boulfelfel; he never told me he was too busy to help me solve a problem and took my phone calls at every hour. For the man taking over my research project, Jonathan Haydak, I want to extend thanks for his renewing my energy for research during the writing of this thesis. He is truly excited about simulations and has a passion for science that is contagious.

There are many other graduate students and Georgia Tech alumni to thank. I especially want to extend my best to Dr. Emmanuel Haldoupis, Dr. Dalar Nazarian, Dr. Jason Gee, Dr. Jeffrey Camp, Dr. Ambarish Kulkarni, Brandon Plaisance, and Brian Pimentel. They were available in their offices to discuss porous materials, simulations, life, and all of the above. It will be exciting to watch our careers develop together and we may even work together again in the future.

My research career would not have been fruitful without the PACE team at Georgia Tech who worked tirelessly to keep our high performance computer cluster functioning at peak performance. I want to acknowledge Dr. Wesley Emeneker, Dr. Mehmet Belgin, Dr. Blake Fleischer, and Dr. Fang Lui for fielding my questions and for allowing me to drop by their offices unannounced. They were always available to help me solve any of my computing problems.

I also had the pleasure of meeting some of the LAMMPS development team during my graduate students, especially Dr. Axel Kohlmeyer and Dr. Giacomo Fiorin. Without their work focused on creating the best performing molecular dynamics code and answering my questions about compilation or coding issues, this thesis would never have

been possible. I even greatly enjoyed trying Axel's homebrewed beer at Temple University (Philadelphia)!

My love of research was instilled by Dr. Joan Brennecke, my undergraduate research advisor. She is an inspiring woman and her mentorship was a blessing. I also want to thank Dr. Bill Schneider and the many Notre Dame graduate students. They taught me the value of atomistic simulations, gave me the fundamentals to succeed at Georgia Tech, showed me firsthand the life of a graduate student, and set me on this path.

I have had some amazing times with my closest friends in Atlanta: Jay Joshi, Colton Moran, Julian Hungerford, Jason Lee, and Keller Smith. They encouraged me to lift weights again, shared many beers with me, taught me how to shoot, and allowed me to vent from time to time. To Jay especially, the years as his roommate have been a blessing and he has become one of my closest friends.

I have also had the fortune to be able to take refuge in the Georgia Tech machine shop. It seems like an unlikely friendship, but I became close with Jeff Andrews and Brad Parker over a ridiculous amount of coffee. There were no limits to the topics of our conversations and they have helped me through some difficult times.

During the last months of my time as a graduate student, I was blessed to meet Ashley Howell. She guided me through some of my most difficult months, the last stretch of my PhD, and has been a never ending source of support. She has an inquisitive mind, always seeks the truth, and is truly a remarkable woman. I am looking forward to the future!

Without the sacrifices of Marie J. and Arthur R. Baum (maternal grandparents), Virginia Radwan Galvez (maternal great grandmother, Nani), and Irene E. and Adrian J. Verploegh (paternal grandparents) I would not have had the opportunity to do this research. My work here at Tech was never possible without their sacrifices as coal miners, farmers, chemists, survivors of the Great Depression, and immigrants. I imagine

they are able to see how the sacrifices of their lives impacted me and I want to be able to extend their legacy of hard work and perseverance to my future children.

To my parents Diane and Jim Verploegh, I love you very much. There are no words to describe their sacrifices to make my Ph.D. a reality. They saw me through the good times and bad and were a constant in an every changing world. They taught me about life and how to question the world around me. They showed me how to examine God's creation and to use that knowledge to help others around me. Without them, none of my journey was possible and I am blessed to have them as parents.

*Ross Verploegh, Atlanta, July 2017*

# TABLE OF CONTENTS

	Page
<b>ACKNOWLEDGEMENTS .....</b>	<b>vii</b>
<b>LIST OF TABLES .....</b>	<b>vix</b>
<b>LIST OF FIGURES .....</b>	<b>xviii</b>
<b>SUMMARY .....</b>	<b>xxxi</b>
 <b><u>CHAPTER</u></b>	
<b>I. INTRODUCTION .....</b>	<b>1</b>
1.1 Energy Efficient Separations using Nanoporous Materials .....	1
1.2 Nanoporous Material of Interest: Metal-Organic Frameworks .....	3
1.3 Zeolitic Imidazolate Frameworks .....	6
1.3.1 ZIF Kinetic Flexibility.....	8
1.3.2 ZIF Thermodynamic Flexibility.....	10
1.4 Intuitive and Heuristic Methods for MOF Screening and Selections for Membrane Applications: The Limitations .....	11
1.5 Overview of Hierarchical Atomistic Simulations and Complementary Experimental Methods for MOF Selection.....	13
1.5.1 Predicting and Measuring Adsorption: Tools and Challenges .....	14
1.5.2 Predicting and Measuring Diffusion: Tools and Challenges.....	15
1.5.3 Predicting and Measuring Membrane Permeabilities: Tools and Challenges .....	17
1.6 Thesis Impact .....	20
<b>II. HYDROCARBON DIFFUSION PREDICTIONS THROUGH ZEOLITIC IMIDAZOLATE FRAMEWORK-8.....</b>	<b>23</b>
2.1 Introduction.....	24
2.2 Theory .....	27

2.2.1 Diffusion Background .....	27
2.2.2 Calculating the Diffusion Hopping Rate at Infinite Dilution .....	28
2.2.3 Coupling of Adsorbate and MOF Framework Motions .....	30
2.2.4 Loading Dependence of the Diffusion Coefficient .....	30
2.3 Computational Methods.....	32
2.3.1 ZIF-8 and Adsorbate Force Fields.....	32
2.3.2 Grand Canonical Monte Carlo .....	33
2.3.3 Free Energy Mapping.....	33
2.3.4 Transmission Coefficient Calculation .....	36
2.3.5 Methods for Measuring Loading-Dependent Self-Diffusivities .....	37
2.4 Results and Discussion .....	38
2.4.1 Infinite Dilution: Hydrocarbons in ZIF-8.....	38
2.4.2 Loading Dependence of Hydrocarbon Diffusion in ZIF-8.....	45
2.4.3 ZIF-8 Membrane Property Predictions.....	51
2.5 Conclusions and Impact.....	57
<b>III. TRANSFERABLE FORCE FIELD DEVELOPMENT DESCRIBING ZEOLITIC IMIDAZOLATE FRAMEWORK FLEXIBILITY .....</b>	<b>59</b>
3.1 Introduction.....	59
3.2 Parameterization of the intraZIF Force Field.....	64
3.2.1 From Bulk Structure to Cluster Models .....	65
3.2.2 van der Waals and Coulombic Interactions.....	66
3.2.3 Stretching and Bending Modes .....	68
3.2.4 Dihedrals and Improper Torsions.....	71
3.3 Five Independent Tests of the intraZIF Force Field .....	74
3.3.1 Structural Properties .....	74
3.3.2 Thermodynamic Stability of Im and mIm ZIF Polymorphs.....	77

3.3.3 Bulk Modulus Predictions .....	78
3.3.4 Reproducibility of Relative Energy and Forces from BOMD Calculations .....	80
3.3.5 Window Diameter Distributions .....	81
3.4 Light Gas Diffusivities in ZIFs with the SOD Topology .....	84
3.4.1 Adsorbate Force Fields and ZIF-Adsorbate Interactions .....	84
3.4.2 Diffusion Theory and Computational Methods.....	85
3.4.3. Screening of Thirty Adsorbates in SALEM-2, ZIF-8, and ZIF-90 ..	86
3.4.4 Diffusion in ZIF-7 .....	92
3.5 Conclusions.....	96
<b>IV. CREATION OF STRUCTURAL MODELS FOR MIXED-LINKER ZEOLITIC IMIDAZOLATE FRAMEWORK 8-90 MATERIALS.....</b>	<b>98</b>
4.1 Introduction.....	99
4.2 Experimental Methods .....	103
4.3 Simulation Methods .....	104
4.3.1 ZIF-8 <sub>x</sub> -90 <sub>100-x</sub> Structure Generation.....	104
4.3.2 Semi-Empirical Fitting of <sup>1</sup> H CRAMPS NMR Intensity Curves ...	105
4.4 Results and Discussion .....	106
4.4.1 Pure ZIF-8 and ZIF-90 NMR Analysis .....	106
4.4.2 ZIF-8 <sub>x</sub> -90 <sub>100-x</sub> Hybrid Materials .....	110
4.5 Conclusions.....	125
<b>V. LATTICE MODEL OF ADSORBATE DIFFUSION THROUGH MIXED- LINKER ZEOLITIC IMIDAZOLATE FRAMEWORKS .....</b>	<b>127</b>
5.1 Introduction.....	127
5.2 Theory .....	131
5.2.1 Quantifying Local Order in Binary Mixed-Linker ZIFs .....	131

5.2.2 Diffusion as an Activated Hopping Process .....	132
5.2.3 Classification of Windows and Hopping Rate Catalogue .....	132
5.3 Simulation Methods .....	135
5.3.1 Lattice Generation .....	135
5.3.2 Kinetic Monte Carlo Procedure.....	136
5.4 Results and Discussion .....	138
5.4.1 Zero Hopping Rates through Window Blocking.....	138
5.4.2 Deriving Hopping Rates through Hybrid Windows based on the Hopping Rates in the Parent ZIFs .....	144
5.4.3 Comparison to Experimental ZIF-8 <sub>x</sub> -90 <sub>100-x</sub> Isobutane and n-Butane Self-Diffusion Data .....	150
5.5 Conclusions.....	153
<b>VI. LIGHT GAS DIFFUSION PREDICTIONS THROUGH MIXED-LINKER ZEOLITIC IMIDAZOLATE FRAMEWORKS .....</b>	<b>155</b>
6.1 Introduction.....	155
6.2 Theory .....	158
6.2.1 Creating Mixed-Linker ZIF Structures.....	158
6.2.2 Modeling Adsorbate Diffusion and Comparisons to Experimental Diffusion Data .....	160
6.3 Simulation Methods .....	161
6.3.1 Binary-Mixed Linker ZIF and Adsorbate Force Fields.....	161
6.3.2 Conventional and Biased Molecular Dynamics .....	163
6.3.3 Lattice-Diffusion Model and Kinetic Monte Carlo .....	164
6.4 Results and Discussion .....	164
6.4.1 ZIF-8-90: The First Experimentally Reported Example of Tunable Diffusion in ZIFs .....	164
6.4.2 ZIF-8/SALEM-2 in the SOD Topology .....	174



6.4.3 ZIF-7-90: Window Blocking By a Bulky Imidazolate Linker .....	178
6.5 Conclusions.....	182
<b>VII. CONCLUSIONS .....</b>	<b>183</b>
7.1 Dissertation Impact .....	183
7.2 Suggestions for Future Work .....	185
<b>APPENDIX A: CHAPTER 2 SUPPORTING INFORMATION .....</b>	<b>188</b>
<b>APPENDIX B: CHAPTER 3 SUPPORTING INFORMATION .....</b>	<b>212</b>
<b>APPENDIX C: CHAPTER 4 SUPPORTING INFORMATION .....</b>	<b>265</b>
<b>APPENDIX D: CHAPTER 5 SUPPORTING INFORMATION .....</b>	<b>279</b>
<b>APPENDIX E: CHAPTER 6 SUPPORTING INFORMATION .....</b>	<b>285</b>
<b>APPENDIX F: PUBLISHED WORK .....</b>	<b>291</b>
<b>APPENDIX G: COPYRIGHT AGREEMENT LETTERS .....</b>	<b>294</b>
<b>REFERENCES.....</b>	<b>296</b>
<b>VITA <i>Ross J. Verploegh</i>.....</b>	<b>322</b>

## LIST OF TABLES

	Page
<b>Table 1.1:</b> Extant examples of kinetic separations of light olefins and paraffins using supported thin films. ....	5
<b>Table 2.1:</b> Comparison of simulated and experimental single-component permeabilities. ....	55
<b>Table 3.1:</b> Comparison of experimental and intraZIF predicted unit cell lattice parameters and volumes ....	68
<b>Table 3.2:</b> Summary of predicted diffusivities in ZIF-7 using both conventional NPT-MD and dynamically corrected TST. ....	95
<b>Table A.1:</b> Molecular diameters, molecular weights, 12-6 Lennard Jones potential parameters and atomic charges for small adsorbates. ....	188
<b>Table A.2:</b> Bonds, angles, and dihedrals for rigid and flexible adsorbates. ....	189
<b>Table A.3:</b> Helmholtz free energy barrier (kJ/mol) at infinite dilution over the 0 to 150 °C temperature range. ....	192
<b>Table A.4:</b> Adsorbate transition state theory (TST) derived hopping rate (jumps/s) at infinite dilution over the 0 to 150 °C temperature range as calculated with Equation A.1. ....	193
<b>Table A.5:</b> Dynamical correction factors for adsorbates at infinite dilution over the 0 to 150 °C temperature range. ....	194
<b>Table A.6:</b> Infinite-dilution self-diffusion coefficients for small non-spherical molecules and light key hydrocarbons at 0°C, 35°C, 100°C, and 150°C derived from the dynamical correction factor and the TST hopping rate. The red region highlights the data pertaining to the C2/C3 separation. ....	195
<b>Table A.7:</b> Self diffusion coefficients as a function of temperature measured with NVT-MD and NVT-dcTST simulations. ....	196
<b>Table A.8:</b> Extant experimental diffusion coefficients for adsorbates in ZIF-8 used in Figure 2.4 of Chapter 2. Listed after the diffusion values respectively is the diffusion coefficient type, temperature, adsorbate loading, experimental technique, and literature reference. ....	198
<b>Table A.9:</b> Mean and standard deviation from a normal distribution fit to the window histograms at 308.15 K for all 15 adsorbates. ....	200

<b>Table A.10:</b> Calculated liquid loadings for C1-C4 hydrocarbons. For CH <sub>4</sub> , the liquid loading of 22 molecules per cage, even though unphysical, was used instead of 19 molecules per cage to theoretically demonstrate the loading at which the diffusivity of methane began to decrease due to steric hindrance. ....	203
<b>Table A.11:</b> Simulated free energies, dynamical correction factors, self-diffusivities, thermodynamic correction factors, and transport diffusivities as a function of adsorbate loading at 35 °C. ....	206
<b>Table B.1:</b> Bonded force field parameters for ZIFs with unfunctionalized imidazolate linkers. Functional forms, spring constants, and equilibrium geometry parameters are listed. ....	212
<b>Table B.2:</b> Bonded force field parameters for ZIFs with 2-methylimidazolate linkers. Functional forms, spring constants, and equilibrium geometry parameters are listed. ....	217
<b>Table B.3:</b> Bonded force field parameters for ZIFs with imidazolate-2-carboxaldehyde linkers. Functional forms, spring constants, and equilibrium geometry parameters are listed. ....	220
<b>Table B.4:</b> Bonded force field parameters for ZIFs with benzimidazolate linkers. Functional forms, spring constants, and equilibrium geometry parameters are listed. ....	224
<b>Table B.5:</b> Buckingham potential parameters taken from the Molecular Mechanics 3 (MM3) force field and used in the intraZIF-FF. ....	229
<b>Table B.6:</b> AMBER van der Waals parameters taken from the parm10.dat file. ....	230
<b>Table B.7:</b> Unscaled and scaled epsilon and sigma 12-6 Lennard Jones parameters from the Universal Force Field (UFF) used to describe adsorbate-adsorbent interactions. ....	230
<b>Table B.8:</b> Charges for periodic ZIFs from the DDEC method used in the intraZIF-FF. ....	231
<b>Table B.9:</b> Pair-wise coulombic interactions utilizing the Debye damping factor. ....	231
<b>Table B.10:</b> SALEM-2 structural parameter comparisons between DFT and FF energy minimizations. ASA (NASA) and AV (NAV) are reported for the simulation volume (2x2x2 supercell). ....	234
<b>Table B.11:</b> ZIF-7 structural parameter comparisons between DFT and FF energy minimizations. ASA (NASA) and AV (NAV) are reported for the simulation volume (2x2x2 supercell). ....	235

<b>Table B.12:</b> ZIF-8 structural parameter comparisons between DFT and FF energy minimizations. ASA (NASA) and AV (NAV) are reported for the simulation volume (2x2x2 supercell). .....	235
<b>Table B.13:</b> ZIF-90 structural parameter comparisons between DFT and FF energy minimizations. ASA (NASA) and AV (NAV) are reported for the simulation volume (2x2x2 supercell). .....	235
<b>Table B.14:</b> Pore limiting diameters [ $\text{\AA}$ ] of Im polymorphs. ....	236
<b>Table B.15:</b> Accessible surface areas [ $\text{m}^2/\text{cm}^3$ ] per unit cell of Im polymorphs. ....	237
<b>Table B.16:</b> Pore limiting diameters [ $\text{\AA}$ ] of mIm polymorphs. ....	238
<b>Table B.17:</b> Accessible surface areas [ $\text{m}^2/\text{cm}^3$ ] per unit cell of mIm polymorphs. ....	239
<b>Table B.18:</b> Relative configurational energies [ $\text{kJ/mol/Zn}$ ] of Im polymorphs ranked according to the PBE-D2 predicted stabilities. ....	242
<b>Table B.19:</b> Relative configurational energies [ $\text{kJ/mol/Zn}$ ] of mIm polymorphs ranked according to the PBE-D2 predicted stabilities. ....	243
<b>Table B.20:</b> Force comparisons for the Zn atom type (n=97992) of the AMBER and intraZIF FFs to BOMD forces. ....	244
<b>Table B.21:</b> Force comparisons for the N atom type (n=391968) of the AMBER and intraZIF FFs to BOMD forces. ....	245
<b>Table B.22:</b> Force comparisons for the $\text{C}_1$ atom type (n=195984) of the AMBER and intraZIF FFs to BOMD forces. ....	245
<b>Table B.23:</b> Force comparisons for the $\text{C}_2$ atom type (n=391968) of the AMBER and intraZIF FFs to BOMD forces. ....	246
<b>Table B.24:</b> Force comparisons for the $\text{H}_1$ atom type (n=195984) of the AMBER and intraZIF FFs to BOMD forces. ....	246
<b>Table B.25:</b> Force comparisons for the $\text{H}_2$ atom type (n=391968) of the AMBER and intraZIF FFs to BOMD forces. ....	247
<b>Table B.26:</b> Full list of adsorbate molecular diameters, LJ sites, molecular weights, LJ parameters, and charges. ....	253
<b>Table B.27:</b> Free energy barriers (FEB) for adsorbates in SALEM-2, ZIF-8, and ZIF-90 at 308 K and 1.01 bar. ....	256
<b>Table B.28:</b> Dynamical correction factors for adsorbates in SALEM-2, ZIF-8, and ZIF-90 at 308 K and 1.01 bar. ....	257

<b>Table B.29:</b> Self-diffusion coefficients for adsorbates in SALEM-2, ZIF-8, and ZIF-90 at 308 K and 1.01 bar.....	258
<b>Table B.30:</b> Comparisons of simulated diffusivities to the experimental diffusivities measured by Zhang et al. The experimental diffusivities are measured at 50 °C and the simulated diffusivities are calculated at 35 °C.....	259
<b>Table C.1:</b> Material quantities for synthesizing ZIF-8-90 mixed-linker materials. ....	266
<b>Table C.2:</b> BET surface areas for several hybrid ZIF-8 <sub>x</sub> -90 <sub>100-x</sub> materials. ....	269
<b>Table C.3:</b> Liquid NMR hydrogen peak locations in ppm.....	270
<b>Table C.4:</b> Summary of fitting results detailing the starting unit cell, A value, scaled initial z-magnetization values, and final short range orders for different ZIF-8-90 hybrids.....	278
<b>Table E.1:</b> Adsorbate force field parameters along with molecular diameters (KD=kinetic diameter, vdW=van der Waals diameter, and LJ=diameter approximated from Lennard-Jones sigma parameters) and molecular weights. ....	286
<b>Table E.2:</b> 12-6 Lennard-Jones parameters on framework atoms used to model adsorbate-framework interactions.....	286
<b>Table E.3:</b> Statistics benchmarking the quality of the intraZIF-FF at describing PBE-D3(BJ) configurational potential energies from BOMD simulations at 700 K and 1.01 bar.....	287

## LIST OF FIGURES

	Page
<b>Figure 1.1:</b> (a) Schematic of a hollow fiber membrane module and (b) a cross-sectional SEM image of a supported thin-film nanoporous membrane (yellow ring on the bore side) as adapted from Brown et al.....	2
<b>Figure 1.2:</b> Several representative MOFs: (a) IRMOF-1, (b) Cu-BTC, (c) MIL-47, (d) MIL-100, (e) UiO-66, and (f) MOF-72. ....	4
<b>Figure 1.3:</b> Structural and chemical diversity of ZIF materials as adapted from Park et al. ....	7
<b>Figure 1.4:</b> Classes of MOF framework flexibility; figure was adapted from Coudert et al.....	8
<b>Figure 1.5:</b> (a) 3D-printed ZIF-8 structure (Zn=light blue, N=dark blue, C=black, H=off-white); molecules diffuse through the 6 MR windows. (b) Activation energy of diffusion as a function of molecular diameter for zeolites 4A and 5A and ZIF-8; figure adapted from Zhang et al. ....	10
<b>Figure 1.6:</b> Screening MOFs for molecular sieving applications based on geometric characteristics such as the global cavity diameter, largest cavity diameter, and the pore limiting diameter under the rigid framework assumption. Figure adapted from Haldoupis et al. ....	12
<b>Figure 1.7:</b> Loading dependent diffusion of ethane through ZIF-8 where solid squares represent the transport diffusivities, closed blue circles represent the corrected diffusivities, and the open blue circles the self-diffusivities measured with IR microscopy; figure adapted from Chemlik et al. ....	16
<b>Figure 1.8:</b> Hierarchical methods for choosing MOFs for membrane applications. Both the transport and adsorption properties are considered first and simultaneously through simulations (blue text) and experiments (red text) to engineer MOF membranes with properties that reach the target performance criteria. ....	19
<b>Figure 2.1:</b> Schematic of the linear reaction coordinate (red vector) traversing the window between two ZIF-8 cages. Umbrellas are idealized as brown discs on the red 1-D RC. The other 14 cages in the 2x2x2 ZIF-8 simulation volume as well as hydrogen atoms have been removed for clarity. Spheres colored in yellow, blue, and black correspond respectively to Zn, N, and C atoms.....	36
<b>Figure 2.2:</b> Free energy curves for propane at infinite dilution as a function of temperature in flexible ZIF-8.....	38

<b>Figure 2.3:</b> Transmission coefficient curves for propane at infinite dilution in flexible ZIF-8 as a function of time for various temperatures. ....	39
<b>Figure 2.4:</b> Infinite-dilution self-diffusion coefficients for small non-spherical molecules and light key hydrocarbons at 35 °C as a function of molecular diameter. Experimental data was taken directly from Zhang et al. and Eum et al. Simulated C <sub>1</sub> -C <sub>4</sub> diffusivities in LTA zeolite taken from Boulfelfel et al. ....	42
<b>Figure 2.5:</b> ZIF-8 window size distributions at 35 °C for configurations with adsorbates constrained to be in the window as described in the text. ....	45
<b>Figure 2.6:</b> Short alkane and alkene self-diffusion coefficients as a function of unary fractional loading in ZIF-8 at 35°C. ....	47
<b>Figure 2.7:</b> Short alkane and alkene transport diffusion coefficients as a function of unary fractional loading in ZIF-8 at 35°C. ....	49
<b>Figure 2.8:</b> Short alkane and alkene permeabilities as a function of feed pressure in ZIF-8 at 35 °C .....	53
<b>Figure 3.1:</b> Cluster models for the (a) imidazole (Im), (b) 2-methylimidazole (mIm), (c) imidazole-2-carboxaldehyde (ImCA), and (d) benzimidazole (BzIm) linkers. C, N, H, O, and Zn atoms represented by grey, purple, off-white, red, and gold spheres. Each of the atom types are labelled according to their unique atomic charges. ....	66
<b>Figure 3.2:</b> Relative energy comparisons between PBE and (a) the intraZIF-FF including Fourier dihedrals from the potential energy fitting and (b) the AMBER-FF using standard cosine proper dihedrals for the Im cluster. Insets represent the concatenated relative energy time series for the simulations with increasing temperature. The color code (black to blue/intraZIF and orange to green/AMBER) is designed to easily identify the low and high energy regions. ....	73
<b>Figure 3.3:</b> Parity plots for (a) PLDs and (b) accessible surface areas as predicted by PBE-D2 and the intraZIF (blue/black closed circles) and AMBER (orange/green) force fields. There are 27 Im polymorphs (black/orange circles) including SALEM-2 and 25 mIm polymorphs (blue/green circles) including ZIF-8. ....	76
<b>Figure 3.4:</b> Relative energy rankings of the hypothetical (a) imidazolate (black/orange) and (b) 2-methylimidazolate (blue/green) polymorphs for PBE-D2, the AMBER-FF (open circles), and the intraZIF-FF (closed circles).....	78

- Figure 3.5:** Pressure dependence of the ZIF-8 unit cell parameters measured by Chapman et al. and predicted by the intraZIF and AMBER FFs. The third-order Birch-Murnaghan isothermal equation of state is fit (solid line) to both the measured and predicted data. The amorphization pressures are indicated by the dashed lines. ....79
- Figure 3.6:** SALEM-2 relative potential energies as predicted by the AMBER-FF (orange to green) and intraZIF-FF (black to blue) in reference to PBE-D3(BJ) relative energies from fully periodic BOMD simulations at 700 K.....81
- Figure 3.7:** Window diameter histograms in SALEM-2 using PBE-D3(BJ) and the AMBER and intraZIF FFs. Solid lines represent the lognormal distribution fits with the mean ( $\mu$ ) and standard deviation (SD) of these lognormal distributions reported in the table insets. There are 2000 samples for each histogram from the AMBER-FF and intraZIF-FF and the sample number for the histograms from PBE-D3(BJ) are reported in the center panel.. ....82
- Figure 3.8:** Window diameter histograms in SALEM-2, ZIF-7, ZIF-8, and ZIF-90 at 1.01 bar and temperatures at which the crystal structures were resolved, using the intraZIF-FF. The inset table compares the PLD ( $\text{\AA}$ ) of the energy minimized structures using PBE-D2 and the intraZIF-FF. Solid lines represent Gaussian distribution fits where the mean ( $\mu$ ) and standard deviation are reported in the legend. ....84
- Figure 3.9:** Self-diffusivities of 14 adsorbates as predicted by the modified AMBER force field using NVT-MD from Verploegh et al. and the intraZIF-FF using NPT-MD (1.01 bar) in comparison to reference experimental diffusivities from Zhang et al. (unmarked) and Eum et al. (marked) at 308 K. The dashed orange lines represent the order-of-magnitude accuracy expected from macroscopic uptake methods. ....87
- Figure 3.10:** Self-diffusivities at infinite dilution of thirty adsorbates in SALEM-2, ZIF-8, and ZIF-90 with fits of Equation 3.13 as solid lines. The intraZIF-FF predicted PLDs from energy-minimized structures are shown as dashed lines. ....88
- Figure 3.11:** Analysis of diffusion in ZIF-7-I phase with (a) a singular truncated octahedron cage viewed perpendicular to (010) along with the one-dimensional reaction coordinate (solid red line). The plane of the minor cage is indicated by the dashed green line and the inaccessible window is indicated by the dashed red lines. (b) Gibbs free energy curves as a function of reaction coordinate. The shaded regions represent the integral used to calculate the TST hopping rate. The inset show the transmission coefficient curves for  $\text{H}_2$ , methane, n-butane, and isobutane. ....94



<b>Figure 4.1:</b> (a) Schematic demonstrating nearest neighbor convention based on bond connectivity where the central mIm linker has 3 OHC-Im and 3 mIm NNs. (b) Schematic of a ZIF-8 <sub>50</sub> -90 <sub>50</sub> hybrid 2×2×2 supercell where the OHC-Im linkers are randomly distributed. Atom representations are as follows: O=red, N=blue, H=off-white, C=black, and Zn=gold. Yellow (a) and purple (b) tetrahedrons are included to illustrate the 4-coordinated Zn atoms. ....	103
<b>Figure 4.2:</b> <sup>1</sup> H-NMR contour plots of (a) ZIF-8 and (b) ZIF-90, measured at 5 kHz MAS and 1 ms mixing time. Diagonal peaks are marked in solid circles and cross-peaks in dashed circles. ....	108
<b>Figure 4.3:</b> Fit of the spin-exchange model (solid curves) to experimental CRAMPS NMR measurements (red circles) for spin exchange between protons in ZIF-8 as a function of the mixing time. ....	110
<b>Figure 4.4:</b> <sup>1</sup> H-NMR spectra of (a) physical mixture of ZIF-8 and ZIF-90 and (b) mixed-linker ZIF-8 <sub>50</sub> -90 <sub>50</sub> , measured at 5 kHz MAS and 50 ms mixing time. Green dotted circle in (a) denotes the absence of transfer between methyl and aldehyde protons in physical ZIF mixture. Red dotted circle in (b) shows the transfer in hybrid material. ....	111
<b>Figure 4.5:</b> Spin diffusion profiles of (a) ZIF-8 and ZIF-90, (b) ZIF-8 <sub>50</sub> -90 <sub>50</sub> , and (c) ZIF-8-90 at various compositions scaled by the anticipated spin diffusion coefficient. ....	114
<b>Figure 4.6:</b> ZIF-8 <sub>50</sub> -90 <sub>50</sub> methyl (gray) and aldehyde (orange) hydrogen maps for 5×5×5 supercells of size 8.47 nm: (a) SRO of $\alpha = 0.87$ demonstrating extreme clustering, (b) SRO of $\alpha = 0.0$ demonstrating a random linker arrangement, and (c) SRO of $\alpha = -0.29$ demonstrating partial ordering. Hydrogens not to scale, in order to enhance clarity. ....	119
<b>Figure 4.7:</b> Experimental (open red circles) and simulated NMR spin exchange peak intensities for ZIF-8 <sub>50</sub> -90 <sub>50</sub> with $\alpha = 0.45$ . ....	120
<b>Figure 4.8:</b> Comparison of experimental NMR spin exchange intensity ratios and simulated curves for several structures with different $\alpha$ values for ZIF-8 <sub>50</sub> -90 <sub>50</sub> . ....	121
<b>Figure 4.9:</b> Comparison of experimental (red circles) and simulated 2D CRAMPS peak ratios of the ‘best-fit’ SRO models (solid black lines), for four different ZIF-8-90 mixed-linker materials. ....	122
<b>Figure 4.10:</b> Short range order $\alpha$ and average number of OHC-Im linkers per mIm linker as a function of the overall composition of the mixed-linker ZIF-8-90 material. ....	123

- Figure 4.11:** Probability distributions of observing the four possible types of pore windows as a function of the short range order parameter ( $\alpha$ ) and the overall composition of the mixed-linker ZIF-8-90 material. Red circles indicate the window type probabilities for the experimental samples. ....125
- Figure 5.1:** Truncated octahedron representing a singular cage of both parent (a) ZIF-8 and (b) ZIF-90. H, C, N, O and Zn atoms colored off-white, black, blue, red, and gold respectively. ....130
- Figure 5.2:** Four window types corresponding to the four possible 6 MR windows in ZIF-8<sub>x</sub>-90<sub>100-x</sub>. Only the windows laying directly in the plane (denoted by the yellow circle and arrows in (a)) are assumed to dictate diffusion. (a) and (b) Parent window types of type 1 and 4 containing all mIm linkers and all ImCA linkers respectively; (c) and (d) Hybrid windows of type 2 containing two mIm/one ImCA linkers and type 3 containing one mIm/two ImCA linkers. H, C, N, O and Zn atoms colored off-white, black, blue, red, and gold; aqua blue and pink inside the imidazolate rings indicate whether the linker is a mIm or ImCA linker respectively. ....134
- Figure 5.3:** Example mixed-linker ZIF-A<sub>50</sub>-B<sub>50</sub> structures in the SOD topology with short-range order values of (a) -0.25 (i.e. alternating/sparse), (b) 0.0 (i.e. random), (c) +0.70 (clustered). Each figure shows a 10x10x10 structure. The yellow and black bonds indicate type A and type B linkers respectively....136
- Figure 5.4:** (a) Diffusivity and (b) percolation probability as a function of the bulky imidazolate mole fraction in lattices with fixed SRO. The rate catalogue is  $k=[1,0,0,0]$ .....141
- Figure 5.5:** Probability of randomly choosing a type 1 window in ZIF-A<sub>x</sub>-B<sub>100-x</sub> lattices with varying SRO. Composition threshold “ranges” from Figure 5.4b are labeled with the red dots and red solid lines. The bond percolation threshold for a bcc lattice with  $\alpha=0$  is 0.1803; this singular value is extrapolated on the contour plot (as indicated by the red dash line) to ZIF-A-B lattices exhibiting non-random SRO. ZIF-A-B materials falling on the left of the line allow adsorbate diffusion; ZIF-A-B materials falling on the right of the line inhibit adsorbate diffusion. For reference, there are 24 imidazolate linkers per unit cell and 24000 per 10x10x10 supercell. ....143
- Figure 5.6:** Diffusivities in ZIF-A-B with random SRO ( $\alpha=0$ ) for the three linker blocking scenarios.....144
- Figure 5.7:** Normalized hopping rates for the four window types using various analytical interpolation schemes. Parent window hopping rates are set to  $10^{-4}$  and  $10^0$  for visual clarity. ....146

- Figure 5.8:** Normalized diffusivities as a function of imidazolate linker mole fraction, interpolation scheme, and ratio of the parent window rates denoted by R1, R2, and R3. SRO  $\alpha$  is set to 0.0 (random ordering) for all curves. Uncertainties are smaller than the symbols.....147
- Figure 5.9:** Hybrid tree diagram and heat map demonstrating the influence of interpolation scheme, local ordering, ratio of the parent window rates, and imidazolate mole fraction on the deviation from predicted diffusivities in randomly ordered lattices. More details are given in the text.....149
- Figure 5.10:** Comparison of normalized experimental infinite dilution diffusivities at 308 K measured by Eum et al. to self-diffusivities predicted by the lattice-gas models with varying local ordering; **(a)** n-butane in ZIF-87-90<sub>93</sub>, **(b)** n-butane in ZIF-828-90<sub>72</sub>, **(c)** n-butane in ZIF-863-90<sub>37</sub>, **(d)** isobutane in ZIF-87-90<sub>93</sub>, **(e)** isobutane in ZIF-828-90<sub>72</sub>, **(f)** isobutane in ZIF-863-90<sub>37</sub>. The red checkerboard rectangle bounded by black dashed lines represents the region in which predicted diffusivities would be considered acceptable as discussed in the text. ....152
- Figure 6.1:** Representative binary mixed-linker ZIF truncated octahedron with random SRO ( $\alpha=0$ ): **(a)** ZIF-850-90<sub>50</sub>, **(b)** ZIF<sub>SOD</sub>-Im<sub>50</sub>-mIm<sub>50</sub> and **(c)** ZIF-740-90<sub>60</sub> in the SOD topology. ....160
- Figure 6.2:** Relative potential energy comparison between PBE-D3(BJ) and the intraZIF-FF for ZIF-850-90<sub>50</sub> (SRO  $\alpha=0$ ) from a 5250 ps BOMD trajectory at 700 K. ....163
- Figure 6.3:** **(a)** Free energy curves with the inset showing the transmission coefficient curves for methane and **(b)** corresponding rates through the four window types for methane in ZIF-8-90 materials exhibiting random local order ( $\alpha=0$ ) at 308 K. Open circles in are the composition-dependent hybrid rates while the black filled circles are the average hopping rates. ....166
- Figure 6.4:** Conventional MD and lattice-diffusion model (LDM) comparison for methane in ZIF-8<sub>x</sub>-90<sub>100-x</sub> at 308.15 K and the infinite dilution limit. MSD plots from the NPT-MD simulations are reported in Appendix E.....168
- Figure 6.5:** Simulated (filled circles) and experimental (open diamonds) self-diffusivities of methanol (magenta) and ethanol (black) in ZIF-8-90 at 313 K. Lines are guides for the eye. ....170
- Figure 6.6:** Simulated (filled circles) and experimental (open diamonds) self-diffusivities of water in ZIF-8-90 at 313 K. Red crosses indicate simulated self-diffusivities of water in the parent ZIFs from dcTST simulations. Lines are guides for the eye. Inset images show water clustering (red spheres) in ZIF-807-90<sub>93</sub> (left) and ZIF-875-90<sub>25</sub> (right). ....172

<b>Figure 6.7:</b> Comparison of predicted (upper panel) and experimental (lower panel) self-diffusivities of n-butane, 1-butanol, and isobutane in ZIF-8 <sub>x</sub> -90 <sub>100-x</sub> . The upper panel features experimentally measured n-butane and isobutane diffusivities by Zhang et al. and Eum et al. to indicate the experimental uncertainties that exist for these materials. Rates used in the lattice-diffusion model are reported in Appendix E (Figure E.2). .....	174
<b>Figure 6.8:</b> (a) Hopping rates of N <sub>2</sub> , methane, n-butane, isobutane, SF <sub>6</sub> , and benzene through the four window types in SALEM-2/ZIF-8 hybrids at 308 K, and (b) corresponding self-diffusion coefficients predicted through the lattice-diffusion model. ....	177
<b>Figure 6.9:</b> (a) Hopping rates of N <sub>2</sub> , methane, propane and n-butane through the four window types in ZIF-7-90 hybrids, and (b) corresponding self-diffusion coefficients predicted through the lattice-diffusion model for ZIF-7-90 structures with SRO $\alpha=0$ . Dashed lines represent the region where the probability of choosing a type one window drops from 52-44% for the “equal” LD model and from 40-25% for the “weighted” diffusion model. The percolation threshold (0.18 for body centered cubic lattice with SRO $\alpha=0$ ) is approached much more quickly with the “weighted” LD model. ....	181
<b>Figure A.1:</b> Free energy curves at infinite dilution and 308.15 K for a representative sample of adsorbates demonstrating a shifting TS location.....	191
<b>Figure A.2:</b> Potential and entropic contributions to the Helmholtz free energy barrier for small non-spherical adsorbates and hydrocarbons in flexible ZIF-8. ....	193
<b>Figure A.3:</b> Mean ZIF-8 window diameter as a function of molecular diameter. ....	199
<b>Figure A.4:</b> Adsorption isotherms of C1-C4 hydrocarbons in the rigid low-loading ZIF-8 structure at 308.15 K. Solid lines represent the GCMC results and the symbols (closed=paraffins and open=olefins) are taken from the experimental results of Zhang et al.....	201
<b>Figure A.5:</b> Difference in the grand potential between the high loading and low loading phases of ZIF-8 upon loading of C1-C4 hydrocarbons at 308.15 K.....	202
<b>Figure A.6:</b> Propane free energy curves as a function of loading. ....	204
<b>Figure A.7:</b> Propane transmission coefficient curves as a function of loading.....	205
<b>Figure A.8:</b> Hydrocarbon thermodynamic correction factors as a function of loading.....	205
<b>Figure A.9:</b> Short alkane and alkene transport diffusion coefficients as a function of molecules per cage in ZIF-8 at 35°C. ....	207

<b>Figure A.10:</b> Comparison of both experimental and simulated methane diffusivities as a function of loading in ZIF-8. We have also included two other simulation studies: NVT-MD calculations at 298 K by Pantatosaki et al. (transport diffusivities, solid blue circles) and NPT-MD calculations at 298 K by Zhang et al. (self-diffusivities, half-filled purple circles). .....	208
<b>Figure A.11:</b> Comparison of both experimental and simulated ethylene and ethane diffusivities as a function of loading in ZIF-8. ....	209
<b>Figure A.12:</b> Comparison of both experimental and simulated propylene and propane diffusivities as a function of loading in ZIF-8. ....	209
<b>Figure A.13:</b> Hydrocarbon sorption coefficients as a function of bulk pressure. ....	211
<b>Figure A.14:</b> Hydrocarbon fluxes through an idealized ZIF-8 membrane as a function of feed pressure with a transmembrane pressure drop equal to the feed pressure. ....	211
<b>Figure B.1:</b> (a) Morse potentials fit (solid black line) to potential energy scans (red dots) along the Zn-N bond. The harmonic potential with the spring constant from the Seminario method is shown for comparison (dashed blue line). The mean absolute error (MAE) of the Morse fit is also reported. (b) Relative coulombic energy for the Zn-N potential energy scans. ....	214
<b>Figure B.2:</b> Harmonic angle potential fit using the spring constant from the Seminario method (dashed blue line) and the direct PES fit (solid black line) to PES scans (red dots) of the C <sub>1,2</sub> -Zn-N angles. The mean absolute error of the PES fit is also reported. (b) Relative coulombic energy for the C <sub>1,2</sub> -Zn-N potential energy scans. ....	215
<b>Figure B.3:</b> (a) Harmonic angle potential fit using the spring constant from the Seminario method (dashed blue line) and the direct PES fit (solid black line) to PES scans (red dots) of the N-Zn-N angles. The mean absolute error of the PES fit is also reported. (b) Relative coulombic energy for the N-Zn-N potential energy scans. ....	215
<b>Figure B.4:</b> Relative energy comparisons between PBE and (a) the intraZIF-FF (black circles) including Fourier dihedrals from the potential energy fitting as well as (b) the AMBER-FF (orange crosses) for the low energy region (<20 kJ mol <sup>-1</sup> ). ....	216
<b>Figure B.5:</b> (a) Morse potentials fit (solid black line) to potential energy scans (red dots) along the Zn-N bond. The harmonic potential with the spring constant from the Seminario method is shown for comparison (dashed blue line). The mean absolute error (MAE) of the Morse fit is also reported. (b) Relative coulombic energy for the Zn-N potential energy scans. ....	219

<b>Figure B.6:</b> Relative energy comparisons between PBE and (a) the intraZIF-FF including Fourier dihedrals from the potential energy fitting and (b) the AMBER-FF using standard cosine proper dihedrals. The color code (black to blue/intraZIF and orange to green/AMBER) is designed to easily identify the low and high energy regions. ....	219
<b>Figure B.7:</b> (a) Morse potentials fit (solid black line) to potential energy scans (red dots) along the Zn-N bond. The harmonic potential with the spring constant from the Seminario method is shown for comparison (dashed blue line). The mean absolute error (MAE) of the Morse fit is also reported. (b) Relative coulombic energy for the Zn-N potential energy scans. ....	222
<b>Figure B.8:</b> Relative energy comparisons between PBE and (a) the intraZIF-FF including Fourier dihedrals from the potential energy fitting and (b) the AMBER-FF using standard cosine proper dihedrals. The color code (black to blue/intraZIF and orange to green/AMBER) is designed to easily identify the low and high energy regions. ....	223
<b>Figure B.9:</b> Cosine potential fit of the PBE energies from potential energy scans involving rotation of the aldehyde group around the C <sub>1</sub> -C <sub>4</sub> axis. ....	223
<b>Figure B.10:</b> (a) Morse potentials fit (solid black line) to potential energy scans (red dots) along the Zn-N bond. The harmonic potential with the spring constant from the Seminario method is shown for comparison (dashed blue line). The mean absolute error (MAE) of the Morse fit is also reported. (b) Relative coulombic energy for the Zn-N potential energy scans. ....	226
<b>Figure B.11:</b> Relative energy comparisons between PBE and (a) the intraZIF-FF including Fourier dihedrals from the potential energy fitting and (b) the AMBER-FF using standard cosine proper dihedrals. The color code (black to blue/intraZIF and orange to green/AMBER) is designed to easily identify the low and high energy regions. ....	227
<b>Figure B.12:</b> Potential energy scan along the C <sub>1</sub> -Zn-N and C <sub>2</sub> -Zn-N angles for the four clusters with the harmonic fit to the unfunctionalized imidazolate cluster scan (black line). ....	228
<b>Figure B.13:</b> Potential energy scan along the N-Zn-N angles for the four clusters with the harmonic fit to the unfunctionalized imidazolate cluster scan (black line). ....	228
<b>Figure B.14:</b> Charges on individual atoms in the Im cluster as compared to periodic charges. ....	232
<b>Figure B.15:</b> Charges on individual atoms in the BzIm cluster as compared to periodic charges. ....	233

<b>Figure B.16:</b> Charges on individual atoms in the mIm cluster as compared to periodic charges. ....	233
<b>Figure B.17:</b> Charges on individual atoms in the ImCA cluster as compared to periodic charges. ....	234
<b>Figure B.18:</b> Parity plots for (a) unit cell densities and (b) LCDs as predicted by PBE-D2 and the intraZIF (blue/black) and AMBER (orange/green) force fields. There are 27 Im polymorphs as well as the SALEM-2 structure (closed circles) and 25 mIm polymorphs (open circles). ....	240
<b>Figure B.19:</b> Analysis of N-Zn-N angles in the 27 Im polymorphs and the SALEM-2 (labeled as taku_h). Error bars on the average angle (black solid circles) represent the standard deviation of all the N-Zn-N angles in the unit cell. ....	241
<b>Figure B.20:</b> Examples of tetrahedral and near square planar Zn coordination environments for the Im-sod and Im-uoc polymorphs. ....	241
<b>Figure B.21:</b> ZIF-8 relative potential energies as predicted by the AMBER-FF and intraZIF-FF in reference to PBE-D3(BJ) relative energies from fully periodic BOMD simulations at 700 K. ....	248
<b>Figure B.22:</b> ZIF-90 relative potential energies as predicted by the AMBER-FF and intraZIF-FF in reference to PBE-D3(BJ) relative energies from fully periodic BOMD simulations at 700 K. ....	249
<b>Figure B.23:</b> Histograms with fitted lognormal distributions of (a) Zn-N bond lengths and (b) N-Zn-N angles in ZIF-90 at temperatures of 308.15, 500, and 700 K and a pressure of 1.0 bar. $\mu$ ( $\mu$ ), $\sigma$ ( $\sigma$ ) are the mean and standard deviation of the lognormal distribution and n is the number of samples. ....	250
<b>Figure B.24:</b> ZIF-7 relative potential energies as predicted by the AMBER-FF and intraZIF-FF in reference to PBE-D3(BJ) relative energies from fully periodic BOMD simulations at 700 K. ....	251
<b>Figure B.25:</b> Molecular weight as a function of molecular diameter for the thirty adsorbates included in this study. ....	253
<b>Figure B.26:</b> Comparisons of simulated and experimental self-diffusivities in ZIF-8 at infinite dilution and at the temperatures listed in the legend. The experimental data is taken from Zhang et al. (open red circles), Eum et al. (open black circles), and Zhang et al. (open blue circles). ....	259
<b>Figure B.27:</b> Gibbs free energy barriers of benzene and p-xylene as a function of temperature. Lines are linear fits to decouple the entropic and enthalpic contributions to diffusion. ....	260

<b>Figure B.28:</b> Simulated XRD patterns for the three stable metaphases of ZIF-7 as reported by Zhao et al. along with routes of formation depending on loading, temperature, and degradation.....	261
<b>Figure B.29:</b> Total and directional MSDs for H <sub>2</sub> diffusion in (a) flexible and (b) rigid ZIF-7-I at a loading of three adsorbates per unit cell, 1.01 bar, and 308 K.....	262
<b>Figure B.30:</b> MSDs for (a) methane and (b) n-butane in flexible ZIF-7-I at a loading of three adsorbates per unit cell, 1.01 bar, and 308 K.....	263
<b>Figure B.31:</b> XY projection of the H <sub>2</sub> trajectories in the flexible ZIF-7-I structure. The XY-plane of the expanded ZIF-7 unit cell was divided into a 250 by 250 rectangular grid. Each grid point was sampled every 500 fs over a 10 ns trajectory, and the intensity of each sampled grid point was increased by the number of H <sub>2</sub> molecules whose XY centroid was within 0.5 Å (calculated using Euclidean Norm). The blue line shows the XY trajectory of a single H <sub>2</sub> sampled every 5 ps over a 750 ps trajectory. The Zn-linker overlay (black lines) on the graph is taken from the empty expanded rigid structure.....	264
<b>Figure B.32:</b> XY projection of the CO <sub>2</sub> trajectories in the flexible ZIF-7-I structure. The blue line shows the XY trajectory of a single CO <sub>2</sub> sampled every 5 ps over a 1000 ps trajectory. All other plot features are the same as shown in Figure B.31.....	264
<b>Figure C.1:</b> Measured and simulated XRD patterns of hybrid ZIF-8 <sub>x</sub> -90 <sub>100-x</sub> materials. ....	267
<b>Figure C.2:</b> Simulated ZIF-8 <sub>50</sub> -90 <sub>50</sub> XRD patterns as a function of SRO with a 3x3x3 supercell. ....	267
<b>Figure C.3:</b> SEM image of ZIF-8 crystals. ....	268
<b>Figure C.4:</b> SEM image of a ZIF-90 crystal. ....	268
<b>Figure C.5:</b> SEM image of ZIF-8 <sub>50</sub> -90 <sub>50</sub> crystals.....	269
<b>Figure C.6:</b> Liquid NMR spectrum for a hybrid ZIF-8 <sub>x</sub> -90 <sub>100-x</sub> material. Peaks are labeled according to each hydrogen type. Other peaks are from the solvent. ....	270
<b>Figure C.7:</b> Schematic of the positions of the protons in the ZIF-8 crystal structure (top). The methyl protons are shown in red, and the imidazole protons are shown in white. <sup>1</sup> H spin diffusion NMR curve for ZIF-8 (bottom left) and ZIF-90 (bottom right) as well as predicted curves using the lamellar morphology for different spin diffusion coefficients. ....	271



<b>Figure C.8:</b> Representative distances used for calculation of intramolecular spin diffusion domains in ZIF-8 and ZIF-90. ....	272
<b>Figure C.9:</b> Single pulse $^1\text{H}$ excitation NMR spectra for ZIF-8-90 materials. ....	272
<b>Figure C.10:</b> Second moment of the NMR spectra calculated as a function of linker composition (left) and predicted spin diffusion coefficient as a geometric average of pure components. ....	273
<b>Figure C.11:</b> T2 curves of ZIF-8 (left) and ZIF-90 (right) using Hahn Echo and CPMG (with rotor synchronization and without rotor synchronization). ....	274
<b>Figure C.12:</b> Pure ZIF-90 fitting results, with model fits given by the solid black lines and experimental NMR data in the open red circles. ....	276
<b>Figure C.13:</b> Relative Mean absolute error (MAE) as a function of SRO for five ZIF-8-90 hybrid materials. ....	277
<b>Figure D.1:</b> Example MSD of a lattice-gas in the parent material with a linear fit. ....	279
<b>Figure D.2:</b> Example MSDs of a lattice-gas in both percolating and non-percolating clusters with characteristic length scales represented by gold lines. ....	280
<b>Figure D.3:</b> (a) Example of window blocking from a bulky imidazolate linker. Diffusivities as a function of composition at fixed SRO for (b) window blocking requiring three bulky linkers, (c) window blocking requiring two linkers, and (d) window blocking requiring only one bulky linker. ....	282
<b>Figure D.4:</b> Normalized self-diffusivities as a function of SRO and the mole fraction of linker type A where (a) utilizes a rate convention of $k=[1,0,0,1]$ to denote blocking of the hybrid windows, (b) utilizes a rate convention of $k=[0,1,1,0]$ to denote blocking of the parent windows, (c) utilizes a rate convection of $k=[1,10^{-2},10^{-2},1]$ to denote reduced diffusion through hybrid windows, and (d) utilizes a rate convection of $k=[10^{-2},1,1,10^{-2}]$ to denote reduced diffusion through parent windows. ....	284
<b>Figure E.1:</b> MSDs for $\text{CH}_4$ in ZIF-8-90 where the square of the cage to cage distance is indicated by the solid black line. These MSDs were calculated at a loading of two methane molecules per unit cell, 308 K, and 1.01 bar. ....	288
<b>Figure E.2:</b> Hopping rates of n-butane, 1-butanol, and isobutane through ZIF-8-90 window types at 308 K and 1.01 bar. ....	289
<b>Figure E.3:</b> Ideal n-butane/isobutane diffusion selectivity as a function of mIm linker in SALEM-2/ZIF-8 hybrids with a SRO $\alpha=0$ (red circles) at 308 K and 1.01 bar. The ideal diffusion selectivities measured by Zhang and Koros at the same conditions are shown as solid black circles. Lines are guides for the eye. ....	290

<b>Figure E.4:</b> Predicted ideal diffusion selectivities of combinations of benzene, isobutane, and SF <sub>6</sub> in SALEM-2/ZIF-8 hybrids at 308 K and 1.01 bar. The dashed line indicates a selectivity of 1. Lines are guides for the eye. ....	290
<b>Figure G.1:</b> Copyright permission for Chapter 2 content. ....	294
<b>Figure G.2:</b> Copyright permission for Chapter 4 content. ....	295

## SUMMARY

Industrial separations of light gases and hydrocarbons are currently performed with well-established but energy and capital intensive distillation. Within the last decade, certain research advances have energy suppliers focused on novel separation techniques using metal-organic frameworks (MOFs) as a possible replacement for traditional distillation. Experimental groups at Georgia Tech have developed techniques for creating thin-film and mixed-matrix MOF membranes that would perform these commodity fuel and reagent separations at ambient temperature and moderate pressures. Zeolitic imidazolate frameworks (ZIFs), a family of MOFs, were shown experimentally to act as excellent molecular sieves for C1-C4 hydrocarbons and other light gases. They also have superior binding properties to polymer supports and are more easily synthesized than zeolites, enhancing large-scale manufacturability. Understanding diffusion properties of light gases and hydrocarbons in ZIFs was needed in determining which ZIFs have the most industrial promise, providing direction for future experimental efforts, and also to contribute to fundamental knowledge of diffusion processes.

In this thesis, I, in collaboration with many talented researchers, established a suite of computational methods that are suited to tackling several significant challenges facing the research community studying ZIFs. ZIFs are flexible materials and this inherent material property required the use of fully flexible molecular dynamics calculations to explain hydrocarbon-ZIF framework interactions during the diffusion process. These computational methods were extended to predict loading-dependent, single-component transport diffusion coefficients of hydrocarbons and membrane permeabilities. Because there was no previous standard flexible force field for ZIF frameworks, a classical force field was developed based on Density Functional Theory (DFT) calculations capable of accurately predicting small molecule diffusivities. In a

joint experimental-computational collaboration, I aided in the development of a protocol for determining the local ordering of the organic linkers in binary mixed-linker ZIFs. This structural knowledge of mixed-linker ZIFs on the unit cell level prompted the creation of a lattice-diffusion model, which was used to qualitatively explain the impact of local ordering on diffusion as well as provide quantitative predictions of diffusion through binary mixed-linker ZIFs. This work enhances scientific knowledge on molecular transport in single and mixed-linker ZIFs and provides energy suppliers with the tools to engineer new separation alternatives of light gases.

# **CHAPTER 1**

## **INTRODUCTION**

### **1.1 Energy Efficient Separations using Nanoporous Materials**

Energy companies are interested in alternative strategies that would eliminate the need for energy intensive and thus expensive distillation separations for molecules with similar relative volatilities (i.e. boiling points). These alternatives would help lower overall project life costs through lower initial capital and operating costs for commodity products such as C3 and C4 hydrocarbons. Light key hydrocarbons, especially the olefins with a reactive double bond, are industrially relevant for use as fuels or the starting reagents for thermoplastic polymers and resins.<sup>1</sup> Separations of C3 and C4 paraffin and olefin mixtures currently utilize cryogenic distillation columns<sup>2</sup> of which energy costs dictate 85% of operating costs<sup>3-5</sup>. Operating costs of distillation columns do depend, however, on the highly volatile price of natural gas.<sup>6</sup>

Alternatives to replace distillation columns fall under two categories which seek to use thermodynamic<sup>7</sup> and kinetic properties of a particular nanoporous adsorbent (e.g. zeolite, activated carbon) system. Separations driven by equilibrium thermodynamics include pressure or temperature swing adsorption processes<sup>5</sup>. These processes require energy input with compressors for high pressures and a regeneration procedure that is dependent on, and thus limited by, the characteristic heats of adsorption. Kinetic separations using mixed matrix membranes<sup>8,9</sup> and thin film membranes<sup>10</sup> can continuously operate at near ambient temperature and pressures without these limitations<sup>11,12</sup>. Pure nanoporous adsorbent membranes on support materials such as hollow fiber membranes provide an extremely attractive option for separations since they require no significant energy input; this attractiveness is lessened if the retentate and

permeate streams require significant compression<sup>13</sup>. These membranes are relatively new devices that have been developed by Andrew Brown and co-workers at the Georgia Institute of Technology in Atlanta, GA<sup>11</sup>. A schematic of a hollow fiber membrane module and a support thin-film nanoporous membrane is shown in Figure 1.1. Within the last decade, advances have been made in four key areas regarding the development of these membranes that make them perfect candidates for large industrial separations: **(1)** development of high-efficiency modules, **(2)** creation of advanced materials, **(3)** control of microscopic transport phenomena, and **(4)** introduction of scalable manufacturing methods.<sup>14,15</sup> **This thesis seeks to understand how to control adsorbate transport through nanoporous membranes and to then select or engineer new nanoporous materials better suited for molecular sieving (i.e. molecular straining) using atomistic simulations.**

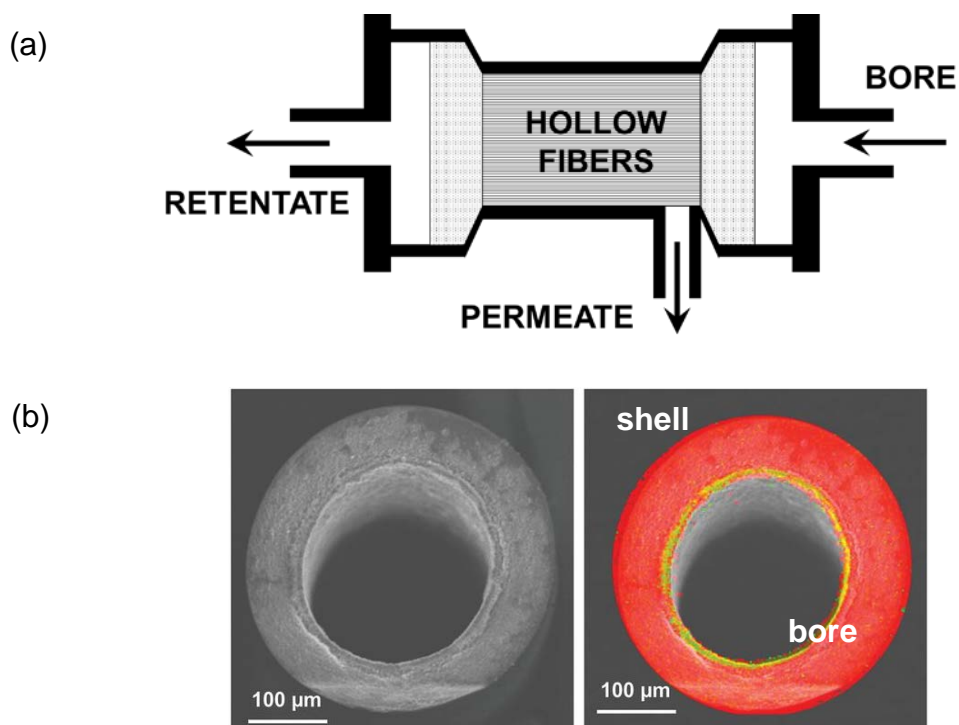


**Figure 1.1 (a)** Schematic of a hollow fiber membrane module and **(b)** a cross-sectional SEM imaged of a supported thin-film nanoporous membrane (yellow ring on the bore side) as adapted from Brown et al.<sup>16</sup>

## 1.2 Nanoporous Material of Interest: Metal-Organic Frameworks

Metal-organic frameworks (MOFs) are a relatively new class of nanoporous materials which are formed through coordination bonds between metal centers and organic linkers<sup>17</sup>. These connections form predictable molecular scaffolds with pores of topologies and dimensions that lend themselves for study by molecular simulations.<sup>18-21</sup> MOFs have many proposed uses such as gas storage<sup>22</sup>, catalysis<sup>23</sup>, chemical sensing<sup>24,25</sup>, drug delivery<sup>26</sup>, and chemical separations<sup>27</sup> all of which are discussed extensively in thorough review articles<sup>28,29</sup>. Many research groups are able to tailor their MOF synthesis to include metal centers or organic functional groups that can enhance, for example, the storage capacity or separation ability. Over 37,000 MOF structures have been reported to date in the Cambridge Structural Database<sup>30</sup> and matching MOFs for use in specific separations is a daunting task. To add another layer of chemical diversity in the MOF family, the Yaghi group has reported making multivariate MOFs that include different proportions of organic linkers<sup>31</sup>. These are beneficial since it is possible to exhibit “hybrid” performance stemming from the properties of the parent materials. Figure 1.2 features several common MOF materials studied by various research groups, demonstrating the topological and chemical diversity that MOFs offer.

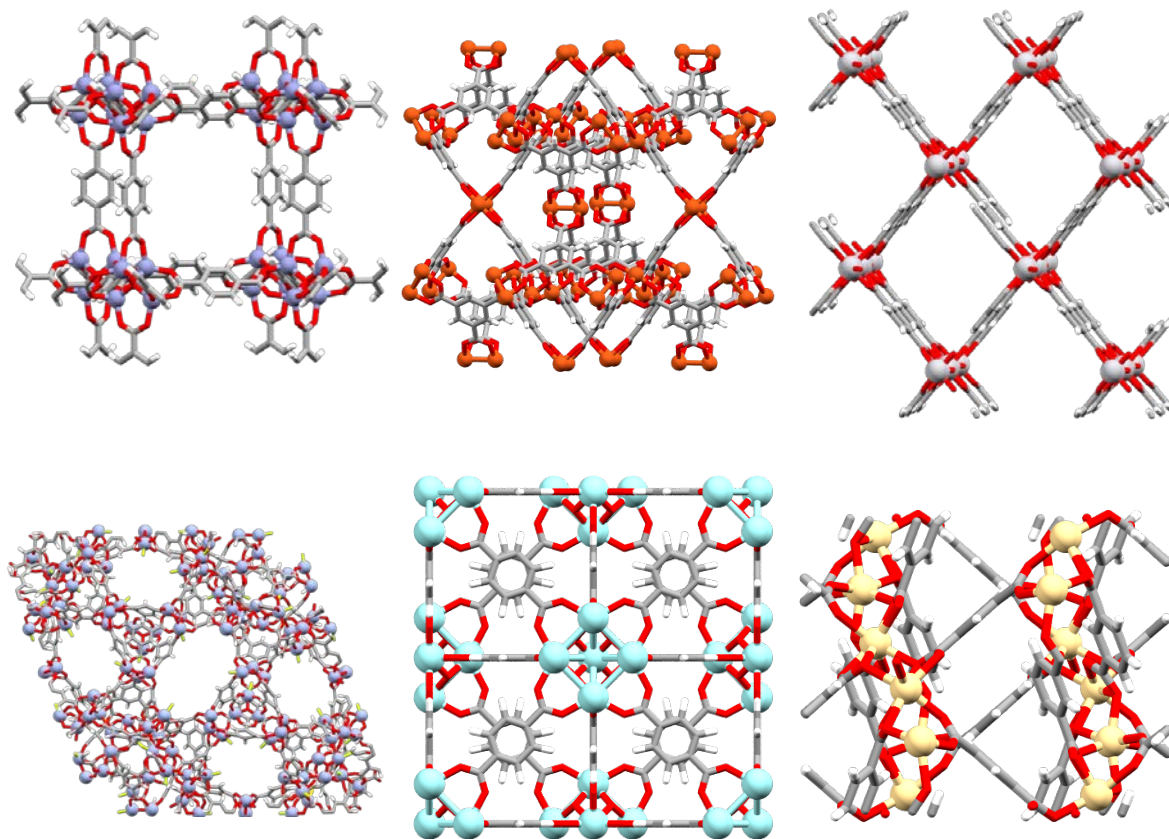


**Figure 1.2** Several representative MOFs: (a) IRMOF-1, (b) Cu-BTC, (c) MIL-47, (d) MIL-100, (e) UiO-66, and (f) MOF-72.

However, not all MOFs are suitable for applications requiring molecular sieving. MOFs exhibiting 2D/3D topologies, small pore limiting diameters, and large cavities have the most potential for molecular sieving based applications.<sup>32</sup> Small pore diameters allow for molecular sieving of molecules with different kinetic diameters and large cavities allow for mixing of species within the cavities, reducing molecule on molecule drag.<sup>33</sup> Open structure MOFs with large channels are characterized by liquid-like diffusion with Knudsen selectivity<sup>33</sup> and are not useful for molecular sieving.

Even with much dedicated research, MOFs are not currently used in any industrial separation.<sup>34</sup> To be truly competitive, MOFs need to perform significantly better than other nanoporous materials, especially zeolites, currently used in industry. One major advantage of focusing on developing MOF membranes is that we do not have to compete



with pre-existing membrane technologies; there is to-date only one zeolite membrane used in an industrial application.<sup>35</sup> Polymer hollow fiber membrane and mixed matrix membrane development has advanced in the last decade but pure MOF thin film hollow fiber membranes have the possibility of attaining even higher product stream purities.<sup>36</sup> My experimental collaborators in Dr. Sankar Nair's laboratory at the Georgia Institute of Technology (Atlanta, GA) have directed research towards creating zeolitic imidazolate frameworks (ZIFs) thin films since they have many of the properties needed to perform molecule sieving.<sup>37</sup> The research groups of Dr. Bill Koros and Dr. Ryan Lively at the Georgia Institute of Technology also seek to use ZIFs in mixed-matrix membrane applications, where ZIF crystals are doped into a polymer matrix. In addition to my experimental collaborators, the separation potential of ZIFs for olefin and paraffin mixtures has been demonstrated by several other research groups. These findings are summarized Table 1.1 below.

**Table 1.1.** Extant examples of kinetic separations of light olefins and paraffins using supported thin films.

MOF [ZIF]	Adsorbates	Measurement Techniques	Loading [bar]/Temperature [K]	Selectivity
ZIF-8 <sup>38</sup>	Propylene/Propane	Gas permeation	1.0 <sup>SC</sup> /298	59 <sup>ID</sup>
ZIF-8 <sup>39</sup>	Propylene/Propane	Wicke-Kallenbach	1.0 <sup>BM</sup> /303	~32 <sup>BM</sup>
ZIF-8 <sup>36</sup>	Propylene/Propane	Wicke-Kallenbach	1.03 <sup>BM</sup> /298	~12 <sup>BM</sup>
ZIF-90 <sup>11</sup>	Hexane/Benzene	Pervaporation	1.0/295	~11 <sup>ID</sup>
ZIF-8 <sup>40</sup>	Ethene/Propane	Wicke-Kallenbach	1.0 <sup>BM</sup> /296	167 <sup>BM</sup>

*ID=ideal, SC=single component, BM=binary mixture*

### 1.3 Zeolitic Imidazolate Frameworks

Zeolitic imidazolate frameworks (ZIFs) are a subclass of MOFs formed through the coordination of Zn or Co metal centers and various functionalized imidazolate linkers.<sup>41</sup> Figure 1.3 below adapted from Park et al. shows the amazing topological and chemical diversity offered by ZIF materials. ZIFs can also be synthesized with combinations of imidazole linkers, and it is possible to alternate linkers to tailor hydrophobicity and window size while keeping the same topology.<sup>42</sup> The imidazole linkers can have a variety of functional groups such as methyl groups for ZIF-8, aldehyde groups for ZIF-90, and benzimidazole linkers for ZIF-7. Thompson et al. and Rashidi et al. demonstrated that hybrids of  $\text{ZIF-8}_x\text{90}_{100-x}$ ,  $\text{ZIF-7}_x\text{8}_{100-x}$  and  $\text{ZIF-7}_x\text{90}_{100-x}$  could be experimentally synthesized.<sup>42,43</sup> Most importantly, experimental collaborators in Dr. Sankar Nair's laboratory have demonstrated that altering the fraction of certain linker types can enhance permeation selectivities of certain alkanes; to model this behavior requires knowledge of the atomic structure.<sup>30,44-46</sup> This thesis elucidates a method for quantifying the local ordering imidazolate in binary mixed-linker ZIFs, crucial input for atomistic models. Because there are so many ZIF materials containing a single imidazolate linker or combinations of imidazolate linkers, computational methods must be developed to quickly and accurately predict which single-linker or mixed-linker ZIFs would be applicable for gas separations.

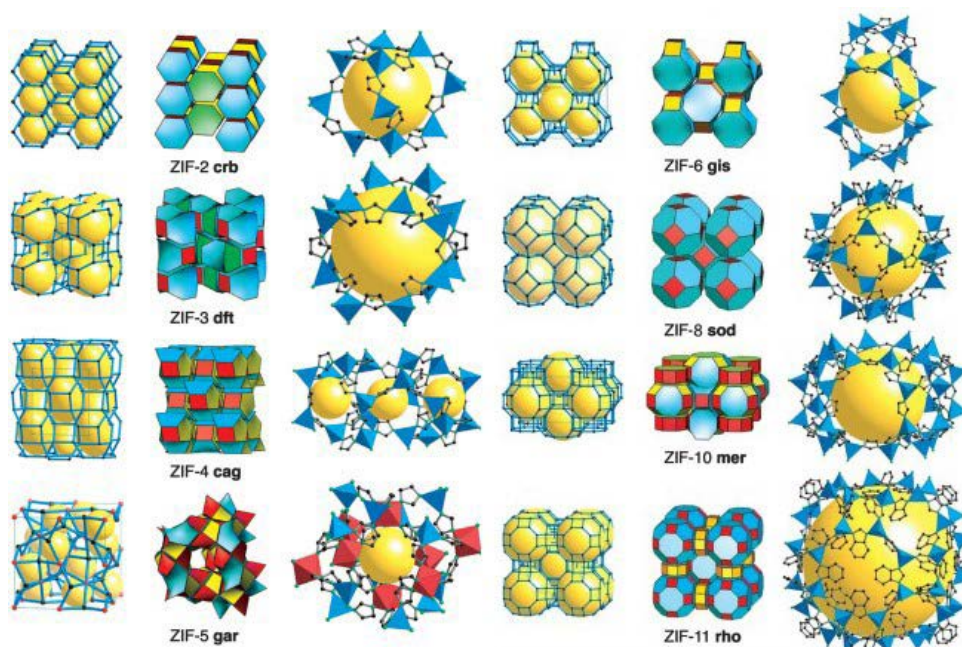


**Figure 1.3** Structural and chemical diversity of ZIF materials as adapted from Park et al.<sup>41</sup>

One feature of ZIF materials makes computational studies into their molecular sieving capabilities challenging: *structural flexibility*. Structural flexibility of any nanoporous system creates challenges for simulation since, at the time work on this thesis began, modeling techniques were just being implemented to accurately describe this flexibility and predict its impact on adsorption and diffusion properties of light gases. Modeling ZIF flexibility requires that classical simulations have the ability to accurately describe flexibility on the unit cell level through classical potentials (i.e. force fields). Coudert summarizes the different classes of flexibility encountered in MOF materials as shown in Figure 1.4 below: several of these flexibility classifications are encountered in ZIFs.

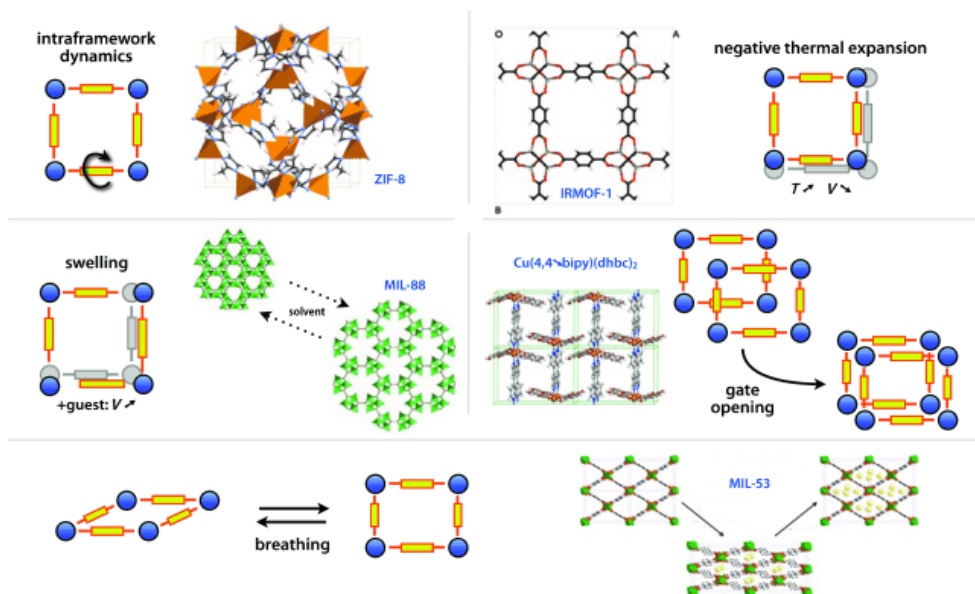


**Figure 1.4** Classes of MOF framework flexibility; figure was adapted from Coudert et al.<sup>47</sup>

### 1.3.1 ZIF Kinetic Flexibility

Kinetic flexibility is defined as the ability of the imidazolate linkers to twist and bend as well as the inherent modes of vibration of the ZIF structure. Many geometric screening studies have identified 2D and 3D ZIFs exhibiting small windows or pore limiting diameters (PLDs) and large cavities. These types of ZIFs, with small openings dictating the passage of molecular species<sup>48</sup>, provide the most suitable avenue for the molecular sieving of adsorbates, but molecular passage through these small openings is largely mediated by imidazolate linker flexibility<sup>49</sup>. Zeolites, MOF predecessors, have largely been modeled as rigid frameworks (i.e. framework atoms are not allowed to move during the simulation) but it is known that molecular transport is significantly affected by kinetic flexibility in zeolites with small windows.<sup>50,51</sup> Several examples of the importance of kinetic flexibility are demonstrated through the surprising separation properties of ZIFs. A “gate opening effect” was experimentally discovered that describes the turning of the benzimidazole linkers of ZIF-7 upon exposure to C2 and C3 olefins and paraffins<sup>52</sup>. This rotational motion allows for the preferred adsorption of paraffins over olefins; this finding can also be attributed to the stronger interaction the paraffin has with

ZIF-7. ZIF-8 has promising adsorption separation characteristics for butanol separation from aqueous mixtures<sup>53</sup> which is made possible through the flexibility of the ZIF-8 methyl-2-imidazolate linkers. It may be possible to utilize this selectivity in membrane pervaporation setups.<sup>54,55</sup> Koros and coworkers demonstrated that ZIF-8 can adsorb hydrocarbons that are larger than the experimental aperture size.<sup>56</sup> Pioneering computational work by Haldoupis et al. showed that including the framework flexibility of ZIF-8 produced orders of magnitude improvement in comparisons of predicted and simulated diffusion coefficients of small molecules.<sup>57</sup> This was further validated through molecular dynamic simulations and transition state theory by Zhu and coworkers for six small molecules<sup>58</sup>. Unfortunately, these computational methods were not easily extended to study the diffusion of larger molecules such as n-butane.

Figure 1.5a shows a singular octahedron cage of ZIF-8 featuring 6 and 4 member rings; this structure was 3D printed by Ross Verploegh and funded by Phillips 66. Figure 1.5b below demonstrates the interesting behavior of ZIF-8 as compared to industrially used zeolites 4A and 5A whose names correspond to their window dimensions. ZIF-8 has an experimentally determined window diameter of 3.42 Å but allows molecules with molecular diameters larger than 7.0 Å to diffuse through its windows.<sup>59</sup> This thesis is focused on including the structural flexibility, which allows this type of diffusion behavior, into computational studies of diffusion.

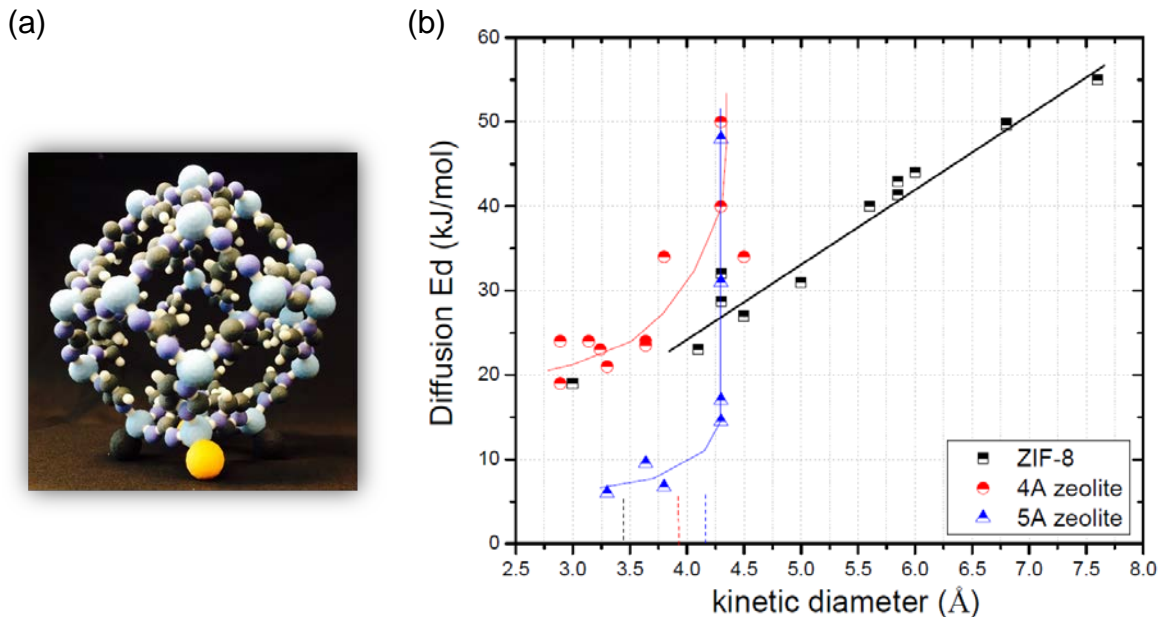


**Figure 1.5** (a) 3D-printed ZIF-8 structure (Zn=light blue, N=dark blue, C=black, H=off-white); molecules diffuse through the 6 MR windows. (b) Activation energy of diffusion as a function of molecular diameter for zeolites 4A and 5A and ZIF-8; figure adapted from Zhang et al.<sup>60</sup>

### 1.3.2 ZIF Thermodynamic Flexibility

Thermodynamic flexibility is characterized as a metastable phase transformation of the MOF to a new configuration under the presence of a particular adsorbate or temperature increase. This transformation must be known when (1) examining a large design space for optimal operating conditions of a particular kinetic separation as well as for (2) developing processes that utilize cyclic operating conditions between which the MOF changes structural phases repeatedly. There are several notable examples of thermodynamic flexibility. ZIF-7 has been shown to expand as adsorbates fill the pores of the structure<sup>4</sup>. This particular behavior results from the nature of the benzimidazole linker positions, which cause the framework to become more dense (shrink) without the presence of adsorbates. With the increased adsorbate pressure, the structure assumes the more favorable “inflated” conformation, which is evident through the step-isotherms. Titus and Farrusseng discussed the thermodynamics of the ZIF-7 transition upon

adsorption of carbon dioxide thus demonstrating why this breathing phenomena is favorable.<sup>61</sup> ZIF-8 has been shown to undergo reversible transitions from a low-loading (LL) to a high-loading (HL) structure through high pressure diamond anvil experiments as well as nitrogen adsorption at 77 K.<sup>62</sup> This transition is characterized by a reorientation of the methyl-imidazole linkers leading to an increase in accessible pore volume as well as the pore limiting diameter; the I43m space-group symmetry is maintained during this transition<sup>62</sup>. Ania and coworkers demonstrated that this effect also happens for oxygen, nitrogen, and carbon monoxide at cryogenic temperatures<sup>63</sup>. Coudert et al. developed the osmotic framework adsorption solution theory (OFAST), which can be used to study guest-induced thermodynamics phase changes of MOF structures such as the MIL-53 series.<sup>64,65</sup> In terms of atomistic simulation progress, Salles et al. applied a bonded FF to MIL-53(Cr) that was capable of reproducing this material's narrow pore (NP) and large pore (LP) structures.<sup>66</sup> In this thesis, we have not focused on modeling thermodynamic flexibility, but have addressed its existence appropriately when examining certain ZIF materials.

## **1.4 Intuitive and Heuristic Methods for MOF Screening and Selections for Membrane Applications: The Limitations**

First and foremost, the usage of a ZIF in membrane separations requires that it produces a high selectivity and high permeability, overcoming the Robeson upper bound of pure polymeric membranes.<sup>67</sup> Both thermodynamic (i.e. adsorption) and kinetic (i.e. transport) information is needed for the selection of an appropriate MOF in a membrane application.<sup>13</sup> A first pass screening procedure using computational methods can identify possible candidate MOFs. MOF atomic structures can be taken from the Cambridge Structural Database,<sup>68</sup> but some structures have disordered atoms or residual solvent. The computation-ready, experimental (CoRE) MOF database provides over 4700 already

synthesized MOF structures that are immediately ready for molecular simulations.<sup>69</sup> To find suitable MOFs that may not have been synthesized, Wilmer et al. demonstrated a computational approach to create hypothetical MOF materials by combining metals and organic linkers.<sup>70</sup>

Geometric criteria such as the molecular diameter of the adsorbates as well as the diameter of the channels and cavities within MOFs can identify candidate MOFs based on size exclusion of one adsorbate over another. Haldoupis et al. described how to calculate the pore limiting diameter (PLD), the largest cavity diameter (LCD), and the global cavity diameter (GCD) using a grid based method as seen in Figure 1.6.<sup>71</sup> Zeo++, a free software package, calculates similar quantities based on Voronoi decomposition.<sup>72</sup> Haldoupis et al.<sup>57</sup>, Awati et al.<sup>73</sup>, and Camp et al.<sup>74</sup> established that screening procedures could include flexibility of windows of ZIFs, zeolites, and porous organic cage crystals respectively. These methods, however, do not account for the interactions of the adsorbates with the window regions of nanoporous materials and therefore incorrectly predict diffusion of large adsorbates.<sup>74</sup>

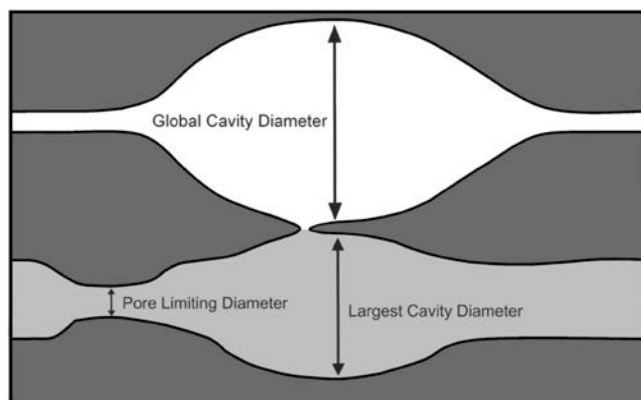


**Figure 1.6** Screening MOFs for molecular sieving applications based on geometric characteristics such as the global cavity diameter, largest cavity diameter, and the pore limiting diameter under the rigid framework assumption. Figure adapted from Haldoupis et al.<sup>59</sup>



To heuristically assess the adsorption selectivity of MOFs, the chemical nature of the organic linkers can provide useful information *a priori*. For example, functional groups that can hydrogen bond with guest molecules can increase the affinity for water or alcohol molecules by providing a significant number of favorable adsorption sites.<sup>75</sup> Quantum chemistry methods have been utilized to measure the binding energies of adsorbates such as H<sub>2</sub>O, NH<sub>3</sub>, and CO<sub>2</sub> with sets of functionalized organic linkers.<sup>76,77</sup> Adsorption selectivity in the low pressure regime can also be determined as the ratio of Henry's coefficients derived from computationally efficient Widom particle insertion simulations using generic force fields (e.g. Universal Force Field).<sup>78</sup> Experimentally, Wollmann et al. have demonstrated the use of an optical detector of heats of adsorption to analyze the porosity of materials with speed and accuracy for high-throughput screening.<sup>79</sup> At this stage of the screening process, stability of the MOF materials under process conditions and impact of structural flexibility on adsorption and diffusion properties are largely ignored.

## 1.5 Overview of Hierarchical Atomistic Simulations and Complementary

### Experimental Methods for MOF Selection

Once several candidate MOF materials are chosen from the first screening pass, more detailed atomistic simulations as well as experiments can be performed. Steady state fluxes ( $J$ ) of an  $n$ -component mixture can be calculated using Fick's law:

$$(J) = -[D_T(c)] \cdot (\nabla c) \quad (1.1)$$

where the gradient of the concentration is based on the feed and permeate gas pressures in the membrane and the transport diffusivities are a function of loading. The next step of the MOF screening process is to simulate adsorption and transport properties as well as

compare to experimental results. For details on the specifics of the classical simulation methods mentioned in the next three sections, readers are referred to the book by Frenkel and Smit.<sup>80</sup>

### 1.5.1 Predicting and Measuring Adsorption: Tools and Challenges

Single component isotherms and heats of adsorption can be simulated using Grand Canonical Monte Carlo (GCMC) or Gibbs Ensemble Monte Carlo (GEMC) using classical force fields.<sup>81</sup> Atomistic simulations can be used to study multicomponent adsorption but the number of simulations required increases substantially if a significant range of bulk gas compositions is examined. Mixing theories utilize single component isotherms fit to a variety of mathematical functions and generate multicomponent isotherms. Ideal adsorbed solution theory (IAST)<sup>82</sup> is a commonly used mixing theory to generate binary isotherms, but it is not rigorously applicable for adsorbents that are energetically heterogeneous to one of the adsorbed species.<sup>83</sup> Classical adsorption simulations such as Grand Canonical Monte Carlo (GCMC) are currently hindered in accuracy by a lack of transferable force fields for adsorbate-MOF pairs<sup>84</sup> and many research groups are focused on addressing this problem.<sup>85</sup> Furthermore, kinetic flexibility of the MOF frameworks has been determined to significantly influence their adsorption properties; this greatly minimizes the predictive capabilities of GCMC simulations using the rigid framework assumption.<sup>86-88</sup> The loading of adsorbates into a MOF can also induce a metastable phase change as previously mentioned. The osmotic framework adsorbed solution theory (OFAST) rationalizes the thermodynamics of loading-induced metastable MOF phase changes, but the MOF phases need to be known for OFAST to be coupled with GCMC simulations.<sup>89</sup> Very few MOF classical force fields can predict MOF phase changes *a priori*.<sup>90,91</sup>

Experimentally, adsorption of guest molecules in MOFs can be measured by a variety of techniques.<sup>92</sup> The most commonly used methods are gravimetric, volumetric or breakthrough experiments. Other techniques including spectroscopic techniques (infra-red (IR), X-ray diffraction (XRD) and synchrotron radiation (SR)), chromatography, and calorimetry can be combined with adsorption experiments to gather information about adsorbent-adsorbate interactions, orientations, structural transitions, and specific adsorption sites.<sup>93-95</sup> These experimental techniques are more complicated and time-consuming; hence not always suitable for screening purposes as opposed to computational studies.

### **1.5.2 Predicting and Measuring Diffusion: Tools and Challenges**

Single component self- and collective (corrected) diffusivities as a function of loading can be simulated using equilibrium molecular dynamics (EMD).<sup>96</sup> Self- and collective diffusion coefficients can also be calculated using transport hopping rates from transition state theory (TST) along with direct analytical expressions or kinetic Monte Carlo (KMC) simulations.<sup>97</sup> Collective diffusivities are related to the transport diffusivities in Equation 1.1 above through Darken's equation.<sup>98</sup> For ZIFs with cage-type architectures allowing for large Maxwell-Stefan self-exchange diffusivities, it is possible to equate the self- and collective diffusivities as shown experimentally in Figure 1.7 for ethane diffusion in ZIF-8.

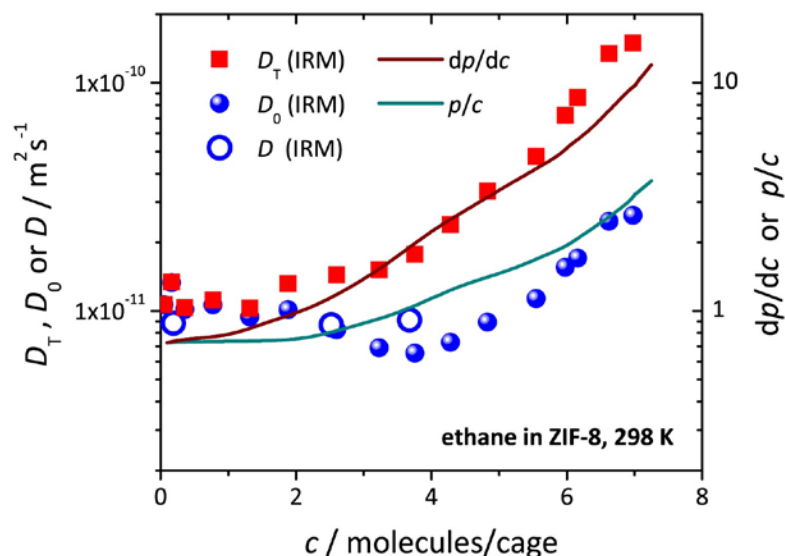


**Figure 1.7** Loading dependent diffusion of ethane through ZIF-8 where solid squares represent the transport diffusivities, closed blue circles represent the corrected diffusivities, and the open blue circles the self-diffusivities measured with IR microscopy; figure adapted from Chemlik et al.<sup>99</sup>

For multicomponent diffusion, EMD can be directly used to predict diffusion or mixing theories similar to those used for multicomponent adsorption can be applied. One mixing theory, the Skoulidas, Sholl, Krishna (SSK) method, can be used to obtain the loading and composition dependent matrix of binary diffusion coefficients from loading-dependent single-component self- and corrected diffusivities along with binary isotherms.<sup>100</sup> Simulations predicting diffusion should also eventually account for point defects (e.g. missing linkers), extended defects (e.g. stacking faults), or surface barriers.<sup>101,102</sup> Atomistic simulations of diffusion through MOFs have also primarily treated the MOF as a rigid entity for computational cost savings. Recent studies, however, have demonstrated that for tight-fitting (small) adsorbates, flexibility of the MOF framework is crucial (less important) for accurately predicting self-diffusivities.<sup>97,103</sup>

Transient curves from adsorption experiments can be fitted to mathematical models to obtain transport as well as the Maxwell-Stefan diffusivities of adsorbate

molecules.<sup>104,105</sup> Direct measurement of microscopic self-diffusion of molecules within MOFs at various length scales is also made possible by techniques like infrared microspectroscopy (IRM), interference microscopy (IFM), pulsed-field-gradient NMR (PFG NMR) and quasi-elastic neutron scattering (QENS).<sup>106,107</sup> Based on the size of diffusion domains and pore hierarchy, some of these techniques can be directly compared to simulated diffusivities from computational methods like Monte Carlo or MD simulations.<sup>108,109</sup>

In addition to adsorption and diffusion data, transient breakthrough experiments and simulations also provide valuable information with respect to the separation performance of a MOF.<sup>110</sup> Multicomponent breakthrough experiments are often critical because certain key factors like cooperative or competitive interplay between adsorbates are missing in single-component experiments. Krishna and Long have shown that dimensionless breakthrough time is a suitable metric for comparing the performance of MOFs for a given separation as well as estimating practical time considerations for using these MOFs in industrial applications.<sup>111</sup>

### **1.5.3 Predicting and Measuring Membrane Permeabilities: Tools and Challenges**

Simple one-dimensional continuum shell models<sup>112</sup> can be used with known adsorption and diffusion data to calculate the flux or permeability if a membrane thickness and the feed and permeate pressures are specified. In addition to pure thin film membrane predictions, single component gas permeabilities in both the polymer matrix and MOF can be used to predict the effective permeability through mixed matrix MOF membranes with either the Maxwell, modified Maxwell, Lewis-Neilson, Pal, Felske, modified Felske, or Bruggeman models.<sup>113,114</sup> Examples of membrane screening studies exist showing that these methods can predict the performance of CuBTC, IRMOF,

Zn(bdc)(ted)<sub>0.5</sub>, and COF-102 membranes for H<sub>2</sub>/CH<sub>4</sub>, CO<sub>2</sub>/CH<sub>4</sub>, and CO<sub>2</sub>/H<sub>2</sub> binary separations.<sup>115</sup>

Once the suitable MOF is selected and a pure-MOF or mixed-matrix membrane is made, they can be tested using single or multicomponent permeation experiments. Gas phase components can be measured using techniques such as permeation cells<sup>116</sup> or the Wicke-Kallenbach method<sup>117</sup>, and liquid phase feed mixtures can be used in pervaporation tests<sup>118</sup>. It is often seen that separation performance predicted by screening experiments or molecular simulations do not match the results of permeation tests. Guest molecules can show different transport properties in pure-MOF or polymer components as compared to heterogeneous membranes.<sup>119</sup> Certain factors like counteracting adsorption and diffusion effects<sup>120</sup> or restricted flexibility of MOF framework after membrane formation<sup>121</sup> can contribute to these variations. Practical considerations like defects in membranes<sup>16</sup> or adhesion of MOF and polymer<sup>122</sup> could also play a role in these experiments. Atomistic and continuum modeling of MOF MMMs, specifically the interfaces between the polymer and embedded MOF crystals, has been attempted but is an active area of research.<sup>123-125</sup> The computational and experimental methods used to select MOFs suitable for use in membrane separations are summarized in Figure 1.8.

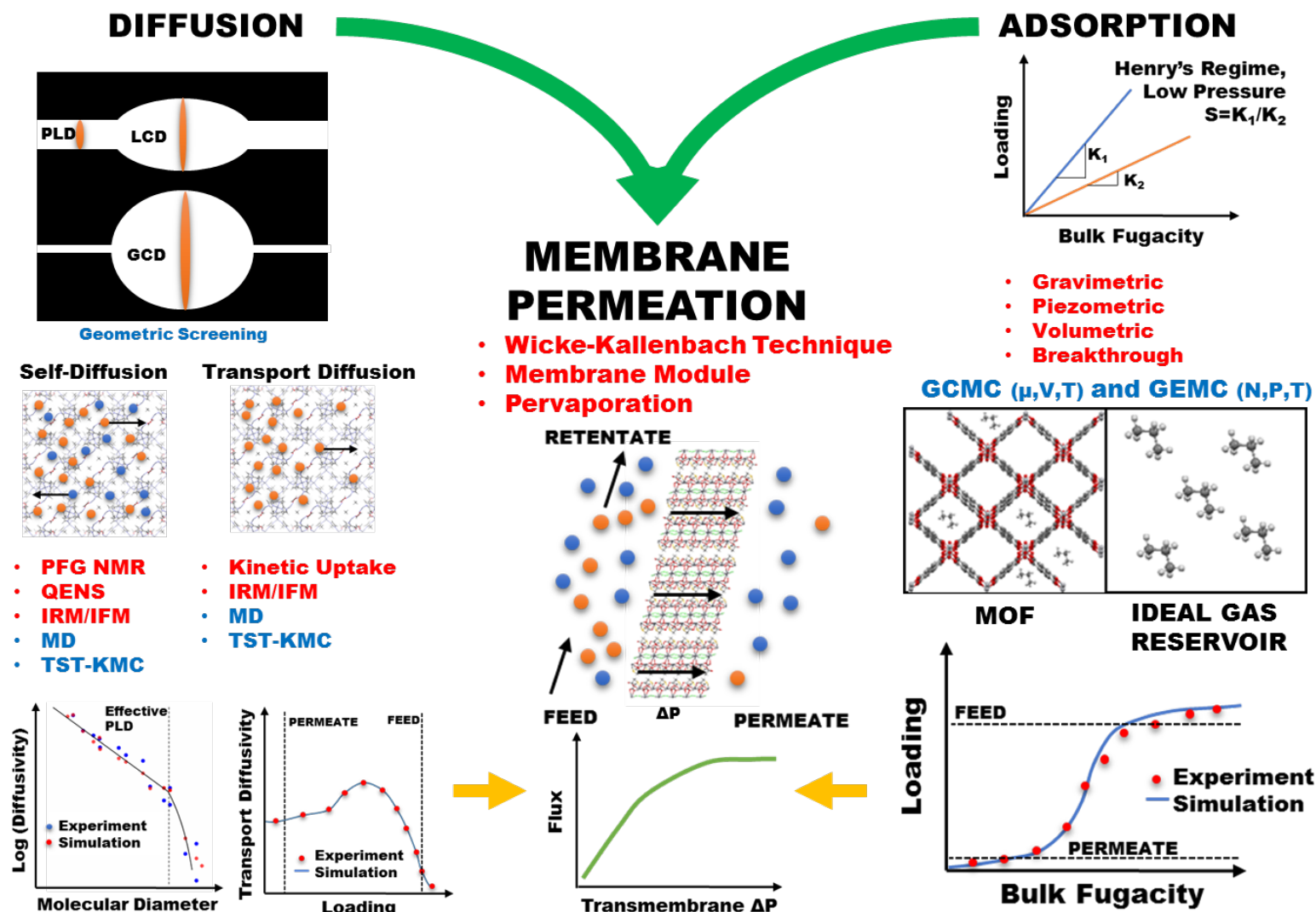


**Figure 1.8** Hierarchical methods for choosing MOFs for membrane applications. Both the transport and adsorption properties are considered first and simultaneously through simulations (blue text) and experiments (red text) to engineer MOF membranes with properties that reach the target performance criteria.

## 1.6 Thesis Impact

The topics addressed in this thesis significantly advance the computational techniques and knowledge needed to accurately model diffusion through single-linker and mixed-linker ZIF materials. Below, the five key scientific advances made in this thesis are highlighted addressing substantial challenges the nanoporous materials community had faced.

**Adsorbates larger than the window of ZIF-8 were able to diffuse. What is the mechanism for this diffusion process and how can we access the entire range of diffusion time scales?**

(1) Studying diffusion of large adsorbates with molecular diameters equal to or larger than the window diameter of ZIF materials required the implementation of computational methods that included ZIF structural flexibility and could access the entire range of diffusion time-scales. We found that large adsorbates brace open the window of ZIF-8 during the diffusion process. These computational methods and insights could be extended to look at other nanoporous materials exhibiting small pores. This work is addressed in Chapter 2.

**There are many other single-linker ZIF materials. How can other ZIFs structurally similar to ZIF-8 be accurately screened for molecular sieving applications?**



(2) No transferable force field capable of accurately predicting the structural flexibility of ZIFs was available in the existing literature. Therefore the intraZIF force field was developed to model structural flexibility and used to screen three single-linker ZIFs for the diffusion properties of thirty adsorbates. This work is addressed in Chapter 3.

**Individual ZIF crystals can contain two types of imidazolate linkers. How are the imidazolate linkers in ZIF-8<sub>x</sub>90<sub>100-x</sub> materials distributed on the unit cell level?**

(3) A combination of NMR experiments and various computational modeling techniques led to the development of mixed-linker ZIF structural models to be used in atomistic simulations. This established protocol could be used to determine the structure of any mixed-linker MOF material assuming hydrogens on the various linkers were chemically distinguishable without isotopic labeling. This work is addressed in Chapter 4.

**Local ordering in solid solutions is known to affect chemical and physical properties. Does the local ordering of imidazolate linkers in binary mixed-linker ZIFs impact diffusion?**

(4) It was unclear what impact the local ordering of imidazolate linkers in binary mixed-linker ZIFs had on diffusion properties of light gases. We therefore proposed a lattice-diffusion model based on four diffusion hopping rates through parent and hybrid parents. It was determined that local ordering had a small impact on diffusion properties and that

the hopping rates through the four windows most strongly controlled diffusion behavior. This work is addressed in Chapter 5.

**Diffusion can be continuously tuned with binary mixed-linker ZIFs. Can the tools and knowledge from Chapters 2-5 be used to accurately predict diffusion in binary mixed-linker ZIFs?**

(5) Combining the computational techniques of Chapter 2 (biased molecular dynamics including framework flexibility) and Chapter 5 (lattice-diffusion model) with the intraZIF force field developed in Chapter 3, we show that it is possible to quantitatively predict diffusion through binary mixed-linker ZIFs. This work can be used to screen any single-linker or binary mixed-linker ZIF for any light gas separation of interest and is addressed in Chapter 6.

## CHAPTER 2

### HYDROCARBON DIFFUSION PREDICTIONS THROUGH ZEOLITIC IMIDAZOLATE FRAMEWORK-8

The below text was reproduced from the article “Temperature and Loading-Dependent Diffusion of Light Hydrocarbons in ZIF-8 as Predicted through Fully Flexible Molecular Simulations” by Ross Verploegh, Sankar Nair, and David Sholl in the *Journal of the American Chemical Society*, 2015, volume, pages 15760-15771. Copyright 2015, American Chemical Society. The copyright permissions letter for this publication can be found in Appendix G. This chapter details the computational methods needed to accurately predict diffusion through cage-type ZIF materials.

Accurate and efficient predictions of hydrocarbon diffusivities in zeolitic imidazolate frameworks (ZIFs) are challenging, due to the small pore size of materials such as ZIF-8 and the wide range of diffusion time scales of hydrocarbon molecules in ZIFs. Here we have computationally measured the hopping rates of 15 different molecules (kinetic diameters of 2.66-5.10 Å) in ZIF-8 *via* dynamically corrected transition state theory (dcTST). Umbrella sampling combined with the one-dimensional weighted histogram analysis method (WHAM) was used to calculate the diffusion free energy barriers. Both the umbrella sampling and dynamical correction calculations included ZIF-8 flexibility, which is found to be critical in accurately describing molecular diffusion in this material. Comparison of the computed diffusivities to extant experimental results shows remarkable agreement within an order of magnitude for all the molecules. The dcTST method was also applied to study the effect of hydrocarbon loadings. Self and transport diffusion coefficients of methane, ethane, ethylene, propane,

propylene, n-butane, and 1-butene in ZIF-8 are reported over a temperature range of 0-150 °C and loadings from infinite dilution to liquid-like loadings.

## 2.1 Introduction

New separation strategies for light paraffin and olefin species that have small differences in relative volatilities could have a significant industrial impact.<sup>126</sup> Currently, the industry standard for olefin/paraffin separations is cryogenic distillation, with approximately 85% of the annual operating cost attributed to energy consumption.<sup>5</sup> One class of proposed alternative processes uses nanoporous materials as adsorbents in thermodynamically-controlled pressure, temperature, and (or) vacuum swing adsorption separations or as size-selective entities in kinetically-controlled membrane or adsorption separations.<sup>127</sup> Regardless of the choice between a thermodynamic or kinetic separation process, it is necessary to know the diffusion coefficients of hydrocarbons in the nanoporous material of choice to accurately design the separation process.

Metal-organic frameworks (MOFs) are a class of nanoporous materials formed through coordination bonds between metal centers and organic linkers.<sup>17</sup> MOFs have many proposed uses such as gas storage, catalysis<sup>23</sup>, chemical sensing<sup>24</sup>, drug delivery<sup>26</sup>, and chemical separations<sup>28</sup> and their ordered pore networks lend themselves to study by molecular simulations<sup>20</sup>. Considerable experimental work has focused on exploiting the molecular sieving characteristics of ZIF-8, a prototypical small pore MOF.<sup>22,45</sup> ZIF-8 is water stable, thermally stable up to 550°C, demonstrates permanent porosity, and is easily synthesized.<sup>41</sup> ZIF-8 has been experimentally shown to exhibit interesting sieving properties with regard to increasing hydrocarbon chain length and morphology.<sup>56</sup> Specifically, ZIF-8 has shown a sharp kinetic separation between propylene and propane with single-component and binary permeation selectivities in a range of 15 to 60 at room temperature and 35 °C.<sup>38,39,128,129</sup> Pan and Lai demonstrated not only a sharp C<sub>3</sub>

olefin/paraffin separation but also a promising ideal  $C_2/C_3$  permeation separation of 6.6 at 1 bar and 298 K.<sup>40</sup> Furthermore, Bux and coworkers showed permeation selectivities of 2.4 for ethylene over ethane for an equimolar bulk gas mixture at room temperature and 6 bar with a ZIF-8 membrane.<sup>130</sup>

Previous simulation studies of molecular diffusion in ZIF-8 have focused on relatively fast diffusing small molecules such as hydrogen<sup>131</sup>, noble gases<sup>132</sup>, carbon dioxide<sup>133</sup>, and small alcohols<sup>134</sup> using both rigid and flexible ZIF-8 frameworks. Diffusion coefficients of such rapidly diffusing species can be calculated in nanoporous materials through straightforward equilibrium molecular dynamics (EMD) simulations.<sup>135</sup> Unfortunately, many of the hydrocarbon species of interest in ZIF-8 have diffusivities lower than  $10^{-12}$  m<sup>2</sup>/s, which are high enough to be of industrial relevance but too low to measure with EMD. To date, only one simulation study has attempted to demonstrate the hydrocarbon sieving properties of ZIF-8. Zheng et al. simulated the self-diffusion of methane, ethane, ethylene, and propane and made a comparison to transport diffusivities experimentally measured using the Wicke-Kallenbach (WK) technique.<sup>136</sup> Their results for propane show poor convergence because of the slow hopping of propane in ZIF-8 on molecular dynamics (MD) timescales. To circumvent this time-scale dilemma, the diffusion of adsorbates may be considered as an activated hopping process of an adsorbate between low energy regions.<sup>137</sup> Within this description, enhanced sampling methods such as transition path sampling or dynamically corrected transition state theory (dcTST) can be applied to characterize the diffusion properties of slowly diffusing adsorbates.<sup>137-149</sup>

MOFs also exhibit a variety of flexible phenomena such as intra-framework dynamics, swelling, negative thermal expansion, gate opening, and breathing.<sup>47</sup> By Coudert's classification<sup>47</sup>, ZIF-8 displays intra-framework dynamics through methyl-imidazole (mIm) organic linker rotation. The swinging of the mIm organic linker is caused by both thermal fluctuations, as shown by *ab initio* MD calculations (AIMD),<sup>18,57</sup>

and forces exerted by adsorbed molecules, as shown by Fairen-Jimenez using *in situ* powder X-ray diffraction (XRD)<sup>150</sup>. The latter phenomenon generates a thermodynamically metastable structure with a larger window diameter (3.81 Å) than the empty ZIF-8 structure (3.42 Å).<sup>150</sup> Uptake experiments and single-component breakthrough measurements have shown that ZIF-8 accepts chemical species (e.g. isobutane, benzene, xylene isomers, and 1,2,4-trimethylbenzene) that have kinetic diameters larger than ZIF-8's measured powder XRD pore size (3.42 Å).<sup>56,60,151</sup> Haldoupis and coworkers demonstrated using a combination of AIMD and TST simulations that it was essential to include thermal intra-framework motions in predicting methane diffusion in ZIF-8.<sup>57</sup> The simulated diffusion coefficient of methane in the rigid ZIF-8 structure is not measurable by standard EMD. The approximate procedure by Haldoupis et al. of thermally averaging the hopping rate over a set of structures predicts a larger diffusion coefficient than that measured in the rigid structure. This is consistent with the results of Hertäg et al. who also demonstrated that inclusion of ZIF-8 framework flexibility in EMD simulations was critical in accurately describing methane mobility<sup>131</sup>. The methods used by Haldoupis et al. do not account for coupling between the diffusing molecule and the ZIF framework.

In this chapter, we have simulated the self and transport diffusivities of methane, ethane, ethylene, propane, propene, n-butane, and 1-butene in ZIF-8 over industrially relevant temperature and loading ranges using molecular simulation techniques that incorporate ZIF-8 intra-framework motions and compared our results to reported experimental results. We begin by briefly discussing the theory behind the calculation of diffusivities as well as define the simulation methods and force fields used in our calculations. The dcTST methodology was then applied to a range of adsorbed species in ZIF-8 and the computed diffusivities are compared to experimental data. We also describe the loading dependence of the self and transport diffusion coefficients of alkanes

and alkenes in ZIF-8 and use this information to predict hydrocarbon permeabilities through a ZIF-8 membrane.

## 2.2 Theory

### 2.2.1 Diffusion Background

Fick's law describes macroscopic transport by combining a single-component transport diffusivity with a concentration gradient as the driving force.<sup>135</sup> Molecular simulations can be used to calculate self-diffusion coefficients  $D_{\text{self},i}$ , as well as collective (corrected) diffusion coefficients  $D_{0,i}$ , where the subscript  $i$  indicates the molecular species.<sup>135,152</sup> Self and collective diffusion coefficients are correlated through the following sum of parallel resistances<sup>153</sup>:

$$\frac{1}{D_{\text{self},i}} = \frac{1}{D_{0,i}} + \frac{1}{D_{i,i}} \quad (2.1)$$

where  $D_{i,i}$  is the Maxwell-Stefan self-exchange diffusivity. MOFs exhibiting one-, two-, or three-dimensional topologies, small pore limiting diameters (PLDs), and large cavities have the most potential for molecular sieving based applications. Small pore diameters allow for molecular sieving of molecules with different molecular diameters and large cavities allow for mixing of species within the cavities. Below, we assume that correlated mixing effects are negligible in cage-type frameworks with large cages and small windows.<sup>59,153</sup> Therefore, it is possible to assume for unary loadings that the Maxwell-Stefan self-exchange diffusivity is large and can be neglected. This means that  $D_{\text{self},i} = D_{0,i}$  at any unary loading and the relationship between the transport diffusivity  $D_{T,i}$  and the self-diffusivity, known as Darken's equation, can then be written as<sup>153</sup>:

$$D_{T,i} = D_{self,i} \left( \frac{\partial \ln p}{\partial \ln c} \right) \quad (2.2)$$

The quantity in parentheses is known as the thermodynamic correction factor where  $c$  is the adsorbate loading and  $p$  is the corresponding pressure. The thermodynamic correction factor is derived from an adsorption isotherm, calculated either with grand canonical Monte Carlo (GCMC) simulations or measured experimentally. In general, both the transport and self-diffusivities are functions of loading and temperature.

We also assume that the diffusion of adsorbates through a cage-type material can be viewed as an activated hopping process.<sup>137</sup> The loading-dependent self-diffusivity can then be written as a function of the loading-dependent overall exit hopping rate:

$$D_{self,i} = \frac{1}{2n} k_{A \rightarrow ALL}^{EXIT} \lambda^2 \quad (2.3)$$

where  $\lambda$  is the distance between low energy sites and  $n$  can take on values of 1, 2 or 3 depending on the dimensionality of diffusion. For ZIF-8,  $n = 3$ . The exit hopping rate in the expression above is the sum of the hopping rates over all windows exiting a cage.

### 2.2.2 Calculating the Diffusion Hopping Rate at Infinite Dilution

Transition state theory (TST) is applicable to describing processes that are characterized by sequences of rare events such as the hopping of adsorbates from cage to cage in ZIF-8.<sup>154,155</sup> To apply TST, one must have a method that efficiently explores the free energy landscape and locates at least approximately the location of a transition state. These methods include, but are not limited to, the nudged elastic band (NEB) method<sup>156</sup>, biased sampling methods such as umbrella sampling (US)<sup>157,158</sup>, temperature accelerated dynamics (TAD)<sup>159</sup>, steered molecular dynamics (SMD)<sup>160</sup>, metadynamics<sup>161</sup>, Monte



Carlo (MC) histogramming methods<sup>162</sup>, and path sampling methods such as transition path sampling (TPS)<sup>163</sup> and transition interface sampling (TIS)<sup>164</sup>. Each method utilizes different simplifying assumptions and can be combined with a variety of approaches to calculate free energies. For example, the NEB method neglects the entropic contribution to the hopping rate yielding only the minimum potential energy barrier. SMD can be combined with thermodynamic integration<sup>165</sup> to yield free energies from the force required to undergo a transition between two metastable microstates. US and MC histogramming both require an *a priori* definition of a reaction coordinate (RC) upon which to map the free energy directly from probabilities. Path sampling methods do not require definition of a reaction coordinate or calculation of a transmission coefficient but can be computationally expensive<sup>146</sup>.

Within TST, the assumption is made that all systems that reach the transition state (TS) starting from one free energy minimum position (state A) will thermalize in the other free energy minimum position (state B) of interest. For consistency, we will refer to the system as the diffusing adsorbate and ZIF-8 atoms that comprise the window region, state A as the exiting cage, and state B as the receiving cage. TST's treatment of the rate typically overestimates the effective rate by neglecting rapid recrossing events. These recrossings are consequences of the adsorbate having a high kinetic energy after the initial crossing, the geometry of the adsorbent around the TS, or the presence of other adsorbates.<sup>148,166</sup> To correct for this phenomena, it is possible to multiply the TST derived rate by the dynamical correction (dc) factor or transmission coefficient.<sup>167</sup> The transmission coefficient is defined as the probability that the system (the adsorbate) will thermalize within state B (receiving cage) from a trajectory starting at the TS. For a single Lennard-Jones (LJ) fluid (spherical) adsorbate in rigid frameworks at infinite dilution where the transition state is known exactly, the transmission coefficient is typically close to unity. However, this dynamical correction becomes non-negligible for more complex adsorbates, higher adsorbate loadings, and situations such as the presence

of a flexible framework where an imperfect reaction coordinate means that the TS dividing surface is not known exactly.

### **2.2.3 Coupling of Adsorbate and MOF Framework Motions**

Adsorbates with kinetic diameters larger than the pore limiting diameter of ZIF-8 have been clearly demonstrated experimentally to diffuse inside ZIF-8.<sup>56,60,151</sup> This can potentially occur due to flexibility inherent in the ZIF-8 windows or due to deformations of the windows induced by adsorbed molecules. It is not unreasonable to consider that during a crossing event, a large adsorbate would effectively brace the window open. The existing literature modeling diffusion in ZIF-8 has not examined the latter effect. Previous simulation studies have considered the effect of framework flexibility on diffusion of spherical adsorbates by assuming a decoupling of framework motions from the hopping trajectory of the adsorbate. Haldoupis et al. and Awati et al. have utilized methods to measure histograms of window sizes in empty ZIF-8<sup>57</sup> and zeolite frameworks<sup>73,168</sup> respectively. In these calculations, only the equilibrium framework motions of the empty (non-loaded) structures are considered. Recent work by Boulfelfel et al. has shown that this approach neglects important adsorbate-induced deformation during diffusion of extended hydrocarbons in small pore zeolites.<sup>51</sup> To accurately describe diffusion of the broadest range of molecules inside ZIF-8, it is important to adopt methods that incorporate all the coupled adsorbate-framework degrees of freedom (DOF).

### **2.2.4 Loading Dependence of the Diffusion Coefficient**

Extending the free energy methods described above to higher loadings has been attempted in only a small number of studies. Tunca and Ford were the first to extend TST to describe high loading diffusion of spherical molecules in nanoporous crystals.<sup>162,169,170</sup> Dubbeldam and coworkers extended dcTST to higher loading alkane

diffusion in rigid zeolites.<sup>148</sup> Beerdsen and coworkers studied the loading dependence of methane diffusion in rigid cage-, channel-, and intersecting-type zeolites.<sup>171</sup> Jee et al. simulated methane/carbon dioxide mixtures in silica zeolite DDR and demonstrated excellent agreement between MD and TST-kinetic Monte Carlo (KMC) methods.<sup>172</sup> Recently, Smit and coworkers followed the TST-KMC approach of Jee et al. in order to calculate the collective (corrected transport) diffusivity of methane in zeolite Si-LTA with excellent agreement to EMD simulations.<sup>166</sup> In all of these studies, one adsorbate molecule was tracked while all other adsorbates, even those in the exiting and receiving cages, were treated as a contributing background potential.

In this chapter, we propose a simplified scheme that assumes the self-diffusion coefficient is a function of only symmetric receiving and exiting cage loadings. Asymmetric cage loadings are not taken into account as they are in the work by Smit and coworkers.<sup>166</sup> The results of Dubbeldam et al. and Jee et al. demonstrated that specific loadings in surrounding cages do not have a strong effect on the local hopping rates in cage-type materials.<sup>148,172</sup> More careful treatment of asymmetric loadings may be justified if high precision information on loading-dependent diffusivities is required in a specific example. It is important to clarify that all the studies of loading-dependent diffusion mentioned above treated the nanoporous framework as rigid. Below, we extend these methods to include framework flexibility. A recent study by Theodorou and coworkers applied umbrella sampling to study infinite dilution benzene diffusion in fully flexible silicalite at three temperatures.<sup>173</sup> To our knowledge, no prior studies have been performed that apply dcTST to investigate the loading-dependent transport properties of adsorbates within fully flexible MOFs.

## 2.3 Computational Methods

### 2.3.1 ZIF-8 and Adsorbate Force Fields

ZIF-8 has been experimentally shown to undergo a low loading (LL) to high loading (HL) structural transition upon adsorption of N<sub>2</sub> at 77 K.<sup>150</sup> This transition is associated with the rotation of the linkers about the N-N axis of the imidazole ring.<sup>136</sup> A force field (FF) developed by Zhang and coworkers was parameterized to reproduce the ZIF-8 LL to HL transition using a hybrid Gibbs Ensemble MC and NPT-MD simulation.<sup>174</sup> The force field of Zhang et al. was used to describe the ZIF-8 framework in our calculation. The starting ZIF-8 crystallographic structure for all the simulations was obtained from the Cambridge Structural Database (structure code OFERUN).<sup>30,175</sup>

The TraPPE united atom force field was applied to describe adsorbate-adsorbate interactions for methane, ethane, ethylene, propane, propylene, n-butane, 1-butene, isobutane, and isobutene.<sup>176,177</sup> The bonds in these molecules were considered to be flexible<sup>178</sup> and charges were not considered. In addition to hydrocarbons, the following small adsorbates were also considered: He, SF<sub>6</sub>, H<sub>2</sub>, N<sub>2</sub>, O<sub>2</sub>, and CO<sub>2</sub>. He was described as a single-site 12-6 LJ fluid.<sup>179</sup> SF<sub>6</sub> was also described as a single-site 12-6 LJ fluid.<sup>180</sup> H<sub>2</sub> was described by the Michels-Degraaff-Tenseldam model with charges from the Darkim-Levesque model and a fixed H-H bond length of 0.741 Å.<sup>181</sup> N<sub>2</sub> was described by the TraPPE FF with a fixed N-N bond length of 1.100 Å.<sup>182</sup> The LJ parameters for N<sub>2</sub> were taken directly from Zhang et al.<sup>174</sup> and are slightly different than the parameters reported from Potoff and Siepmann<sup>182</sup>. O<sub>2</sub> was described by the TraPPE FF with a fixed O-O bond length of 1.210 Å.<sup>183</sup> CO<sub>2</sub> was described by the rigid EPM2 FF with a fixed C-O bond length of 1.160 Å.<sup>184</sup> H<sub>2</sub>, N<sub>2</sub>, O<sub>2</sub>, and CO<sub>2</sub> were modeled as rigid molecules. All adsorbate FF parameters can be found in Appendix A.

All calculations were carried out in 2x2x2 ZIF-8 unit cell simulation volume with periodic boundary conditions (PBCs). Lorentz-Berthelot mixing rules described all adsorbate-framework 12-6 LJ interactions in both MC and MD simulations. Lennard-

Jones potential interactions were truncated at a spherical radius of 16.5 Å and analytical tail corrections were applied. Ewald summation was used to compute long range Coulombic interactions with a desired relative error in forces of  $10^{-6}$ . In every case, the simulation volumes used were charge neutral.

### 2.3.2 Grand Canonical Monte Carlo

GCMC calculations were performed using RASPA to measure adsorption isotherms in ZIF-8.<sup>185</sup> ZIF-8 was modeled as a rigid structure with the energy minimized structure given by the Zhang FF in these calculations. Park et al. reported a LL ZIF-8 structure, determined by XRD at 258 K and 1 atm, with unit cell parameters of  $a=b=c=16.991$  Å.<sup>41</sup> Unit cell parameters for the LL FF minimized ZIF-8 structure were  $a=b=c=16.991$  Å. The HL form of ZIF-8 as reported by Fairen-Jimenez has unit cell parameters of  $a=b=c=17.107$  Å.<sup>150</sup> Our HL ZIF-8 FF minimized structure has unit cell parameters of  $a=17.09$  Å,  $b=17.16$  Å, and  $c=17.07$  Å. These minor differences in lattice parameters have a negligible effect on the adsorption of hydrocarbons. Pre-tabulated energy and Coulombic grids were generated with a 0.1 Å spacing to enhance computational efficiency. Further simulation details can be found in Appendix A.

### 2.3.3 Free Energy Mapping

Umbrella sampling was chosen as the biased sampling method. To implement umbrella sampling, a one-dimensional RC was chosen that starts in cage A, passes through the narrow window, and ends in cage B. The window region is loosely defined as a geometric plane in the center of the 6 member ring of ZIF-8. In flexible structures this plane is a  $3N-1$  dimensional surface where  $N$  is the number of atoms and the position of which is time-varying. Any reference to the TS location with the one-dimensional RC is therefore an approximate description of the true TS. The RC is defined by the vector

between the geometric centers of cage A and cage B. Figure 2.1 shows a schematic of ZIF-8 and an idealized representation of how umbrella sampling is performed.

All NVT EMD simulations were performed using LAMMPS.<sup>186</sup> The velocity-Verlet integration algorithm was used with a 1 fs time step. For NVT simulations, a Nose-Hoover thermostat was applied with a temperature damping parameter of 100.0 fs. The framework lattice constants and atomic positions were optimized prior to each simulation using the Zhang FF. The conjugate gradient (CG) algorithm as implemented in LAMMPS was used to anisotropically relax both the unit cell parameters and atomic positions. A second minimization step involved using Hessian-free truncated Newton Raphson algorithm to relax only the atomic positions. Both minimization steps adhered to a force cutoff of 0.231 kcal/molÅ<sup>2</sup>. The velocities of all atoms were then initialized from a Maxwell-Boltzmann distribution representative of the specified temperature.

The collective variables (colvars) package developed by Fiorin and coworkers was utilized within LAMMPS to perform the umbrella sampling calculations.<sup>187</sup> During umbrella sampling, an adsorbate is constrained to a 3-D region orthogonal to the reaction coordinate by a spring. The larger the spring constant, the thinner the 3-D region is, with thinner regions requiring more overlapping umbrella simulations. For faster moving adsorbates (He, H<sub>2</sub>, N<sub>2</sub>, CO<sub>2</sub>), a spring constant of 10 kcal mol<sup>-1</sup>Å<sup>-2</sup> was used. A spring constant of 25 kcal mol<sup>-1</sup> Å<sup>-2</sup> was used for the O<sub>2</sub>, methane, ethane, ethylene, propane, propylene, n-butane, and 1-butene simulations. For both these sets of adsorbates, simulations utilized 30 umbrellas with an approximate spacing of 0.508 Å. Isobutane, isobutene, and SF<sub>6</sub> simulations used a spring constant of 150 kcal mol<sup>-1</sup>Å<sup>-2</sup>, with 50 umbrellas each having an approximate spacing of 0.301 Å. For adsorbates with multiple DOFs, the constraining harmonic potential was applied to the molecule's center of mass (COM). A 100 ps equilibration simulation was performed before the 250-500 ps production period for each umbrella. Adsorbates with more DOFs required longer production runs for efficient sampling. The weighted histogram analysis method

(WHAM) was utilized to combine the different umbrella simulations into a free energy curve.<sup>188</sup>

In simulations with the smaller adsorbates, we found that the tracked adsorbate was able to hop to another cage if the umbrella plane was positioned orthogonal to another ZIF-8 window. This led to poor sampling of the specified microstates. Using a Monte Carlo histogramming method (e.g. Awati et al.<sup>168</sup>), the integral over the free energies associated with those microstates of interest is calculated to determine a hopping rate; likewise, only the likelihood of molecular positions within this localized region should be sampled when performing umbrella sampling. For example, if a plane is placed parallel to the window region, one finds that the plane dissects the center of neighboring cages. Sampling these low energy regions would predict a much lower energy barrier when combining umbrella simulations with WHAM. To constrain faster moving adsorbates to the specified cage, a blocking potential (repulsive spherical wall) was created around the cage with a radius of 9 Å. Any tracked adsorbate exiting the microstate experienced a repulsive harmonic potential with a force constant of 200 kcal/mol Å<sup>2</sup> when approaching within 1 Å of the spherical wall. No other atoms within the simulation were subjected to this artificial blocking potential. The total potential energy of the system was analyzed to detect unrealistic spikes that would indicate high forces and therefore, corresponding unphysical velocities. Unwanted adsorbate hopping only occurred one or two times during specific umbrella simulations and we concluded that the brief sampling of these high energy regions had a negligible effect on the final free energy curve.

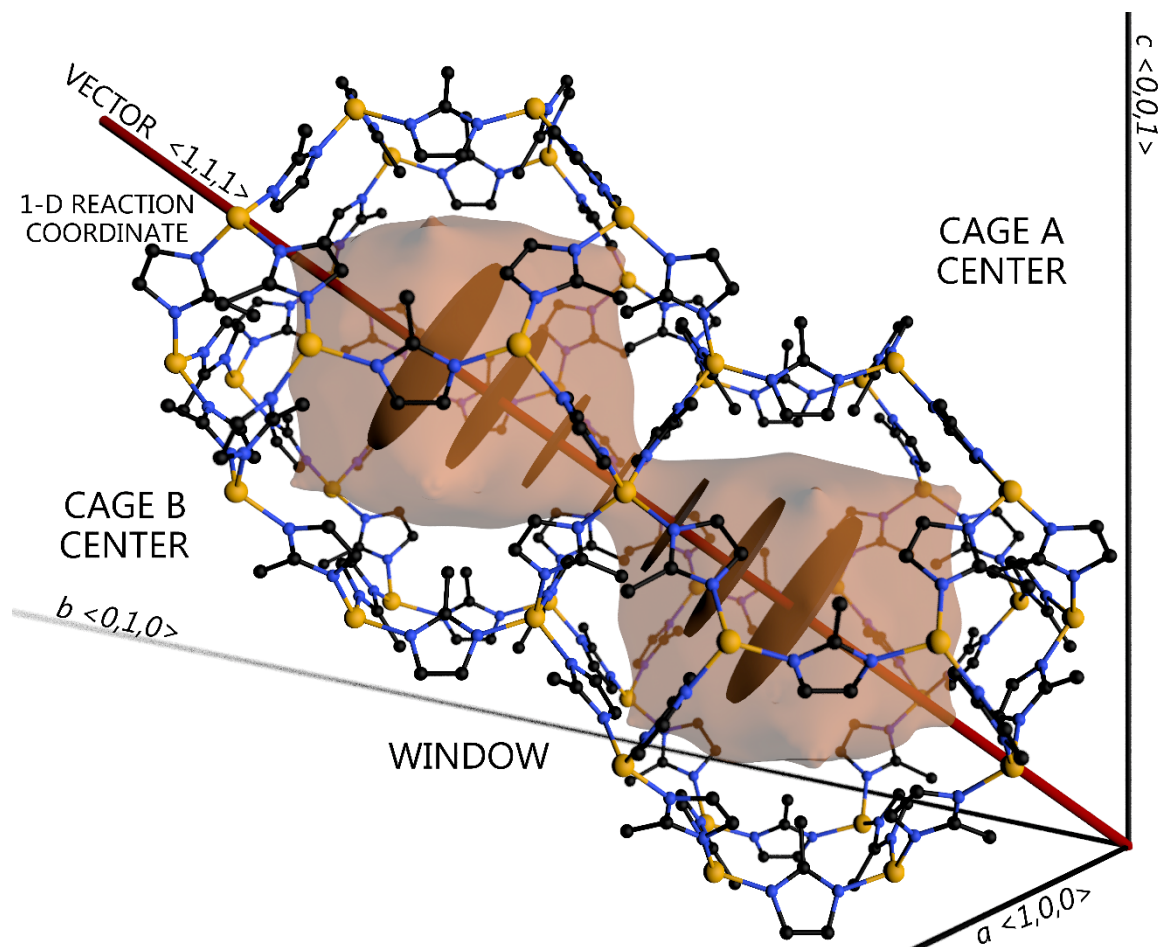


**Figure 2.1** Schematic of the linear reaction coordinate (red vector) traversing the window between two ZIF-8 cages. Umbrellas are idealized as brown discs on the red 1-D RC. The other 14 cages in the 2x2x2 ZIF-8 simulation volume as well as hydrogen atoms have been removed for clarity. Spheres colored in yellow, blue, and black correspond respectively to Zn, N, and C atoms.

### 2.3.4 Transmission Coefficient Calculation

Transmission coefficients were calculated using the procedure described by Frenkel and Smit.<sup>154</sup> To begin, an ensemble of starting configurations of the adsorbate at the TS must be recorded. We used an umbrella sampling simulation during which the tracked adsorbate is held fixed by a tight spring of  $1000 \text{ kcal mol}^{-1} \text{ \AA}^2$  to a plane orthogonal to the TS RC. A 100 ps equilibration simulation is performed before one thousand snapshots are recorded with a sampling frequency of 0.25 ps. A starting snapshot for each trajectory was chosen from the 1000 snapshots using a uniform



distribution. Before running the short MD simulations, the velocities of all atoms, both adsorbate and framework, are randomized according to the Maxwell-Boltzmann distribution at the specified temperature. Each trajectory was run for a total of 6ps, 3ps backwards and forwards in time. Through trial and error, this length was found to be sufficient for the transmission coefficient curves to reach a plateau. The adsorbate COM distance from the TS barrier was tracked to determine whether it was in the exiting or receiving cage. A minimum of 1500 trajectories were gathered for the reported transmission coefficients.

### **2.3.5 Methods for Measuring Loading-Dependent Self-Diffusivities**

The simulation method for measuring loading-dependent self-diffusivities is almost identical to the description of free energy mapping and calculation of the transmission coefficient at infinite dilution. In both calculations, only one adsorbate is tracked. All the extra adsorbates are considered simply as a background potential. A fixed number of adsorbate molecules are added to the system using Widom insertion as implemented in RASPA. The number of molecules placed in both the exiting and receiving cages is set to the total number of adsorbates in the simulation volume divided by the number of ZIF-8 cages (16 cages for the 2x2x2 simulation volume). An adsorbate is then randomly chosen from the other adsorbates not in the receiving or exiting cages, and its coordinates are set approximately at the TS region between the exiting and receiving cages. This adsorbate becomes the tracked adsorbate. Placing the tracked adsorbate at the TS at the beginning of the simulation ensures that the tracked adsorbate does not initially overlap with any other adsorbates and allows for a smooth relaxation into the appropriate cage based on the location of the spring. All other simulation details are the same as described in Section 3.3.

## 2.4 Results and Discussion

### 2.4.1 Infinite Dilution: Hydrocarbons in ZIF-8

Figure 2.2 shows representative free energy curves of propane at infinite dilution in ZIF-8. The free energy curves for other adsorbates are similar and several examples are reported in Appendix A. RC values of 0 and 14.72 Å correspond to the center of the exiting cage and the receiving cage, respectively. The TS is located at approximately 7.6 Å on the RC. This value was used to generate trajectories for the transmission coefficient calculations.

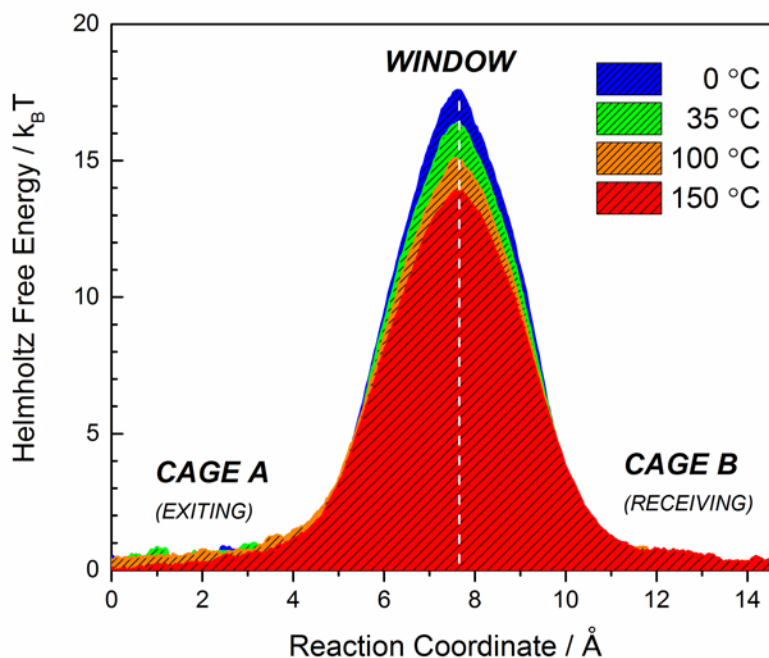


**Figure 2.2** Free energy curves for propane at infinite dilution as a function of temperature in flexible ZIF-8.

Figure 2.3 shows how the transmission coefficient curves for propane vary with respect to time. In general, the transmission coefficient increases as temperature is increased. At 35 °C and infinite dilution, transmission coefficients for the 15 adsorbates

ranges from 0.843 to 0.025 as reported in Table A.5 of Appendix A. Generally, adsorbates with smaller kinetic diameters such as He, H<sub>2</sub>, N<sub>2</sub>, and O<sub>2</sub> have transmission coefficients closer to 1. Isobutane and isobutene have the lowest transmission coefficients. Dubbeldam et al. reported transmission coefficients for propane in a rigid model of zeolite LTL around 0.5 at 300 K and infinite dilution.<sup>148</sup> This is comparable to our result for propane shown in Figure 2.3 for flexible ZIF-8. Abouelnasr et al. reported a transmission coefficient of almost unity for methane in rigid LTA-type zeolite at 300 K.<sup>166</sup>

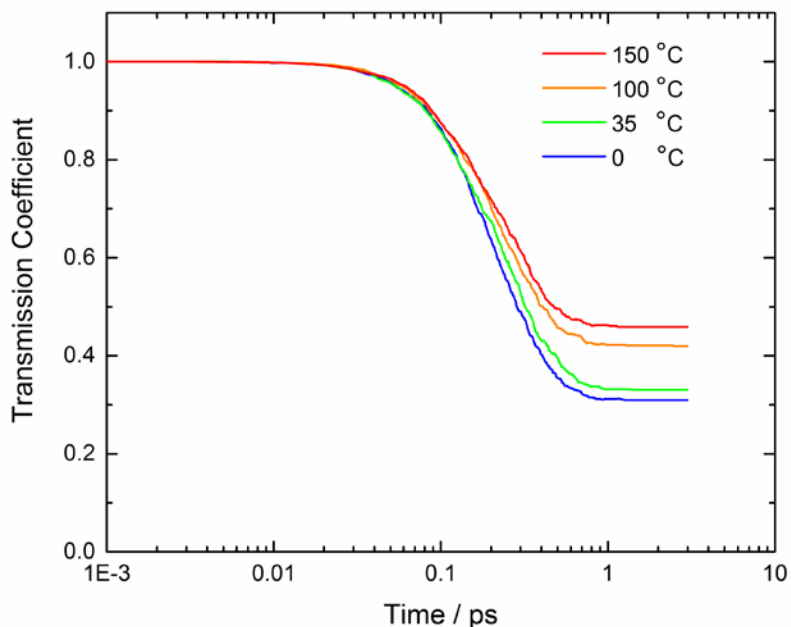


**Figure 2.3** Transmission coefficient curves for propane at infinite dilution in flexible ZIF-8 as a function of time for various temperatures.

Our computed infinite-dilution diffusivities for 15 molecules at 35 °C are shown in Figure 2.4. The self-diffusivities at 0, 35, 100, and 150 °C, along with diffusion activation energies predicted through an Arrhenius fit, are reported in Table A.6 of Appendix A. The diffusion activation energies increase roughly linearly ( $R^2=0.875$ ) as a

function of increasing molecular diameter. For the linear hydrocarbons, the greatest differences in the activation energies occur between C2/C3= (5.4 kJ/mol) and C3=/C3 (4.7 kJ/mol), supporting experimental claims that ZIF-8 can be used to kinetically separate these species. A key observation from Figure 2.4 is that the methods we have used here give results for a range of diffusivities that greatly exceeds what is possible with standard MD calculations. The slowest diffusing species we examined, SF<sub>6</sub>, diffuses 9-10 orders of magnitude more slowly than can be observed with simple MD. The large range of diffusivities than can be assessed with the methods we have used makes it possible for the first time to compare computed diffusivities in ZIF-8 to experimental data in a comprehensive way.

Figure 2.4 shows a comparison between the experimentally measured diffusion data from Zhang and coworkers and our simulated self-diffusivities at infinite dilution and 35 °C. Zhang and coworkers collected data using two different methods: (1) kinetic uptake with a pressure decay cell for adsorbates diffusing slower than 10<sup>-8</sup> cm<sup>2</sup>s<sup>-1</sup> and (2) mixed-matrix membrane permeation for faster diffusing species.<sup>56</sup> The overall agreement between the experimental and simulated results is excellent, with the simulation results for each adsorbate lying within an order of magnitude of the experimental results. There are some quantitative differences between the computed and experimental results. For example, Zhang et al. predicted the ideal diffusion selectivity, defined as the ratio of the self-diffusion coefficients, of propylene over propane to be 145, while our calculations predict this ratio to be 19. Pressure decay cell diffusion data from Eum et al. for *n*-butane and isobutane in ZIF-8 has also been included in Figure 2.4.<sup>189</sup> The difference between the data by Eum et al. and Zhang et al. highlights the observation that measuring slow diffusion in materials of this kind experimentally can be challenging. It also points to the risks associated with drawing overly strong conclusions about the accuracy (or inaccuracy) of computational predictions based on comparisons with a single experimental measurement.

It is interesting to compare our results for ZIF-8 with data from similar calculations in small pore zeolites. Figure 2.4 includes results from recent calculations by Boulfelfel et al.<sup>51</sup> for C<sub>1</sub>-C<sub>4</sub> hydrocarbons in Si-LTA. The PLD of this silica zeolite (ITQ-29), defined using Zeo++ with atomic radii of 1.35 Å for both Si and O atoms<sup>190</sup>, is 3.995 Å<sup>191</sup>, so the window size in Si-LTA is comparable to the window size of ZIF-8 (3.42 Å). Surprisingly, the computed diffusivities in Si-LTA follow the trend observed in our calculations for ZIF-8 with almost quantitative accuracy. In both materials, flexibility of the windows is critical to diffusion; that is, calculations using rigid structures yield vastly lower diffusivities. It is conventional to think of zeolites as “more rigid” than MOFs. The data in Figure 2.4 suggest that at least in this example, carrying this concept to its logical conclusion would lead to incorrect predictions for the trend in diffusion for adsorbates as a function of size.

The red line in Figure 2.4 shows a linear fit to our simulated diffusivities for the species with molecular diameters less than 4.5 Å. Our linear fit assumes that the reported molecular diameters best represent the true morphology of the molecules presented in this chapter. This assumption captures the overall trend among the different molecules well, although there are clearly examples such as N<sub>2</sub>, CO<sub>2</sub>, and CH<sub>4</sub> where this simple trend is not adequate to completely describe the data. Molecules with kinetic diameters larger than 4.5 Å diffuse much more slowly than would be suggested by this empirical linear fit.

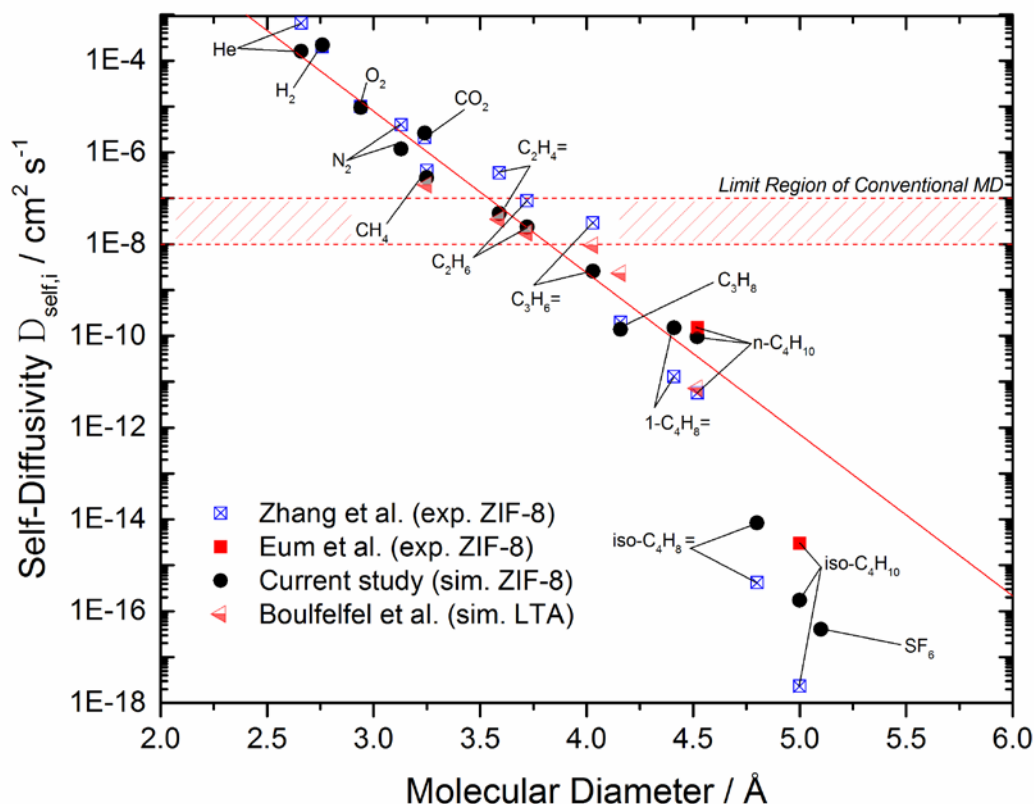


**Figure 2.4** Infinite-dilution self-diffusion coefficients for small non-spherical molecules and light key hydrocarbons at 35 °C as a function of molecular diameter. Experimental data was taken directly from Zhang et al.<sup>56</sup> and Eum et al.<sup>189</sup> Simulated C<sub>1</sub>-C<sub>4</sub> diffusivities in LTA zeolite taken from Boulfelfel et al.<sup>51</sup>

It is useful to consider whether the adsorbates passing through windows in ZIF-8 affect the window size. Intuitively, it seems possible that adsorbates, especially those with extended geometries, may be able to brace the window open while they are close to the dividing surface. Figure 2.5 shows the observed window size distributions when an adsorbate is constrained by a harmonic spring at the dividing surface defined above. Snapshots from the starting configurations used to compute transmission coefficients were used for this analysis. Using the same window diameter finding algorithm of

Haldoupis and coworkers<sup>59</sup> and the percolation algorithm of Ziff and Newman<sup>192</sup>, the window diameter of the relevant window was determined for each configuration. Grid based percolation methods underestimate the true window diameters, unlike methods that yield graph representations of the void space through Voronoi decomposition (Zeo++).<sup>190</sup> When using a specific grid spacing in a grid based method, one can more accurately determine the true window diameter as

$$D_w = D_{w,grid} + \sqrt{3}d_{grid} \quad (2.4)$$

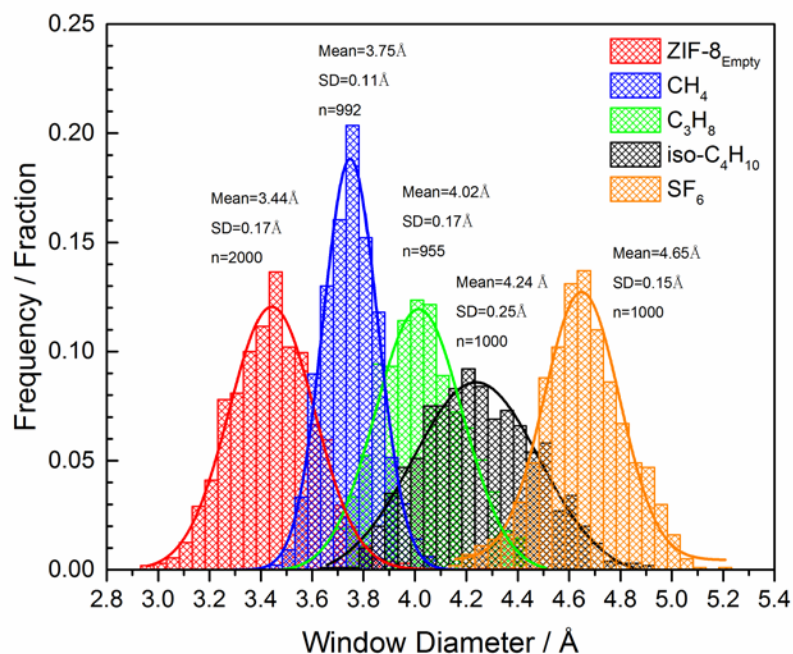
where  $D_w$  is the true window diameter,  $D_{w,grid}$  is the window diameter measured at a particular grid spacing, and  $d_{grid}$  is the grid spacing. The factor of  $\sqrt{3}$  is derived from geometric arguments based on an imperfect three-dimensional grid placement. Using Equation 2.4, we compared grid based PLD measurements at grid spacings of 0.1 and 0.25 Å for the experimentally reported ZIF-8 structures (structure codes VELVOY and OFERUN) to those predicted by Zeo++ and found differences of no greater than 0.028 Å. We therefore used Equation 2.4 with a grid spacing of 0.25 Å for computational efficiency in the calculations reported below. The average window diameter of  $3.44 \pm 0.17$  Å in the empty ZIF-8 structure calculated using the Zhang FF agrees well with the AIMD derived window diameter of  $3.41 \pm 0.16$  Å reported by Haldoupis et al.<sup>57</sup>

Figure 2.5 shows there is a considerable overlap between the window sizes seen in the empty framework and those seen when CH<sub>4</sub> is constrained to be in the window. This suggests that even without including the influence of CH<sub>4</sub> on the ZIF-8 window, configurations occur that allow CH<sub>4</sub> to hop through the window. This concept is central to earlier approximate calculations by Haldoupis et al. for ZIF-8<sup>57</sup> and Awati et al. for eight member ring zeolites<sup>73,168</sup> that use a collection of snapshots from an empty structure to estimate the impact of framework flexibility on diffusion. For the larger molecules

shown in Figure 2.5, however, there is almost no overlap between the window size distribution of the empty framework and the configurations with molecules constrained in the window. For SF<sub>6</sub>, for example, the window diameters three standard deviations above the mean for the empty framework (3.95 Å) and three standard deviations below the mean for the configurations including SF<sub>6</sub> (4.20 Å) are separated by 0.25 Å. It is clear from this gap that calculations that ignore coupling between adsorbates and the framework DOFs will not be able to give accurate diffusion coefficients for large molecules of this kind.

It is important to note that the diffusion of the largest molecules in Figure 2.5 is not associated with a structural transition of ZIF-8 from the LL to HL structure discussed above. We present evidence below that hydrocarbon adsorption in ZIF-8 near room temperature does not promote this transition. Even if ZIF-8 did convert to the HL structure upon adsorption of large molecules, the pore size of this structure is still considerably smaller than the values observed in Figure 2.5 for the largest diffusing species: Zeo++ yields a PLD of 3.35 (3.88) Å in the FF energy minimized LL (HL) structure and the HL structure reported by Fairen-Jimenez et al.<sup>150</sup> has a PLD of 3.81 Å.





**Figure 2.5** ZIF-8 window size distributions at 35 °C for configurations with adsorbates constrained to be in the window as described in the text.

### 2.4.2 Loading Dependence of Hydrocarbon Diffusion in ZIF-8

The self-diffusion coefficients of hydrocarbons in cage-type MOFs are a function of loading and understanding this loading dependence is necessary in determining optimal separation conditions. One issue not addressed in the current literature is whether the ZIF-8 framework adopts the HL form upon adsorption of hydrocarbons at 35°C. This LL to HL transition, as evident through a stepped isotherm, has not been observed experimentally for hydrocarbon adsorption.<sup>56</sup> Duren and coworkers, however, concluded from simulated adsorption of C<sub>2</sub>-C<sub>4</sub> paraffins in LL and HL structures of ZIF-8 at 0°C that experimental adsorption data qualitatively fit the simulated LL (HL) structure isotherm well at low (high) pressures.<sup>193</sup> To resolve this question, calculations that establish the thermodynamic stability of the LL and HL structures in the presence of

adsorbed species are needed. Osmotic framework adsorbed solution theory (OFAST) provides a method to achieve this goal.<sup>64</sup> We performed OFAST calculations and found that the transition from the LL to HL structure was not thermodynamically favorable for any C<sub>1</sub>-C<sub>4</sub> hydrocarbon at 35°C. Details of these calculations are given in Appendix A. As a result of these observations, all of our simulations for hydrocarbon diffusion were performed in the LL ZIF-8 structure.

Figure 2.6 shows alkane and alkene self-diffusion coefficients as a function of fractional loading. Liquid-like loadings,  $\theta_L$ , for all the alkanes and alkenes were computed from each species' bulk liquid density and the pore volume of ZIF-8, and they are tabulated in Appendix A. A higher loading of 22 molecules per cage was used for CH<sub>4</sub>. This allowed us to include a loading at which the methane self-diffusion begins to decrease due to steric hindrance in Figure 2.6. The CH<sub>4</sub> self-diffusivities computed with dcTST are fast enough that these quantities are also accessible from straightforward MD. The self-diffusivities of methane at 6 loadings were gathered using MD simulations during which self-diffusivities were computed using a computationally efficient order-n algorithm<sup>194</sup> as well as with our dcTST method. These MD derived self-diffusion coefficients agree quantitatively with the dcTST derived self-diffusion coefficients at higher loadings, validating our accounting for only the hopping rates of symmetric cage loadings. dcTST also accurately predicts a decrease in the methane self-diffusivity at high loadings. The error bars on the methane and *n*-butane data in Figure 2.6 were generated by running 3 simulations at each loading, and we expect the uncertainties on all the other data in Figure 2.6 to be similar.

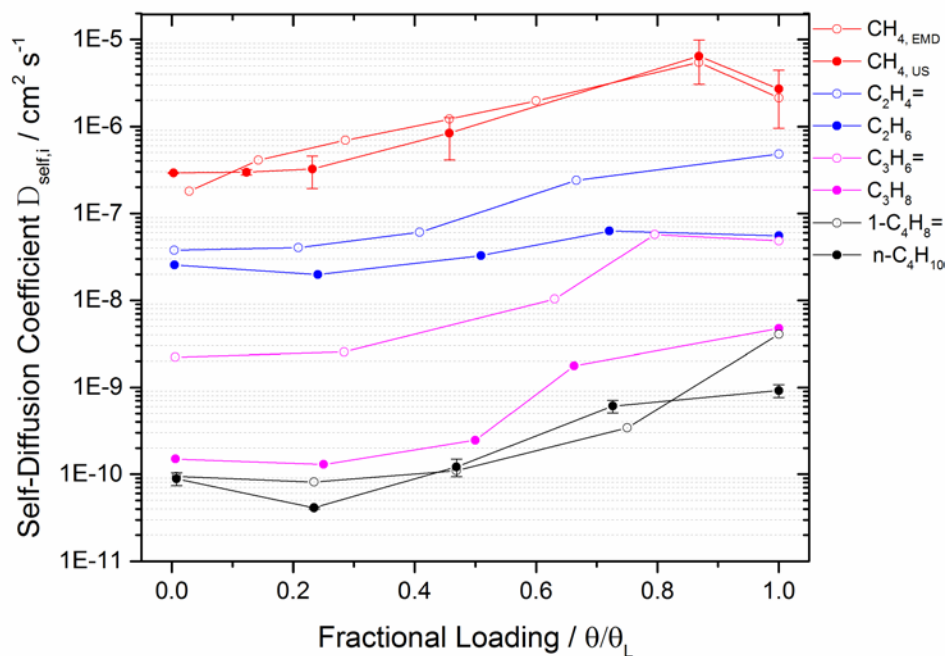


**Figure 2.6** Short alkane and alkene self-diffusion coefficients as a function of unary fractional loading in ZIF-8 at 35°C.

Over most of the fractional loading range, an increase in the self-diffusion coefficient is observed for all hydrocarbons. This behavior is attributed to a larger decrease in the free energy barrier of diffusion than the opposing decrease in the transmission coefficient due to adsorbate-adsorbate interactions. Examples of the free energy and transmission coefficient as a function of loading for propane are reported in Appendix A. Pusch and coworkers measured methane self-diffusivities in ZIF-8 using pulsed field gradient nuclear magnetic resonance (PFG NMR) over the loading range of 2.1 to 4.0 molec/cage, corresponding to bulk gas pressures of 7 and 14 bar respectively.<sup>195</sup> Their results indicate a modest increase in the self-diffusivity from  $8.8 \times 10^{-11}$  to  $1.4 \times 10^{-10}$  m<sup>2</sup>/s over the reported loading range while our calculations predict methane self-diffusivities of  $2.97 \times 10^{-11}$  to  $3.24 \times 10^{-11}$  m<sup>2</sup>/s over a loading range of 2.7-5.1

molec/cage. Pantatosaki et al. reported a methane self-diffusion coefficient of  $1.45 \times 10^{-10}$  m<sup>2</sup>/s at a loading of 5.0 molec/cage using PFG NMR at 298 K<sup>196</sup> while we report a self-diffusion coefficient of  $3.24 \times 10^{-11}$  m<sup>2</sup>/s at the same loading. Jobic et al. measured methane self-diffusivities in ZIF-8 using quasi-electric neutron scattering (QENS) at 200 K and over a loading range of 0.5-7.0 molec/cage.<sup>197</sup> They extrapolated this data to 298 K with an activation energy of diffusion of 5 kJ/mol. At 200 K and 298 K respectively, their reported self-diffusivities range from  $2.7 \times 10^{-11}$  to  $1.6 \times 10^{-10}$  m<sup>2</sup>/s (200 K) and  $7.3 \times 10^{-11}$  to  $4.1 \times 10^{-10}$  m<sup>2</sup>/s (298 K).

Zhang et al. reported methane self-diffusivities in ZIF-8 of  $4.2 \times 10^{-11}$  to  $3.1 \times 10^{-10}$  m<sup>2</sup>/s over a loading range of 0.3 to 12.5 molec/cage using an fully flexible NPT-MD simulations at 298 K.<sup>198</sup> We calculated methane self-diffusivities of  $2.9 \times 10^{-11}$  to  $6.5 \times 10^{-10}$  m<sup>2</sup>/s over a loading range of 0.1 to 19.0 molec/cage showing, as expected because they use the same force field, that our calculations are consistent with those of Zhang et al. Consistent with our finding that the free energy barrier for methane decreases by 11 kJ/mol over a loading of 5 to 19 molec/cage, they determined that the free energy barrier decreases by 10.3 kJ/mol over a loading range of 3 to 12.5 molec/cage.<sup>198</sup> Chmelik and coworkers measured ethane self-diffusivities of  $8.81 \times 10^{-12}$  to  $9.14 \times 10^{-12}$  m<sup>2</sup>/s in ZIF-8 at 298 K over a loading range of 0.2-3.7 molec/cage using infrared microscopy (IRM).<sup>199,200</sup> Similarly, we observed almost constant ethane self-diffusion coefficients of  $2.57 \times 10^{-12}$  to  $1.99 \times 10^{-12}$  m<sup>2</sup>/s (the decrease observed is within the uncertainty of the dcTST calculations) over a loading range of 0.1-3.1 molec/cage. All comparisons of simulated to experimental self-diffusivities for C<sub>1</sub>-C<sub>2</sub> hydrocarbons at higher loadings in ZIF-8 are reported as figures in Appendix A.

Figure 2.7 shows the alkane and alkene transport diffusivities in ZIF-8 as a function of fractional loading at 35 °C. These values were calculated with Equation 2.2 using the self-diffusivities in Figure 2.6 as well as GCMC derived adsorption isotherms of the hydrocarbons in ZIF-8. Very high fractional loadings were not included for

several of the hydrocarbons since the isotherms were only calculated up to 10 bar. This cut-off pressure was arbitrarily chosen but is not without meaning. Having to compress a gas stream is costly, and a separation process operating at high pressures may be financially unattractive.

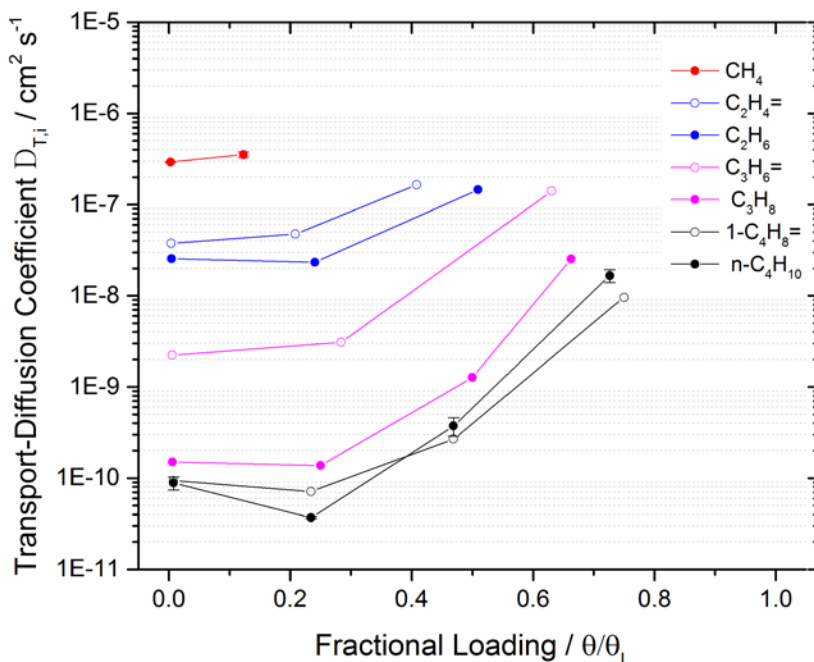


**Figure 2.7** Short alkane and alkene transport diffusion coefficients as a function of unary fractional loading in ZIF-8 at 35°C.

The transport diffusivities at finite loadings are greater than their self-diffusivity counterparts due to an increasing thermodynamic factor for all C1-C4 adsorbates. Chmelik and coworkers reported increasing unary methane transport diffusivities of  $8.8 \times 10^{-11}$  to  $3.78 \times 10^{-10}$   $m^2/s$  from infinite dilution to a loading of 2.1 methane molec/cage in ZIF-8 using IRM at 298K.<sup>201-203</sup> We observed a less sharp methane transport diffusivity increase of  $2.93 \times 10^{-11}$  to  $3.54 \times 10^{-11}$   $m^2/s$  over the loading range of 0.1-2.7 molec/cage. Pantatosaki et al. reported an increase in the methane transport diffusion in

ZIF-8 of  $3.70 \times 10^{-10}$  to  $1.62 \times 10^{-9}$  m<sup>2</sup>/s over a loading range of 0.1-5.3 molec/cage using fully flexible NVT-MD simulations.<sup>196</sup> For these simulations, Pantatosaki et al. utilized the generic DREIDING FF and allowed for quasi-free motion of the 2-methylimidazolate linker. Bux et al. measured single-component ethylene and ethane transport diffusivities in ZIF-8 using IRM at 25 °C.<sup>130,201</sup> For ethylene, they measured transport diffusivities of  $4.97 \times 10^{-11}$  to  $6.68 \times 10^{-10}$  m<sup>2</sup>/s in the loading range of 0.9-6.7 molec/cage while we report ethylene transport diffusivities of  $3.79 \times 10^{-12}$  to  $1.64 \times 10^{-11}$  m<sup>2</sup>/s in the loading range of 0.1-6.1 molec/cage. For ethane, they reported transport diffusivities of  $1.11 \times 10^{-11}$  to  $1.48 \times 10^{-10}$  m<sup>2</sup>/s in the loading range of 0.8-7.0 molec/cage while we calculated ethane transport diffusivities of  $2.57 \times 10^{-12}$  to  $1.46 \times 10^{-11}$  m<sup>2</sup>/s in the loading range of 0.1-6.6 molec/cage. They determined that the transport diffusivity is approximately constant for loadings of up to 4 molecules per cage, after which it increases rapidly for both adsorbates. We observe similar behavior, with both the ethylene and ethane simulated transport diffusivities increasing sharply over a loading range of 3-6 molecules per cage. The order of magnitude disagreement between the simulated and experimental ethylene/ethane results may indicate lack of fidelity in the force fields used in our calculations, although further studies will be needed to clarify this issue.

Chmelik measured propylene and propane transport diffusion coefficients using IRM at 298 K<sup>201</sup>, and reported propylene transport diffusivities of  $1.76 \times 10^{-13}$  to  $2.85 \times 10^{-12}$  m<sup>2</sup>/s over a loading range of 0.4-4.9 molec/cage. We report propylene transport diffusivities of  $2.22 \times 10^{-13}$  to  $1.41 \times 10^{-11}$  m<sup>2</sup>/s over a loading range of 0.1-7 molec/cage, in very good agreement with Chmelik's data. For propane, Chmelik reported transport diffusivities of  $4.86 \times 10^{-16}$  to  $2.48 \times 10^{-15}$  over a loading range of 0.8 to 4.5 molec/cage. We reported propane diffusivities of  $1.49 \times 10^{-14}$  to  $2.54 \times 10^{-12}$  m<sup>2</sup>/s in the loading range of 0.1-6.6 molec/cage. Chmelik reports that a diffusion mediated mixing solvothermal synthesis procedure used to produce 300 µm ZIF-8 crystals yielded propane diffusivities closer to  $10^{-14}$  m<sup>2</sup>/s but a conventional synthesis procedure<sup>204</sup> yielding smaller ZIF-8

crystals produced the diffusivities reported above. The propylene diffusivities measured in both sets of crystals, however, were in agreement. Chmelik attributed the slow diffusion of propane in the non-conventionally synthesized materials to defects, although the reason that this did not similarly effect propylene diffusion is unclear. Zhang et al. reported a propane corrected transport diffusivity of  $2.0 \times 10^{-14} \text{ m}^2/\text{s}$  in  $162 \text{ }\mu\text{m}$  ZIF-8 crystals, measured using the pressure decay kinetic uptake method<sup>56</sup>; our simulated values are in good agreement with this result. All comparisons of simulated to experimental transport diffusivities for C1-C3 hydrocarbons at higher loadings in ZIF-8 are reported as figures in Appendix A.

### 2.4.3 ZIF-8 Membrane Property Predictions

With the above treatment of the transport diffusivities and the adsorption isotherms, it is possible to make direct comparisons to experimental permeance data for ZIF-8 membranes. This is motivated by recent advances in engineering nanoporous materials that act as the selective layer in membrane separations.<sup>11,14,16</sup> Unary permeabilities were calculated numerically using the following relationship from Crank's derivation of concentration-dependent diffusion through a plane sheet<sup>112</sup>:

$$P = \frac{J}{\Delta P / l} = \frac{1}{\Delta P} \int_{C_{low}}^{C_{high}} D_{T,i}(c) dc \quad (2.5)$$

where  $P$  is the permeability,  $J$  is the flux,  $l$  is the membrane thickness,  $\Delta P$  is the transmembrane pressure drop, and  $C_{high}(C_{low})$  is the concentration of the adsorbate at the feed (permeate) sides of the membrane. Figure 2.8 shows unary permeabilities of C1-C4 hydrocarbons as a function of feed pressure with a constant permeate pressure of 0 bar. Unary ZIF-8 membrane fluxes with respect to feed pressure are reported in Appendix A

with an assumed membrane thickness of 1  $\mu\text{m}$ . At pressures above 0.1 bar in Figure 2.8, an increase in the propylene and propane permeabilities is observed whereas a sharp decrease is observed in the 1-butene and n-butane permeabilities. According to GCMC-derived adsorption isotherms, near-saturation is observed at bulk pressures of  $\sim 0.4$  bar for both 1-butene and n-butane. As the bulk pressure increases above  $\sim 0.4$  bar, the loading, and correspondingly, the transport diffusion of the C4 hydrocarbons, does not change significantly. However, according to Equation 2.5, there is a penalty in the permeability from an increasing pressure drop across the ZIF-8 film. At bulk pressures between 1 and 10 bar, an increase in the permeability is observed for the C3 hydrocarbons since the transport diffusion coefficient increases under increased loadings in that pressure range. Pressures above 10 bar would provide a similar decrease in the C3 hydrocarbon permeabilities as that observed for the C4 hydrocarbons. At pressures below 1 bar, several qualitative features are observed. Ethane has a higher permeability than ethylene through its stronger interaction with the ZIF-8 pore surface. This behavior is also observed for n-butane over both 1-butene and propane. Above 1 bar, however, we find that the order of permeabilities follows from the diffusion ranking (fastest to slowest): methane, ethylene, ethane, propylene, propane, n-butane/1-butene. The difference between the permeabilities of ethylene/ethane and n-butane/1-butene are within the uncertainty of the GCMC and MD calculations.



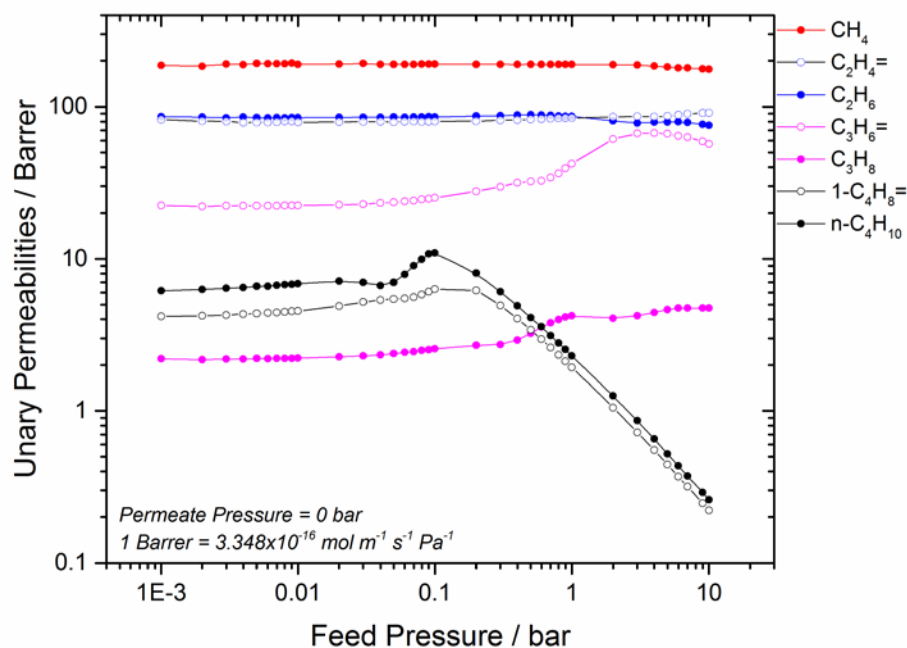


**Figure 2.8** Short alkane and alkene permeabilities as a function of feed pressure in ZIF-8 at 35 °C.

Table 2.1 shows permeability data from experiments with ZIF-8 membranes by Zhang et al.<sup>56</sup>, Pan et al.<sup>39,40,205</sup>, Brown et al.<sup>16</sup>, and Bux et al.<sup>130,131,204</sup> along with simulated permeabilities at corresponding pressure drops and 35 °C. We have included studies that measured the permeances of at least 2 linear hydrocarbons. For each comparison, the limits of integration in Equation 2.5 for the calculations were specifically set to match the experimentally reported feed and permeate bulk pressures. The four research groups noted here measured unary permeances using several different experimental methods: mixed matrix membrane permeation interpreted with a Maxwell model fitting, piezometric uptake rate measurement combined with adsorption isotherm data, the WK technique, and single gas permeation (SGP) with no sweep stream. Zhang et al. fabricated mixed matrix dense films containing 23.8 vol% ZIF-8 crystals and

obtained permeabilities for C<sub>1</sub>-C<sub>3</sub> hydrocarbons using the Maxwell model.<sup>56</sup> They also reported permeabilities for C<sub>3</sub>-C<sub>4</sub> hydrocarbons calculated using their measured corrected transport diffusivities and Langmuir isotherm fits to hydrocarbon adsorption data. Both methods yielded similar C<sub>3</sub>=/C<sub>3</sub> permeabilities, validating their use of the Maxwell model. Brown et al. grew pure 8.8±1.4 μm ZIF-8 membranes on the bore side of Torlon® hollow fibers and measured permeances for propylene, propane, and n-butane using the WK technique.<sup>16</sup> Pan et al. grew pure 2.5 μm thick ZIF-8 membranes on alumina discs and measured methane, ethylene, ethane, propylene, propane, and n-butane permeances with the WK technique with argon as a sweep gas.<sup>40</sup> Pan et al. also performed a follow-up study in which they grew pure ~2 μm thick ZIF-8 membranes on the outer surface of ceramic (yttria-stabilized zirconia) hollow fibers and measured methane, ethane, and propane permeances using the WK technique with argon at 1 bar as a sweep gas.<sup>205</sup> Bux et al. measured methane, ethylene and ethane unary permeances using SPG through a pure 25 μm thick ZIF-8 membrane on a alumina support covered by a smooth titania layer.<sup>130,131,204</sup> Most of these studies have reported permeances at 20-25 °C (room temperature) but we have assumed that the comparison with our simulated 35 °C permeabilities are warranted.

**Table 2.1** Comparison of simulated and experimental single-component hydrocarbon permeabilities through ZIF-8 thin-film membranes.

Adsorbate	Author	Technique	$l$ ( $\mu\text{m}$ ) / Support	T ( $^{\circ}\text{C}$ )	$P_{\text{Feed}}$ (bar)	$P_{\text{Drop}}$ (bar)	Exp. P (Barrer)	Sim. P (Barrer)
<b>CH<sub>4</sub></b>	Zhang <sup>56</sup>	M <sup>3</sup> P	- / M <sup>2</sup> DF	35	2.0	2.0	270±26	188
	Pan <sup>40</sup>	WK	2.5 / AD	23	1.01	1.01	576	189
	Pan <sup>205</sup>	WK	2 / CHF	25	1.01	1.01	717±60	189
	Bux <sup>131,204</sup>	WK	25 / TA	25	1.00	1.00	567	189
<b>C<sub>2</sub>H<sub>4</sub>=</b>	Bux <sup>130</sup>	SGP	25 / TA	20	6.0	5.0	1270	89
	Zhang <sup>56</sup>	M <sup>3</sup> P	- / M <sup>2</sup> DF	35	2.0	2.0	1100±500	85
	Pan <sup>40</sup>	WK	2.5 / AD	23	1.01	1.01	994	85
<b>C<sub>2</sub>H<sub>6</sub></b>	Bux <sup>130</sup>	SGP	25 / TA	20	6.0	5.0	299	78
	Zhang <sup>56</sup>	M <sup>3</sup> P	- / M <sup>2</sup> DF	35	2.0	2.0	430±130	81
	Pan <sup>40</sup>	WK	2.5 / AD	23	1.01	1.01	503	87
	Pan <sup>205</sup>	WK	2 / CHF	25	1.01	1.01	538±30	87
<b>C<sub>3</sub>H<sub>6</sub>=</b>	Zhang <sup>56</sup>	M <sup>3</sup> P	- / M <sup>2</sup> DF	35	2.0	2.0	210±95	42
	Zhang <sup>56</sup>	PURM•AI	-	35	2.0	2.0	390	42
	Brown <sup>16</sup>	WK	8.8 / THF	25	1.03	1.03	201.5	42
	Pan <sup>40</sup>	WK	2.5 / AD	23	1.01	1.01	77	42
<b>C<sub>3</sub>H<sub>8</sub></b>	Zhang <sup>56</sup>	M <sup>3</sup> P	- / M <sup>2</sup> DF	35	2.0	2.0	2.5±1.1	4
	Zhang <sup>56</sup>	PURM•AI	-	35	2.0	2.0	2.9	4
	Brown <sup>16</sup>	WK	8.8 / THF	25	1.03	1.03	22.0	4
	Pan <sup>40</sup>	WK	2.5 / AD	23	1.01	1.01	5	4
	Pan <sup>205</sup>	WK	2 / CHF	25	1.01	1.01	8±1	4
<b>1-C<sub>4</sub>H<sub>8</sub>=</b>								
<b>n-C<sub>4</sub>H<sub>10</sub></b>	Zhang <sup>56</sup>	PURM•AI	-	35	2.0	2.0	0.3	1
	Brown <sup>16</sup>	WK	8.8 / THF	25	1.03	1.03	18.5	2
	Pan <sup>40</sup>	WK	2.5 / AD	25	1.01	1.01	4.0	2

\*Simulated permeabilities calculated at 35°C with a transmembrane pressure drop corresponding to the experimental pressure drop. M<sup>3</sup>P=mixed matrix membrane permeation interpreted with a Maxwell Model; PURM•AI=piezometric uptake rate measurement combined with adsorption isotherm data; WK=Wicke-Kallenbach technique; SGP=single gas permeation; T=Torlon<sup>®</sup>, C=ceramic + HF=hollow fiber; M<sup>2</sup>DF=mixed matrix dense film; TA=titania on an alumina support; AD= $\alpha$ -alumina discs; 1 Barrer=3.348x10<sup>-16</sup> mol m<sup>-1</sup> s<sup>-1</sup> Pa<sup>-1</sup>=10<sup>-10</sup> cm<sup>3</sup>(STP)cm/(cm<sup>2</sup> s cmHg)

On the whole, we find order of magnitude agreement between our simulated values and those reported experimentally. We report  $C_2/C_3 = (\sim 2)$ , and  $C_3/C_3 = (\sim 11)$  predicted ideal selectivities at a feed pressure of 1 bar, a transmembrane pressure drop of 1 bar, and a temperature of 35 °C. This behavior was previously known through experimental results, but for the first time has been demonstrated with simulations. Contrary to our findings, most experimental studies report higher ethylene permeabilities than methane permeabilities and similar methane/ethane permeabilities. Our results predict that methane has a higher permeability than both ethylene/ethane. Bux et al. reported an ideal permeance separation factor of 4.2 of ethylene over ethane at a feed pressure of 6 bar, transmembrane pressure drop of 5 bar, and temperature of 20 °C whereas our simulated ideal permeance selectivity is 1.14. Comparison between the simulated and experimental adsorption isotherms reveals that the GCMC simulations underestimate both ethylene and ethane loading. Adsorbate-framework LJ interactions that more accurately reflect experimentally observed adsorption isotherms would likely improve our permeability predictions and possibly yield self-diffusivities in better agreement with experimental results. Such an investigation would be warranted but is outside the scope of this current study.

In considering the data above, it is important to note that experimental permeance studies are also fraught with possible uncertainties. Experimental papers typically report permeances since it is difficult to measure membrane thicknesses accurately. However, for consistency in Table 2.1, we have multiplied their experimentally measured permeances by their reported membrane thicknesses as visually measured from cross-sectional SEM images. MOF membranes grown on support materials can contain a variety of defects such as missing linkers within the MOF film on the unit cell scale<sup>206</sup> and exposed support material (e.g. pinhole defects) leading to higher than expected fluxes<sup>13</sup>. While still an ongoing subject of research, it is also possible that different

synthesis methods yield different chemical environments on the MOF film interfaces leading to non-negligible surface resistances.

## 2.5 Conclusions and Impact

In this chapter, we have computed the self-diffusivities of 15 adsorbates in flexible ZIF-8 as a function of temperature using dcTST and made extensive comparisons to reported experimental results. These calculations include the diffusion of a much wider range of adsorbates than had previously been examined in ZIF-8 while incorporating the effects of framework flexibility. Our results show that it is possible to compute self-diffusivities using “off the shelf” force fields (FFs) with computationally efficient methods that allow diffusion that is much slower than can be probed with conventional MD. Our simulations show that large adsorbates brace open the window of ZIF-8, effectively rendering prior methodologies including empty framework flexibility unsuitable for the calculation of tight-fitting adsorbate diffusivities. This work is also the first to use dcTST to study the effect of finite loadings on hydrocarbon diffusion while maintaining full flexibility of the nanoporous framework. While we examined only unary loadings of hydrocarbons in ZIF-8, our methods can be extended to study multi-component mixtures. The simulation techniques presented are well suited to predict MOF membrane properties in cage-type MOFs.

As is well known, the quality of MD predictions relies heavily on the quality of the FF. The diffusion activation energy barrier in materials like ZIF-8 is an exponential function of window size<sup>57</sup> and as a result even small changes in the adsorbate-adsorbent FF parameters can yield order of magnitude differences in diffusivity values in some cases.<sup>57,131,196,198</sup> In our calculations, we have used standard FFs without attempting to tune their properties in any way. These FFs appear to capture many features of adsorbate-framework interactions and framework flexibility effects accurately. The inability to directly compute diffusion coefficients for relevant molecules with previous methods,

however, means that these FFs have not been parameterized with methods that generate high quality information for configurations near the transition state that are crucial to diffusion. Combining the simulation methods we have demonstrated in this chapter with recent advances in deriving accurate adsorbate-framework FFs from DFT and other quantum chemistry calculations<sup>85,207</sup> may create a useful means to improve on the FFs available for simulating adsorbate diffusion in MOFs.

## CHAPTER 3

### TRANSFERABLE FORCE FIELD DEVELOPMENT DESCRIBING ZEOLITIC IMIDAZOLATE FRAMEWORK FLEXIBILITY

Quantitatively modeling adsorbate diffusion through zeolitic imidazolate frameworks (ZIFs) must account for the inherent flexibility of these materials. The lack of a transferable intramolecular ZIF force field (FF) for use in classical simulations has previously made accurate simulation of adsorbate diffusion in many ZIFs impossible. We resolve this problem by introducing a density functional theory (DFT) parameterized force field (FF) for ZIFs named the intraZIF-FF, which includes perturbations to the class I force fields previously used to model ZIFs. This FF outperforms ad hoc force fields at predicting ab initio relative energies and atomic forces taken from fully periodic ab initio molecular dynamics (MD) simulations of SALEM-2, ZIF-7, ZIF-8, and ZIF-90. We use the intraZIF-FF to predict the infinite dilution self-diffusion coefficients of thirty adsorbates with molecular diameters ranging from 2.66 to 7.0 Å in these four ZIFs. These results greatly increase the number of adsorbates for which accurate information about molecular diffusion in ZIFs is available.

#### 3.1 Introduction

Although metal-organic frameworks (MOFs)<sup>17,208</sup> have potential for use in molecular sieving<sup>209,210</sup>, catalytic<sup>23,211</sup>, liquid separation<sup>212</sup>, gas adsorption and storage<sup>213</sup>, electronic<sup>214</sup>, and sensing<sup>24</sup> applications, better engineering of MOF-based applications requires atomic-scale insight. MOFs are neither static nor rigid nanoporous materials. Coudert et al. classified the flexibility of MOFs that occurs upon thermal activation, pressure-induced strain, and adsorbate loading.<sup>47,215</sup> Flexibility categories include intraframework dynamics, negative thermal expansion, swelling, breathing, gate opening,

and topology-conserving metastable phase transitions. Some especially notable MOFs demonstrating these behaviors include zeolitic imidazolate frameworks (ZIFs), a chemically and thermally stable family of MOFs.<sup>41,216</sup> Representative examples of ZIF flexibility include, but are certainly not limited to, ZIF-4, ZIF-7, ZIF-8, and ZIF-90. ZIF-4 undergoes a reversible phase transition upon cooling through a cooperative rotation of the imidazolate linkers.<sup>217</sup> ZIF-7 exhibits a phase transition upon thermal activation<sup>218</sup> and gate opening when exposed to light alkenes and alkanes.<sup>4,52</sup> Tight-fitting adsorbates with kinetic diameters ( $> 4.5 \text{ \AA}$ ), larger than the pore limiting diameter (PLD) of ZIF-8 ( $3.4 \text{ \AA}$ ), can enter the ZIF-8 cavities due to the flexibility of the 2-methylimidazolate linkers.<sup>56</sup> ZIF-8 and ZIF-90 both undergo a metastable phase transition upon nitrogen loading at 77 K.<sup>42</sup>

The diffusivities of molecules in ZIFs are critical to the potential of these materials to be used for chemical separations.<sup>2</sup> Any effort to use ZIFs or other MOFs in membranes relies directly on the potential for these materials to achieve diffusion-based separations.<sup>11,16</sup> We recently used free energy sampling methods along with a force field (FF) describing the flexibility of ZIF-8 to simulate diffusion of 15 molecules in this widely studied material<sup>219</sup>. Our results showed good agreement with experimental data over a broad range of molecular sizes, including molecules considerably larger than ZIF-8's nominal pore diameter. They also showed that including the flexibility of ZIF-8 was critical in making accurate predictions of molecular diffusion. This implies that efforts to screen libraries of materials for diffusion-based separations based on simulations in rigid materials<sup>59,220</sup> cannot be expected to be quantitative.

Force fields (FFs) allowing modeling of flexibility in a number of MOFs have been developed. Greathouse and Allendorf implemented a FF for IRMOF-1 that reproduced framework collapse upon addition of water<sup>221</sup> and used it to examine negative thermal expansion, benzene self-diffusion, vibrational frequencies, and other structural properties<sup>222</sup>. They treated the intramolecular degrees of freedom (DOFs) of the benzene



dicarboxylate (BDC) organic linker with the consistent valence force field (CVFF) and the Zn-O interactions with nonbonded 12-6 Lennard-Jones (LJ) and coulombic interactions. Dubbeldam et al. examined negative thermal expansion of IRMOF-1, IRMOF-10, and IRMOF-16, using a hybrid nonbonded/bonded force field similar to that of Greathouse and Allendorf.<sup>223</sup> They departed from Greathouse and Allendorf by treating the oxygen atoms in the linkers with different parameters from the oxygen atoms in the metal-oxide cluster. Salles et al. implemented a FF for MIL-53(Cr) treating the organic moiety with the CVFF and parameterized bonded Cr-O interactions, using DREIDING<sup>224</sup> parameters as starting values, to reproduce structural features of the narrow and large pore structures upon energy minimization.<sup>66</sup> This FF predicted the large-narrow-large pore phase transition upon increased CO<sub>2</sub> loading as well as an activated transition from the narrow pore to large pore phases at 600 K. Gee et al. used FFs to model the intraframework dynamics of MIL-47 and MOF-48 and demonstrated better agreement of C<sub>8</sub> aromatic simulated and experimental adsorption selectivities.<sup>225</sup> Molecular mechanics (MM) simulations of MOF materials, however, are hindered by a lack of transferrable empirical potentials (force fields), but there has been progress on intramolecular MOF force field development.

The studies mentioned above provided insight into MOF flexibility but the FFs are not readily applicable to other materials. Several procedures are available for obtaining force fields using, for example, empirical methods, experimental data, or theoretically calculated Hessian matrices.<sup>226</sup> In the examples above general force field parameters (e.g. the Universal force field (UFF)<sup>227</sup>, DREIDING<sup>224</sup>, and AMBER<sup>228</sup>) were modified in an *ad hoc* manner to obtain experimentally observed MOF properties. This approach leads to what can be termed empirical force fields. Recently, Couprie et al. developed the Universal Force Field for Metal-Organic Frameworks (UFF4MOF), using the standard UFF parameterization procedure, that encompasses >99% of all MOFs in the Computation-Ready Experimental (CoRE) MOF database<sup>45</sup>; Couprie et al. noted that

dynamic properties may not be well modeled using UFF4MOF. An alternative is to develop a FF based on underlying quantum mechanical (QM) calculations. QM frequency based methods have been developed that identify bonded force constants from the diagonal elements of the dynamical (i.e., Hessian) matrix. These methods can be sensitive to the choice of internal coordinates.<sup>229</sup> Other methods include potential energy and force matching of empirical potentials to ab initio molecular dynamics (AIMD) data.<sup>230</sup> The ForceBalance FF fitting package of Wang et al. enables a hybrid approach that combines any available ab initio and experimental data.<sup>231</sup>

The first ab initio parameterized MOF FF was developed by Tafipolsky et al. for MOF-5,<sup>232</sup> which Amirjalayer et al. subsequently used to accurately predict the self-diffusion coefficient of benzene<sup>233</sup>. Bureekaew et al. developed the MOF-FF based purely on ab initio frequency reference data and a genetic algorithm (GA) to fit only the bonded terms, having predetermined the non-bonded terms, for several MOF families.<sup>234</sup> Bristow et al. parameterized the so-called BTW-FF for MOFs, using Molecular Mechanics 3 (MM3) empirical potential<sup>235</sup>, also with a frequency based method.<sup>236</sup> QuickFF, developed by Vanduyfhuys et al., utilizes a frequency based method with purely harmonic potential describing bonded interactions.<sup>237</sup> Rogge et al. studied the mechanical stability of UiO-66, -67, and -68 MOFs containing missing linker defects using force fields derived from QuickFF.<sup>238</sup>

Multiple studies have modeled ZIF frameworks using flexible FFs. Hertäg et al. performed the first molecular dynamics (MD) simulation of flexible ZIF-8 using the DREIDING and AMBER FFs, demonstrating that flexibility was important in predicting the diffusion of H<sub>2</sub> and CH<sub>4</sub>.<sup>131</sup> Battisti et al. made self-diffusion predictions for CO<sub>2</sub>, CH<sub>4</sub>, N<sub>2</sub>, and H<sub>2</sub> in ZIF-2, -4, -5, -8, and -9 using the DREIDING FF to model flexibility; their predictions did not include charges on the ZIF framework.<sup>239</sup> Thornton et al. screened seven ZIF materials for the separation of H<sub>2</sub>, CO<sub>2</sub>, N<sub>2</sub>, and CH<sub>4</sub>, modeling ZIF flexibility with the DREIDING force field.<sup>240</sup> Zheng et al. used the AMBER FF to model

ZIF-8 with atomic charges and more accurately predicted CO<sub>2</sub> self-diffusion as a function of loading.<sup>133</sup> Gee et al. studied small alcohol diffusion in ZIF-8 and ZIF-90, comparing both the AMBER and DREIDING FFs.<sup>134</sup> Zhang et al. introduced a ZIF-8 FF comprised of AMBER parameters with specifically tuned N-Zn-N-C proper dihedrals that reproduces the reversible structural transition upon high N<sub>2</sub> loading at 77 K.<sup>174</sup> Chokbunpiam et al. used the Hertäg's AMBER version of the ZIF-8 FF to predict ethane diffusion.<sup>241</sup> Krokidas et al. parameterized a harmonic ZIF-8<sup>242</sup> and ZIF-67<sup>243</sup> FF using a frequency based method for stretching and bending terms and AMBER parameters for the dihedrals. Du et al. extended Zhang et al.'s ZIF-8 FF to treat the temperature-induced reversible phase change of ZIF-7.<sup>218</sup> Phuong et al. used the AMBER and DREIDING variants of the ZIF-90 FF proposed by Gee et al. to predict CH<sub>4</sub> diffusion in ZIF-90.<sup>244</sup> Gao et al. proposed a coarse-grained FF and studied pressure and temperature induced structural changes for various ZIF structures.<sup>245</sup>

Here we introduce a flexible ZIF force field (i.e., intraZIF-FF) from a series of density functional theory (DFT) calculations. Our FF is constructed to reproduce the static and dynamic behavior of ZIFs observed in ab initio simulations. We have added perturbations to the traditional class I ZIF force fields by including a Morse potential describing the Zn-N bonds and a 3-term Fourier series describing the N-Zn-N-C proper torsions. We make thorough comparisons of the ability of our intraZIF-FF to the AMBER FF to predict various thermodynamic and kinetic properties of ZIFs. Although the studies mentioned above have examined diffusion of a small number of molecules in flexible models of ZIFs, there is limited information available on how molecular diffusion varies as a function of molecular size, shape and functionality. Below, we use the intraZIF-FF to predict the self-diffusivities at room temperature of thirty adsorbates with molecular diameters ranging from 2.66 to 7.0 Å in four chemically distinct ZIFs with the SOD topology, SALEM-2, ZIF-7, ZIF-8, and ZIF-90. For the majority of adsorbates we examined, there exists no prior experimental or predicted diffusion data,

therefore our results greatly expand the number of examples for which diffusivities are available. For the ZIFs studied, it would appear from simple geometric arguments that the suitability of these materials as molecular sieves would be comparable. However, local chemical structure differences arising from flexibility as well as the interaction of adsorbates in the ZIF windows lead to drastically different diffusion characteristics than expected. Our study provides the basis for screening diffusion quantitatively in a large variety of ZIF materials, offering a clear path forward for identifying kinetic chemical separations where ZIFs may be useful.

### 3.2 Parameterization of the intraZIF Force Field

Our ab initio derived class I intraZIF-FF is intended to represent all DOF in an adsorbate-free ZIF and uses the general form

$$E_{\text{intraZIF}} = \sum E_{\text{stretch}} + \sum E_{\text{bend}} + \sum E_{\text{proper}} + \sum E_{\text{coul}} + \sum E_{\text{vdW}} \quad (3.1)$$

Bonded potentials include stretching and bending modes and proper dihedrals. Nonbonded potentials include electrostatic interactions through assignment of point charges and van der Waals interactions through a Buckingham potential. Fitting of bond and angle parameters was performed through a frequency based method while proper dihedral parameters were fit according to a potential energy matching; both using QM cluster calculations. Representation of metal-linker interactions is challenging since there are substantial polarization effects from the charge on the metal ions as well as changes in the coordination sphere.<sup>246</sup> Metal-linker interactions can be described by bonded, nonbonded, and semi-bonded approaches, each approach having certain advantages and limitations.<sup>247-250</sup> The intraZIF-FF neglects local polarization effects and charge transfer, which could potentially better describe Zn-imidazolate interactions.<sup>251</sup> A comparison of intraZIF-FF parameters to the AMBER-FF parameters and additional information is reported in Appendix B (Tables B.1, B.2, B.3, and B.4).

### 3.2.1 From Bulk Structure to Cluster Models

Here we describe our method for creating clusters representing the parent ZIFs. The experimentally determined crystal structures with disorder resolved and solvent removed were taken from the Cambridge Structural Database (CSD) with the following structure identifiers<sup>44</sup>: ZIF-7 (Park et al., *VELVIS*)<sup>41</sup>, ZIF-8 (Park et al., *VELVOY* and Wu et al., *OFERUN*)<sup>41,175</sup>, ZIF-90 (Morris et al., *WOJGEI*)<sup>252</sup>, and SALEM-2 (Hupp et al., *IMIDZB10*)<sup>253</sup>. The geometries of these four bulk ZIF structures were energy minimized using plane wave density functional theory (DFT) as implemented in the Vienna Ab initio package (VASP),<sup>155,254</sup> version VASP5.3.5, using the PBE-GGA<sup>255,256</sup> functional with D2 dispersion corrections<sup>257</sup>. We also optimized all periodic structures with the D3(BJ) dispersion correction including damping.<sup>258,259</sup> Reciprocal space was sampled at the  $\Gamma$ -point and all calculations used a 700 eV energy cutoff. Atomic forces were converged to  $< 0.03$  eV/Å for both unit cell and atomic position relaxations.

Using these energy minimized parent structures, clusters were excised containing a central imidazole linker and the 6 nearest neighbor (NN) linkers that share the two common Zn atoms. No terminations on the terminal imidazolate linkers were necessary. The atomic positions of these clusters were energy minimized using VASP with the PBE functional without D2 corrections with an energy cutoff of 400 eV with an atomic force convergence of  $< 0.01$  eV/Å. A cubic  $25 \times 25 \times 25$  Å supercell was used for the imidazolate (Im), imidazolate-2-carboxaldehyde (ImCA), and 2-methylimidazolate (mIm) clusters while a cubic  $30 \times 30 \times 30$  Å supercell was used for benzimidazolate (BzIm) clusters. These VASP settings were also applied to the potential energy scans described below. Figure 3.1 shows the four optimized clusters containing the Im, BzIm, ImCA, and mIm linkers. Atomic charges on the clusters were assigned using the Density Derived Electrostatic and Chemical (DDEC) method of Manz et al.<sup>260</sup> As shown in Appendix B (Figures B.14, B.15, B.16, and B.17), the charges on the central linker in these clusters were similar to those from the bulk structures.

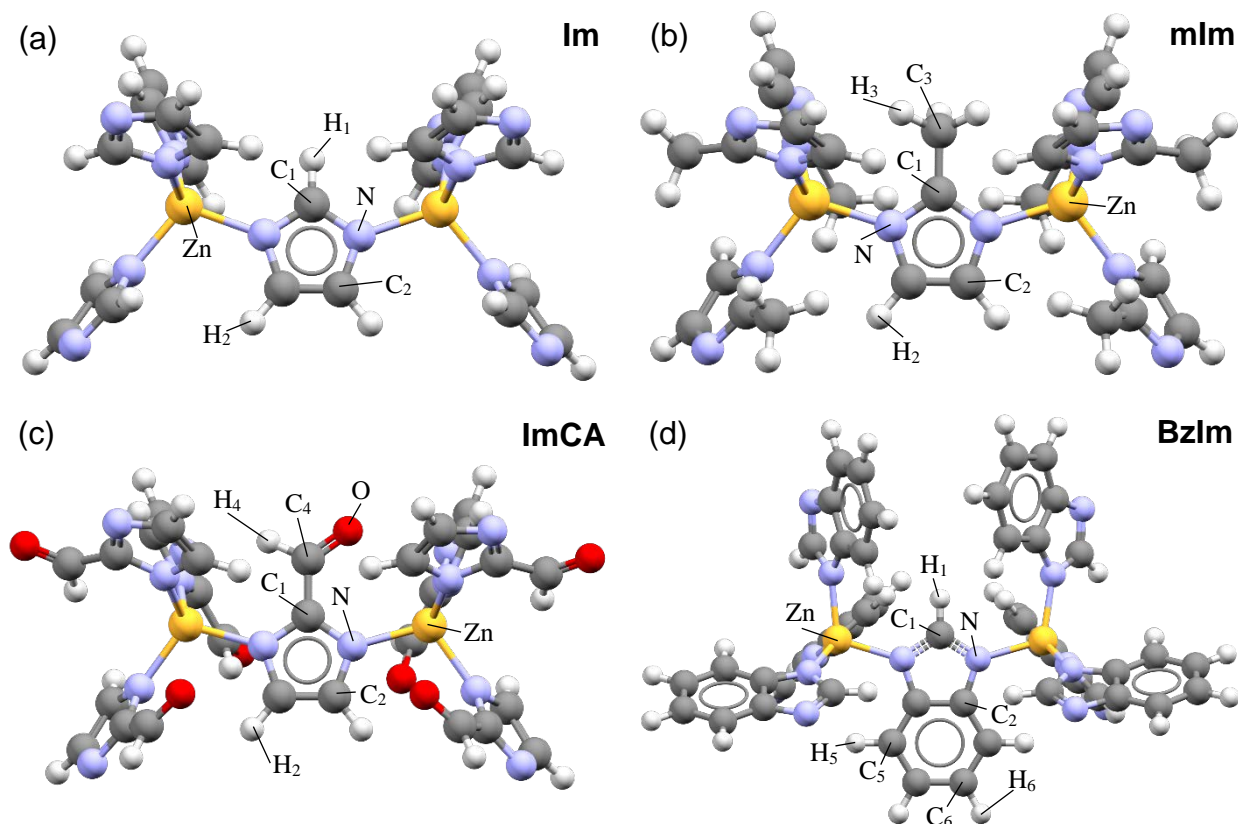


**Figure 3.1** Cluster models for the (a) imidazole (Im), (b) 2-methylimidazole (mIm), (c) imidazole-2-carboxaldehyde (ImCA), and (d) benzimidazole (BzIm) linkers. C, N, H, O, and Zn atoms represented by grey, purple, off-white, red, and gold spheres. Each of the atom types are labelled according to their unique atomic charges.

### 3.2.2 van der Waals and Coulombic Interactions

Since stretching and bend terms account for short range interactions, we chose to exclude bonded pairs (1-2 interactions) and valence angles (1-3 interactions) from van der Waals and electrostatic interactions. Pairs of atoms separated by 3 consecutive bonds (1-4 interactions) were also excluded from pair interactions. For comparison, the AMBER FF<sup>261</sup> scales the 1-4 van der Waals and electrostatic interactions by a factor of 1/2 and 5/6 respectively. Intraframework van der Waals interactions were modeled using a Buckingham potential

$$E_{\text{vdW},ij} = Ae^{-r_{ij}/\rho} - \frac{C}{r_{ij}^6} \quad (3.2)$$

Following the MM3<sup>235,262</sup> FF, the three parameters in the Buckingham potential correspond to an energy parameter  $\varepsilon_{ij}$  and the sum of the vdW radii of the two interacting atoms  $r_{ij}^0$ :

$$A = 1.84 \times 10^5 \varepsilon_{ij}, \rho = \frac{r_{ij}^0}{12}, C = 2.25 \varepsilon_{ij} (r_{ij}^0)^6 \quad (3.3)$$

The vdW parameters used for the intraZIF-FF are reported in Table B.5, and Lorentz-Berthelot mixing rules were applied to generate cross terms. Coulombic interactions were modeled using a hybrid approach, with some atomic interactions modeled with a standard coulombic interaction potential and others with a Debye damping factor added to the coulombic interaction:

$$E_{\text{coul},ij} = \frac{Cq_i q_j}{\varepsilon r_{ij}} \quad \text{and} \quad E_{\text{Debye},ij} = \frac{Cq_i q_j}{\varepsilon r_{ij}} e^{-\kappa r_{ij}} \quad (3.4)$$

The Debye length  $\kappa$  is set to  $0.33 \text{ \AA}^{-1}$ . The 1-4 interactions are included for atomic interactions that use the Coulombic interaction potential with the Debye damping parameter.

We set specific Debye interactions to obtain  $< 1.0\%$  error between the experimental unit cell volume and the volume predicted by the intraZIF-FF. These specific interactions only include Zn-Zn and Zn- $X_{\text{organic}}$  interactions, where  $X_{\text{organic}}$ =H, C, N, or O. Setting these interactions was performed through a pseudo-bisection method (i.e. targeted trial-and-error) procedure during which attractive (repulsive) coulombic interactions are treated with a Debye interaction when the unit cell volume was greater than (less than) the experimental unit cell volume. The experimental ZIF unit cells were determined at specific temperatures and pressures as recorded in Table 3.1. We therefore performed a series of NPT simulations on the empty parent ZIFs using LAMMPS with a vdW and coulomb cutoff of  $15.5 \text{ \AA}$  and a 1.0 fs timestep. Cell parameters were allowed to change anisotropically but the cell angles were fixed. Coulombic interactions utilizing the Debye damping parameter are summarized in Appendix B (Table B.9).

**Table 3.1** Comparison of experimental and intraZIF predicted unit cell lattice parameters and volumes.

ZIF, Conditions	Exptl. XRD	intraZIF-FF				Volume		
	T / K, P / atm	a (c)/ Å	a / Å	b / Å	c / Å	XRD V / Å <sup>3</sup>	FF V / Å <sup>3</sup>	% Error
SALEM-2	100, 1.0	16.83	16.88±0.06	16.85±0.07	16.80±0.07	4767	4778	+0.23
ZIF-7	258, 1.0	22.99	22.84±0.08	22.84±0.09	16.10±0.04	7214	7275	+0.84
		(15.76)						
ZIF-8	258, 1.0	16.99	16.96±0.07	16.97±0.08	16.97±0.06	4904	4883	-0.44
ZIF-90	100, 1.0	17.27	17.40±0.04	17.36±0.04	17.08±0.04	5151	5159	+0.16

### 3.2.3 Stretching and Bending Modes

The Seminario method, based on the Cartesian Hessian matrix, was used for determining bond and angle force constants.<sup>229</sup> Hessian matrices were generated using the finite difference method implemented in VASP using two displacements of 0.005 Å on either side of the minimum. Only translation DOF of atoms associated with the central linker and the tetrahedral metal centers (i.e. two Zn's and the three N's on terminal linkers) were probed. The resulting bonding and angle force constants are reported in Appendix B.

Bonds and angles with low spring constants are poorly described by harmonic functions. The Zn-N coordination has a harmonic spring constant of 67.16 kcal mol<sup>-1</sup> Å<sup>-2</sup> for the mIm cluster according to the Seminario method. The ZIF-8 FFs of Zheng et al. and Zhang et al. respectively use spring constants of 78.5 kcal mol<sup>-1</sup> Å<sup>-2</sup> and 86.0 kcal mol<sup>-1</sup> Å<sup>-2</sup>. To better understand the Zn-imidazolate interactions, Born-Oppenheimer molecular dynamics (BOMD) on the parent ZIFs were carried out using CP2K (version 2.6)<sup>263</sup>. Energies and forces were computed from density functional theory (DFT) as implemented in the module QUICKSTEP<sup>264</sup>. In these calculations, the self-consistent field (SCF) minimizer was based on the orbital transformation method<sup>265</sup>, and a mixed



Gaussian and Plane-Wave (GPW) method<sup>266,267</sup> was used in combination with PBE<sup>255</sup> Goedecker-Teter-Hutter (GTH) pseudopotentials<sup>268,269</sup>. The plane wave and DZVP-MOLOPT-GTH auxiliary basis set cutoffs used for SALEM-2, ZIF-7, and ZIF-8 were 550 and 70 Ry, respectively. 600 and 70 Ry cutoffs were used for ZIF-90 due to the presence of oxygen atoms. The dispersion correction DFT-D3 with damping from Becke and Johanson<sup>258</sup> (BJ) was applied to all simulations with a cutoff of 16 Å. First-principles molecular dynamics (MD) simulations were propagated for the four ZIF structures at 700 K and 1 bar in the NPT ensemble using the Nosé-Hoover thermostat<sup>270</sup> and a time-step of 1 fs. Additional NPT BOMD simulations were also performed at 1 bar and 308.15 and 500 K for only ZIF-90 and SALEM-2. In all BOMD simulations, the simulation volume was a unit cell of the structure with periodic boundary conditions (PBC). This defined a simulation volume containing 204, 522, 276, and 252 atoms for SALEM-2, ZIF-7, ZIF-8, and ZIF-90, respectively.

The mean of the Zn-N bond length is temperature-dependent (Figure B.23a) indicating that an anharmonic description is needed. To this end, we parameterized a Morse potential

$$E_{\text{Zn-N},ij} = \sum D_e (1 - e^{-\alpha(r_{ij} - r_{ij}^0)})^2 \quad (3.5)$$

where  $D_e$  is the depth of the potential well,  $\alpha$  is the stiffness parameter, and  $r_{ij}^0$  is the equilibrium bond distance. A potential energy (PE) scan was performed along the Zn-N bond for bond lengths from 1.8-2.6 Å. The total differential energy determined from the PE scan with the energy minimized cluster as the reference state was decomposed into three contributions:

$$\Delta E_{\text{total}}^{\text{PBE}} = \Delta E_{\text{bond}} + \Delta E_{\text{electrostatic}} + \Delta E_{\text{vDW}} \quad (3.6)$$

In Equation 3.6 above, we assume that vDW contributions are negligible since D2 corrections were not included in our cluster calculations. To decompose the total differential PBE energy between the bonded and electrostatic contributions,

LAMMPS<sup>186,271</sup> was used to determine the electrostatic contribution using the tags coul/cut with a cutoff of 25 Å and special bonds in a 50×50×50 Å supercell. Charges were obtained for the individual atoms in the clusters using the DDEC method. Small deviations from the energy optimized structure were found to have a negligible electrostatic contribution to the PBE potential energy as shown in Appendix B (Figures B.1b, B.5b, B.7b, and B.10b). We therefore assumed for simplicity that  $\Delta E_{total}^{PBE} \approx \Delta E_{bond}$ . The bond dissociation energies were not treated as a fitting parameter. Instead, the four clusters were cleaved along one Zn-N bond with the N on the central linker; this yielded two fragments termed “large” and “small” accordingly. An energy optimization was performed for both fragments according to the methods described already. Bond dissociation energies were determined as:

$$D_e = E_{cluster}^{PBE} - (E_{large\_frag}^{PBE} + E_{small\_frag}^{PBE}) \quad (3.7)$$

The resulting bond dissociation energies, stiffness parameters, and equilibrium bond lengths for all the clusters are reported in Appendix B.

The spring constants for N-Zn-N and Zn-N-C angles were also found to be low. The N-Zn-N angle distributions have a mean that is essentially temperature-independent (Figure B.23b), implying that a harmonic potential is appropriate. While the histograms for ZIF-90 in Figure B.23b imply that a harmonic potential is the appropriate functional form, the N-Zn-N and Zn-N-C were reparametrized using fits to potential energy scans using

$$\Delta E_{total}^{PBE} = \sum \Delta E_{angle} + \Delta E_{coul} + \Delta E_{vdW} \quad (3.8)$$

In a similar fashion to the Zn-N bond fitting procedure, we assume for simplification that  $\Delta E_{total}^{PBE} \approx \sum \Delta E_{angle}$ . The fitting procedure yields lower spring constants ( $\sim 18 \text{ kcal mol}^{-1} \text{ deg}^{-2}$ ) than the Seminario method ( $\sim 37 \text{ kcal mol}^{-1} \text{ deg}^{-2}$ ), probably due to imprecision in

the calculation of the Hessian for these modes in the DFT data underlying our application of the Seminario method.

### 3.2.4 Dihedrals and Improper Torsions

To obtain relevant configurations and potential energies for fitting dihedral parameters, BOMD simulations of the clusters in the NVT ensemble were performed using VASP allowing only the DOF on the central linker and the two Zn atoms to move with a No  -Hoover thermostat, a 1.0 fs time step and an energy cutoff of 400 eV. Using only the cluster rather than the full unit cell greatly reduces the number of dihedrals involved in our fitting. BOMD simulations of the clusters were performed at 100, 300, 500, and 700 K to access a representative range of relative energies (Figures 3.2a and 3.2b insets).

When determining our quality of fit as well as comparing the AMBER and intraZIF FFs, we report the mean absolute deviation (MAE), root mean squared deviation (RMSD), and mean signed difference (MSD). We also include a normalized root mean squared deviation (NRMSD)

$$NRMSD = 100 \left( \frac{RMSD}{\sigma_{QM}} \right) \quad (3.9)$$

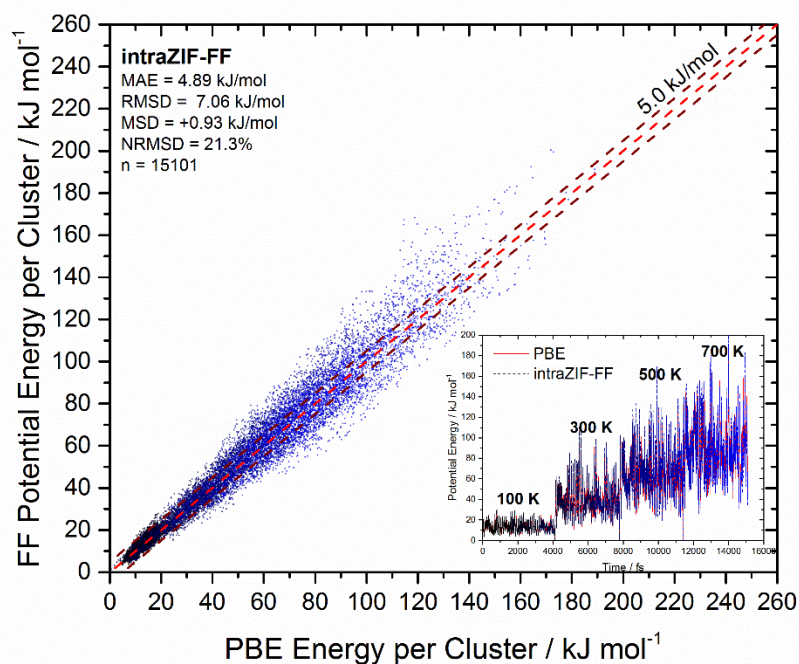
where the RMSD is calculated between the MM and QM energies and  $\sigma_{QM}$  is the standard deviation of the QM energies. As a heuristic, an NRMSD approaching ~20% has been identified as acceptable for a force field utilizing fixed point charges.<sup>272</sup>

We used a potential energy matching procedure developed by Guvench and Mackerell<sup>273</sup> to parameterize the force constants for the proper dihedrals. No improper dihedrals are included in the intraZIF-FF. We assumed that the PBE relative energies for each cluster include only stretching, bending, proper dihedrals, and Coulombic interactions. LAMMPS was used to determine the FF contribution of the stretching, bending, and Coulombic terms and the difference between the PBE and these FF energies

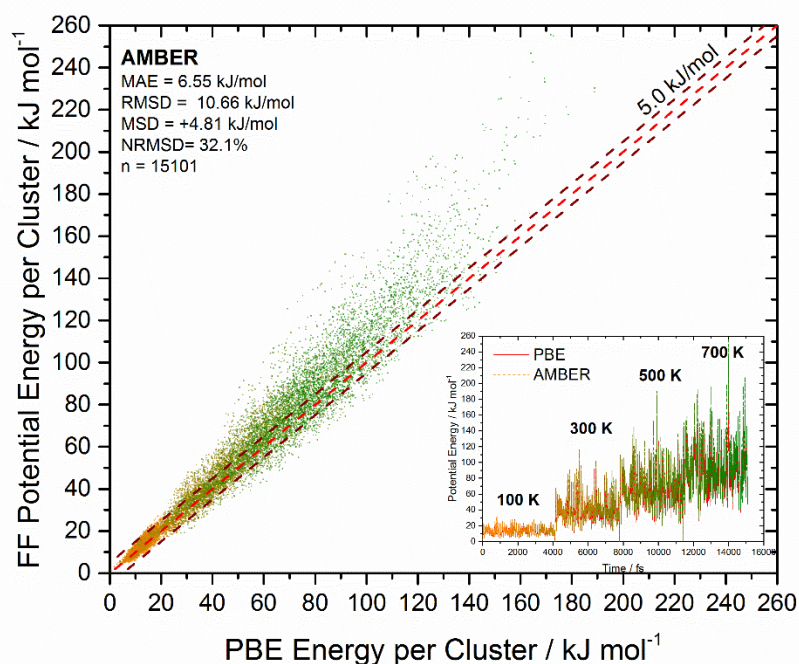
was attributed to the proper dihedrals. A simulated-annealing Monte Carlo procedure with exponential cooling was used to fit a Fourier series for each dihedral (e.g. 59 dihedrals for the Im cluster).<sup>273</sup> The optimization protocol used a starting temperature of 5000 K with four  $0.5 \times 10^6$ -step simulated-annealing runs, and spring constant constraint of [0.0, 4.5] kcal mol<sup>-1</sup> with fixed phase angles. For the imidazole ring dihedrals, the multiplicity (i.e. number of energy minima) of the Fourier series was fixed at  $n=2$  for all the imidazole ring dihedrals and the N-Zn-N-C dihedrals contain multiplicities of  $n=1, 2$ , and 3. All optimized spring constants are reported in Tables B.1, B.2, B.3, and B.4. As a representative example, the RMSD and NRMSD for the Im cluster was 8.90 kJ mol<sup>-1</sup> and 26.8% before the inclusion of any proper dihedrals and the RMSD was 7.06 kJ mol<sup>-1</sup> and 21.3% after inclusion of the dihedrals from the dihedral fitting procedure.

Figure 3.2 compares the PBE energies with results from the intraZIF-FF and AMBER-FF for the BOMD simulations on the Im cluster. The NRMSD for the AMBER force field is greater at 32.1%, demonstrating the ability of the intraZIF-FF to better represent relative energies. Closer examination of low energies ( $< 20$  kJ mol<sup>-1</sup>) reveals that the AMBER and intraZIF FFs represent low energies with similar accuracy (Figure B.4). Similar plots are available for the BzIm, mIm, and ImCA clusters in Appendix B (Figures B.6, B.8, and B.11). In Section 3.3.4 we also compare the intraZIF and AMBER FFs to fully periodic BOMD data, not to be confused with the BOMD simulations of the clusters. BOMD simulations on the full unit cells were not used to fit the intraZIF-FF.

(a)



(b)



**Figure 3.2** Relative energy comparisons between PBE and (a) the intraZIF-FF including Fourier dihedrals from the potential energy fitting and (b) the AMBER-FF using standard cosine proper dihedrals for the Im cluster. Insets represent the concatenated relative energy time series for the simulations with increasing temperature. The color code (black to blue/intraZIF and orange to green/AMBER) is designed to easily identify the low and high energy regions.

### 3.3 Five Independent Tests of the IntraZIF Force Field

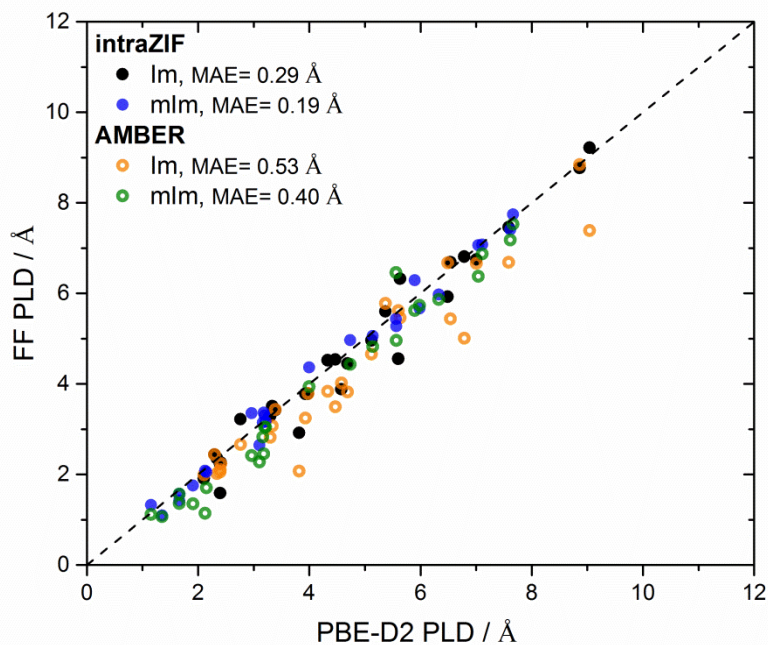
#### 3.3.1 Structural Properties

There are many criteria for assessing the quality of a MOF FF. An initial approach is to measure structural properties for energy minimized structures. To this end, we compared densities ( $\rho$ ), pore limiting diameters (PLDs)<sup>59</sup>, largest cavity diameters (LCDs), and accessible surface areas (ASA) predicted by PBE-D2 and PBE-D3(BJ) to those predicted by the AMBER and intraZIF FFs. Energy minimizations for each FF were performed in LAMMPS using both the conjugate gradient and Hessian-free truncated Newton Raphson algorithms to relax both the unit cell parameters and atomic positions. Zeo++<sup>190</sup> was used to determine the PLDs, LCDs, ASAs, and AVs, with a probe radius of 1.3 Å and 10000 and 50000 Monte Carlo cycles for the ASA and AV calculations. Tables B.10, B.11, B.12, and B.13 summarize these structural properties of SALEM-2, ZIF-7, ZIF-8, and ZIF-90. We find better agreement to the DFT predicted structural properties using the intraZIF-FF since the AMBER-FF predicts that the unit cell parameters contract significantly for the four materials. We fit the intraZIF-FF to experimental crystal structure lattice parameters at the temperatures these structures were refined; these structural comparisons are made with the energy minimized structures so the intraZIF-FF was expected to yield better agreement than the AMBER-FF.

To expand the set of structures used for comparisons, we also performed energy minimizations using PBE-D2, the AMBER-FF, and the intraZIF-FF for the Im and mIm hypothetical ZIF polymorphs reported by Baburin et al.<sup>274,275</sup> The structural information gleaned from these two sets of polymorphs was not used to fit the intraZIF-FF. Figures 3.3a and 3.3b compares the PLDs and ASA of the PBE-D2 polymorphs to those of the intraZIF and AMBER polymorphs. Figures B.18a and B.18b compare the densities and LCDs. The intraZIF-FF more closely reproduces structural features of both sets of polymorphs than the AMBER-FF. For all the Im and mIm polymorphs, the AMBER-FF over predicts the densities (i.e. under predicts unit cell volume). Even more important for

adsorption and diffusion screening studies are accurate prediction of PLDs and LCDs; the intraZIF-FF lowers the MAE for these two quantities by nearly 50% as seen in Figures 3.3a and 3.3b. Furthermore, several of the AMBER-FF energy minimized structures predict a zero accessible surface area for a 2.6 Å diameter spherical probe. The intraZIF-FF only predicts a significantly reduced accessible surface area for the Im-*qtz* polymorph.

(a)



(b)

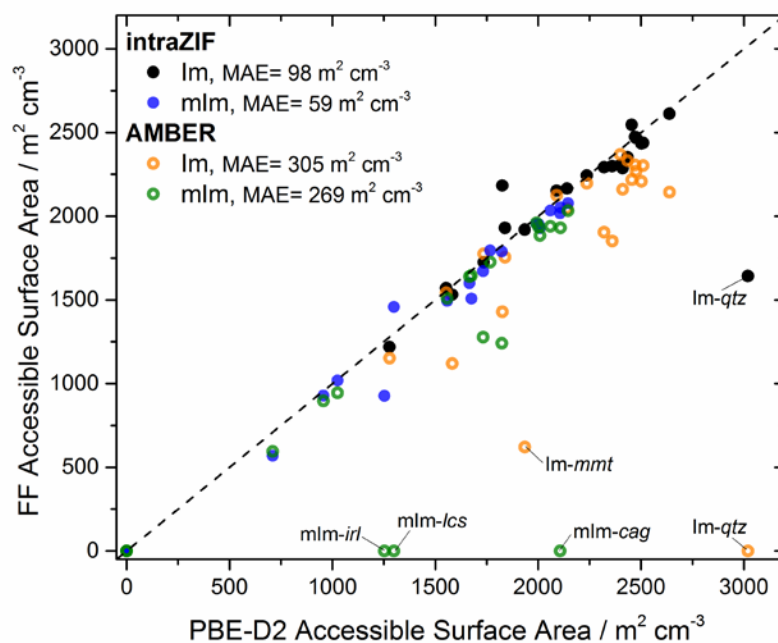


**Figure 3.3** Parity plots for (a) PLDs and (b) accessible surface areas as predicted by PBE-D2 and the intraZIF (blue/black closed circles) and AMBER (orange/green) force fields. There are 27 Im polymorphs (black/orange circles) including SALEM-2 and 25 mIm polymorphs (blue/green circles) including ZIF-8.



### 3.3.2 Thermodynamic Stability of Im and mIm ZIF Polymorphs

ZIFs exhibit polymorphism<sup>41</sup> and there are abundant experimental and computational studies examining their thermodynamic stability<sup>274,275</sup>. Methods such as the osmotic adsorbed solution theory<sup>276</sup> (OFAST) and thermodynamic cycles examining relative stability<sup>276</sup> require the relative configurational potential energies of different polymorphs and even different metastable phases of specific polymorphs<sup>218</sup>. Studying the thermodynamics of extended ZIF defects and predicting how these extended defects influence diffusion requires the use of a FF due to large system sizes.<sup>277</sup> For these reasons, it is useful to have a force field that predicts the correct thermodynamic stability trends. Therefore, we predicted the relative configurational potential energy ranking of the twenty-seven Im and twenty-five mIm ZIF polymorphs mentioned above with respect to the dense *zni* polymorph using PBE-D2 as well as the AMBER and intraZIF FFs, as shown in Figure 3.4. Our DFT calculations predict the *zni* topology to be the most stable polymorph of both ZIFs, in agreement with prior computational studies.<sup>274,275,278</sup> We also compared the relative energy ranking to PBE-D3(BJ) calculations as reported in Tables B.18 and B.19 finding that both dispersion correction methods yield the similar rankings.

Neither the AMBER nor the intraZIF FFs are capable of accurately predicting the PBE-D2/PBE-D3(BJ) thermodynamic stability ranking. This is not terribly surprising given both FFs are parameterized to reproduce the tetrahedral coordination environment of the Zn (see Figure B.20 for representative coordination environments). Figure B.19 shows that the average N-Zn-N angle is  $\sim 109.4^\circ$  for all the Im polymorphs. However, the maximum and minimum angles deviate greatly for some structures; for example, the UOC polymorph has minimum and maximum N-Zn-N angles of  $91^\circ$  and  $162^\circ$  respectively. Even with this limitation, only the intraZIF-FF correctly predicts that the Im-*zni* and mIm-*zni* polymorphs have the lowest configurational potential energy for each of the two polymorph sets as shown in Figure 3.4. The AMBER incorrectly predicts that the mIm-*dia* polymorph is the most thermodynamically stable of the mIm polymorph

set. The intraZIF-FF could be improved by fitting the van der Waals interactions as well as modeling the near square planar and tetrahedral coordination environments with separate harmonic potentials.

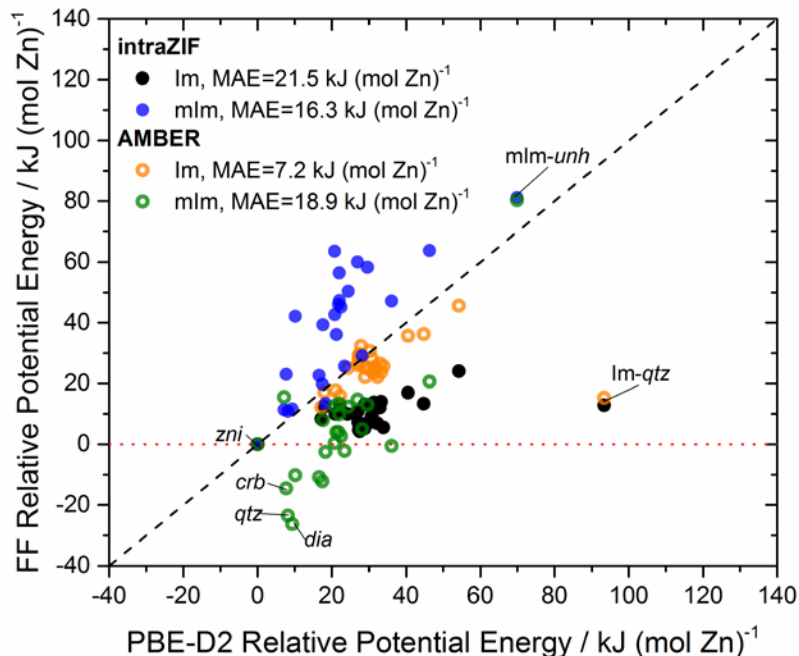


**Figure 3.4** Relative energy rankings of the hypothetical (a) imidazolate (black/orange) and (b) 2-methylimidazolate (blue/green) polymorphs for PBE-D2, the AMBER-FF (open circles), and the intraZIF-FF (closed circles).

### 3.3.3 Bulk Modulus Predictions

The ability of a force field to predict mechanical stability is another important metric. Figure 3.5 shows the pressure dependence of the ZIF-8 unit cell parameters at 308 K as well as the amorphization pressure as first described by Chapman et al.<sup>279</sup> We define the amorphization pressure as the pressure at which the unit cell volume decreases by over 25% from the beginning to the end of a 1 ns NPT-MD simulation with a 100 ps equilibration period. The intraZIF-FF captures the nonlinearity in the unit cell parameter pressure dependence and predicts the amorphization pressure range from 0.3-0.5 GPa

(the experimental amorphization pressure is 0.34 GPa). The AMBER-FF does not predict an amorphization pressure less than 0.6 GPa and the pressure-dependence of the unit cell parameters is exactly linear. The pressure-induced changes in the unit cell parameters were fit to the third-order Birch-Murnaghan equation of state to determine the bulk modulus and the derivative the bulk modulus:

$$K = -V \left( \frac{\partial P}{\partial V} \right)_{P=0} = \frac{\sigma_V}{\epsilon_V} \text{ and } K' = \left( \frac{\partial K}{\partial P} \right)_{P=0} \quad (3.10)$$

The bulk modulus and  $K'$  predicted by the intraZIF-FF and Chapman et al. are 5.53 GPa and -2.68 and 6.52±0.35 GPa and -4.6±0.14 respectively.<sup>279</sup> The AMBER-FF predicts a bulk modulus and  $K'$  of 9.05 GPa and -0.02. Zhang et al. using a modified version of the AMBER-FF estimated the bulk modulus as 8.37±0.05 GPa.<sup>174</sup>

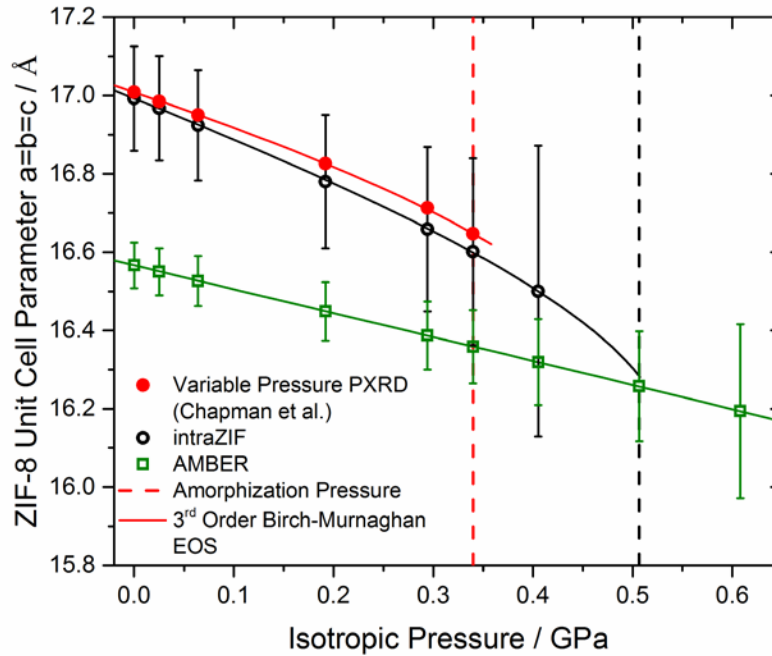


**Figure 3.5** Pressure dependence of the ZIF-8 unit cell parameters measured by Chapman et al.<sup>279</sup> and predicted by the intraZIF and AMBER FFs. The third-order Birch-Murnaghan isothermal equation of state is fit (solid line) to both the measured and predicted data. The amorphization pressures are indicated by the dashed lines.

### 3.3.4 Reproducibility of Relative Energy and Forces from BOMD Calculations

The intraZIF and AMBER force fields were compared for their ability to reproduce PBE-D3(BJ) reference potential energies and atomic forces from BOMD simulations at 700 K and 1.0 bar on the full unit cells. Development of the intraZIF-FF used fitting based on BOMD data from small clusters (as described above), but the BOMD simulation data on the full unit cells was not used in fitting the intraZIF-FF. This test is different from the BOMD simulations of the clusters because these comparisons also include van der Waals pair-wise interactions. Figure 3.6 below shows the comparison between PBE-D3(BJ) relative energies and those predicted by the AMBER and intraZIF FFs for SALEM-2. The time series of the data is represented by the black to blue (intraZIF) and orange to green (AMBER) fade. The AMBER-FF and intraZIF-FF yield NRMSDs of 159.0% and 29.6% respectively, clearly showing that the intraZIF-FF outperforms the AMBER-FF. Similar plots for ZIF-7, ZIF-8, ZIF-90 are in Appendix B.

Tables B.20-B.25 show the comparisons of the AMBER and intraZIF FF predicted atomic forces for the six atom types that comprise SALEM-2 in reference to PBE-D3(BJ) atomic forces. The intraZIF-FF more accurately presents atomic forces on the following atom types: Zn, N, C<sub>1</sub>, and H<sub>1</sub> while the AMBER force field more accurately represents atomic forces on the C<sub>2</sub> and H<sub>2</sub> atom types. Using the intraZIF-FF, we find atomic force NRMSD values of approximately 50% or less for the different atom types. While this comparison of energies and forces is meant to provide concrete proof that the intraZIF-FF more accurately represents kinetic flexibility of ZIFs than the AMBER-FF, this PBE-D3(BJ) reference data could be used to fit more realistic force field parameters through force matching<sup>280</sup>. As a reference for exceptional atomic force NRMSD values, Wang et al. performed a fitting procedure for water that is capable of achieving an atomic force NRMSD of 26%, with the claim that atomic force NRMSDs are capable of reaching values as low as 10-15%.<sup>272</sup> This suggests that the intraZIF-FF

can be improved even further but most likely with diminishing returns with the current functional form.

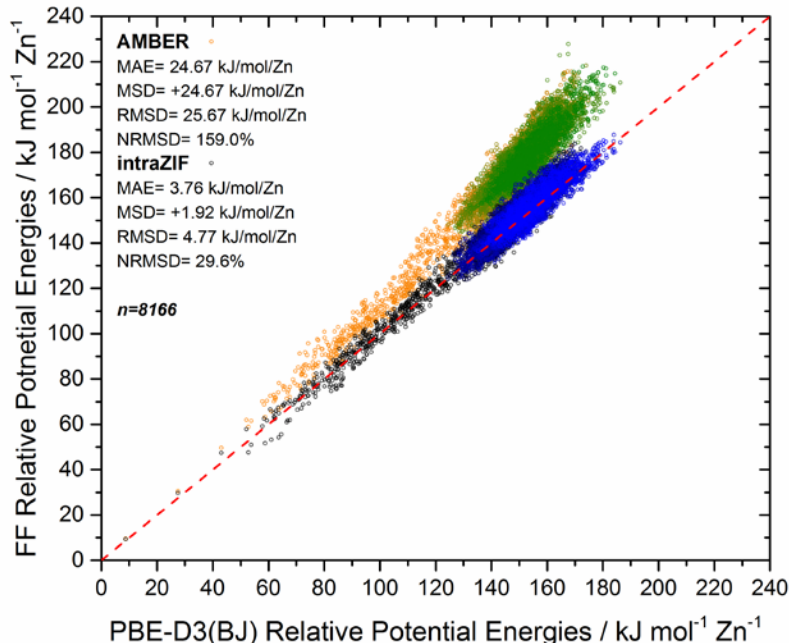


**Figure 3.6** SALEM-2 relative potential energies as predicted by the AMBER-FF (orange to green) and intraZIF-FF (black to blue) in reference to PBE-D3(BJ) relative energies from fully periodic BOMD simulations at 700 K.

### 3.3.5 Window Diameter Distributions

Examining the distribution of window diameters in small pore ZIFs can yield insights into the kinetic separation capabilities of these materials.<sup>18,220</sup> As our final independent test of the intraZIF-FF, we compare individual window diameter histograms measured from fully periodic BOMD simulations as well as MD simulations with both the AMBER and intraZIF FFs. The window diameters were calculated using a grid based percolation method sampling only an individual window.<sup>219</sup> Figure 3.7 (middle panel) shows window diameter histograms for SALEM-2 simulated with BOMD at 300, 500, and 700 K and 1.0 bar from a 15 ps simulation (5 ps equilibration period). We also

simulated the window diameter histograms with the AMBER and intraZIF FFs using conventional NPT-MD with snapshots taken every 0.5 ps over a 1000 ps trajectory. SALEM-2's large spread of window sizes ( $> 2 \text{ \AA}$ ), in contrast to the spread of zeolite window diameters ( $\sim 1 \text{ \AA}$ )<sup>281</sup>, makes it difficult to obtain well converged histograms from computationally expensive BOMD trajectories. From Figure 3.7, we conclude that the AMBER-FF performs slightly better than the intraZIF-FF at predicting the window diameter histograms of SALEM-2 from BOMD trajectories.

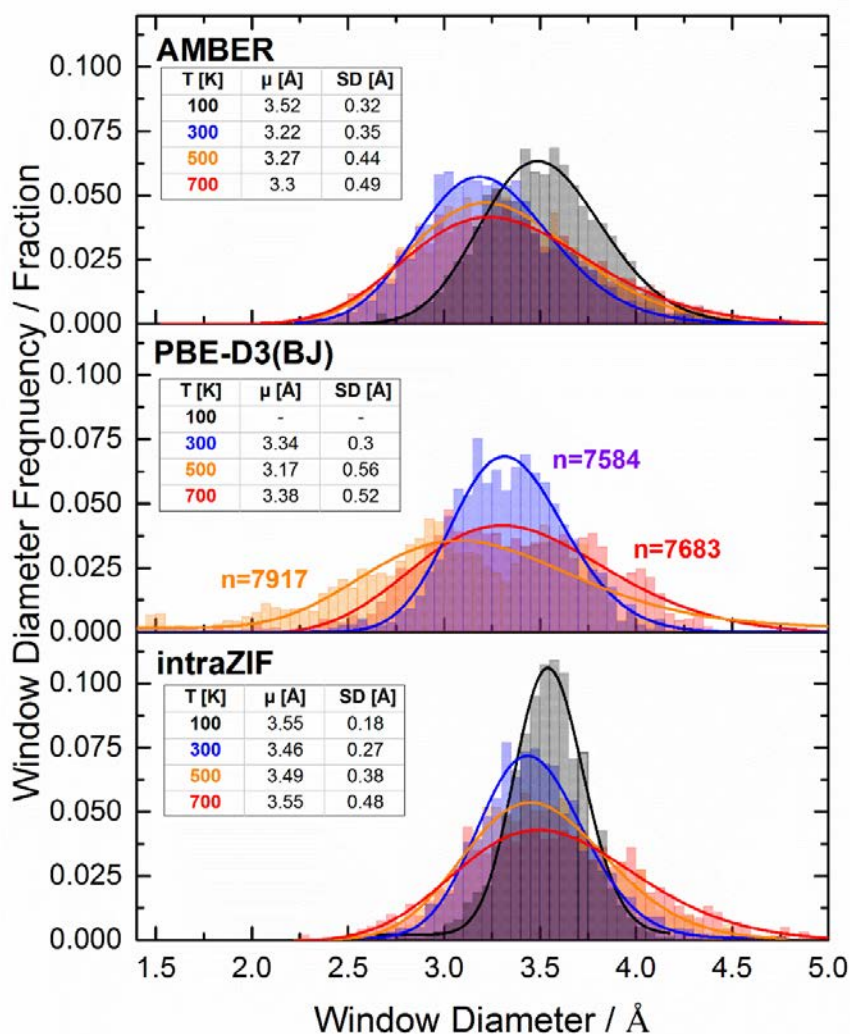


**Figure 3.7** Window diameter histograms in SALEM-2 using PBE-D3(BJ) and the AMBER and intraZIF FFs. Solid lines represent the lognormal distribution fits with the mean ( $\mu$ ) and standard deviation (SD) of these lognormal distributions reported in the table insets. There are 2000 samples for each histogram from the AMBER-FF and intraZIF-FF and the sample number for the histograms from PBE-D3(BJ) are reported in the center panel.

The results above provide evidence that the intraZIF-FF is useful for predicting structural properties of ZIFs. We therefore used this FF to examine its ability to predict experimental PLDs. Since many researchers use PLDs from the experimental unit cells to guide their research, we provide careful treatment in comparing those PLDs to average window diameters predicted by the intraZIF-FF. Figure 3.8 shows the window diameter distributions of the 6 MR for ZIF-8, ZIF-90, ZIF-7 and SALEM-2 at the same temperatures that single-crystal XRD refinements are available. We also include the PLDs from the PBE-D2 and intraZIF-FF energy minimized structures for reference. We note that the mean and standard deviation of the Gaussian distribution for ZIF-8 ( $3.43 \pm 0.19$  Å) matches well with previously reported Gaussian distribution using the AMBER-FF ( $3.44 \pm 0.17$  Å) as reported previously by Verploegh et al.<sup>219</sup> An interesting outlier in the PLD data comparisons in the inset table of Figure 3.8 is ZIF-90. The intraZIF-FF predicts a slightly larger PLD ( $3.77$  Å) than the PLD predicted using PBE-D2 ( $3.45$  Å) of ZIF-90. Inspection of the energy minimized structure from the intraZIF-FF shows that the imidazolate linkers lie  $\sim 18^\circ$  outside the plane formed by the six Zn atoms. We defined the swing angle as the  $C_2-Zn_1-Zn_2-Zn_3$  dihedral angle, which is similar to the dihedral angle defined by Coudert for analyzing the swinging motion of ZIF-8<sup>282</sup>. The imidazolate linkers in the ZIF-90 experimental and PBE-D2 structures are  $\sim 4^\circ$  and  $\sim 6^\circ$  outside the 6 MR window plane. The slight tilting of the linkers causes this increase in the intraZIF-FF PLD.

The experimental PLDs rank as ZIF-7 ( $2.40$  Å) < SALEM-2 ( $3.30$  Å) < ZIF-8 ( $3.43$  Å) < and ZIF-90 ( $3.49$  Å). This data from the crystallographic structures suggested that diffusion in SALEM-2 would be depressed in relation to the ZIF-8 and ZIF-90 structures. However, Karagiari et al. soaked ZIF-8 and SALEM-2 crystals in liquid n-hexane, cyclohexane, and toluene for 24 h at  $25^\circ\text{C}$  and then performed TGA-MS, determining that SALEM-2 crystals, unlike ZIF-8, adsorbed appreciable amounts of both cyclohexane or toluene.<sup>253</sup> The SALEM-2 distribution measured at 300 K (Figure 3.7)

accesses window sizes up to 4.5 Å whereas the ZIF-8 window distribution measured at 258 K only accesses window diameters up to 4.0 Å. These window distributions suggest that larger molecules would diffuse more easily in SALEM-2 than ZIF-8. With these observations, we directly explore the diffusion properties of these ZIFs in Section 3.4.

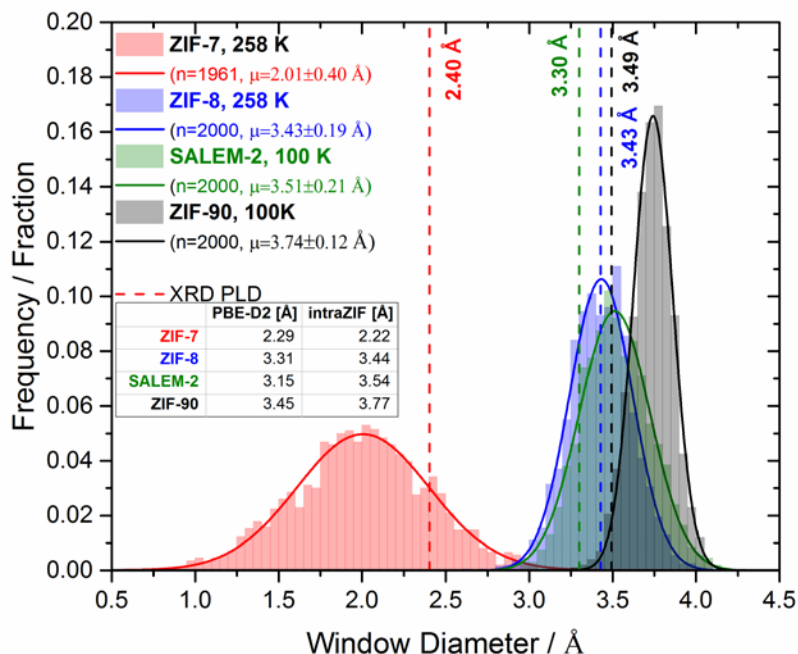


**Figure 3.8** Window diameter histograms in SALEM-2, ZIF-7, ZIF-8, and ZIF-90 at 1.01 bar and temperatures at which the crystal structures were resolved, using the intraZIF-FF. The inset table compares the PLD (Å) of the energy minimized structures using PBE-D2 and the intraZIF-FF. Solid lines represent Gaussian distribution fits where the mean ( $\mu$ ) and standard deviation are reported in the legend.

### 3.4 Light Gas Diffusivities in ZIFs with the SOD Topology

#### 3.4.1 Adsorbate Force Fields and ZIF-Adsorbate Interactions

We selected thirty adsorbates that exhibit various molecular sizes, morphologies, and interaction strengths. Specifically, we examined He, Kr, Xe, Rn, SF<sub>6</sub>, H<sub>2</sub>, O<sub>2</sub>, N<sub>2</sub>, CO<sub>2</sub>, CH<sub>3</sub>OH (methanol), C<sub>2</sub>H<sub>5</sub>OH (ethanol), C<sub>4</sub>H<sub>9</sub>OH (1-butanol), CH<sub>3</sub>-CO-CH<sub>3</sub> (acetone), CH<sub>4</sub>, C<sub>2</sub>H<sub>4</sub>, C<sub>2</sub>H<sub>6</sub>, C<sub>3</sub>H<sub>6</sub>, C<sub>3</sub>H<sub>8</sub>, 1-C<sub>4</sub>H<sub>8</sub>, n-C<sub>4</sub>H<sub>10</sub>, iso-C<sub>4</sub>H<sub>8</sub>, iso-C<sub>4</sub>H<sub>10</sub>, C<sub>6</sub>H<sub>6</sub>, m-C<sub>8</sub>H<sub>10</sub>, o-C<sub>8</sub>H<sub>10</sub>, p-C<sub>8</sub>H<sub>10</sub>, water, N,N-dimethylformamide (DMF), imidazole,



and 1,3,7-trimethylxanthine (caffeine,  $\text{C}_8\text{H}_{10}\text{N}_4\text{O}_2$ ). Figure B.25 in Appendix B shows the molecular weights of these 30 molecules as a function of their molecular diameters. The molecular diameters are a combination of previously reported van der Waals and kinetic diameters;<sup>56,60</sup> those not found in literature are approximated using the Lennard-Jones sigma parameters summed across the second shortest molecular dimension. The FFs used to define adsorbate-adsorbate interactions and adsorbate-ZIF interactions for these species are described in Appendix B.

### 3.4.2 Diffusion Theory and Computational Methods

Self-diffusion of adsorbates through cage-type ZIFs can be modeled as an activated hopping process from cage to cage through connecting windows. The self-diffusion coefficient can be written as<sup>137</sup>

$$D_{\text{self}} = \left( \frac{n_{\text{windows}}}{2d} \right) \kappa k_{i \rightarrow j}^{\text{TST}} \lambda^2 \quad (3.11)$$

where  $n_{\text{windows}}$  is the number of possible windows an adsorbate can exit from its current cage ( $n_{\text{windows}} = 8$  for SALEM-2, ZIF-8, and ZIF-90),  $d$  takes on values of 1, 2, or 3 based on the diffusion dimensionality, ( $d=3$  for SALEM-2, ZIF-8, and ZIF-90),  $\kappa$  is the dynamical correction to the hopping rate  $k_{i \rightarrow j}^{\text{TST}}$  from transition state theory (TST)<sup>148</sup>, and  $\lambda$  is the cage to cage distance. An average  $\lambda$  of 14.75 Å was utilized for SALEM-2, ZIF-8, and ZIF-90.

To produce the Gibbs free energy curve for calculation of the TST hopping rate, umbrella sampling calculations were performed with LAMMPS using the collective variables (colvars) package by Fiorin and coworkers.<sup>187</sup> Spring constants of 10, 25, and 50 kcal mol<sup>-1</sup> Å<sup>-2</sup> were used for adsorbates exhibiting small (e.g. He), medium (e.g. CH<sub>4</sub>) and large (e.g. isobutane) diffusion barriers. Sixty umbrellas were used over the 1-dimensional reaction coordinate with spacings of 0.25 Å. Each simulation was equilibrated for 200 ps with 500 ps of sampling during an NPT simulation. Blocking

potentials were applied to constrain the molecules to the immediate two cage system, ensuring that small adsorbates only sampled the microstates of interest. The weighted histogram analysis method (WHAM) was used to combine umbrella simulations into a free energy curve.<sup>188</sup> Dynamical corrections were measured using the algorithm detailed by Frenkel and Smit.<sup>154</sup> Further details of these methods are discussed in Chapter 2.<sup>219</sup>

### 3.4.3 Screening of Thirty Adsorbates in SALEM-2, ZIF-8, and ZIF-90

To our knowledge, this is the most comprehensive screening study of adsorbate diffusion in ZIFs with simulations that include the flexibility of the ZIF frameworks. Figure 3.9 compares the intraZIF-FF's capability of predicting these reference experimental diffusivities to the AMBER-FF's capability at predicting these experimental self-diffusivities. The MAE for the intraZIF-FF and the AMBER-FF are 0.82 and 0.69 (log base 10 scale) respectively, with the intraZIF-FF predicting slightly faster self-diffusion. It is important to note that the accuracy (not the precision) of self-diffusion coefficients from experimental macroscopic uptake methods is typically at best an order of magnitude.<sup>283</sup> This is particularly apparent when comparing the results in Figure 3.9 from independent experiments by Eum et al. and Zhang et al. for n-butane and isobutane diffusion in ZIF-8. Given this level of experimental uncertainty, it is reasonable to conclude that both sets of FF-based results in Figure 3.9 show good agreement with experimentally observed diffusivities in ZIF-8.

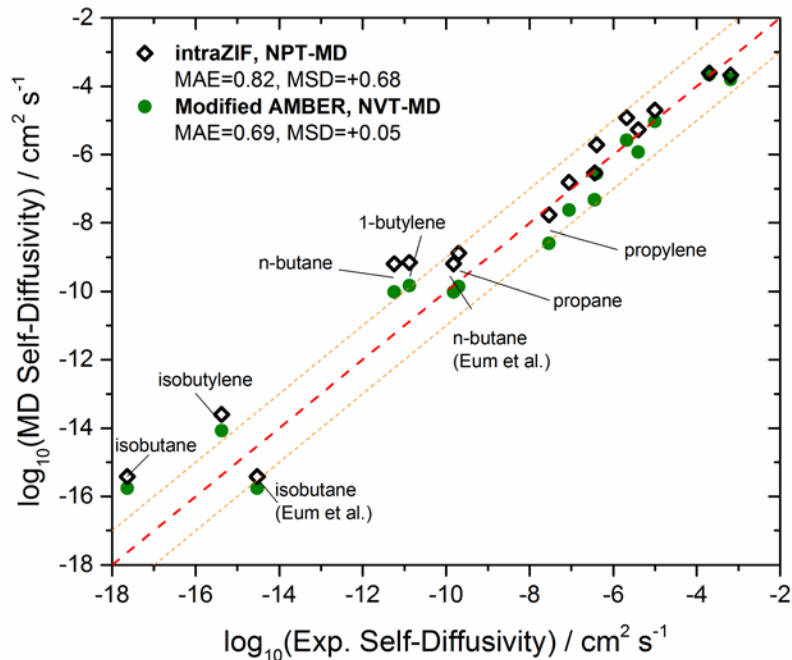


**Figure 3.9** Self-diffusivities of 14 adsorbates as predicted by the modified AMBER force field using NVT-MD from Verploegh et al.<sup>219</sup> and the intraZIF-FF using NPT-MD (1.01 bar) in comparison to reference experimental diffusivities from Zhang et al.<sup>56</sup> (unmarked) and Eum et al.<sup>189</sup> (marked) at 308 K. The dashed orange lines represent the order-of-magnitude accuracy expected from macroscopic uptake methods.

Figure 3.10 shows the self-diffusivities at infinite dilution of all thirty adsorbates in SALEM-2, ZIF-90, and ZIF-8 at 308.15 K. All the predicted diffusion coefficients are reported in Table B.29. For reference, we have plotted the PLDs from intraZIF-FF energy minimized structures as dashed lines. Consistent with previous studies<sup>57,284</sup>, it is clear that adsorbates with molecular diameters much larger than the PLDs can diffuse readily. A key observation from the data in Figure 3.10 is that SALEM-2 shows the fastest self-diffusivities for large molecules. This is supported by the window distributions of SALEM-2 and ZIF-90 in Figure 3.8. Both distributions are measured at 100 K, but the standard deviation of the distribution for SALEM-2 is 50% larger than the distribution for ZIF-90. SALEM-2, while having an average window diameter 0.23 Å less than the

average window diameter of ZIF-90, is able to access the same range of window diameters as ZIF-90. Coudert found that the libration angle<sup>285</sup> for SALEM-2 is 35° while for ZIF-8 it is 15°, with free energy barriers to rotation of 3.5 and 15 kJ mol<sup>-1</sup> respectively, at 77 K using BOMD simulations.<sup>282</sup> However, these observations about the linker rotation and subsequent window distributions do not explain why a molecule as large as caffeine (~7 Å) is predicted to diffuse twelve (eighteen) orders of magnitude faster in SALEM-2 than ZIF-90 (ZIF-8). Clearly, the interaction of the adsorbates in the window region influences the predicted self-diffusivities in a way that cannot even be predicted from structural features of the empty material.

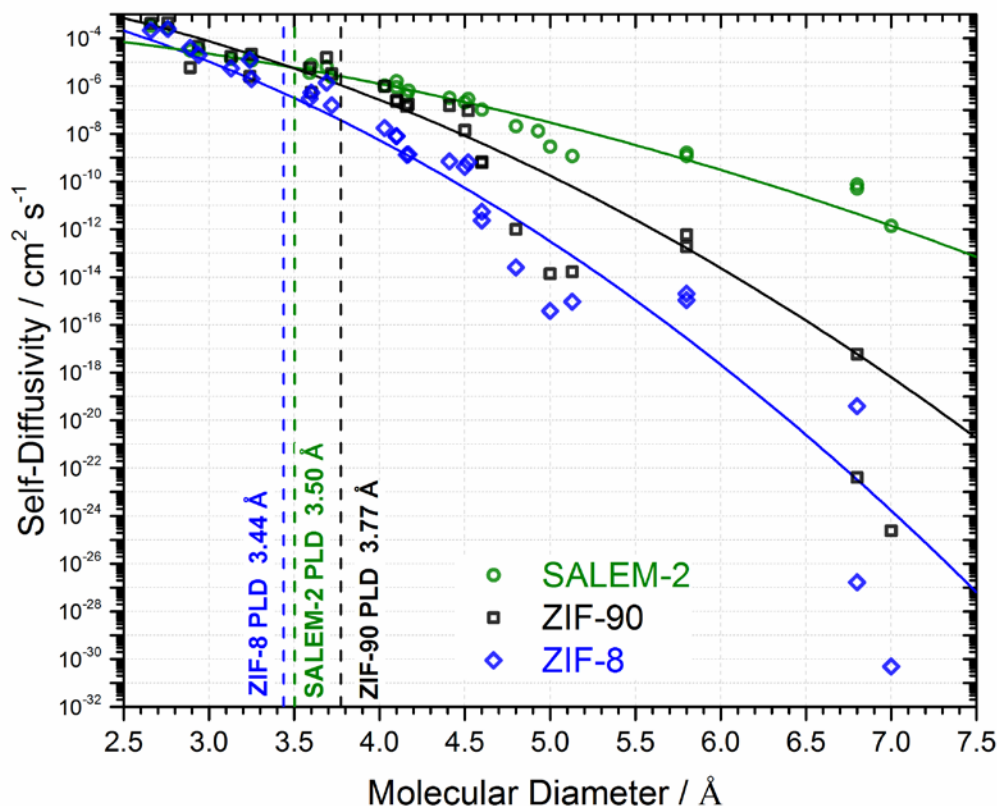


**Figure 3.10** Self-diffusivities at infinite dilution of thirty adsorbates in SALEM-2, ZIF-8, and ZIF-90 with fits of Equation 3.13 as solid lines. The intraZIF-FF predicted PLDs from energy-minimized structures are shown as dashed lines.

In Chapter 2, we made a thorough comparison of simulation results in ZIF-8 to experiments for C1-C4 hydrocarbons and light gases<sup>219</sup>. There are few experimental works to which we can make direct comparisons to experiments for the larger adsorbates in Figure 3.10. These experiments utilize macroscopic uptake methods that measure transport diffusivities, which can be related to the corrected diffusivity using Darken's equation<sup>153</sup>. Corrected diffusivities measured experimentally at infinite dilution can be directly compared to our predicted self-diffusivities, with the assumption that Maxwell-Stefan self-exchange diffusivities are large for cage-type ZIF materials.<sup>99</sup> Zhang et al. reported corrected diffusivities in ZIF-8 for water, ethanol, 1-butanol, benzene, *p*-xylene, *m*-xylene, and *o*-xylene using vapor-phase kinetic uptake experiments at 50 °C.<sup>60</sup> Table B.30 and Figure B.26 compare our simulated self-diffusivities to those measured by Zhang et al. Our predicted self-diffusivities follow the same ranking as those measured by Zhang et al.; however, most direct comparisons are different by several orders of magnitude. When measuring diffusion experimentally of large adsorbates using macroscopic uptake methods<sup>283</sup>, external heat<sup>286</sup> and mass transfer effects<sup>287</sup> can have a large impact on the accuracy of the reported diffusivities. Significant disagreement could also arise from significant surface barriers as Tanaka et al. reported observing for 1-butanol in ZIF-8 at 323 K.<sup>288</sup>

Several of our predicted self-diffusivities of adsorbates reaching molecular diameters equal to or greater than 5.8 Å are worth examining in closer detail. Interestingly, we predicted that *p*-xylene diffuses 2× faster than benzene in ZIF-8, in disagreement with Zhang et al. Unfortunately, it is difficult to draw the definitive conclusion that benzene truly diffuses faster than *p*-xylene from the experimental data based on known uncertainties. To investigate this further, we calculated Gibbs free energy barriers of benzene and *p*-xylene at 275, 300, 325, 350, 375, and 400 K and predicted a lower enthalpic barrier for *p*-xylene than benzene (Figure B.27). This observation is in concert with the work of Kolokathis et al. that determined *p*-xylene

diffuses 100× faster than benzene at low occupancies in silicalite-1 because it exhibits both a lower entropic and internal energy barrier.<sup>289</sup> We also predict extremely low diffusivities for o-xylene, m-xylene, and caffeine in ZIF-8 compared with the uptake experiments of Zhang et al. and Liédana et al.<sup>290</sup> Liédana et al. reported only caffeine uptake data at 80 °C so a caffeine transport diffusivity in ZIF-8 was estimated by fitting published data<sup>290</sup> to the analytical solution for diffusion into a sphere. For this calculation, average ZIF-8 particle radii were estimated at 125 nm from the reported characterization and were modeled as experiencing an instantaneous step change at the surface<sup>112</sup> with no depletion effects. The resulting transport diffusivity was approximately  $1 \times 10^{-17} \text{ cm}^2 \text{ s}^{-1}$ . We predicted a much slower self-diffusion coefficient for caffeine of  $4.91 \times 10^{-31} \text{ cm}^2 \text{ s}^{-1}$  with a Gibbs free energy barrier of  $150 \text{ kJ mol}^{-1}$  and transmission coefficient of 0.003. While we cannot make a direct comparison, we note that the extreme deformability of the ZIF-8 window is demonstrated with such a large molecule ( $\sim 7 \text{ Å}$  diameter). The 6 MR window resembles an oval-shape from visualization of the MD trajectories upon the hopping event. The intraZIF-FF, particularly the adsorbate-adsorbent interactions, may not be applicable for such intimate chemical interactions of these very large molecules with the ZIF-8 window. Defects could also exist in the ZIF-8 crystals that result in the faster diffusion observed experimentally.<sup>291</sup>

There have been fewer diffusion studies involving ZIF-90, and we are aware of no experimental diffusion data in SALEM-2. In an extant experimental study, Eum et al. reported corrected diffusivities of n-butane, 1-butanol, and isobutane (from fastest to slowest) in ZIF-90 at 35 °C.<sup>189</sup> The diffusivities for these three molecules in ZIF-90 are one, two, and three orders of magnitude faster than the diffusivities in ZIF-8. We correctly predict the order of diffusivities as well as predicting that diffusion for these three adsorbates is faster in ZIF-90 than ZIF-8. It is interesting to note that the reported PLDs from the XRD-derived structures are nearly identical (ZIF-90:  $3.5 \text{ Å}$ , ZIF-8:  $3.4$

Å)<sup>292</sup> yet minute differences in the window region can yield significantly faster diffusion. The only computational study examining diffusion in ZIF-90 was performed by Chokbunpiam et al. who simulated H<sub>2</sub> and CH<sub>4</sub> self-diffusion using conventional NPT-MD (AMBER-FF) at low loading (2.5 molecules per cage) and 300 K. They reported self-diffusivities of  $5.5 \times 10^{-4}$  and  $1.2 \times 10^{-5}$  cm<sup>2</sup> s<sup>-1</sup> for H<sub>2</sub> and CH<sub>4</sub> respectively;<sup>293</sup> in excellent agreement, our simulated diffusivities for H<sub>2</sub> and CH<sub>4</sub> in ZIF-90 and 308 K are  $4.54 \times 10^{-4}$  and  $2.14 \times 10^{-5}$  cm<sup>2</sup> s<sup>-1</sup> respectively. These comparisons demonstrate that our simulations predict the correct diffusion trends as seen experimentally and are in agreement with other computational groups performing similar studies.

It is interesting to consider whether there are simple scaling relationships that describe the large collection of diffusivities in Figure 3.10. An empirical relation between self-diffusivity and molecular diameter for penetrant diffusion in polymers was given in a seminal analysis of gas permeation in polymer membranes by Freeman.<sup>294</sup>

$$\log(D_{s,i}) = -\left(\frac{1-a}{RT}\right)cd_i^2 + f\left(\frac{1-a}{RT}\right) - b \quad (3.12)$$

where the constants a, b, c, and d are independent of the adsorbate and depend only on the material in which the molecules are diffusing. By comparing this prediction to that of a reference adsorbate the following relationship is obtained

$$\log\left(\frac{D_{s,i}}{D_{s,ref}}\right) = -c'(d_i^2 - d_{ref}^2) \quad (3.13)$$

where  $c'$  is dependent on temperature and the porous material, but is independent of the adsorbate. Fits to this function using methane as the reference adsorbate are shown as solid lines in Figure 3.10. Our fit parameters  $c'$  are 0.415, 0.810, and 1.08 Å<sup>-2</sup> for SALEM-2, ZIF-90, and ZIF-8 respectively. These values are similar in magnitude with those of polymers, where Freeman reported that  $c'$  parameters at 308 K for polymers range between 0.15 Å<sup>-2</sup> for extremely flexible polydimethylsiloxane to 1.41 Å<sup>-2</sup> for a high-performance glassy polyimide.

### 3.4.4 Diffusion in ZIF-7

Little is known about the transport of adsorbates through ZIF-7. ZIF-7 has a rhombohedral sodalite topology, unlike the cubic unit cells of ZIF-8 and ZIF-90. ZIF-7 was first synthesized by Yaghi and coworkers<sup>292</sup> and is not stable in liquid water.<sup>295</sup> Gascon and coworkers determined that ZIF-7 unit cell expands through adsorption of CO<sub>2</sub> as well as C2 and C3 hydrocarbons at room temperature, revealing that these larger hydrocarbons can diffuse through the small windows (PLD of 2.2 Å)<sup>4</sup>. ZIF-7 also exhibits a gate opening mechanism that selectively adsorbs C4 paraffins over olefins.<sup>52</sup> It also has been shown that solvents used in the synthesis can adsorb in the apparently inaccessible regions of ZIF-7 as seen from the templating solvents in the original reported crystal structure.<sup>41</sup> To complicate computational studies, ZIF-7 has three known stable phases depending on sample activation as demonstrated by Zhao et al. (simulated XRD patterns in Figure B.28).<sup>296</sup> We chose to examine diffusion only in the ZIF-7-I phase for which we successfully performed a DFT energy minimization. We attempted a DFT energy minimization on the ZIF-7-II phase reported by Zhao et al. and were unable to obtain a converged structure. This further supports Du et al. who noted that solving the structure of ZIF-7-II is challenging given its complexity and low symmetry.<sup>218</sup>

Inspection of ZIF-7-I reveals what we will call minor cages formed by the six benzimidazolate linkers surrounding the 6-MR window, the plane of which is shown by the dashed green line in Figure 3.11a. We propose that self-diffusion proceeds in ZIF-7 as a hopping process controlled by the rate from the minor cages into the center of the major sodalite cage. This is supported by the calculated Gibbs free energy barriers from minor cage to minor cage as shown in Figure 3.11b. The distance from the center of one minor cage to another is 15.95 Å. From Zeo++ calculations on the rigid structure, the 6MR window outlined in red dashed lines in Figure 3.11a is hypothesized to be inaccessible to adsorbates larger than 1.8 Å in diameter. Zhao et al. previously denoted the minor cage as cavity A and the inaccessible 6MR window as cavity B.<sup>296</sup> They



showed using high-resolution neutron powder diffraction that cavity B opens upon adsorption of CO<sub>2</sub> at high loadings, and therefore we assume that this gate-opening is not observed at near infinite dilution. Even if motion of the BzIm linkers allows diffusion through cavity B, we hypothesize that diffusion is dominated by hopping through cavity A, which has the larger PLD.

When calculating a diffusivity with Equation 3.11, we assume the number of windows is 2 and the diffusion occurs in the z-direction (i.e. the dimensionality is 1). The integral of the free energy curve use to calculate the hopping rate in Equation 3.11 is performed over the minor cage microstate. Transmission coefficients were calculated along the [001] vector for trajectories leaving from the minor cage at the point designated 0 Å as in Figure 3.11a. To validate this approach, we have also calculated the self-diffusivities as well as the diagonal components of the diffusivity tensor ( $D_{xx}, D_{yy}, D_{zz}$ ) using conventional NPT-MD in combination with the Einstein relation<sup>152</sup>. All the predicted self-diffusivities from both dynamically corrected TST and conventional NPT-MD are reported in Table 3.2.

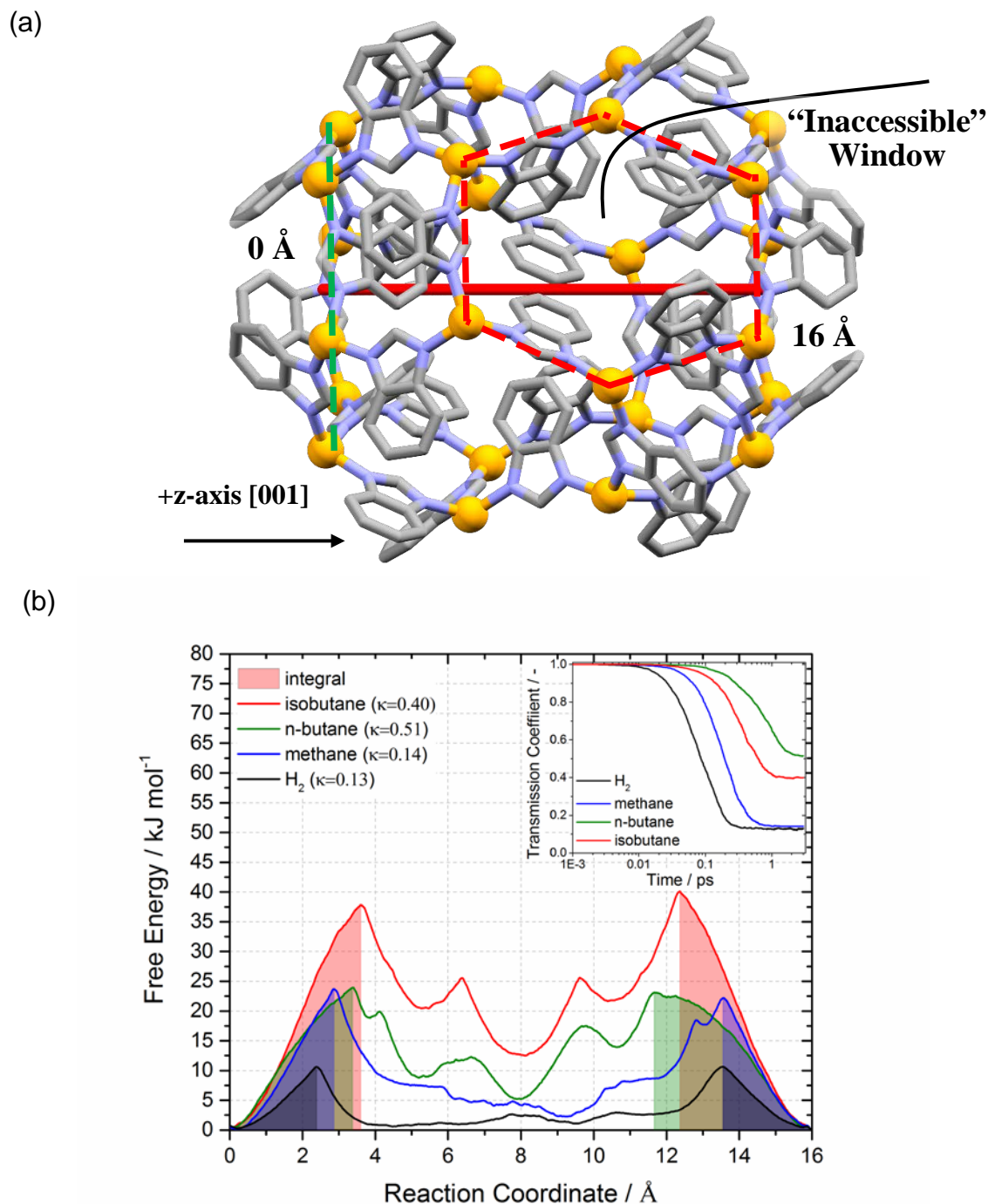


**Figure 3.11** Analysis of diffusion in ZIF-7-I phase with (a) a singular truncated octahedron cage viewed perpendicular to (010) along with the one-dimensional reaction coordinate (solid red line). The plane of the minor cage is indicated by the dashed green line and the inaccessible window is indicated by the dashed red lines. (b) Gibbs free energy curves as a function of reaction coordinate. The shaded regions represent the integral used to calculate the TST hopping rate. The inset show the transmission coefficient curves for  $\text{H}_2$ , methane, n-butane, and isobutane.

**Table 3.2** Summary of predicted diffusivities in ZIF-7 using both conventional NPT-MD and dynamically corrected TST.

Adsorbate (Molecular Diameter / Å)	$D_{self}^{MD}$ [cm <sup>2</sup> s <sup>-1</sup> ]	$D_{self,xx}^{MD}$ [cm <sup>2</sup> s <sup>-1</sup> ]	$D_{self,yy}^{MD}$ [cm <sup>2</sup> s <sup>-1</sup> ]	$D_{self,zz}^{MD}$ [cm <sup>2</sup> s <sup>-1</sup> ]	$D_{self,zz}^{TST}$ [cm <sup>2</sup> s <sup>-1</sup> ]
H <sub>2</sub> (2.76)	$(2.6 \pm 0.3) \times 10^{-5}$	$(2.5 \pm 0.7) \times 10^{-5}$	$(2.9 \pm 0.5) \times 10^{-5}$	$(2.4 \pm 0.8) \times 10^{-5}$	$1.39 \times 10^{-4}$
N <sub>2</sub> (3.13)	$(1.5 \pm 0.2) \times 10^{-6}$	$(1.7 \pm 0.7) \times 10^{-6}$	$(2.1 \pm 0.4) \times 10^{-6}$	$(6.7 \pm 0.6) \times 10^{-7}$	-
CO <sub>2</sub> (3.24)	$(4.6 \pm 1.4) \times 10^{-7}$	$(4.6 \pm 3.1) \times 10^{-7}$	$(7.0 \pm 1.5) \times 10^{-7}$	$(2.3 \pm 0.8) \times 10^{-7}$	-
CH <sub>4</sub> (3.25)	$(1.8 \pm 0.4) \times 10^{-6}$	$(1.6 \pm 0.9) \times 10^{-6}$	$(2.7 \pm 1.2) \times 10^{-6}$	$(9.9 \pm 0.5) \times 10^{-7}$	$4.74 \times 10^{-7}$
n-butane (4.52)	$(1.1 \pm 0.1) \times 10^{-6}$	$(1.5 \pm 0.6) \times 10^{-6}$	$(1.3 \pm 0.3) \times 10^{-6}$	$(4.9 \pm 1.6) \times 10^{-7}$	$9.66 \times 10^{-7}$
isobutane (5.0)	-	-	-	-	$1.48 \times 10^{-9}$

Several observations are apparent from the diffusivity data in Table 3.2. It is clear our approach to predict diffusion using dcTST does not yield the same self-diffusivities as predicted by conventional NPT-MD. We examined MD trajectories (Figures B.31 and B.32) and determined that adsorbates were hopping through what we described above as the “inaccessible” side windows of the ZIF-7-I major cage that were not considered in our dcTST self-diffusivity predictions. We also measured H<sub>2</sub> diffusion in the rigid structure using MD, finding  $D_{self,xx}^{MD}, D_{self,yy}^{MD} \sim 0$  and  $D_{self,zz}^{MD} = 9.25 \times 10^{-8}$  cm<sup>2</sup> s<sup>-1</sup> (MSDs reported in Figure B.29), demonstrating that diffusion does not occur through cavity B in the rigid structure. The surprising flexibility of ZIF-7 can also be seen in the large standard deviation (0.4 Å) of the window diameter histogram for ZIF-7 reported in Figure 3.8. These results run counter to the notion that because ZIF-7 has a small PLD and is therefore restricted to sieving small molecules such as H<sub>2</sub>, CO<sub>2</sub>, N<sub>2</sub>, and CH<sub>4</sub>. Our results strongly suggest that the “inaccessible” 6MR windows must be accounted for when predicting diffusion, so the results from TST calculations with based on a one-dimensional reaction coordinate are not able to accurately describe this material.

In an effort to examine whether we predict reasonable diffusion trends in ZIF-7 with conventional MD, we compare to available computational and experimental literature regarding transport in ZIF-7. Using fully flexible MD simulations, Pilvar et al.<sup>297</sup> predicted a self-diffusion coefficient for H<sub>2</sub> in ZIF-7 of  $2.7 \times 10^{-5}$  cm<sup>2</sup> s<sup>-1</sup>, in excellent

agreement with our MD predicted self-diffusivity; they did not report the mechanism of H<sub>2</sub> diffusion or through which windows it was observed to diffuse. Wu et al. examined the adsorption kinetics of CO<sub>2</sub> and CH<sub>4</sub> in ZIF-7 at 298 K and predicted CH<sub>4</sub> diffuses more quickly than CO<sub>2</sub>, in agreement with our NPT-MD self-diffusivities.<sup>298</sup> Rashidi et al. reported experimental transport diffusivities of  $(3\pm1)\times10^{-15}$  and  $(4\pm1)\times10^{-16}$  cm<sup>2</sup> s<sup>-1</sup> respectively for n-butane and isobutane at 308 K in the ZIF-7-II phase.<sup>43</sup> A direct comparison cannot be made to our results for the ZIF-7-I phase, but it is surprising that these diffusivities are many orders of magnitude slower in the ZIF-7-II phase than the ZIF-7-I phase. Du et al. reported that ZIF-7-II is a relatively dense phase and could possibly contain even smaller PLDs and experience more restricted flexibility than the ZIF-7-I phase<sup>218</sup>, leading to these extremely low experimental transport diffusivities. It is also possible that significant surface barrier resistances exist for ZIF-7 crystals.<sup>101</sup> More comprehensive investigations of adsorbate diffusion through the various ZIF-7 phases are warranted, preferably using a combination of pulsed field gradient (PFG) NMR and molecular dynamics.

### 3.5 Conclusions

This study provides the basis for diffusion screening studies in flexible MOF materials with emphasis on the thoroughly studied ZIF family. To provide a consistent way of modeling ZIF flexibility, we have developed the intraZIF force field using DFT reference calculations as fitting and test data. We thoroughly demonstrated that the intraZIF-FF provides better prediction of various geometric and energetic properties than the AMBER-FF. The intraZIF-FF also more accurately reproduces kinetic flexibility through comparison of relative energies and atomic forces from BOMD simulations. Our piece-wise force field fitting process can be used to easily develop extensions of the intraZIF force field, enabling modeling of ZIFs with different imidazolate functionalities. The intraZIF force field was used to produce the largest quantitative screening of

diffusion in ZIFs, and essentially MOF as a whole, by including framework flexibility. Our predicted diffusion coefficients access a range of twenty-four orders of magnitude, made possible only through the use of biased molecular dynamics sampling methods. Our examination of the diffusion mechanism in ZIF-7 should guide further computational studies seeking to examine diffusion in this highly flexible material.

There have been many quantitative screening studies examining adsorption in MOFs<sup>45,299</sup> but it is difficult to perform this type of accurate screening to determine MOFs with molecular sieving potential. While it is increasingly possible to access superb computational capabilities, analytical models will need to be developed that merge empty framework flexibility characteristics with specific adsorbate-adsorbent interactions at transition states encountered along the diffusion pathway. A motivating study performed by Witman et al. develops a simple analytical model to predict the influence of pore size distributions on Henry's constants.<sup>87</sup> In a similar fashion, the intraZIF-FF could be used to develop structure-property relationships between diffusivities and flexibility observables (e.g. linker swing angles, window size distributions, etc.) possibly using hypothetical ZIF polymorphs, a list that easily extends to well over a million structures based on zeolite analogues<sup>300</sup>. Our study provides a possible basis for predicting diffusion quantitatively in ZIFs with a range of topologies and imidazolate functionalities, by providing an representative force field, proving the ability of this force field, and predicting the diffusivities of thirty small molecules.

## CHAPTER 4

### CREATION OF STRUCTURAL MODELS FOR MIXED-LINKER ZEOLITIC IMIDAZOLATE FRAMEWORK 8-90 MATERIALS

The below text was reproduced from the article “Structure Elucidation of Mixed-Linker Zeolitic Imidazolate Frameworks by Solid-State  $^1\text{H}$  CRAMPS NMR Spectroscopy and Computational Modeling” by Krishna C. Jayachandrababu, Ross J. Verploegh, Johannes Leisen, Ryan C. Nieuwendaal, David S. Sholl, and Sankar Nair in the *Journal of the American Chemical Society*, 2016, volume, pages 7325-7336. Copyright 2016, American Chemical Society. The copyright permissions letter for this publication can be found in Appendix G. I participated as a co-first author to Dr. Jayachandrababu, providing all the computational modeling and data analysis in this study. This chapter details the combination of experimental and computational methods needed to determine the local ordering of imidazolate linkers in binary mixed-linker ZIFs on the unit cell level (sub-nanometer length scales).

Mixed-linker zeolitic imidazolate frameworks (ZIFs) are nanoporous materials that exhibit continuous and controllable tunability of properties like effective pore size, hydrophobicity and organophilicity. The structure of mixed-linker ZIFs has been studied on macroscopic scales using gravimetric and spectroscopic techniques. However, it has so far not been possible to obtain information on unit-cell-level linker distribution, an understanding of which is key to predicting and controlling their adsorption and diffusion properties. We demonstrate the use of  $^1\text{H}$ -CRAMPS NMR spin exchange measurements in combination with computational modeling to elucidate potential structures of mixed-linker ZIFs, particularly the ZIF 8-90 series. All the compositions studied have structures that have linkers mixed at a unit-cell-level as opposed to separated or highly clustered phases within the same crystal, and compositional modeling was utilized to vet potential

structures at this high level of mixing. Direct experimental observations of linker mixing were accomplished by measuring the proton spin exchange behavior between functional groups on the linkers. The data was then fitted to a kinetic spin exchange model using proton positions from candidate mixed-linker ZIF structures that were generated computationally using the short-range order (SRO) parameter as a measure of the ordering, clustering, or randomization of the linkers. The present method offers the advantages of sensitivity without requiring isotope enrichment, a straightforward NMR pulse sequence, and an analysis framework that allows one to relate spin diffusion behavior to proposed atomic positions. We find that structures close to equimolar composition of the two linkers show a greater tendency for linker clustering than what would be predicted based on random models. Using computational modeling we have also shown how the window-type distribution in experimentally synthesized mixed-linker ZIF-8-90 materials varies as a function of their composition. The structural information thus obtained can be further used for predicting, screening, or understanding the tunable adsorption and diffusion behavior of mixed-linker ZIFs, for which the knowledge of linker distributions within the framework is key.

#### 4.1 Introduction

Zeolitic imidazolate frameworks (ZIFs) are a sub-class of metal organic frameworks (MOFs)<sup>301-303</sup> that have created great interest for potential use as adsorbents and membrane materials in gas and liquid separation processes.<sup>304-312</sup> ZIFs have metal-atom centers (such as Zn or Co) which are connected by imidazolate linkers to form 3D frameworks. ZIF structures exist in a wide variety of zeolite-like topologies, with a range of cage and window sizes appropriate for molecular separations.<sup>303</sup> In addition to their structural diversity as well as selective adsorption and transport properties for hydrocarbons, other organic molecules, and water, several ZIFs also exhibit good thermal and chemical stability.<sup>313,314</sup> In contrast to ZIFs containing a single type of linker, it has

been shown that by incorporating two linkers in the same framework in different relative compositions, one can finely and continuously tune the pore size and host-guest interactions of ZIF frameworks.<sup>315,316</sup> This considerably increases the possibilities for using ZIF structures as a platform for engineering optimal materials for target separation applications without undertaking extensive *de novo* design and synthesis of ZIFs. For example, Eum et al.<sup>317</sup> and Rashidi et al.<sup>318</sup> recently demonstrated the continuous tuning of hydrocarbon and alcohol diffusivities over several orders of magnitude by varying the relative composition of ZIF-7, ZIF-8 and ZIF-90 linkers in mixed-linker ZIF-8-90 and ZIF-7-90 materials. Based on evidence from water adsorption and micro-Raman measurements, it was also shown that these mixed-linker ZIF materials incorporate both types of linkers in the same crystal and are not physical mixtures of single-linker ZIFs. However, no direct information about the unit-cell-level distribution/mixing of linkers could be gained from these measurements. The distribution of linkers lining the windows determines the pore sizes and shapes, and thereby the diffusion rate of molecules through the pores. In related work, several studies have demonstrated the use of computational techniques to screen ZIFs as potential candidates for specific separation processes.<sup>103,319-322</sup> However, it is not currently possible to simulate or predict the properties of experimental mixed-linker ZIFs, since the molecular-level linker mixing characteristics of these materials are unknown. Understanding the spatial distribution of the linkers in mixed-linker frameworks is critical in understanding how adsorption and diffusion properties can be controlled, and furthermore in selecting or designing appropriate linker combinations and compositions for a targeted separation process.

Due to the large degree of compositional disorder in mixed-linker ZIFs, crystallographic techniques cannot be used as a primary method for elucidating their structure. However, solid-state NMR spectroscopy can distinguish between the nuclear environments of different functional groups, for example in the study of domain sizes in block copolymers.<sup>323-326</sup> Recently several groups have successfully demonstrated the use



of NMR spectroscopy to study structural properties of MOFs. Baías et al. used  $^1\text{H}$  NMR spectroscopy in conjunction with X-ray crystallography to determine the local structure of a substituted imidazole based MOF (SIM-1).<sup>327</sup> With this technique, it was possible to deduce the relative orientation of functional groups that were present on the same linker molecule and their distribution within the framework. Recently, it was shown by Kong et al. that REDOR NMR can be used to estimate the linker distribution in multivariate (MTV) MOFs.<sup>328</sup> This technique requires isotopic labeling with  $^{13}\text{C}$  and  $^{15}\text{N}$  nuclei, since  $^{13}\text{C}$  is only 1.1 % naturally abundant (and hence insensitive), and  $^{14}\text{N}$  is a spin-1 nucleus (which is less amenable to REDOR).  $^1\text{H}$  NMR spin diffusion experiments performed by Kranjc et al. showed that the coarseness of the spatial distributions of linkers in two aluminum-based MOFs (DUT-5) could be distinguished when using 20 kHz magic angle spinning (MAS) and RFDR  $^1\text{H}$ - $^1\text{H}$  recoupling.<sup>329</sup> Here, we demonstrate the use of  $^1\text{H}$  CRAMPS spin diffusion experiments with 5 kHz MAS and no recoupling in conjunction with computational modeling of mixed-linker ZIFs for estimating linker distributions in multiple mixed-linker ZIF materials that are all mixed on size scales of  $\approx 1$  nm, which is a significant departure from the Kranjc study. We focus particularly on ZIF-8-90 hybrids as a typical example for such a challenging system and note that, unlike the previous work by Kranjc, routine Fickian-based spin diffusion analysis protocols cannot be used for vetting structures on these short length scales ( $< 1$  nm). The linker distributions in these materials are unknown *a priori*. This methodology does not require isotopic enrichment for the NMR measurements, and allows a generalized way of determining the structures of mixed-linker MOFs when one assumes a relatively simple, phenomenological spin exchange model. When two different types of linkers (with NMR-distinguishable protons) are distributed ('mixed') in the framework, the distribution of nearest neighbor inter-nuclear distances between the two functional groups will depend upon the degree of mixing. For example, in a clustered linker distribution (where each type of linker forms isolated phases) the distance distribution between

linkers of two different types will be very different from more random or highly ordered linker distributions. By measuring spin exchange rates using NMR, and matching them to dipolar couplings calculated from the proton positions from computationally generated models, one can ascertain the level of linker mixing in the materials of interest.

We have used the short-range order (SRO) as defined by the Warren-Cowley parameter  $\alpha$  to quantify the degree of linker mixing.<sup>330</sup> This parameter is defined as:

$$\alpha_j = 1 - \frac{P_j^{A(B)}}{x_B} \quad (4.1)$$

where  $P_j^{A(B)}$  is the conditional probability of finding the linker of type B at the  $j^{th}$  neighbor site given a linker of type A, and  $x_B$  is the fractional composition of linker type B in the material. For hybrid ZIF-8-90 systems, we have selected the nearest neighbor ( $j=1$ ) to define  $\alpha$ . Nearest neighbors (NNs) are not assigned based on the value of the distance but are based upon the sharing of a common  $Zn^{2+}$  center; therefore, each organic linker has 6 NNs. The contribution of second order NNs, (*i.e.*, those connected through two Zn metal centers) are assumed to be negligible (see below). Figure 4.1a shows the NN convention and Figure 4.1b shows a schematic of a ZIF-8<sub>50</sub>-90<sub>50</sub> hybrid 2×2×2 unit cell in which the linkers are randomly distributed. The experimentally measured spin diffusion curves of different mixed-linker ZIFs can be compared to the computationally generated spin diffusion curves of structures with different SROs to identify the value of  $\alpha$  that best describes the synthesized material. Note that for the calculation of spin exchange rates, multiple quantum effects, magic angle spinning effects, molecular dynamics, and long range couplings are ignored. The physical significance of this short-range order is demonstrated by showing how the window-type distribution varies as a function of  $\alpha$ . Since the diffusion of guest molecules through the cages of a ZIF material is governed by

the type of linkers that line the window, this distribution is critical in determining how material transport is a function of the relative composition of constituent linkers.

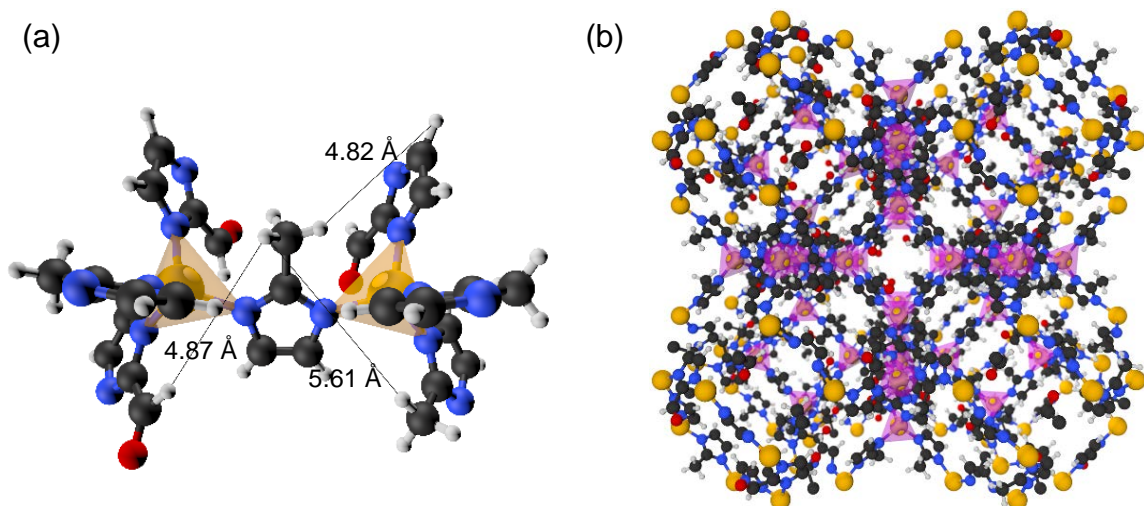


**Figure 4.1** (a) Schematic demonstrating nearest neighbor convention based on bond connectivity where the central mIm linker has 3 OHC-Im and 3 mIm NNs. (b) Schematic of a ZIF-8<sub>50</sub>-90<sub>50</sub> hybrid 2×2×2 supercell where the OHC-Im linkers are randomly distributed. Atom representations are as follows: O=red, N=blue, H=off-white, C=black, and Zn=gold. Yellow (a) and purple (b) tetrahedrons are included to illustrate the 4-coordinated Zn atoms.

## 4.2 Experimental Methods<sup>1</sup>

Pure ZIF-8 and ZIF-90 were synthesized according to a previously reported procedure.<sup>75</sup> The ZIF-8<sub>x</sub>-90<sub>100-x</sub> ( $0 < x < 100$ ) hybrid materials were made by the procedures given in Thompson et al.<sup>315</sup> Zinc nitrate hexahydrate and 2-methylimidazole (mIm, ZIF-8 linker) were obtained from Sigma Aldrich; imidazole-2-carboxaldehyde (OHC-Im, ZIF-90 linker) and sodium formate from Alfa Aesar; methanol and N, N-dimethylformamide were obtained from BDH Chemicals. All chemicals were used in the syntheses without further modifications or purification.

---

<sup>1</sup>All experimental work reported in this chapter was performed by Dr. Krishna C. Jayachandrababu in Dr. Sankar Nair's laboratory at the Georgia Institute of Technology, Atlanta, GA

Details of the synthesis of ZIF-8-90 materials, and characterization procedures for all the materials, are given in Appendix C. NMR measurements were performed on a Bruker Avance III 400 MHz spectrometer using a standard broadband H/X MAS probe. The samples (~5 mg) were loaded into 4 mm ZrO<sub>2</sub> rotors, and the magic angle spinning was intentionally set to a relatively low rate (5 KHz) so as to avoid the quenching of spin diffusion; experiments performed at faster rates exhibited long onset times. No recoupling was applied during the mixing time. 2D CRAMPS experiments were conducted using the phase modulated Lee-Goldburg decoupling during the evolution and detection times (Bruker Pulse sequence: wpmlg2d).<sup>331,332</sup> Mixing times ranging from 0.05-50 ms were used to study the temporal evolution of spin diffusion. Other typical experimental parameters were 399.92 MHz Larmor frequency, 2.5  $\mu$ s  $\pi/2$  pulse width, 56.57 kHz frequency offset, 12.5  $\mu$ s Lee-Goldburg  $2\pi$  pulse, receiver gain of 8, 4 scans, 512x128 2D points with sine apodization.

### 4.3 Simulation Methods

#### 4.3.1 ZIF-8<sub>x</sub>-90<sub>100-x</sub> Structure Generation

The starting ZIF-8 unit cell (structure code VELVOY<sup>301</sup>), and the ZIF-90 unit cell (structure code WOJGEI<sup>333</sup>) were taken from the Cambridge structural database (CSD).<sup>30</sup> As a standard self-consistency check, the geometries of these two bulk ZIF structures were energy minimized using plane wave density functional theory (DFT) calculations as implemented in the Vienna Ab initio package (VASP)<sup>155,334</sup> version 5.2.12. The generalized gradient approximation (GGA) Perdew-Burke-Ernzerhof (PBE)<sup>335</sup> functional was applied along with D2 dispersion corrections by Grimme.<sup>336</sup> Calculations were performed at the  $\Gamma$ -point with a 700 eV energy cutoff. Atomic forces were converged to < 0.03 eV/Å during both unit cell and atomic position relaxations. The unit cells for the two ZIFs were subsequently expanded into 5×5×5 supercells. The 5x5x5 supercells were not re-optimized after linker swapping since they comprised anywhere between 31500

(pure ZIF-90) and 34500 (pure ZIF-8) atoms, depending on the composition. A DFT structure optimization would have been computationally infeasible on a supercell this large. Small displacements ( $\sim 0.1$  Å) in the atomic positions of the hydrogens are not expected to have a large effect on the final spin diffusion predictions. Interatomic distances between the  $-\text{CH}_3$  and  $-\text{OHC}$  hydrogens on the order of  $>10$  Å would have a greater impact on the spin diffusion behavior.

A linker NN library was generated through the mIm connectivity determined using a fast percolation algorithm.<sup>337</sup> Using this library of linker NNs a simple Reverse Monte Carlo (RMC) procedure was implemented to generate a new linker NN library with a characteristic SRO and specified composition. A candidate linker swap that generated a NN library with a SRO closer to the target SRO,  $\alpha_t$ , was accepted with unit probability and unfavorable moves were accepted with probability  $\exp(-\beta/|\alpha-\alpha_t|)$  following from the Metropolis criterion. Values of  $\beta$  ranged from 1 to 1000 for different target SRO values and a total of  $1 \times 10^6$  MC steps were used. A fraction of mIm linkers were then chosen to be swapped with OHC-Im linkers using the final linker NN library. This procedure was implemented by aligning the imidazole ring plane normal vectors as well as the vectors defined by the primary carbon and the nitrogen-nitrogen centers-of-mass of an OHC-Im fragment and chosen mIm linker. Organic linker fragments were taken from the DFT energy optimized bulk structures. Several representative hybrid ZIF- $8_x$ -90 $_{100-x}$  XRD patterns calculated using Mercury CSD 3.5.1<sup>338-341</sup> are available in Appendix C.

#### 4.3.2 Semi-Empirical Fitting of $^1\text{H}$ CRAMPS NMR Intensity Curves

Simulated NMR intensity fit curves were generated using a kinetic model of spin exchange/diffusion using modeled proton positions as described by Perrin and Dwyer as well as Elena and Emsley.<sup>329,342-344</sup> This analysis assumes that relaxation of the  $z$ - (longitudinal) magnetization (parallel to the applied static magnetic field) back to its

equilibrium value during spin diffusion experiments can be modeled through a system of coupled differential equations. All details of the model along with relevant equations and parameters are given in Appendix C. This set of kinetic equations models the spin exchange behavior using the  $r^{-6}$  dependence of the exchange rate due to the dipolar coupling and assumes spin lattice relaxation occurs on time scales greater than even the longest mixing time.<sup>345-347</sup> To assess agreement between simulated and experimental  $^1\text{H}$  NMR spectral intensities at various values of  $r$ , we utilized the mean absolute error (MAE):

$$MAE = \frac{1}{n} \sum_{k=1}^n |I_{sim} - I_{exp}| \quad (4.2)$$

where  $n$  is the number of data points and the subscripts ‘sim’ and ‘exp’ refer to simulated and experimental values respectively. We generated mixed-linker ZIF structures spanning the range of SRO values for a fixed composition. From this set, we determined the structure with the minimum MAE and reported a confidence interval on the corresponding SRO. The SRO confidence interval is defined from the SROs that correspond to structures that yield MAE values within  $\pm 5\%$  of the minimum MAE structure.

## 4.4 Results and Discussion

### 4.4.1 Pure ZIF-8 and ZIF-90 NMR Analysis

The  $^1\text{H}$  chemical shift signatures of the methyl group (2.6 ppm), aldehyde group (9.8 ppm) and the protons on the 4- and 5- positions of the imidazole rings (7.3 ppm) in ZIF-8 and ZIF-90 were first identified using solution NMR of samples digested in  $d_4$ -acetic acid. Based upon initial survey measurements, the spinning frequency for spin diffusion data collection was fixed at an optimum of 5 kHz. The selection of spinning

frequency is important since there is a trade-off between the spectral resolution and strong dipolar coupling. At lower frequencies, the solid-state spectra were not sufficiently resolved whereas at higher frequencies the averaging of dipolar couplings slowed down spin diffusion and yielded a significant deviation from  $t^{1/2}$  behavior. Figures 4.2a-4.2b show  $^1\text{H}$ -NMR spectra for ZIF-8 and ZIF-90 and example contour plots of the two materials from the CRAMPS experiment at 1 ms mixing time. The diagonal peaks (marked by solid circles) are a result of direct observation of methyl and imidazole protons. The cross peak (marked by dashed circle) is caused by magnetization transfer between the nuclei corresponding to the diagonal peaks. The presence of this cross peak shows that there is intimate contact between the imidazole protons and the methyl protons in ZIF-8 as well as the imidazole protons and aldehyde proton in ZIF-90.

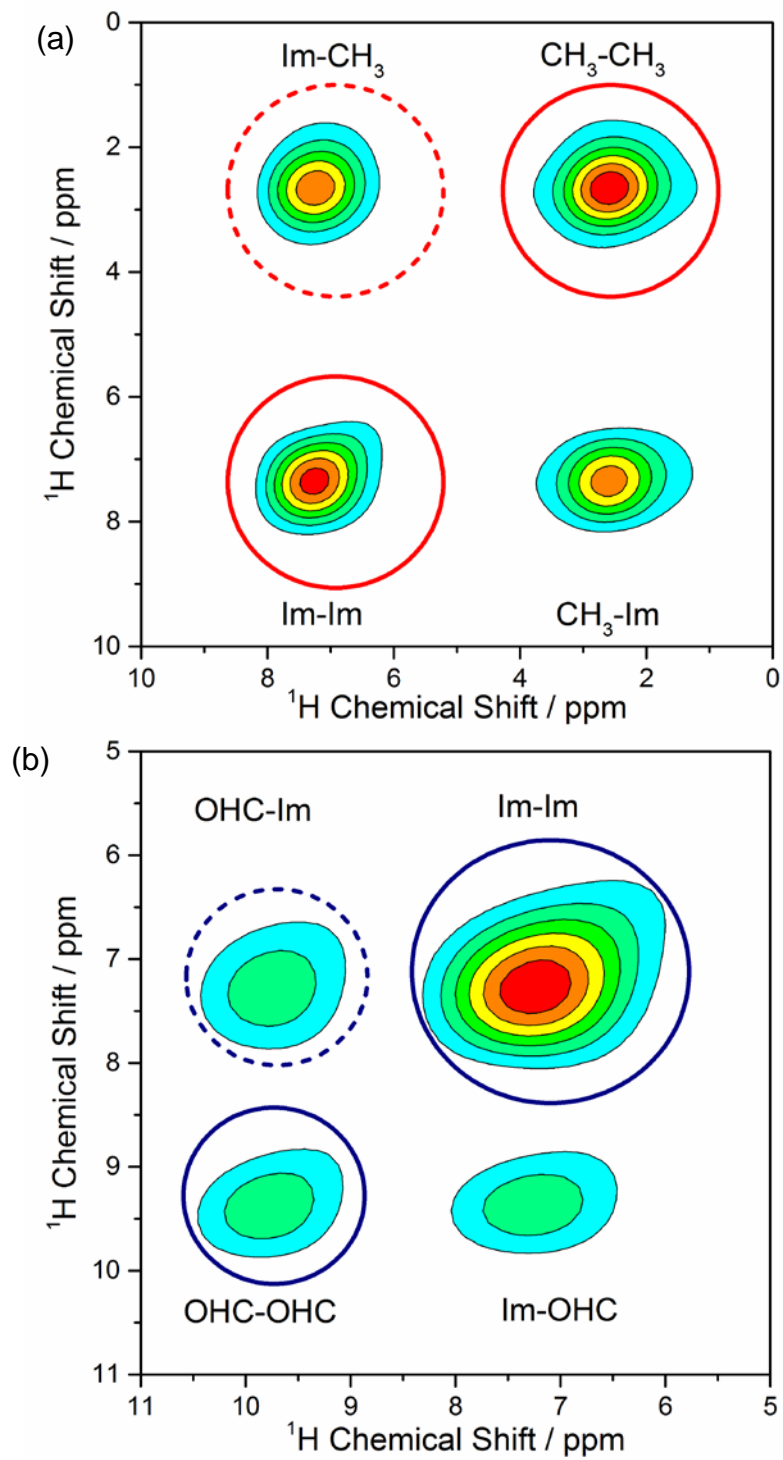


**Figure 4.2**  $^1\text{H}$ -NMR contour plots of (a) ZIF-8 and (b) ZIF-90, measured at 5 kHz MAS and 1 ms mixing time. Diagonal peaks are marked in solid circles and cross-peaks in dashed circles.



The CRAMPS NMR data from the two pure ZIFs were fitted to the kinetic spin exchange model (Equations C.2-C.8, Appendix C) to determine the single parameter  $A$  in the spin exchange rate-constant matrix (Equation C.6, Appendix C). Scaled experimental diagonal and cross-peak volumes as a function of mixing time, along with the model fits, are reported for ZIF-8 in Figure 4.3, and the results for ZIF-90 are shown in Appendix C. The obtained values for ZIF-8 and ZIF-90 are  $101.8 \pm 5.7$  and  $120.7 \pm 8.1$ , respectively. The values of initial  $z$ -magnetization (Equation C.5, Appendix C) for the  $-\text{Im}$  and  $-\text{CH}_3$  diagonal peaks were set as the average values from the sum of the diagonal and cross peak volumes (*e.g.*,  $\text{CH}_3\text{-Im} + \text{CH}_3\text{-CH}_3$  and  $\text{Im-Im} + \text{Im-CH}_3$ ) at mixing times between 2 to 40 ms. While the  $A$  values for the hybrid (mixed-linker) ZIFs are expected to all be similar based on the end-member ZIFs, for completeness we calculated  $A$  parameters for each of the mixed-linker ZIFs using a weighted geometric mean based upon the fractions of each type of linker in the mixed-linker material. The three initial  $z$ -magnetization values for the hybrid materials were set using the same methodology as described above. Only the interatomic distances between the  $-\text{CH}_3$ ,  $-\text{Im}$ , and  $-\text{OHC}$  hydrogens were changed in the various atomic models based on their different short range order values.

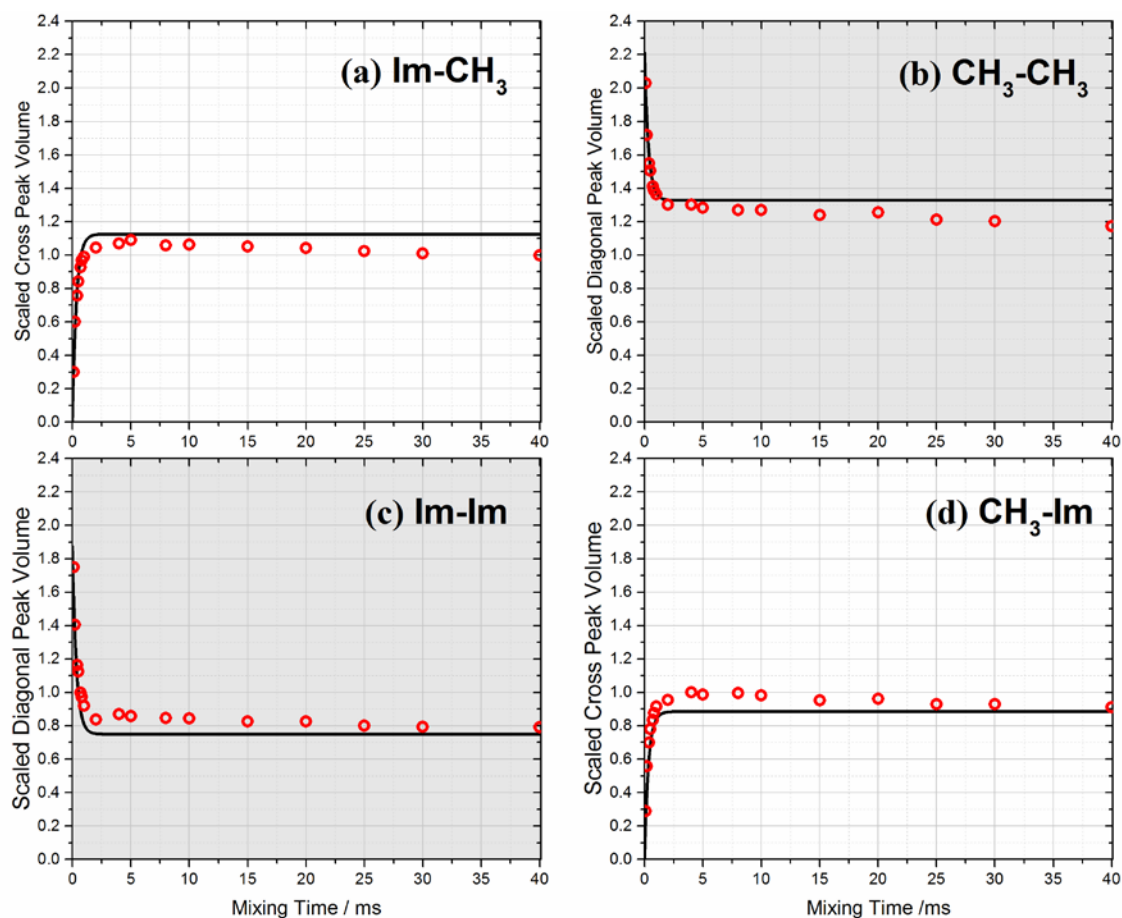


**Figure 4.3** Fit of the spin-exchange model (solid curves) to experimental CRAMPS NMR measurements (red circles) for spin exchange between protons in ZIF-8 as a function of the mixing time.

#### 4.4.2 ZIF-8<sub>x</sub>-90<sub>100-x</sub> Hybrid Materials

Figure 4.4a shows the CRAMPS contour plot at 50 ms mixing time from a sample consisting of equal amounts of pure ZIF-8 and pure ZIF-90 crystals mixed physically. As expected, cross-peaks for the methyl-to-imidazole-ring and aldehyde-to-imidazole-ring spin transfers are observed to arise from within the individual ZIF-8 and ZIF-90 phases since spin transfer occurs over length scales ranging from a few angstroms to tens of nanometers (within the time window of the experiment). However no methyl-to-aldehyde exchange is observed (dashed green circle) which is consistent with the crystal sizes of the ZIF samples being above 100 nm. In contrast, the 2D CRAMPS contour profile for a

ZIF-8<sub>50</sub>-90<sub>50</sub> sample collected at 1 ms mixing time is shown in Figure 4.4b. Spin transfer between methyl protons and aldehyde protons is clearly observed from the cross-peak at the expected position (dashed red circle).

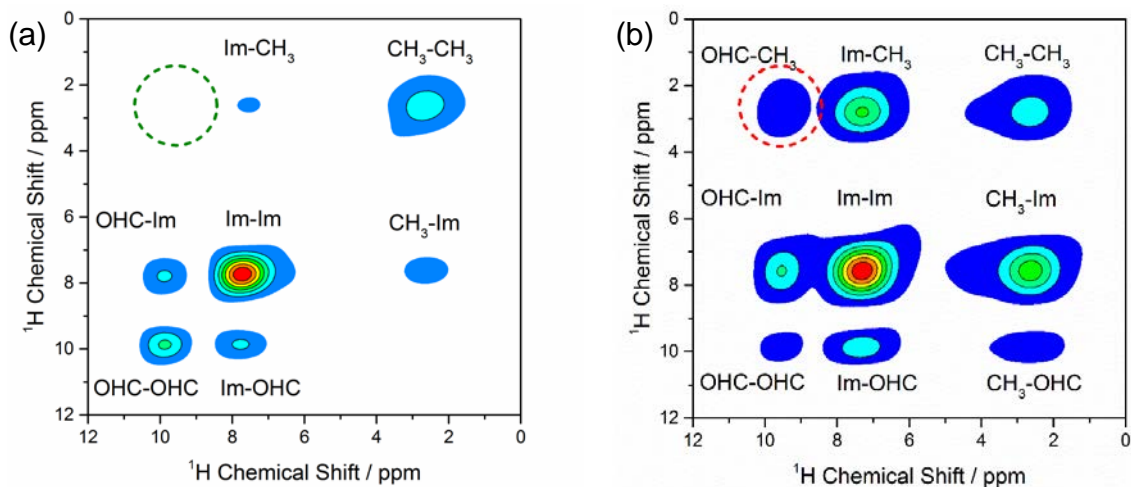


**Figure 4.4**  $^1\text{H}$ -NMR spectra of (a) physical mixture of ZIF-8 and ZIF-90 and (b) mixed-linker ZIF-8<sub>50</sub>-90<sub>50</sub>, measured at 5 kHz MAS and 50 ms mixing time. Green dotted circle in (a) denotes the absence of transfer between methyl and aldehyde protons in physical ZIF mixture. Red dotted circle in (b) shows the transfer in hybrid material.

Intensity profiles at several mixing times were used to study the spin diffusion and quantify the length scale of these transfer processes. ZIF-8 and ZIF-90 were used for calibration since the distances between the functional group and imidazole ring protons on each linker are known from their crystal structures.<sup>51</sup> Spin diffusion is the spontaneous exchange of spin polarization between nuclear spins, and the rate of this exchange is a function of the domain sizes that comprise the participating nuclei.<sup>345</sup> The intensity, which is defined as the ratio of the cross-peak area to the cross-peak and source-peak sum, is plotted versus the square root of the mixing time and shown in Figure 4.5a for both ZIF-8 and ZIF-90. Each spin diffusion profile shows an approximately linear increase from 0 – 2 ms<sup>1/2</sup> followed by a plateau at longer mixing times. The saturation

levels of these curves are defined by the relative ratio of protons in the source and the sink, which in this case are the methyl and aldehyde protons, respectively.<sup>323</sup>

For an estimation of the spatial distribution of linkers, one can adopt a Fickian-based spin diffusion approach. The advantage of this approach is that the domain size(s) of hybrids can be determined simply by the extrapolation of the early time, linear portion of the slope to the x-asymptote when plotted as a function of the square root of time.<sup>348</sup> In this case, the two unknowns are the dimensionality of the domains (spheres, rods, fractals, lamella, etc.) and the spin diffusion coefficient. An alternative technique such as transmission electron microscopy or small angle x-ray diffraction is required to determine the dimensionality of the domains. The spin diffusion coefficient can be estimated via empirical relations or using standards of known length scales of mixing.<sup>323</sup> We estimated the spin diffusion coefficients in the ZIF-8 and ZIF-90 neat materials by inspecting the proton positions in the crystal structures and performing finite element calculations of the spatial polarization changes using a lamellar model of packing of protons (Figure C.7 Appendix C) for various spin diffusion coefficient values. The best fit values were 0.25 nm<sup>2</sup>/ms and 0.2 nm<sup>2</sup>/ms for ZIF-8 and ZIF-90, respectively, which is on the lower end of reported <sup>1</sup>H spin diffusion coefficients (0.05 to 0.8 nm<sup>2</sup>/ms) and is likely due to proton diluteness compared to typical polymers.<sup>325,349</sup>

An alternative way for determining the spin diffusion coefficient  $D$  was introduced by White et al.<sup>325</sup>

$$D = \frac{\pi x^2}{4\varepsilon\tau_{eq}} \quad (4.3)$$

where  $x$  is the distance of the defined irreducible unit or domain as measured from the crystal structure,  $\varepsilon$  is the dimensionality of spin transfer, and  $\tau_{eq}$  is the observed

magnetization equilibration time. For intramolecular spin diffusion the characteristic dimension  $\langle x \rangle$  of the domain was estimated using

$$\langle x \rangle = (L \times d)^{0.5} \quad (4.4)$$

where  $L$  is the length and  $d$  is the diameter of the domain. For ZIF-8 and ZIF-90,  $x$  was estimated at 0.35 nm and 0.34 nm respectively from the crystallographic structures (Figure C.8, Appendix C).  $\tau_{eq}$  was evaluated by extrapolating the linear region of the spin diffusion curve to the saturation level as shown in Figure 4.5a, and was found to be 0.43 ms for ZIF-8 and 0.74 ms for ZIF-90. The values of  $D_{ZIF-8}$  and  $D_{ZIF-90}$  obtained using these parameters and Equation 4.3 are 0.2 nm<sup>2</sup>/ms and 0.1 nm<sup>2</sup>/ms, respectively.

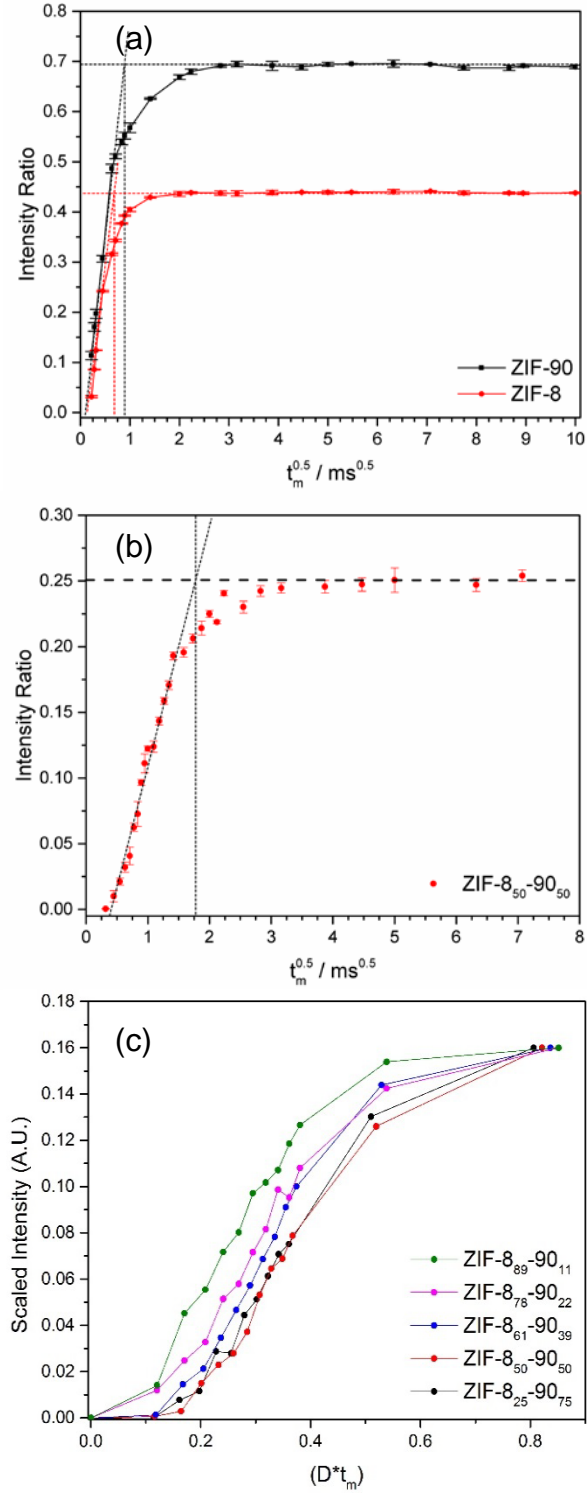


**Figure 4.5** Spin diffusion profiles of (a) ZIF-8 and ZIF-90, (b) ZIF-8<sub>50</sub>-90<sub>50</sub>, and (c) ZIF-8-90 at various compositions scaled by the anticipated spin diffusion coefficient.

Figure 4.5b shows the spin diffusion plot for a ZIF-8<sub>50</sub>-90<sub>50</sub> mixed-linker material. The expected saturation level (at long mixing times) of the spin diffusion curve for this composition is also shown. This can be calculated purely from the bulk composition by taking the ratio of numbers of source and sink protons. For example, in ZIF-8<sub>50</sub>-90<sub>50</sub> there are 3 methyl protons for every aldehyde proton and hence the expected saturation ratio was calculated as  $1/(1+3) = 0.25$ .  $\tau_{eq}$  was estimated at 3.1 ms by extrapolating the slope to the asymptote. The corresponding value of  $x$  calculated using Equation 4.3 is  $\approx 1$  nm; note that the dimensionality ( $\epsilon$ ) is not known *a priori*.

We also compared the spin diffusion data for the multiple compositions of ZIF-8<sub>x</sub>-90<sub>100-x</sub>. Since the spin diffusivity is likely to change (subtly) amongst the samples because of changes in the proton density and (potentially) molecular dynamics, we scaled the spin diffusion data for the multiple compositions by the anticipated spin diffusion coefficient. The spin diffusion coefficients were calculated by either interpolating between the ZIF-8 and ZIF-90 using either a geometric average or by using the second moment of the single pulse excitation spectra (Figures C.9 and C.10, Appendix C) for use in known equations of the spin diffusion coefficient. Both methods yielded similar results. The data is shown in Figure 4.5c, where we have scaled the asymptotes to coincide and have zoomed into the early time points. As shown in the figure, all of the compositions have nearly the same total equilibration time,  $(Dt)^{0.5} \approx 0.9$ , which suggests that the total repeat units of the domains in ZIF-8<sub>x</sub>-90<sub>100-x</sub> materials are nearly identical at a length scale comparable to their XRD-derived cavity diameters as measured with Zeo++<sup>72</sup> for ZIF-8 (1.14 nm)<sup>301</sup> and ZIF-90 (1.136 nm)<sup>333</sup>, and also to the size of their unit cells (1.699 nm and 1.727 nm respectively). Previously, there had been no direct evidence of linker mixing in ZIFs at sub-unit-cell length scales. While previous findings that employed techniques including micro-Raman spectroscopy<sup>17</sup>, photothermal induced resonance (PTIR)<sup>58</sup>, and aerosol time-of-flight mass spectrometry (ATOF-MS)<sup>59</sup> for observing spatial uniformity in mixed-linker MOFs have been limited to length scales greater than 100 nm, the above

NMR spin diffusion measurements conclusively establish that there is sub-unit-cell linker mixing in these mixed-linker ZIFs. However, in order to delineate further between these structures, we turned to a kinetic exchange model.

The spin equilibration times (scaled by the estimated spin diffusion coefficients) are approximately the same amongst the compositions, which denotes the same total repeat distance in each of the samples. The 50:50 composition exhibits the slowest initial slope, denotes the largest possible domain, and decreases in composition of either of the components only serve to decrease the average cluster size and increase the slope, an observation consistent with previously determined Fickian models. However, we also observe a drastic deviation from the classic Fickian  $t^{1/2}$  dependence upon decreasing the ZIF-8 fraction. Chen et al.<sup>350</sup> has shown that local ( $< 1$  nm) spin diffusion coefficients can be slower than those at longer length scales due to non-diffusive, exponential behavior due to discrete exchange events. Here, it seems the time window over which this occurs varies with sample and is likely due to the composition-dependent change in the uniformity of local dipolar fields under MAS. Upon inspection of the single pulse excitation  $^1\text{H}$  MAS NMR spectra (Appendix C), the ZIF-8-heavy materials exhibit only weak MAS sideband intensity, which would suggest a strong network of dipolar coupled protons, little appreciable dipolar field averaging, and more uniform dipolar fields. The ZIF-90-heavy hybrids, on the other hand, exhibit NMR spectra with strong sideband intensities with no appreciable underlying broadened features, which suggests significant averaging of weak couplings in the presence of strong couplings and less uniform dipolar fields.

Next we explore the possibility of determining more quantitatively the short-range linker mixing patterns. Several groups have used  $^1\text{H}$  spin diffusion NMR as a method for predicting proton positions using rates of exchange between neighboring protons using kinetic equations. We created models of mixed-linker ZIFs that had the same relative linker compositions but different SRO ( $\alpha$ ) values, *via* methods described in a previous



section. The Warren Cowley parameter, used to quantify SRO, is normalized to cover the range from [-1, 1]. A system with an  $\alpha$  value of 1 (-1) is completely clustered (ordered). For the periodic systems under consideration, the SRO of clustered structures can asymptotically approach 1 with increasing unit cell size since there will always be an interface between regions containing only linkers of one type. The lower bound ( $\sim -0.29$ ), as determined through our RMC procedure, is observed to be constant for a composition range of 0.21 to 0.79 mole fraction of OHC-Im linkers. We attribute this observable lower limit to our definition of nearest neighbors as well as the specific topology of our ZIF system. The lower limit on the SRO parameter may not be possible to determine *a priori* for 3D periodic systems and would change depending on our definition of linker coordination. Figure 4.6 shows how the functional group protons ( $-\text{CH}_3$  for ZIF-8 and  $-\text{CHO}$  for ZIF-90) are distributed in space over a  $5 \times 5 \times 5$  unit-cell volume for ZIF-8<sub>50</sub>-90<sub>50</sub> with three different values of  $\alpha$  representing clustering, randomization, and significant ordering respectively. While Fickian models of spin diffusion could eliminate such a highly clustered model as shown in Figure 4.6a (SRO = 0.87) as a possibility for the structures here, kinetic models may offer a more precise estimate of varying degrees of randomization and clustering (Figures 4.6b-4.6c). For each overall composition, simulated  $^1\text{H}$  CRAMPS NMR intensity patterns for the mixed-linker structures with different  $\alpha$  values were directly calculated using nearest-neighbor dipolar couplings (see Appendix C). No fitting parameters are used, since the spin exchange parameter  $A$  is already known from the calibrations with ZIF-8 and ZIF-90. For example, Figure 4.7 shows the experimentally measured and calculated peak intensities of ZIF-8<sub>50</sub>-90<sub>50</sub> for  $\alpha = 0.45$ . The subplots shaded in pink represent NMR spin exchange between methyl protons on the ZIF-8 linker and the aldehyde protons on the ZIF-90 linker, the transfer processes that are of most interest for structure determination; although all the exchange processes are measured and calculated. The agreement between experimental and simulated NMR curves was quantified using MAE (Equation 4.2), which was used to

determine the structure that most closely reproduces the experimental data for each mixed-linker ZIF composition. Specifically, we used the intensity ratio of the cross peak corresponding to the methyl-to-aldehyde (CH<sub>3</sub>-CHO) transfer to the sum of the intensities of the methyl diagonal peak (CH<sub>3</sub>) and the CH<sub>3</sub>-CHO peak (as plotted earlier in Figure 4.5) for assignment of an SRO value. Simulated curves were generated for several structures with identical composition but different short-range-order values.

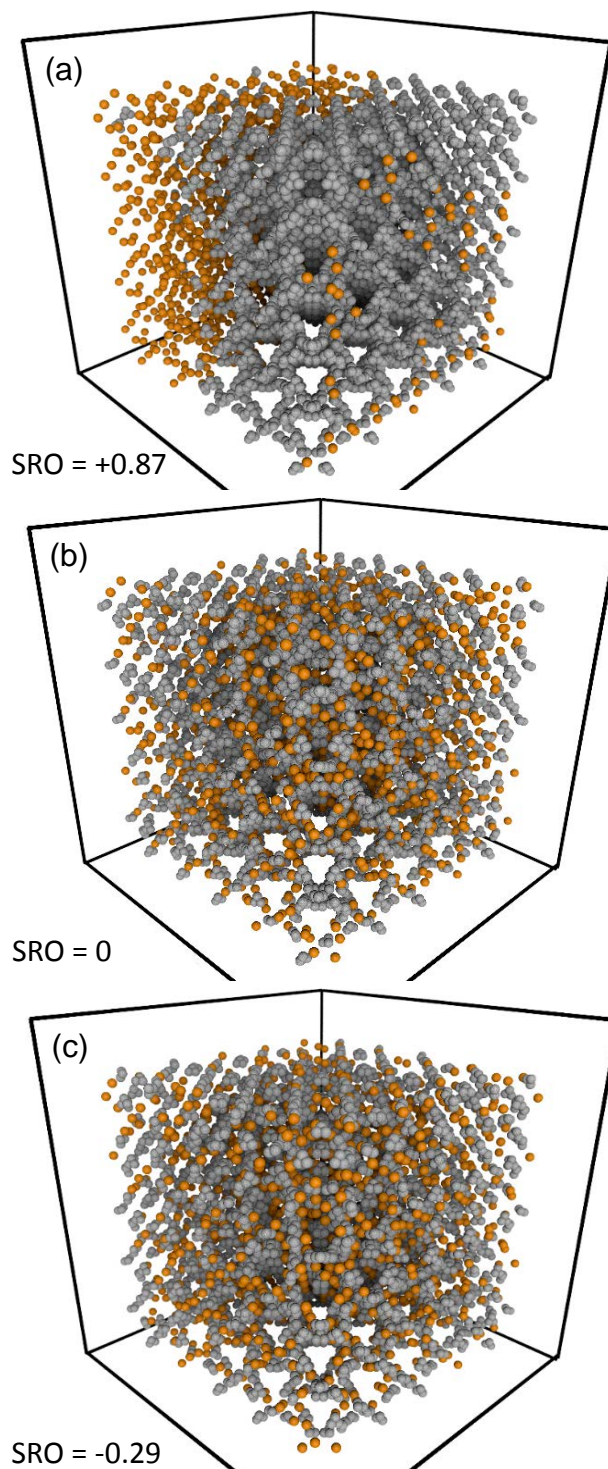


**Figure 4.6** ZIF-8<sub>50</sub>-90<sub>50</sub> methyl (gray) and aldehyde (orange) hydrogen maps for 5×5×5 supercells of size 8.47 nm: (a) SRO of  $\alpha = 0.87$  demonstrating extreme clustering, (b) SRO of  $\alpha = 0.0$  demonstrating a random linker arrangement, and (c) SRO of  $\alpha = -0.29$  demonstrating partial ordering. Hydrogens not to scale, in order to enhance clarity.

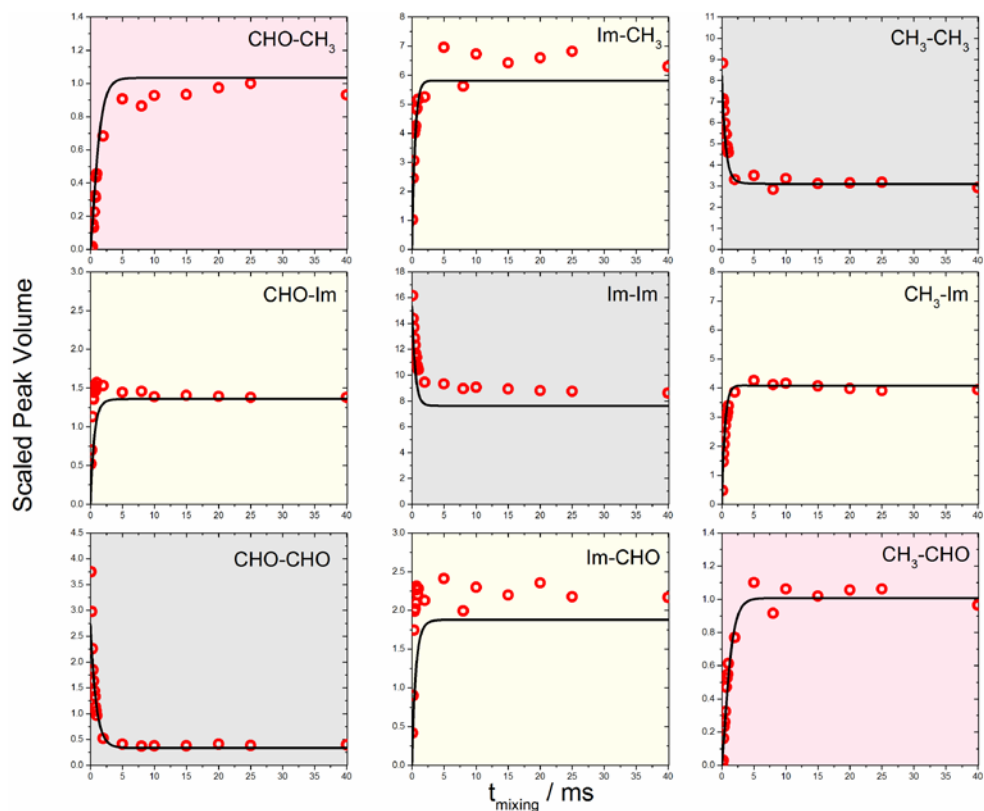


**Figure 4.7** Experimental (open red circles) and simulated NMR spin exchange peak intensities for ZIF-8<sub>50</sub>-90<sub>50</sub> with  $\alpha = 0.45$ .

The comparisons for ZIF-8<sub>50</sub>-90<sub>50</sub> are shown in Figure 4.8. The best minimum MAE between experimental and simulated curves for this material is given by the structure with  $\alpha = 0.45$  (Figure C.13, Appendix C). From the definition of  $\alpha$ , it follows that the two linkers in ZIF-8<sub>50</sub>-90<sub>50</sub> exhibit some tendency for clustering. The value of  $\alpha = 0.45$  indicates that given a methyl linker in ZIF-8<sub>50</sub>-90<sub>50</sub>, there is a 28% probability that there is an aldehyde linker present in each of its six nearest neighbor sites. A  $\pm 5\%$  deviation was chosen as the tolerance limit for describing the structure with reasonable accuracy. It was found that structures with  $0.40 < \alpha < 0.55$  fell in this range.

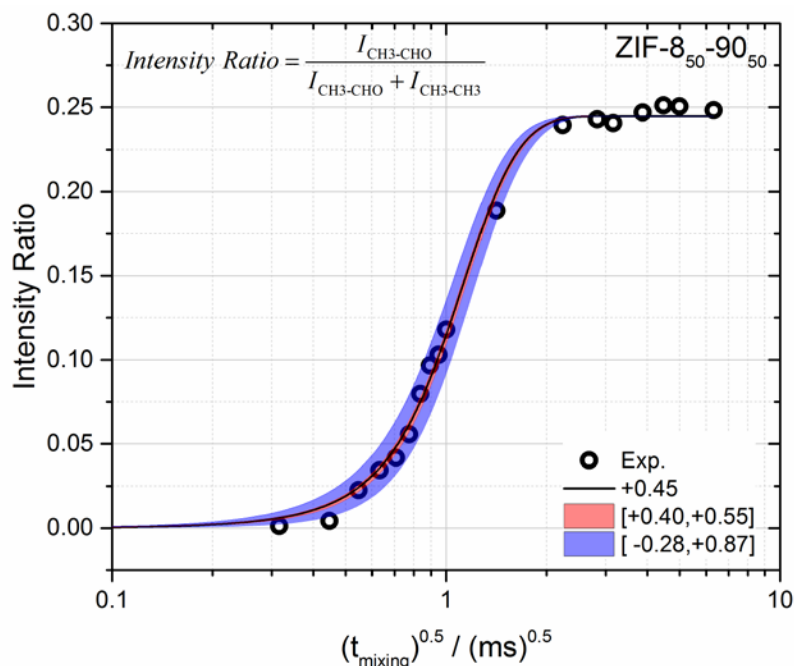


**Figure 4.8** Comparison of experimental NMR spin exchange intensity ratios and simulated curves for several structures with different  $\alpha$  values for ZIF-8<sub>50</sub>-90<sub>50</sub>.

Figure 4.9 shows the best fits of the spin exchange plots for the various compositions of mixed-linker ZIF-8<sub>x</sub>-90<sub>100-x</sub> materials, and Figure C.13 (Appendix C) shows the MAE versus  $\alpha$  for each composition. The model yields good fits for ZIF-8<sub>25</sub>-90<sub>75</sub>, ZIF-8<sub>61</sub>-90<sub>39</sub>, and ZIF-8<sub>78</sub>-90<sub>22</sub> yield good fits, but ZIF-8<sub>89</sub>-90<sub>11</sub> shows greater deviation. Recall that ZIF-8<sub>89</sub>-90<sub>11</sub> yielded a spin diffusion curve with a strong  $t^{1/2}$  dependence (Figure 4.5c) and weak spinning sideband intensity at 5 kHz MAS (Appendix C), suggesting the strongest network of dipolar couplings of the ZIF-8<sub>x</sub>-90<sub>100-x</sub> compositions. Since the kinetic exchange model is based solely on direct couplings and ignores multiple quantum, molecular dynamics, and MAS effects, we therefore posit that the model is most accurate when studying sample sets with less appreciable variation in the local proton density and/or dynamics.

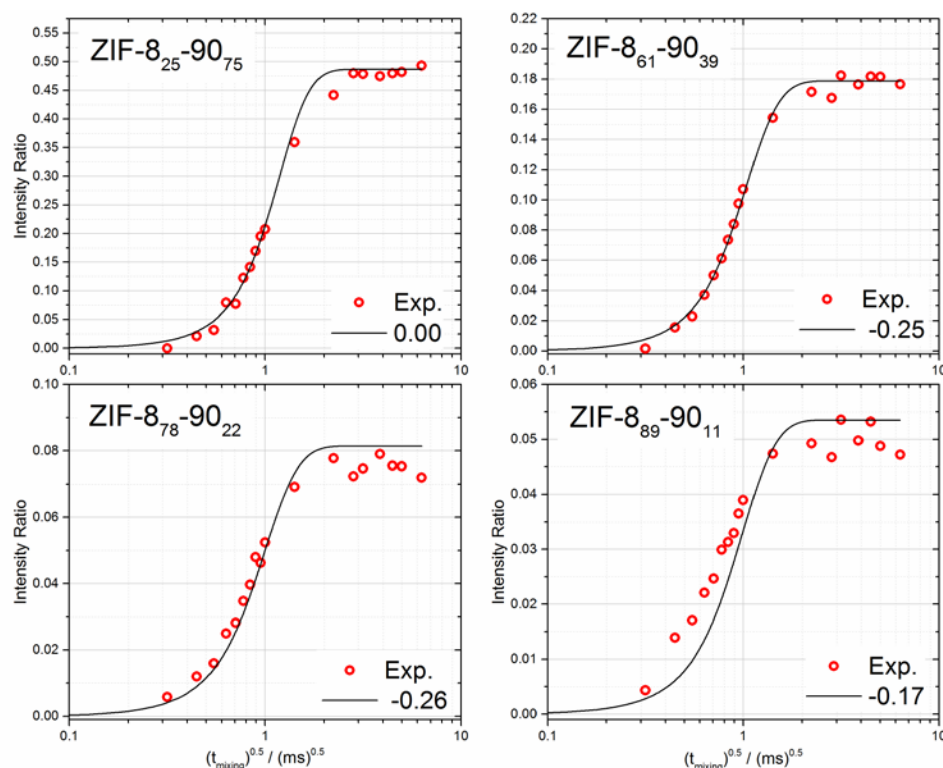


**Figure 4.9** Comparison of experimental (red circles) and simulated 2D CRAMPS peak ratios of the ‘best-fit’ SRO models (solid black lines), for four different ZIF-8-90 mixed-linker materials.

For the compositions that the model is most successful, it was observed that the best-fit  $\alpha$  value falls in the range that indicated a close to randomly distributed structure, with the exception of ZIF-8<sub>50</sub>-90<sub>50</sub>. This is represented graphically in Figure 4.10 in relation to the ‘nearest neighbor’ concept. The anomalous behavior of ZIF-8<sub>50</sub>-90<sub>50</sub> is not clearly understood at this point. It must be noted that this material certainly shows linker mixing at a unit-cell level and has long-range compositional homogeneity. The variation in  $\alpha$  is directly translated to a slightly higher tendency for pore windows to have exclusively ZIF-8 or ZIF-90 linkers (see below). Even though individual windows have different compositions, there are multiple windows of each type within each unit cell and at length-scales higher than that of each unit cell, the compositional homogeneity is

preserved. We can offer the hypothesis that when both linkers are present in roughly equal amounts, there may be an increased thermodynamic or kinetic driving force that tends towards cluster formation during synthesis. On the other hand, when one linker is in the minority, it may prefer to be more randomly distributed within the ‘matrix’ of the majority linker. Experimentally, it has been observed that the rate of formation of ZIF-8<sub>x</sub>-90<sub>100-x</sub> goes from slow (observable product formation in a duration of many minutes) to fast (nearly instantaneous) as the relative content of the OHC-Im linker is increased from 0 to 100%. The observed deviation from near-random mixing of ZIF-8<sub>50</sub>-90<sub>50</sub> could be attributed to competing effects of heats-of-mixing and the reaction kinetics. Although uncommon, such deviations from the expected value of order parameter for binary materials are known. For example, an almost-equiatomic Pd-Pt alloy was shown (*via* X-ray scattering measurements) to exhibit a more ordered behavior than what was expected based on phase transition thermodynamics.<sup>351</sup>

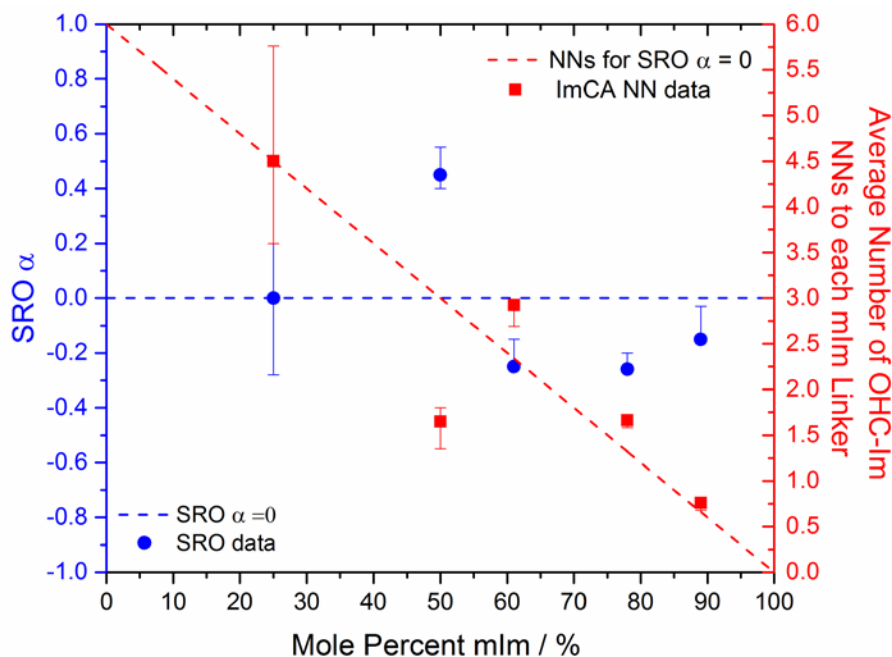


**Figure 4.10** Short range order  $\alpha$  and average number of OHC-Im linkers per mIm linker as a function of the overall composition of the mixed-linker ZIF-8-90 material.

It has been clearly shown that hybrid cage-type ZIF-8-90 materials allow for drastic tunability of molecular diffusion<sup>317</sup>, implying that diffusion is primarily influenced by the three imidazolate linkers lining the pore windows between cages. These windows can be classified into 4 types: Type 1 (lined by 3 mIm linkers), Type 2 (2 mIm linkers and 1 OHC-Im linker), Type 3 (1 mIm linker and 2 OHC-Im linkers), and Type 4 (3 OHC-Im linkers). The various structure models generated with different compositions and short-range orders can then be differentiated according to the probability distribution of these windows in the structure. A set of 166 unique 5x5x5 supercells were generated to represent the entire composition and accessible SRO parameter ranges to provide a qualitative understanding of the effect of SRO on window type probability. The probability of window types was determined in a two-step method. A depth-first search (DFS) algorithm was applied that identified cycles of size N (i.e. all 6 member rings) in an undirected graph (i.e. SOD topology with Zn centers as nodes and linkers as edges). Once all the 6 member rings were identified and the mIm/OHC-Im linkers had been assigned according to the RMC procedure described above, an assignment algorithm identifies which three linkers (i.e. those with imidazole ring hydrogens in the plane of the window) belong to each 6 member ring window. The type of these three linkers determines the window type. No energetic parameters were taken into account for this analysis. Figure 4.11 below shows four contour plots representing the fractional probabilities of observing each of the four window types for a structure with a given composition and short-range order. For example, structures with positive SROs (*i.e.*, more clustered linkers) demonstrate lower probabilities of observing Type 2 and Type 3 windows. The locations of the five experimentally studied hybrid materials are shown by the red circles in each plot. The ZIF-8<sub>50</sub>-90<sub>50</sub> structure has very similar window probability profiles whether the linkers are clustered (+0.45) or alternating (-0.25). While outside the scope of the present study, the above method of differentiating the structural



models based on window type distributions could be used to qualitatively predict the influence of SRO on diffusion properties.

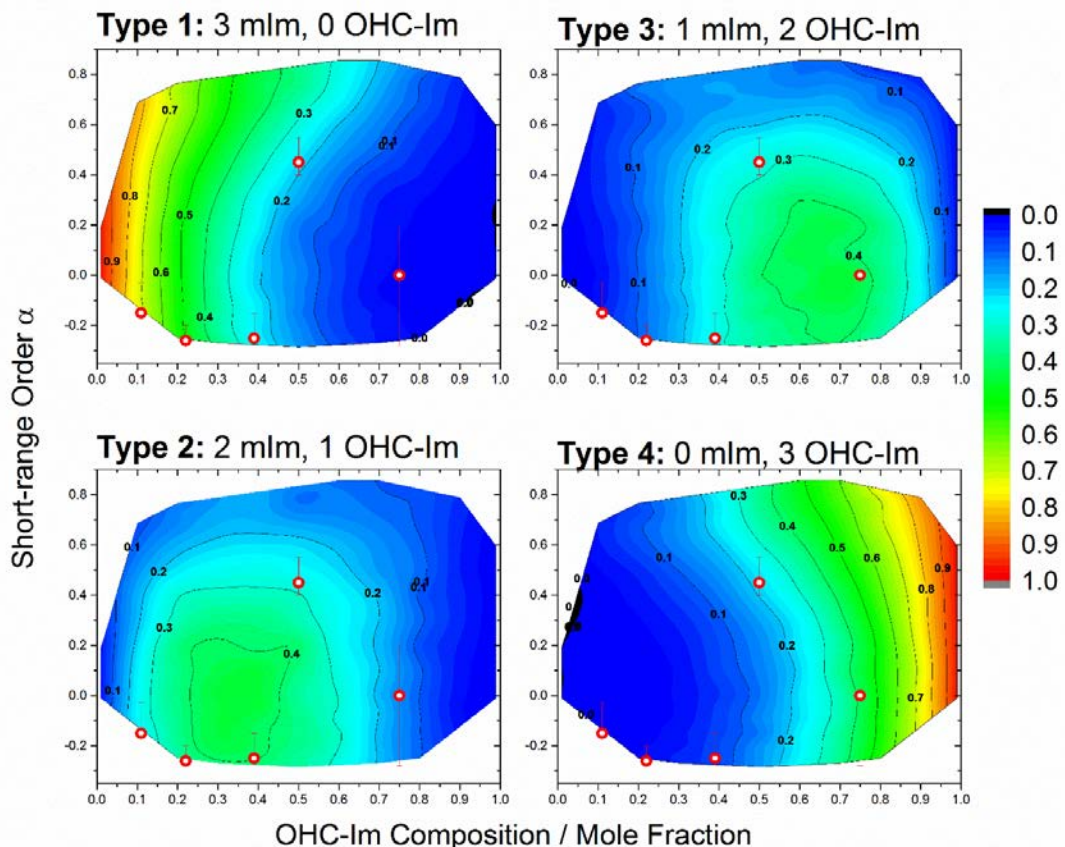


**Figure 4.11** Probability distributions of observing the four possible types of pore windows as a function of the short range order parameter ( $\alpha$ ) and the overall composition of the mixed-linker ZIF-8-90 material. Red circles indicate the window type probabilities for the experimental samples.

## 4.5 Conclusions

We have determined the unit-cell-level mixing of linkers in mixed-linker ZIFs (specifically ZIF-8-90) using a combination of  $^1\text{H}$  CRAMPS NMR spectroscopy and computational techniques. Direct experimental observations of linker mixing were accomplished by measuring the spin diffusion behavior between functional groups on the linkers. The experimental data was then compared to simulations based on a spin

exchange model and proton positions from computationally generated mixed-linker ZIF structure models that use the short-range order (SRO) parameter as a measure of the ordering, clustering, or randomization of the linkers. The present method offers the advantages of not requiring isotope enrichment as well as a potentially reasonable way of predicting how subtle changes in structure can affect the pore/window-type distribution in mixed-linker materials. Our findings undeniably indicate that the linkers in ZIF-8-90 hybrids are mixed on the sub-unit cell length scale, and provide conclusive evidence that the synthesis of these mixed-linker ZIFs results in true hybrid materials as opposed to separated or clustered phases within the same crystal. When using the kinetic spin exchange model, we find that the mixed-linker ZIFs exhibit slightly different levels of linker mixing depending on the bulk composition. Furthermore, structures close to equimolar composition of the two linkers appear to have greater tendency for linker clustering than those with a majority content of one linker. Using the mixed-linker ZIF structures determined by the NMR experiments and modeling, we have also shown how the window-type distribution in experimentally synthesized mixed-linker ZIF-8-90 materials varies as a function of their composition. The above structural information can be further used for predicting, screening, or understanding the tunable adsorption and diffusion behavior of mixed-linker ZIFs. This technique can be potentially applied to any MOF system with linker functional groups containing protons that are distinguishable by NMR and topologies known *a priori* through crystallographic techniques.

## CHAPTER 5

# LATTICE MODEL OF ADSORBATE DIFFUSION THROUGH MIXED-LINKER ZEOLITIC IMIDAZOLATE FRAMEWORKS

The below text was reproduced from the article “Lattice-Gas Modeling of Adsorbate Diffusion in Mixed-Linker Zeolitic Imidazolate Frameworks: Effect of Local Imidazolate Ordering” by Ross J. Verploegh, Ying Wu, and David S. Sholl in *Langmuir*, 2017. Copyright 2017, American Chemical Society. This article was selected as an ACS Editor’s Choice® article; as a result, this is an open access article published under an ACS AuthorChoice License. This license permits copying and redistribution of the article or any adaptations for non-commercial purposes. Ying participated as a co-first author. This chapter details how the local ordering of imidazolate linkers in binary mixed-linker ZIFs influences diffusion properties.

The rates of adsorbate diffusion in zeolitic imidazolate frameworks (ZIFs) can be varied by several orders of magnitude by incorporating two different imidazolate linkers in the ZIF crystals. Although some prior measurements of short-range order in these mixed-linker materials have been reported, it is unclear how this short-range order impacts the net diffusion of adsorbates. We introduce a lattice diffusion model that treats diffusion in ZIF-8<sub>x</sub>-90<sub>100-x</sub> crystals as a series of activated hops between cages, allowing us to assess the effects of short range imidazolate order on molecular diffusion.

### 5.1 Introduction

Metal-organic frameworks (MOFs)<sup>208</sup>, a class of nanoporous materials that form through the coordination of metal nodes and organic linkers<sup>352</sup>, have demonstrated potential for use in gas storage<sup>353</sup>, adsorption<sup>27</sup>, catalysis<sup>23</sup>, molecular sieving<sup>354</sup>, drug

delivery<sup>355</sup>, and sensing applications<sup>356</sup>. Adding to an already large set of synthesized MOFs, researchers have created MOFs with two or more types of organic linkers, termed multivariate (MTV), mixed-linker, mixed-ligand, or hybrid MOFs.<sup>357</sup> Mixed-linker MOFs fall under Yaghi et al.'s "heterogeneity within order" description applied to MOFs that exhibit multiple building units (i.e. metal nodes or organic linkers) or demonstrate deviations from perfect order (i.e. defects).<sup>358</sup> Some mixed-linker MOFs are synthesized with combinations of linkers and the arrangement of these linkers is known on the unit cell level through single crystal X-ray diffraction (XRD) refinement techniques.<sup>359</sup> We describe these MOFs as having a long-range ordering of their organic linkers. Examples of mixed-linker MOFs with long-range order include the DMOF family, whose structures contain both the 1,4-benzenedicarboxylic acid (BDC) and the pillar linker 1,4-diazabicyclo[2.2.2]octane (DABCO) ligands.<sup>360</sup> There are also mixed-linker MOFs that exhibit only local (short-range) ordering, with the apportionment of organic linkers varying within the region of several unit cells. Numerous examples exist including MTV-MOF-5,<sup>357</sup> MTV-MOF-177,<sup>361</sup> and various MOFs from the MIL<sup>362</sup>, UiO<sup>363</sup>, and ZIF<sup>42</sup> families. Determining the local ordering of these mixed-linker MOFs is experimentally challenging. Kong et al. used solid-state NMR measurements combined with molecular simulations to determine the ordering of organic linkers in MTV-MOF-5 materials.<sup>31</sup> Krajnc et al. performed <sup>1</sup>H spin-diffusion MAS NMR to determine the local ordering of biphenyl and bipyridyl dicarboxylic linkers in MOF DUT-5 containing AlO<sub>6</sub> octahedra.<sup>364</sup> Jayachandrababu et al. determined the local ordering of 2-methylimidazolate and carboxaldehyde-2-imidizolate linkers in ZIF-8-90 materials using <sup>1</sup>H CRAMPS NMR and computational modeling.<sup>46</sup>

The presence of local order in solid solutions (e.g. metal alloys<sup>365</sup>) has been shown to have non-negligible effects on various physical and chemical properties (e.g. electrical resistivity, strength, diffusion, etc. in metal alloys).<sup>366</sup> As an example, Kamakoti et al. studied hydrogen diffusion through binary face centered cubic (fcc) Pd<sub>x</sub>-

Cu<sub>100-x</sub> alloys and determined that local ordering had a measurable impact on the diffusion rates of interstitial H atoms.<sup>330</sup> Little is known about how the local ordering of linkers in mixed-linker MOFs impact properties such as guest diffusion and adsorption. Because considerable experimental and computational effort must be devoted to quantifying the local ordering of organic linkers, there is merit in understanding how strongly this kind of local ordering affects properties of interest. In this chapter, we focus on one subclass of MOFs, zeolitic imidazolate frameworks (ZIFs), which have been demonstrated to operate as molecular sieves in both membrane<sup>16,367</sup> and kinetic adsorption<sup>368</sup> separations. Pimentel et al. summarized common single-linker and mixed-linker ZIFs that form an array of topologies based on the coordination environment of either Zn or Co metal ions with various functionalized imidazolate linkers.<sup>369</sup> Binary mixed-linker ZIFs with short-range order have been shown experimentally to provide tunability of guest diffusion rates. Eum et al. demonstrated that it was possible to tune the diffusion properties of water, small alcohols, *n*-butane and isobutane through ZIF-8-90 materials.<sup>189</sup> Rashidi et al. examined *n*-butane and isobutane diffusion tunability in ZIF-7-90 materials.<sup>43</sup> Zhang and Koros demonstrated that *n*-butane, isobutane, and SF<sub>6</sub> diffusion can be tuned in a binary ZIF containing both 2-methylimidazolate and imidazolate linkers.<sup>370</sup>

The aim of this chapter is to determine if the local ordering of a binary mixture of imidazolate linkers affects intracrystalline adsorbate diffusion in mixed-linker ZIFs. Our study focuses on ZIF-8<sub>x</sub>-90<sub>100-x</sub>, which has been extensively characterized through powder XRD, <sup>1</sup>H NMR, and various adsorption and diffusion experiments.<sup>42,189</sup> Parent ZIF-8 and ZIF-90 materials, as shown in Figure 5.1, are comprised of 2-methylimidazolate linkers (mIm) and carboxaldehyde-2-imidazolate (ImCA) linkers respectively. ZIF-8 and ZIF-90 both form in the sodalite (SOD) zeolite topology, exhibit cubic unit cells with similar volumes (ZIF-8: 4904 Å<sup>3</sup>, ZIF-90: 5151 Å<sup>3</sup>), and have almost identical powder XRD patterns according to the refined structures from the Cambridge

Structural Database (CSD).<sup>371</sup> Because of the similarity of the unit cells and distances between cage centers, it is possible to readily study how the local ordering of ImCA and mIm linkers impacts diffusion properties.

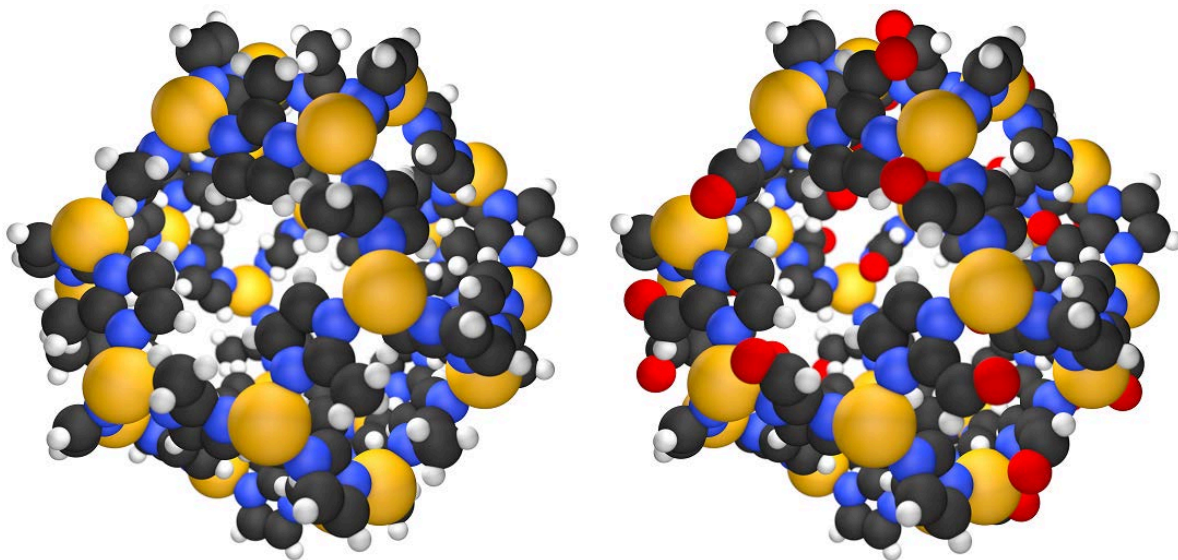


**Figure 5.1** Truncated octahedron representing a singular cage of both parent (a) ZIF-8 and (b) ZIF-90. H, C, N, O and Zn atoms colored off-white, black, blue, red, and gold respectively.

We first define our methods for creating mixed-linker  $\text{ZIF-8}_x\text{-90}_{100-x}$  of various compositions with quantitatively defined short-range order. We describe the basic theory behind adsorbate diffusion in these materials and how we use kinetic Monte Carlo (KMC) to measure infinite dilution self-diffusion coefficients of molecules in these structures. We begin by examining how the existence of percolation pathways with window blocking impacts diffusion in ZIF-8-90. While this limiting case is conceptually appealing, real binary mixed-linker ZIFs have non-zero diffusivities in both parent ZIFs. Thus, examining diffusion through the hybrid materials means deriving the catalogue of diffusion rates, which are presumably functions of the distributions of 6 member-ring (MR) window (i.e. pore) types in ZIF-8-90 systems. Rates through “hybrid” windows in the ZIF-8-90 system that are not present in the parent ZIFs require interpolation of the

rates through the “parent” windows. We studied five such interpolation schemes and compare their predictive capability to experimental n-butane and isobutane diffusion in ZIF-8-90. We demonstrate that a simple model based on this approach can be used to predict tunable diffusion properties, with only a weak dependence on the interpolation scheme applied.

## 5.2 Theory

### 5.2.1 Quantifying Local Order in Binary Mixed-Linker ZIFs

We will refer to the two imidazolate linkers as type A and type B linkers and denote the composition of crystals as ZIF-A<sub>x</sub>-B<sub>100-x</sub>. This notation is used when referring to general quantities and ZIF-8<sub>x</sub>-90<sub>100-x</sub> is used when referring to material specific characteristics. To quantify local order, also referred to as short-range order (SRO), we adopted the Warren-Cowley parameter  $\alpha$ ,<sup>330,372</sup> which is defined as

$$\alpha = 1 - \frac{\langle P_j^{A(B)} \rangle}{x_B} \quad (5.1)$$

where  $P_j^{A(B)}$  is the conditional probability of finding the linker of type B at the  $j^{th}$  neighbor site given a linker of type A, and  $x_B$  is the fractional composition of linker type B in the material. An  $\alpha < 0$ ,  $\alpha = 0$ , or  $\alpha > 0$  indicates alternating, fully random, or clustered ordering of imidazolate linkers respectively. The conditional probability is taken as an ensemble average over all the type A linkers in the material. We have selected the nearest neighbor ( $j=1$ ) to define  $\alpha$ . Nearest neighbors (NNs) are based upon the sharing of a common Zn node and not based on any distance criteria; therefore, each organic linker has six NNs. Second order NNs, or those connected through two or more Zn metal centers, are not considered. This treatment is the same as previously presented by Jayachandrababu et al. in Chapter 4.<sup>46</sup>

### 5.2.2 Diffusion as an Activated Hopping Process

For ZIF-8<sub>x</sub>-90<sub>100-x</sub>, diffusion of adsorbates can be described as an activated hopping process from cage to cage through narrow window regions.<sup>99,201,219</sup> Cages in ZIF-8<sub>x</sub>-90<sub>100-x</sub> materials are connected through a body centered cubic (bcc) lattice (i.e. eight nearest neighbor cages). For a parent ZIF material with a single cage and window type, the self-diffusion coefficient can be written as<sup>137</sup>

$$D_{self} = \frac{N_{cages}}{2n} k_{i \rightarrow j} \lambda^2 \quad (5.2)$$

where  $N_{cages}$  is the number of nearest neighbor cages (e.g.  $N_{cages}=8$ ),  $n$  takes on values of 1, 2, or 3 based on the diffusion dimensionality (e.g.  $n=3$  for ZIF-8 and ZIF-90),  $k_{i \rightarrow j}$  is the hopping rate from cage  $i$  to cage  $j$ , and  $\lambda$  is the distance between cage centers. For simplicity, we report all our findings in normalized units:

$$\begin{aligned} D_{self}^* &= k^* (\lambda^*)^2 \\ k^* &= \frac{k}{k^\alpha} \\ \lambda^* &= \frac{\lambda}{\lambda^\alpha} \end{aligned} \quad (5.3, 5.4, 5.5)$$

where the reduced self-diffusivity is a product of the normalized hopping rate and squared normalized distance between the cages,  $k^\alpha$  is the largest local hopping rate, and  $\lambda^\alpha$  is the distance between cages (14.76 Å for both ZIF-8 and ZIF-90).

### 5.2.3 Classification of Windows and Hopping Rate Catalogue

Figure 5.2 illustrates the 6 member rings (MRs) that can separate adjacent cages in ZIF-8<sub>x</sub>-90<sub>100-x</sub>. Each window is surrounded by six linkers, but only the imidazole rings



of three linkers lie within the plane of the window. We make the simplifying assumption that these three linkers control the hopping rate of molecules through the window. Under this assumption, there are only four different windows as shown in Figure 5.2: 3-mIm (type 1), 2-mIm/1-ImCA (type 2), 1-mIm/2-ImCA (type 3), and 3-ImCA (type 4). We will refer to the 3-mIm and 3-ImCA windows as “parent windows” and the 2-mIm/1-ImCA and 1-mIm/2-ImCA windows as “hybrid windows.” We use a normalized rate notation to denote the rate catalogue for these windows. For example,  $k=[10^0,10^{-1},10^{-2},10^{-3}]$  would refer to the rates being 1, 0.1, 0.01 and 0.001 hops per unit time through windows of type 1, 2, 3, and 4, respectively.

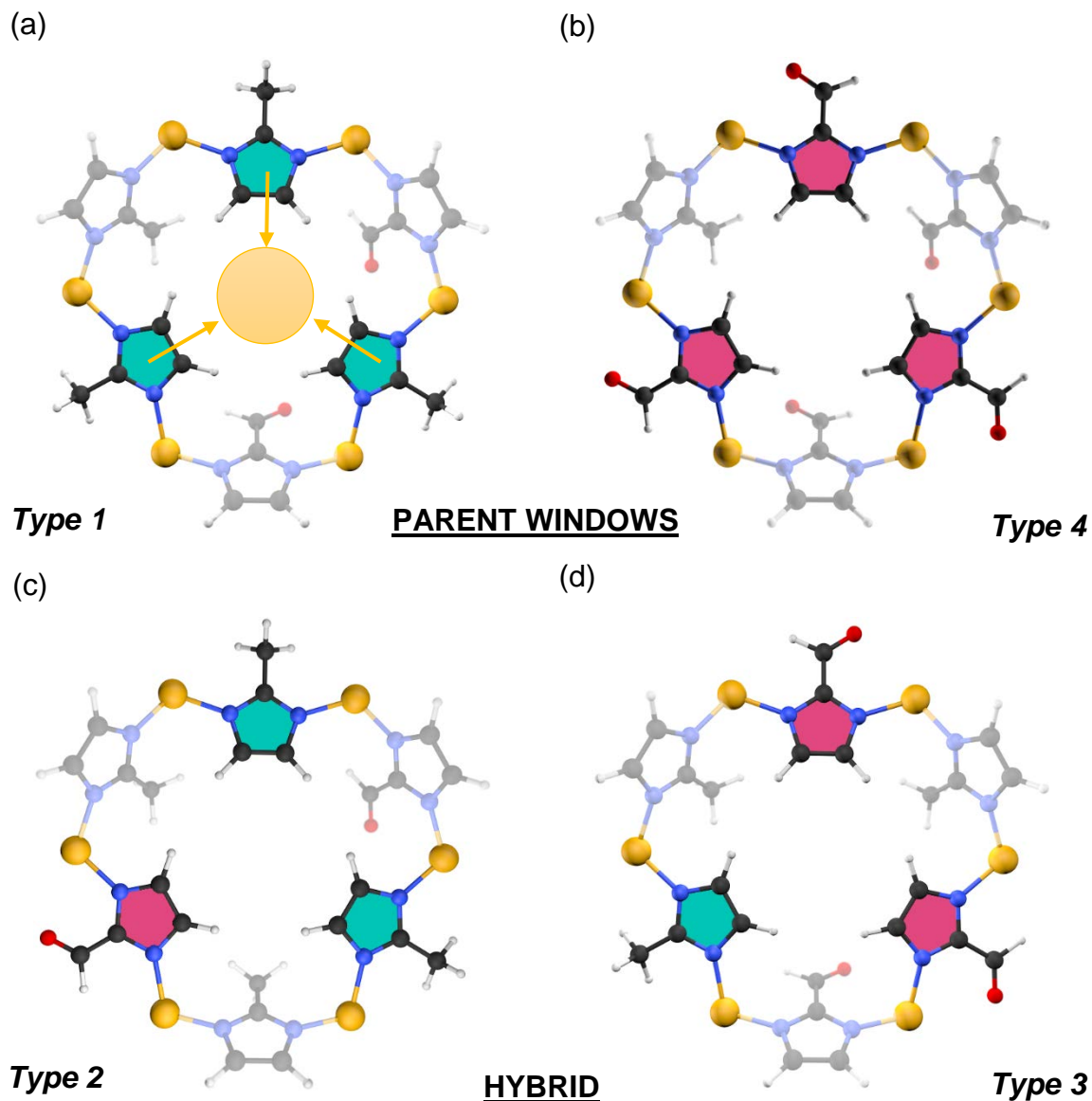


**Figure 5.2** Four window types corresponding to the four possible 6 MR windows in ZIF- $8_x-90_{100-x}$ . Only the windows laying directly in the plane (denoted by the yellow circle and arrows in (a)) are assumed to dictate diffusion. (a) and (b) Parent windows windows of type 1 and 4 containing all mIm linkers and all ImCA linkers respectively; (c) and (d) Hybrid windows of type 2 containing two mIm/one ImCA linkers and type 3 containing one mIm/two ImCA linkers. H, C, N, O and Zn atoms colored off-white, black, blue, red, and gold; aqua blue and pink inside the imidazolate rings indicate whether the linker is a mIm or ImCA linker respectively.

## 5.3 Simulation Methods

### 5.3.1 Lattice Generation

The starting ZIF-8 unit cell (structure code VELVOY<sup>373</sup>) was taken from the Cambridge structural database (CSD).<sup>371</sup> The atomic coordinates of the 12 Zn atoms in the unit cell were then expanded into 10x10x10 supercells with periodic boundary conditions. There are 24 imidazolate linkers per unit cell and therefore, 24000 per supercell. We make the assumption that the ZIF-8 and ZIF-90 unit cells have the same cell lengths and maintain the SOD topology through the entire composition range. These assumptions are well supported by experimental observations.<sup>42,373,374</sup>

Window types were assigned using a multi-step method. The organic linkers were replaced by “pseudo-bonds” between pairs of Zn atoms separated by 6.0 Å. A depth-first search algorithm was applied to identify all 6 MRs. A window-assignment algorithm then identified which three linkers are located in specific window planes. The arbitrary assignment of three linkers in the first window then uniquely defines to which windows all the other linkers are assigned. For a pre-specified composition, an initially random distribution of type A (mIm) and type B (ImCA) linkers in the structure was created. To generate structures with a target SRO  $\alpha_t$ , candidate linker swaps were performed using a reverse Monte Carlo (RMC) algorithm.<sup>46,330</sup> The RMC algorithm accepted a linker swap that changed the system’s SRO from  $\alpha_{i-1}$  to  $\alpha_i$  with a Metropolis criterion, that is, with unit probability when  $|\alpha_i - \alpha_t| < |\alpha_{i-1} - \alpha_t|$  and with probability  $\exp(-\beta|\alpha_i - \alpha_t|)$  when  $|\alpha_i - \alpha_t| \geq |\alpha_{i-1} - \alpha_t|$ .  $\beta$  was fixed at 100 and the RMC procedure was performed for  $2 \times 10^6$  steps. Example ZIF-A<sub>50</sub>-B<sub>50</sub> structures are shown in Figure 5.3. This approach allows crystals with arbitrary composition and SRO to be generated.

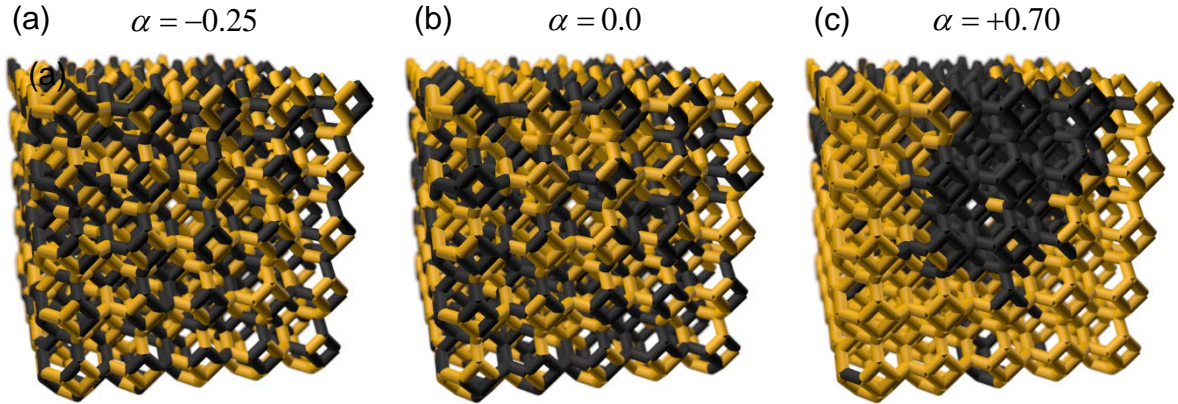


**Figure 5.3** Example mixed-linker ZIF-A<sub>50</sub>-B<sub>50</sub> structures in the SOD topology with short-range order values of (a) -0.25 (i.e. alternating/sparse), (b) 0.0 (i.e. random), (c) +0.70 (clustered). Each figure shows a 10x10x10 structure. The yellow and black bonds indicate type A and type B linkers respectively.

### 5.3.2 Kinetic Monte Carlo Procedure

Kinetic Monte Carlo (KMC) methods have been widely applied for studying diffusion of adsorbates through nanoporous materials such as zeolites.<sup>375-380</sup> Below we only consider diffusion in the infinite dilution limit, that is, for an isolated adsorbate. We follow the  $n$ -fold algorithm, also known as the direct or rejection-free method<sup>381</sup>, by Bortz et al.<sup>382,383</sup> The  $n$ -fold KMC scheme was chosen for computational efficiency since null-events are not allowed. According to percolation<sup>384</sup> (graph) theory terminology, sites (vertices) in the model correspond to the cage centers and bonds (edges) correspond to the various windows, each assigned one of four rates based on the generated structure. The cage to cage distance was defined as 14.76 Å for ZIF-8-90. Groups of cages connected together through the same window type are referred to as clusters. The algorithm begins by defining the probability  $P$  of choosing the  $n^{th}$  event (i.e. adsorbate hop from the current to cage  $l$  through one of 8 windows) as

$$P(\text{cage}_{\text{current}} \rightarrow \text{cage}_l) = \sum_{l=1}^8 \frac{k_l}{k_{\text{total}}} \quad (5.6)$$

where  $k_l$  is the rate through one window and  $k_{total}$  is the sum of the rates through the possible eight windows exiting the current cage. A random number  $r_l$  is selected from a uniform distribution and the  $n^{th}$  event is then chosen based on

$$P(cage_{current} \rightarrow cage_{l-1}) < r_1 \leq P(cage_{current} \rightarrow cage_l) \quad (5.7)$$

Time is updated after each hopping event with a time increment following a Poisson distribution:

$$\tau = \frac{-\ln(r_2)}{k_{total}} \quad (5.8)$$

where  $r_2$  is a second random number drawn from a uniform distribution. Five hundred non-interacting adsorbates were initially uniformly distributed among the 2000 sites of the lattice. Each KMC simulation was performed for  $0.5 \times 10^6$  steps, during which the mean squared displacement (MSD) of the non-interacting adsorbates was tracked. The self-diffusivity was calculated using the Einstein relation<sup>152</sup>:

$$D_{self} = \lim_{t \rightarrow \infty} \left[ \frac{1}{6N \langle t \rangle} \sum_{i=1}^N \left\langle |R_i(t) - R_i(0)|^2 \right\rangle \right] \quad (5.9)$$

where  $N$  is the number of adsorbates,  $\langle t \rangle$  is the average time,  $R_i(t)$  is the final position, and  $R_i(0)$  is the initial position in Cartesian coordinates. In practice, the real time and MSD of each lattice gas are recorded, which are then arithmetically averaged across parallel snapshots for the 500 molecules. The number of KMC steps and adsorbates were

chosen such that KMC simulations in the parent materials combined with Equation 5.9 yielded the same self-diffusivity as Equation 5.2 for a given rate. For KMC simulations involving mixed-linker lattices, the self-diffusivities were considered converged once the coefficient of variation (ratio of the standard deviation to the mean) was below 10%. Verification of our KMC algorithm implementation by comparison to Equation 5.2 is provided in Appendix D.

## 5.4 Results and Discussion

### 5.4.1 Zero Hopping Rates through Window Blocking

We begin by considering a conceptually simple scenario where adsorbate diffusion through the mixed-linker ZIF is blocked (i.e. a hopping rate of zero) through one or more types of ZIF windows. We refer to this as ‘window blocking.’ Keffer et al. examined adsorbate diffusion on zeolite sorption lattices, referring to ‘window blocking’ as generic ‘bond-blocking’.<sup>385</sup> They suggested cations located in the window regions of zeolites or the presence of slower moving adsorbates can block adsorbate diffusion. Analogous window blocking can occur when adsorbates preferentially adsorb at window regions. Jee and Sholl demonstrated that CO<sub>2</sub>, by adsorbing in the 8 MR window of pure silica zeolite DDR, reduces the rate of CH<sub>4</sub> hopping to close to zero.<sup>172</sup>

When the non-interacting adsorbates are initially placed in the lattice, there is a finite probability that they are placed into a non-percolating cluster. These adsorbates would observe a “confined” diffusion regime and not a linear diffusion regime<sup>148</sup> in their MSDs (refer to Appendix D for representative MSDs). It is unphysical that adsorbates would be located in these non-percolating clusters, given that they can neither enter nor exit. Various cluster wrapping identification algorithms<sup>192,386,387</sup> could be used to identify which cages belong to percolating clusters, thus furthering computational efficiency by allowing targeted initial placement of the adsorbates; however, these percolation schemes were not implemented in this chapter. Instead, the final MSD of each adsorbate was

compared to the longest possible mean squared displacement ( $3l_i^2$  where  $i=x, y, \text{ or } z$  for the cubic unit cell) within the three-dimensional bcc lattice of ZIF- $A_xB_{100-x}$ . For the  $10 \times 10 \times 10$  supercell,  $3l_i^2 = 86598 \text{ \AA}^2$  with a unit cell length of  $a=b=c=16.99 \text{ \AA}$ . Adsorbates having final MSDs less than  $3l_i^2$  after  $0.5 \times 10^6$  KMC steps were not included in calculating the averaged self-diffusivity from Equation 5.9.

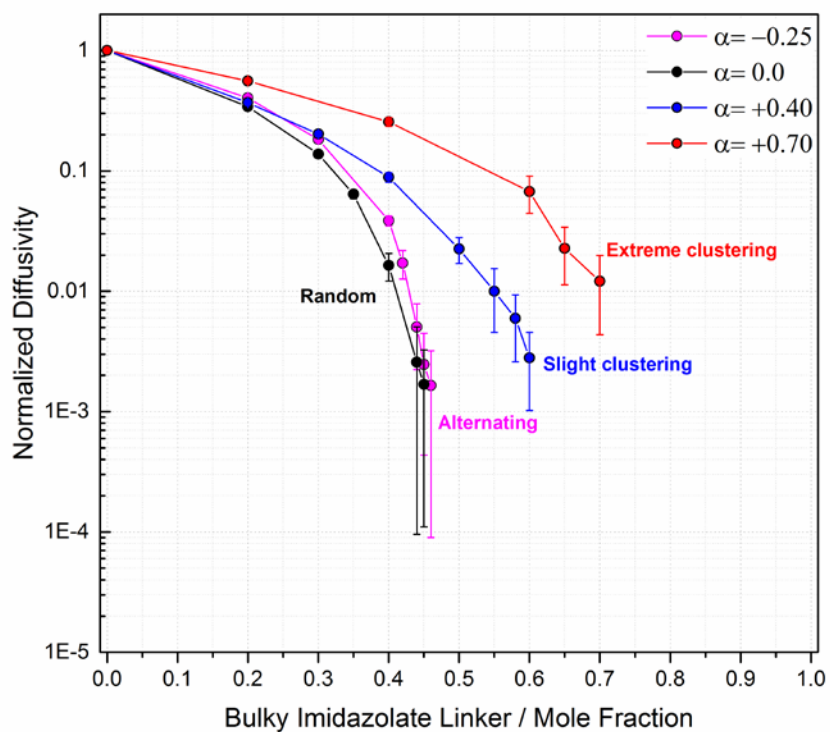
Figure 5.4a shows the normalized self-diffusivity as a function of the bulky imidazolate linker composition. Here the rates are set to  $k=[1,0,0,0]$ , implying that the presence of one or more bulky imidazolate linkers completely obstructs adsorbate diffusion. In all cases, increasing the proportion of the linkers that are bulky reduces the self-diffusion rate. The SRO of the bulky imidazolate linkers, however, has a significant impact on self-diffusion. ZIF lattices with an alternating ( $\alpha < 0$ ) and random ( $\alpha = 0$ ) SRO exhibit a faster reduction in adsorbate self-diffusion than ZIF lattices with clustering ( $\alpha > 0$ ) as the amount of the bulky imidazolate linker increases. To qualitatively explain this observation, the normalized self-diffusivity in the mixed-linker ZIF lattices can also be equated with the diffusibility factor  $Q$ ,<sup>388</sup> or ratio of the diffusivity in the mixed-linker ZIF to the diffusivity in the parent ZIF containing no bulky imidazolate linkers. The diffusibility  $Q$ , according to literature examining percolation through porous media<sup>388</sup>, is a function of three dimensionless quantities, namely porosity  $\varepsilon$ , tortuosity  $\tau$ , and constrictivity  $\delta$  with the condition that  $\tau \geq 1$ . In generating lattices with different local orderings, we do not alter porosity or constrictivity. By blocking windows, we alter tortuosity<sup>389</sup> by increasing the lengths of the diffusion paths the adsorbates must traverse, thus decreasing the diffusivities. Increasing the mole fraction of the bulky imidazolate group increases the number of blocked windows and directly the lengths of the diffusion pathways. Lattices with alternating and random SRO demonstrated a larger increase in the tortuosity as compared to lattices with clustered SRO. The diffusivities at varying SROs terminate at particular compositions where the simulated diffusivity drops to zero

(not plotted with the log-scale in Figure 5.4a). Error bars represent the uncertainty of measuring the diffusion through 50 independent realizations.

Figure 5.4b illustrates the probability of percolation as a function of the bulky imidazolate mole fraction. The probability of percolation is defined as the ratio of lattices that allow net diffusion to the total number of generated lattices for a particular composition. Results are only shown for 10x10x10 simulation volumes; we have not attempted to quantify the finite size effects that are important in highly precise studies of bond percolation thresholds<sup>390-393</sup>. The probability of percolation reaches zero at different compositions as the SRO of the lattice is changed. Lattices with alternating and random SRO have a similar composition threshold (~45-50 mole percent) whereas the composition threshold shifts to higher values (~70-75 mole percent) for lattices with clustered SRO ( $\alpha=+0.70$ ).



(a)



(b)

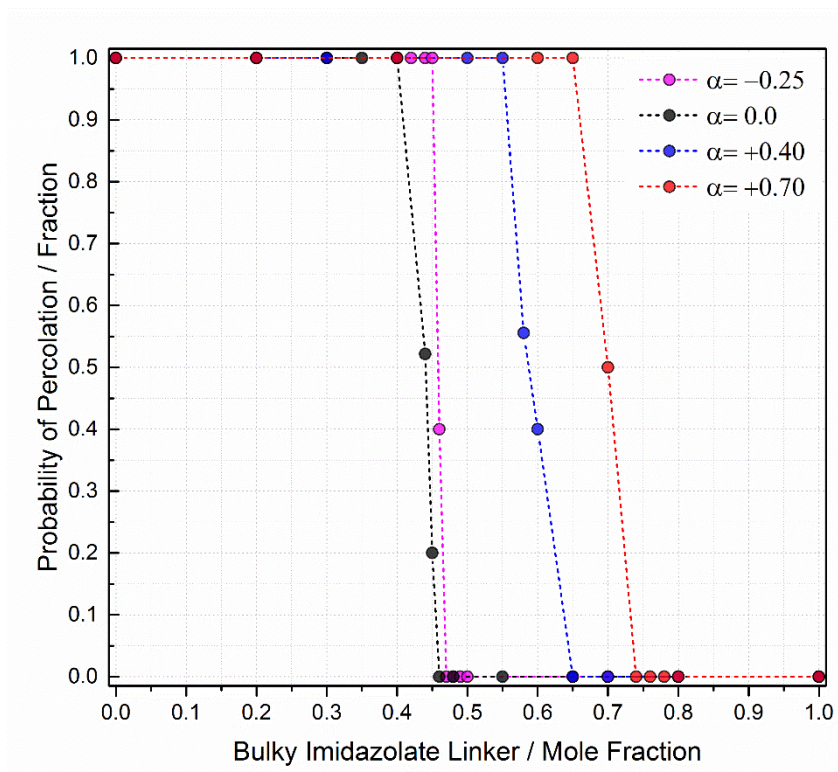


**Figure 5.4** (a) Diffusivity and (b) percolation probability as a function of the bulky imidazolate mole fraction in lattices with fixed SRO. The rate catalogue is  $k=[1,0,0,0]$ .

The data in Figures 5.4a and 5.4b can be recast to understand why the diffusivity values reach zero at different composition thresholds with varying SRO. Figure 5.5 shows the probability of randomly selecting a window of type 1 (i.e. the window through which hopping occurs) as a function of both SRO and composition. The composition “ranges” at fixed SRO where adsorbate diffusion becomes zero are overlaid on the plot as red dots. The bond percolation threshold for a bcc lattice is reported by Lorenz and Ziff to be  $0.1802875 \pm 0.0000010^{390}$ , when the bonds are placed (removed) randomly ( $\alpha=0.0$ ) on the lattice. Although this threshold will vary in structures with non-random short-range order, this value gives a useful way to estimate where percolation will occur. The red dashed line in Figure 5.5 denotes a window type probability of 0.180, and it is clear that our simulated bond percolation thresholds are consistent with this value over the full range of SRO.

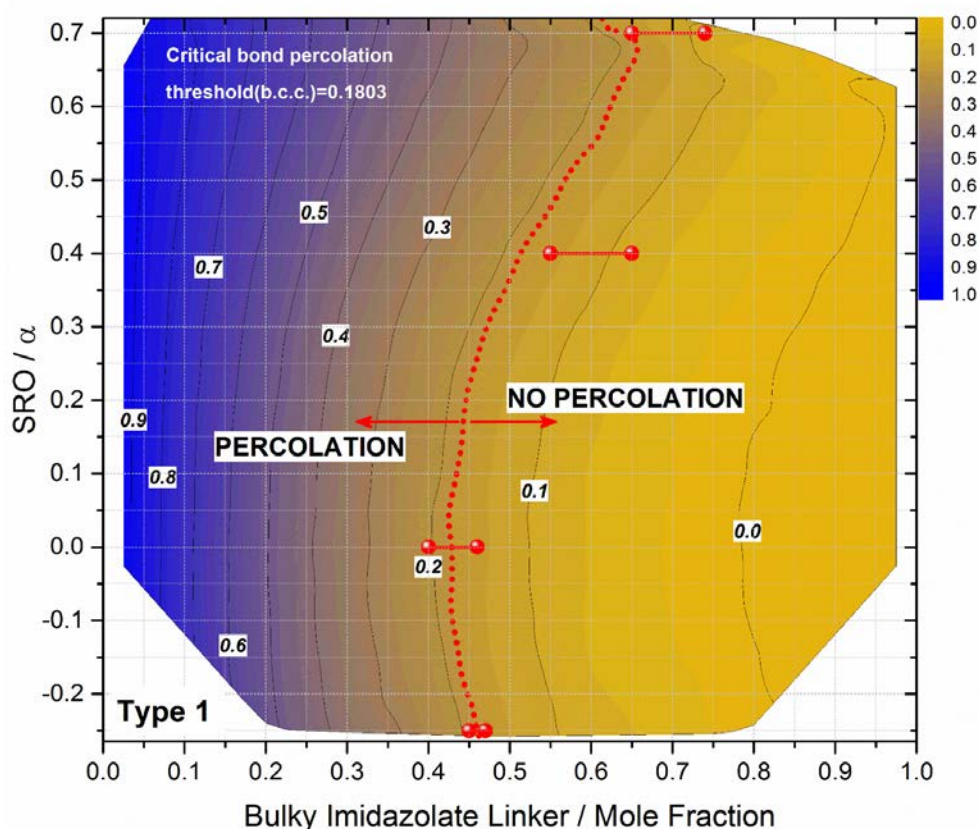


**Figure 5.5** Probability of randomly choosing a type 1 window in ZIF-A<sub>x</sub>-B<sub>100-x</sub> lattices with varying SRO. Composition threshold “ranges” from Figure 5.4b are labeled with the red dots and red solid lines. The bond percolation threshold for a bcc lattice with  $\alpha=0$  is 0.1803; this singular value is extrapolated on the contour plot (as indicated by the red dash line) to ZIF-A-B lattices exhibiting non-random SRO. ZIF-A-B materials falling on the left of the line allow adsorbate diffusion; ZIF-A-B materials falling on the right of the line inhibit adsorbate diffusion. For reference, there are 24 imidazolate linkers per unit cell and 24000 per 10x10x10 supercell.

A logical extension of the single blocking case would be to consider the scenario when more than one bulky imidazolate linker is needed for window blocking. We report in Figure 5.6 normalized diffusivities in ZIF-A<sub>x</sub>-B<sub>100-x</sub> with random SRO ( $\alpha=0$ ) for the three possible window blocking scenarios. Decreasing the probability of blocked windows shifts the composition threshold to higher bulky imidazolate linker mole fractions. Similar results are reported in Appendix D for ZIF-A<sub>x</sub>-B<sub>100-x</sub> lattices with SRO of -0.25 and +0.70. We also examined adsorbate diffusion when the hopping rates

through the hybrid windows are accelerated (depressed) with respect to the rates through the parent windows. These results are reported in Appendix D and show that it is possible to non-monotonically tune adsorbate diffusion.

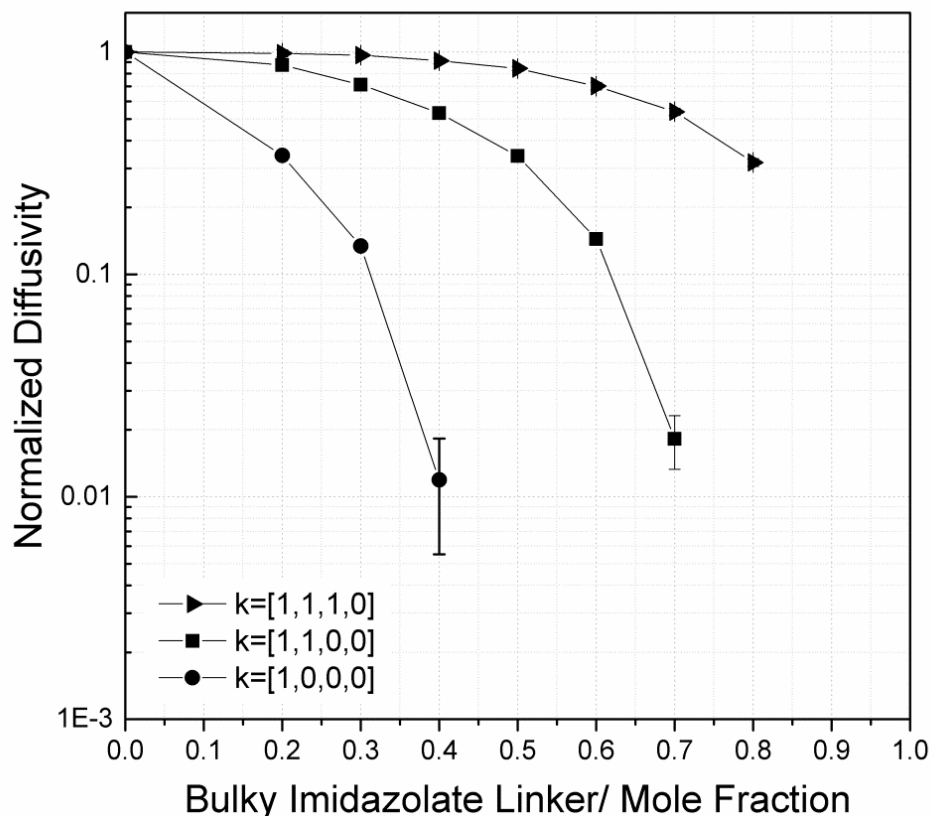


**Figure 5.6** Diffusivities in ZIF-A-B with random SRO ( $\alpha=0$ ) for the three linker blocking scenarios.

#### 5.4.2 Deriving Hopping Rates through Hybrid Windows based on the Hopping Rates in the Parent ZIFs

We now turn to the more physically realistic situation where the hopping rates through windows of all types are non-zero. Our model requires four hopping rates as inputs. The hopping rates for the parent materials can be back calculated using Equation 5.2 if experimental data is available. Unfortunately, there is currently no experimental method that can directly measure hopping rates through hybrid windows. Rather than

attempting to determine these rates from more detailed models (e.g. atomistic simulations), we instead explored several plausible functional forms for these rates. Specifically, we used the following interpolation functions:

$$k_i = mi^n + b \text{ where } n = 1, 2, 3...$$

$$\log(k_i) = mi + b \quad (5.10, 5.11, 5.12)$$

$$k_i = \frac{(mb)i}{1+bi}$$

where Equation 5.10 corresponds to a linear, quadratic, and cubic power law with  $n = 1, 2$  and  $3$  respectively, Equation 5.11 is a logarithmic interpolation function, and Equation 5.12 is a Langmuir interpolation function. The variables  $m$  and  $b$  are obtained by specifying the parent rates  $k_1$  and  $k_4$  and solving the set of linear equations, and the variable  $i$  is the rate index taking values of  $1, 2, 3$ , or  $4$ . Figure 5.7 shows the normalized hopping rate through the four window types according to these five functions with the parent window hopping rates arbitrarily set to  $k_1=10^{-4}$  and  $k_4=1$ .

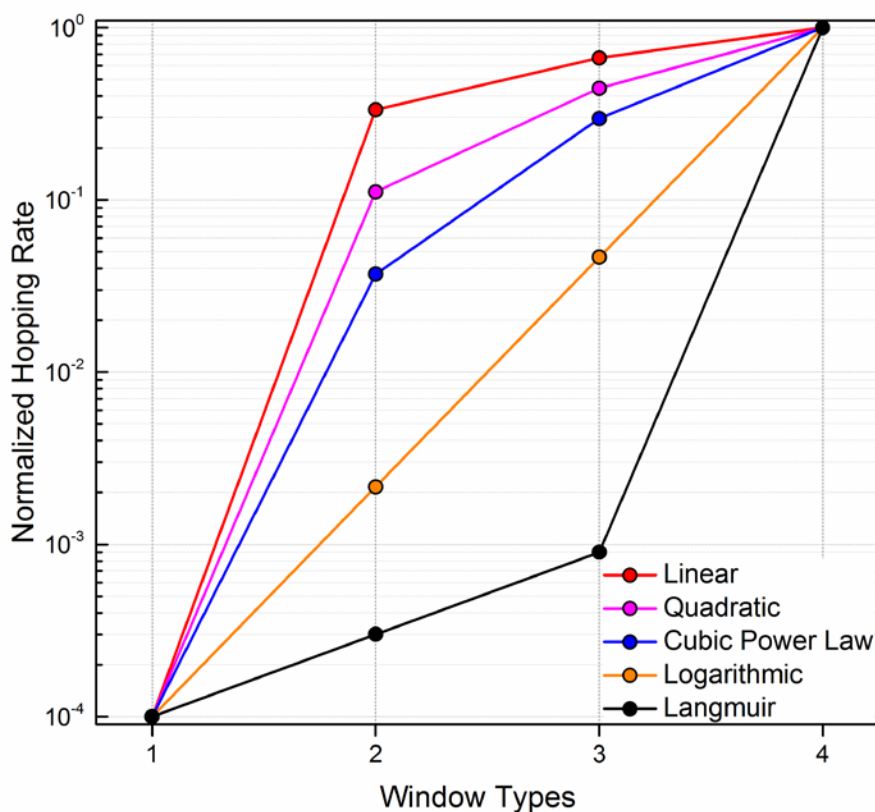


**Figure 5.7** Normalized hopping rates for the four window types using various analytical interpolation schemes. Parent window hopping rates are set to  $10^{-4}$  and  $10^0$  for visual clarity.

Figure 5.8 shows the normalized diffusivities as a function of imidazolate linker mole fraction on ZIF lattices with random ordering ( $\alpha=0$ ). Large differences in the diffusivity can be seen depending on the interpolation scheme used to define the hopping rates through hybrid windows. For an equimolar linker composition, for example, the diffusivities in Figure 5.8 vary by more than two orders of magnitude from a linear to Langmuir interpolation. This observation highlights the need to develop atomistic models capable of accurately predicting the hopping rates through the hybrid windows if quantitative predictions of diffusion in these materials are to be made.

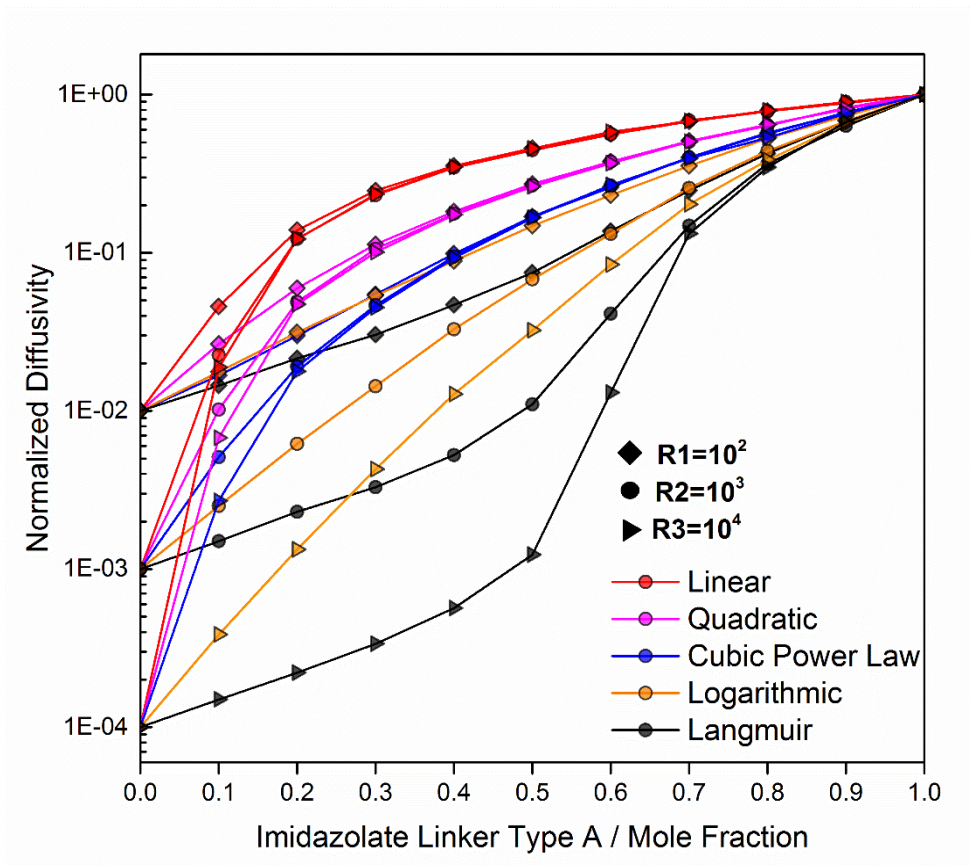


**Figure 5.8** Normalized diffusivities as a function of imidazolate linker mole fraction, interpolation scheme, and ratio of the parent window rates denoted by R1, R2, and R3. SRO  $\alpha$  is set to 0.0 (random ordering) for all curves. Uncertainties are smaller than the symbols.

We now consider the impact of short-range order on diffusion in ZIF-A-B for which hopping is possible through all window types. Our intent is to determine how adsorbate diffusion deviates in ZIF-A-B lattices with non-random SRO from adsorbate diffusion in ZIF-A-B lattices with random SRO. We generated ZIF-A<sub>x</sub>-B<sub>100-x</sub> lattices with SROs of -0.25, +0.4, and +0.7 and predicted diffusivities using the five interpolation schemes and three ratios of the parent window rates. This procedure generated 405 diffusivities (not including the diffusivities in the parent structures) to supplement the data for ZIF-A<sub>x</sub>-B<sub>100-x</sub> with  $\alpha=0$  shown in Figure 8. A succinct way of representing this data is shown in the tree diagram and heat map of Figure 5.9. Moving from left to right,

Figure 5.9 is read by first selecting the interpolation scheme, the SRO, the ratio of the parent rates, and finally the material's composition. The heat map's colors in Figure 5.9 indicate the ratio of the diffusivity in the ZIF-A-B lattice with non-random SRO to the diffusivity in the ZIF-A-B lattice with random SRO on a log scale. More specifically the heat map shows the diffusion ratio:

$$DR = \log_{10} \left( \frac{D_{\alpha=x}}{D_{\alpha=0.0}} \right) \quad (5.13)$$

Diffusion ratio values close to zero (gold squares in Figure 5.9) indicate that SRO has a minimal impact on the diffusivity as compared to a random distribution of imidazolate linkers. Diffusion ratio values approaching -1 or 1, as represented by blue or red squares in Figure 5.9, respectively, demonstrate that the SRO alters the diffusivity by an order of magnitude or more.

For most plausible binary mixed-linker ZIFs, the local ordering of imidazolate linkers does not impact diffusivities significantly in reference to the lattices with random SRO. This result is clear from the large swathes of gold in Figure 5.9. These results suggest that adsorbate diffusion will have a weak dependence on the SRO in many binary mixed-linker ZIF materials. There are, however, notable examples when the local ordering of imidazolate linkers impacts diffusion properties significantly. Diffusion is depressed for the linear, quadratic, and power law interpolation schemes and diffusion is accelerated for the logarithmic and Langmuir schemes most significantly when the ratio of the parent rates increases and the local ordering becomes clustered (i.e.  $\alpha > 0.4$ ). When clustering of the imidazolate linkers occurs, the population of window types 1 and 4 (parent rates) increases,<sup>46</sup> and adsorbates preferentially percolate in the dominant clusters (featuring the larger hopping rate) depending on composition.



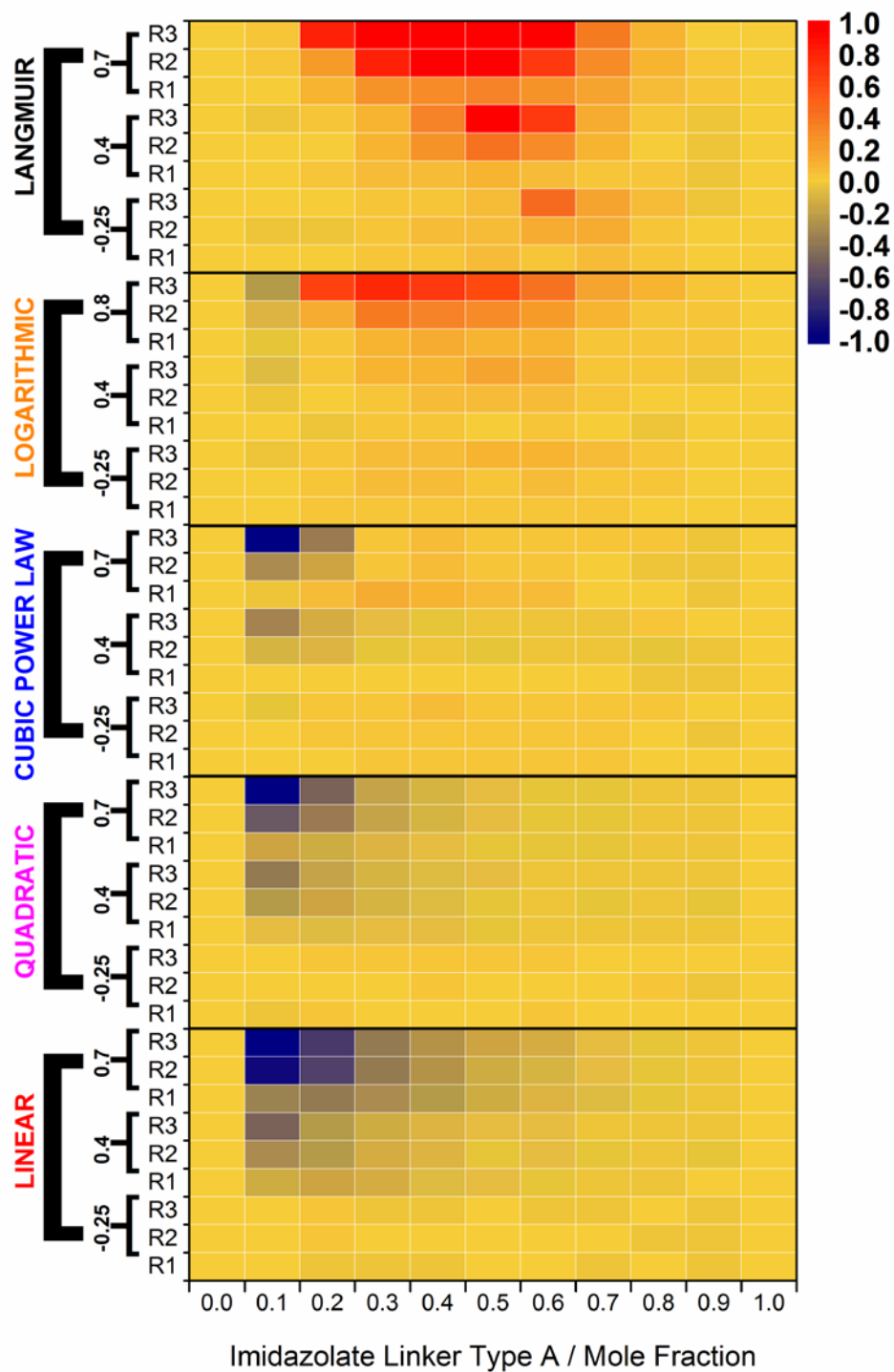


**Figure 5.9** Hybrid tree diagram and heat map demonstrating the influence of interpolation scheme, local ordering, ratio of the parent window rates, and imidazolate mole fraction on the deviation from predicted diffusivities in randomly ordered lattices. More details are given in the text.

### 5.4.3 Comparison to Experimental ZIF-8<sub>x</sub>-90<sub>100-x</sub> Isobutane and n-Butane Self-Diffusion Data

We now use the information above to qualitatively predict self-diffusion of *n*-butane and isobutane in the binary mixed-linker ZIF-8-90 system. First, we normalized all the *n*-butane and isobutane experimental diffusivities from Eum et al.<sup>189</sup> in the parent and hybrid ZIFs according to the larger parent diffusivity. This data is shown in Figures 5.10a-5.10f as a solid black line. We used Equation 5.2 to calculate the parent hopping rates from the normalized experimental diffusion data of both *n*-butane and isobutane. The ratios of the parent ZIF-90 hopping rate to the parent ZIF-8 hopping rate for *n*-butane and isobutane are  $\sim 10^1$  and  $\sim 10^3$  respectively; diffusion of both molecules is faster in ZIF-90 than in ZIF-8. To put our analysis in context, it is important to define the accuracy that is possible with experimental measurements of these diffusivities. Studies by Eum et al.<sup>189</sup> and Zhang et al.<sup>394</sup> utilized identical pressure decay cell experiments but gave over an order of magnitude disagreement between their reported self-diffusion measurements for *n*-butane and isobutane. Diffusion coefficients from macroscopic methods are influenced by possible external heat and mass transfer effects as well as surface barriers on the ZIF powders resulting from slightly different synthesis techniques.<sup>283,395</sup> We therefore view the experimental data as accurate within an order of magnitude. We represent this uncertainty by bounding the experimental data in Figures 5.10a-5.10f with a red region and dashed black lines.

Using the normalized parent hopping rates, we defined the hybrid hopping rates for *n*-butane and isobutane in ZIF-8-90 using the five interpolation functions. We created lattices with compositions ZIF-8<sub>7</sub>-90<sub>93</sub>, ZIF-8<sub>28</sub>-90<sub>72</sub>, and ZIF-8<sub>63</sub>-90<sub>37</sub> to allow direct comparison to experimental data. For each composition we considered SRO values from -0.25 to +0.70. Figures 5.10a, 5.10b, and 5.10c show our predictions for *n*-butane self-diffusion in ZIF-8<sub>7</sub>-90<sub>93</sub>, ZIF-8<sub>28</sub>-90<sub>72</sub>, and ZIF-8<sub>63</sub>-90<sub>37</sub>. For *n*-butane, where the ratio of the diffusivities between the parent materials is an order of magnitude, we are able to

accurately predict the monotonic decrease of n-butane diffusivity with increasing 2-methylimidazolate content in the hybrid materials. Within the inherent accuracy of the kinetic uptake experiments, our prediction is unaffected by the choice of local ordering or the interpolation scheme for the hybrid hopping rates. Figures 5.10d, 5.10e, and 5.10f show our predictions for isobutane self-diffusion in ZIF-87-90<sub>93</sub>, ZIF-828-90<sub>72</sub>, and ZIF-863-90<sub>37</sub>. It is clear that in Figures 5.10e and 5.10f that local ordering and the choice of interpolation scheme have a non-negligible influence on the diffusion predictions. We note in Figure 5.10f that our diffusivity prediction with the Langmuir interpolation and a clustered SRO ( $\alpha \sim 0.60$ ) best matches the normalized experimental diffusivity. The suggestion from this result of a clustered SRO for compositions close to the ZIF-863-90<sub>37</sub> is in disagreement, however, with the alternating SRO ( $\alpha = -0.25$ ) for ZIF-861-90<sub>39</sub> directly measured by Jayachandrababu et al. in the previous chapter.<sup>46</sup> We can speculate that an interpolation function intermediate between the logarithmic and Langmuir functions would provide a better diffusivity prediction for this material.

Ultimately, however, there is a need to be able to determine the hopping rates through hybrid windows in a quantitative way in order to make meaningful predictions about the SRO in binary mixed-linker ZIFs using data such as in Figure 5.10. As to our simplification that diffusion is controlled by four hopping rates, objections could be made that the hopping rates through hybrid windows would be influenced by second or third nearest neighbor linkers. These distant linkers through intermediate range ( $\sim 5\text{-}10$  Å) dispersion or electrostatic interactions would influence the immediate linker's flexibility and effectively the hopping rate. Thorough comparison between conventional molecular dynamics and our lattice diffusion model, using rates measured through free energy sampling methods in combination with dynamically corrected transition state theory<sup>219</sup>, should validate our assumption that only four window types are necessary.

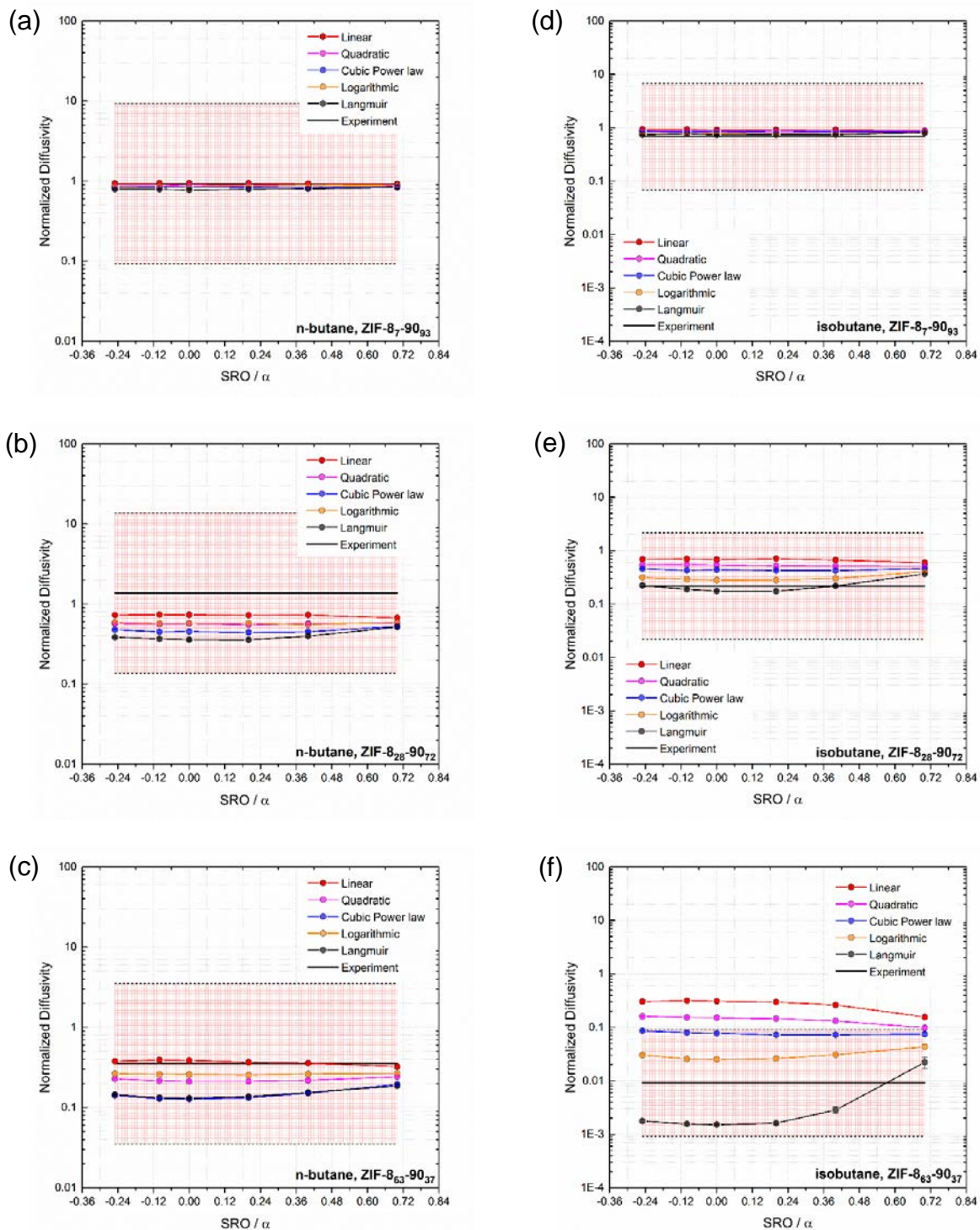


**Figure 5.10** Comparison of normalized experimental infinite dilution diffusivities at 308 K measured by Eum et al.<sup>189</sup> to self-diffusivities predicted by the lattice-gas models with varying local ordering; (a) n-butane in ZIF-87-90<sub>93</sub>, (b) n-butane in ZIF-828-90<sub>72</sub>, (c) n-butane in ZIF-863-90<sub>37</sub>, (d) isobutane in ZIF-87-90<sub>93</sub>, (e) isobutane in ZIF-828-90<sub>72</sub>, (f) isobutane in ZIF-863-90<sub>37</sub>. The red checkerboard rectangle bounded by black dashed lines represents the region in which predicted diffusivities would be considered acceptable as discussed in the text.

## 5.5 Conclusions

We have developed a lattice-gas model well-suited for qualitatively predicting the influence of short-range linker order on self-diffusion in binary mixed-linker ZIF materials. This model would be easily extended to other cage-type nanoporous materials with different windows and connectivity. Short-range order has the most influence on diffusion when window blocking occurs through only one bulky imidazolate group, and the percolation threshold can be tuned through varying window populations. For lattices with non-monotonic diffusion behavior, only those with severe clustering of linkers demonstrate strongly different diffusion behavior as compared to the lattices with random ordering. We suggested multiple representative interpolation schemes to extract hopping rates through hybrid windows from the hopping rates through the two parent ZIFs. Ultimately, the SRO of the lattice is of less importance than the actual rates through the hybrid windows. Comparing our predictions to normalized n-butane and isobutane experimental diffusivities through ZIF-8-90 materials further demonstrate that knowledge of the exact SRO of a binary mixed-linker ZIF is unnecessary to make diffusion predictions in many instances.

Our conclusions have several implications for both the experimental and computational communities examining mixed-linker MOFs. Recent reviews by Qin et al.<sup>359</sup> as well as Osborn Popp and Yaghi<sup>396</sup> highlight progress in developing synthesis techniques that selectively place different functional groups at desired positions within the MOF framework. Developing experimental synthesis procedures, such as sequential linker installation (SLI)<sup>397</sup>, for ZIF materials would allow for increased tunability of “bulky” linker placement and ultimately adsorbate diffusion. This study should help motivate synthesis procedures that allow for the control of the local ordering of organic linkers in mixed-linker MOFs. For binary mixed-linker ZIF systems exhibiting monotonic tunability of adsorbate diffusion, significant effort to quantify precisely the local ordering of the ZIF for diffusion predictions is an unnecessary undertaking as SRO

has modest influence on adsorbate self-diffusion. More important than SRO quantification or control is knowledge of the “true” hopping rates through the hybrid windows, currently only accessible using either ab initio or classical molecular dynamics simulations. Ab initio MD simulations are most likely computationally intractable with the large number of atoms required in the simulations so “mixed-linker” force fields must be developed for binary MOF materials. These force fields only have to be sensitive enough to predict hopping through hybrid windows, thus providing quantitative predictions of adsorbate diffusion. This study provides the first step required for quantitatively predicting adsorbate diffusion in binary mixed-linker ZIFs.

## **CHAPTER 6**

### **LIGHT GAS DIFFUSION PREDICTIONS THROUGH MIXED-LINKER ZEOLITIC IMIDAZOLATE FRAMEWORKS**

This chapter uses all the computational methods in Chapter 2, the intraZIF force field of Chapter 3, knowledge of the binary mixed-linker ZIF structures determined in the work of Chapter 4, and the lattice-diffusion modeling in Chapter 5 to quantitatively predict adsorbate diffusion in binary mixed-linker ZIFs. This is a culmination of my entire research at Georgia Tech, and proves that the methods and insights to accurately select ZIFs for molecular sieving have been well-established.

Experimental studies have shown that adsorbate diffusion in zeolitic imidazolate frameworks (ZIFs) can be tuned by incorporating two different imidazolate linkers in the ZIF crystals. We demonstrate for the first time that atomistic simulations are capable of quantitatively predicting self-diffusion in binary mixed-linker ZIFs. Diffusion coefficients of various adsorbates for which prior experimental data exists are predicted in ZIF-8-90, ZIF-8/SALEM-2 (imidazole and 2-methylimidazole in the cubic SOD topology), and ZIF-7-90. A combination of conventional and biased molecular dynamics simulations as well as a previously developed lattice-diffusion model allows us to access the full range of diffusion time scales for various adsorbates such as small hydrocarbons, alcohols, benzene, and water.

#### **6.1 Introduction**

Metal-organic frameworks (MOFs)<sup>398</sup>, a class of nanoporous materials formed through the linking of metal ions and organic linkers, will increasingly find themselves useful for molecular storage, delivery, catalytic, sieving, and sensing applications<sup>208</sup> as

enterprising researchers and engineers identify strong product/market fits<sup>399</sup>. Continually adding to an already expansive set of synthesized MOFs, researchers are engineering MOFs with heterogeneous building units, such combinations of metal nodes, organic linkers, and defects.<sup>357,358,396,400</sup> One subset of MOFs exhibiting heterogeneity are mixed-linker MOFs, also termed hybrid, mixed-ligand, or multivariate MOFs. These mixed-linker MOFs have demonstrated enhanced adsorption properties over their parent MOFs.<sup>357</sup> Synthesis protocols for controlling linker placement are being reported such as “programmed pores” by Lei et al.<sup>401</sup> and sequential linker installation (SLI)<sup>402</sup>. One challenge associated with mixed-linker MOFs is that they can potentially exhibit both long and short-range ordering of their linkers. The structure of mixed-linker MOFs exhibiting long-range order can be determined using single crystal X-ray diffraction (XRD) techniques.<sup>41</sup> Determining the structure of MOFs exhibiting short-range order (SRO) is experimentally demanding but can be determined by various NMR methods. There are only a handful of mixed-linker MOF families (ZIFs, MTV-MOFs, DUT-5, UiO-66) for which the short-range ordering of organic linkers has been experimentally determined.<sup>31,46,364,403</sup>

In this chapter, we concentrate on zeolitic imidazolate frameworks (ZIFs)<sup>41</sup>, a well-studied family of MOFs comprised of Zn or Co metal centers and various functionalized imidazolate linkers. ZIFs have demonstrated potential as adsorbents or molecular sieves in both adsorption<sup>368</sup> and membrane based separations<sup>11,16,404</sup>. ZIFs can form in a multitude of topologies while containing single or multiple types of imidazolate linkers (i.e. mixed-linker ZIFs).<sup>216,405</sup> Mixed-linker ZIFs have been synthesized *de novo* with binary combinations of functionalized imidazolate linkers such as 2-methylimidazole (mIm), benzimidazole (BzIm), and carboxaldehyde-2-imidazole (ImCA).<sup>42,43</sup> Post-synthetic modifications such as solvent assisted linker exchange (SALE)<sup>406</sup>, thermal treatment,<sup>370</sup> or chemical transformations<sup>252</sup> on single-linker ZIFs can also be used to create mixed-linker ZIFs. These methods can create mixed-linker ZIFs



exhibiting either long-range order (e.g. ZIF-68, ZIF-69)<sup>405</sup> as determined through single crystal x-ray diffraction (XRD) or short-range order (e.g. ZIF-8-90)<sup>189</sup>. Methods using a combination of NMR techniques and computational modeling have been developed to quantify the short-range ordering (SRO) of imidazolate linkers in binary mixed-linker ZIFs.<sup>46</sup> The incorporation of multiple functionalized imidazole linkers allows for tunability of properties such as adsorption and diffusion when compared to the parent single-linker ZIF materials.<sup>42,43,407</sup>

To our knowledge, only three experimental studies have thoroughly examined diffusion in binary mixed-linker ZIFs. Eum et al. demonstrated that varying the mixed-linker composition of ZIF-8<sub>x</sub>-90<sub>100-x</sub> allowed for continuous tuning of the diffusion and adsorption of water, alcohol, and C4 isomers.<sup>408</sup> Rashidi et al. synthesized ZIF-7<sub>x</sub>-90<sub>100-x</sub> materials and showed that by increasing the mole fraction of benzimidazolate linkers, the transport diffusivities of n-butane and isobutane were decreased by seven and four orders of magnitude, respectively, relative to the diffusivities in parent ZIF-90.<sup>43</sup> Zhang and Koros used thermal modifications to make a SALEM-2/ZIF-8 hybrid material.<sup>370</sup> They found that upon conversion of 17% of 2-methylimidazolate linkers to unfunctionalized imidazolate linkers, the transport diffusivities of SF<sub>6</sub> and isobutane increased three orders of magnitude and those of n-butane increase two orders of magnitude relative to the parent material. It would be useful to be able to use computational methods to efficiently and quantitatively treat mixed-linker ZIF materials in order to predict tunable diffusion characteristics as well as to possibly identify hybrid materials that exhibit more favorable diffusion characteristics relative to the parent materials.

We present in this chapter the first quantitative predictions of adsorbate diffusion in binary mixed-linker ZIFs using molecular simulations. This work extends our previous study that qualitatively examined the impact of local imidazolate ordering on the self-diffusion of adsorbates at infinite dilution using a lattice-based model.<sup>409</sup> The molecular simulations we present here simulations use the intraZIF force field (FF) to

describe the kinetic flexibility of the imidazolate linkers. We show that the intraZIF-FF represents relative potential energies from Born-Oppenheimer molecular dynamics (BOMD) simulations of the ZIF-8-90 framework. We demonstrate that our previously reported lattice-diffusion (LD) model accurately reproduces self-diffusivities from conventional molecular dynamics (MD) simulations for methane in ZIF-8-90 materials. We also make direct comparisons to all existing experimental diffusion data measured using both PFG-NMR and macroscopic uptake methods for ZIF-8-90 materials. For adsorbates that diffuse on time scales inaccessible to conventional MD, we use local hopping rates from biased MD simulations in combination with our LD model to predict diffusion in the binary mixed-linker ZIFs. We then predict the kinetic separation performance of SALEM-2/ZIF-8 and ZIF-7-90 hybrid materials for several representative adsorbates.

## 6.2 Theory

### 6.2.1 Creating Mixed-Linker ZIF Structures

We refer to mixed-linker ZIFs with combinations of ImCA and mIm linkers as ZIF-8<sub>x</sub>-90<sub>100-x</sub> materials and those with combinations of BzIm and ImCA linkers as ZIF-7<sub>x</sub>-90<sub>100-x</sub> materials. Since a common name for the SALEM-2/ZIF-8 structure does not exist, we will refer to this structure as ZIF<sub>SOD</sub>-Im<sub>x</sub>-mIm<sub>100-x</sub> since it contains both unfunctionalized imidazolate (Im) and 2-methylimidazolate (mIm) linkers and is in the SOD topology. When referencing nonspecific ZIFs, we will refer to the two imidazolate linkers as type A and type B. The structures of the single-linker parent ZIFs (structure codes *VELVOY*<sup>41</sup> for ZIF-8, *WOJGEI*<sup>252</sup> for ZIF-90, and *IMIDZB10* for SALEM-2<sup>253</sup>) were obtained from the Cambridge Structural Database (CSD)<sup>44</sup>. These structures exist in the SOD topology with cubic unit cells, similar unit cell volumes of 4767, 4904, and 5159 Å<sup>3</sup>, and pore limiting diameters<sup>59</sup> (PLDs) of 3.30, 3.43, and 3.45 Å for SALEM-2, ZIF-8, and ZIF-90 respectively. The SALEM-2, ZIF-8, and ZIF-90 unit cells each

contain 24 imidazolate linkers and 12 Zn metal centers. Using the parent ZIFs as starting structures, fully atomistic mixed-linker ZIF structures were created with predetermined binary imidazolate compositions and short-range ordering (SRO) of the imidazolate linkers. We quantify SRO using the Warren-Cowley parameter<sup>372,410</sup>

$$\alpha = 1 - \frac{\langle P_j^{A(B)} \rangle}{x_B} \quad (6.1)$$

where  $P_j^{A(B)}$  is the conditional probability of selecting a linker of type B at the  $j^{th}$  neighbor site of a linker of type A, and  $x_B$  is the fractional composition of linker type B. With this definition, a SRO  $\alpha > 0$ ,  $\alpha = 0$ , or  $\alpha < 0$  represents a clustered, uniformly random, or an ordering that favors alternating linker types, respectively. Nearest neighbors for a given imidazolate linker are determined based on their bonding to shared Zn metal centers ( $j=1$ ), so each linker has six nearest neighbors. A percolation algorithm was used to identify all the atoms belonging to each imidazolate linker in the parent structure and create a nearest neighbor list. To achieve a specified composition, type A linkers in the starting structure that was made of only type A linkers are randomly selected to be converted to type B linkers. Using the nearest neighbor list, a reverse Monte Carlo (RMC) algorithm is applied setting the SRO at a given composition.<sup>46,409</sup> Once the target SRO is achieved, atomistic detail is obtained by replacing type A linkers with type B linkers by aligning a stand-alone linker of type B with the selected type A linker. This is performed by aligning the type A and type B linkers' imidazolate plane normal vectors and the vectors formed by the C atom bonded to two N atoms and the N-N midpoint. Figure 6.1 shows representative mixed-linker cages for ZIF-8-90, ZIF-Im-mIm, and ZIF-7-90 with random placements of imidazolate linkers (SRO  $\alpha=0$ ).

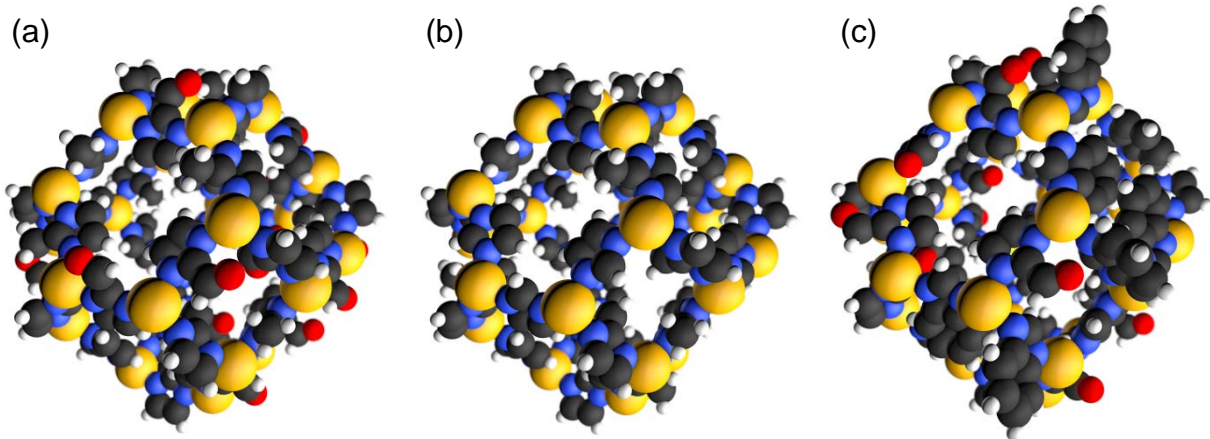


**Figure 6.1** Representative binary mixed-linker ZIF truncated octahedron with random SRO ( $\alpha=0$ ): (a) ZIF-8<sub>50</sub>-90<sub>50</sub>, (b) ZIF<sub>SOD</sub>-Im<sub>50</sub>-mIm<sub>50</sub> and (c) ZIF-7<sub>40</sub>-90<sub>60</sub> in the SOD topology.

## 6.2.2 Modeling Adsorbate Diffusion and Comparisons to Experimental Diffusion Data

Adsorbate diffusion was modeled using both conventional molecular dynamics (MD)<sup>154</sup>, free energy sampling based on biased MD<sup>219</sup> and a lattice-diffusion model<sup>375,377-379,411</sup> using the techniques discussed in Section 6.3.2 and 6.3.3. Self-diffusivities were calculated using the Einstein relation<sup>135,152</sup>:

$$D_{self} = \lim_{t \rightarrow \infty} \left[ \frac{1}{6N \langle t \rangle} \sum_{i=1}^N \left\langle |R_i(t) - R_i(0)|^2 \right\rangle \right] \quad (6.2)$$

where  $N$  is the number of adsorbates,  $t$  is time, and  $R_i$  is the Cartesian coordinate vector of the adsorbate center of mass at  $t$  and  $t=0$ . Self-diffusivities lower than  $\sim 10^{-8} \text{ cm}^2 \text{ s}^{-1}$  cannot be readily measured with conventional molecular dynamics. In this case, self-diffusion in cage-type ZIFs may be treated as an activated hopping process from cage to cage.<sup>99,137,201,219</sup> Diffusion in SALEM-2, ZIF-7, ZIF-8, and ZIF-90 mixed-linker hybrids occurs through the 6 member rings (MRs), each surrounded by three imidazolate linkers that lie directly in the window plane. As described in our earlier work for diffusion in binary mixed-linker ZIFs<sup>46,409</sup>, we hypothesized that diffusion is most affected by these

three linkers and reported that combinations of these three linkers yield four types of windows that include two parent windows and two hybrid windows.

Some of the experimental diffusion data we compare to measured self-diffusion using pulsed field gradient (PFG) NMR; our predicted self-diffusivities can be directly compared to this data.<sup>283,412</sup> Kinetic uptake experiments<sup>56,153,413</sup> were also used to measure transport diffusivities. To make direct simulation and experimental comparisons for this data, corrected transport diffusivities can be calculated through Darken's equation, relating corrected diffusivities to transport diffusivities through the thermodynamic correction factor.<sup>153</sup> If drag between counter-diffusing adsorbates is negligible as has been demonstrated for cage-type materials<sup>99</sup>, corrected transport diffusivities equal corrected self-diffusivities at a fixed temperature and adsorbate loading.

## **6.3 Simulation Methods**

### **6.3.1 Binary-Mixed Linker ZIF and Adsorbate Force Fields**

The intraZIF force field (FF) developed previously was used to model the ZIF systems. A hybrid intraZIF force field is introduced here where the force fields for the parent ZIF materials are combined to model the hybrids. Atomic point charges are kept constant on the organic linkers; however, using the Zn charges from the parent materials yields a net charge. Charges are therefore balanced by assigning five Zn atom types: two Zn types for the parent ZIFs and three Zn types representing the possible combinations of bonded N atoms. The atomic charges on the Zn atoms are taken as weighted arithmetic average according to the number of bonded N atoms (two types representing linker A and linker B) between charges on the parent Zn types. All other bonded and pair-wise interactions are the same as the previously reported intraZIF force field. The following eleven adsorbates were considered: N<sub>2</sub>, water, methanol, ethanol, 1-butanol, CH<sub>4</sub>, propane, n-butane, isobutane, SF<sub>6</sub>, and benzene. All adsorbate force fields are reported in

Appendix E. Adsorbate-framework interactions were modeled with a 12-6 Lennard-Jones (LJ) potential with parameters derived from Lorentz-Berthelot mixing rules. This treatment is the same as previously reported and all adsorbate-framework interactions are reported in the Appendix E.

As a validation of the hybrid intraZIF force field, Born-Oppenheimer molecular dynamics (BOMD) on the parent ZIFs were carried out using CP2K (version 2.6)<sup>263</sup>. Energies were computed from density functional theory (DFT) as implemented in the module QUICKSTEP<sup>264</sup>. In these calculations, the self-consistent field (SCF) minimizer was based on the orbital transformation method<sup>265</sup>, and a mixed Gaussian and Plane-Wave (GPW) method<sup>266,267</sup> was used in combination with PBE<sup>255</sup> Goedecker-Teter-Hutter (GTH) pseudopotentials<sup>268,269</sup>. The plane wave and DZVP-MOLOPT-GTH auxiliary basis sets cutoff used were 600 and 70 Ry cutoffs due to the presence of oxygen atoms. The dispersion correction DFT-D3 with damping from Becke and Johnson<sup>258</sup> (BJ) was applied to all simulations with a cutoff of 16 Å. First-principles molecular dynamics (MD) simulations were propagated for the three ZIF-8-90 structures at 700 K and 1 bar in the NPT ensemble using the Nosé-Hoover thermostat<sup>154</sup> and a time-step of 1 fs. In all MD simulations, the unit cell of each structure was used as a simulation box and periodic boundary conditions (PBC) were applied. The box contained 258, 264, and 270 atoms for ZIF-80<sub>25</sub>-90<sub>75</sub>, ZIF8<sub>50</sub>-90<sub>50</sub>, and ZIF-8<sub>75</sub>-90<sub>25</sub>, respectively. Figure 6.2 shows potential energy comparisons between PBE-D3(BJ) and the intraZIF-FF for the ZIF-8<sub>50</sub>-90<sub>50</sub> system, demonstrating reasonable agreement with a mean absolute error (MAE) of 9.02 kJ mol Zn<sup>-1</sup>. Table E.3 reports the mean absolute error, mean signed deviation (MSD), root mean squared deviation (RMSD), and the normalized root mean squared deviation (NRMSD) for the parent ZIFs and the three mixed-linker ZIFs. These results demonstrate that the intraZIF-FF performs adequately at describing binary mixed-linker ZIF flexibility.

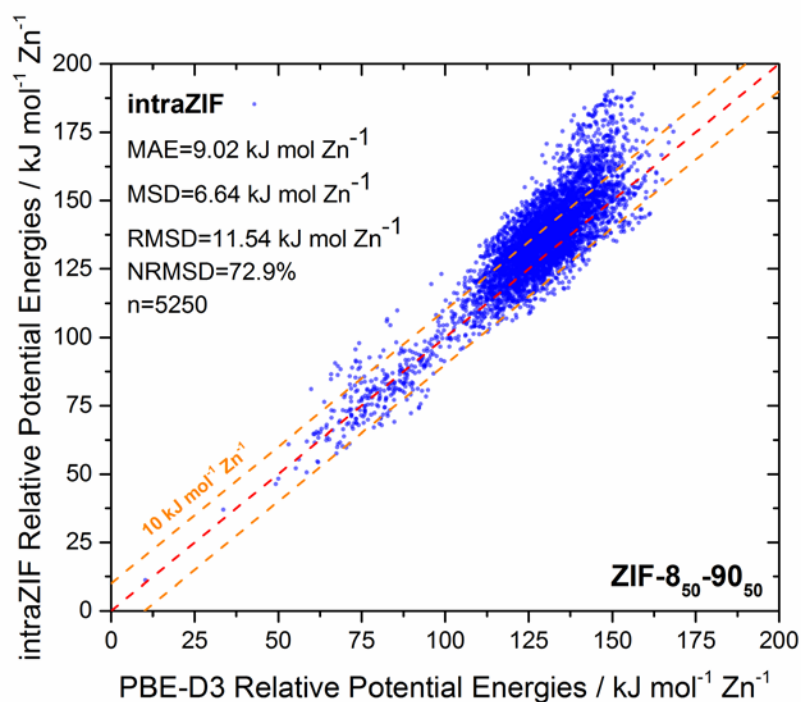


**Figure 6.2** Relative potential energy comparison between PBE-D3(BJ) and the intraZIF-FF for ZIF-8<sub>50</sub>-90<sub>50</sub> (SRO  $\alpha=0$ ) from a 5250 ps BOMD trajectory at 700 K.

### 6.3.2 Conventional and Biased Molecular Dynamics

Molecular dynamics were performed using LAMMPS<sup>186,271</sup> in the NPT ensemble with fixed simulation cell angles using a pairwise cutoff of 15.5 Å, timestep of 1 fs, and temperature and stress damping parameters of 100 and 1000 fs respectively. We applied an order-N scheme<sup>194</sup> with adsorbate snapshots taken every 10 fs to obtain accurate statistics on the MSDs. The MSDs were used to calculate single-component self-diffusivities with Equation 6.2. For conventional MD simulations, an equilibration time of 500 ps was used with 25 ns of production sampling.

For adsorbates diffusing on time scales slower than those readily measurable with standard MD, dynamically correct transition state theory (dcTST)<sup>148</sup> was utilized to calculate the diffusion hopping rates. We applied the collective variables<sup>187</sup> package of Fiorin et al. to perform umbrella sampling along a one-dimensional reaction coordinate

during an NPT-MD simulation. Umbrellas were spaced every 0.25 Å and used a spring constant of 50 kcal mol A<sup>-2</sup>. An equilibration of 200 ps with production of 500 ps was performed for each umbrella. The adsorbate position histograms were reweighted to create a Gibbs free energy using the weighted histogram analysis method (WHAM)<sup>188</sup>. Dynamical corrections were measured using the algorithm provided by Frenkel and Smit<sup>154</sup> with a sampling of 1500 trajectories, each 3 ps in length. Further details of these methods are discussed in Chapter 2.<sup>219</sup>

### 6.3.3 Lattice-Diffusion Model and Kinetic Monte Carlo

We previously developed a lattice-diffusion (LD) model to describe diffusion at infinite dilution in binary mixed-linker ZIFs.<sup>409</sup> Lattices were created with a specified mixed-linker composition and SRO  $\alpha$ . One of four possible rates is assigned to each cage-cage connection (i.e. window) based on the three linkers lining the window; the four hopping rates through the four different windows were calculated using the procedure detailed in Section 6.3.2. The cage-to-cage distance is 14.75 Å, an average distance taken from the SALEM-2, ZIF-8, and ZIF-90 unit cells. The kinetic Monte Carlo (KMC) algorithm used to propagate diffusion across the lattice follows the n-fold algorithm of Bortz et al.<sup>382</sup> with the utilization of five hundred non-interacting adsorbates and  $0.5 \times 10^6$  MC steps. Equation 6.2 was used to calculate self-diffusivities. Specific details of the lattice creation and KMC algorithm are reported in Chapter 5.<sup>409</sup>

## 6.4 Results and Discussion

### 6.4.1 ZIF-8-90: The First Experimentally Reported Example of Tunable Diffusion in ZIFs

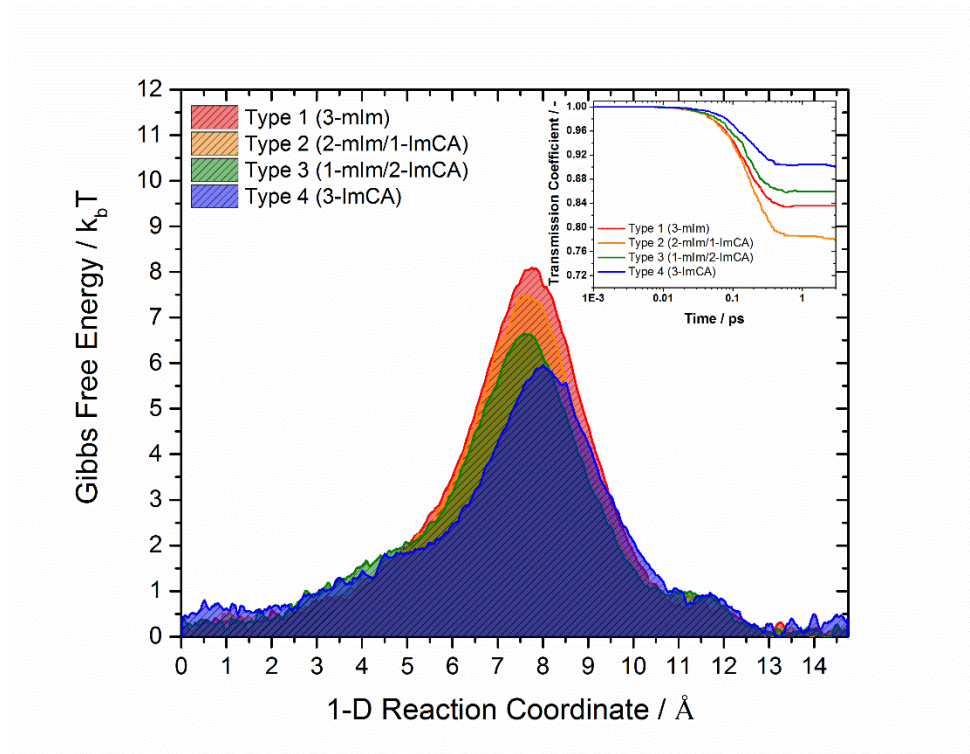
The structure of ZIF-8-90 materials has been characterized extensively and was the first mixed-linker MOF material in which tunable adsorption and diffusion was observed.<sup>42,46,189</sup> Before we predict any adsorbate diffusion in ZIF-8-90, we first address



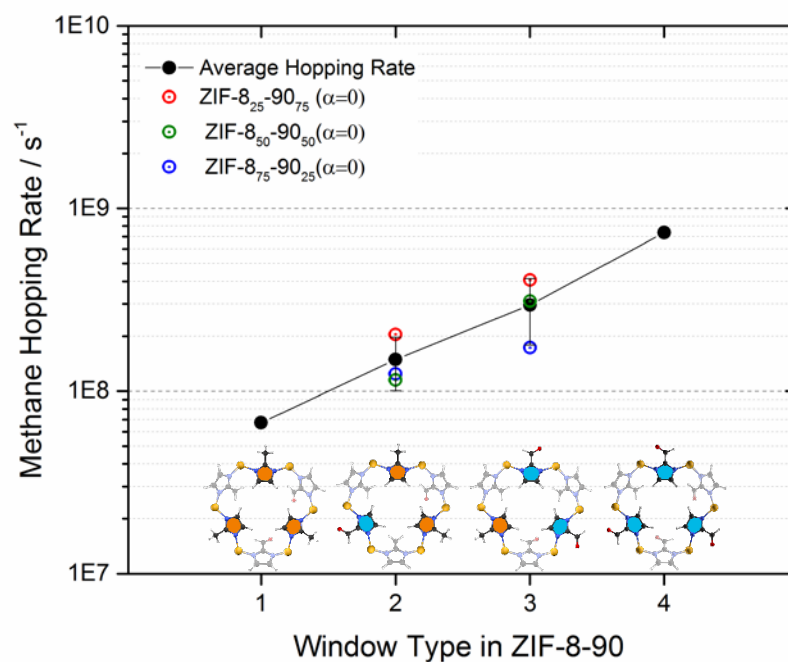
the underlying assumption of our LD model that diffusion is controlled by the rates through four types of windows. To test this hypothesis, we begin by calculating the hopping rates through the parent and hybrid windows. Hybrid windows were selected in ZIF-8<sub>50</sub>-90<sub>50</sub> through which dynamically corrected diffusion hopping rates were measured. We also selected hybrid windows in atomistic models of ZIF-8<sub>25</sub>-90<sub>75</sub> and ZIF-8<sub>75</sub>-90<sub>25</sub> with  $\alpha = 0$ . We denote windows that contain 3 mIm, 2 mIm/1 ImCA, 1 mIm/2 ImCA, and 3 ImCA linkers as type 1, 2, 3, and 4 windows, respectively. If the hopping rates through these windows was only a function of the local composition of the window, the hopping rates through each window type would be independent of the overall composition of the material.

Figure 6.3a shows the Gibbs free energy barriers for methane diffusion for windows in the parent ZIFs and hybrid windows in ZIF-8<sub>50</sub>-90<sub>50</sub> at 308 K and infinite dilution. As the number of ImCA linkers in the window increases, a decrease in the Gibbs free energy barrier is observed; an expected result since the ZIF-90 window exhibits slightly larger window diameters (3.45 Å) than the window diameters of ZIF-8 (3.43 Å) according to the experimental structures. The transmission coefficients all plateau at trajectory lengths of  $\sim 3$  ps.<sup>74,166</sup> Figure 6.3b shows the resulting methane hopping rates as determined by dcTST for the four window types. Uncertainties for hopping rates measured at infinite dilution are  $<20\%$ <sup>219</sup>. The hybrid rates measured in the ZIF-8-90 materials with varying composition are reported as open circles in Figure 6.3b. For type 2 and 3 windows, the rates for ZIF-8<sub>25</sub>-90<sub>75</sub> and ZIF-8<sub>75</sub>-90<sub>25</sub> differ by roughly a factor of two. We find, however, that the average of the three hybrid rates (filled black circles) is very similar to the rate measured in the ZIF-8<sub>50</sub>-90<sub>50</sub> material. These results indicate that the assumption that hopping rates are dictated solely by the window type is not exact, but the variations in window hopping rates due to deviations from this approximation are small.

(a)



(b)



**Figure 6.3** (a) Free energy curves with the inset showing the transmission coefficient curves for methane and (b) corresponding rates through the four window types for methane in ZIF-8-90 materials exhibiting random local order ( $\alpha=0$ ) at 308 K. Open circles in are the composition-dependent hybrid rates while the black filled circles are the average hopping rates.

Methane diffuses fast enough in ZIF-8-90 to be accurately measured using conventional NPT-MD, but also on time-scales long enough for dcTST to be applicable. As a result, we can directly compare observations from MD simulations with results from our LD model that use the average methane hopping rates described above. Figure 6.4 compares methane self-diffusivity as a function of mIm mole fraction in ZIF-8-90 materials using both methods. The loading of the conventional NPT-MD simulations was 1 CH<sub>4</sub> per cage to obtain reasonable MSD statistics while the LD model measures directly predicts self-diffusion at infinite dilution. The self-diffusivities predicted from our LD model agree quantitatively with those computed with conventional NPT-MD simulations. To assess the influence of finite size effects, we calculated diffusion with our LD model for simulation volumes with 2×2×2 and 10×10×10 unit cells. The self-diffusivities measured in both simulation volumes agree almost exactly, demonstrating the negligible influence of finite size effects. Each of the self-diffusivities from the LD model was predicted in five different lattice realizations, showing self-diffusion uncertainties smaller than the symbols.

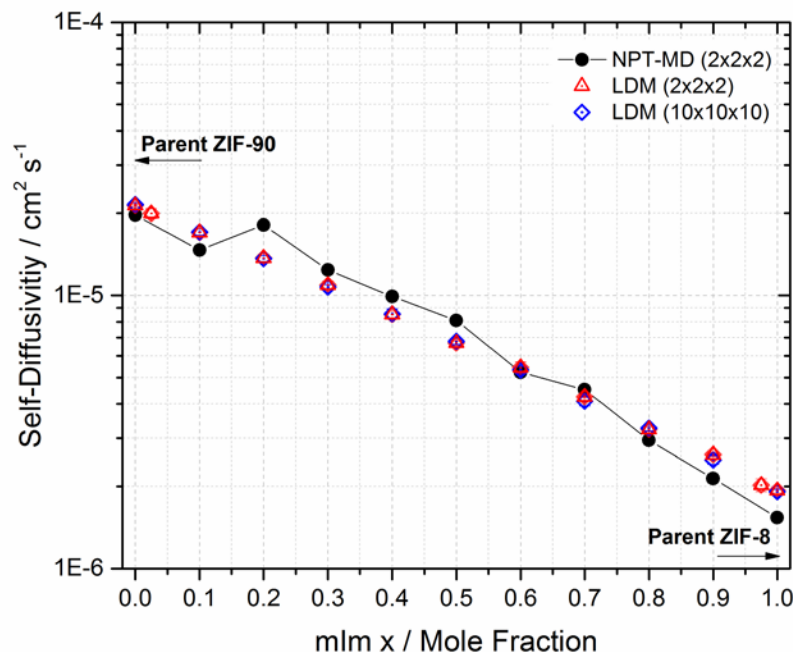


**Figure 6.4** Conventional MD and lattice-diffusion model (LDM) comparison for methane in ZIF-8<sub>x</sub>-90<sub>100-x</sub> at 308.15 K and the infinite dilution limit. MSD plots from the NPT-MD simulations are reported in Appendix E.

Using a combination of conventional molecular dynamics and lattice-diffusion simulations, we compared our predicted self-diffusion coefficients to experimental diffusion coefficients of water, methanol, ethanol, n-butane, 1-butanol, and isobutane in ZIF-8-90. The experimentally reported self- and corrected diffusivities were obtained using a combination of experimental methods. Water, methanol, and ethanol self-diffusivities were measured with PFG-NMR at finite loadings at 313 K.<sup>189</sup> The n-butane, 1-butanol, and isobutane corrected diffusivities were measured using macroscopic uptake measurements at low loadings near infinite dilution and 308 K.<sup>189</sup> We compared our predicted self-diffusivities directly to these experimental corrected diffusivities since corrected diffusivities are exactly equal to self-diffusivities at infinite dilution.<sup>152</sup> Since water, methanol, and ethanol diffuse on time scales accessible through conventional MD, we simulated the self-diffusivities using NPT-MD at 313 K and the loadings reported by

Eum et al.<sup>189</sup>: 16 mmol/g of ZIF-8<sub>0</sub>-90<sub>100</sub> (44 molecules per unit cell), 16 mmol/g of ZIF-8<sub>7</sub>-90<sub>93</sub> (44 molecules per unit cell), 18 mmol/g of ZIF-8<sub>25</sub>-90<sub>75</sub> (49 molecules per unit cell), 18 mmol/g of ZIF-8<sub>50</sub>-90<sub>50</sub> (49 molecules per unit cell), 4 mmol/g of ZIF-8<sub>75</sub>-90<sub>25</sub> (11 molecules per unit cell), and 0.5 mmol/g ZIF-8<sub>100</sub>-90<sub>0</sub> (1 molecule per unit cell). Methanol and ethanol loadings were assumed to be constant with the ZIF-8-90 composition with 8.0 mmol/g methanol of ZIF (22 molecules per unit cell) and 5 mmol/g of ethanol of ZIF (14 molecules per unit cell). These loadings were estimated from experimental isotherms.<sup>189,414</sup> Gee et al. reported that 10% variation of loading around 4.5 mmol/g of methanol and 2.25 mmol/g of ethanol of ZIF had a negligible impact on the predicted self-diffusivities these small alcohols in ZIF-8 and ZIF-90.<sup>134</sup> We predicted the diffusivities of n-butane, 1-butanol, and isobutane using our LD model since diffusion is too slow to measure with conventional MD. Rates through the four window types in ZIF-8-90 materials are measured with biased sampling molecular dynamics. All the NPT-MD and LD model simulations in ZIF-8-90 materials were performed in structures with random short-range order ( $\alpha=0$ ). Jayachandrababu et al. experimentally determined the SRO of ZIF-8-90 materials and reported SRO  $\alpha$  values near 0.0 over most of the composition range with slight clustering ( $\alpha= +0.45$ ) observed in ZIF-8<sub>50</sub>-90<sub>50</sub>.<sup>46</sup> In our previous study, we determined that diffusion predictions are a weak function of SRO<sup>409</sup>; we therefore predict diffusivities in ZIF-8-90 materials with random SRO.

Figure 6.5 compares our predicted methanol and ethanol self-diffusivities to those measured with PFG-NMR in ZIF-8-90. Quantitative agreement is observed between our predicted methanol and ethanol self-diffusivities and the experimental measurements. The AMBER force field was previously used to predict methanol and ethanol diffusivities in the parent ZIF-8 and ZIF-90 materials.<sup>134</sup> The AMBER-FF under-predicted the methanol self-diffusivities by over an order of magnitude and predicted that ethanol diffusivities were lower than  $1 \times 10^{-12} \text{ m}^2 \text{ s}^{-1}$ . This example provides evidence that

the hybrid intraZIF-FF provides quantitative diffusion predictions in hybrid ZIF materials.

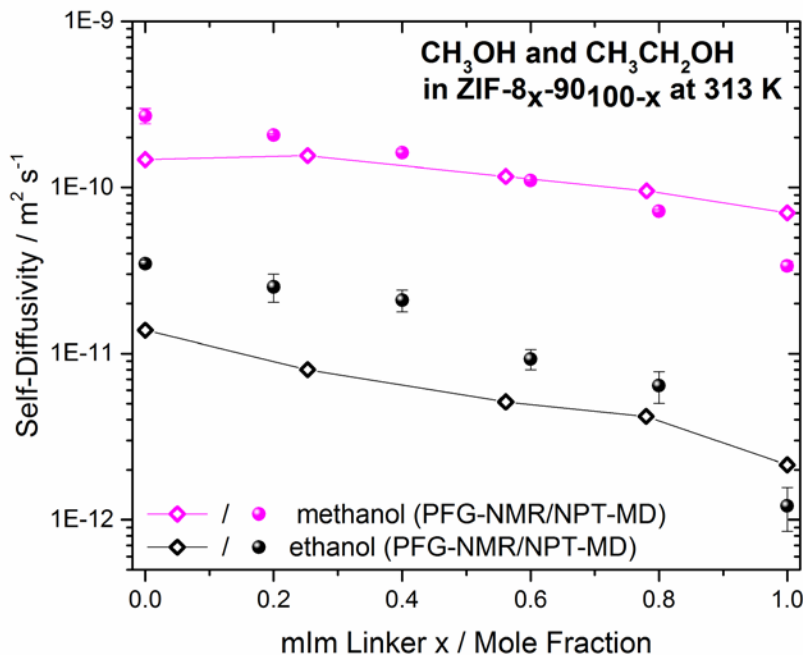


**Figure 6.5** Simulated (filled circles) and experimental<sup>189</sup> (open diamonds) self-diffusivities of methanol (magenta) and ethanol (black) in ZIF-8-90 at 313 K. Lines are guides for the eye.

Figure 6.6 shows the self-diffusivities of water measured from PFG-NMR (open diamonds) and predicted with NPT-MD simulations (filled blue circles) in ZIF-8-90. Quantitative agreement between the PFG-NMR results and the predicted self-diffusivities is obtained over the composition range from ZIF-90 to ZIF-8<sub>50</sub>-90<sub>50</sub>. The water loading is high for each instance considered in this range of compositions. However, our calculations predict that water diffusion decreases significantly in ZIF-8<sub>75</sub>-90<sub>25</sub> relative to the ZIF-90-rich materials. Water is known to undergo cluster formation and cage-filling upon adsorption in nanoporous materials, especially materials with some hydrophobic character in their pores.<sup>415</sup> Examination of the MD trajectories revealed that water clustering occurs in ZIF-8<sub>75</sub>-90<sub>25</sub> (right inset of Figure 6.6), leading to a significant

decrease in the predicted diffusivity. In this material, the locally hydrophobic regions associated with ZIF-8 linkers<sup>291</sup> induce the formation of localized water clusters. In ZIF-8, the eight water molecules cluster in a similar manner, but we were unable to accurately measure water self-diffusivities due to poor MSD statistics. This result implies that water diffusion occurs in ZIF-8 on much longer time-scales than is measurable with NPT-MD simulations at near infinite dilution loadings. When significant clustering of adsorbates occurs, simulations of diffusion can be strongly impacted by finite size effects.<sup>416,417</sup> We did not attempt to explore these effects for water diffusion in ZIF-8-90.

In Chapter 3, we calculated infinite dilution self-diffusivities of water in ZIF-90 and ZIF-8 using dcTST. These self-diffusivities are reported as red crosses in Figure 6.6. Infinite dilution dcTST predicts a water self-diffusivity of  $4 \times 10^{-9} \text{ m}^2 \text{ s}^{-1}$  in ZIF-8 at infinite dilution and 308 K. Zhang et al. performed detailed experimental studies of water uptake in ZIF-8 crystals using gravimetric uptake experiments.<sup>414</sup> They determined the corrected diffusivity of water to be  $\sim 1 \times 10^{-10} \text{ m}^2 \text{ s}^{-1}$  at a loading of 0.2 mmol H<sub>2</sub>O per g ZIF-8 ( $P/P_0=0.95$ ) and 308 K. Their corrected diffusivity is slightly lower than our self-diffusivity at infinite dilution predicted with dcTST. Macroscopic uptake experiments often have order-of-magnitude uncertainties.<sup>219</sup> It is possible that diffusion of water at low loadings in real ZIF-8 samples is influenced by the presence of defects in this hydrophobic material, which would be expected to reduce diffusion relative to the defect-free material.<sup>291</sup> Overall, our results show that molecular simulations perform well in predicting water diffusion in hybrid materials at conditions where water adsorption is not highly localized.

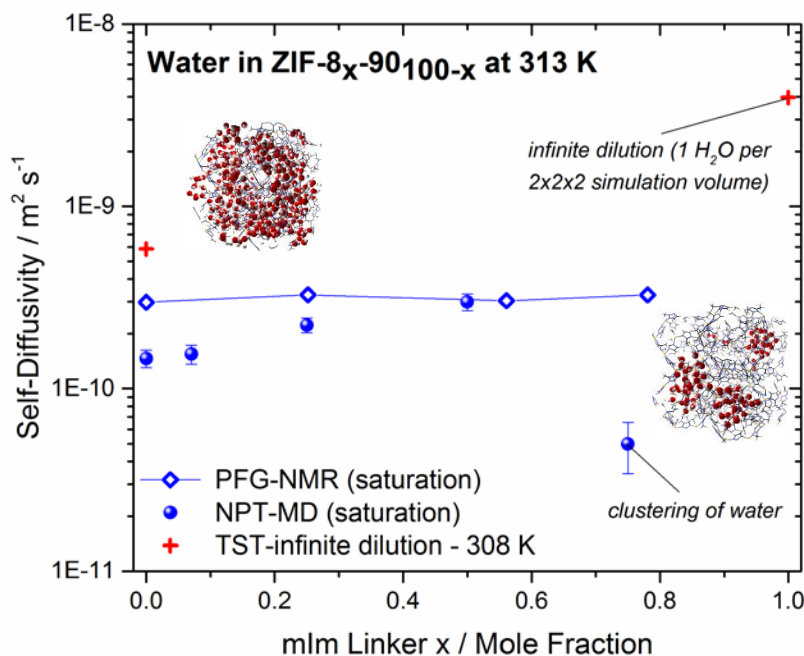


**Figure 6.6** Simulated (filled circles) and experimental<sup>189</sup> (open diamonds) self-diffusivities of water in ZIF-8-90 at 313 K. Red crosses indicate simulated self-diffusivities of water in the parent ZIFs from dcTST simulations. Lines are guides for the eye. Inset images show water clustering (red spheres) in ZIF-8<sub>07</sub>-90<sub>93</sub> (left) and ZIF-8<sub>75</sub>-90<sub>25</sub> (right).

Figure 6.7 shows the self-diffusivities of n-butane, 1-butanol, and isobutane as predicted by our LD model (upper panel) and experimentally measured using macroscopic uptake methods (lower panel) in ZIF-8-90. The transport diffusivities of n-butane and isobutane were experimentally measured with a pressure decay cell and the transport diffusivities of 1-butanol were measured using gravimetric uptake. These values were reported as corrected diffusivities using Darken's equation and thermodynamic corrections obtained from experimental isotherms. As discussed in Section 6.2.2, we make the assumption that corrected and self-diffusivities are equivalent given that the experimental corrected diffusivities are measured at low loadings and our predicted self-diffusivities are measured at infinite dilution. We predict the same trends as the experimental measurements that the diffusivity rankings are n-butane > 1-butanol



> isobutane and that diffusion of all three adsorbates is slower in ZIF-8 than in ZIF-90. Our calculations predict faster diffusion coefficients of n-butane and 1-butanol and slower diffusion of isobutane than the experimental diffusivities. Eum et al.<sup>189</sup> and Zhang et al.<sup>56</sup> independently measured n-butane and isobutane corrected diffusivities in ZIF-8 using the same kinetic uptake methodology and found two and three orders of magnitude difference in the diffusivities for n-butane and isobutane respectively. This experimental uncertainty is shown in the upper panel of Figure 6.7. Measuring slow adsorbate diffusion experimentally has the potential for significant uncertainties, possibly from external heat<sup>286</sup> or mass transfer<sup>287</sup> effects. For example, Tanaka et al. reported that 1-butanol diffusion in ZIF-8 crystals measured with macroscopic uptake measurements was significantly influenced by surface barriers.<sup>288</sup> Similar observations have been made by Remi et al. for 1-butanol diffusion in zeolite SAPO-34.<sup>101</sup> Overall, we quantitatively predict self-diffusion of adsorbates when comparing to PFG-NMR measurements and provide the same qualitative trends of diffusion as revealed experimentally with macroscopic measurements of adsorbate diffusion in binary mixed-linker ZIF-8-90.

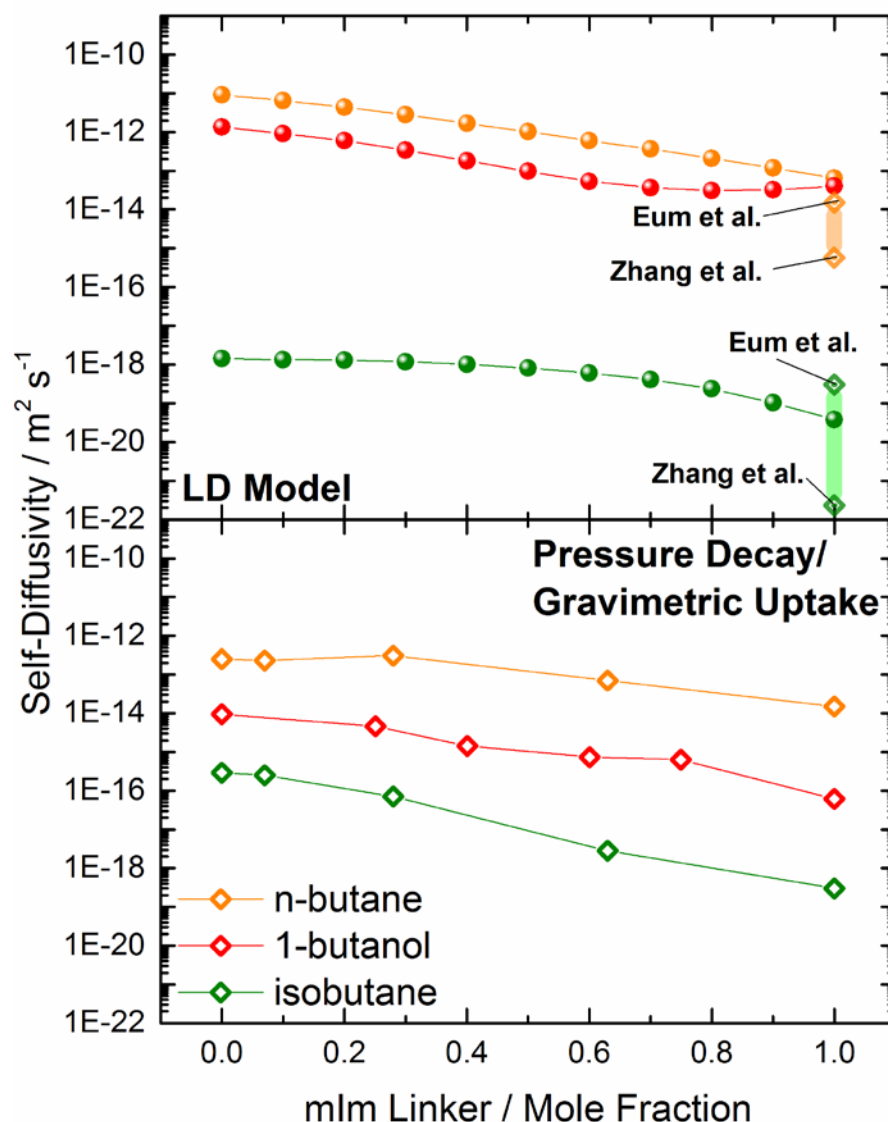


**Figure 6.7** Comparison of predicted (upper panel) and experimental<sup>189</sup> (lower panel) self-diffusivities of n-butane, 1-butanol, and isobutane in ZIF-8<sub>x</sub>-90<sub>100-x</sub>. The upper panel features experimentally measured n-butane and isobutane diffusivities by Zhang et al.<sup>56</sup> and Eum et al.<sup>189</sup> to indicate the experimental uncertainties that exist for these materials. Rates used in the lattice-diffusion model are reported in Appendix E (Figure E.2).

#### 6.4.2 ZIF-8/SALEM-2 in the SOD Topology

Zhang and Koros measured transport diffusivities of n-butane, isobutane, and SF<sub>6</sub> in hybrid SALEM-2/ZIF-8 materials created through thermal modification of the parent ZIF-8 material.<sup>370</sup> They report two significant findings as the mole fraction of

unfunctionalized imidazolate linker increases from 0% to 17%: (1) the transport diffusivities of n-butane, isobutane, and SF<sub>6</sub> increase by ~28, 400, and 432 times respectively and (2) the ideal diffusion selectivity of n-butane/isobutane decreases by over an order of magnitude. As a further test of our modeling approach, we attempted to predict both these observed trends separate from any experimental input. Since the short-range order of the hybrid SALEM-2/ZIF-8 materials used in these experiments has not been experimentally measured, we used structures with random SRO ( $\alpha=0$ ). As discussed above, diffusion is typically a weak function of SRO unless severe clustering of linkers is occurring.<sup>409</sup> Karagiari et al. synthesized SALEM-2 through solvent assisted linker exchange (SALE) and reported that in a structure containing 15% mIm linkers that these linkers were randomly dispersed as determined through XRD refinement.<sup>253</sup>

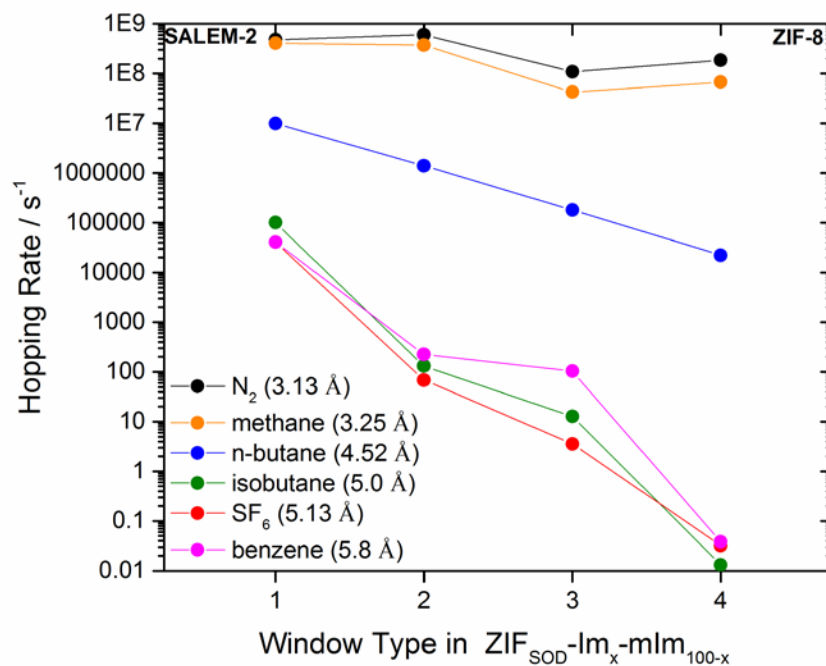
Figure 6.8a shows the rates of N<sub>2</sub>, methane, n-butane, isobutane, SF<sub>6</sub>, and benzene hopping through the four window types present in ZIF<sub>SOD</sub>-Im<sub>x</sub>-mIm<sub>100-x</sub> materials. Windows labeled type 1, 2, 3, and 4 have 3 Im, 2 Im/1 mIm, 1 Im/2 mIm, and 3 mIm linkers lining the plane of the window. The rates are calculated using the same procedure as described for the ZIF-8-90 materials and the molecules studied were chosen not only based on the original experimental study but also for their molecular diameters, shape, and charge characteristics. As observed in Figure 6.8a, the hopping rates for each of adsorbates monotonically decrease from type 1 to type 4 windows. The rate behavior for small molecules such as N<sub>2</sub> and CH<sub>4</sub> decreases monotonically from type 1 to type 4 windows. One surprising feature of these results is that the type 3 window hopping rate for benzene, which has a molecular diameter of 5.8 Å, is almost two orders of magnitude faster than SF<sub>6</sub>, which has a molecular diameter of 5.13 Å.

Figure 6.8b shows the self-diffusivities for N<sub>2</sub>, methane, n-butane, isobutane, SF<sub>6</sub>, and benzene in ZIF<sub>SOD</sub>-Im<sub>x</sub>-mIm<sub>100-x</sub> at 308 K and infinite dilution. We correctly predict the two trends observed from the experimental single-component n-butane, isobutane, and SF<sub>6</sub> transport diffusion data presented by Zhang and Koros. We determine that as the

fraction of Im linkers increases from 0% to 20%, that the self-diffusivities of n-butane, isobutane, and SF<sub>6</sub> increase by ~5, 476, and 59 times respectively and the ideal diffusion selectivity of n-butane/isobutane decreases by almost two orders of magnitude (Figure E.3). Unfortunately, direct comparison of the experimental transport diffusion coefficients to our predicted self-diffusivities is not possible without experimental isotherms to calculate corrected diffusivities. Grand canonical Monte Carlo (GCMC) simulations could be performed using rigid SALEM-2/ZIF-8 hybrids to approximate the thermodynamic correction factors. However, it is unclear how significantly SRO influences the adsorption properties of hybrid ZIF materials, introducing significant uncertainty in a direct comparison.

While these experimental studies clearly demonstrate the tunable diffusion properties of binary mixed-linker ZIFs, the conclusion may be drawn from ideal diffusion selectivities that one or the other parent ZIF has the highest potential for molecular sieving, not the hybrid material. The self-diffusivities in Figure 6.8b also show interesting behavior when considering benzene. SALEM-2/ZIF-8 hybrids with mIm mole fractions between 0.4-0.9 have larger ideal diffusion selectivities for binary combinations of isobutane, SF<sub>6</sub>, and benzene than the parent ZIF materials (Figure E.4). Even though the separations shown in the data have little practical interest, they illustrate the possibility that properties of a hybrid ZIF may improve upon the separation capability of the single-linker ZIFs.

(a)



(b)

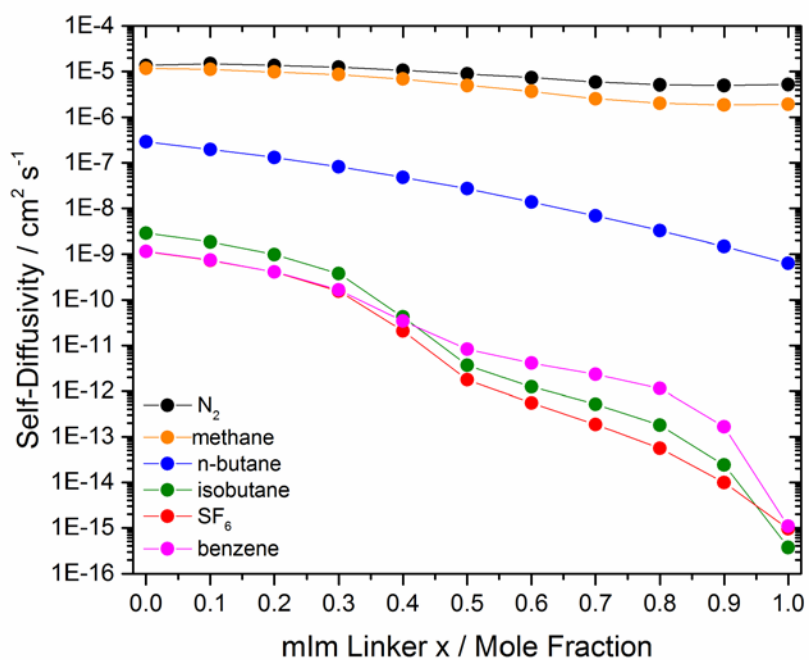


**Figure 6.8** (a) Hopping rates of  $\text{N}_2$ , methane, n-butane, isobutane,  $\text{SF}_6$ , and benzene through the four window types in SALEM-2/ZIF-8 hybrids at 308 K, and (b) corresponding self-diffusion coefficients predicted through the lattice-diffusion model.

### 6.4.3 ZIF-7-90: Window Blocking By a Bulky Imidazolate Linker

Rashidi et al. extensively characterized ZIF-7-90 and measured n-butane and isobutane transport diffusivities in these materials.<sup>43</sup> They determined that ZIF-7-90 forms in a different topology than the parent ZIF-90 SOD materials for compositions exceeding 40% of benzimidazole (BzIm) linkers. We have therefore only examined diffusion over the composition range 0-0.4 BzIm mole fraction in the cubic SOD topology.<sup>43</sup> In Chapter 5, we presented a conceptually simple case for which adsorbate diffusion is “blocked” by a bulky imidazolate linker.<sup>409</sup> The ZIF-7-90 material has the most potential for this type of behavior among the examples we have studied since benzimidazole is a large linker that can block the aperture. The experimental data presented by Rashidi et al. indirectly supports this claim as transport diffusivities of n-butane and isobutane decreased by several orders of magnitude relative to the parent material when 40% mole fraction of BzIm linker was added. Figure 6.9a shows the hopping rates for N<sub>2</sub>, methane, propane, and n-butane as a function of window type in ZIF-7-90 where windows of type 1, 2, 3, and 4 contain 3 ImCA, 2 ImCA/1 BzIm, 1 ImCA/2 BzIm, and 3 BzIm linkers respectively. The hopping rates through the hybrid windows are measured in ZIF-7<sub>40</sub>-90<sub>60</sub>. The type 4 window hopping rate is also measured in the ZIF-7<sub>40</sub>-90<sub>60</sub> structure rather than the parent ZIF-7 structure, since that structure maintains a rhombohedral unit cell and not the cubic SOD topology.<sup>41</sup> A surprising outcome from these calculations is that the hopping rate decreases significantly from a window of type 1 to a window of type 2 but then increases for all four adsorbates in windows of type 3 and 4. Using the hopping rates in Figure 6.9a, we have predicted the self-diffusion coefficients for N<sub>2</sub>, methane, propane, and n-butane in ZIF-7<sub>x</sub>-90<sub>100-x</sub> as shown in Figure 6.9b. The self-diffusivities calculated with our standard LD model are in the filled circles. We find that even with hopping rates increasing for windows of type 3 and 4, the self-diffusion monotonically decreases over the entire composition range.

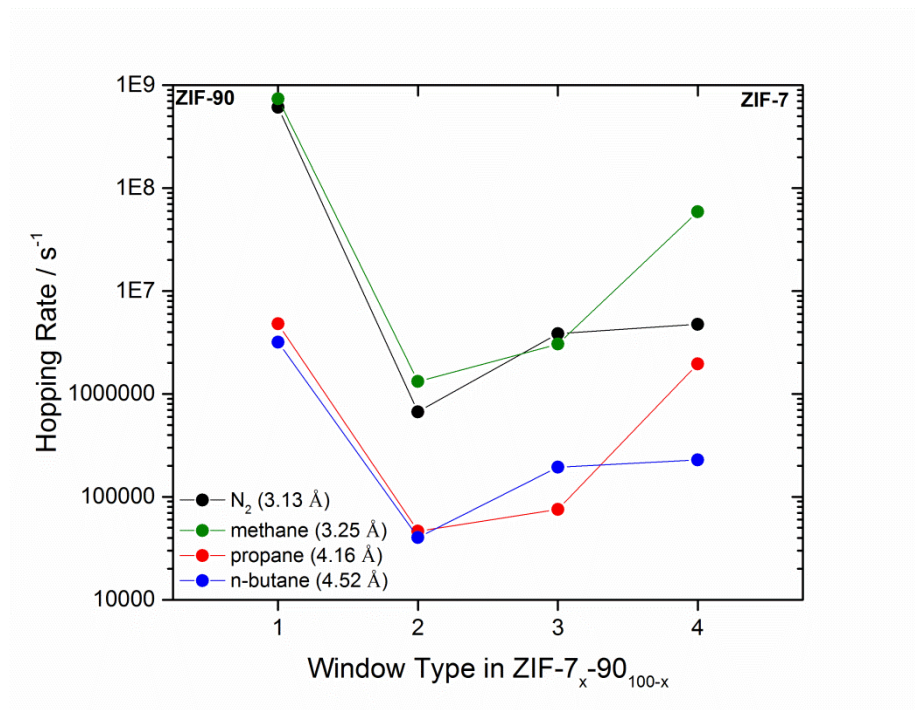
One possible explanation for the sharp decrease in transport diffusivities reported by Rashidi et al. could be that during crystallization of the hybrid material BzIm linkers located themselves preferentially within “empty” windows. The probability of selecting a window of type 2 at a composition of 0.33 BzIm mole fraction and SRO  $\alpha=0.0$  is ~50% when using our original LD model.<sup>46</sup> We term our original LD model as having “equal” window probabilities. We also considered a “weighted” LD model where BzIm linkers are placed randomly in windows that do not contain a BzIm linker. This idea is somewhat analogous to Lowenstein’s rule, which is often invoked in aluminosilicate zeolites as prohibiting occupation of neighboring tetrahedral sites by Al atoms.<sup>418,419</sup> This method produces structures with compositions ranging from 0.0 to 0.33 BzIm mole fraction and  $\alpha=0.0$  where every window is a type 2 window (i.e. one BzIm linker per window) and type 3 and type 4 windows are not allowed to form. ZIF-7-90 structures formed with this restriction with compositions between 0.0 and 0.33 BzIm mole fraction can still have SRO  $\alpha$  exactly equal to 0.0. Structures with compositions between 0.33 and 0.4 BzIm mole fraction are allowed to form windows of type 3 and type 4 only after all windows are initially type 2. The SRO  $\alpha$  values are slightly positive for structures with compositions between 0.33 and 0.4 BzIm mole fraction. For example, a structure containing 35% BzIm yields  $\alpha=+0.02$  and a structure containing 40% BzIm yields  $\alpha=+0.08$ .

Figure 6.9b shows the self-diffusivities predicted by the equal and weighted LD models. For BzIm mole fractions larger than 0.2, diffusion is predicted to be orders of magnitude different between the two LD models. This decrease in diffusivity cannot be attributed to a different short-range order because, as noted above, the weighted and equal LD models generated structures with very similar SRO. This is an example in which knowledge of the SRO is insufficient to completely describe the resulting diffusion properties of a mixed linker material. The methods that are currently available for measuring SRO in these materials experimentally are unfortunately not sufficient to

assess the kind of local ordering that distinguishes the two models we have considered here.<sup>46</sup>



(a)



(b)

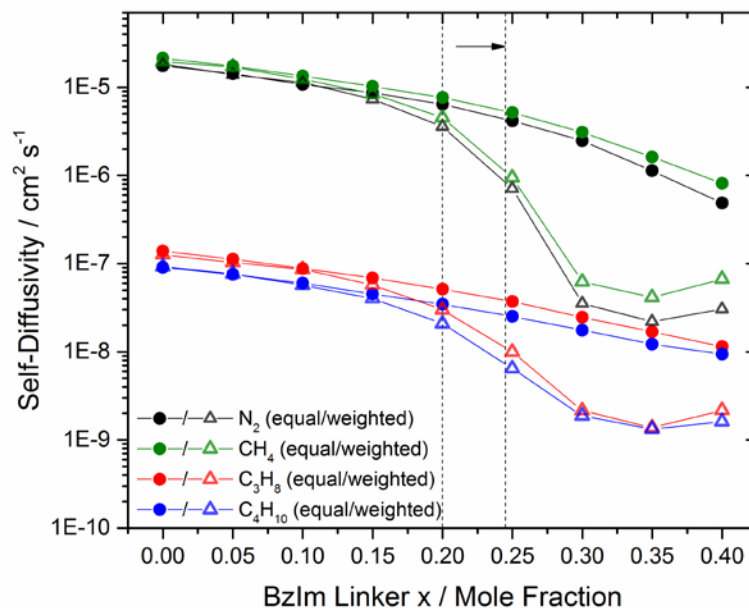


**Figure 6.9** (a) Hopping rates of  $N_2$ , methane, propane and n-butane through the four window types in ZIF-7-90 hybrids, and (b) corresponding self-diffusion coefficients predicted through the lattice-diffusion model for ZIF-7-90 structures with SRO  $\alpha=0$ . Dashed lines represent the region where the probability of choosing a type one window drops from 52-44% for the “equal” LD model and from 40-25% for the “weighted” diffusion model. The percolation threshold (0.18 for body centered cubic lattice with SRO  $\alpha=0$ ) is approached much more quickly with the “weighted” LD model.<sup>409</sup>

## 6.5 Conclusions

In this work, we presented for the first time quantitative diffusion predictions in binary mixed-linker ZIF materials. We accomplished this by first introducing a hybrid intraZIF force field that is capable of representing configurational potential energies from Born-Oppenheimer molecular dynamics simulations. We used this force field to self-consistently demonstrate that our previously developed lattice-diffusion model yields the same self-diffusivities as fully detailed NPT-MD simulations for methane in ZIF-8-90 materials. We proved that it is possible to quantitatively predict diffusion of several adsorbates through ZIF-8-90 by thorough comparison to experimental data taken using PFG-NMR and macroscopic kinetic uptake methods. We qualitatively predicted diffusion trends in SALEM-2/ZIF-8 and ZIF-7-90 hybrids. In the SALEM-2/ZIF-8 materials, we correctly predicted diffusion trends seen experimentally. We also determined that a hybrid of this material is capable of higher ideal diffusion selectivities than the parent materials for adsorbates with similar molecular diameters. For ZIF-7-90 materials, we demonstrated our hypothesized window blocking scenario and that the preferential formation of certain window types can lead to large differences in diffusion predictions. Overall, this suite of methods and conclusions demonstrates that atomistic simulations can quantitatively predict diffusion in mixed-linker MOFs and can be used to identify hybrid MOFs suitable for molecular sieving applications.

## CHAPTER 7

### CONCLUSIONS

#### 7.1 Dissertation Impact

The content in this dissertation allows for the accurate prediction of diffusion in single-linker and mixed-linker MOFs and the methods introduced can ultimately be used to guide experimental work on these materials. While the focus of this work was on zeolitic imidazolate frameworks (ZIFs), the methods and insights from studying ZIFs is applicable to study diffusion in any nanoporous material exhibiting long-range or short-range order of its structural components. We obtained fundamental insights into adsorbate diffusion in ZIFs by examining a range of adsorbates and ZIF materials.

It had been observed experimentally that diffusion of large molecules (e.g. isobutane) occurs in ZIF-8 even though the molecular diameters of these molecules were much larger than the pore aperture. The computational tools available when work on this thesis began were not capable of accurately predicting this phenomenon. Chapter 2 introduced the use of biased molecular dynamics sampling methods, which are required to examine the entire range of diffusion time scales encountered by various molecules in ZIF-8. These unique computational methods, when coupled with models describing the thermally-induced structural flexibility of the ZIF-8 framework, were able to predict self-diffusivities within an order of magnitude agreement of experimentally determined self-diffusivities. It was also determined that large adsorbates significantly brace open the window of ZIF-8 during the diffusion process. This study provided the basis for studying the diffusion of any molecules, small or large, within nanoporous materials containing small window apertures and large cavities.

The work in Chapter 2 was focused on describing diffusion in ZIF-8 accurately and required the use of a previously reported force field to model flexibility. It was

determined that modifications of this “off the shelf” force field were not adequate for modeling the flexibility of a large range of ZIF materials. Chapter 3 discusses the development of a force field modeling the flexibility of ZIFs based on density functional theory (DFT) calculations. We have named this the intraZIF force field and it more accurately reproduces lattice parameters, configurational potential energies, window diameter distributions, pore limiting diameters, and surface areas as compared to the previously available generic force field. The intraZIF force field was used to screen diffusion of thirty adsorbates with molecular diameters ranging of 2.6 to 7.0 Å in four ZIF materials: SALEM-2, ZIF-7, ZIF-8, and ZIF-90. We found that neither pore limiting diameters nor window diameter distributions could be used to accurately predict *a priori* whether an adsorbate would diffuse faster or slower in one ZIF material over another. Extending these calculations to other single-linker ZIF materials with different topologies is one direction of future work that would be fruitful.

During my thesis work, experiments had shown that the diffusion of light gases could be monotonically tuned using binary-mixed linker ZIFs and that individual crystals contained both types of linker. We required structural information on the unit cell level to perform detailed atomistic studies of diffusion in these materials. Chapter 4 details a combined 2D NMR and computational approach for elucidating structural information on the unit cell level. We determined over the entire composition range the local ordering on the unit cell level of 2-methylimidazolate and carboxaldehyde-2-imidazolate linkers in ZIF-8-90 materials. This protocol did not require isotopic labeling of the imidazolate linkers and could be used to study the local ordering of n-component organic linkers in MOFs, assuming the hydrogens were in chemically distinguishable environments.

A logical extension of this work was to determine how the local ordering of linkers influenced diffusion properties. Chapter 5 proposes a lattice-diffusion model combined with kinetic Monte Carlo to study diffusion. We determined that diffusion was typically a weak function of the local ordering of organic linkers but highly dependent on

the hopping rates through various types of pores encountered in mixed-linker ZIF materials. With the establishment of the various computational methods and insights garnered in Chapters 2-5 and the experimental demonstration that diffusion is monotonically tunable in binary mixed-linker ZIFs, we proceeded to predict diffusion quantitatively in binary mixed linker ZIFs. Chapter 6 demonstrates that this suite of computational methods can be applied to accurately predict diffusion in binary mixed-linker ZIFs.

## 7.2 Suggestions for Future Work

The work performed in Chapters 2-6 can lead to many interesting research projects as proposed below:

**(1) Validate flexible MOF force fields with one-dimensional NMR.** The rotation of the imidazolate linker directly impacts diffusion properties and it has been shown that the rotation is influenced by temperature as well as the presence of adsorbates.<sup>285</sup> Quantities such as the linker libration angles or reorientation correlation functions can be measured using atomistic simulations. The challenge will be in making sure the quantities measured in the molecular dynamics simulations correspond directly to NMR observables.<sup>420,421</sup> It may be possible to use linker libration angles and the frequency of rotation to experimentally determined window size distributions of MOFs if these issues are understood in sufficient detail.

**(2) Impact of polymer confinement on ZIF materials and light gas diffusion.** Mueller et al. determined that diffusion of ethylene was decreased when traveling inside of ZIF-8 crystals embedded in a polymer film.<sup>422</sup> The intraZIF force field accurately models ZIF-8 under compression and therefore could be used to model

diffusion as a function of pressure. The effect of pressure may influence the diameter of ZIF apertures and could yield improved ideal diffusion selectivities.

**(3) Automate the prediction of diffusion coefficients.** Screening nanoporous materials for adsorption separations has been almost trivial with access to robust codes that simulate adsorption. The codes to measure diffusion accurately are neither widely accessible to the computational chemistry community nor are they conducive to screening libraries of even hundreds of nanoporous materials. It would be advantageous to produce a suite of Python scripts using the LAMMPS molecular dynamics package<sup>271</sup> (or a similar set of software tools) to predict diffusion occurring at any time scale in any nanoporous material.

**(4) Use hypothetical ZIF polymorphs to develop a pseudo-empirical model capable of predicting diffusion.** In Chapter 3, we determined that a relationship between the square of the molecular diameter and the logarithm of self-diffusivities yields similar fitting parameters as those seen for polymers. These fit parameters are a function of the ZIF flexibility and temperature. This model would relate intrinsic ZIF flexibility characteristics and adsorbate molecular diameters to predict self-diffusivities, without the need to perform many computationally expensive atomistic simulations.

**(5) Use mixed-linker force fields and lattice-diffusion models to investigate all difficult light gas separations.** Chapter 6 establishes the methods to examine diffusion in mixed-linker ZIFs and explores the predictive capability of simulations by comparing to experimental diffusion data. It would be interesting to screen pore apertures with combinations of organic linkers to determine if ideal diffusion

selectivities are enhanced or reduced in relationship to pore apertures containing only one type of organic linker.

**(6) Probe surface barriers that may exist using path sampling techniques.** It has been suggested that surface barriers exist on crystal surfaces of nanoporous materials.<sup>101</sup> It may be possible to build slab models and use the biased sampling molecular dynamics techniques discussed in Chapter 2 to examine the rates of diffusion from a gas phase into the first layer of a ZIF slab model. Computationally expensive methods such as transition path or interface sampling could be applied to tackle this problem since it features an ill-defined reaction coordinate.

**(7) Extend the lattice-diffusion model to examine the impact of defects in MOFs on diffusion.** Defects in MOF crystals are hypothesized to have a significant impact on their diffusion properties.<sup>277,291</sup> The lattice-diffusion model discussed in Chapter 5 could be altered to examine how the density and placement of point and extended defects influence diffusion.

The implementation of computational methods for studying diffusion as well as the merging of experimental and computational procedures to create models for mixed-linker materials has led to fundamental insights of how diffusion occurs in nanoporous materials. This information has extended the knowledge of diffusion processes and leads the community developing novel kinetic separation techniques closer to finding the proper nanoporous material for any separation of interest.

## APPENDIX A

### SUPPORTING INFORMATION FOR CHAPTER 2

#### A.1 Force Field Parameters

Intramolecular 1-2, 1-3, and 1-4 Lennard-Jones and Coulomb interactions were removed for all adsorbates. Molecular kinetic or van der Waals diameters combined with a nanoporous material's pore limiting diameter are useful metrics for deciding whether a kinetic separation is feasible. The diameters listed in Table A.1 were taken from Zhang et al.<sup>56</sup> and *Advances in Nanoporous Materials*<sup>423</sup>.

**Table A.1** Molecular diameters, molecular weights, 12-6 Lennard Jones potential parameters and atomic charges for small adsorbates.

Adsorbate	Kinetic Diameter (Å)	van der Waals Diameter (Å)	LJ Site	MW (g/mol)	$\sigma$ (Å)	$\epsilon$ (K)	$\epsilon$ (kcal/mol)	q (e)
Helium	2.6	2.66*	He	4.00	2.64	10.9	0.0217	0.0
N <sub>2</sub>	3.64	3.13*	2xN <sub>N2</sub>	14.01	3.32	36.43	0.0724	-0.482
			N <sub>COM</sub>	0.0	0.0	0.0	0.0	+0.964
O <sub>2</sub>	3.46	2.94*	2xO <sub>O2</sub>	16.00	49.0	3.02	0.0974	-0.113
			O <sub>COM</sub>	0.0	0.0	0.0	0.0	+0.226
H <sub>2</sub>	2.89	2.76*	2xH <sub>H2</sub>	1.01	2.958	36.7	0.0729	+0.468
			H <sub>COM</sub>	0.0	0.0	0.0	0.0	-0.936
CO <sub>2</sub>	3.3	3.24*	C <sub>CO2</sub>	12.01	2.757	28.129	0.0559	+0.6512
			2xO <sub>CO2</sub>	16.00	3.033	80.507	0.1600	-0.3256
SF <sub>6</sub>	5.1 <sup>a</sup>	-	SF <sub>6</sub>	146.06	5.13	222.10	0.4414	0.0
CH <sub>4</sub>	3.8	3.25*	CH <sub>4</sub>	16.04	3.730	148.0	0.2941	0.0
C <sub>2</sub> H <sub>4</sub>	3.9	3.59*	2xCH <sub>2</sub> =	14.03	3.675	85.0	0.1689	0.0
C <sub>2</sub> H <sub>6</sub>	-	3.72*	2xCH <sub>3</sub>	15.03	3.750	98.0	0.1947	0.0
C <sub>3</sub> H <sub>6</sub>	4.5	4.03*	CH <sub>2</sub>	14.03	3.675	85.0	0.1689	0.0
			CH	13.02	3.730	47.0	0.0934	0.0
			CH <sub>3</sub>	15.03	3.750	98.0	0.1947	0.0
C <sub>3</sub> H <sub>8</sub>	4.3	4.16*	2xCH <sub>3</sub>	15.03	3.750	98.0	0.1947	0.0
			CH <sub>2</sub>	14.03	3.950	46.0	0.0914	0.0
1-C <sub>4</sub> H <sub>8</sub>	4.5	4.41*	CH <sub>2</sub> =	14.03	3.675	85.0	0.1689	0.0
			CH	13.02	3.730	47.0	0.0934	0.0
			CH <sub>2</sub>	14.03	3.950	46.0	0.0914	0.0
			CH <sub>3</sub>	15.03	3.750	98.0	0.1947	0.0
n-C <sub>4</sub> H <sub>10</sub>	4.3	4.52*	2xCH <sub>3</sub>	15.03	3.750	98.0	0.1947	0.0
			2xCH <sub>2</sub>	14.03	3.950	46.0	0.0914	0.0
iso-C <sub>4</sub> H <sub>8</sub>	4.8*	4.42	CH <sub>2</sub> =	14.03	3.675	85.0	0.1689	0.0
			C	12.01	3.850	20.0	0.0397	0.0
			2xCH <sub>3</sub>	15.03	3.750	98.0	0.1947	0.0
iso-C <sub>4</sub> H <sub>10</sub>	5.0*	4.52	3xCH <sub>3</sub>	15.03	3.750	98.0	0.1947	0.0
			CH	13.02	4.680	10.0	0.0199	0.0

Note: "a" subscript refers to the use of the Lennard-Jones sigma parameter to describe the kinetic diameter; "\*" labeled diameters were used to construct Figure 2.4 in Chapter 2.



**Table A.2** Bonds, angles, and dihedrals for rigid and flexible adsorbates.

<b>Bond Stretch</b>					
$U_{stretching} = \sum k_r (r_{ij} - r_{ij}^0)^2$					
<b>i-j</b>	<b>k<sub>r</sub> (kcal/mol Å<sup>2</sup>)</b>	<b>r<sub>0</sub>(Å)</b>	<b>Notes</b>		
CH <sub>x</sub> -CH <sub>y</sub>	95.882	1.540	Single bond		
CH <sub>x</sub> =CH <sub>y</sub>	95.882	1.330	Double bond		
H <sub>H2</sub> -H <sub>COM</sub>	NA	0.371	Rigid		
O <sub>O2</sub> -O <sub>COM</sub>	NA	0.605	Rigid		
N <sub>N2</sub> -N <sub>COM</sub>	NA	0.550	Rigid		
C <sub>CO2</sub> -O <sub>CO2</sub>	NA	1.160	Rigid		

<b>Harmonic Bend</b>			
$U_{bending} = \sum k_{\theta} (\theta_{ijk} - \theta_{ijk}^0)^2$			
<b>i-j-k</b>	<b>k<sub>θ</sub> (kcal/mol rad<sup>2</sup>)</b>	<b>θ<sub>0</sub>(Å)</b>	<b>Notes</b>
CH <sub>x</sub> -(CH <sub>2</sub> )-CH <sub>y</sub>	62.099	114.0	Linear
CH <sub>x</sub> =(CH)-CH <sub>y</sub>	69.969	119.7	Linear/iso-C <sub>4</sub> H <sub>8</sub>
CH <sub>x</sub> -(CH <sub>2</sub> )-CH <sub>y</sub>	62.099	112.0	iso-C <sub>4</sub> H <sub>10</sub>

<b>Proper Torsions</b>					
$U_{proper} = k_0 + \frac{1}{2} k_1 [1 + \cos(\phi)] + \frac{1}{2} k_2 [1 - \cos(2\phi)] + \frac{1}{2} k_3 [1 + \cos(3\phi)]$					
<b>i-j-k-l</b>	<b>k<sub>0</sub> (kcal/mol)</b>	<b>k<sub>1</sub> (kcal/mol)</b>	<b>k<sub>2</sub> (kcal/mol)</b>	<b>k<sub>3</sub> (kcal/mol)</b>	<b>Notes</b>
CH <sub>x</sub> -(CH <sub>2</sub> )-(CH)=CH <sub>y</sub>	1.3682	0.3432	-0.4363	-1.1217	n-C <sub>4</sub> H <sub>8</sub>
CH <sub>x</sub> -(CH <sub>2</sub> )-(CH <sub>2</sub> )-CH <sub>y</sub>	0.0	1.4110	-0.2710	3.4150	n-C <sub>4</sub> H <sub>10</sub>

## A.2 Additional Simulation Methodology Details

Hopping rates were calculated with Equation A.1 below:

$$k_{A \rightarrow B}^{TST} = \frac{1}{\sqrt{2\beta\pi m}} \frac{\exp[-\beta F^\ddagger(\lambda)]}{\int_{state A} \exp[-\beta F(\lambda)] d\lambda} \quad (A.1)$$

where  $k$  is the hopping rate,  $m$  is the mass of the adsorbate,  $\beta$  is the inverse of the  $k_bT$ ,  $\lambda$  is the reaction coordinate, and  $F$  is the free energy. The free energy can be related to the probability of observing the adsorbate at any position along the reaction coordinate with Equation A.2:

$$\beta F(\lambda) = -\log \langle P(\lambda) \rangle \quad (A.2)$$

The dynamical correction was calculated using Equation A.3<sup>167</sup>:

$$f_d = \frac{\left\langle \dot{\lambda}(0) \delta[\lambda^\ddagger - \lambda(0)] H[\lambda(t) - \lambda^\ddagger] \right\rangle}{\left\langle \dot{\lambda}(0) \delta[\lambda^\ddagger - \lambda(0)] H[\lambda(0^+) - \lambda^\ddagger] \right\rangle} \quad (A.3)$$

where  $t$  is time,  $H$  represents the Heaviside step function, and  $\delta$  represents the Dirac delta function. The rate calculated from Equation A.1 is then corrected with the dynamical correction:

$$k_{A \rightarrow B}^{dcTST} = f_d k_{A \rightarrow B}^{TST} \quad (A.4)$$

The overall rate is then calculated by multiplying the hopping rate through one window by the total number of windows exiting any particular cage (e.g.  $n=8$  for ZIF-8):

$$k_{A \rightarrow EXIT}^{dcTST} = n_{windows} k_{A \rightarrow B}^{dcTST} \quad (\text{A.5})$$

As shown in Figure A.1, the transition state location was observed to change depending on the adsorbate. A TS location of 7.37 Å was used for isobutane, isobutene, and SF<sub>6</sub> where a TS location of 7.66 Å was used for the other 12 adsorbates when performing the dynamical correction calculations.

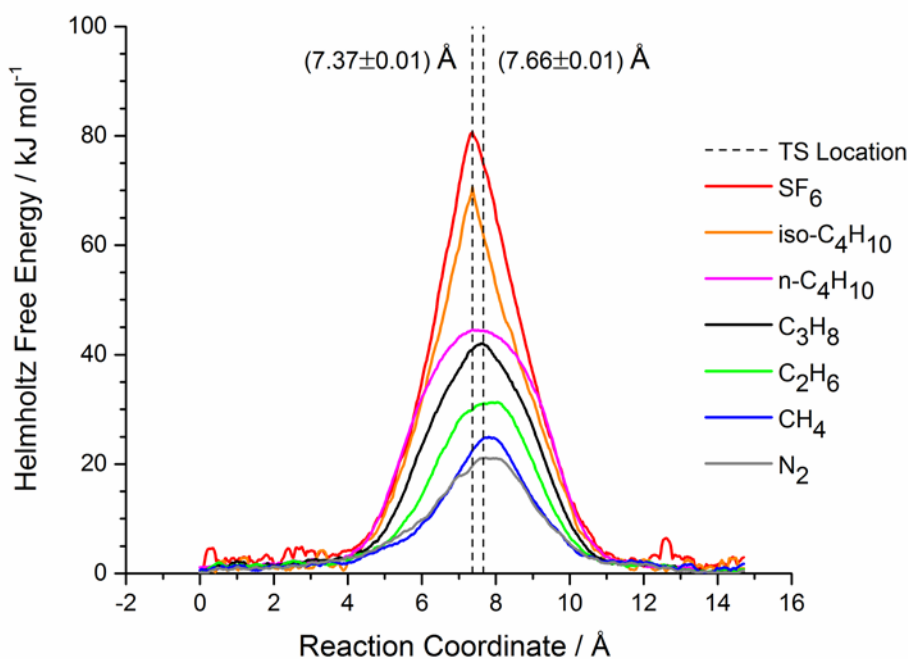


**Figure A.1** Free energy curves at infinite dilution and 308.15 K for a representative sample of adsorbates demonstrating a shifting TS location.

### A.3 Infinite Dilution Temperature Dependent Diffusivities

The Helmholtz free energy barrier can be decomposed into an entropic and potential contribution by measuring the free energy barrier at multiple temperatures and fitting the equation below:

$$\Delta A = \Delta U - T\Delta S \quad (\text{A.6})$$

where the intercept represents the potential contribution ( $\Delta U$ ) and the slope represents the entropic contribution ( $\Delta S$ ) to the hopping rate. This analysis has been performed for the 15 adsorbates and shown in Table A.3 as well as plotted in Figure A.2.

**Table A.3** Helmholtz free energy barrier (kJ/mol) at infinite dilution over the 0 to 150 °C temperature range.

Adsorbate	Temperature (°C)				$\Delta S$ (J mol <sup>-1</sup> K <sup>-1</sup> )	$\Delta U$ (kJ mol <sup>-1</sup> )	Linear Fit R <sup>2</sup>
	0	35	100	150			
He	9.3	10.9	12.4	12.9	23.8	3.2	0.93
H <sub>2</sub>	11.3	11.5	14.9	16.4	37.2	0.7	0.96
O <sub>2</sub>	14.3	16.4	18.9	21.1	43.9	2.6	0.99
N <sub>2</sub>	20.7	21.2	23.9	26.7	40.5	9.1	0.97
CO <sub>2</sub>	17.5	19.5	23.2	26.1	57.2	1.9	1.00
CH <sub>4</sub>	23.8	25.0	27.4	29.8	39.7	12.8	0.99
SF <sub>6</sub>	78.2	80.60	86.8	88.4	72.0	58.7	0.97
C <sub>2</sub> H <sub>4</sub> =	27.8	29.8	32.3	35.3	48.4	14.6	0.99
C <sub>2</sub> H <sub>6</sub>	29.6	31.3	34.9	37.4	52.9	15.1	1.00
C <sub>3</sub> H <sub>6</sub> =	35.0	36.2	40.0	43.1	55.1	19.6	0.99
C <sub>3</sub> H <sub>8</sub>	39.9	42.0	46.9	48.9	62.2	23.0	0.99
1-C <sub>4</sub> H <sub>8</sub> =	40.2	42.0	47.2	50.2	69.2	21.1	1.00
n-C <sub>4</sub> H <sub>10</sub>	42.3	44.5	49.0	53.1	72.0	22.4	1.00
iso-C <sub>4</sub> H <sub>8</sub> =	59.8	62.1	66.7	67.9	56.2	44.8	0.97
iso-C <sub>4</sub> H <sub>10</sub>	69.2	70.6	79.0	81.9	91.9	43.5	0.97

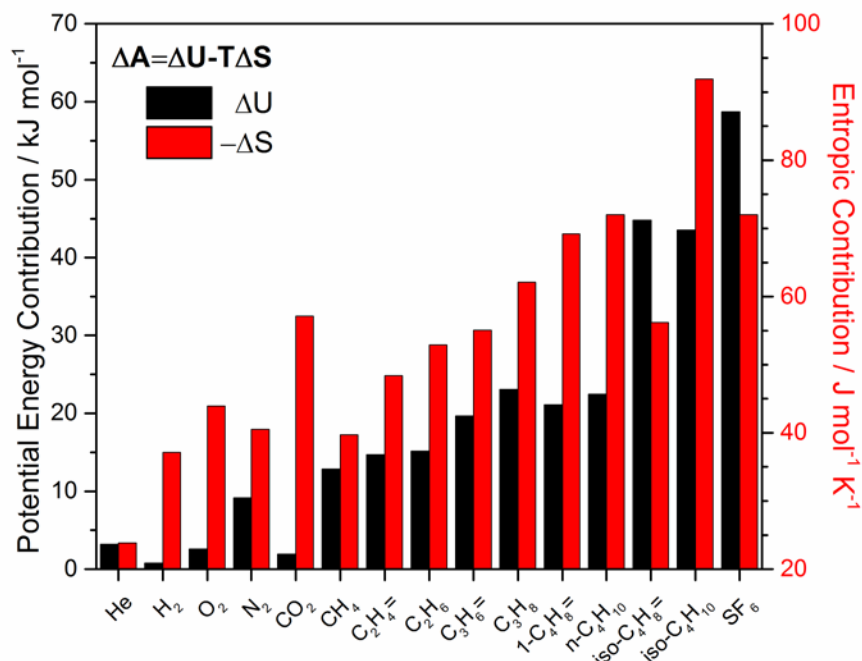


**Figure A.2** Potential and entropic contributions to the Helmholtz free energy barrier for small non-spherical adsorbates and hydrocarbons in flexible ZIF-8.

**Table A.4** Adsorbate transition state theory (TST) derived hopping rate (jumps/s) at infinite dilution over the 0 to 150 °C temperature range as calculated with Equation A.1.

Adsorbate	Temperature (°C)			
	0	35	100	150
He	9.47E+09	7.02E+09	9.88E+09	1.34E+10
H <sub>2</sub>	4.32E+09	7.52E+09	5.83E+09	6.92E+09
O <sub>2</sub>	3.68E+08	3.86E+08	4.93E+08	5.50E+08
N <sub>2</sub>	2.79E+07	5.35E+07	1.07E+08	1.30E+08
CO <sub>2</sub>	1.07E+08	1.44E+08	1.18E+08	1.49E+08
CH <sub>4</sub>	8.49E+06	1.69E+07	4.97E+07	1.10E+08
SF <sub>6</sub>	1.64E-04	3.54E-03	1.19E-01	2.24E+00
C <sub>2</sub> H <sub>4</sub> =	1.03E+06	2.24E+06	6.86E+06	1.13E+07
C <sub>2</sub> H <sub>6</sub>	4.50E+05	1.09E+06	2.81E+06	6.24E+06
C <sub>3</sub> H <sub>6</sub> =	4.34E+04	1.48E+05	5.10E+05	1.17E+06
C <sub>3</sub> H <sub>8</sub>	4.18E+03	1.44E+04	6.15E+04	1.98E+05
1-C <sub>4</sub> H <sub>8</sub> =	4.33E+03	1.24E+04	6.06E+04	1.59E+05
n-C <sub>4</sub> H <sub>10</sub>	1.23E+03	5.10E+03	2.66E+04	6.02E+04
iso-C <sub>4</sub> H <sub>8</sub> =	1.55E+00	7.69E+00	1.25E+02	1.03E+03
iso-C <sub>4</sub> H <sub>10</sub>	2.17E-02	1.91E-01	4.19E+00	3.58E+01

**Table A.5** Dynamical correction factors for adsorbates at infinite dilution over the 0 to 150 °C temperature range.

Adsorbate	Temperature (°C)			
	0	35	100	150
He	0.819	0.792	0.757	0.719
H <sub>2</sub>	0.825	0.826	0.812	0.808
O <sub>2</sub>	0.843	0.843	0.840	0.847
N <sub>2</sub>	0.742	0.764	0.771	0.773
CO <sub>2</sub>	0.617	0.632	0.666	0.658
CH <sub>4</sub>	0.548	0.570	0.615	0.670
SF <sub>6</sub>	0.364	0.364	0.230	0.473
C <sub>2</sub> H <sub>4</sub> =	0.696	0.723	0.738	0.746
C <sub>2</sub> H <sub>6</sub>	0.726	0.750	0.758	0.763
C <sub>3</sub> H <sub>6</sub> =	0.518	0.602	0.638	0.655
C <sub>3</sub> H <sub>8</sub>	0.310	0.331	0.420	0.459
1-C <sub>4</sub> H <sub>8</sub> =	0.403	0.412	0.453	0.499
n-C <sub>4</sub> H <sub>10</sub>	0.486	0.646	0.651	0.647
iso-C <sub>4</sub> H <sub>8</sub> =	0.006	0.027	0.043	0.044
iso-C <sub>4</sub> H <sub>10</sub>	0.028	0.025	0.045	0.074

The diffusion rates for C1-C4 hydrocarbons demonstrate Arrhenius behavior as a function of temperature, which were evaluated using Equation A.7 below:

$$\ln(D_{self,i}) = \frac{-E_d}{RT} + \ln(D_{o,i}) \quad (\text{A.7})$$

where  $E_d$  is the diffusion activation energy,  $D_o$  is the Arrhenius prefactor,  $R$  is the ideal gas constant, and  $T$  is temperature. Both the diffusion prefactor and activation energy barrier of diffusion for each molecule are reported in Table A.6 below. Poor linear fits are observed for smaller molecules where diffusion does not follow Arrhenius behavior. This is not surprising, since the activation energies for hopping of these species are small and the temperature range over which a straightforward TST description is accurate is also limited as a result. Table A.8 includes a compilation of experimentally derived diffusion coefficients for the adsorbates in this study.

**Table A.6** Infinite-dilution self-diffusion coefficients for small non-spherical molecules and light key hydrocarbons at 0°C, 35°C, 100°C, and 150°C derived from the dynamical correction factor and the TST hopping rate. The red region highlights the data pertaining to the C2/C3 separation.

Adsorbate	Temperature (°C)				$E_D$ (kJ mol <sup>-1</sup> )	$D_{o,i}$ (cm <sup>2</sup> s <sup>-1</sup> )	Linear Fit R <sup>2</sup>
	0	35	100	150			
He	2.24E-04	1.61E-04	2.16E-04	2.78E-04	1.72	4.01E-04	0.28
H <sub>2</sub>	1.03E-04	1.80E-04	1.37E-04	1.62E-04	1.86	2.78E-04	0.29
O <sub>2</sub>	8.97E-06	9.41E-06	1.20E-05	1.35E-05	2.73	2.88E-05	0.96
N <sub>2</sub>	6.00E-07	1.18E-06	2.38E-06	2.92E-06	10.23	5.88E-05	0.98
CO <sub>2</sub>	1.92E-06	2.63E-06	2.27E-06	2.84E-06	1.79	4.55E-06	0.52
CH <sub>4</sub>	1.35E-07	2.79E-07	8.84E-07	2.13E-06	17.50	2.77E-04	0.99
SF <sub>6</sub>	1.73E-18	3.73E-17	7.87E-16	3.06E-14	59.56	3.90E-07	0.98
C <sub>2</sub> H <sub>4</sub> =	2.07E-08	4.69E-08	1.47E-07	2.44E-07	<b>15.97</b>	2.38E-05	1.00
C <sub>2</sub> H <sub>6</sub>	9.46E-09	2.36E-08	6.16E-08	1.38E-07	<b>16.66</b>	1.48E-05	0.99
C <sub>3</sub> H <sub>6</sub> =	6.50E-10	2.58E-09	9.40E-09	2.21E-08	<b>22.09</b>	1.21E-05	0.99
C <sub>3</sub> H <sub>8</sub>	3.74E-11	1.38E-10	7.47E-10	2.63E-09	<b>26.81</b>	4.84E-06	1.00
1-C <sub>4</sub> H <sub>8</sub> =	5.05E-11	1.48E-10	7.95E-10	2.29E-09	24.42	2.21E-06	1.00
n-C <sub>4</sub> H <sub>10</sub>	1.73E-11	9.53E-11	5.01E-10	1.13E-09	26.52	2.40E-06	0.99
iso-C <sub>4</sub> H <sub>8</sub> =	2.54E-16	5.92E-15	1.54E-13	1.31E-12	53.73	5.69E-06	1.00
iso-C <sub>4</sub> H <sub>10</sub>	1.78E-17	1.36E-16	5.51E-15	7.66E-14	53.47	2.22E-07	0.99

The predicted 1.8 kJ/mol diffusion activation barrier for CO<sub>2</sub> was surprising and attributed to a possible deficiency in the force field and not in the dcTST simulation method. We first checked our dcTST predicted CO<sub>2</sub> diffusivities against those measured with standard NVT-MD simulations to see if the predicted activation energy from dcTST was incorrect. To check reproducibility, we also re-measured the self-diffusivities again using our dcTST method. The results at the four temperatures are reported in Table A.7 below.

**Table A.7** Self diffusion coefficients as a function of temperature measured with NVT-MD and NVT-dcTST simulations.

Temperature / °C	$D_{\text{self}}$ (cm <sup>2</sup> /s) / NVT-MD (1 molec./cage)	$D_{\text{self}}$ (cm <sup>2</sup> /s) / dcTST (1 molec./16 cages) – First Simulation	$D_{\text{self}}$ (cm <sup>2</sup> /s) / dcTST (1 molec./16 cages) – Second Simulation
0	$(3.5 \pm 0.3) \times 10^{-6}$	$1.9 \times 10^{-6}$	$1.9 \times 10^{-6}$
35	$(4.6 \pm 0.8) \times 10^{-6}$	$2.6 \times 10^{-6}$	$2.7 \times 10^{-6}$
100	$(7.6 \pm 0.7) \times 10^{-6}$	$2.3 \times 10^{-6}$	$2.2 \times 10^{-6}$
150	$(8.5 \pm 0.6) \times 10^{-6}$	$2.8 \times 10^{-6}$	$4.6 \times 10^{-6}$

NVT-MD at a loading of 1 molec./cage predicts a diffusion activation energy of 5.9 kJ/mol and NVT-dcTST (with only one CO<sub>2</sub> molecule per 16 cages) predicts of diffusion activation energy barrier of 1.8 kJ/mol. As observed, dynamically corrected TST does a poor job predicting the CO<sub>2</sub> diffusion over a large temperature because of the low activation energy barrier of diffusion. A clear indication of this is the large scatter of the CO<sub>2</sub> diffusion data especially at higher temperatures leading to poor Arrhenius equation fits. We also observe poor fits of He and H<sub>2</sub> diffusion coefficients to the Arrhenius equation which we expected since these small molecules are assumed to have very low activation energy barriers to diffusion in ZIF-8. Dubbeldam and coworkers<sup>148</sup> found that for low energy barriers ( $\sim 3\text{kT}$ ), his dcTST-derived diffusivities still matched those derived from EMD simulations. Our measured barriers for CO<sub>2</sub> using NVT-dcTST are  $\sim 1\text{kT}$  and using NVT-MD are  $\sim 2\text{kT}$  at 35 °C. It is not surprising that we see some deviation in the dcTST derived diffusivities from those measured with NVT-MD since our assumption of activated hopping is less applicable in this limit. Our results for CO<sub>2</sub> are also comparable to those measured by Zhang et al. whom, using the same force field<sup>174</sup>, reported an NPT-EMD derived CO<sub>2</sub> self-diffusivity of  $(7 \pm 2) \times 10^{-6} \text{cm}^2/\text{s}$  (298 K and infinite dilution)<sup>198</sup> where we report  $2.63 \times 10^{-6} \text{cm}^2/\text{s}$  (308 K and infinite dilution) using NVT-dcTST. Zhang et al. predicted a diffusion energy barrier of  $\sim 4\text{kT}$  at 25°C with histogram sampling using the same ZIF-8 and CO<sub>2</sub> FF parameters.<sup>198</sup> These results



would suggest that this is a limitation in the Zhang et al. force field to predict the correct temperature dependence of CO<sub>2</sub> diffusion, and not a deficiency of our dcTST simulation method.

To our knowledge, there have been no studies examining the ability of different FFs to predict the activation energy barrier of CO<sub>2</sub> in ZIF-8 or studies with experimental data on the temperature dependence of CO<sub>2</sub> diffusion in ZIF-8. It therefore, makes it difficult to comment on which pieces of the FF could be further improved to give more accurate results. In general the simulated diffusion coefficients can be different if a different force field was used. It happens that Zheng's ZIF-8 FF predicts a CO<sub>2</sub> diffusivity of  $2 \times 10^{-6} \text{cm}^2/\text{s}$  (1 molecule per cage) using NVT-EMD simulations<sup>133</sup>, which is in good agreement with our result. This agreement is not surprising since the Zheng and Zhang ZIF-8 force fields are very similar except for the N-Zn-N-C torsions added in the Zhang FF.

**Table A.8** Extant experimental diffusion coefficients for adsorbates in ZIF-8 used in Figure 2.4 of Chapter 2. Listed after the diffusion values respectively is the diffusion coefficient type, temperature, adsorbate loading, experimental technique, and literature reference.

Adsorbate	Diffusion Coefficient (cm <sup>2</sup> s <sup>-1</sup> )	Type	Temp. (°C)	Loadin g	Technique	Ref.
He	(6.5±5.2)E-4	Corrected	35	ID	M <sup>3</sup> P	Zhang
H <sub>2</sub>	2.0E-4	Corrected	35	ID	M <sup>3</sup> P	Zhang
O <sub>2</sub>	(1.0±0.5)E-5	Corrected	35	ID	M <sup>3</sup> P	Zhang
N <sub>2</sub>	(4.0±3.0)E-6	Corrected	35	ID	M <sup>3</sup> P	Zhang
CO <sub>2</sub>	(2.1±0.5)E-6	Corrected	35	ID	M <sup>3</sup> P	Zhang
CH <sub>4</sub>	(4.0±0.4)E-7	Corrected	35	ID	M <sup>3</sup> P	Zhang
C <sub>2</sub> H <sub>4</sub> =	(3.6±1.6)E-7	Corrected	35	ID	M <sup>3</sup> P	Zhang
C <sub>2</sub> H <sub>6</sub>	(8.8±2.7)E-8	Corrected	35	ID	M <sup>3</sup> P	Zhang
C <sub>3</sub> H <sub>6</sub> =	(1.6±0.3)E-8/ 2.9E-8	Corrected	35	ID	M <sup>3</sup> P / PURM	Zhang
C <sub>3</sub> H <sub>8</sub>	(1.7±0.8)E-10/ 2.0E-10	Corrected	35	ID	M <sup>3</sup> P/ PURM	Zhang
1-C <sub>4</sub> H <sub>8</sub> =	1.3E-11	Corrected	35	ID	PURM	Zhang
n-C <sub>4</sub> H <sub>10</sub>	5.7E-12	Corrected	35	ID	PURM	Zhang
	(1.5±0.3)E-10	Corrected	35	ID	PURM	Eum
iso-C <sub>4</sub> H <sub>8</sub> =	4.2E-16	Corrected	35	ID	PURM	Zhang
iso-C <sub>4</sub> H <sub>10</sub>	2.3E-18	Corrected	35	ID	PURM	Zhang
	(3±1)E-15	Corrected	35	ID	PURM	Eum

*ID=infinite dilution (low loading); M<sup>3</sup>P=mixed matrix membrane permeation with Maxwell model; PURM=piezometric uptake rate measurement.*

#### A.4 Adsorbate Induced Window Size Distributions

Figure A.3 shows the measured mean ZIF-8 window diameters (black dots, Table A.9 below) as a function of molecular diameter (same as reported in Table A.1 above). The empty ZIF-8 mean window size has been plotted as a blue dashed line. Viewing 1 and 2 (light blue dashed lines) standard deviations away from the mean empty ZIF-8 window size still does not encompass mean window sizes observed for molecular diameters above 4.0 Å.

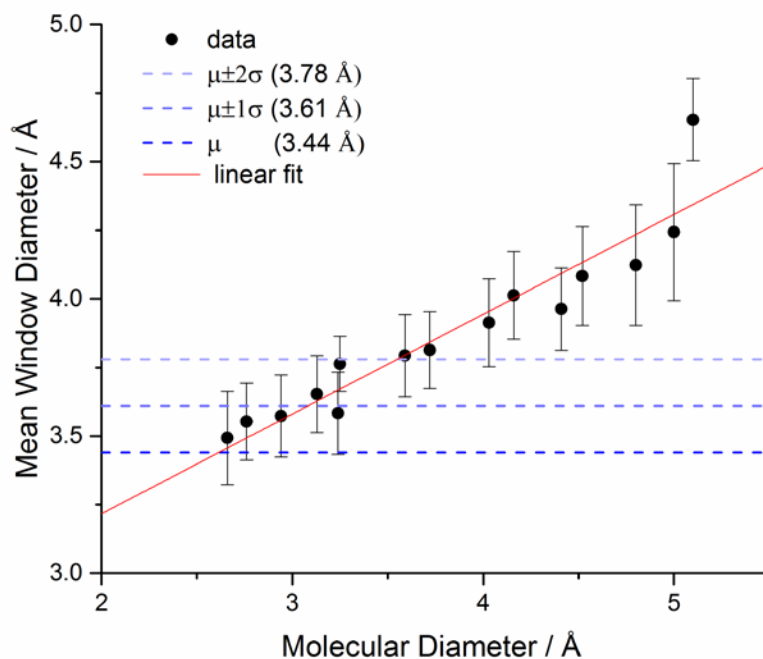


**Figure A.3** Mean ZIF-8 window diameter as a function of molecular diameter.

**Table A.9** Mean and standard deviation from a normal distribution fit to the window histograms at 308.15 K for all 15 adsorbates.

<b>Adsorbate</b>	<b>Sample Size</b>	<b>Mean [<math>\text{\AA}</math>]</b>	<b>Standard Deviation [<math>\text{\AA}</math>]</b>
<b>Empty</b>	2000	3.44	0.17
<b>He</b>	1000	3.49	0.17
<b>H<sub>2</sub></b>	1000	3.55	0.14
<b>O<sub>2</sub></b>	1000	3.57	0.15
<b>N<sub>2</sub></b>	1000	3.65	0.14
<b>CO<sub>2</sub></b>	1000	3.58	0.15
<b>CH<sub>4</sub></b>	992	3.75	0.11
<b>SF<sub>6</sub></b>	1000	4.65	0.15
<b>C<sub>2</sub>H<sub>4</sub>=</b>	1000	3.79	0.15
<b>C<sub>2</sub>H<sub>6</sub></b>	1000	3.81	0.14
<b>C<sub>3</sub>H<sub>6</sub>=</b>	1000	3.91	0.16
<b>C<sub>3</sub>H<sub>8</sub></b>	955	4.02	0.17
<b>1-C<sub>4</sub>H<sub>8</sub>=</b>	1000	3.96	0.15
<b>n-C<sub>4</sub>H<sub>10</sub></b>	1000	4.08	0.18
<b>iso-C<sub>4</sub>H<sub>8</sub>=</b>	1000	4.12	0.22
<b>iso-C<sub>4</sub>H<sub>10</sub></b>	1000	4.24	0.25

### A.5 Adsorption Isotherms and OFAST Calculations

The Peng Robinson equation of state as implemented in RASPA<sup>185</sup> was used to convert fugacities to pressures for the GCMC calculations. All adsorbate specific critical pressures, critical temperatures, and acentric factors were taken from the NIST database<sup>424</sup> and are reported in Table A.9. A total of 250,000 MC cycles was used for the initialization period and 100,000 MC cycles were used for the equilibration period. Both the LL and HL ZIF-8 structures were determined through a FF energy-minimization routine.

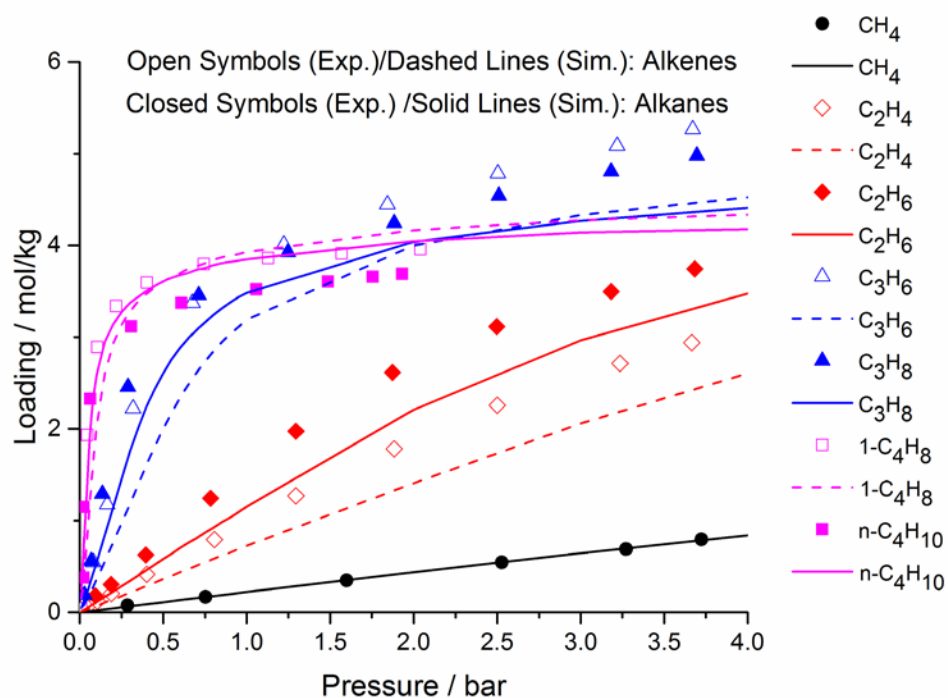


**Figure A.4** Adsorption isotherms of C1-C4 hydrocarbons in the rigid low-loading ZIF-8 structure at 308.15 K. Solid lines represent the GCMC results and the symbols (closed=paraffins and open=olefins) are taken from the experimental results of Zhang et al.<sup>56</sup>

Osmotic Framework Adsorbed Solution Theory (OFAST) can be generally used to predict the thermodynamically favorable adsorbent phase over a range of adsorbate loadings, and we refer the reader to manuscripts by Coudert et al. for calculation details.<sup>47,64,65,276,425,426</sup> In summary, the grand potential  $\Omega$  (normalized by the number of Zn atoms per simulation volume) is calculated under guest adsorption, and the structure with the lower grand potential is thermodynamically favored. We conclude from the OFAST calculations that the ZIF-8 HL is never seen under hydrocarbon loading at 35 °C. The difference in the grand potential between the HL and LL ZIF-8 structure under no hydrocarbon loading is positive and further increases for higher hydrocarbon loadings making the hydrocarbon-loaded HL ZIF-8 structure not thermodynamically favorable.

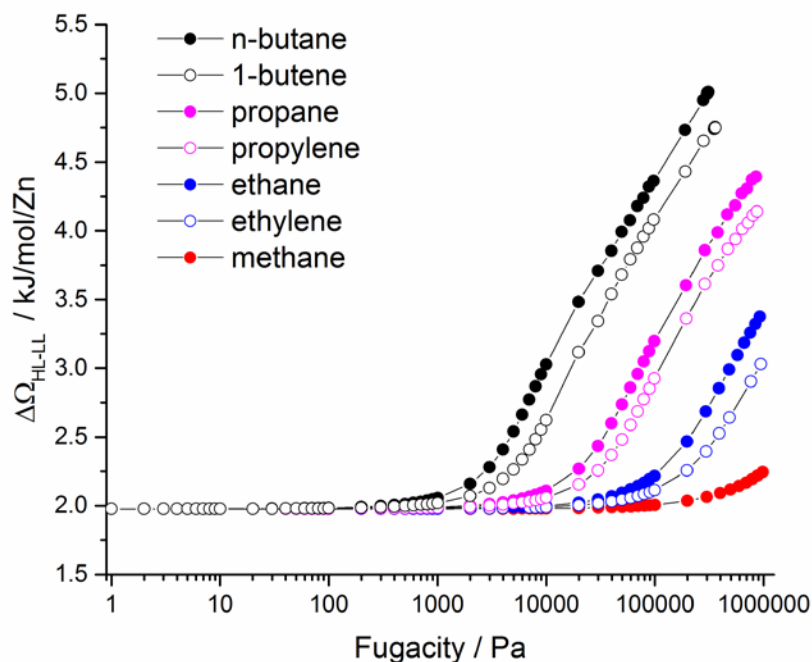


**Figure A.5** Difference in the grand potential between the high loading and low loading phases of ZIF-8 upon loading of C1-C4 hydrocarbons at 308.15 K.

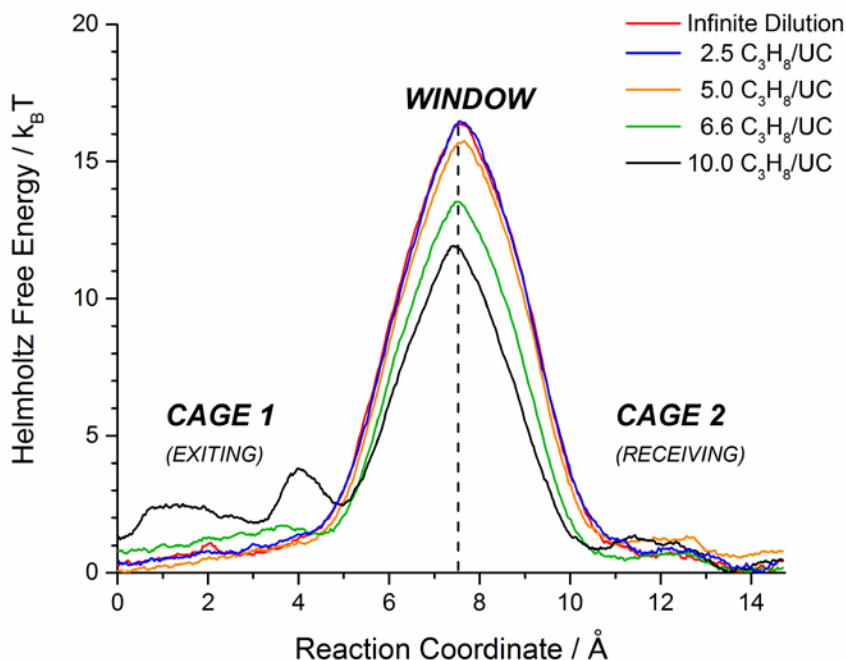
### A.6 Finite-Loading Diffusivities at 35 °C

For the gases, we calculated liquid loadings by assuming liquid densities. This approach was also applied to adsorbate vapors for consistency instead of taking the saturation loading from the GCMC derived isotherms. Liquid densities at the normal boiling points taken from the NIST database<sup>424</sup>. The liquid-like loading (number of molecules) per ZIF-8 unit cell was calculated using a void volume of 2363.3 Å<sup>3</sup> per unit cell where there are 2 cages per unit cell. The unit cell total volume is 4923.5 Å<sup>3</sup> with a helium void fraction of 0.48 and density of 924 kg/m<sup>3</sup> as calculated using RASPA. Liquid-like loadings have been rounded to the nearest whole molecule.

**Table A.10** Calculated liquid loadings for C1-C4 hydrocarbons. For CH<sub>4</sub>, the liquid loading of 22 molecules per cage, even though unphysical, was used instead of 19 molecules per cage to theoretically demonstrate the loading at which the diffusivity of methane began to decrease due to steric hindrance.

Adsorbate	MW [g/mol]	T <sub>c</sub> [K] / P <sub>c</sub> [Pa] / ω [-]	Normal T <sub>boil</sub> [K]	Liquid Density [kg/m <sup>3</sup> ]	Liquid Loading per UC	Liquid Loading per Cage
Methane	16.04	190.564 / 4599200 / 0.01142	111.00	423.30	38	19 (22)
Ethane	30.07	305.33 / 4871800 / 0.0993	184.55	543.97	26	13
Ethylene	28.05	282.35 / 5041800 / 0.0866	169.00	568.20	29	15
Propane	44.1	369.825 / 4247660 / 0.1524	231.03	580.93	19	10
Propylene	42.08	365.57 / 4664600 / 0.1408	225.46	609.05	21	11
Butane	58.12	425.125 / 3796000 / 0.201	273.00	601.26	15	8
1-Butene	56.11	419.60 / 4022602.5 / 0.208	266.80	625.63	16	8

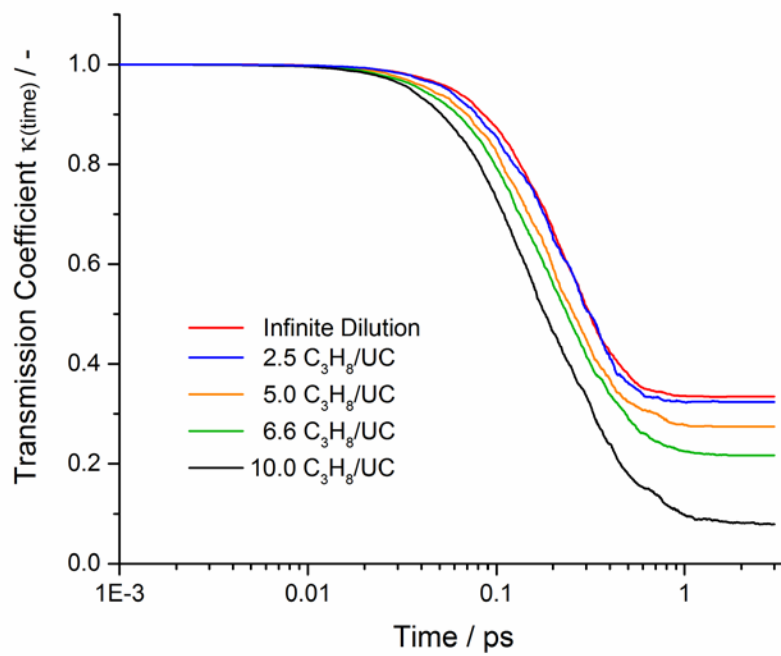
Figure A.6 shows representative free energy curves of propane under increased propane loading at 35 °C. Higher loadings yield lower free energy barriers and small barriers within the cage region begin to appear at very high loadings due to small pore blocking effects.



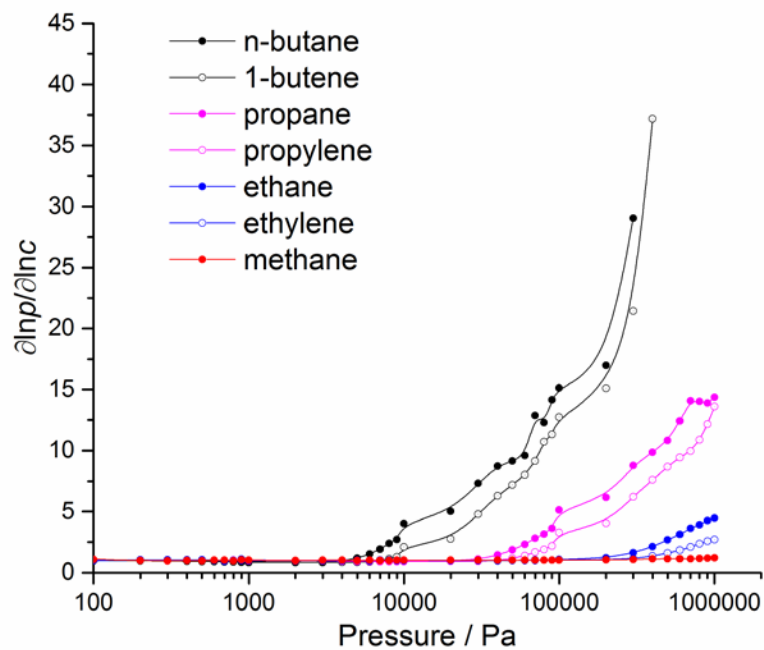
**Figure A.6** Propane free energy curves as a function of loading.

Figure A.7 shows representative transmission coefficient curves of propane under increased propane loading at 35 °C. Higher loadings yield decreased transmission coefficients through an increased probability of propane collisions. Figure A.8 shows the thermodynamic correction factors calculated using GCMC derived-adsorption data (Figure A.4). N-butane and 1-butene are stopped respectively at their bulk pressures that correspond to saturation. Table A.11 summarizes all the thermodynamic and kinetic data calculated at higher hydrocarbon loadings.





**Figure A.7** Propane transmission coefficient curves as a function of loading.



**Figure A.8** Hydrocarbon thermodynamic correction factors as a function of loading.

**Table A.11** Simulated free energies, dynamical correction factors, self-diffusivities, thermodynamic correction factors, and transport diffusivities as a function of adsorbate loading at 35 °C.

Pressure (bar)	Loading $\langle n / \text{cage} \rangle$	Free Energy Barrier (kJ mol <sup>-1</sup> )	$D_{self,i}^{TST}$ (cm <sup>2</sup> s <sup>-1</sup> )	DCF*	$D_{self,i}$ (cm <sup>2</sup> s <sup>-1</sup> )	TCF*	$D_{T,i}$ (cm <sup>2</sup> s <sup>-1</sup> )
<b>METHANE (CH<sub>4</sub>)</b>							
0.20	0.06	24.89±0.03	(4.99±0.17)E-07	0.58±0.01	(2.92±0.03)E-07	1.00	(2.93±0.03)E-07
10.00	2.69	25.19±0.30	(5.31±0.20)E-07	0.56±0.02	(2.97±0.21)E-07	1.19	(3.54±0.25)E-07
-	5.06	25.21±2.51	(5.84±2.26)E-07	0.55±0.02	(3.24±1.32)E-07	-	-
-	10.00	22.65±2.26	(1.58±0.79)E-06	0.53±0.01	(8.39±4.27)E-07	-	-
-	19.00	14.08±0.35	(3.32±0.59)E-05	0.19±0.07	(6.47±3.40)E-06	-	-
-	21.88	16.73±2.10	(2.19±1.01)E-05	0.11±0.01	(2.71±1.75)E-06	-	-
<b>ETHYLENE (C<sub>2</sub>H<sub>4</sub>)</b>							
0.06	0.06	29.86	5.39E-08	0.70	3.79E-08	1.00	3.79E-08
3.15	3.13	29.68	6.25E-08	0.65	4.04E-08	1.18	4.77E-08
10.00	6.13	27.71	1.19E-07	0.51	6.10E-08	2.69	1.64E-07
-	10.00	24.03	5.69E-07	0.42	2.40E-07	-	-
-	15.00	20.65	4.48E-06	0.11	4.84E-07	-	-
<b>ETHANE (C<sub>2</sub>H<sub>6</sub>)</b>							
0.04	0.06	31.60	3.64E-08	0.71	2.57E-08	1.00	2.57E-08
1.92	3.13	31.56	3.00E-08	0.66	1.99E-08	1.18	2.34E-08
10.00	6.63	28.96	7.11E-08	0.46	3.28E-08	4.45	1.46E-07
-	9.38	27.87	1.47E-07	0.43	6.29E-08	-	-
-	13.00	28.45	2.87E-07	0.19	5.55E-08	-	-
<b>PROPYLENE (C<sub>3</sub>H<sub>6</sub>)</b>							
1.25E-02	0.06	36.35	4.61E-09	0.48	2.22E-09	1.00	2.22E-09
0.52	3.13	35.48	5.69E-09	0.45	2.55E-09	1.20	3.07E-09
10.00	6.94	31.66	2.40E-08	0.43	1.04E-08	13.59	1.41E-07
-	8.75	26.77	1.72E-07	0.33	5.73E-08	-	-
-	11.00	25.09	2.89E-07	0.17	4.85E-08	-	-
<b>PROPANE (C<sub>3</sub>H<sub>8</sub>)</b>							
8.55E-03	0.06	41.95	4.47E-10	0.33	1.49E-10	1.00	1.49E-10
0.28	2.50	42.20	4.32E-10	0.32	1.40E-10	1.06	1.48E-10
1.05	5.00	40.36	8.99E-10	0.27	2.47E-10	5.17	1.28E-09
10.00	6.63	34.68	8.18E-09	0.22	1.77E-09	14.35	2.54E-08
-	10.00	30.56	6.05E-08	0.08	4.76E-09	-	-
<b>1-BUTYLENE (1-C<sub>4</sub>H<sub>8</sub>)</b>							
2.79E-03	0.06	42.39	3.57E-10	0.26	9.40E-11	1.00	9.40E-11
5.75E-02	1.88	42.51	3.83E-10	0.21	8.13E-11	0.88	7.12E-11
0.15	3.75	41.35	5.35E-10	0.21	1.10E-10	2.45	2.69E-10
3.42	6.00	36.52	3.39E-09	0.10	3.42E-10	28.13	9.61E-09
-	8.00	30.56	3.35E-08	0.12	4.06E-09	-	-
<b>BUTANE (n-C<sub>4</sub>H<sub>10</sub>)</b>							
1.78E-03	0.06	44.22±0.95	(1.66±0.31)E-10	0.53±0.01	(8.85±1.48)E-11	1.00	(8.85±1.48)E-11
3.53E-02	1.88	45.48±0.16	(9.26±0.39)E-11	0.44±0.01	(4.11±0.11)E-11	0.90	(3.69±0.10)E-11
9.28E-02	3.75	42.25±0.60	(3.54±0.64)E-10	0.34±0.02	(1.22±0.28)E-10	3.08	(3.74±0.86)E-10
2.86	5.81	35.60±1.00	(4.13±0.71)E-09	0.15±0.01	(6.09±0.98)E-10	27.39	(1.67±0.27)E-08
-	8.00	32.30±1.10	(2.58±1.35)E-08	0.04±0.01	(9.20±1.54)E-10	-	-

\*DCF= Dynamical correction factor, TCF=Thermodynamic correction factor

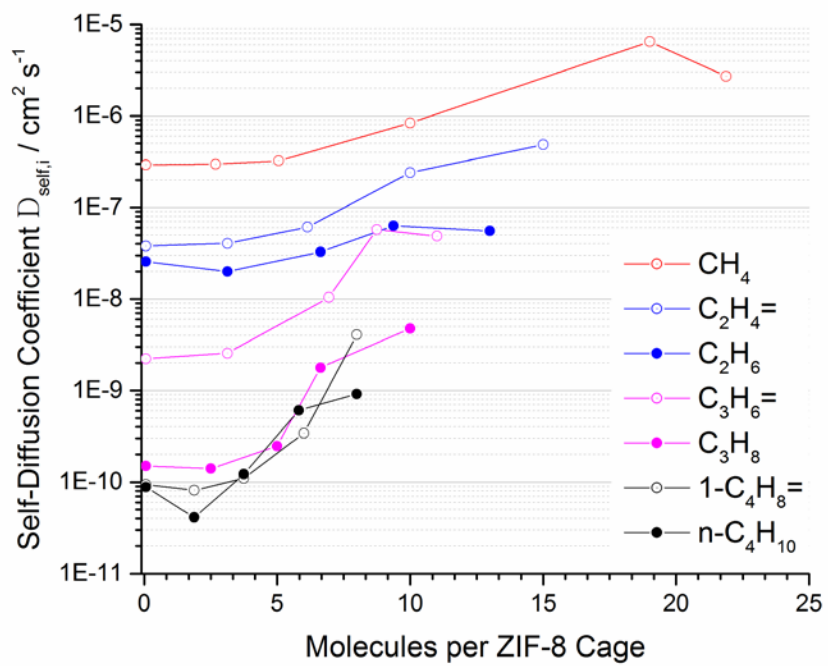


**Figure A.9** Short alkane and alkene transport diffusion coefficients as a function of molecules per cage in ZIF-8 at 35°C.

### A.7 Comparison to Extant Experimental Measurements of Diffusion

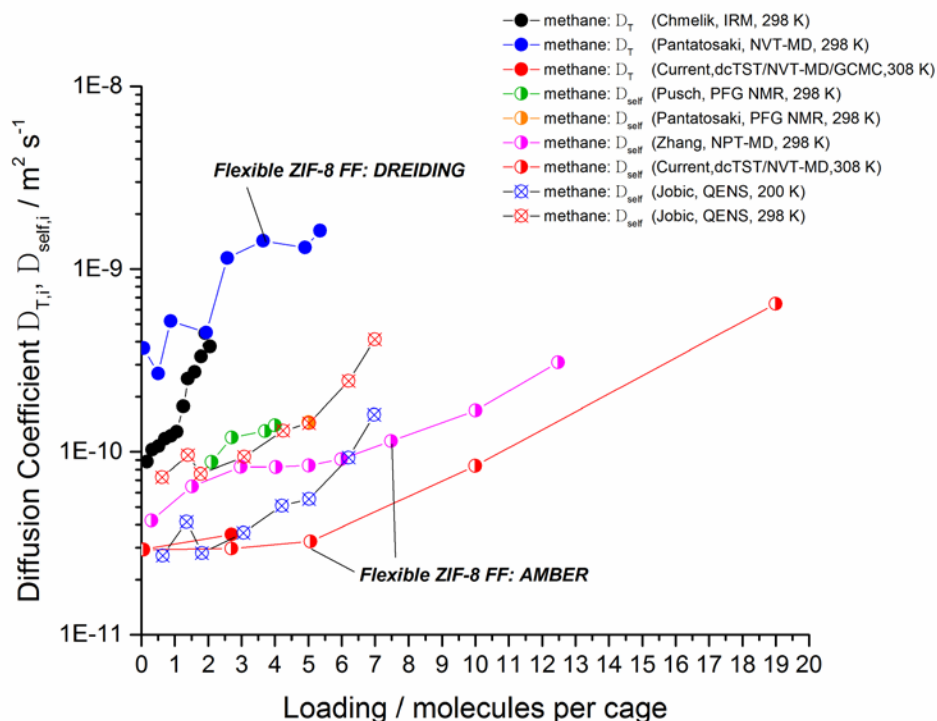


**Figure A.10** Comparison of both experimental and simulated methane diffusivities as a function of loading in ZIF-8. We have also included two other simulation studies: NVT-MD calculations at 298 K by Pantatosaki et al.<sup>196</sup> (transport diffusivities, solid blue circles) and NPT-MD calculations at 298 K by Zhang et al.<sup>198</sup> (self-diffusivities, half-filled purple circles).

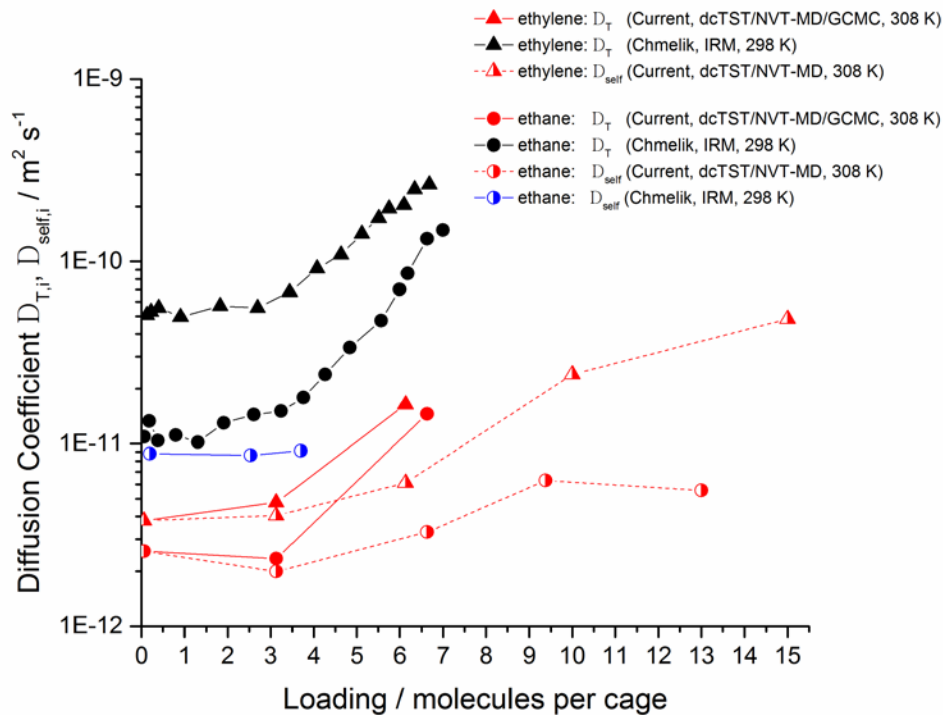


**Figure A.11** Comparison of both experimental and simulated ethylene and ethane diffusivities as a function of loading in ZIF-8.

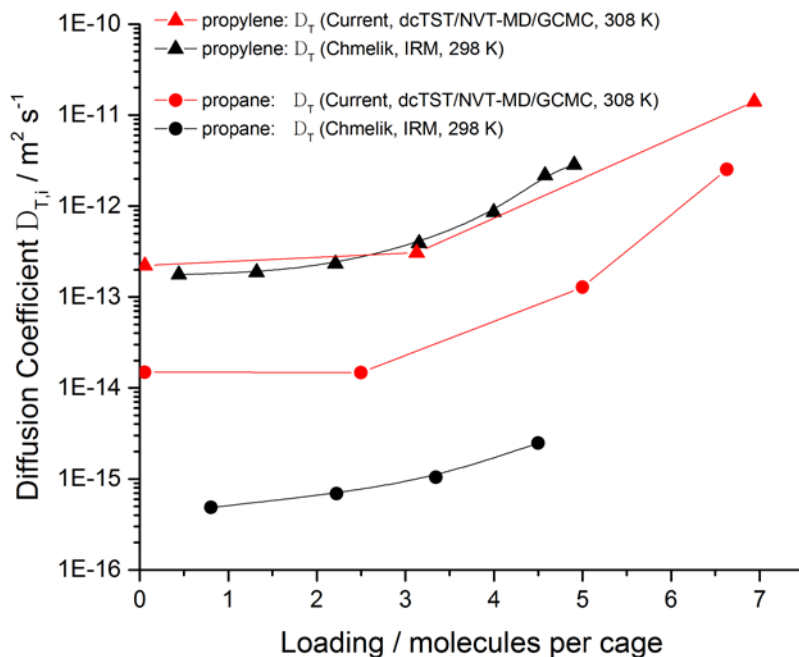


**Figure A.12** Comparison of both experimental and simulated propylene and propane diffusivities as a function of loading in ZIF-8.

### A.8 ZIF-8 Membrane Flux Calculations

Fick's law states:

$$J = -D_{T,i} \frac{\partial c}{\partial x} = \text{constant} \quad (\text{A.8})$$

A separation of variables and integration of Fick's Law yields:

$$J = \frac{1}{l} \int_{C_{low}}^{C_{high}} D_{T,i} dc \quad (\text{A.9})$$

Permeance is defined as the flux across the membrane divided by the pressure drop:

$$\frac{P_i}{l} = \frac{J}{\Delta P} = \frac{1}{l \Delta P} \int_{C_{low}}^{C_{high}} D_{T,i}(c) dc \quad (\text{A.10})$$

Permeance can be multiplied by the membrane thickness to yield permeability. Permeability is difficult to quantify since it is difficult to measure the membrane thickness. It can be re-written as the product of the effective membrane transport diffusivity and the sorption coefficient:

$$P_i = \frac{J}{\Delta P / l} = \frac{1}{\Delta P} \int_{C_{low}}^{C_{high}} D_{T,i}(c) dc = D_{T,i,eff} \left[ \frac{m^2}{s} \right] S \left[ \frac{mol}{m \cdot s \cdot Pa} \right] \quad (\text{A.11})$$

The effective membrane diffusivity is defined as:

$$D_{T,i,eff} = \frac{1}{C_{high} - C_{low}} \int_{C_{low}}^{C_{high}} D_{T,i}(c) dc \quad (\text{A.12})$$

The sorption coefficient is defined as:

$$S = (C_{high} - C_{low}) / (P_{high} - P_{low}) \quad (\text{A.13})$$

To calculate the permeability, the concentration dependence of the transport diffusivity was determined by linearly interpolating between the common logarithm of the transport diffusivities as a function of average loading. The integral in Equation A.11 was numerically calculated using the trapezoid rule with the concentration limits corresponding to the desired pressure drop. The relationship between the pressure and concentration was numerically calculated from linear interpolation of the GCMC-derived isotherm.

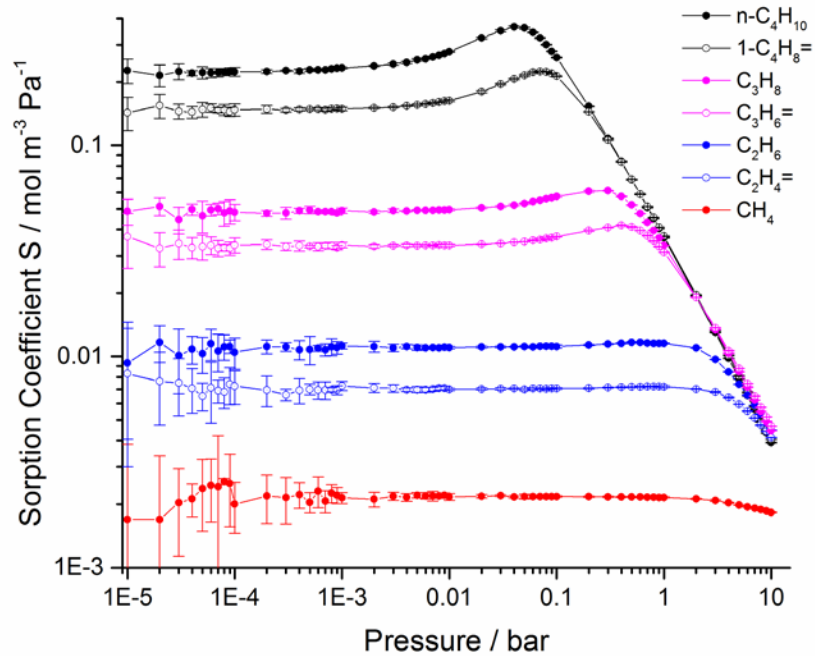


**Figure A.13** Hydrocarbon sorption coefficients as a function of bulk pressure.

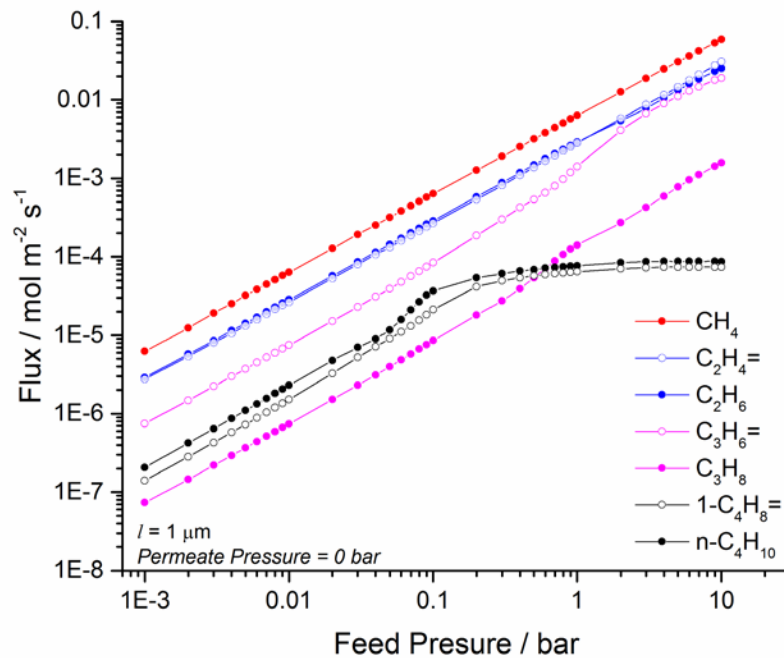


**Figure A.14** Hydrocarbon fluxes through an idealized ZIF-8 membrane as a function of feed pressure with a transmembrane pressure drop equal to the feed pressure.

## APPENDIX B

### SUPPORTING INFORMATION FOR CHAPTER 3

#### B.1 Unfunctionalized Imidazolate (Im) ZIF Intramolecular Force Field Parameters

Table B.1 below contains all the intramolecular force field functions and parameters implemented for unfunctionalized ZIFs. Green (red) shaded regions indicated which degrees of freedom are (not) included in the intraZIF-FF. Comparison of spring constants between the AMBER and intraZIF FFs are also included.

**Table B.1** Bonded force field parameters for ZIFs with unfunctionalized imidazolate linkers. Functional forms, spring constants, and equilibrium geometry parameters are listed.

BOND STRETCHES (6 types)			
Type I-J (N*)	Harmonic: $U_{stretching} = \sum k_r (r_{ij} - r_{ij}^0)^2$		$r_{ij}^0 / \text{\AA}$
	intraZIF $k_r / \text{kcal mol}^{-1} \text{\AA}^{-2}$	AMBER $k_r / \text{kcal mol}^{-1} \text{\AA}^{-2}$	
C <sub>1</sub> -H <sub>1</sub> (1)	373.06	367.0	1.09
C <sub>1</sub> -N (2)	362.69	488.0	1.35
C <sub>2</sub> -N (2)	299.01	410.0	1.38
C <sub>2</sub> -H <sub>2</sub> (2)	381.32	367.0	1.09
C <sub>2</sub> -C <sub>2</sub> (1)	389.86	518.0	1.38
Zn-N (2)	70.67 <sup>H</sup>	78.5 <sup>A,133</sup> , 86.0 <sup>A,174</sup>	2.00
Type I-J (N*)	Morse: $U_{Zn-N} = \sum D_r (1 - e^{-\alpha(r_{ij} - r_{ij}^0)})^2$		$r_{ij}^0 / \text{\AA}$
	$D_r / \text{kcal mol}^{-1}$	$\alpha / \text{\AA}^{-1}$	
Zn-N (2)	26.08	2.09	2.00
ANGLE BENDING (9 types)			



Table B.1. (continued)

Harmonic: $U_{bend} = \sum k_{\theta} (\theta_{ijk} - \theta_{ijk}^0)^2$			
	intraZIF-FF	AMBER	
Type I-J-K ( $N^*$ )	$k_{\theta} / \text{kcal mol}^{-1} \text{rad}^{-2}$	$k_{\theta} / \text{kcal mol}^{-1} \text{rad}^{-2}$	$\theta_{ijk}^0 / ^{\circ} \text{degrees}$
C <sub>2</sub> -C <sub>2</sub> -H <sub>2</sub> (2)	65.15	50.0	130.66
N-C <sub>1</sub> -N (1)	104.91	70.0	112.49
N-C <sub>2</sub> -C <sub>2</sub> (2)	121.85	70.0	108.18
N-C <sub>2</sub> -H <sub>2</sub> (2)	63.42	50.0	121.16
C <sub>1</sub> -N-C <sub>2</sub> (2)	105.54	70.0	105.58
H <sub>1</sub> -C <sub>1</sub> -N (2)	52.84	50.0	123.75
C <sub>1</sub> -N-Zn (2)	38.65 <sup>H</sup> /18.28 <sup>P</sup>	50.0 <sup>A</sup>	127.25
C <sub>2</sub> -N-Zn (2)	39.84 <sup>H</sup> /18.84 <sup>P</sup>	35.0 <sup>A</sup>	127.17
N-Zn-N (3)	33.39 <sup>H</sup> /18.20 <sup>P</sup>	10.5 <sup>A</sup>	109.43

## DIHEDRAL ANGLES (13 types)

Cosine: $U_{proper} = \sum k_{\phi} [1 + \cos(m \phi_{ijkl} - \phi_{ijkl}^0)]$				
	intraZIF	AMBER		
Type I-J-K-L ( $N^*$ )	$k_{\phi} / \text{kcal mol}^{-1}$	$k_{\phi} / \text{kcal mol}^{-1}$	$\phi_{ijkl}^0 / ^{\circ} \text{degrees}$	$m / -$
N-C <sub>1</sub> -N-C <sub>2</sub> (2)	3.97±0.56	4.80	180.0	2
H <sub>1</sub> -C <sub>1</sub> -N-C <sub>2</sub> (2)	3.61±0.98	4.80	180.0	2
C <sub>2</sub> -C <sub>2</sub> -N-C <sub>1</sub> (2)	2.72±1.24	4.80	180.0	2
H <sub>2</sub> -C <sub>2</sub> -N-C <sub>1</sub> (2)	3.43±0.75	4.80	180.0	2
N-C <sub>2</sub> -C <sub>2</sub> -H <sub>2</sub> (2)	2.61±0.71	4.00	180.0	2
N-C <sub>2</sub> -C <sub>2</sub> -N (1)	1.85±1.74	4.00	180.0	2
H <sub>2</sub> -C <sub>2</sub> -C <sub>2</sub> -H <sub>2</sub> (1)	0.00	4.00	180.0	2
H <sub>1</sub> -C <sub>1</sub> -N-Zn (2)	0.00	NA	180.0	2
H <sub>2</sub> -C <sub>2</sub> -N-Zn (2)	0.00	NA	180.0	2
N-C <sub>1</sub> -N-Zn (2)	0.00	NA	180.0	2
C <sub>2</sub> -C <sub>2</sub> -N-Zn (2)	0.00	NA	180.0	2

$$\text{Fourier series: } U_{proper} = \sum_{n=1}^6 k_{\phi,n} [1 + \cos(m_n \phi_{ijkl} - d_n)]$$

Type I-J-K-L ( $N^*$ )	$k_{\phi} / \text{kcal mol}^{-1}$	$d_n / ^{\circ} \text{degrees}$	$m / -$
C <sub>1</sub> -N-Zn-N (6)	3.02±1.48, 2.26±1.42, 0.08±0.05	0.0, 180.0, 0.0	1, 2, 3
C <sub>2</sub> -N-Zn-N (6)	3.39±0.74, 1.92±0.79, 0.02±0.02	0.0, 0.0, 0.0	1, 2, 3

## IMPROPER ANGLES (3 types)

Cosine: $U_{improper} = \sum k_{\xi} [1 + \cos(m \xi_{ijkl} - \xi_{ijkl}^0)]$				
	intraZIF	AMBER		
Type I-J-K-L ( $N^*$ )	$k_{\xi} / \text{kcal mol}^{-1}$	$k_{\xi} / \text{kcal mol}^{-1}$	$\xi_{ijkl}^0 / ^{\circ} \text{degrees}$	$m / -$
N-H <sub>2</sub> -C <sub>2</sub> <sup>P</sup> -C <sub>2</sub> (2)	0.00	1.1	180.0	2
H <sub>1</sub> -N-C <sub>1</sub> <sup>P</sup> -N (1)	0.00	1.1	180.0	2
C <sub>1</sub> -C <sub>2</sub> -N <sup>P</sup> -Zn (2)	0.00	0.00	180.0	2

Improper term I-J-K-L refers to the angle between planes I-J-K and J-K-L, with J-K axis of rotation and K being the central/primary atom (noted by subscript <sup>P</sup>);  $N^*$ =number of bonds, angles, or dihedrals in the linker-metal complex. Superscripts H, P, and A refer to Hessian matrix, potential energy scan, or AMBER in reference to where certain spring constants were obtained.

Figures B.1a, B.2a, and B.3a show the single point potential energy scans for the Zn-N bond, the N-Zn-C<sub>1,2</sub> angles, and the N-Zn-N angle along with harmonic and Morse potential fits. Figures B.1b, B.2b, and B.3b show the contribution of the electrostatic energy for “fixed” and “varying” charges. “Fixed charges” refer to using only one set of charges as derived from the DDEC<sup>260</sup> method on the minimum energy cluster. “Varying charges” refer to the recalculation of charges for each snapshot along the scan using the DDEC method. Figure B.4 shows the low energy region of the BOMD simulations on the Im cluster.

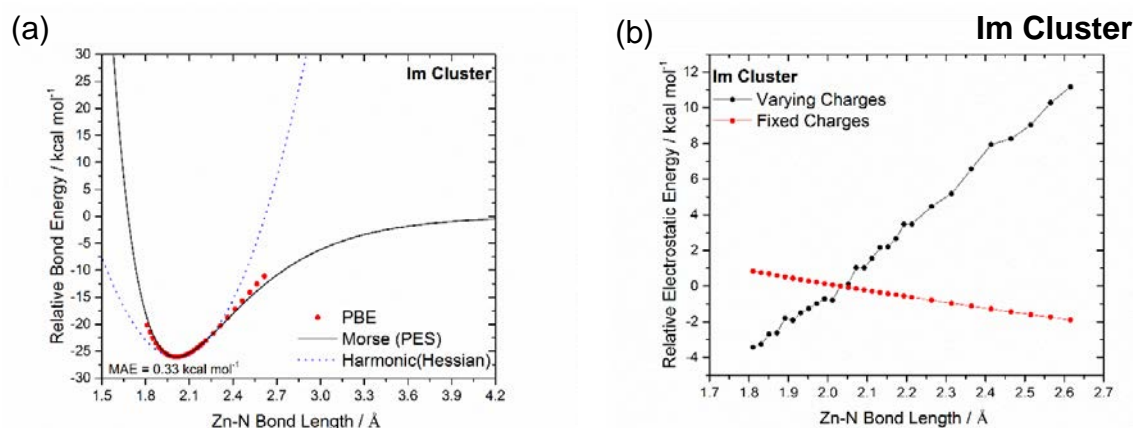


**Figure B.1** (a) Morse potentials fit (solid black line) to potential energy scans (red dots) along the Zn-N bond. The harmonic potential with the spring constant from the Seminario method is shown for comparison (dashed blue line). The mean absolute error (MAE) of the Morse fit is also reported. (b) Relative coulombic energy for the Zn-N potential energy scans.

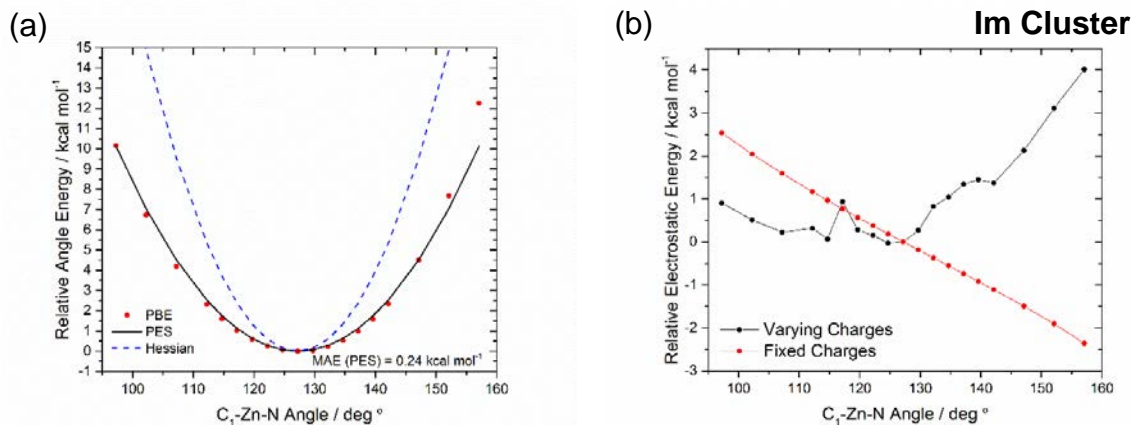


**Figure B.2** Harmonic angle potential fit using the spring constant from the Seminario method (dashed blue line) and the direct PES fit (solid black line) to PES scans (red dots) of the C<sub>1,2</sub>-Zn-N angles. The mean absolute error of the PES fit is also reported. **(b)** Relative coulombic energy for the C<sub>1,2</sub>-Zn-N potential energy scans.

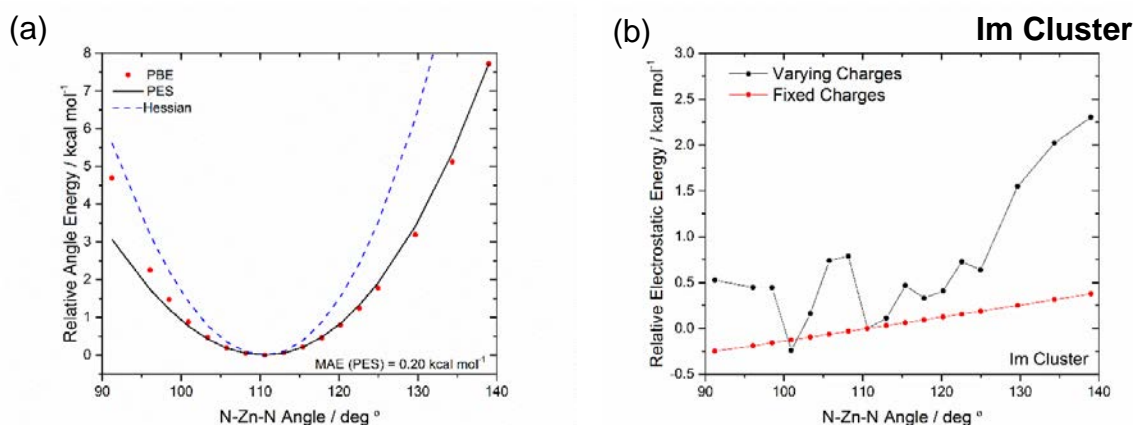


**Figure B.3** (a) Harmonic angle potential fit using the spring constant from the Seminario method (dashed blue line) and the direct PES fit (solid black line) to PES scans (red dots) of the N-Zn-N angles. The mean absolute error of the PES fit is also reported. **(b)** Relative coulombic energy for the N-Zn-N potential energy scans.

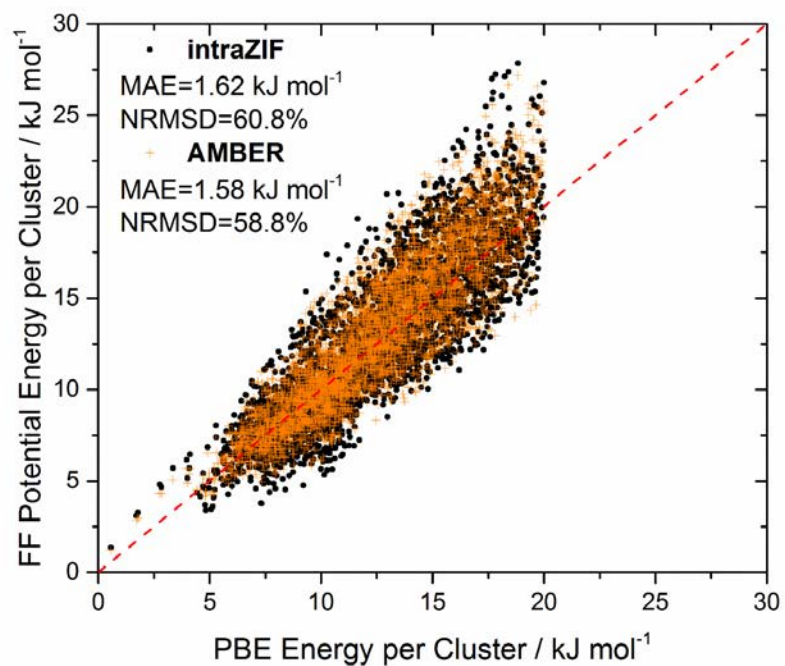


**Figure B.4** Relative energy comparisons between PBE and (a) the intraZIF-FF (black circles) including Fourier dihedrals from the potential energy fitting as well as (b) the AMBER-FF (orange crosses) for the low energy region ( $<20 \text{ kJ mol}^{-1}$ ).

## B.2 2-Methylimidazole (mIm) ZIF Intramolecular Force Field Parameters

Table B.2 below contains all the intramolecular force field functions and parameters implemented for ZIFs with 2-methylimidazole linkers. Green (red) shaded regions indicted which degrees of freedom are (not) included in the intraZIF-FF. Comparison of spring constants between the AMBER and intraZIF FFs are also included.

**Table B.2** Bonded force field parameters for ZIFs with 2-methylimidazole linkers. Functional forms, spring constants, and equilibrium geometry parameters are listed.

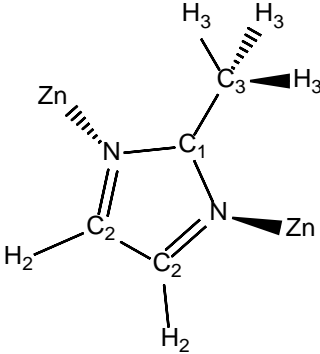
			
<b>BOND STRETCHES (7 types)</b>			
<b>Harmonic:</b> $U_{stretching} = \sum k_r (r_{ij} - r_{ij}^0)^2$			
	<b>intraZIF</b>	<b>AMBER</b>	
Type I-J (N*)	$k_r / \text{kcal mol}^{-1} \text{\AA}^{-2}$	$k_r / \text{kcal mol}^{-1} \text{\AA}^{-2}$	$r_{ij}^0 / \text{\AA}$
C <sub>3</sub> -H <sub>3</sub> (3)	332.52	340.0	1.10
C <sub>1</sub> -C <sub>3</sub> (1)	248.76	346.543/317.0	1.49
C <sub>1</sub> -N (2)	336.56	488.0/535.55	1.35
C <sub>2</sub> -N (2)	298.63	410.0/440.21	1.38
C <sub>2</sub> -H <sub>2</sub> (2)	380.11	367.0	1.09
C <sub>2</sub> -C <sub>2</sub> (1)	402.91	540.249/518.0	1.38
Zn-N (2)	67.16 <sup>H</sup>	78.5 <sup>A,133</sup> , 86.0 <sup>A,174</sup>	1.99
<b>Morse:</b> $U_{Zn-N} = \sum D_r (1 - e^{-\alpha(r_{ij} - r_{ij}^0)})^2$			
Type I-J (N*)	$D_r / \text{kcal mol}^{-1}$	$\alpha / \text{\AA}^{-1}$	$r_{ij}^0 / \text{\AA}$
Zn-N (2)	27.13	2.01	1.99
<b>ANGLE BENDING (11 types)</b>			
<b>Harmonic:</b> $U_{bend} = \sum k_\theta (\theta_{ijk} - \theta_{ijk}^0)^2$			
	<b>intraZIF</b>	<b>AMBER</b>	
Type I-J-K (N*)	$k_\theta / \text{kcal mol}^{-1} \text{rad}^{-2}$	$k_\theta / \text{kcal mol}^{-1} \text{rad}^{-2}$	$\theta_{ijk}^0 / ^\circ \text{degrees}$
H <sub>3</sub> -C <sub>3</sub> -H <sub>3</sub> (3)	35.88	35.0	107.95
H <sub>3</sub> -C <sub>3</sub> -C <sub>1</sub> (3)	54.59	50.0	110.95

Table B.2 (continued)

H <sub>2</sub> -C <sub>2</sub> -C <sub>2</sub> (2)	64.14	50.0	130.95
H <sub>2</sub> -C <sub>2</sub> -N (2)	63.06	50.0	121.23
C <sub>2</sub> -N-C <sub>1</sub> (2)	112.17	70.0	106.27
C <sub>2</sub> -C <sub>2</sub> -N (2)	117.58	70.0	108.04
N-C <sub>1</sub> -N (1)	111.76	70.0	111.38
N-C <sub>1</sub> -C <sub>3</sub> (2)	106.35	70.0	124.28
Zn-N-C <sub>1</sub> (2)	44.58 <sup>H</sup> /18.28 <sup>P</sup>	50.0	126.91
Zn-N-C <sub>2</sub> (2)	44.45 <sup>H</sup> /18.84 <sup>P</sup>	35.0	126.81
N-Zn-N (3)	36.62 <sup>H</sup> /18.20 <sup>P</sup>	10.5	109.45

## DIHEDRAL ANGLES (14 types)

Cosine: $U_{proper} = \sum k_{\phi} [1 + \cos(m \phi_{ijkl} - \phi_{ijkl}^0)]$					
	intraZIF	AMBER			
Type I-J-K-L (N*)	$k_{\phi} / \text{kcal mol}^{-1}$	$k_{\phi} / \text{kcal mol}^{-1}$	$\phi_{ijkl}^0 / ^{\circ} \text{degrees}$	$m / -$	
C <sub>3</sub> -C <sub>1</sub> -N-C <sub>2</sub> (2)	1.48	4.15	180.0	2	
N-C <sub>1</sub> -N-C <sub>2</sub> (2)	3.97	4.80	180.0	2	
C <sub>2</sub> -C <sub>2</sub> -N-C <sub>1</sub> (2)	2.72	4.80	180.0	2	
H <sub>2</sub> -C <sub>2</sub> -N-C <sub>1</sub> (2)	3.43	4.80	180.0	2	
N-C <sub>2</sub> -C <sub>2</sub> -H <sub>2</sub> (2)	2.61	4.00	180.0	2	
N-C <sub>2</sub> -C <sub>2</sub> -N (1)	1.85	4.00	180.0	2	
H <sub>2</sub> -C <sub>2</sub> -C <sub>2</sub> -H <sub>2</sub> (1)	0.00	4.00	180.0	2	
N-C <sub>1</sub> -C <sub>3</sub> -H <sub>3</sub> (6)	0.00	NA (free rotation of methyl-group)	180.0	2	
C <sub>3</sub> -C <sub>1</sub> -N-Zn (2)	0.00	NA	180.0	2	
N-C <sub>1</sub> -N-Zn (2)	0.00	NA	180.0	2	
C <sub>2</sub> -C <sub>2</sub> -N-Zn (2)	0.00	NA	180.0	2	
H <sub>2</sub> -C <sub>2</sub> -N-Zn (2)	0.00	NA	180.0	2	

$$\text{Fourier series: } U_{proper} = \sum_{n=1}^6 k_{\phi,n} [1 + \cos(m_n \phi_{ijkl} - d_n)]$$

Type I-J-K-L (N*)	$k_{\phi} / \text{kcal mol}^{-1}$	$d_n / ^{\circ} \text{degrees}$	$m / -$
C <sub>1</sub> -N-Zn-N (6)	3.02±1.48, 2.26±1.42, 0.08±0.05	0.0, 180.0, 0.0	1, 2, 3
C <sub>2</sub> -N-Zn-N (6)	3.39±0.74, 1.92±0.79, 0.02±0.02	0.0, 0.0, 0.0	1, 2, 3

## IMPROPER ANGLES (3 types)

Fourier series: $U_{improper} = \sum k_{\xi} [1 + \cos(m \xi_{ijkl} - \xi_{ijkl}^0)]$					
	intraZIF	AMBER			
Type I-J-K-L (N*)	$k_{\xi} / \text{kcal mol}^{-1}$	$k_{\xi} / \text{kcal mol}^{-1}$	$\xi_{ijkl}^0 / ^{\circ} \text{degrees}$	$m / -$	
N-H <sub>2</sub> -C <sub>2</sub> <sup>P</sup> -C <sub>2</sub> (2)	0.00	1.1	180.0	2	
C <sub>3</sub> -N-C <sub>1</sub> <sup>P</sup> -N (1)	0.00	1.1	180.0	2	
C <sub>1</sub> -C <sub>2</sub> -N <sup>P</sup> -Zn (2)	0.00	NA	180.0	2	

Improper term I-J-K-L refers to the angle between planes I-J-K and J-K-L, with J-K axis of rotation and K being the central/primary atom (noted by subscript <sup>P</sup>); N\*=number of bonds, angles, or dihedrals in the linker-metal complex. Superscripts H, P, and A refer to Hessian matrix, potential energy scan, or AMBER in reference to where certain spring constants were obtained.

Figure B.5a shows the single point potential energy scans for the Zn-N bond along with harmonic and Morse potential fits. Figure B.5b shows the contribution of the electrostatic energy for “fixed” and “varying” charges. Figure B.6 shows the comparison of the (a) intraZIF and (b) AMBER FF predicted configurational potential energies from BOMD simulations on the cluster.

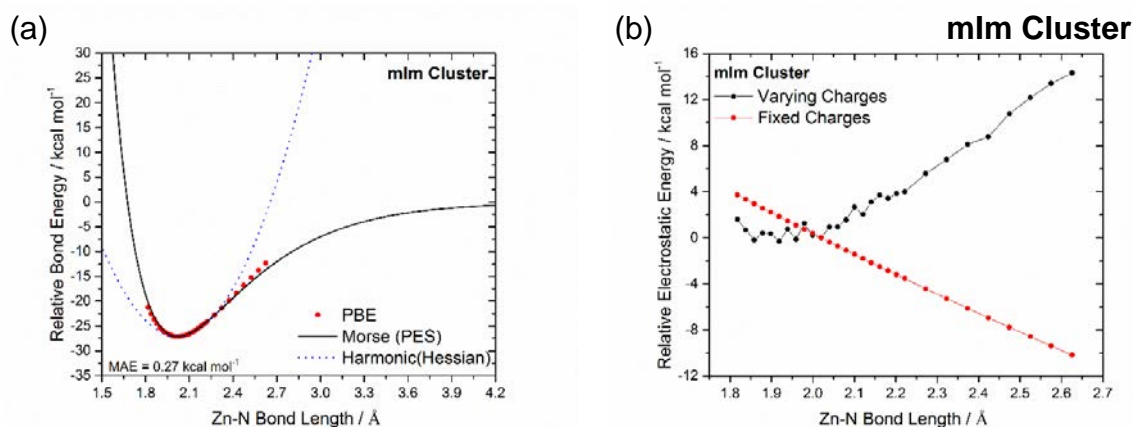


**Figure B.5** (a) Morse potentials fit (solid black line) to potential energy scans (red dots) along the Zn-N bond. The harmonic potential with the spring constant from the Seminario method is shown for comparison (dashed blue line). The mean absolute error (MAE) of the Morse fit is also reported. (b) Relative coulombic energy for the Zn-N potential energy scans.

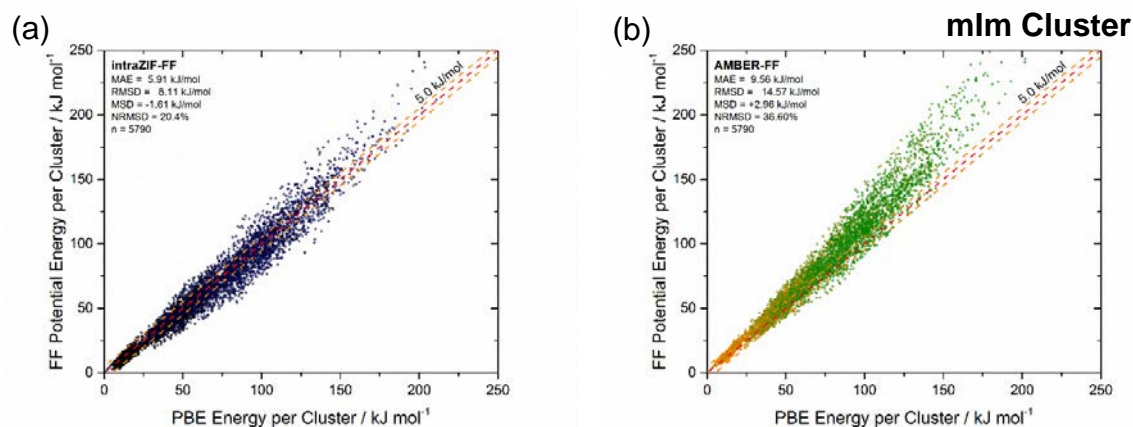


**Figure B.6** Relative energy comparisons between PBE and (a) the intraZIF-FF including Fourier dihedrals from the potential energy fitting and (b) the AMBER-FF using standard cosine proper dihedrals. The color code (black to blue/intraZIF and orange to green/AMBER) is designed to easily identify the low and high energy regions.

### B.3 Imidazolate-2-Carboxaldehyde (ImCA) ZIF Intramolecular Force Field

#### Parameters

Table B.3 below contains all the intramolecular force field functions and parameters implemented for ZIFs with imidazolate-2-carboxaldehyde linkers. Green (red) shaded regions indicated which degrees of freedom are (not) included in the intraZIF-FF. Comparison of spring constants between the AMBER and intraZIF FFs are also included.

**Table B.3** Bonded force field parameters for ZIFs with imidazolate-2-carboxaldehyde linkers. Functional forms, spring constants, and equilibrium geometry parameters are listed.

BOND STRETCHES (8 types)			
<b>Harmonic:</b> $U_{stretching} = \sum k_r (r_{ij} - r_{ij}^0)^2$			
Type I-J (N*)	intraZIF $k_r / \text{kcal mol}^{-1} \text{\AA}^{-2}$	AMBER $k_r / \text{kcal mol}^{-1} \text{\AA}^{-2}$	$r_{ij}^0 / \text{\AA}$
C <sub>4</sub> -O (1)	692.30	570.0	1.23
C <sub>4</sub> -H <sub>4</sub> (1)	293.42	367.0	1.12
C <sub>1</sub> -C <sub>4</sub> (1)	254.22	357.2	1.45
C <sub>1</sub> -N (2)	312.81	488.0	1.36
N-C <sub>2</sub> (2)	348.16	410.0	1.36
C <sub>2</sub> -H <sub>2</sub> (2)	384.32	367.0	1.09
C <sub>2</sub> -C <sub>2</sub> (1)	353.87	518.0	1.39
Zn-N (2)	62.63 <sup>H</sup>	78.5 <sup>A,133</sup> , 86.0 <sup>A,174</sup>	2.00
<b>Morse:</b> $U_{Zn-N} = \sum D_r (1 - e^{-\alpha(r_{ij} - r_{ij}^0)})^2$			
Type I-J (N*)	$D_r / \text{kcal mol}^{-1}$	$\alpha / \text{\AA}^{-1}$	$r_{ij}^0 / \text{\AA}$
Zn-N (2)	29.25	1.87	2.00
ANGLE BENDING (12 types)			



Table B.3 (continued)

Harmonic: $U_{bend} = \sum k_{\theta} (\theta_{ijk} - \theta_{ijk}^0)^2$			
	intraZIF	AMBER	
Type I-J-K (N*)	$k_{\theta} / \text{kcal mol}^{-1} \text{rad}^{-2}$	$k_{\theta} / \text{kcal mol}^{-1} \text{rad}^{-2}$	$\theta_{ijk}^0 / ^{\circ} \text{degrees}$
O-C <sub>4</sub> -H <sub>4</sub> (1)	82.10	50.0	121.52
O-C <sub>4</sub> -C <sub>1</sub> (1)	104.06	80.0	124.02
H <sub>4</sub> -C <sub>4</sub> -C <sub>1</sub> (1)	98.74	50.0	114.47
C <sub>4</sub> -C <sub>1</sub> -N (2)	129.33	70.0	124.18
C <sub>1</sub> -N-C <sub>2</sub> (2)	123.56	70.0	105.80
N-C <sub>2</sub> -H <sub>2</sub> (2)	64.50	50.0	121.64
N-C <sub>2</sub> -C <sub>2</sub> (2)	129.12	70.0	108.38
N-C <sub>1</sub> -N (1)	94.24	70.0	111.63
C <sub>2</sub> -C <sub>2</sub> -H <sub>2</sub> (2)	68.10	50.0	129.97
C <sub>1</sub> -N-Zn (2)	40.69 <sup>H</sup> /18.28 <sup>P</sup>	50.0	127.89
C <sub>2</sub> -N-Zn (2)	41.06 <sup>H</sup> /18.84 <sup>P</sup>	35.0	126.05
N-Zn-N (3)	30.68 <sup>H</sup> /18.20 <sup>P</sup>	10.5	109.46

## DIHEDRAL ANGLES (15 types)

Cosine: $U_{proper} = \sum k_{\phi} [1 + \cos(m\phi_{ijkl} - \phi_{ijkl}^0)]$				
	intraZIF	AMBER		
Type I-J-K-L (N*)	$k_{\phi} / \text{kcal mol}^{-1}$	$k_{\phi} / \text{kcal mol}^{-1}$	$\phi_{ijkl}^0 / ^{\circ} \text{degrees}$	$m / -$
O-C <sub>4</sub> -C <sub>1</sub> -N (2)	2.02	2.325	180.0	2
H <sub>4</sub> -C <sub>4</sub> -C <sub>1</sub> -N (2)	1.39	2.325	180.0	2
C <sub>4</sub> -C <sub>1</sub> -N-C <sub>2</sub> (2)	1.48±0.45	4.15	180.0	2
N-C <sub>1</sub> -N-C <sub>2</sub> (2)	3.97	4.80	180.0	2
C <sub>2</sub> -C <sub>2</sub> -N-C <sub>1</sub> (2)	2.72	4.80	180.0	2
H <sub>2</sub> -C <sub>2</sub> -N-C <sub>1</sub> (2)	3.43	4.80	180.0	2
N-C <sub>2</sub> -C <sub>2</sub> -H <sub>2</sub> (2)	2.61	4.00	180.0	2
N-C <sub>2</sub> -C <sub>2</sub> -N (1)	1.85	4.00	180.0	2
H <sub>2</sub> -C <sub>2</sub> -C <sub>2</sub> -H <sub>2</sub> (1)	0.00	4.00	180.0	2
C <sub>4</sub> -C <sub>1</sub> -N-Zn (2)	0.00	NA	180.0	2
N-C <sub>1</sub> -N-Zn (2)	0.00	NA	180.0	2
C <sub>2</sub> -C <sub>2</sub> -N-Zn (2)	0.00	NA	180.0	2
H <sub>2</sub> -C <sub>2</sub> -N-Zn (2)	0.00	NA	180.0	2

$$\text{Fourier series: } U_{proper} = \sum \sum_{n=1}^6 k_{\phi,n} [1 + \cos(m_n \phi_{ijkl} - d_n)]$$

Type I-J-K-L (N*)	$k_{\phi} / \text{kcal mol}^{-1}$	$d_n / ^{\circ} \text{degrees}$	$m / -$
C <sub>1</sub> -N-Zn-N (6)	3.02±1.48, 2.26±1.42, 0.08±0.05	0.0, 180.0, 0.0	1, 2, 3
C <sub>2</sub> -N-Zn-N (6)	3.39±0.74, 1.92±0.79, 0.02±0.02	0.0, 0.0, 0.0	1, 2, 3

## IMPROPER ANGLES (3 types)

Fourier series: $U_{improper} = \sum k_{\xi} [1 + \cos(m\xi_{ijkl} - \xi_{ijkl}^0)]$				
	intraZIF	AMBER		
Type I-J-K-L (N*)	$k_{\xi} / \text{kcal mol}^{-1}$	$k_{\xi} / \text{kcal mol}^{-1}$	$\xi_{ijkl}^0 / ^{\circ} \text{degrees}$	$m / -$

**Table B.3 (continued)**

N-H <sub>2</sub> -C <sub>2</sub> <sup>P</sup> -C <sub>2</sub> (2)	0.00	1.10	180.0	2
C <sub>4</sub> -N-C <sub>1</sub> <sup>P</sup> -N (1)	0.00	1.10	180.0	2
C <sub>1</sub> -C <sub>2</sub> -N <sup>P</sup> -Zn (2)	0.00	NA	180.0	2

*Improper term I-J-K-L refers to the angle between planes I-J-K and J-K-L, with J-K axis of rotation and K being the central/primary atom (noted by subscript <sup>P</sup>); N\*=number of bonds, angles, or dihedrals in the linker-metal complex. Superscripts H, P, and A refer to Hessian matrix, potential energy scan, or AMBER in reference to where certain spring constants were obtained.*

Figure B.7a shows the single point potential energy scans for the Zn-N bond along with harmonic and Morse potential fits. Figure B.7b shows the contribution of the electrostatic energy for “fixed” and “varying” charges. Figure B.8 shows the comparison of the (a) intraZIF and (b) AMBER FF predicted configurational potential energies from BOMD simulations on the cluster. Figure B.9 shows the fitting of the rotation of the aldehyde group around the C<sub>1</sub>-C<sub>4</sub> axis.

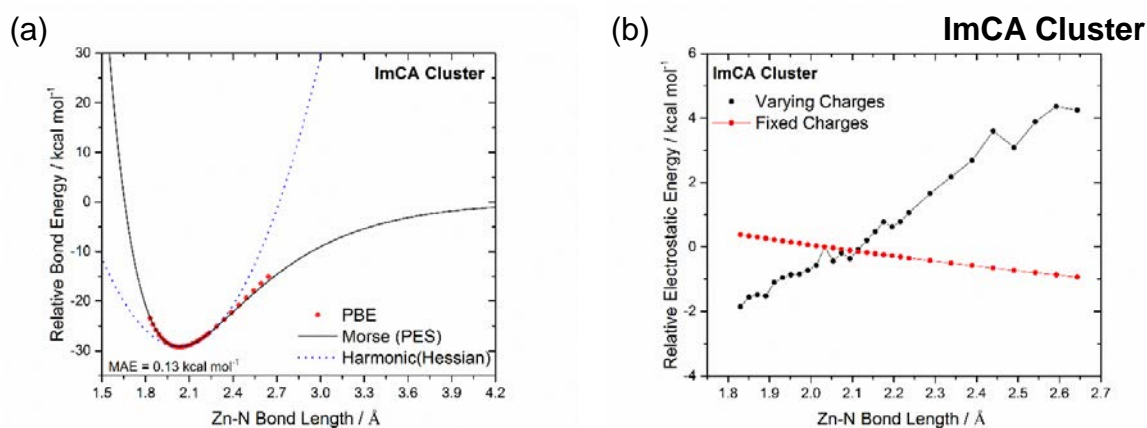


**Figure B.7** (a) Morse potentials fit (solid black line) to potential energy scans (red dots) along the Zn-N bond. The harmonic potential with the spring constant from the Seminario method is shown for comparison (dashed blue line). The mean absolute error (MAE) of the Morse fit is also reported. (b) Relative coulombic energy for the Zn-N potential energy scans.

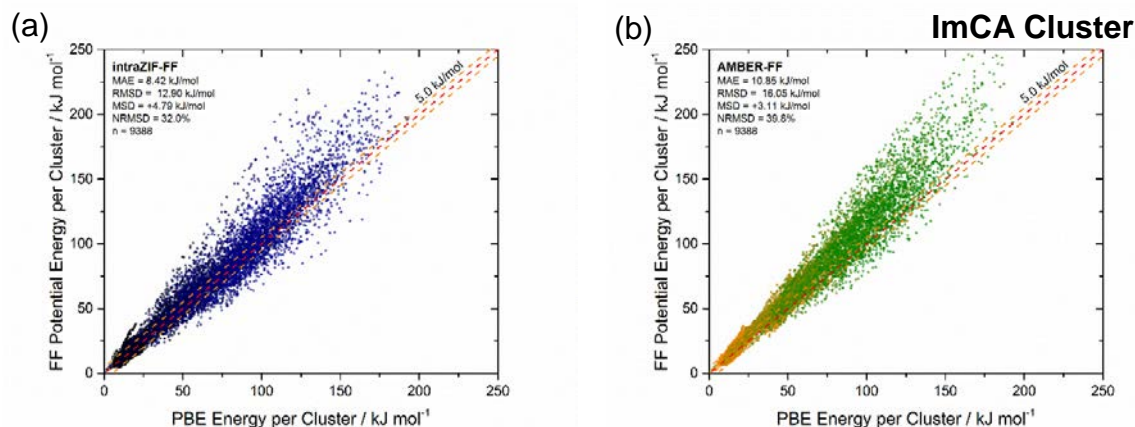


**Figure B.8** Relative energy comparisons between PBE and (a) the intraZIF-FF including Fourier dihedrals from the potential energy fitting and (b) the AMBER-FF using standard cosine proper dihedrals. The color code (black to blue/intraZIF and orange to green/AMBER) is designed to easily identify the low and high energy regions.

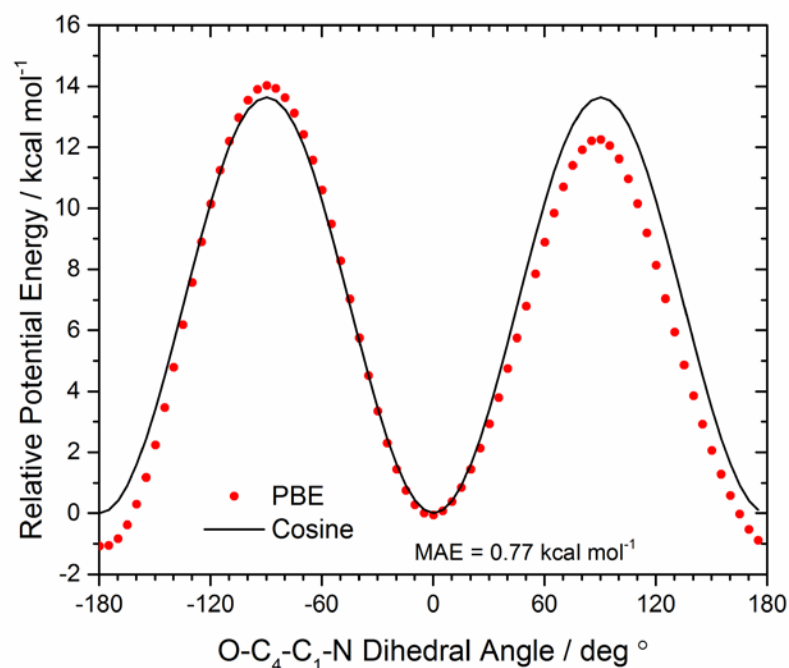


**Figure B.9** Cosine potential fit of the PBE energies from potential energy scans involving rotation of the aldehyde group around the  $C_1$ - $C_4$  axis.

### B.4 Benzimidazole (BzIm) ZIF Intramolecular Force Field Parameters

Table B.4 below contains all the intramolecular force field functions and parameters implemented for ZIFs with benzimidazole linkers. Green (red) shaded regions indicated which degrees of freedom are (not) included in the intraZIF-FF. Comparison of spring constants between the AMBER and intraZIF FFs are also included.

**Table B.4** Bonded force field parameters for ZIFs with benzimidazole linkers. Functional forms, spring constants, and equilibrium geometry parameters are listed.

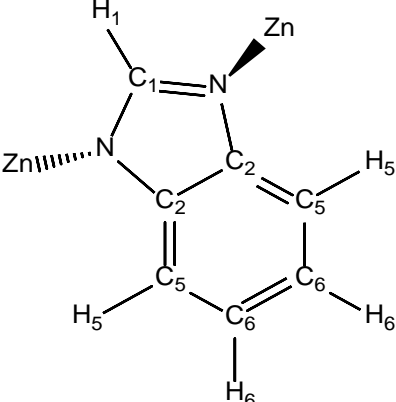
			
<b>BOND STRETCHES (10 types)</b>			
<b>Harmonic:</b> $U_{stretching} = \sum k_r (r_{ij} - r_{ij}^0)^2$			
	<b>intraZIF</b>	<b>AMBER</b>	
Type I-J (N*)	$k_r / \text{kcal mol}^{-1} \text{ \AA}^{-2}$	$k_r / \text{kcal mol}^{-1} \text{ \AA}^{-2}$	$r_{ij}^0 / \text{\AA}$
C <sub>1</sub> -H <sub>1</sub> (1)	369.37	367.0	1.09
C <sub>1</sub> -N (2)	351.24	488.0	1.34
C <sub>2</sub> -N (2)	274.22	410.0	1.39
C <sub>2</sub> -C <sub>2</sub> (1)	288.33	518.0	1.42
C <sub>2</sub> -C <sub>5</sub> (2)	350.29	469.0	1.40
C <sub>5</sub> -H <sub>5</sub> (2)	361.76	367.0	1.09
C <sub>5</sub> -C <sub>6</sub> (2)	366.93	469.0	1.39
C <sub>6</sub> -H <sub>6</sub> (2)	360.81	367.0	1.09
C <sub>6</sub> -C <sub>6</sub> (1)	339.98	469.0	1.41
Zn-N (2)	64.32 <sup>H</sup>	78.5 <sup>A,133</sup> , 86.0 <sup>A,174</sup>	1.99
<b>Morse:</b> $U_{Zn-N} = \sum D_r (1 - e^{-\alpha(r_{ij} - r_{ij}^0)})^2$			
Type I-J (N*)	$D_r / \text{kcal mol}^{-1}$	$\alpha / \text{\AA}^{-1}$	$r_{ij}^0 / \text{\AA}$
Zn-N (2)	26.06	1.98	1.99

Table B.4. (continued)

ANGLE BENDING (15 types)			
Type I-J-K (N*)	Harmonic: $U_{bend} = \sum k_{\theta} (\theta_{ijk} - \theta_{ijk}^0)^2$		
	intraZIF	AMBER	$\theta_{ijk}^0 / ^\circ \text{ degrees}$
	$k_{\theta} / \text{kcal mol}^{-1} \text{rad}^{-2}$	$k_{\theta} / \text{kcal mol}^{-1} \text{rad}^{-2}$	
N-C <sub>1</sub> -H <sub>1</sub> (2)	54.40	50.0	122.77
N-C <sub>1</sub> -N (1)	113.26	70.0	114.47
N-C <sub>2</sub> -C <sub>5</sub> (2)	150.32	70.0	131.01
N-C <sub>2</sub> -C <sub>2</sub> (2)	121.99	70.0	107.68
C <sub>1</sub> -N-C <sub>2</sub> (2)	143.04	70.0	105.09
C <sub>2</sub> -C <sub>5</sub> -H <sub>5</sub> (2)	60.12	50.0	121.52
C <sub>2</sub> -C <sub>5</sub> -C <sub>6</sub> (2)	157.37	63.0	117.01
C <sub>5</sub> -C <sub>6</sub> -C <sub>6</sub> (2)	190.48	63.0	121.67
C <sub>5</sub> -C <sub>6</sub> -H <sub>6</sub> (2)	60.10	50.0	119.17
C <sub>6</sub> -C <sub>6</sub> -H <sub>6</sub> (2)	60.55	50.0	119.15
C <sub>6</sub> -C <sub>5</sub> -H <sub>5</sub> (2)	63.88	50.0	121.48
C <sub>2</sub> -C <sub>2</sub> -C <sub>5</sub> (2)	145.80	63.0	120.93
N-Zn-N (3)	32.04 <sup>H</sup> /18.20 <sup>P</sup>	10.5	109.42
Zn-N-C <sub>1</sub> (2)	49.24 <sup>H</sup> /18.28 <sup>P</sup>	50.0	126.76
Zn-N-C <sub>2</sub> (2)	51.17 <sup>H</sup> /18.84 <sup>P</sup>	35.0	127.94

DIHEDRAL ANGLES (24 types)				
Type I-J-K-L (N*)	Fourier series: $U_{proper} = \sum k_{\phi} [1 + \cos(m\phi_{ijkl} - \phi_{ijkl}^0)]$			
	intraZIF	AMBER	$\phi_{ijkl}^0 / ^\circ \text{ degrees}$	$m / -$
	$k_{\phi} / \text{kcal mol}^{-1}$	$k_{\phi} / \text{kcal mol}^{-1}$		
N-C <sub>2</sub> -C <sub>5</sub> -C <sub>6</sub> (2)	0.38±0.36	4.80	180.0	2
H <sub>1</sub> -C <sub>1</sub> -N-C <sub>2</sub> (2)	2.37±1.29	4.80	180.0	2
C <sub>1</sub> -N-C <sub>2</sub> -C <sub>2</sub> (2)	0.69±0.57	4.80	180.0	2
H <sub>5</sub> -C <sub>5</sub> -C <sub>2</sub> -N (2)	0.22±0.11	4.80	180.0	2
C <sub>2</sub> -C <sub>2</sub> -C <sub>5</sub> -H <sub>5</sub> (2)	0.26±0.19	4.80	180.0	2
C <sub>5</sub> -C <sub>2</sub> -C <sub>2</sub> -C <sub>5</sub> (1)	0.62±0.32	4.00	180.0	2
H <sub>5</sub> -C <sub>5</sub> -C <sub>6</sub> -C <sub>6</sub> (2)	0.22±0.21	4.80	180.0	2
H <sub>6</sub> -C <sub>6</sub> -C <sub>6</sub> -C <sub>5</sub> (2)	0.56±0.30	4.80	180.0	2
C <sub>5</sub> -C <sub>6</sub> -C <sub>6</sub> -C <sub>5</sub> (1)	1.06±1.10	4.80	180.0	2
N-C <sub>2</sub> -C <sub>2</sub> -N (1)	1.10±1.14	4.00	180.0	2
N-C <sub>2</sub> -C <sub>2</sub> -C <sub>5</sub> (2)	0.49±0.41	4.00	180.0	2
C <sub>1</sub> -N-C <sub>2</sub> -C <sub>5</sub> (2)	0.59±0.46	4.80	180.0	2
C <sub>2</sub> -C <sub>5</sub> -C <sub>6</sub> -H <sub>6</sub> (2)	1.24±1.33	4.80	180.0	2
C <sub>6</sub> -C <sub>5</sub> -C <sub>2</sub> -C <sub>2</sub> (2)	0.22±0.32	4.80	180.0	2
C <sub>6</sub> -C <sub>6</sub> -C <sub>5</sub> -C <sub>2</sub> (2)	0.58±0.44	4.80	180.0	2
N-C <sub>1</sub> -N-C <sub>2</sub> (2)	2.30±1.25	4.80	180.0	2
H <sub>5</sub> -C <sub>5</sub> -C <sub>6</sub> -H <sub>6</sub> (2)	0.00	4.80	180.0	2
H <sub>6</sub> -C <sub>6</sub> -C <sub>6</sub> -H <sub>6</sub> (1)	0.00	4.80	180.0	2
Zn-N-C <sub>1</sub> -H <sub>1</sub> (2)	0.00	NA	180.0	2
Zn-N-C <sub>2</sub> -C <sub>5</sub> (2)	0.00	NA	180.0	2
Zn-N-C <sub>1</sub> -N (2)	0.00	NA	180.0	2
Zn-N-C <sub>2</sub> -C <sub>2</sub> (2)	0.00	NA	180.0	2

$$\text{Fourier series: } U_{proper} = \sum_{n=1}^6 \sum k_{\phi,n} [1 + \cos(m_n \phi_{ijkl} - d_n)]$$

**Table B.4. (continued)**

Type I-J-K-L (N*)	$k_{\phi} / \text{kcal mol}^{-1}$	$d_n / ^\circ \text{degrees}$	m / -
C <sub>1</sub> -N-Zn-N (6)	3.02±1.48, 2.26±1.42, 0.08±0.05	0.0, 180.0, 0.0	1, 2, 3
C <sub>2</sub> -N-Zn-N (6)	3.39±0.74, 1.92±0.79, 0.02±0.02	0.0, 0.0, 0.0	1, 2, 3

**IMPROPER ANGLES (5 types)**

Fourier series: $U_{\text{improper}} = \sum k_{\xi} [1 + \cos(m \xi_{ijkl} - \xi_{ijkl}^0)]$				
Type I-J-K-L (N*)	intraZIF $k_{\xi} / \text{kcal mol}^{-1}$	AMBER $k_{\xi} / \text{kcal mol}^{-1}$	$\xi_{ijkl}^0 / ^\circ \text{degrees}$	m / -
N-C <sub>2</sub> -C <sub>2</sub> <sup>P</sup> -C <sub>5</sub> (2)	0.00	1.10	180.0	2
H <sub>1</sub> -N-C <sub>1</sub> <sup>P</sup> -N (1)	0.00	1.10	180.0	2
H <sub>6</sub> -C <sub>5</sub> -C <sub>6</sub> <sup>P</sup> -C <sub>6</sub> (2)	0.00	1.10	180.0	2
H <sub>5</sub> -C <sub>6</sub> -C <sub>5</sub> <sup>P</sup> -C <sub>2</sub> (2)	0.00	1.10	180.0	2
C <sub>1</sub> -C <sub>2</sub> -N <sup>P</sup> -Zn (2)	0.00	NA	180.0	2

Improper term I-J-K-L refers to the angle between planes I-J-K and J-K-L, with J-K axis of rotation and K being the central atom (noted by subscript <sup>P</sup>); N\*=number of bonds, angles, or dihedrals in the linker-metal complex. Superscripts H, P, and A refer to Hessian matrix, potential energy scan, or AMBER in reference to where certain spring constants were obtained.

Figure B.10a shows the single point potential energy scans for the Zn-N bond along with harmonic and Morse potential fits. Figure B.10b shows the contribution of the electrostatic energy for “fixed” and “varying” charges. Figure B.11 shows the comparison of the (a) intraZIF and (b) AMBER FF predicted configurational potential energies from BOMD simulations on the cluster.

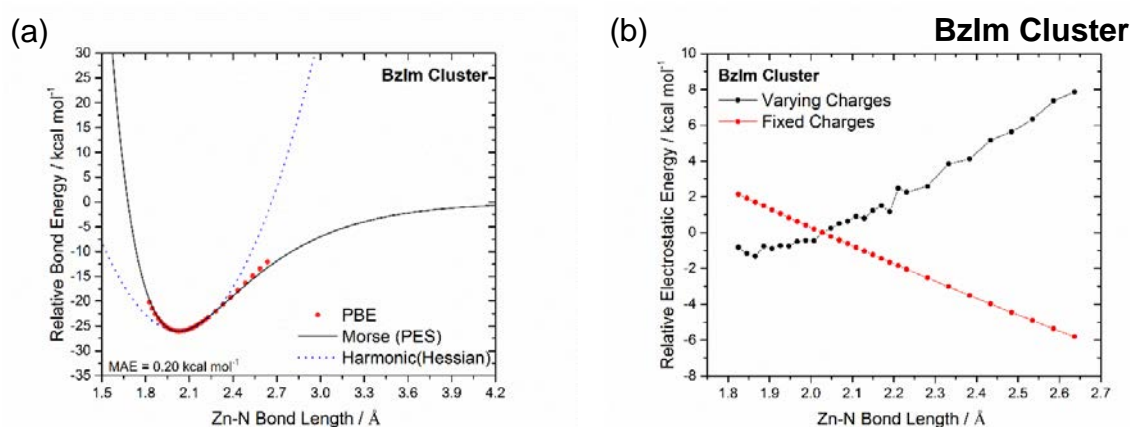


**Figure B.10** (a) Morse potentials fit (solid black line) to potential energy scans (red dots) along the Zn-N bond. The harmonic potential with the spring constant from the Seminario method is shown for comparison (dashed blue line). The mean absolute error (MAE) of the Morse fit is also reported. (b) Relative coulombic energy for the Zn-N potential energy scans.

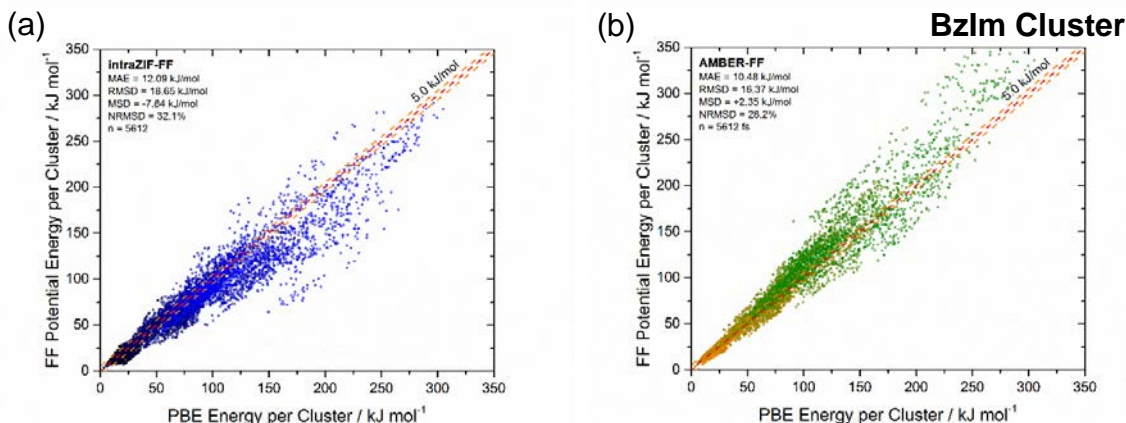


**Figure B.11** Relative energy comparisons between PBE and (a) the intraZIF-FF including Fourier dihedrals from the potential energy fitting and (b) the AMBER-FF using standard cosine proper dihedrals. The color code (black to blue/intraZIF and orange to green/AMBER) is designed to easily identify the low and high energy regions.

### ***B.5 Modeling Zn-N-C<sub>1,2</sub> and N-Zn-N Bending by Fitting to Potential Energy Scans***

Single point potential energy scans along the Zn-N-C<sub>1,2</sub> and N-Zn-N bending degrees of freedom of the Im, mIm, BzIm, and ImCA clusters. The axis of rotation was defined as the normal vector to the plane formed by the three carbon atoms of the central linker's imidazolate five member ring. The origin for the axis of rotation was defined as location of the N atom on the central linker for the Zn-N-C<sub>1,2</sub> bending and the Zn atom for the N-Zn-N bending. To test how symmetrical the clusters were, two potential energy scans were performed on both N and Zn atoms of the ImCA cluster. The "O" and "H" subscripts on Figures B.12 and B.13 below indicate whether the N, Zn atoms closer to the O or H atoms on the aldehyde group respectively were used as the origin of rotation. The relative angle energy is a sum of all the angles changing in the scan.

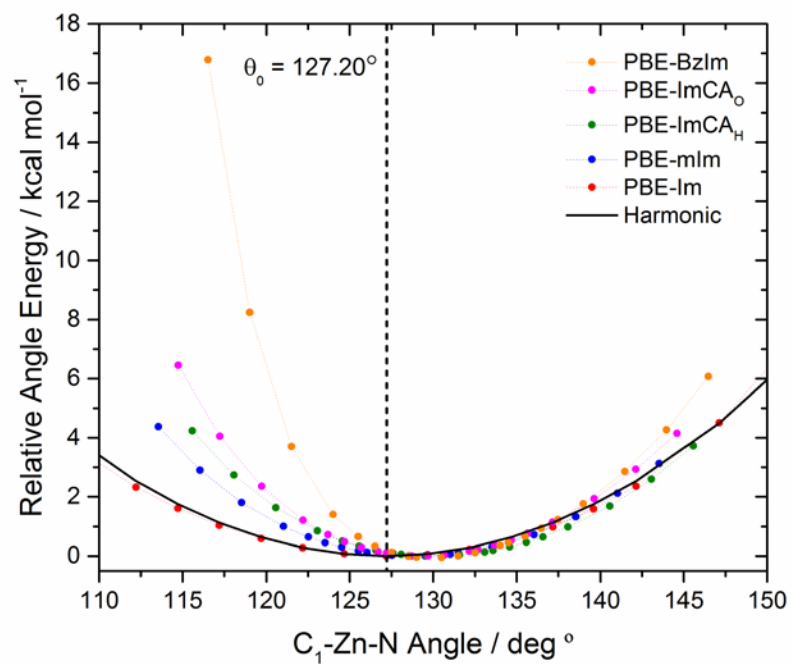


**Figure B.12** Potential energy scan along the  $C_1$ -Zn-N and  $C_2$ -Zn-N angles for the four clusters with the harmonic fit to the unfunctionalized imidazolate cluster scan (black line).

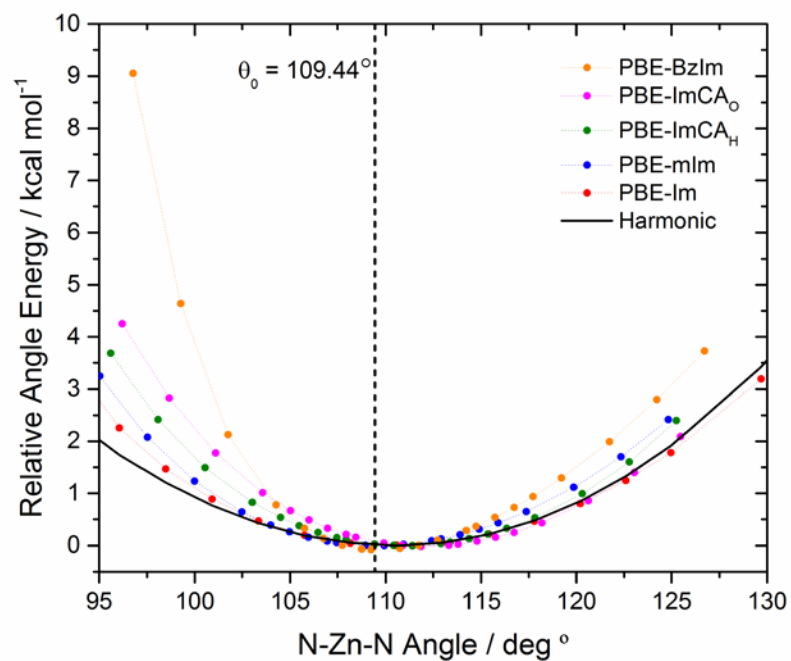


**Figure B.13** Potential energy scan along the N-Zn-N angles for the four clusters with the harmonic fit to the unfunctionalized imidazolate cluster scan (black line).



## ***B.6 Nonbonded Force Field Parameters for ZIFs***

### ***B.6.1 Van der Waals Pair-Wise Interactions***

Adsorbent-adsorbent van der Waals interactions were modeled using a Buckingham potential (intraZIF) and compared to 12-6 Lennard-Jones parameters from the AMBER-FF. All parameters are listed in Tables B.5 and B.6. Van der Waals parameters on the ZIF framework atoms for adsorbent-adsorbate interactions (Table B.7) were modeled using parameters from the Universal force field where all epsilon values were scaled by 0.54, which was demonstrated to more accurately reproduce N<sub>2</sub>, CH<sub>4</sub>, and CO<sub>2</sub> adsorption<sup>174</sup> and hydrocarbon diffusion in ZIF-8<sup>219</sup>. We have not parameterized any adsorbate-adsorbent interactions, instead using Lorentz-Berthelot mixing rules. This provides a standard method for modeling framework-adsorbate interactions. For those seeking to parameterize more accurate adsorbate-adsorbent interactions, we direct the reader to a review article by Fang et al. detailing methods for developing force fields that model adsorbate-adsorbent interactions.<sup>85</sup> To describe diffusion with true accuracy, adsorbate-adsorbent configurations at transition states (e.g. isobutane in the ZIF-8 window) must be included in any force field fitting procedure.

**Table B.5** Buckingham potential parameters taken from the Molecular Mechanics 3 (MM3) force field and used in the intraZIF-FF.

<b>Atom Type</b>	<b><math>\epsilon_{ii}</math> [kcal/mol]</b>	<b><math>r_{ii}^0</math> [Å]</b>
Zn	0.0276	2.29
N	0.043	1.93
C <sub>1,2,5,6</sub>	0.056	1.94
C <sub>3,4</sub>	0.027	2.04
H <sub>1,2,3,5,6</sub>	0.020	1.50
H <sub>4</sub>	0.020	1.62
O	0.059	1.82

**Table B.6** AMBER van der Waals parameters taken from the parm10.dat file.

Atom Type	$\epsilon$ [kcal/mol]	$\sigma$ [Å]
Zn	0.0125	1.96
N	0.1700	3.25
C <sub>1,2,3,4,5</sub>	0.0860	3.40
H <sub>1,2,5,6</sub>	0.0150	2.51
H <sub>3,4</sub>	0.0157	2.65
O	0.2100	2.96

**Table B.7** Unscaled and scaled epsilon and sigma 12-6 Lennard Jones parameters from the Universal Force Field (UFF) used to describe adsorbate-adsorbent interactions.

Atom Type	$\epsilon$ [kcal/mol]	$0.54\epsilon$ [kcal/mol]	$\sigma$ [Å]
Zn	0.124	0.067	2.462
N	0.069	0.037	3.261
C <sub>x</sub>	0.105	0.057	3.431
H <sub>x</sub>	0.044	0.024	2.571
O	0.060	0.032	3.118

### B.6.2 Electrostatic Pair-Wise Interactions

Table B.8 shows the DDEC charges for periodic ZIFs used in the intraZIF-FF. Table B.9 shows which pair-wise coulombic interactions include the Debye damping factor.

**Table B.8** Charges for periodic ZIFs from the DDEC method used in the intraZIF-FF.

Atom Type	Im	BzIm	mIm	ImCA
Zn	0.7294	0.7826	0.7599	0.7136
N	-0.3621	-0.4502	-0.4312	-0.3455
C1	0.1636	0.2432	0.4280	0.1994
C2	-0.0529	0.1722	-0.0571	0.0095
C3	-	-	-0.4676	-
C4	-	-	-	0.2450
C5	-	-0.0881	-	-
C6	-	-0.1982	-	-
H1	0.0931	0.0988	-	-
H2	0.1043	-	0.1083	0.1096
H3	-	-	0.1399	-
H4	-	-	-	0.0459
H5	-	0.0988	-	-
H6	-	0.0988	-	-
O	-	-	-	-0.3942

**Table B.9** Pair-wise coulombic interactions utilizing the Debye damping factor.

ZIF	Atom i (charge / e)	Atom j (charge / e)	Short Range Interaction
<b>SALEM-2</b>	Zn (+0.7294)	Zn (+0.7294)	Repulsive
	Zn (+0.7294)	C2 (-0.0529)	Attractive
<b>ZIF-7</b>	Zn (+0.7826)	Zn (+0.7826)	Repulsive
	Zn (+0.7826)	C2 (+0.1722)	Repulsive
	Zn (+0.7826)	C5 (-0.0881)	Attractive
<b>ZIF-8</b>	Zn (+0.7599)	Zn (+0.7599)	Repulsive
	Zn (+0.7599)	N (-0.4312)	Attractive
	Zn (+0.7599)	C1(+0.4280)	Repulsive
	Zn (+0.7599)	C2 (-0.0571)	Attractive
	Zn (+0.7599)	C3(-0.4676)	Attractive
	Zn (+0.7599)	H2(+0.1083)	Repulsive
	Zn (+0.7599)	H3(+0.1399)	Repulsive
<b>ZIF-90</b>	Zn (+0.7136)	Zn (+0.7136)	Repulsive
	Zn (+0.7136)	C1 (+0.1994)	Repulsive
	Zn (+0.7136)	C2 (+0.0095)	Repulsive

For those seeking to use the intraZIF-FF, below is the required LAMMPS setting for the Debye interactions:

```
##NONBONDED LMP POTENTIAL PARAMETERS##
pair_style hybrid/overlay lj/cut 15.5 buck 15.5 coul/long 15.5
coul/debye 0.33 15.5
special_bonds lj 1.0e-10 1.0e-10 1.0e-10 coul 1.0e-10 1.0e-10 1.0e-10
kspace_style ewald/disp 1.0E-06
pair_modify tail yes
pair_modify pair coul/debye special coul 0.0 0.0 1.0
include VDW_LAMMPS.data
include CHARGES_LAMMPS.data
##END NONBONDED LMP POTENTIAL PARAMETERS##
```

Figures B.14-B.17 compare the charges derived from the central linker in the clusters to charges derived from the periodic ZIFs.

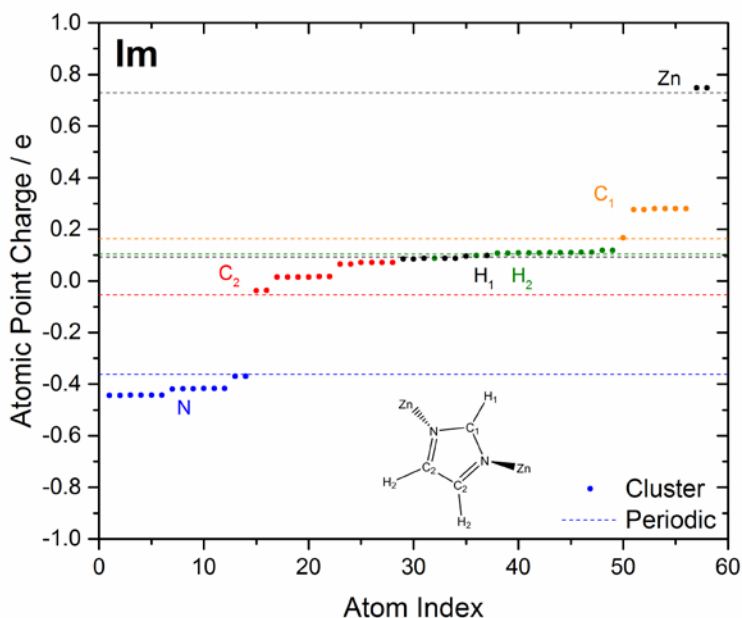


**Figure B.14** Charges on individual atoms in the Im cluster as compared to periodic charges.

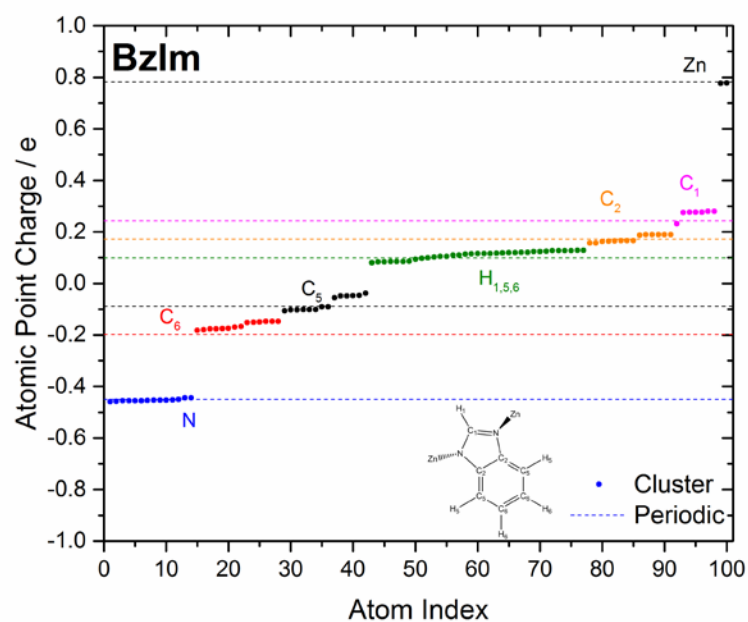


**Figure B.15** Charges on individual atoms in the BzIm cluster as compared to periodic charges.

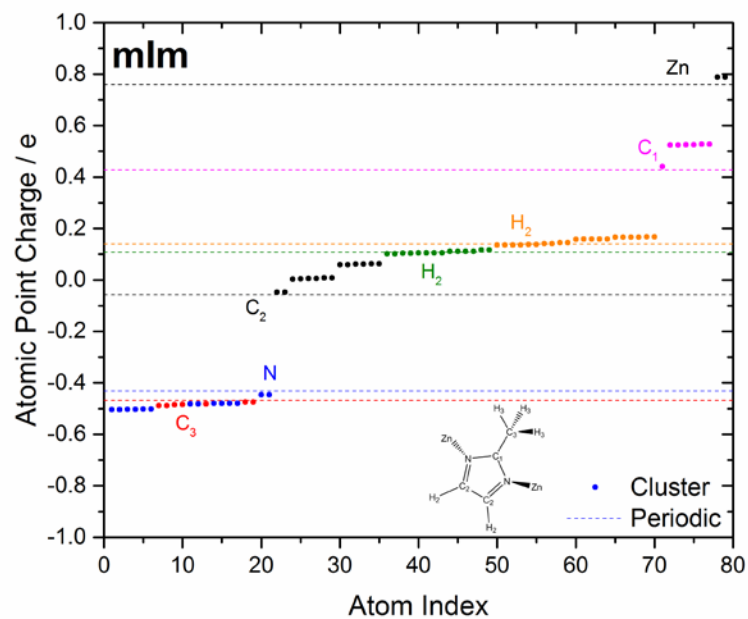


**Figure B.16** Charges on individual atoms in the mIm cluster as compared to periodic charges.

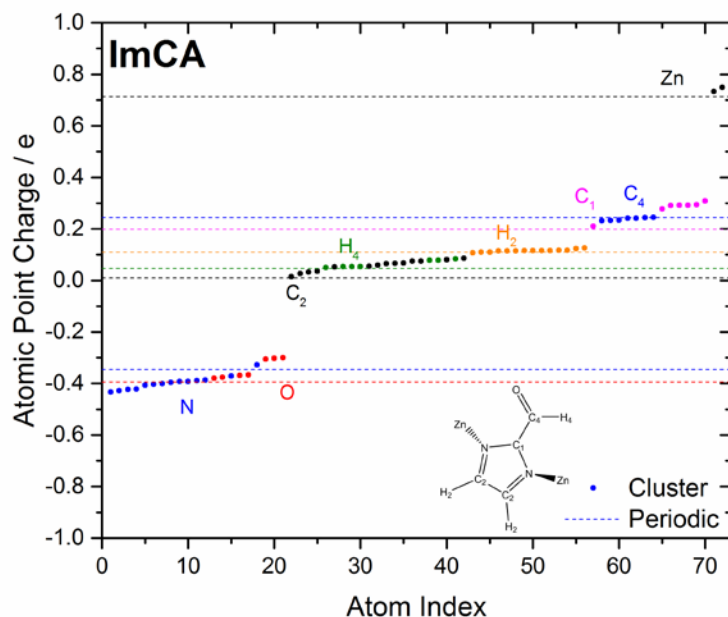


**Figure B.17** Charges on individual atoms in the ImCA cluster as compared to periodic charges.

### B.7 Geometric Predictions of SALEM-2, ZIF-7, ZIF-8, ZIF-90

Below in Tables B.10-B.13, we report the lattice parameters, pore limiting diameter (PLD), largest cavity diameter (LCD), accessible surface area (ASA), non-accessible surface area (NASA), accessible volume (AV), non-accessible volume (NAV), and density calculated using Zeo++ with a probe radius of 1.3 Å.<sup>190</sup>

**Table B.10** SALEM-2 structural parameter comparisons between DFT and FF energy minimizations. ASA (NASA) and AV (NAV) are reported for the simulation volume (2x2x2 supercell).

Structural Parameter	PBE-D2	PBE-D3(BJ)	intraZIF	AMBER
<b>a</b> [Å]	16.84	16.86	16.83	16.55
<b>b</b> [Å]	16.84	16.86	16.83	16.48
<b>c</b> [Å]	16.84	16.86	16.83	16.51
<b>PLD</b> [Å]	3.15	3.17	3.54	3.16
<b>LCD</b> [Å]	11.74	11.75	11.52	10.86
<b>ASA (NASA)</b> [Å <sup>2</sup> ]	8004.72 (0)	8041.04 (0)	8206.25 (0)	7527.33 (0)
<b>AV (NAV)</b> [Å <sup>3</sup> ]	10775.36 (0)	10846.00 (0)	10561.4 (0)	8995.95 (0)
<b>ρ</b> [g cm <sup>-3</sup> ]	0.8326	0.8299	0.8337	0.8828

**Table B.11** ZIF-7 structural parameter comparisons between DFT and FF energy minimizations. ASA (NASA) and AV (NAV) are reported for the simulation volume (2x2x2 supercell).

Structural Parameter	PBE-D2	PBE-D3(BJ)	intraZIF	AMBER
<b>a</b> [ $\text{\AA}$ ]	22.46	22.51	22.50	21.53
<b>b</b> [ $\text{\AA}$ ]	22.46	22.51	22.50	21.54
<b>c</b> [ $\text{\AA}$ ]	15.95	15.99	16.08	15.63
<b>PLD</b> [ $\text{\AA}$ ]	2.29	2.27	2.22	1.65
<b>LCD</b> [ $\text{\AA}$ ]	5.52	5.50	4.95	4.38
<b>ASA (NASA)</b> [ $\text{\AA}^2$ ]	0 (4899.51)	0 (4953.79)	0 (3963.8)	0 (2097.59)
<b>AV (NAV)</b> [ $\text{\AA}^3$ ]	0 (1767.99)	0 (1863.49)	0 (1093.92)	0 (481.195)
<b><math>\rho</math></b> [ $\text{g cm}^{-3}$ ]	1.2855	1.2766	1.2707	1.4265

**Table B.12** ZIF-8 structural parameter comparisons between DFT and FF energy minimizations. ASA (NASA) and AV (NAV) are reported for the simulation volume (2x2x2 supercell).

Structural Parameter	PBE-D2	PBE-D3(BJ)	intraZIF	AMBER
<b>a</b> [ $\text{\AA}$ ]	16.94	16.98	16.90	16.46
<b>b</b> [ $\text{\AA}$ ]	16.94	16.98	16.91	16.46
<b>c</b> [ $\text{\AA}$ ]	16.94	16.98	16.90	16.46
<b>PLD</b> [ $\text{\AA}$ ]	3.31	3.32	3.44	3.05
<b>LCD</b> [ $\text{\AA}$ ]	11.39	11.42	10.89	10.91
<b>ASA (NASA)</b> [ $\text{\AA}^2$ ]	6976.22 (0)	6987.86 (0)	7038.57 (0)	6156.93 (0)
<b>AV (NAV)</b> [ $\text{\AA}^3$ ]	9109.63 (0)	9222.16 (0)	8670.51 (0)	7246.57 (0)
<b><math>\rho</math></b> [ $\text{g cm}^{-3}$ ]	0.9324	0.9271	0.9390	1.0169

**Table B.13** ZIF-90 structural parameter comparisons between DFT and FF energy minimizations. ASA (NASA) and AV (NAV) are reported for the simulation volume (2x2x2 supercell).

Structural Parameter	PBE-D2	PBE-D3(BJ)	intraZIF	AMBER
<b>a</b> [ $\text{\AA}$ ]	17.14	17.20	17.34	16.97
<b>b</b> [ $\text{\AA}$ ]	17.16	17.22	17.29	16.98
<b>c</b> [ $\text{\AA}$ ]	17.05	17.11	17.09	16.55
<b>PLD</b> [ $\text{\AA}$ ]	3.45	3.49	3.77	3.40
<b>LCD</b> [ $\text{\AA}$ ]	10.91	10.97	10.95	10.30
<b>ASA (NASA)</b> [ $\text{\AA}^2$ ]	7245.54 (0)	7304.22 (0)	7661.72 (0)	6916.94 (0)
<b>AV (NAV)</b> [ $\text{\AA}^3$ ]	9376.08 (0)	9612.72 (0)	9470.43 (0)	7727.50 (0)
<b><math>\rho</math></b> [ $\text{g cm}^{-3}$ ]	1.0151	1.0046	0.9940	1.0678

### ***B.8 Im and mIm ZIF Polymorphs: Geometric and Stability Predictions***

Tables B.14 and B.15 show the PLDs and accessible surfaces respectively of the PBE-D2, PBE-D3(BJ), the intraZIF-FF, and the AMBER-FF energy optimized Im polymorphs. Tables B.16 and B.17 show the PLDs and accessible surfaces respectively of the PBE-D2, PBE-D3(BJ), the intraZIF-FF, and the AMBER-FF energy optimized mIm polymorphs. Figure B.18 shows the parity plots for (a) unit cell densities and (b) LCDs as predicted by PBE-D2 and the intraZIF and AMBER force fields.

**Table B.14** Pore limiting diameters [ $\text{\AA}$ ] of Im polymorphs.

<b>Polymorph</b>	<b>PBE-D2</b>	<b>PBE-D3(BJ)</b>	<b>intraZIF</b>	<b>AMBER</b>
afw	3.93	3.90	3.78	3.25
cag_exp	2.11	2.11	1.92	2.00
cfc	4.58	4.58	3.88	4.02
coe	2.40	2.36	2.24	2.06
crb_exp	5.12	5.12	4.96	4.66
dft_exp	5.60	5.60	4.56	5.62
dia	3.98	3.98	3.78	3.79
gis_exp	5.37	5.37	5.60	5.78
gsi	2.41	2.40	2.26	2.24
irl	2.34	2.33	2.36	2.02
lcs	2.76	2.76	3.22	2.66
lon	4.47	4.46	4.54	3.50
lta	9.04	9.06	9.22	7.39
mer_exp	7.58	7.59	7.46	6.69
mmt	3.30	3.30	3.30	2.82
neb	2.30	2.31	2.44	2.44
pcb	5.63	5.63	6.32	5.46
pcl	6.54	6.52	6.69	5.44
qtz	3.82	3.73	2.92	2.08
sod	3.39	3.39	3.42	3.44
sra	6.79	6.87	6.81	5.01
unc	4.69	4.70	4.45	3.82
unh	8.86	8.86	8.77	8.85
uni	7.00	7.01	6.75	6.66
unj	6.49	6.44	5.93	6.68
uoc	4.33	4.33	4.52	3.84
zni_exp	2.40	2.40	1.59	2.11



**Table B.15** Accessible surface areas [ $\text{m}^2/\text{cm}^3$ ] per unit cell of Im polymorphs.

<b>Polymorph</b>	<b>PBE-D2</b>	<b>PBE-D3(BJ)</b>	<b>intraZIF</b>	<b>AMBER</b>
afw	2638.22	2626.04	2611.59	2143.95
cag_exp	0	0	0	0
cfc	2360.46	2366.97	2299.06	1851.99
coe	0	0	0	0
crb_exp	2454.38	2454.60	2546.25	2217.79
dft_exp	2475.44	2475.80	2468.06	2269.16
dia	2410.58	2413.00	2286.11	2160.64
gis_exp	2434.78	2434.68	2352.52	2332.26
gsi	0	0	0	0
irl	0	0	0	0
lcs	1825.88	1830.81	2183.13	1429.3
lon	2320.14	2323.24	2291.85	1904.69
lta	1735.93	1733.54	1725.08	1775.87
mer_exp	2236.55	2237.10	2243.45	2197.59
mmt	1935.19	1940.68	1918.98	620.652
neb	0	0	0	0
pcb	2399.1	2399.19	2304.84	2368.83
pcl	2502.03	2503.26	2433.51	2208.51
qtz	3019.71	3015.36	1642.29	0
sod	2090.02	2088.74	2152.79	2125.25
sra	2510.26	2511.82	2437.83	2303.12
unc	1582.4	1596.55	1530.85	1119.69
unh	1838.93	1839.39	1929.91	1755.2
uni	1277.84	1278.16	1218.88	1152.15
unj	1553.01	1524.95	1570.54	1542.67
uoc	2471.62	2476.30	2473.89	2306.17
zni_exp	0	0.00	0	0

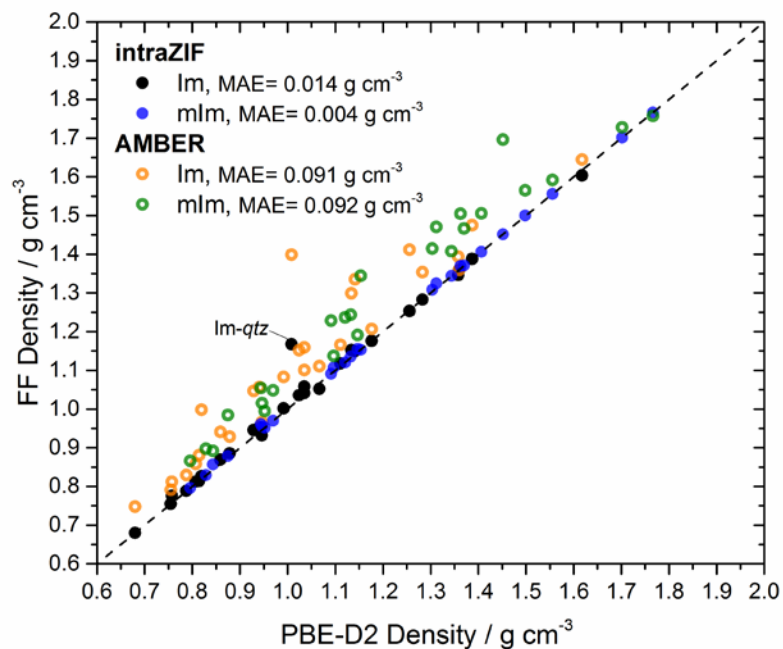
**Table B.16** Pore limiting diameters [ $\text{\AA}$ ] of mIm polymorphs.

Polymorph	PBE-D2	PBE-D3(BJ)	intraZIF	AMBER
cag	3.18	3.21	3.37	2.46
cfc	3.21	3.21	3.17	3.05
coi	1.15	1.18	1.33	1.12
crb	4.00	3.96	4.37	3.94
dft	5.56	5.58	5.44	6.46
dia	1.66	1.69	1.57	1.36
gis	7.04	7.06	7.07	6.38
gsi	2.15	2.17	2.06	1.71
irl	3.10	3.08	2.65	2.28
lcs	2.96	2.97	3.36	2.42
lon	3.16	3.21	3.15	2.83
lta	7.11	7.14	7.08	6.88
mer	7.61	7.69	7.41	7.18
mmt	1.66	1.70	1.43	1.57
neb	1.91	1.96	1.76	1.35
pcb	5.90	6.06	6.29	5.63
pcl	5.56	5.58	5.28	4.96
qtz	2.12	2.19	2.08	1.14
sod	3.20	3.20	3.30	3.05
sra	6.33	6.39	5.98	5.87
unc	4.73	4.86	4.97	4.43
unh	7.66	7.52	7.75	7.53
uni	5.14	5.28	5.06	4.83
unj	5.98	5.91	5.67	5.74
zni	1.35	1.36	1.10	1.07

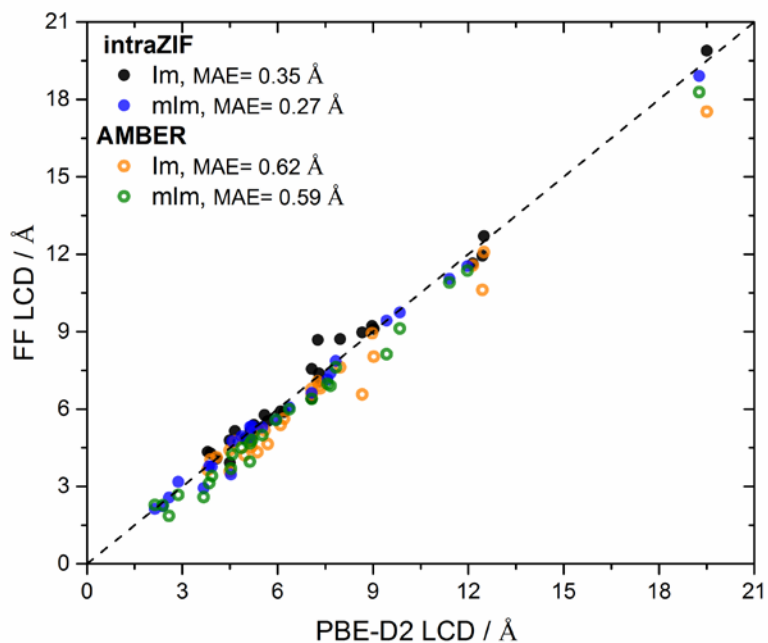
**Table B.17** Accessible surface areas [m<sup>2</sup>/cm<sup>3</sup>] per unit cell of mIm polymorphs.

Polymorph	PBE-D2	PBE-D3(BJ)	intraZIF	AMBER
cag	2106.68	2120.01	2018.05	0
cfc	1733.02	1770.02	1672.21	1277.91
coi	0	0.00	0	0
crb	956.277	959.53	928.74	896.423
dft	2008.39	2024.84	1929.82	1884.71
dia	0	0	0	0
gis	1991.79	1992.04	1954.44	1960.52
gsi	0	0	0	0
irl	1252.53	1266.31	927.183	0
lcs	1298.88	1313.57	1458.14	0
lon	1823.6	1863.03	1789.27	1240.99
lta	1666.26	1666.18	1600.35	1638.78
mer	2002.26	1998.65	1951.01	1936.13
mmt	0	0	0	0
neb	0	0	0	0
pcb	2145.14	2137.28	2078.04	2032.57
pcl	2059.46	2067.06	2034.1	1939.3
qtz	0	0.00	0	0
sod	1766.77	1767.72	1795.15	1726.43
sra	2108.41	2110.03	2052.57	1930.88
unc	1024.83	1094.01	1018.65	944.765
unh	1675.84	1643.96	1508.06	1646.08
uni	709.902	717.81	568.809	594.674
unj	1557.88	1540.00	1494.24	1509.49
zni	0	0	0	0

(a)

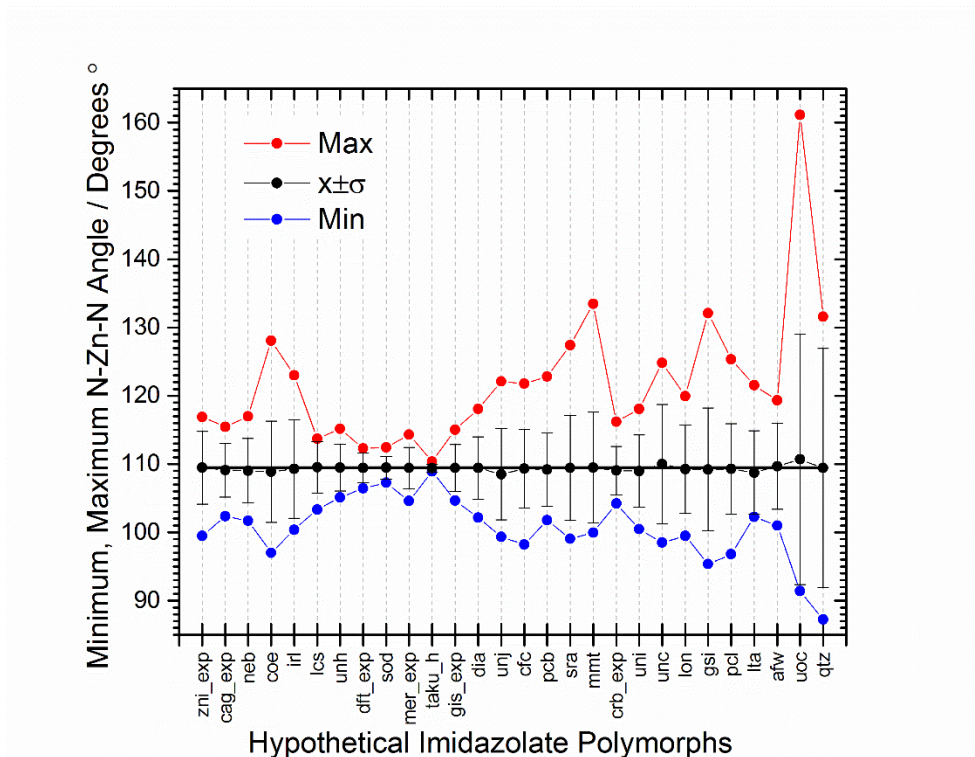


(b)



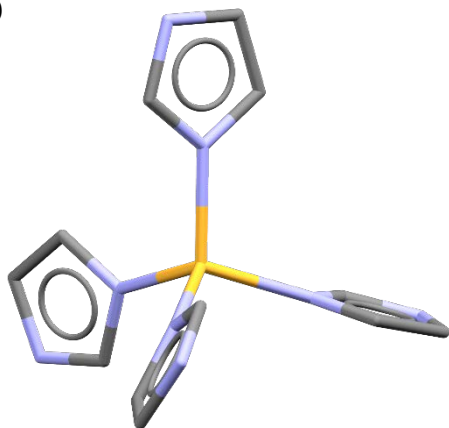
**Figure B.18** Parity plots for (a) unit cell densities and (b) LCDs as predicted by PBE-D2 and the intraZIF (blue/black) and AMBER (orange/green) force fields. There are 27 Im polymorphs as well as the SALEM-2 structure (closed circles) and 25 mIm polymorphs (open circles).

Figure B.19 below shows the minimum, mazimum, and average N-Zn-N angle for the 27 Im polymorphs as well as SALEM-2 (labeled as taku\_h). Figure B.20 shows the coordination environment for two different Im polymorphs.



**Figure B.19** Analysis of N-Zn-N angles in the 27 Im polymorphs and the SALEM-2 (labeled as taku\_h). Error bars on the average angle (black solid circles) represent the standard deviation of all the N-Zn-N angles in the unit cell.

**SOD**



**UOC**

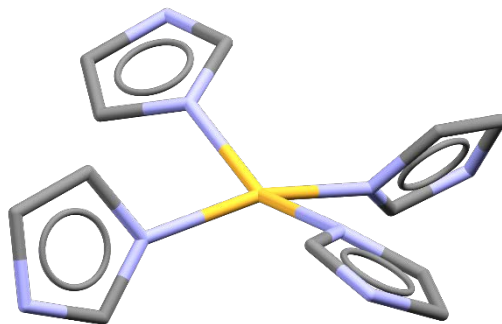


**Figure B.20** Examples of tetrahedral and near square planar Zn coordination environments for the Im-sod and Im-uoc polymorphs.

Tables B.18 and B.19 show the relative configuration energies for Im and mIm polymorphs with the *zni* polymorph as the reference.

**Table B.18** Relative configurational energies [kJ/mol/Zn] of Im polymorphs ranked according to the PBE-D2 predicted stabilities.

Polymorph	PBE-D2	PBE-D3(BJ)	intraZIF	AMBER
zni_exp	0.0	0.0	0.0	0.0
cag_exp	17.2	14.9	8.4	12.2
neb	18.0	18.4	12.3	17.0
coe	21.0	20.0	10.0	17.7
irl	22.2	22.8	12.6	16.0
lcs	24.3	20.8	10.0	25.0
unh	27.2	26.1	10.9	26.0
dft_exp	27.2	24.3	7.4	26.9
sod (SALEM-2)	27.3	24.4	4.7	28.7
mer_exp	27.3	24.8	6.7	29.4
gis_exp	27.9	25.5	5.0	32.3
dia	28.8	27.8	5.1	25.4
unj	29.0	28.3	13.2	22.1
cfc	30.2	29.2	7.3	24.4
pcb	30.3	27.6	7.6	30.6
sra	30.8	29.7	9.2	28.1
mmt	31.4	30.9	13.8	23.5
crb_exp	31.6	30.4	7.2	25.5
uni	31.9	30.9	11.7	24.9
unc	32.3	30.4	7.0	22.1
lon	32.9	33.5	12.1	26.5
gsi	33.3	31.9	14.0	23.7
pcl	33.9	32.5	5.5	25.6
lta	40.5	40.9	17.0	35.7
afw	44.8	45.5	13.3	36.2
uoc	54.3	55.7	24.0	45.6
qtz	93.4	96.4	12.8	15.3

**Table B.19** Relative configurational energies [kJ/mol/Zn] of mIm polymorphs ranked according to the PBE-D2 predicted stabilities.

Polymorph	PBE-D2	PBE-D3(BJ)	intraZIF	AMBER
zni	0.0	0.0	0.0	0.0
coi	7.1	12.5	11.4	15.5
crb	7.7	0.4	23.0	-14.5
qtz	8.1	5.1	10.8	-23.5
dia	9.3	-6.7*	11.6	-26.3
sod (ZIF-8)	10.1	3.6	42.1	-10.2
unc	16.6	3.0	22.6	-10.9
uni	17.4	16.4	19.8	-12.2
unj	17.6	16.4	39.3	8.0
mmt	18.3	16.6	13.4	-2.5
gis	20.8	18.5	63.5	12.6
cfc	20.8	14.2	42.7	0.4
irl	21.3	19.0	36.1	4.0
cag	21.8	17.4	46.0	4.0
mer	22.0	21.2	56.4	9.8
sra	22.1	19.5	47.3	13.4
lon	22.5	15.5	45.1	2.7
neb	23.4	20.3	25.6	-2.2
pcl	24.5	19.7	50.3	12.3
dft	27.0	23.2	60.0	14.7
gsi	28.2	23.8	29.1	5.0
pcb	29.6	26.9	58.3	13.0
lcs	36.1	32.2	47.1	-0.6
lta	46.3	41.5	63.7	20.6
unh	69.9	74.4	81.1	80.3

*\*The dia polymorphs is predicted to be slightly lower in energy than the zni polymorph when using PBE-D3(BJ).*

## ***B.9 Born-Oppenheimer Molecular Dynamics (BOMD) Data for SALEM-2, ZIF-7, ZIF-8, and ZIF-90***

The sections below show analysis of the BOMD simulations involving the periodic ZIF structures. This analysis examines some combination of relative potential energies, atomic forces, N-Zn bond lengths, and N-Zn-N angle bending for each structure in order to compare the intraZIF-FF to the AMBER-FF as well as justify the functional form of the intraZIF-FF. **This BOMD data was not used to fit the intraZIF-FF and is only used as reference data for benchmarking.**

### ***B.9.1 SALEM-2***

For the SALEM-2 structure, we have made comparisons between atomic forces predicted by the AMBER-FF (pink) and the intraZIF-FF (light blue) in reference to PBE-D3(BJ) forces from BOMD simulations at 700 K and 1.0 bar. These comparisons are shown in Tables B.20-B.25 for the six atom types.

**Table B.20** Force comparisons for the Zn atom type (n=97992) of the AMBER and intraZIF FFs to BOMD forces.

<b>AMBER</b>	<b>F<sub>x</sub>_MAE</b>	<b>F<sub>y</sub>_MAE</b>	<b>F<sub>z</sub>_MAE</b>	<b>F<sub>mag</sub>_MAE</b>
	41.60	42.43	43.47	59.35
	<b>F<sub>x</sub>_MSD</b>	<b>F<sub>y</sub>_MSD</b>	<b>F<sub>z</sub>_MSD</b>	<b>F<sub>mag</sub>_MSD</b>
	-0.04	-1.49	-0.53	51.33
	<b>F<sub>x</sub>_RMSD</b>	<b>F<sub>y</sub>_RMSD</b>	<b>F<sub>z</sub>_RMSD</b>	<b>F<sub>mag</sub>_RMSD</b>
	53.95	55.33	56.49	75.18
	<b>F<sub>x</sub>_NRMSD</b>	<b>F<sub>y</sub>_NRMSD</b>	<b>F<sub>z</sub>_NRMSD</b>	<b>F<sub>mag</sub>_NRMSD</b>
	65.56	66.67	69.21	127.51
<b>intraZIF</b>	<b>F<sub>x</sub>_MAE</b>	<b>F<sub>y</sub>_MAE</b>	<b>F<sub>z</sub>_MAE</b>	<b>F<sub>mag</sub>_MAE</b>
	33.07	34.37	34.30	50.75
	<b>F<sub>x</sub>_MSD</b>	<b>F<sub>y</sub>_MSD</b>	<b>F<sub>z</sub>_MSD</b>	<b>F<sub>mag</sub>_MSD</b>
	2.47	1.20	-1.47	48.46
	<b>F<sub>x</sub>_RMSD</b>	<b>F<sub>y</sub>_RMSD</b>	<b>F<sub>z</sub>_RMSD</b>	<b>F<sub>mag</sub>_RMSD</b>
	41.90	43.45	43.07	60.41
	<b>F<sub>x</sub>_NRMSD</b>	<b>F<sub>y</sub>_NRMSD</b>	<b>F<sub>z</sub>_NRMSD</b>	<b>F<sub>mag</sub>_NRMSD</b>
	50.92	52.35	52.76	102.46

*MAE, MSD, and RMSD have units of kJ mol A<sup>-1</sup>. NRMSD is a percent.*



**Table B.21** Force comparisons for the N atom type (n=391968) of the AMBER and intraZIF FFs to BOMD forces.

<b>AMBER</b>	<b>F<sub>x</sub>_MAE</b>	<b>F<sub>y</sub>_MAE</b>	<b>F<sub>z</sub>_MAE</b>	<b>F<sub>mag</sub>_MAE</b>
	53.92	54.02	54.35	65.10
	<b>F<sub>x</sub>_MSD</b>	<b>F<sub>y</sub>_MSD</b>	<b>F<sub>z</sub>_MSD</b>	<b>F<sub>mag</sub>_MSD</b>
	0.87	0.90	-0.60	35.32
	<b>F<sub>x</sub>_RMSD</b>	<b>F<sub>y</sub>_RMSD</b>	<b>F<sub>z</sub>_RMSD</b>	<b>F<sub>mag</sub>_RMSD</b>
<b>intraZIF</b>	70.53	70.14	71.20	86.03
	<b>F<sub>x</sub>_NRMSD</b>	<b>F<sub>y</sub>_NRMSD</b>	<b>F<sub>z</sub>_NRMSD</b>	<b>F<sub>mag</sub>_NRMSD</b>
	51.16	50.63	51.99	83.41
	<b>F<sub>x</sub>_MAE</b>	<b>F<sub>y</sub>_MAE</b>	<b>F<sub>z</sub>_MAE</b>	<b>F<sub>mag</sub>_MAE</b>
	45.00	44.28	44.95	46.90
<b>intraZIF</b>	<b>F<sub>x</sub>_MSD</b>	<b>F<sub>y</sub>_MSD</b>	<b>F<sub>z</sub>_MSD</b>	<b>F<sub>mag</sub>_MSD</b>
	0.08	-0.08	0.02	-3.12
	<b>F<sub>x</sub>_RMSD</b>	<b>F<sub>y</sub>_RMSD</b>	<b>F<sub>z</sub>_RMSD</b>	<b>F<sub>mag</sub>_RMSD</b>
	57.29	56.05	56.96	60.16
	<b>F<sub>x</sub>_NRMSD</b>	<b>F<sub>y</sub>_NRMSD</b>	<b>F<sub>z</sub>_NRMSD</b>	<b>F<sub>mag</sub>_NRMSD</b>
	41.55	40.46	41.59	58.33

MAE, MSD, and RMSD have units of  $\text{kJ mol}^{-1}$ . NRMSD is a percent.

**Table B.22** Force comparisons for the C<sub>1</sub> atom type (n=195984) of the AMBER and intraZIF FFs to BOMD forces.

<b>AMBER</b>	<b>F<sub>x</sub>_MAE</b>	<b>F<sub>y</sub>_MAE</b>	<b>F<sub>z</sub>_MAE</b>	<b>F<sub>mag</sub>_MAE</b>
	57.48	56.54	56.02	69.49
	<b>F<sub>x</sub>_MSD</b>	<b>F<sub>y</sub>_MSD</b>	<b>F<sub>z</sub>_MSD</b>	<b>F<sub>mag</sub>_MSD</b>
	1.68	0.18	-2.86	42.73
	<b>F<sub>x</sub>_RMSD</b>	<b>F<sub>y</sub>_RMSD</b>	<b>F<sub>z</sub>_RMSD</b>	<b>F<sub>mag</sub>_RMSD</b>
<b>intraZIF</b>	74.75	73.15	72.77	91.78
	<b>F<sub>x</sub>_NRMSD</b>	<b>F<sub>y</sub>_NRMSD</b>	<b>F<sub>z</sub>_NRMSD</b>	<b>F<sub>mag</sub>_NRMSD</b>
	46.64	46.50	44.45	74.73
	<b>F<sub>x</sub>_MAE</b>	<b>F<sub>y</sub>_MAE</b>	<b>F<sub>z</sub>_MAE</b>	<b>F<sub>mag</sub>_MAE</b>
	51.50	49.57	50.52	55.44
<b>intraZIF</b>	<b>F<sub>x</sub>_MSD</b>	<b>F<sub>y</sub>_MSD</b>	<b>F<sub>z</sub>_MSD</b>	<b>F<sub>mag</sub>_MSD</b>
	1.02	0.10	-3.10	7.95
	<b>F<sub>x</sub>_RMSD</b>	<b>F<sub>y</sub>_RMSD</b>	<b>F<sub>z</sub>_RMSD</b>	<b>F<sub>mag</sub>_RMSD</b>
	65.82	63.12	64.32	71.58
	<b>F<sub>x</sub>_NRMSD</b>	<b>F<sub>y</sub>_NRMSD</b>	<b>F<sub>z</sub>_NRMSD</b>	<b>F<sub>mag</sub>_NRMSD</b>
	41.07	40.12	39.29	58.28

MAE, MSD, and RMSD have units of  $\text{kJ mol}^{-1}$ . NRMSD is a percent.

**Table B.23** Force comparisons for the C<sub>2</sub> atom type (n=391968) of the AMBER and intraZIF FFs to BOMD forces.

<b>AMBER</b>	<b>F<sub>x</sub>_MAE</b>	<b>F<sub>y</sub>_MAE</b>	<b>F<sub>z</sub>_MAE</b>	<b>F<sub>mag</sub>_MAE</b>
	57.17	56.41	57.92	72.18
	<b>F<sub>x</sub>_MSD</b>	<b>F<sub>y</sub>_MSD</b>	<b>F<sub>z</sub>_MSD</b>	<b>F<sub>mag</sub>_MSD</b>
	0.07	2.12	0.34	53.28
	<b>F<sub>x</sub>_RMSD</b>	<b>F<sub>y</sub>_RMSD</b>	<b>F<sub>z</sub>_RMSD</b>	<b>F<sub>mag</sub>_RMSD</b>
	73.99	73.50	75.66	94.71
	<b>F<sub>x</sub>_NRMSD</b>	<b>F<sub>y</sub>_NRMSD</b>	<b>F<sub>z</sub>_NRMSD</b>	<b>F<sub>mag</sub>_NRMSD</b>
	46.69	46.34	47.01	74.50
<b>intraZIF</b>	<b>F<sub>x</sub>_MAE</b>	<b>F<sub>y</sub>_MAE</b>	<b>F<sub>z</sub>_MAE</b>	<b>F<sub>mag</sub>_MAE</b>
	60.35	60.14	61.22	69.87
	<b>F<sub>x</sub>_MSD</b>	<b>F<sub>y</sub>_MSD</b>	<b>F<sub>z</sub>_MSD</b>	<b>F<sub>mag</sub>_MSD</b>
	0.99	2.80	-0.34	34.73
	<b>F<sub>x</sub>_RMSD</b>	<b>F<sub>y</sub>_RMSD</b>	<b>F<sub>z</sub>_RMSD</b>	<b>F<sub>mag</sub>_RMSD</b>
	77.39	77.49	79.33	91.11
	<b>F<sub>x</sub>_NRMSD</b>	<b>F<sub>y</sub>_NRMSD</b>	<b>F<sub>z</sub>_NRMSD</b>	<b>F<sub>mag</sub>_NRMSD</b>
	48.83	48.85	49.29	71.67

MAE, MSD, and RMSD have units of kJ mol A<sup>-1</sup>. NRMSD is a percent.

**Table B.24** Force comparisons for the H<sub>1</sub> atom type (n=195984) of the AMBER and intraZIF FFs to BOMD forces.

<b>AMBER</b>	<b>F<sub>x</sub>_MAE</b>	<b>F<sub>y</sub>_MAE</b>	<b>F<sub>z</sub>_MAE</b>	<b>F<sub>mag</sub>_MAE</b>
	18.33	17.51	18.43	23.26
	<b>F<sub>x</sub>_MSD</b>	<b>F<sub>y</sub>_MSD</b>	<b>F<sub>z</sub>_MSD</b>	<b>F<sub>mag</sub>_MSD</b>
	-0.44	0.19	2.05	10.70
	<b>F<sub>x</sub>_RMSD</b>	<b>F<sub>y</sub>_RMSD</b>	<b>F<sub>z</sub>_RMSD</b>	<b>F<sub>mag</sub>_RMSD</b>
	28.58	29.35	34.50	44.30
	<b>F<sub>x</sub>_NRMSD</b>	<b>F<sub>y</sub>_NRMSD</b>	<b>F<sub>z</sub>_NRMSD</b>	<b>F<sub>mag</sub>_NRMSD</b>
	32.91	36.43	38.02	55.71
<b>intraZIF</b>	<b>F<sub>x</sub>_MAE</b>	<b>F<sub>y</sub>_MAE</b>	<b>F<sub>z</sub>_MAE</b>	<b>F<sub>mag</sub>_MAE</b>
	17.52	16.35	17.36	21.39
	<b>F<sub>x</sub>_MSD</b>	<b>F<sub>y</sub>_MSD</b>	<b>F<sub>z</sub>_MSD</b>	<b>F<sub>mag</sub>_MSD</b>
	-0.11	0.87	1.91	7.63
	<b>F<sub>x</sub>_RMSD</b>	<b>F<sub>y</sub>_RMSD</b>	<b>F<sub>z</sub>_RMSD</b>	<b>F<sub>mag</sub>_RMSD</b>
	24.47	22.37	24.59	31.86
	<b>F<sub>x</sub>_NRMSD</b>	<b>F<sub>y</sub>_NRMSD</b>	<b>F<sub>z</sub>_NRMSD</b>	<b>F<sub>mag</sub>_NRMSD</b>
	28.18	27.76	27.10	40.06

MAE, MSD, and RMSD have units of kJ mol A<sup>-1</sup>. NRMSD is a percent.

**Table B.25** Force comparisons for the H<sub>2</sub> atom type (n=391968) of the AMBER and intraZIF FFs to BOMD forces.

<b>AMBER</b>	<b>F<sub>x</sub>_MAE</b>	<b>F<sub>y</sub>_MAE</b>	<b>F<sub>z</sub>_MAE</b>	<b>F<sub>mag</sub>_MAE</b>
	22.46	22.61	22.36	28.04
	<b>F<sub>x</sub>_MSD</b>	<b>F<sub>y</sub>_MSD</b>	<b>F<sub>z</sub>_MSD</b>	<b>F<sub>mag</sub>_MSD</b>
	-1.54	-2.84	0.77	17.18
	<b>F<sub>x</sub>_RMSD</b>	<b>F<sub>y</sub>_RMSD</b>	<b>F<sub>z</sub>_RMSD</b>	<b>F<sub>mag</sub>_RMSD</b>
<b>intraZIF</b>	31.07	32.37	33.64	43.51
	<b>F<sub>x</sub>_NRMSD</b>	<b>F<sub>y</sub>_NRMSD</b>	<b>F<sub>z</sub>_NRMSD</b>	<b>F<sub>mag</sub>_NRMSD</b>
	36.69	36.49	40.22	53.13
	<b>F<sub>x</sub>_MAE</b>	<b>F<sub>y</sub>_MAE</b>	<b>F<sub>z</sub>_MAE</b>	<b>F<sub>mag</sub>_MAE</b>
	26.14	26.50	26.10	32.80
<b>intraZIF</b>	<b>F<sub>x</sub>_MSD</b>	<b>F<sub>y</sub>_MSD</b>	<b>F<sub>z</sub>_MSD</b>	<b>F<sub>mag</sub>_MSD</b>
	-2.14	-3.50	1.26	22.35
	<b>F<sub>x</sub>_RMSD</b>	<b>F<sub>y</sub>_RMSD</b>	<b>F<sub>z</sub>_RMSD</b>	<b>F<sub>mag</sub>_RMSD</b>
	35.45	36.22	35.08	46.02
	<b>F<sub>x</sub>_NRMSD</b>	<b>F<sub>y</sub>_NRMSD</b>	<b>F<sub>z</sub>_NRMSD</b>	<b>F<sub>mag</sub>_NRMSD</b>
	41.87	40.83	41.94	56.21

*MAE, MSD, and RMSD have units of kJ mol A<sup>-1</sup>. NRMSD is a percent.*

### B.9.2 ZIF-8 BOMD Analysis

For the ZIF-8 structure, we have made comparisons between the relative potential energies from BOMD simulations and the AMBER-FF as well as the intraZIF-FF as shown in Figure B.21.

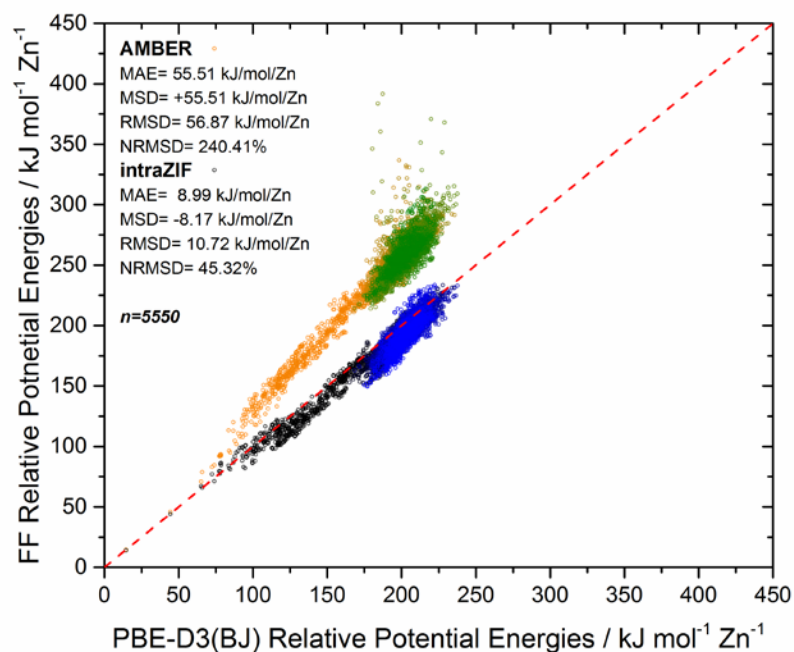


**Figure B.21** ZIF-8 relative potential energies as predicted by the AMBER-FF and intraZIF-FF in reference to PBE-D3(BJ) relative energies from fully periodic BOMD simulations at 700 K.

### B.9.3 ZIF-90 BOMD Analysis

For the ZIF-90 structure, we have made comparisons between the relative potential energies from BOMD simulations and the AMBER-FF as well as the intraZIF-FF as shown in Figure B.22. We also examined the Zn-N stretch and the N-Zn-N bend as a function of temperature to verify the functional form used in the intraZIF-FF as shown in Figure B.23.

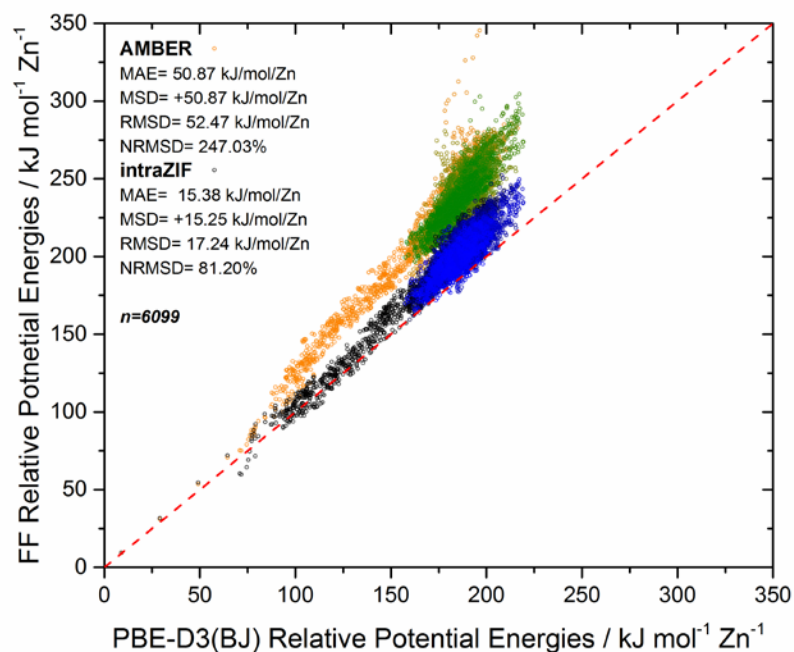
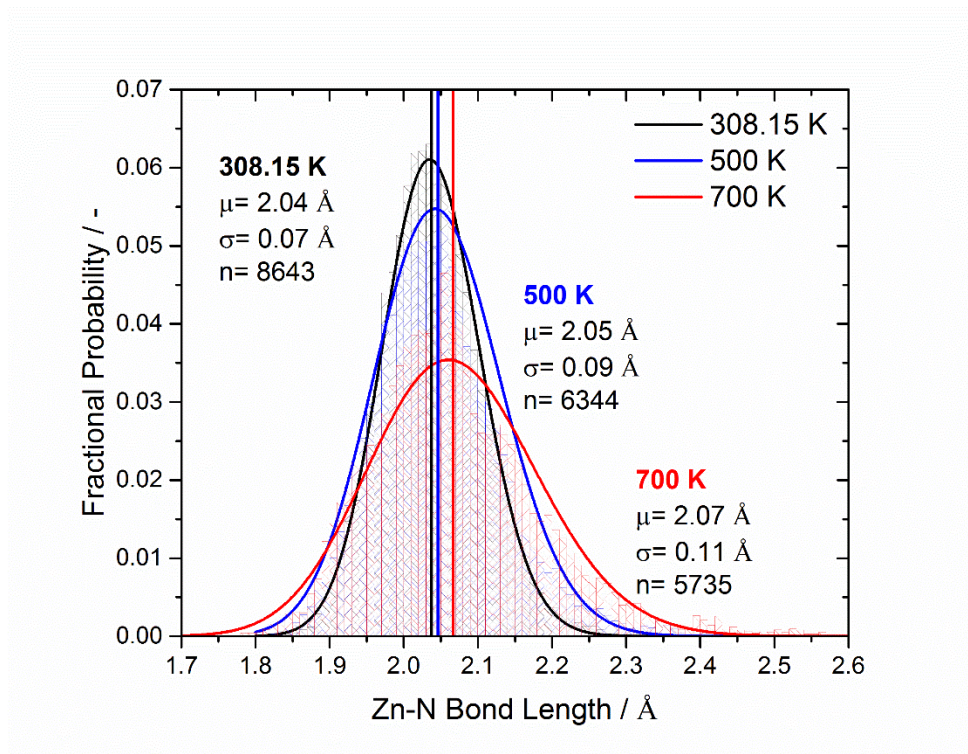


**Figure B.22** ZIF-90 relative potential energies as predicted by the AMBER-FF and intraZIF-FF in reference to PBE-D3(BJ) relative energies from fully periodic BOMD simulations at 700 K.

(a)



(b)

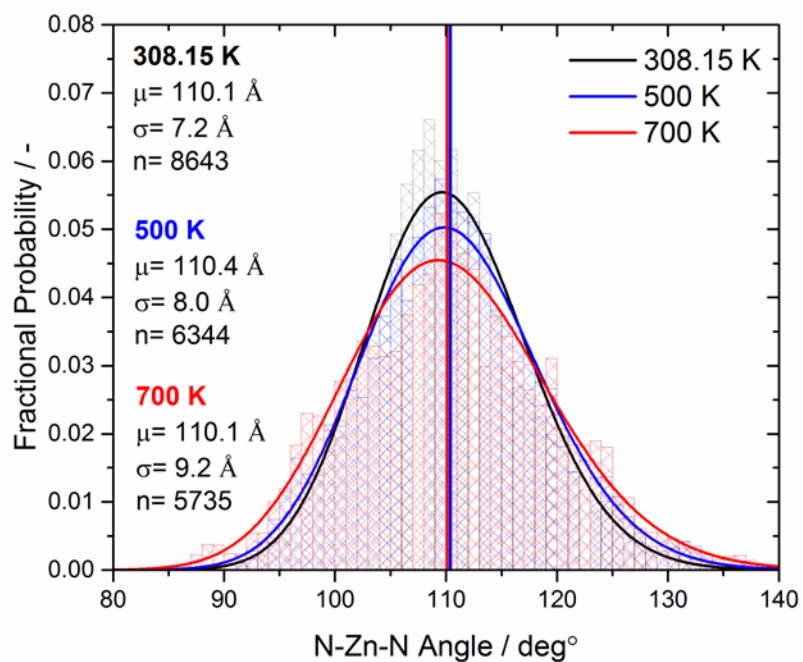


**Figure B.23** Histograms with fitted lognormal distributions of (a) Zn-N bond lengths and (b) N-Zn-N angles in ZIF-90 at temperatures of 308.15, 500, and 700 K and a pressure of 1.0 bar.  $\mu$  ( $\mu$ ),  $\sigma$  ( $\sigma$ ) are the mean and standard deviation of the lognormal distribution and  $n$  is the number of samples.

#### B.9.4 ZIF-7 BOMD Analysis

For the ZIF-7 structure, we have made comparisons between the relative potential energies from BOMD simulations and the AMBER-FF as well as the intraZIF-FF as shown in Figure B.24.

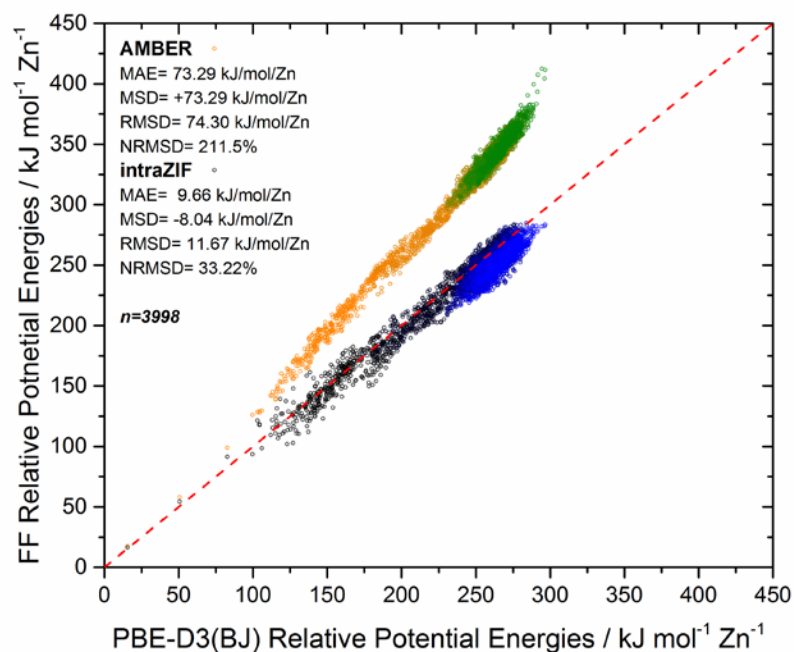


**Figure B.24** ZIF-7 relative potential energies as predicted by the AMBER-FF and intraZIF-FF in reference to PBE-D3(BJ) relative energies from fully periodic BOMD simulations at 700 K.

## ***B.10 Light Gas Diffusion in SALEM-2, ZIF-8, ZIF-90, and ZIF-7***

### ***B.10.1 Adsorbate Force Fields***

We examined five single-site 12-6 LJ fluids of increasing molecular size (He<sup>179</sup>, Kr<sup>74</sup>, Xe<sup>74</sup>, Rn<sup>74</sup>, and SF<sub>6</sub><sup>427</sup>), four small 3-site rigid linear molecules (H<sub>2</sub><sup>181</sup>, O<sub>2</sub><sup>183</sup>, N<sub>2</sub><sup>174,182</sup>, CO<sub>2</sub><sup>184</sup>) and thirteen alcohols paraffins, olefins were modeled using the united atom TraPPE FF<sup>176,177,428</sup>: CH<sub>3</sub>OH (methanol), C<sub>2</sub>H<sub>5</sub>OH (ethanol), C<sub>4</sub>H<sub>9</sub>OH (1-butanol), CH<sub>3</sub>-CO-CH<sub>3</sub> (acetone)<sup>429</sup>, CH<sub>4</sub>, C<sub>2</sub>H<sub>4</sub>=, C<sub>2</sub>H<sub>6</sub>, C<sub>3</sub>H<sub>6</sub>=, C<sub>3</sub>H<sub>8</sub>, 1-C<sub>4</sub>H<sub>8</sub>=, n-C<sub>4</sub>H<sub>10</sub>, iso-C<sub>4</sub>H<sub>8</sub>=, and iso-C<sub>4</sub>H<sub>10</sub>. The single and double C-C bonds were modeled with a harmonic potential<sup>178</sup>, a departure from the original TraPPE implementation to facilitate implementation in LAMMPS. The OPLS force field was used to model rigid C<sub>6</sub>H<sub>6</sub>, m-C<sub>8</sub>H<sub>10</sub>, o-C<sub>8</sub>H<sub>10</sub>, and p-C<sub>8</sub>H<sub>10</sub>.<sup>430,431</sup> We also examined water, N,N-dimethylformamide (DMF), imidazole, and 1,3,7-trimethylxanthine (caffeine, C<sub>8</sub>H<sub>10</sub>N<sub>4</sub>O<sub>2</sub>). We have also included H<sub>2</sub>O modeled using the SPC/E FF designed to work with long range electrostatic solvers (Ewald)<sup>432,433</sup>. N,N-Dimethylformamide (DMF) was modeled using the six-interaction site OPLS model (CS2) by Chalaris and Samios.<sup>434</sup> Imidazole was modeled using the explicit hydrogen TraPPE FF.<sup>435</sup> 1,3,7-trimethylxanthine (caffeine, C<sub>8</sub>H<sub>10</sub>N<sub>4</sub>O<sub>2</sub>) was modeled using the rigid force field of Sanjeewa and Weerasinghe with the methyl functionalities as united atom groups.<sup>436</sup> A hybrid approach was adopted for determining molecular diameters. Molecular diameter definitions include kinetic diameters (KD), van der Waals diameters (vdW), as well as Lennard-Jones (LJ) diameters. Figure B.25 shows the adsorbates examined according to their molecular diameter and molecular weight. Table B.26 shows all the adsorbate LJ parameters. For those seeking to replicate these calculations, the bond lengths, angles, and dihedrals used are in the original references.



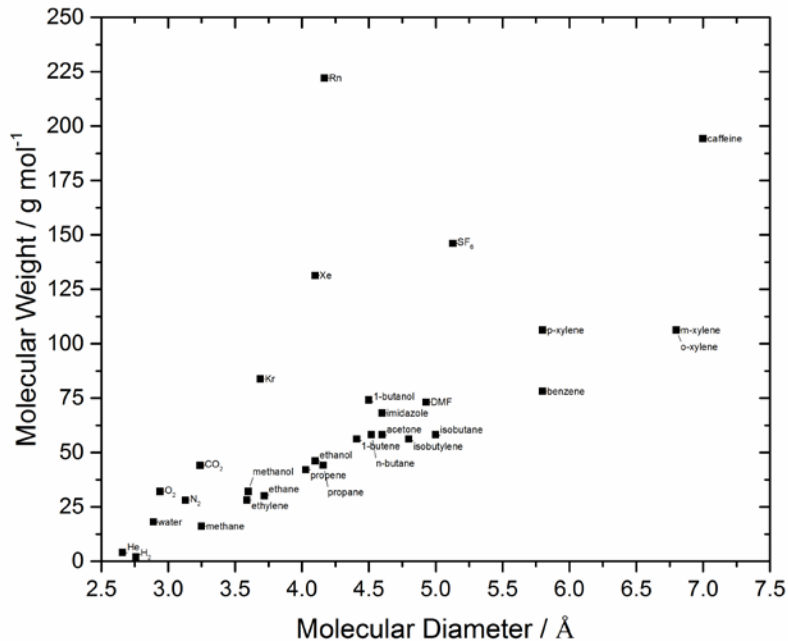


**Figure B.25** Molecular weight as a function of molecular diameter for the thirty adsorbates included in this study.

**Table B.26** Full list of adsorbate molecular diameters, LJ sites, molecular weights, LJ parameters, and charges.

Index	Adsorbate	Molecular Diameter [Å]	LJ Site (name)	MW [g mol <sup>-1</sup> ]	$\sigma$ [Å]	$\epsilon$ [kcal mol <sup>-1</sup> ]	$\epsilon$ [K]	q [e]
1	He	2.66 <sup>vdWD,56</sup>	He	4.00	2.64	0.0217	10.9	0.0
2	Kr	3.69 <sup>LJ</sup>	Kr	83.80	3.69	0.3378	170.0	0.0
3	Xe	4.10 <sup>LJ</sup>	Xe	131.29	4.10	0.4193	211.0	0.0
4	Rn	4.17 <sup>LJ</sup>	Rn	222.00	4.17	0.5962	300.0	0.0
5	SF <sub>6</sub>	5.13 <sup>LJ</sup>	SF <sub>6</sub>	146.06	5.13	0.4414	222.1	0.0
6	H <sub>2</sub>	2.76 <sup>vdWD,56</sup>	2xH <sub>H2</sub>	1.01	0.0	0.0	0.0	+0.468
			H <sub>COM</sub>	0.0	2.958	0.0729	36.7	-0.936
7	O <sub>2</sub>	2.94 <sup>vdWD,56</sup>	2xO <sub>O2</sub>	16.00	3.02	0.0974	49.0	-0.113
			O <sub>COM</sub>	0.0	0.0	0.0	0.0	+0.226
8	N <sub>2</sub>	3.64 <sup>KD,56</sup>	2xN <sub>N2</sub>	14.01	3.32	0.0724	36.43	-0.482
			N <sub>COM</sub>	0.00	0.0	0.0	0.0	+0.964
9	H <sub>2</sub> O	2.89 <sup>vdWD</sup>	O <sub>H2O</sub>	16.00	3.166	0.15535	78.18	-0.8476
			2xH <sub>H2O</sub>	1.01	0.0	0.0	0.0	0.4238
10	CO <sub>2</sub>	3.24 <sup>vdWD,56</sup>	C <sub>CO2</sub>	12.01	2.757	0.0559	28.12	+0.651
							9	2
			2xO <sub>CO2</sub>	16.00	3.033	0.1600	80.50	-0.3256
11	CH <sub>3</sub> OH	3.60 <sup>vdWD,437</sup>	CH <sub>3</sub> _sp3 <sup>a</sup>	15.03	3.750	0.1947	98.0	0.265
			O	16.00	3.020	0.1848	93.0	-0.700
			H	1.01	0.0	0.0	0.0	0.435

Table B.26 (continued)

12	C <sub>2</sub> H <sub>5</sub> OH	4.10 <sup>KD,60</sup>	CH <sub>3</sub> _sp3	15.03	3.750	0.1947	98.0	0.0
			CH <sub>2</sub> _sp3 <sup>a</sup>	14.02	3.950	0.0914	46.0	0.265
			O	16.00	3.020	0.1848	93.0	-0.700
			H	1.01	0.0	0.0	0.0	0.435
13	CH <sub>4</sub>	3.25 <sup>vdWD,56</sup>	CH <sub>4</sub>	16.04	3.73	0.2941	148.0	0.0
14	C <sub>2</sub> H <sub>4</sub> =	3.59 <sup>vdWD,56</sup>	2xCH <sub>2</sub>	14.02	3.675	0.1689	85.0	0.0
15	C <sub>2</sub> H <sub>6</sub>	3.72 <sup>vdWD,56</sup>	2xCH <sub>3</sub>	15.03	3.750	0.1947	98.0	0.0
16	C <sub>3</sub> H <sub>6</sub> =	4.03 <sup>vdWD,56</sup>	CH <sub>2</sub>	14.02	3.675	0.1689	85.0	0.0
			CH	13.02	3.730	0.0934	47.0	0.0
			CH <sub>3</sub>	15.03	3.750	0.1947	98.0	0.0
17	C <sub>3</sub> H <sub>8</sub>	4.16 <sup>vdWD,56</sup>	CH <sub>3</sub>	15.03	3.750	0.1947	98.0	0.0
			CH <sub>2</sub>	14.02	3.950	0.0914	46.0	0.0
18	1-C <sub>4</sub> H <sub>8</sub> =	4.41 <sup>vdWD,56</sup>	CH <sub>2</sub>	14.02	3.675	0.1689	85.0	0.0
			CH	13.02	3.730	0.0934	47.0	0.0
			CH <sub>2</sub>	14.02	3.950	0.0914	46.0	0.0
			CH <sub>3</sub>	15.03	3.750	0.1947	98.0	0.0
19	n-C <sub>4</sub> H <sub>10</sub>	4.52 <sup>vdWD,56</sup>	2x CH <sub>3</sub>	15.03	3.750	0.1947	98.0	0.0
			2xCH <sub>2</sub>	14.02	3.950	0.0914	46.0	0.0
20	iso-C <sub>4</sub> H <sub>8</sub> =	4.8 <sup>KD,56</sup>	2xCH <sub>3</sub>	15.03	3.750	0.1947	98.0	0.0
			C	12.01	3.850	0.0397	20.0	0.0
			CH <sub>2</sub>	14.02	3.675	0.1689	85.0	0.0
21	iso-C <sub>4</sub> H <sub>10</sub>	5.0 <sup>KD,56</sup>	CH <sub>3</sub> _sp3	15.03	3.750	0.1947	98.0	0.0
			CH_sp3	13.02	4.680	0.0199	10.0	0.0
22	C <sub>6</sub> H <sub>6</sub>	5.80 <sup>KD,437</sup>	6xC_xyl	12.01	3.55	0.0700	35.24	-0.115
			6xH_xyl	1.01	2.42	0.0299	15.03	0.115
23	m-C <sub>8</sub> H <sub>10</sub>	6.80 <sup>KD,437</sup>	6xC_xyl	12.01	3.55	0.0700	35.24	-0.115
			4xH_xyl	1.01	2.42	0.0299	15.03	0.115
			2xCH <sub>3</sub> _xyl	15.03	3.80	0.1699	85.51	0.115
24	o-C <sub>8</sub> H <sub>10</sub>	6.80 <sup>KD,437</sup>	6xC_xyl	12.01	3.55	0.0700	35.24	-0.115
			4xH_xyl	1.01	2.42	0.0299	15.03	0.115
			2xCH <sub>3</sub> _xyl	15.03	3.80	0.1699	85.51	0.115
25	p-C <sub>8</sub> H <sub>10</sub>	5.80 <sup>KD,437</sup>	6xC_xyl	12.01	3.55	0.0700	35.24	-0.115
			4xH_xyl	1.01	2.42	0.0299	15.03	0.115
			2xCH <sub>3</sub> _xyl	15.03	3.80	0.1699	85.51	0.115
26	(CH <sub>3</sub> ) <sub>2</sub> NC(O)H DMF	4.93 <sup>vdWD</sup>	2xCH <sub>3</sub> _dmf	15.03	3.80	0.1600	80.0	0.28
			N_dmf	14.01	3.20	0.1600	80.0	-0.57
			C_dmf	12.01	3.70	0.100	50.0	0.45
			O_dmf	16.00	2.96	0.2000	100.0	-0.50
			H_dmf	1.01	2.20	0.0160	8.0	0.06
27 <sup>EH</sup>	C <sub>3</sub> H <sub>4</sub> N <sub>2</sub>	4.6 <sup>LJ</sup>	N1_im	14.01	3.40	0.2820	141.0	-0.416
			C2_im	12.01	3.60	0.0614	30.7	0.224
			N3_im	14.01	3.20	0.1140	57.0	-0.485
			C4_im	12.01	3.60	0.0614	30.7	0.005
			C5_im	12.01	3.60	0.0614	30.7	0.030
			H6_im	1.01	0.50	0.0240	12.0	0.336
			H7_im	1.01	2.360	0.0510	25.5	0.097
			H8_im	1.01	2.360	0.0510	25.5	0.092
			H9_im	1.01	2.360	0.0510	25.5	0.117
28	1-butanol	4.5 <sup>LJ</sup>	CH <sub>3</sub>	15.03	3.75	0.1947	98.0	0.00
			2xCH <sub>2</sub>	14.02	3.95	0.0914	46.0	0.00
			CH <sub>2</sub> _sp3 <sup>a</sup>	14.02	3.95	0.0914	46.0	0.265
			O	16.00	3.02	0.1848	93.0	-0.700
			H	1.01	0.0	0.0	0.0	0.435

**Table B.26 (continued)**

29	acetone	4.6 <sup>LJ</sup>	2xCH <sub>3</sub> _sp <sup>3k</sup>	15.03	3.750	0.1947	98.0	0.00
			C_sp <sup>2k</sup>	12.01	3.820	0.0795	40.0	0.424
			O	16.00	3.050	0.1570	79.0	-0.424
30	caffeine	7.0 <sup>LJ</sup>	N1_caf	14.01	3.341	0.10466	52.67	-0.8395
			C2_caf	12.01	3.581	0.0908	45.69	0.9538
			N3_caf	14.01	3.341	0.10466	52.67	-0.7907
			C4_caf	12.01	3.581	0.0908	45.69	0.7944
			C5_caf	12.01	3.581	0.0908	45.69	0.3580
			C6_caf	12.01	3.581	0.0908	45.69	0.9451
			N7_caf	14.01	3.341	0.10466	52.67	-0.7854
			C8_caf	12.01	3.581	0.0908	45.69	0.4905
			N9_caf	14.01	3.341	0.10466	52.67	-0.6598
			C10_caf	12.01	3.581	0.0663	33.36	0.2768
			O11_caf	16.00	2.76	0.3057	153.8	-0.6036
			C12_caf	12.01	3.581	0.0663	33.36	0.2827
			O13_caf	16.00	2.76	0.3057	153.8	-0.7090
			C14_caf	12.01	3.581	0.0663	33.36	0.2866

### B.10.2 Free Energy Barriers for SALEM-2, ZIF-8, and ZIF-90

**Table B.27** Free energy barriers (FEB) for adsorbates in SALEM-2, ZIF-8, and ZIF-90 at 308 K and 1.01 bar.

Adsorbate	Im FEB [kJ mol <sup>-1</sup> ]	mIm FEB [kJ mol <sup>-1</sup> ]	ImCA FEB [kJ mol <sup>-1</sup> ]
He	8.7	10.4	8.6
H <sub>2</sub>	10.0	11.0	9.3
H <sub>2</sub> O	10.9	13.3	17.1
O <sub>2</sub>	11.5	13.8	12.0
N <sub>2</sub>	14.2	17.6	14.5
CO <sub>2</sub>	12.1	14.4	19.8
Methane	15.4	20.7	15.3
Ethylene	18.1	25.0	17.7
Methanol	14.0	20.8	18.8
Kr	15.3	19.6	13.9
Ethane	19.3	26.6	18.9
Propylene	20.9	31.4	21.3
Xe	19.6	32.6	24.4
Ethanol	18.4	32.2	25.2
Propane	22.8	37.6	26.5
Rn	19.3	35.3	24.2
1-Butene	23.3	37.9	26.3
1-Butanol	23.2	39.7	30.4
<i>n</i> -butane	23.9	39.2	26.5
Acetone	24.4	49.2	39.5
Imidazole	23.9	48.0	38.1
Isobutylene	30.7	57.9	49.3
DMF	25.3	61.9	60.0
Isobutane	34.0	66.7	57.3
SF <sub>6</sub>	36.2	71.4	64.1
Benzene	37.5	72.6	60.6
<i>p</i> -xylene	35.6	70.3	56.5
<i>m</i> -xylene	39.8	133.1	114.8
<i>o</i> -xylene	41.7	92.9	78.3
Caffeine	49.0	150.0	128.1

### B.10.3 Dynamical Correction Factors for SALEM-2, ZIF-8, and ZIF-90

**Table B.28** Dynamical correction factors for adsorbates in SALEM-2, ZIF-8, and ZIF-90 at 308 K and 1.01 bar.

Adsorbate	Im DCF [-]	mIm DCF [-]	ImCA DCF [-]
He	0.85	0.88	0.95
H <sub>2</sub>	0.77	0.88	0.89
H <sub>2</sub> O	0.35	0.83	0.70
O <sub>2</sub>	0.74	0.90	0.90
N <sub>2</sub>	0.66	0.87	0.91
CO <sub>2</sub>	0.47	0.75	0.84
Methane	0.61	0.84	0.90
Ethylene	0.64	0.86	0.88
Methanol	0.38	0.29	0.11
Kr	0.67	0.86	0.88
Ethane	0.64	0.83	0.83
Propylene	0.60	0.70	0.78
Xe	0.58	0.75	0.85
Ethanol	0.37	0.44	0.68
Propane	0.59	0.59	0.74
Rn	0.59	0.57	0.85
1-Butene	0.56	0.39	0.72
1-Butanol	0.40	0.52	0.42
<i>n</i> -butane	0.63	0.66	0.63
Acetone	0.33	0.11	0.60
Imidazole	--	0.18	0.27
Isobutylene	0.53	0.04	0.05
DMF	0.07	--	--
Isobutane	0.26	0.01	0.01
SF <sub>6</sub>	0.40	0.36	0.34
Benzene	0.48	0.60	0.47
<i>p</i> -xylene	0.44	0.48	0.42
<i>m</i> -xylene	0.08	0.02	0.22
<i>o</i> -xylene	0.30	0.07	0.02
Caffeine	0.07	0.004	0.24

*\*We were unable to obtain accurate statistics on the dynamical corrections for imidazole in SALEM-2 and DMF in ZIF-8 and ZIF-90 from computational challenges with sampling the starting positions of the trajectories.*

### B.10.4 Self-Diffusion Coefficients for SALEM-2, ZIF-8, and ZIF-90

**Table B.29** Self-diffusion coefficients for adsorbates in SALEM-2, ZIF-8, and ZIF-90 at 308 K and 1.01 bar.

Adsorbate	Im	mIm	ImCA
	$D_{\text{self}} [\text{cm}^2 \text{s}^{-1}]$	$D_{\text{self}} [\text{cm}^2 \text{s}^{-1}]$	$D_{\text{self}} [\text{cm}^2 \text{s}^{-1}]$
He	3.42E-04	2.11E-04	4.28E-04
H <sub>2</sub>	2.71E-04	2.43E-04	4.54E-04
H <sub>2</sub> O	3.13E-05	3.97E-05	5.86E-06
O <sub>2</sub>	3.50E-05	2.00E-05	4.74E-05
N <sub>2</sub>	1.39E-05	5.42E-06	1.77E-05
CO <sub>2</sub>	1.69E-05	1.22E-05	2.53E-06
Methane	1.19E-05	1.95E-06	2.14E-05
Ethylene	3.55E-06	2.93E-07	5.72E-06
Methanol	7.83E-06	5.29E-07	5.45E-07
Kr	6.52E-06	1.37E-06	1.58E-05
Ethane	2.38E-06	1.55E-07	3.28E-06
Propylene	1.04E-06	1.73E-08	9.75E-07
Xe	8.88E-07	8.10E-09	2.57E-07
Ethanol	1.60E-06	7.85E-09	2.26E-07
Propane	4.15E-07	1.32E-09	1.39E-07
Rn	6.49E-07	1.38E-09	1.71E-07
1-Butene	3.18E-07	7.00E-10	1.53E-07
1-Butanol	2.08E-07	4.11E-10	1.40E-08
<i>n</i> -butane	2.88E-07	6.45E-10	9.26E-08
Acetone	1.03E-07	2.34E-12	6.00E-10
Imidazole	--	5.43E-12	6.98E-10
Isobutylene	2.09E-08	2.51E-14	9.88E-13
DMF	1.32E-08	--	--
Isobutane	2.91E-09	3.80E-16	1.38E-14
SF <sub>6</sub>	1.17E-09	9.28E-16	1.67E-14
Benzene	1.19E-09	1.09E-15	1.86E-13
<i>p</i> -xylene	1.60E-09	2.02E-15	5.94E-13
<i>m</i> -xylene	5.11E-11	1.66E-27	4.08E-23
<i>o</i> -xylene	7.49E-11	3.92E-20	5.95E-18
Caffeine	1.39E-12	4.91E-31	2.37E-25

*\*We were unable to obtain accurate statistics on the dynamical corrections for imidazole in SALEM-2 and DMF in ZIF-8 and ZIF-90 from computational issues with sampling the starting positions of the trajectories. The reaction coordinate value corresponding to the barrier was incorrectly identified from the Gibbs free energy curves during our automated screening process. The RC was chosen simply by finding the maximum corresponding Gibbs free energy value along the curve; however, small deviations of this selection to the left (right) of the barrier led to a low acceptance of trajectories. The correct barrier could be selected through trial and error and this computational limitation will be addressed in future screening studies of diffusion.*

### B.10.5 Comparison to Prior Experimental Diffusion Data

Table B.30 shows a comparison between simulated diffusivities and those experimentally measured by Zhang et al.<sup>60</sup> Figure B.26 show a comparison between simulated diffusivities and those measured experimentally by Zhang et al.<sup>60</sup>, Eum et al.<sup>189</sup>, and Zhang et al.<sup>56</sup> Figure B.27 shows the Gibbs free energy barriers as a function of temperature for benzene and p-xylene.

**Table B.30** Comparisons of simulated diffusivities to the experimental diffusivities measured by Zhang et al.<sup>60</sup> The experimental diffusivities are measured at 50 °C and the simulated diffusivities are calculated at 35 °C.

Adsorbate	Experimental Data <sup>60</sup> [cm <sup>2</sup> s <sup>-1</sup> ]	NPT-MD (intraZIF-FF) [cm <sup>2</sup> s <sup>-1</sup> ]
water	$2.2 \times 10^{-7}$	$3.97 \times 10^{-5}$
ethanol	$3.9 \times 10^{-8}$	$7.85 \times 10^{-9}$
1-butanol	$3.8 \times 10^{-13}$	$4.1 \times 10^{-10}$
benzene	$5 \times 10^{-17}$	$1.09 \times 10^{-15}$
p-xylene	$3.4 \times 10^{-17}$	$2.02 \times 10^{-15}$
m-xylene	$1.4 \times 10^{-17}$	$1.66 \times 10^{-27}$
o-xylene	$8.5 \times 10^{-18}$	$3.92 \times 10^{-20}$

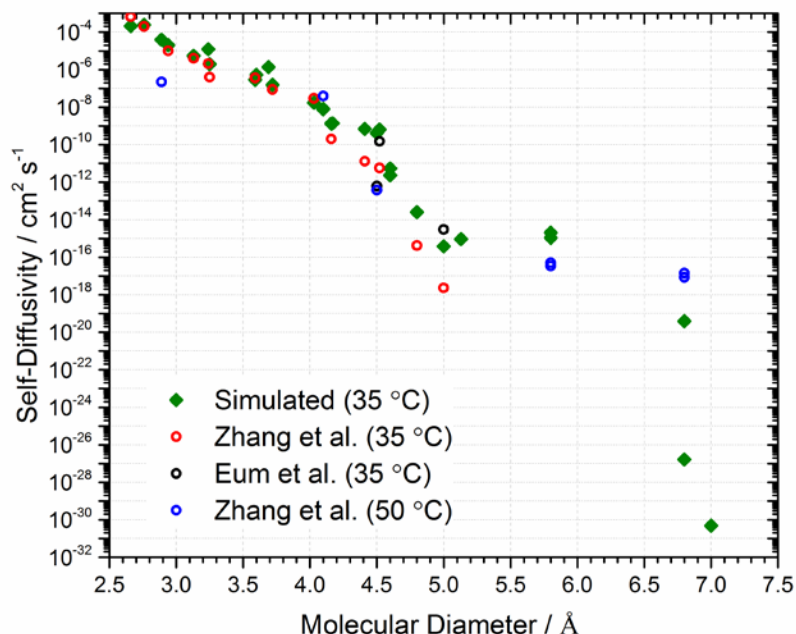


**Figure B.26** Comparisons of simulated and experimental self-diffusivities in ZIF-8 at infinite dilution and at the temperatures listed in the legend. The experimental data is taken from Zhang et al.<sup>56</sup> (open red circles), Eum et al.<sup>189</sup> (open black circles), and Zhang et al.<sup>60</sup> (open blue circles).

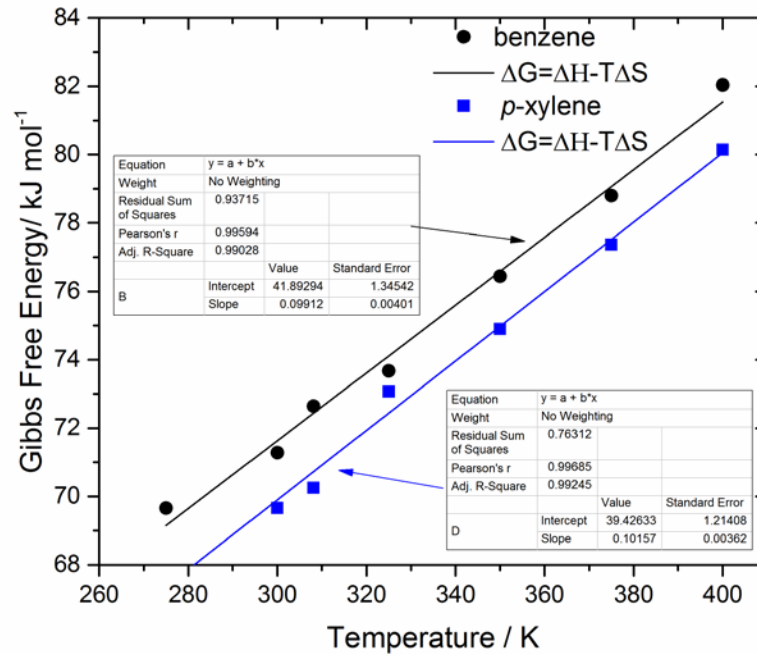


**Figure B.27** Gibbs free energy barriers of benzene and p-xylene as a function of temperature. Lines are linear fits to decouple the entropic and enthalpic contributions to diffusion.

#### B.10.6 Freeman Fitting Parameters

When fitting Equation 3.13 in Chapter 3, we use methane as our reference adsorbate where  $d_{ref}$  is 3.25 Å and  $D_{s,ref}$  is  $1.19 \times 10^{-5}$ ,  $2.14 \times 10^{-5}$ , and  $1.95 \times 10^{-6}$  cm<sup>2</sup> s<sup>-1</sup> for SALEM-2, ZIF-90, and ZIF-8 respectively. The fit parameters  $c'$  are 0.415, 0.810, and 1.08 Å<sup>-2</sup> with MAEs calculated by

$$\log\left(\frac{D_{s,i}}{D_{s,ref}}\right) \quad (B.1)$$

yielding 0.76, 2.70, and 2.79 for SALEM-2, ZIF-90, and ZIF-8 respectively. For the calculation of  $c'$  using

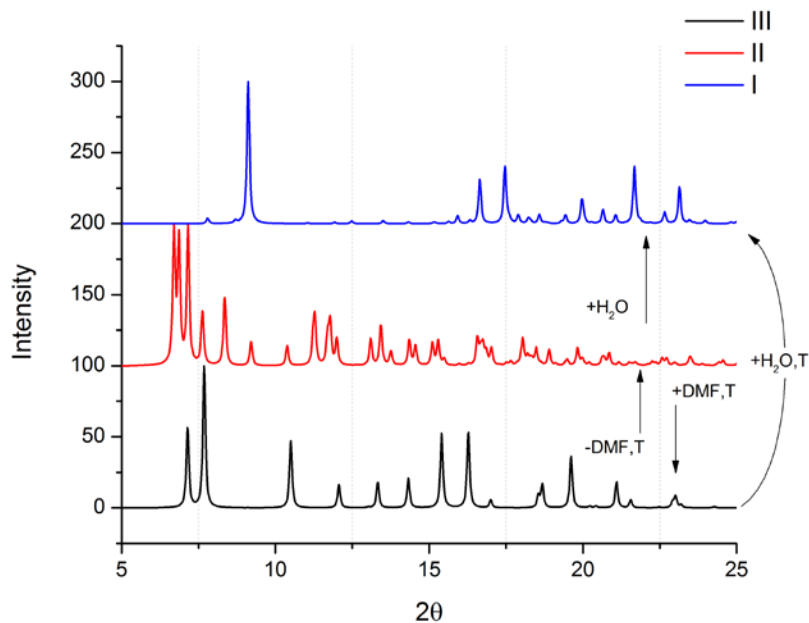
$$c' = \left(\frac{1-a}{RT}\right)c \quad (B.2)$$

for polymers,  $a=0.64$  and  $c=250-2400$  cal mol<sup>-1</sup> Å<sup>-2</sup> according to Freeman.<sup>294</sup>



### B.10.7 Focused Discussion of Diffusion in ZIF-7

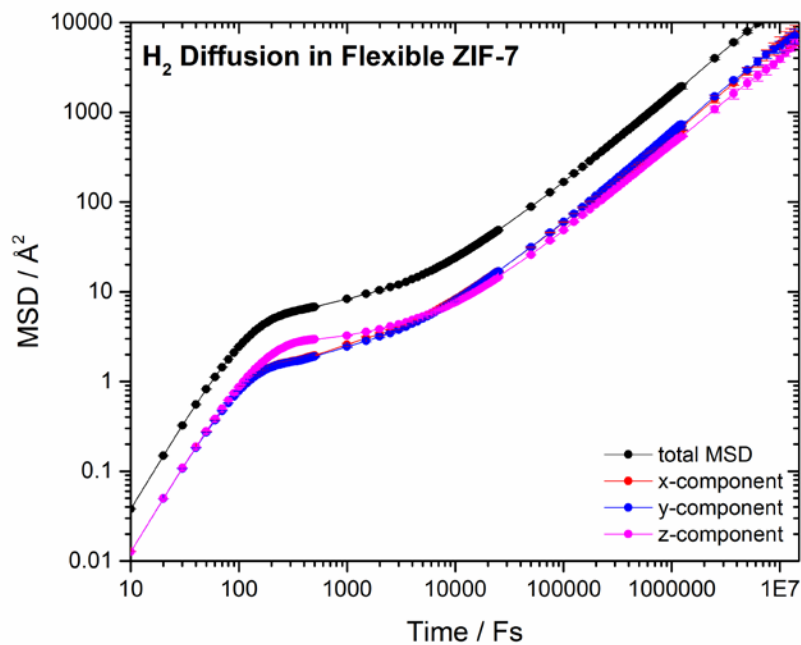
Figure B.28 shows the simulated XRD patterns for the three metastable phases of ZIF-7.



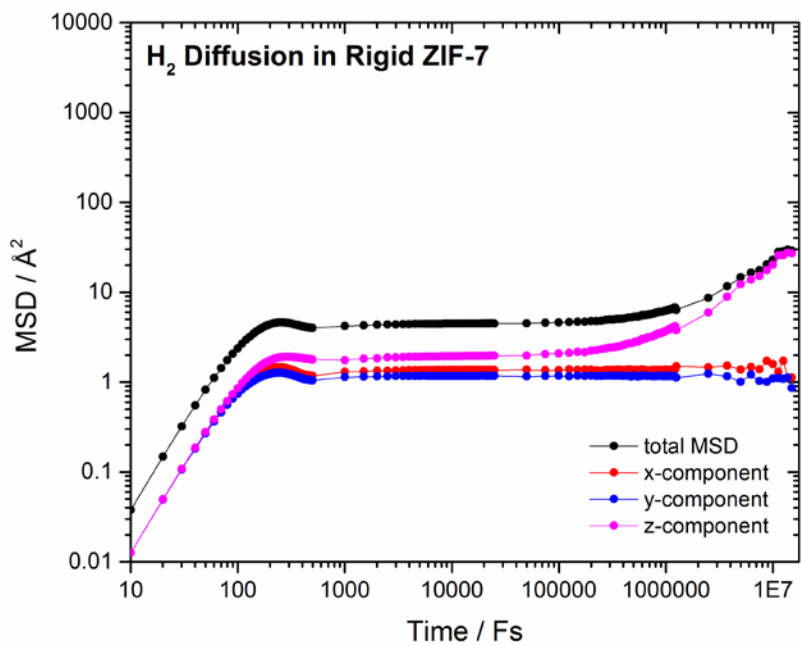
**Figure B.28** Simulated XRD patterns for the three stable metaphases of ZIF-7 as reported by Zhao et al. along with routes of formation depending on loading, temperature, and degradation.<sup>295</sup>

Figure B.29 shows MSDs for H<sub>2</sub> in flexible and rigid ZIF-7-I at 308 K. Figure B.30 shows the MSDs for methane and n-butane in flexible ZIF-7-I at 308 K. Figures B.31 and B.32 show trajectories taken by H<sub>2</sub> and CO<sub>2</sub> molecules respectively in flexible ZIF-7-I at 308 K.

(a)

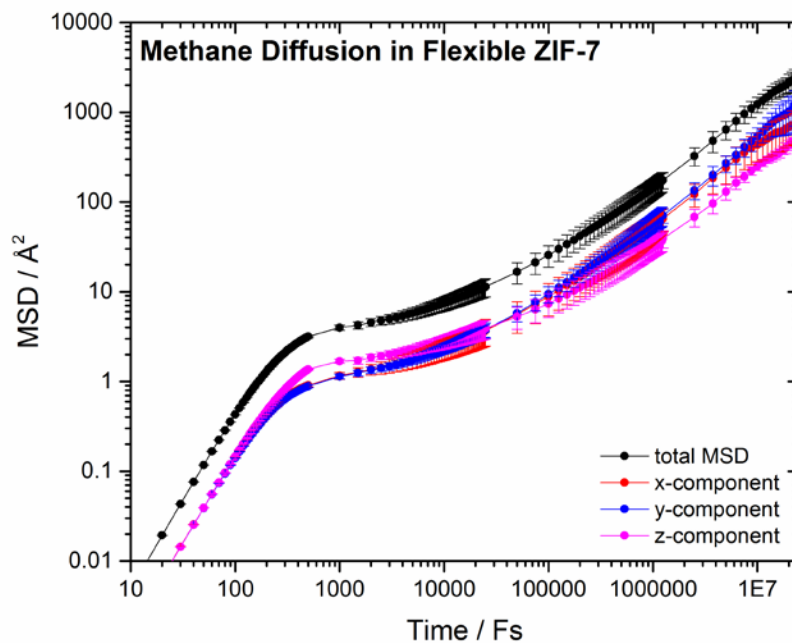


(b)



**Figure B.29** Total and directional MSDs for H<sub>2</sub> diffusion in (a) flexible and (b) rigid ZIF-7-I at a loading of three adsorbates per unit cell, 1.01 bar, and 308 K.

(a)



(b)

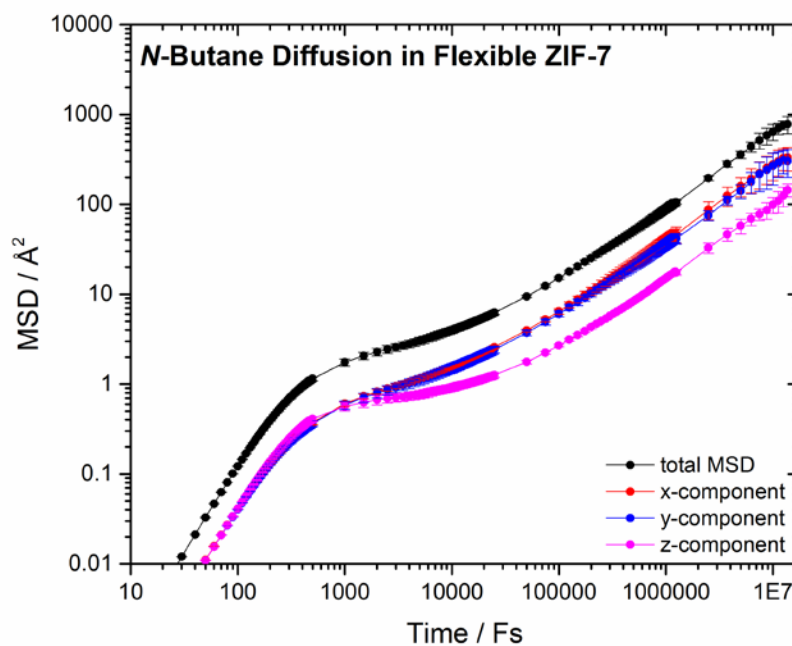


**Figure B.30** MSDs for (a) methane and (b) n-butane in flexible ZIF-7-I at a loading of three adsorbates per unit cell, 1.01 bar, and 308 K.

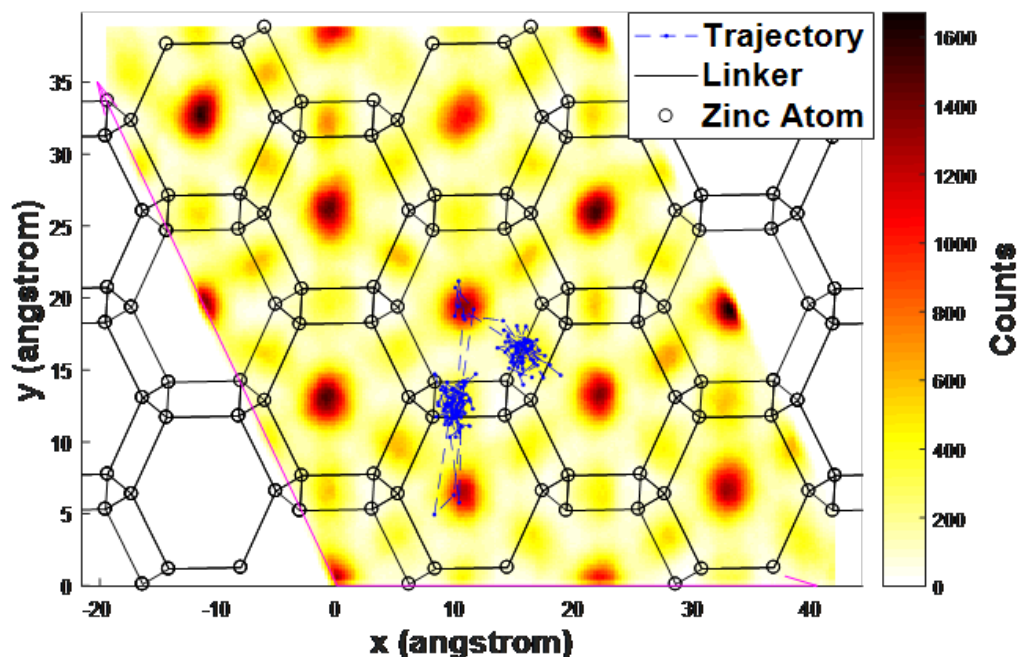


**Figure B.31** XY projection of the H<sub>2</sub> trajectories in the flexible ZIF-7-I structure. The XY-plane of the expanded ZIF-7 unit cell was divided into a 250 by 250 rectangular grid. Each grid point was sampled every 500 fs over a 10 ns trajectory, and the intensity of each sampled grid point was increased by the number of H<sub>2</sub> molecules whose XY centroid was within 0.5 Å (calculated using Euclidean Norm). The blue line shows the XY trajectory of a single H<sub>2</sub> sampled every 5 ps over a 750 ps trajectory. The Zn-linker overlay (black lines) on the graph is taken from the empty expanded rigid structure.

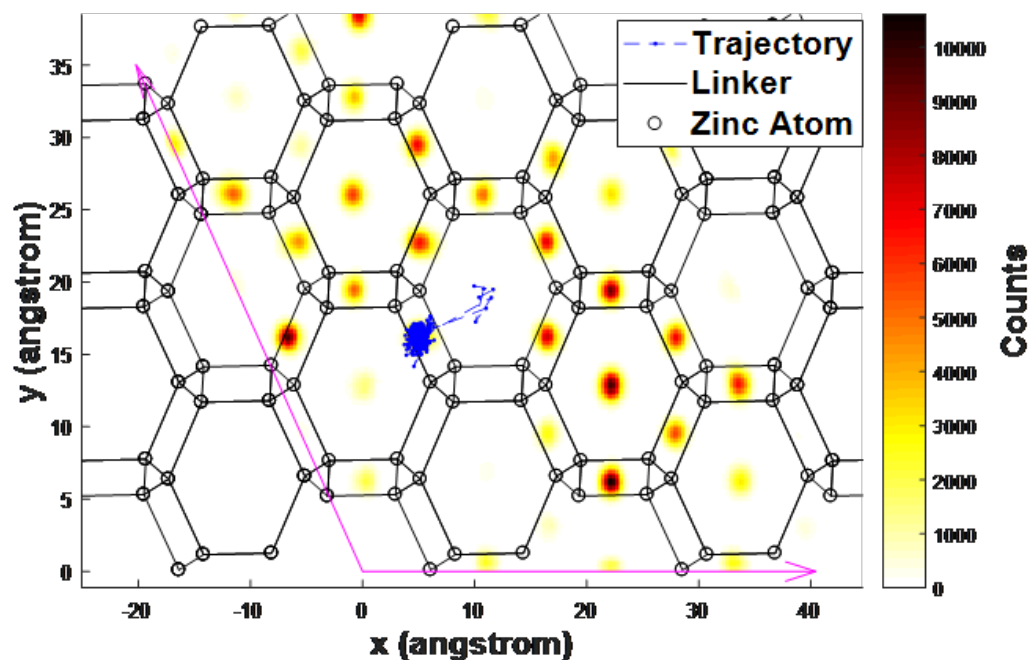


**Figure B.32** XY projection of the CO<sub>2</sub> trajectories in the flexible ZIF-7-I structure. The blue line shows the XY trajectory of a single CO<sub>2</sub> sampled every 5 ps over a 1000 ps trajectory. All other plot features are the same as shown in Figure B.31.

## APPENDIX C

### SUPPORTING INFORMATION FOR CHAPTER 4

#### *C.1 Synthesis of ZIF materials*

*ZIF-8*: 0.324 g 2-methylimidazole and 0.538 g sodium formate were dissolved in 40 mL methanol. This solution was mixed with another solution of 0.588 g zinc nitrate hexahydrate in 40 mL methanol. The resulting mixture was stirred for 1 minute and then sealed in a jar and heated to 90° C for 24 hours. The crystals formed were collected and washed with fresh methanol. The washing process was followed by centrifugation at 7500 rpm for 5 minutes. The washing-centrifugation process was repeated twice more. The crystals were air dried at 60° C and then degassed in vacuum at 160° C for 24 hours.

*ZIF-90*: 5.952 g zinc nitrate hexahydrate and 7.684 g imidazole-2-carboxaldehyde were dissolved in 200 mL N,N-dimethylformamide. The resulting solution was then heated to 120° C for held at that temperature for 10 minutes. The solution was then cooled down to room temperature and then left undisturbed for 2 days. The resulting crystals were then collected and washed in methanol. The washing process was followed by centrifugation at 7500 rpm for 5 minutes. The washing-centrifugation process was repeated twice more. The crystals were air dried at 60° C and then degassed in vacuum at 160° C for 24 hours.

*ZIF-8-90*: Table C.1 describes the synthesis compositions.

**Table C.1** Material quantities for synthesizing ZIF-8-90 mixed-linker materials.

<b>Material</b>	<b>Zn(NO<sub>3</sub>)<sub>2</sub>·6H<sub>2</sub>O</b>	<b>Imidazole-2-carboxaldehyde</b>	<b>2-methylimidazole</b>	<b>Sodium formate</b>
ZIF-8 <sub>25</sub> -90 <sub>75</sub>	2.974 g	0.962 g	2.464 g	2.72 g
ZIF-8 <sub>50</sub> -90 <sub>50</sub>	2.974 g	0.480 g	2.874 g	2.72 g
ZIF-8 <sub>61</sub> -90 <sub>39</sub>	2.974 g	0.384 g	2.956 g	2.72 g
ZIF-8 <sub>78</sub> -90 <sub>22</sub>	2.974 g	0.173 g	3.136 g	2.72 g
ZIF-8 <sub>89</sub> -90 <sub>11</sub>	2.974 g	0.076 g	3.218 g	2.72 g

The linkers and sodium formate were mixed in 100 mL methanol and dissolved completely by heating to 60° C. The solution was allowed to cool down to room temperature. Zinc nitrate was dissolved in 100 mL deionized water. The two solutions were mixed and stirred for 24 hours. The crystals were recovered by centrifugation at 7500 rpm. The crystals were then washed with fresh methanol and centrifuged thrice followed by air drying at 60° C. The crystals were degassed in vacuum at 160° C for 24 hours.

## ***C.2 Characterization of ZIF materials***

### ***C.2.1 Experimental and Simulated X-Ray Diffraction (XRD) Patterns***

Figure C.1 compares the experimental to simulated XRD patterns for several hybrid ZIF materials. The simulated XRD patterns were generated from 3x3x3 supercell atomic structures with random placement of linkers. Figure C.2 demonstrates that changing the SRO does not induce any significant change in the XRD pattern.

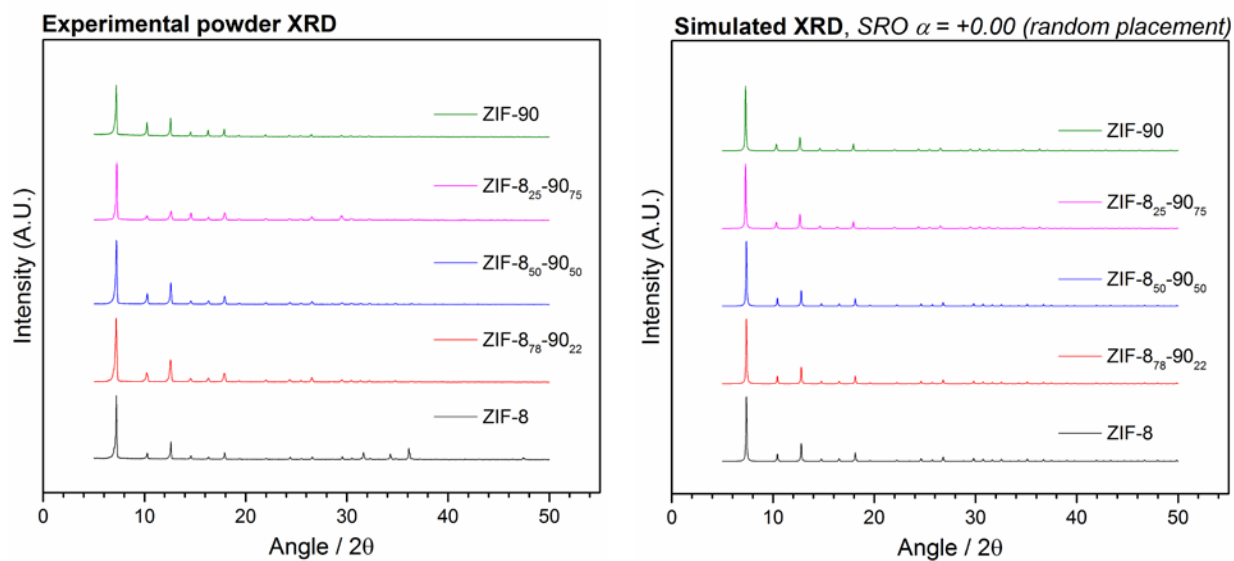


**Figure C.1** Measured and simulated XRD patterns of hybrid ZIF-8<sub>x</sub>-90<sub>100-x</sub> materials.

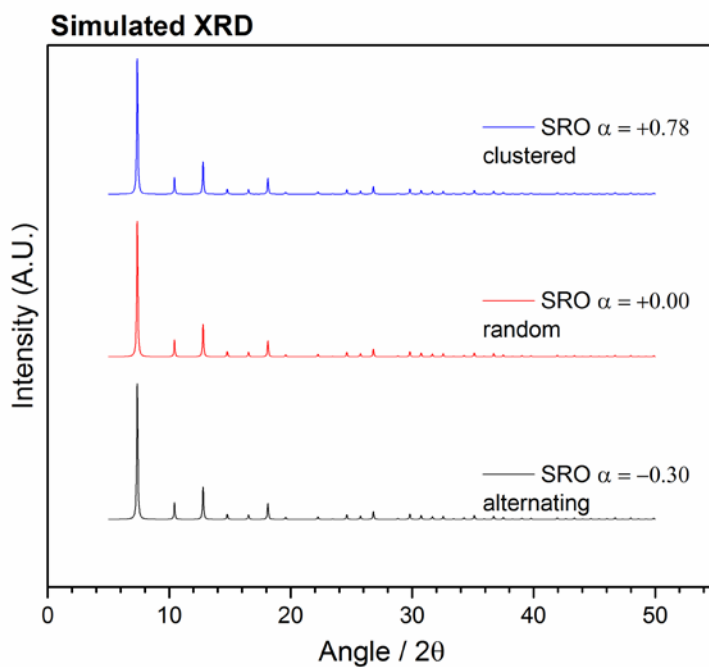


**Figure C.2** Simulated ZIF-8<sub>50</sub>-90<sub>50</sub> XRD patterns as a function of SRO with a 3x3x3 supercell.

### *C.2.2 SEM Imaging*

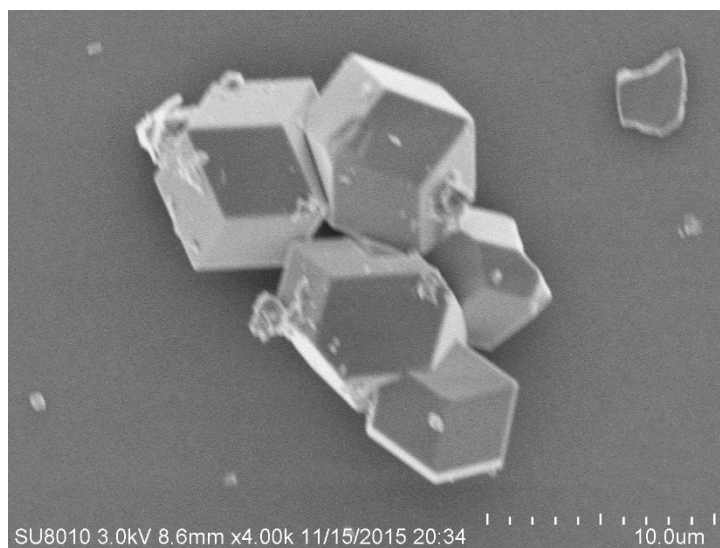


**Figure C.3** SEM image of ZIF-8 crystals.

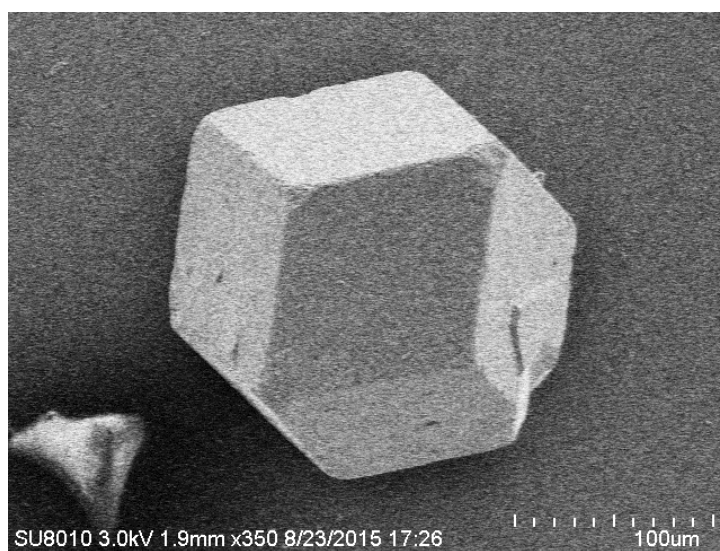


**Figure C.4** SEM image of a ZIF-90 crystal.



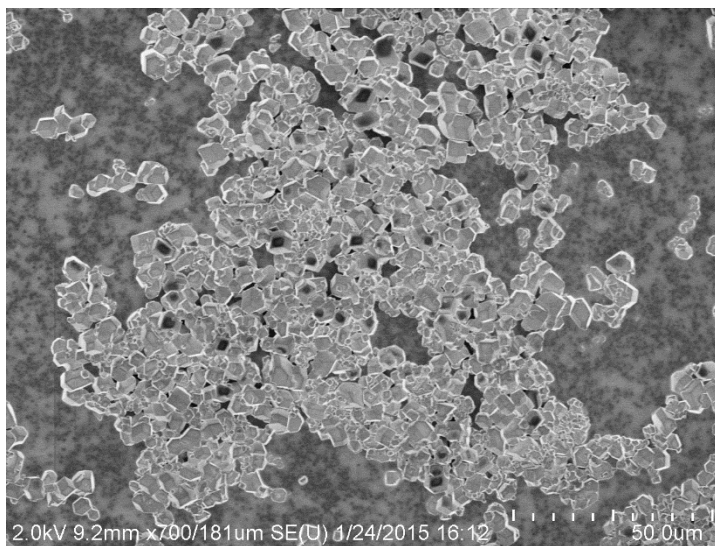


**Figure C.5** SEM image of ZIF-8<sub>50</sub>-90<sub>50</sub> crystals.

### *C.2.3 BET Surface Areas*

The BET surface areas of representative samples as measured on a TriStar nitrogen physisorption apparatus at 77 K are given in Table C.2.

**Table C.2** BET surface areas for several hybrid ZIF-8<sub>x</sub>-90<sub>100-x</sub> materials.

Sample	BET Surface Area (m <sup>2</sup> /g)
ZIF-8	1577
ZIF-8 <sub>78</sub> -90 <sub>22</sub>	1348
ZIF-8 <sub>50</sub> -90 <sub>50</sub>	1478
ZIF-8 <sub>25</sub> -90 <sub>75</sub>	1425
ZIF-90	1100

### *C.2.4 Solution NMR*

The composition of all mixed-linker ZIF samples were analyzed by <sup>1</sup>H-solution NMR. Samples were digested in deuterated (d<sub>4</sub>) acetic acid (Sigma Aldrich). The relative

composition of linkers were calculated by comparing the peak integrals for the respective proton signals. The ppm levels of relevant peaks are given in Table S3. Figure S.6 demonstrates an example liquid NMR spectrum for a hybrid ZIF-8<sub>x</sub>-90<sub>100-x</sub> material.

**Table C.3** Liquid NMR hydrogen peak locations in ppm.

Chemical entity (number of protons)	ppm
Methyl group on ZIF-8 linker (3)	2.7
Aldehyde group on ZIF-90 linker (1)	9.8
Proton on imidazolate ring (2)	7.3

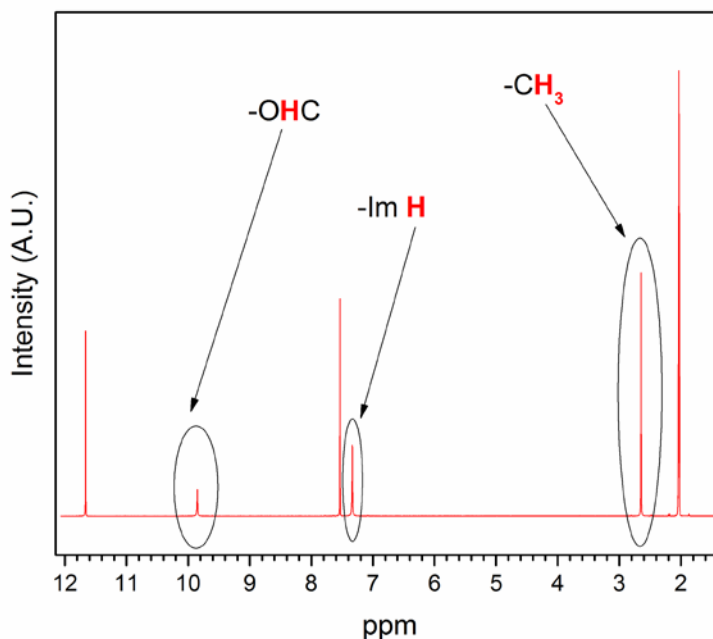


**Figure C.6** Liquid NMR spectrum for a hybrid ZIF-8<sub>x</sub>-90<sub>100-x</sub> material. Peaks are labeled according to each hydrogen type. Other peaks are from the solvent.

### C.2.5 Solid-State NMR

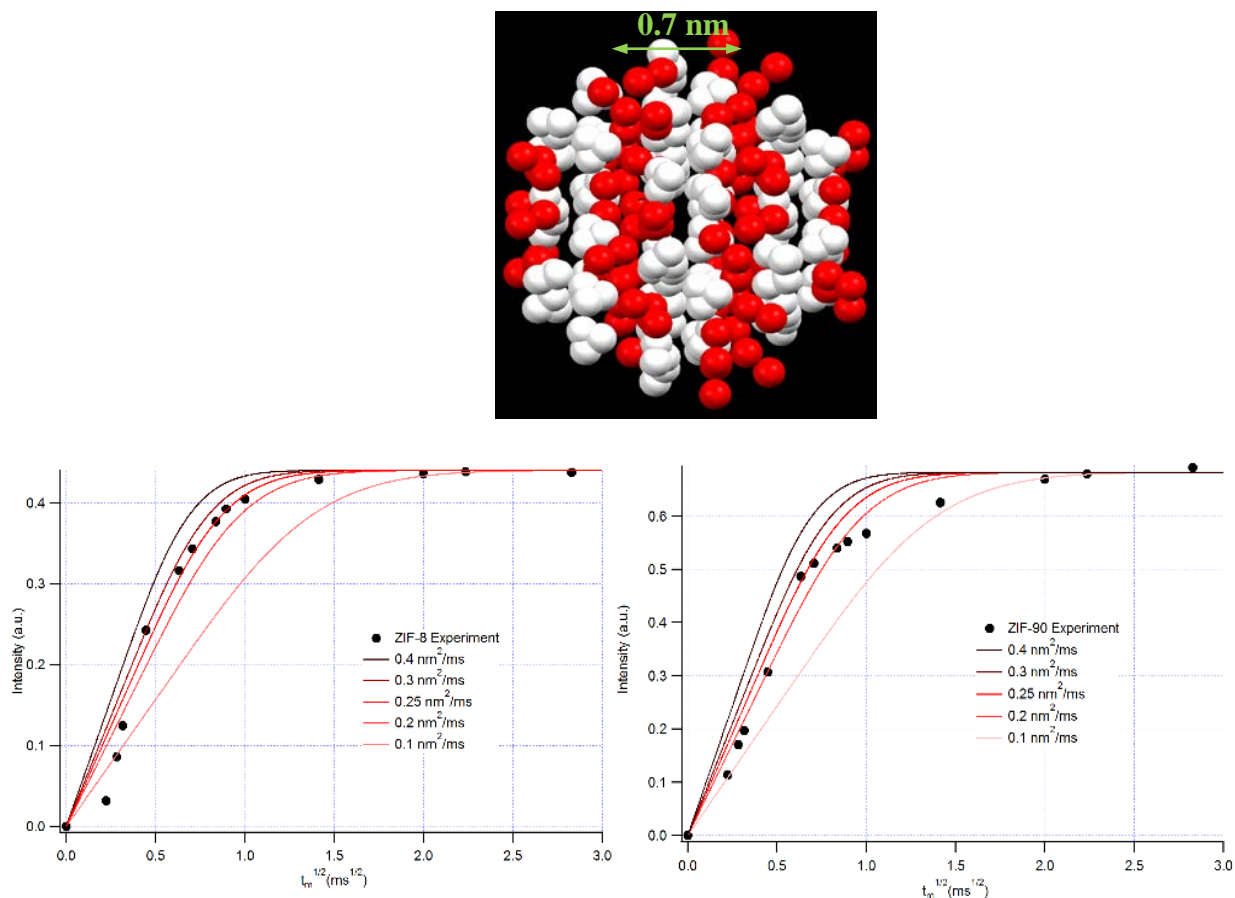


**Figure C.7** Schematic of the positions of the protons in the ZIF-8 crystal structure (top). The methyl protons are shown in red, and the imidazole protons are shown in white.  $^1\text{H}$  spin diffusion NMR curve for ZIF-8 (bottom left) and ZIF-90 (bottom right) as well as predicted curves using the lamellar morphology for different spin diffusion coefficients.

*C.2.6 Dimensions used in domain size calculations for intramolecular spin diffusion in ZIF-8 and ZIF-90*

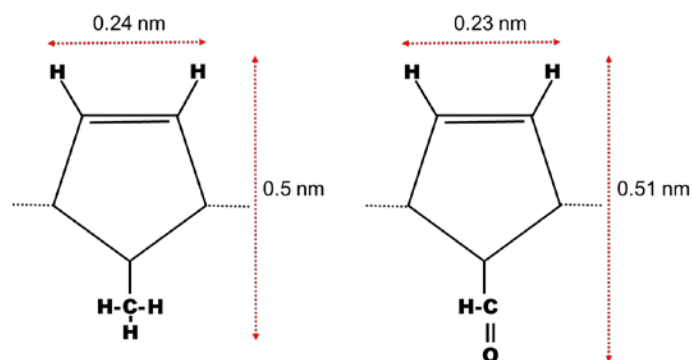


**Figure C.8** Representative distances used for calculation of intramolecular spin diffusion domains in ZIF-8 and ZIF-90.

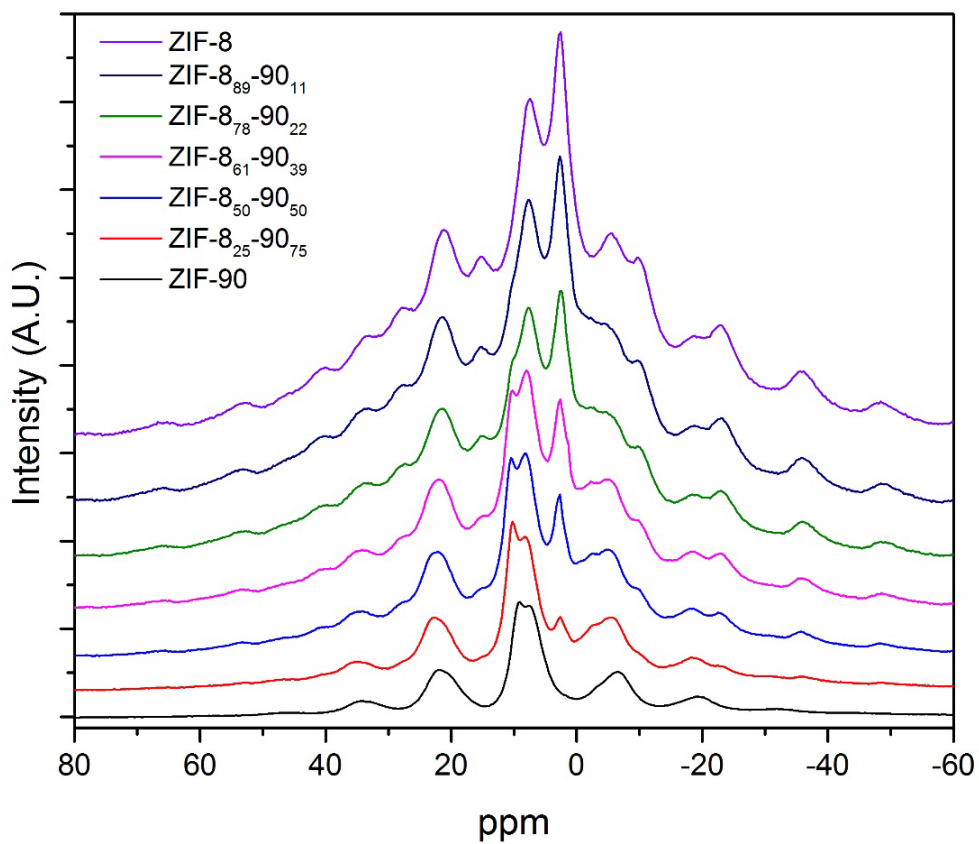


**Figure C.9** Single pulse <sup>1</sup>H excitation NMR spectra for ZIF-8-90 materials.

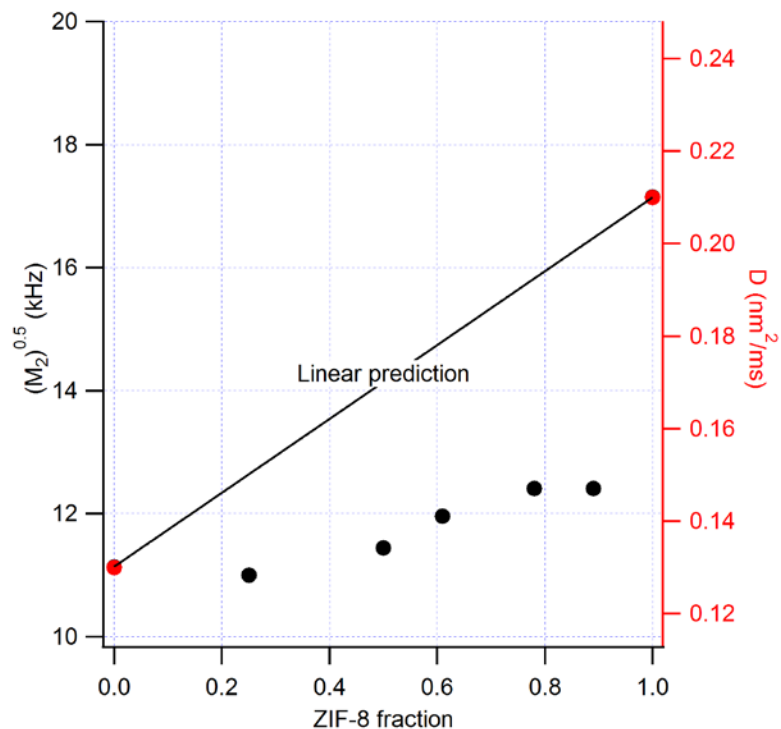


**Figure C.10** Second moment of the NMR spectra calculated as a function of linker composition (left) and predicted spin diffusion coefficient as a geometric average of pure components.

### C.2.7 Second moment calculation

The second moment of the NMR spectra in Figure C.7 were calculated using the following equations:

$$\sigma^2 = \frac{\left[ \sum (x - \mu)^2 \times y \right]}{\sum (y)}$$

$$\mu = \frac{\sum (x \times y)}{\sum (y)}$$
(C.1)

where x and y are the abscissa and ordinate of the NMR spectra from Figure C.9.

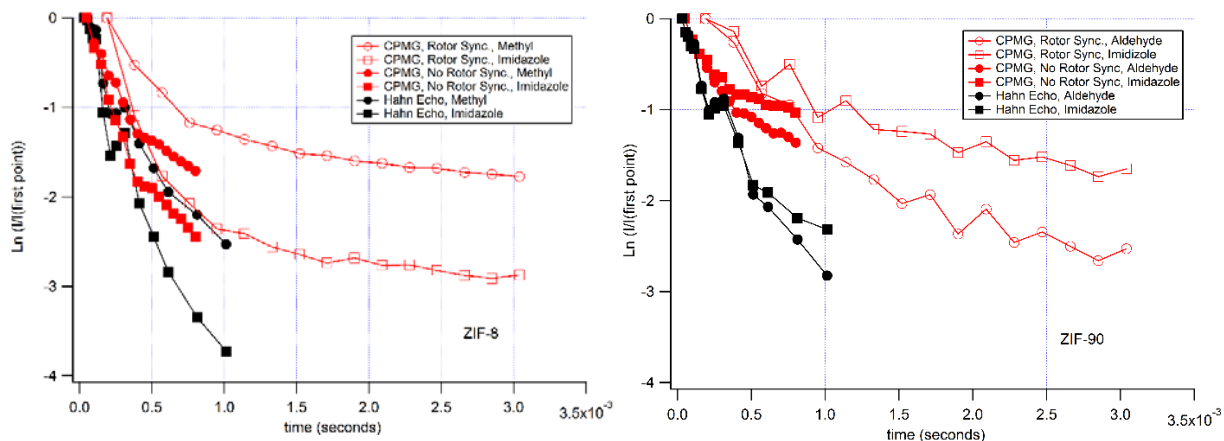


**Figure C.11** T2 curves of ZIF-8 (left) and ZIF-90 (right) using Hahn Echo and CPMG (with rotor synchronization and without rotor synchronization).

Note that the T2 curves shown in Figure C.11 are calculated from the center peaks only. These are the longest possible T2s. A more robust approximation of T2 can be obtained from the second moment calculation in Figure C.10 since it takes into account all the side-band peaks as well.

### C.3 Modeling of $^1\text{H}$ CRAMPS NMR Intensity Curves

Here we summarize the derivation as given by Perrin and Dwyer<sup>438</sup> as well as Elena and Emsley<sup>439</sup> for modeling the relaxation of z (longitudinal)-magnetization back to its equilibrium value during the mixing time period of an NMR experiment. The following system of coupled differential equations can be used to model the relaxation:

$$\begin{aligned}
 \frac{dm_1}{dt} &= -(T_{1,1}^{-1} + \sum_l k_{1l}) m_1 + k_{21} m_2 + \dots + k_{N2} m_N \\
 \frac{dm_2}{dt} &= k_{12} m_1 - (T_{1,2}^{-1} + \sum_l k_{2l}) m_2 + \dots + k_{N2} m_N \\
 \frac{dm_N}{dt} &= k_{1N} m_1 + \dots + k_{2N} m_2 + \dots - (T_{1,N}^{-1} + \sum_l k_{Nl}) m_N
 \end{aligned}
 \tag{C.2}$$

where  $N$  is the total number of spin types (e.g.  $N=2$  for ZIF-8),  $m_N$  is the deviation of the z-magnetization away from its equilibrium value,  $T_{1,N}$  is the spin lattice relation and  $k_{ij}$  is the rate constant for exchange from spin site  $i$  to spin site  $j$ . We assume that spin lattice relaxation happens on time scales much greater than mixing times for this analysis. The coupled first order differential equations are then reduced into the following form:

$$\frac{dm}{dt} = -Rm \quad (C.3)$$

where  $m$  is an  $N \times 1$  vector of z-magnetizations and  $R$  is an  $N \times N$  matrix of rate constants of spin transfer. The solution to this first order differential equation through a matrix exponential is given by:

$$m(t_m) = e^{-Rt_m} m(0) \quad (C.4)$$

where  $t_m$  is the mixing time. By including the initial condition of the deviation of magnetization from its equilibrium value and assuming conservation of magnetization, the cross and diagonal peak intensities follow as:

$$I_{ij}(t_m) = M_z^{j,0} (e^{-Rt_m})_{ij} \quad (C.5)$$

where  $M_z^{j,0}$  are the initial z-magnetization values and  $I_{ij}$  are the intensity values corresponding to the NMR diagonal and cross peak volumes. Cross-terms are calculated using the following formulation:

$$k_{ij} = A \frac{1}{N_i} \left\langle \sum_{l=1}^{N_j} \frac{1}{r_{kl}^n} \right\rangle_{k=1,2,\dots,N_i} \quad (C.6)$$

where  $A$  is a fitting parameter with units of  $m^6/s$ ,  $N_i$ ,  $N_j$  are the number of hydrogens with spin type  $i, j$ ,  $r_{kl}$  is the distance between hydrogen  $k$  (source: spin type  $i$ ) and hydrogen  $l$  (sink: spin type  $j$ ),  $n$  is the power scaling of the distance ( $n=6$ ), and the average is taken over all hydrogen  $k$ 's with spin type  $i$  in an effort to include thermal fluctuations. This

averaging can be ignored if a crystal cell with uniform spacing of hydrogens is observed. The Levenberg-Marquardt least squares fitting routine as implemented in the LMFIT Python module was used to determine the  $A$  parameter for the pure materials. Diagonal rate constants are calculated as:

$$k_{ii} = - \sum_{\substack{j \\ j \neq i}}^{\# \text{ spins}} k_{ij} \quad (\text{C.7})$$

As a self-consistency check, the forward and reverse rates must satisfy detailed balance:

$$k_{ij} p_i = k_{ji} p_j \quad (\text{C.8})$$

where  $p_i$  and  $p_j$  are relative populations of spin type  $i, j$ .

#### C.4 Pure ZIF-90 Spin Exchange Fitting Results

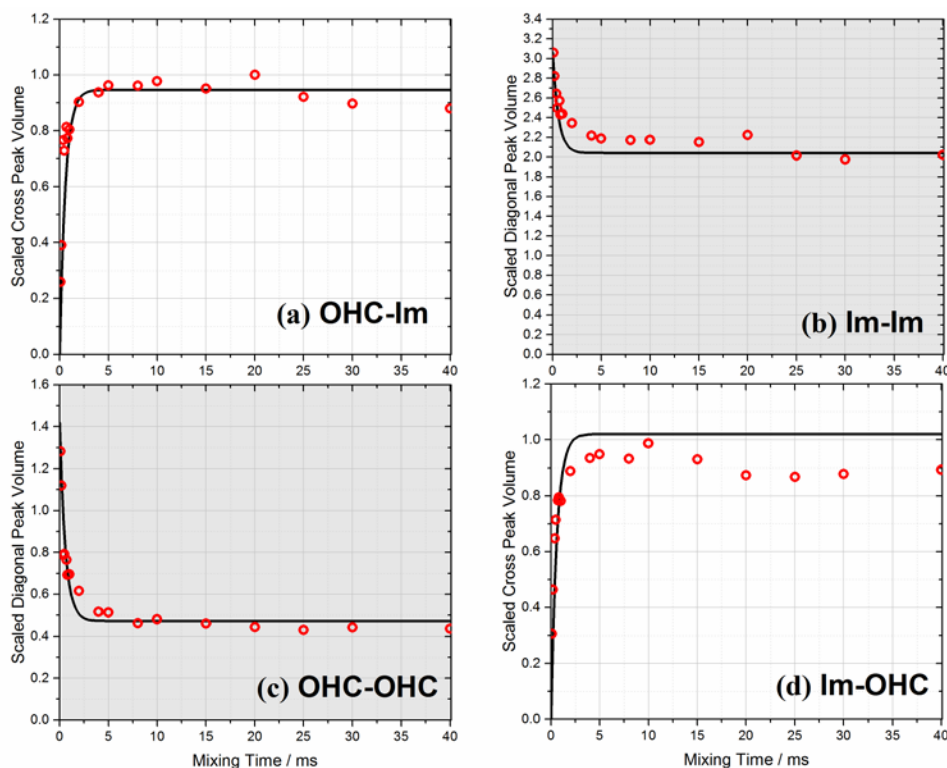


**Figure C.12** Pure ZIF-90 fitting results, with model fits given by the solid black lines and experimental NMR data in the open red circles.



Figure C.13 shows the mean absolute error as a function of SRO. Three experiments of ZIF-8<sub>50</sub>-90<sub>50</sub> (label A, B, C) were done, each yielding the same minimum SRO value/range. Table C.4 gives a complete summary of all the fitting parameters and results of the pure and hybrid ZIF materials.

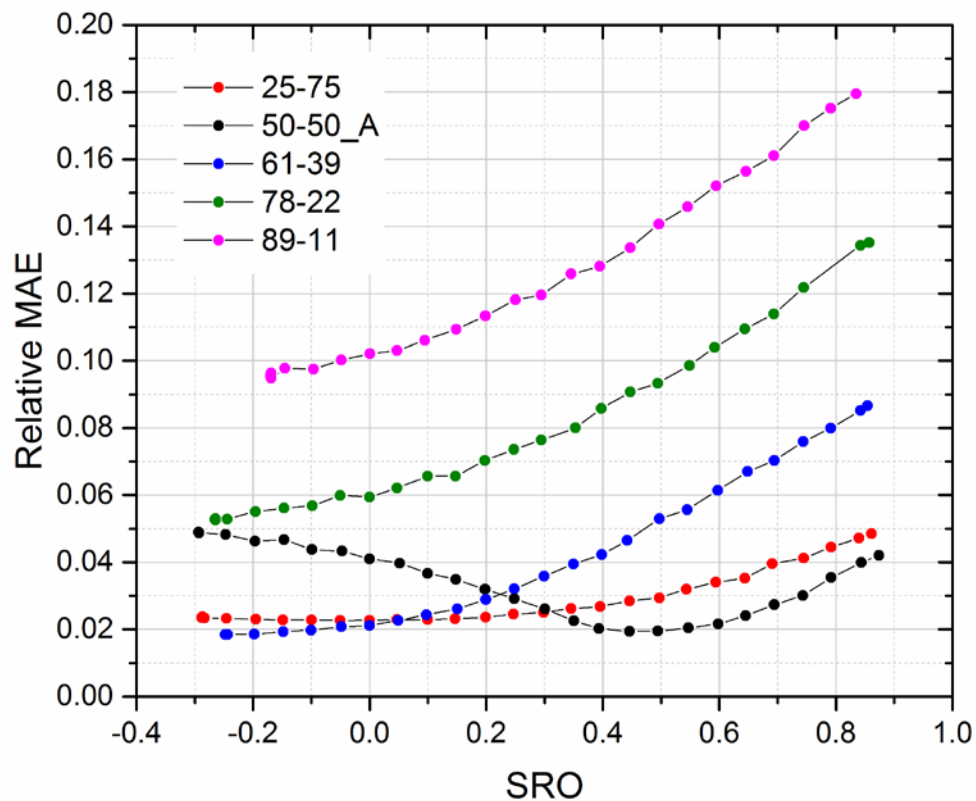


**Figure C.13** Relative Mean absolute error (MAE) as a function of SRO for five ZIF-8-90 hybrid materials.

**Table C.4** Summary of fitting results detailing the starting unit cell, A value, scaled initial z-magnetization values, and final short range orders for different ZIF-8-90 hybrids.

Sample	Starting Unit Cell	A	$M_z^{\text{Im},0}$	$M_z^{\text{OHC},0}$	$M_z^{\text{CH}_3,0}$	SRO $\alpha$ [range]
<b>ZIF-8<sub>100</sub>-90<sub>0</sub></b>	ZIF-8	(101.8±5.7)*	1.875	-	2.212	-
<b>ZIF-8<sub>0</sub>-90<sub>100</sub></b>	ZIF-90	(120.7±8.1)*	3.061	1.420	-	-
<b>ZIF-8<sub>25</sub>-90<sub>75</sub></b>	ZIF-90	115.6	0.660	0.205	0.085	<b>0.00, [-0.29,+0.20]</b>
<b>ZIF-8<sub>50</sub>-90<sub>50</sub><sup>A</sup></b>	ZIF-8	110.8	0.665	0.104	0.311	<b>+0.45, [+0.40,+0.55]</b>
<b>ZIF-8<sub>50</sub>-90<sub>50</sub><sup>B</sup></b>	ZIF-8	110.8	0.660	0.103	0.304	<b>+0.45, [+0.40,+0.50]</b>
<b>ZIF-8<sub>50</sub>-90<sub>50</sub><sup>C</sup></b>	ZIF-8	110.8	0.651	0.103	0.302	<b>+0.45, [+0.40,+0.55]</b>
<b>ZIF-8<sub>61</sub>-90<sub>39</sub></b>	ZIF-8	108.8	0.644	0.063	0.451	<b>-0.25, [-0.25,-0.15]</b>
<b>ZIF-8<sub>78</sub>-90<sub>22</sub></b>	ZIF-8	105.7	0.558	0.001	0.569	<b>-0.26, [-0.26,-0.20]</b>
<b>ZIF-8<sub>89</sub>-90<sub>11</sub></b>	ZIF-8	103.7	0.604	0.000	0.696	<b>-0.17, [-0.17,-0.05]</b>

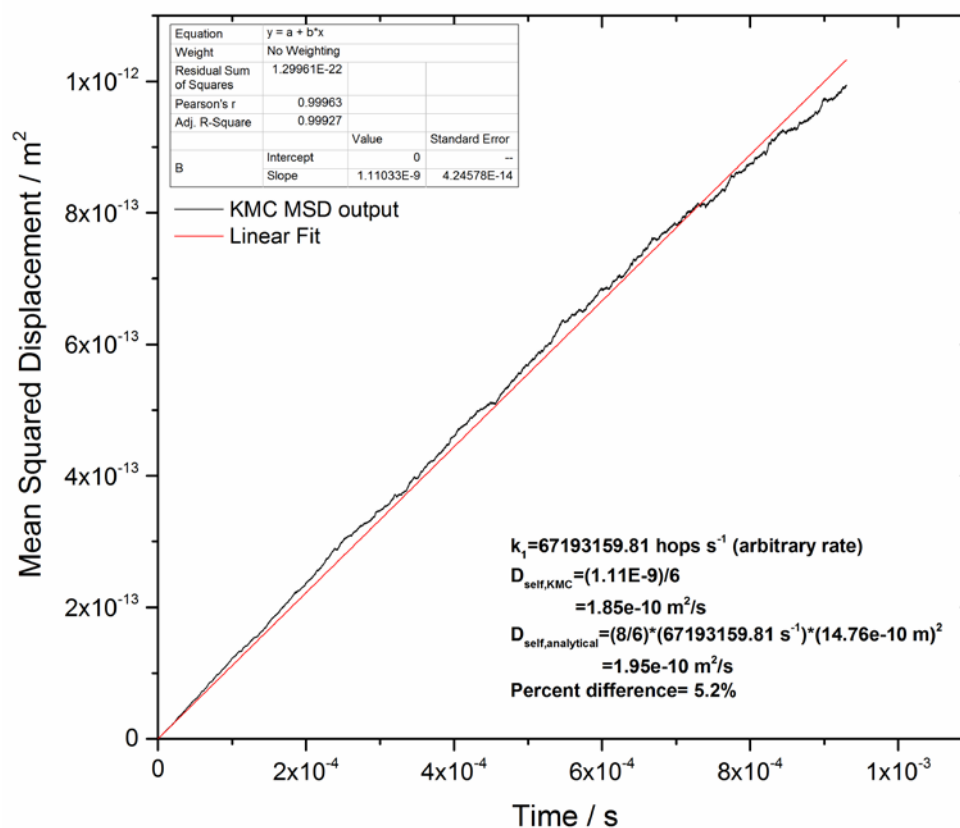
\*These A parameter values were determined through the fitting procedure of the pure ZIF data and used to calculate the A parameter values for the hybrid ZIF materials; <sup>A,B,C</sup>Three different ZIF-8<sub>50</sub>-90<sub>50</sub> experiments, each yielding the same SRO.

## APPENDIX D

### SUPPORTING INFORMATION FOR CHAPTER 5

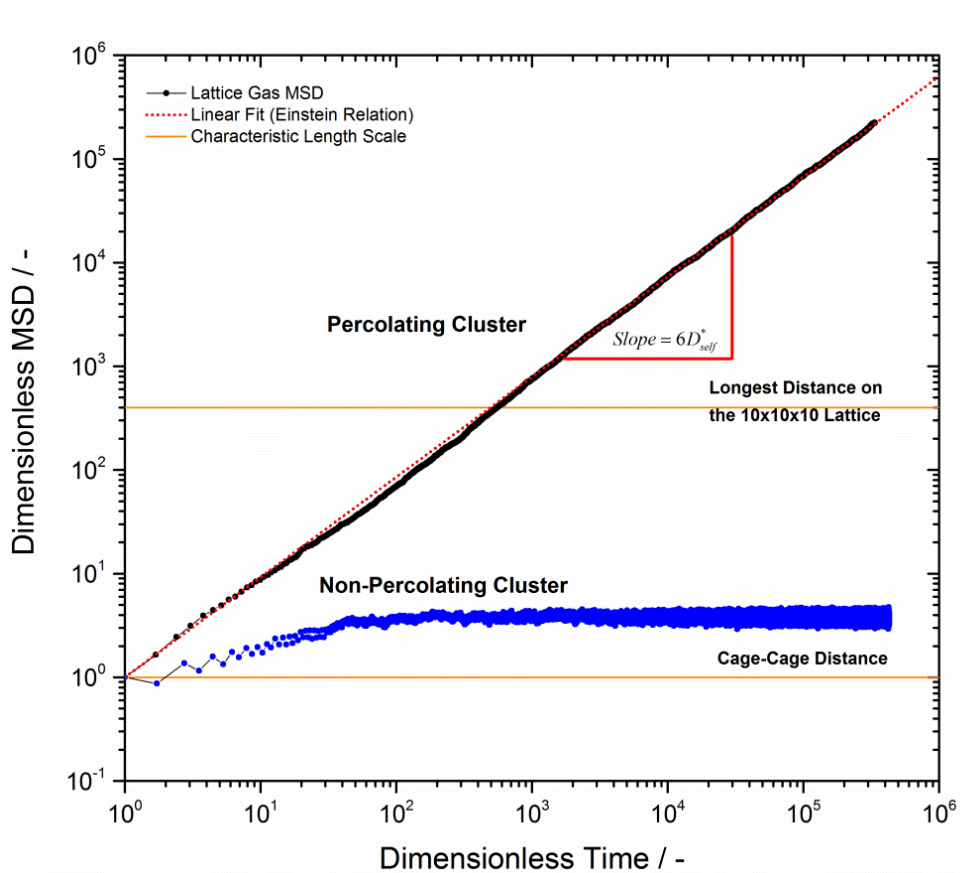
#### *D.1 KMC Implementation Validation and Percolating Cluster Determination*

Figure D.1 shows a representative MSD plot of an adsorbate in a parent material. The analytical self-diffusivity and the KMC self-diffusivity have a percent difference of ~5%.



**Figure D.1** Example MSD of a lattice-gas in the parent material with a linear fit.

Figure D.2 shows representative MSD plots of an adsorbate in a percolating (black) and non-percolating (blue) cluster. Adsorbates with final MSD values not larger than the longest distance on the 10x10x10 lattice were not included in the averaged diffusivity calculation.



**Figure D.2** Example MSDs of a lattice-gas in both percolating and non-percolating clusters with characteristic length scales represented by gold lines.

## *D.2 Alternative Window Blocking Scenarios*

A logical extension of the single blocking case would be to consider the scenario when more than one bulky imidazolate linker is needed for window blocking (e.g. a benzimidazolate linker in  $\text{ZIF-7}_x\text{-8}_{100-x}$  as shown in Figure D.3a). We report in Figures D.3b, D.3c, and D.3d normalized diffusivities as a function of the bulky imidazolate mole fraction for lattices with constant SRO. Figure D.3b demonstrates the influence of SRO when 3 bulky imidazolate linkers are required for window blocking ( $k_4=0$ ), and Figure D.3c demonstrates the influence when 2 or 3 bulky imidazolate linkers are required for window blocking ( $k_3, k_4=0$ ). Figure D.3d contains the same information as Figure 5.4a of Chapter 5, but is duplicated for direct comparison. Window blocking with only  $k_4=0$  shows that clustered linkers result in a faster decrease of the diffusivity as opposed to randomly placed or alternating linkers. Clustered linkers create lattices with a large population of blocked type 4 windows, hence lengthening diffusion pathways. Interestingly, the composition thresholds are the same for the three lattices. Window blocking with  $k_3, k_4=0$  demonstrates that SRO has a negligible influence on the simulated diffusivities; interestingly, the composition threshold for lattices with clustered linkers is shifted to a larger mole fraction than the lattices with alternating or random SRO. These results suggest that window blocking requiring only one bulky imidazolate linker has the most promise for tuning adsorbate diffusion with SRO control.

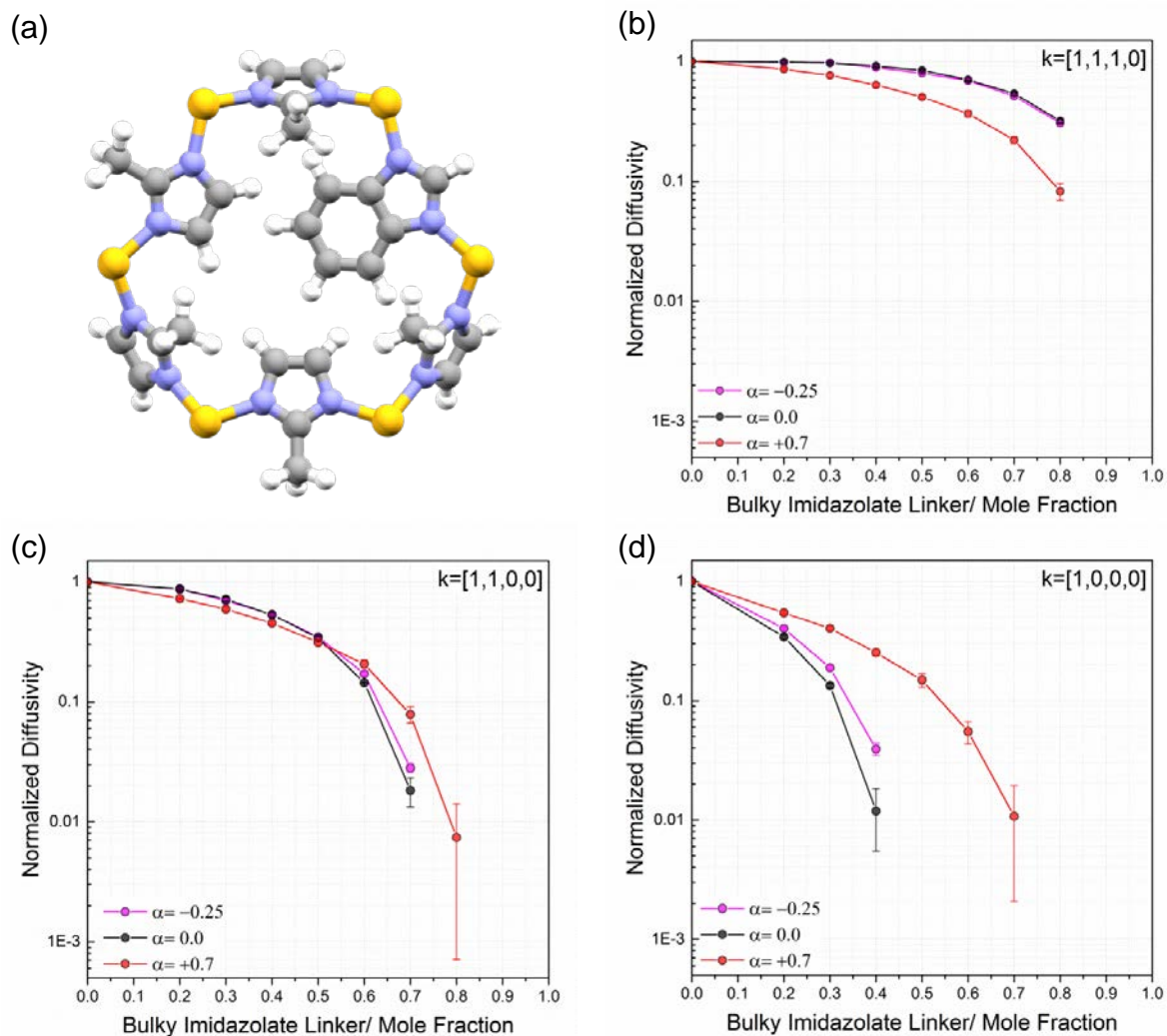


**Figure D.3** (a) Example of window blocking from a bulky imidazolate linker. Diffusivities as a function of composition at fixed SRO for (b) window blocking requiring three bulky linkers, (c) window blocking requiring two linkers, and (d) window blocking requiring only one bulky linker.

### ***D.3 Divergent Hopping Rates through Hybrid and Parent Windows***

To our knowledge, existing experimental data of adsorbate transport in binary mixed-linker ZIFs presents diffusion coefficients as monotonic functions of the organic linker composition. It is reasonable to consider that adsorbate diffusion may also be blocked (allowed) through either the hybrid or parent windows resulting in nonlinear diffusion behavior. This behavior is plausible when two distinct linkers surrounding a window interact in a cooperative manner. These interactions either impact linker flexibility (i.e. amplitude or frequency characteristics<sup>440</sup>) or (broaden) narrow the window aperture through attractive (repulsive) pair-wise interactions (e.g. van der Waals or electrostatics). Figures D.4a and D.4b demonstrate the impact of SRO when considering window blocking through the two hybrid windows and the two parent windows respectively. Figure D.4a demonstrates that adsorbate diffusion is most reduced (by one order of magnitude) for SROs close to 0.0 (i.e. random local ordering). More striking is the observation that adsorbates can percolate through the structure over the entire range of compositions. This is a direct consequence of the window type probabilities as a function of composition<sup>46</sup>. Figure D.4b demonstrates that structures with random local orderings enhance the diffusion properties over a composition range from 0.2-0.8 mole fractions. Percolation is only completely inhibited in the near parent ZIF lattices where the probability of observing a hybrid window of either type drops to near zero. Figures D.4c and D.4d demonstrate the impact of local ordering when adsorbate diffusion is depressed (accelerated) through the hybrid windows. Similar observations as those discussed for Figures D.4a and D.4b are made, with a difference that percolation in the parent materials in Figure D.4d is not impeded completely, merely reduced according to the predetermined rates. Said another way, there are two percolation thresholds in Figure D.4b and no percolation thresholds in Figure D.4d. Ultimately, to predict this diffusion behavior, one needs the knowledge that the rates through the hybrid windows are faster (slower) than the rates in the parent materials; the magnitude of the hybrid window rates is not an important parameter.

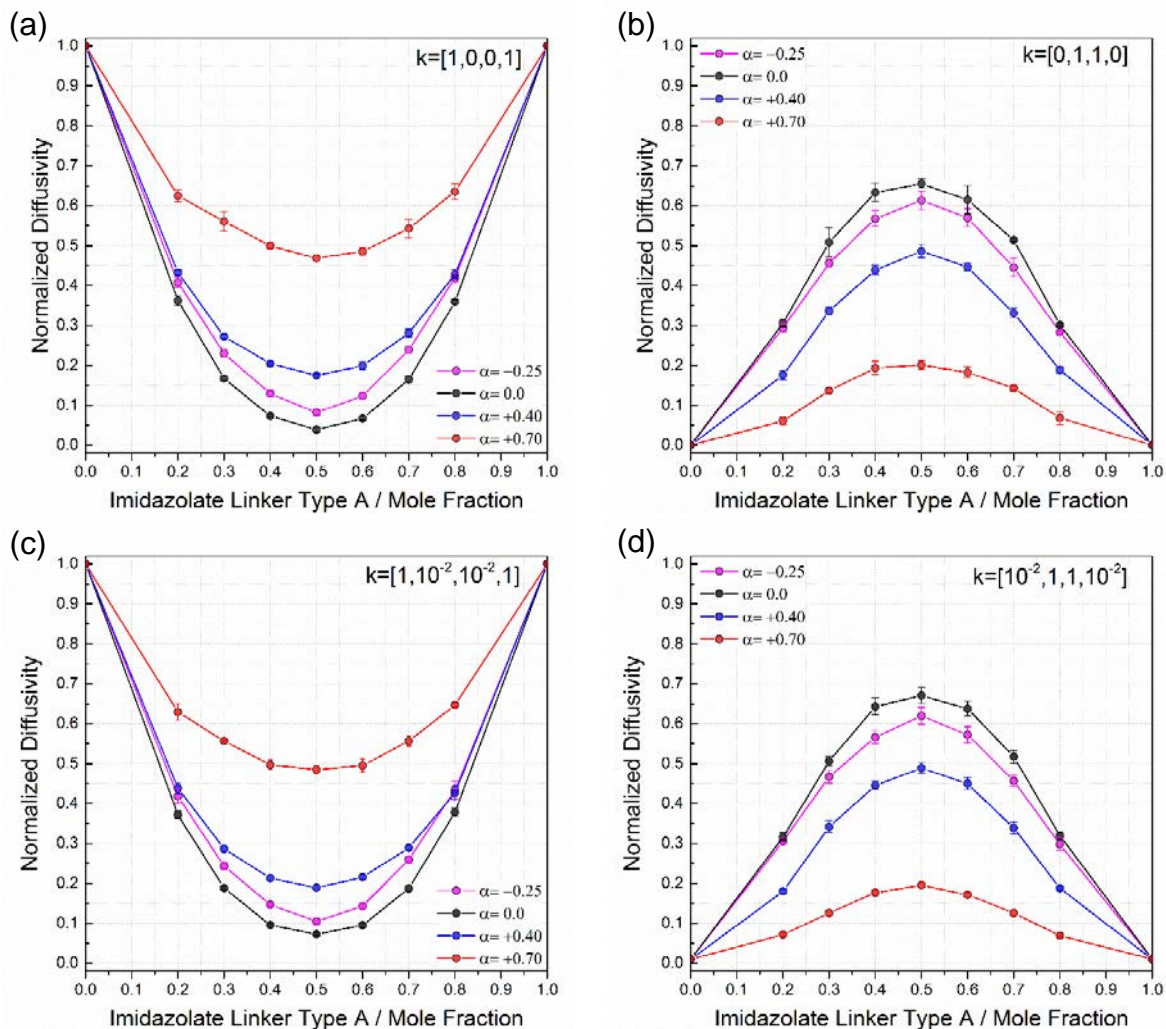


**Figure D.4** Normalized self-diffusivities as a function of SRO and the mole fraction of linker type A where (a) utilizes a rate convention of  $k=[1,0,0,1]$  to denote blocking of the hybrid windows, (b) utilizes a rate convention of  $k=[0,1,1,0]$  to denote blocking of the parent windows, (c) utilizes a rate convention of  $k=[1,10^{-2},10^{-2},1]$  to denote reduced diffusion through hybrid windows, and (d) utilizes a rate convention of  $k=[10^{-2},1,1,10^{-2}]$  to denote reduced diffusion through parent windows.



## APPENDIX E

### SUPPORTING INFORMATION FOR CHAPTER 6

#### *E.1 Adsorbate Force Fields and Adsorbate-Framework Interactions*

We modeled SF<sub>6</sub> as a single-site 12-6 Lennard-Jones (LJ) fluid<sup>427</sup> and N<sub>2</sub> as a 3-site rigid linear molecule<sup>174,182</sup>. We modeled methanol, ethanol, 1-butanol, methane, propane, n-butane, and isobutane using the united atom TraPPE FF<sup>176,177,428</sup>. The single and double C-C bonds were modeled with a harmonic potential<sup>178</sup>, a departure from the original TraPPE implementation to facilitate implementation in LAMMPS. The OPLS force field was used to model rigid benzene (C<sub>6</sub>H<sub>6</sub>).<sup>430,431</sup> We have also included H<sub>2</sub>O modeled using the SPC/E FF designed to work with long range electrostatic solvers (Ewald)<sup>432,433</sup>. Table E.1 shows all the adsorbate LJ parameters and Table E.2 shows all the ZIF 12-6 LJ parameters used only to describe framework-adsorbate interactions. For those seeking to replicate these calculations, the bond lengths, angles, and dihedrals used are in the original references.

**Table E.1** Adsorbate force field parameters along with molecular diameters (KD=kinetic diameter, vdW=van der Waals diameter, and LJ=diameter approximated from Lennard-Jones sigma parameters) and molecular weights.

Index	Adsorbate	Molecular Diameter [Å]	LJ Site (name)	MW [g mol <sup>-1</sup> ]	$\sigma$ [Å]	$\epsilon$ [kcal mol <sup>-1</sup> ]	$\epsilon$ [K]	q [e]
1	SF <sub>6</sub>	5.13 <sup>LJ</sup>	SF <sub>6</sub>	146.06	5.13	0.4414	222.1	0.0
2	N <sub>2</sub>	3.64 <sup>KD,56</sup>	2xN <sub>N2</sub>	14.01	3.32	0.0724	36.43	-0.482
			N <sub>COM</sub>	0.00	0.0	0.0	0.0	+0.964
3	H <sub>2</sub> O	2.89 <sup>vdWD</sup>	O <sub>H2O</sub>	16.00	3.166	0.15535	78.18	-0.8476
			2xH <sub>H2O</sub>	1.01	0.0	0.0	0.0	0.4238
4	CH <sub>3</sub> OH	3.60 <sup>vdWD,437</sup>	CH <sub>3</sub> _sp3 <sup>a</sup>	15.03	3.750	0.1947	98.0	0.265
			O	16.00	3.020	0.1848	93.0	-0.700
			H	1.01	0.0	0.0	0.0	0.435
5	C <sub>2</sub> H <sub>5</sub> OH	4.10 <sup>KD,60</sup>	CH <sub>3</sub> _sp3	15.03	3.750	0.1947	98.0	0.0
			CH <sub>2</sub> _sp3 <sup>a</sup>	14.02	3.950	0.0914	46.0	0.265
			O	16.00	3.020	0.1848	93.0	-0.700
			H	1.01	0.0	0.0	0.0	0.435
6	CH <sub>4</sub>	3.25 <sup>vdWD,56</sup>	CH <sub>4</sub>	16.04	3.73	0.2941	148.0	0.0
7	C <sub>3</sub> H <sub>8</sub>	4.16 <sup>vdWD,56</sup>	CH <sub>3</sub>	15.03	3.750	0.1947	98.0	0.0
			CH <sub>2</sub>	14.02	3.950	0.0914	46.0	0.0
8	n-C <sub>4</sub> H <sub>10</sub>	4.52 <sup>vdWD,56</sup>	2x CH <sub>3</sub>	15.03	3.750	0.1947	98.0	0.0
			2xCH <sub>2</sub>	14.02	3.950	0.0914	46.0	0.0
9	iso-C <sub>4</sub> H <sub>10</sub>	5.0 <sup>KD,56</sup>	CH <sub>3</sub> _sp3	15.03	3.750	0.1947	98.0	0.0
			CH_sp3	13.02	4.680	0.0199	10.0	0.0
10	C <sub>6</sub> H <sub>6</sub>	5.80 <sup>KD,437</sup>	6xC_xyl	12.01	3.55	0.0700	35.24	-0.115
			6xH_xyl	1.01	2.42	0.0299	15.03	0.115
11	1-butanol	4.5 <sup>LJ</sup>	CH <sub>3</sub>	15.03	3.75	0.1947	98.0	0.00
			2xCH <sub>2</sub>	14.02	3.95	0.0914	46.0	0.00
			CH <sub>2</sub> _sp3 <sup>a</sup>	14.02	3.95	0.0914	46.0	0.265
			O	16.00	3.02	0.1848	93.0	-0.700
			H	1.01	0.0	0.0	0.0	0.435

**Table E.2** 12-6 Lennard-Jones parameters on framework atoms used to model adsorbate-framework interactions.

Atom Type	$\epsilon$ [kcal/mol]	$\sigma$ [Å]
Zn	0.067	2.462
N	0.037	3.261
C <sub>x</sub>	0.057	3.431
H <sub>x</sub>	0.024	2.571
O	0.032	3.118

## ***E.2 PBE-D3(BJ) and the intraZIF-FF Potential Energy Comparisons***

Table E.3 shows the statistics used to benchmark the intraZIF-FF at predicting configurational potential energies from BOMD simulations. The mean absolute error (MAE), mean signed deviation (MSD), root mean squared deviation (RMSD), and the normalized root mean squared deviation (NRMSD). The NRMSD is defined as the RMSD divided by the standard deviation of the PBE-D3(BJ) energies and is reported as a percentage.

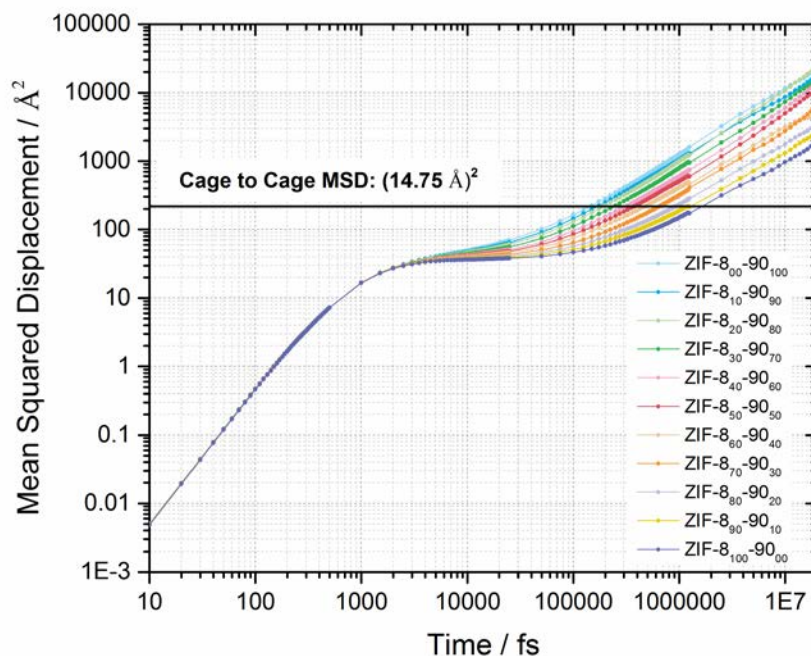
**Table E.3** Statistics benchmarking the quality of the intraZIF-FF at describing PBE-D3(BJ) configurational potential energies from BOMD simulations at 700 K and 1.01 bar.

<b>Material</b>	<b>MAE</b>	<b>MSD</b>	<b>RMSD</b>	<b>NRMSD</b>	<b>N samples</b>
ZIF-8	8.99	-8.17	10.72	45.32	5550
ZIF-8 <sub>75</sub> -90 <sub>25</sub>	7.33	0.09	9.03	45.96	4708
ZIF-8 <sub>50</sub> -90 <sub>50</sub>	9.02	6.64	11.54	72.94	5250
ZIF-8 <sub>25</sub> -90 <sub>75</sub>	16.62	16.46	18.89	166.85*	5509
ZIF-90	15.38	15.25	17.25	81.20	6099

*\*The NRMSD for ZIF-8<sub>25</sub>-90<sub>75</sub> is larger than ZIF-90 because a lower standard deviation of the PBE-D3(BJ) energies is observed*

### *E.3 Mean Squared Displacement Analysis from NPT-MD Simulations for Methane in ZIF-8-90*

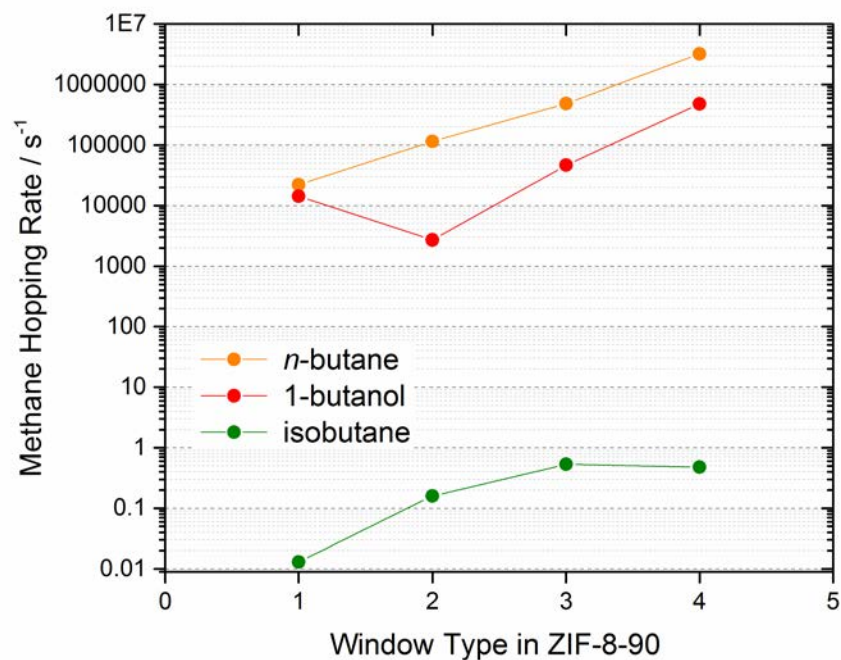
Figure E.1 below shows MSD plots for methane measured over the composition range of ZIF-8-90 materials. Methane diffusion in ZIF-90 is faster than in ZIF-8.



**Figure E.1** MSDs for CH<sub>4</sub> in ZIF-8-90 where the square of the cage to cage distance is indicated by the solid black line. These MSDs were calculated at a loading of two methane molecules per unit cell, 308 K, and 1.01 bar.

#### *E.4 Hopping Rates of N-Butane, 1-Butanol, and Isobutane in ZIF-8-90*

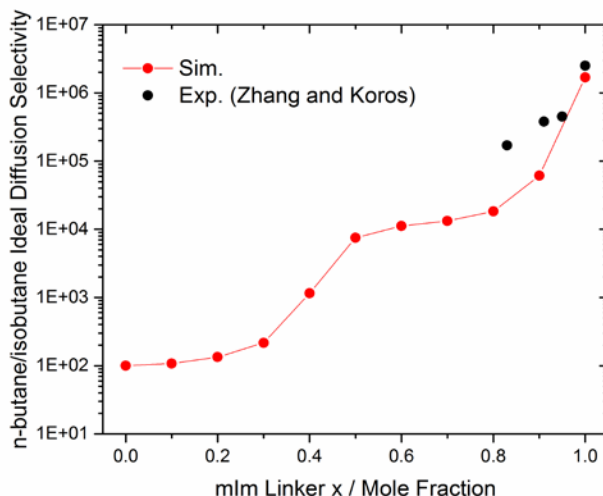
Figure E.2 below shows the hopping rates of n-butane, 1-butanol, and isobutane in the four window types of ZIF-8-90. A type 1 window contains 3 mIm linkers and a type 4 window contains 3 ImCA linkers as described in Chapter 6.



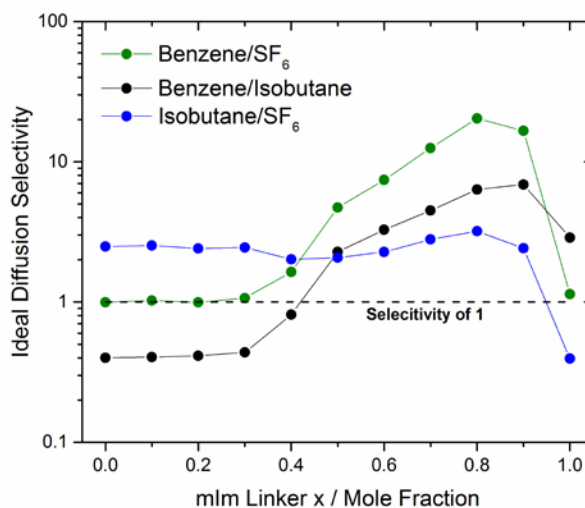
**Figure E.2** Hopping rates of n-butane, 1-butanol, and isobutane through ZIF-8-90 window types at 308 K and 1.01 bar.

### E.5 Ideal Diffusion Selectivities in SALEM-2/ZIF-8 Hybrids

Figure E.3 below shows the n-butane/isobutane ideal diffusion selectivities experimentally measured<sup>370</sup> and simulated for SALEM-2/ZIF-8 hybrids. Figure E.4 shows the ideal diffusion selectivities for combinations of benzene, isobutane, and SF<sub>6</sub> in SALEM-2/ZIF-8 hybrids at 308 K and 1.01 bar.



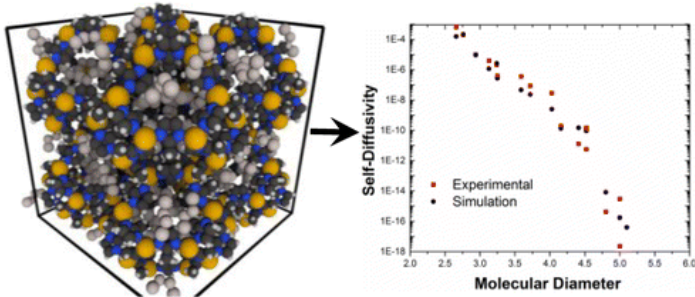
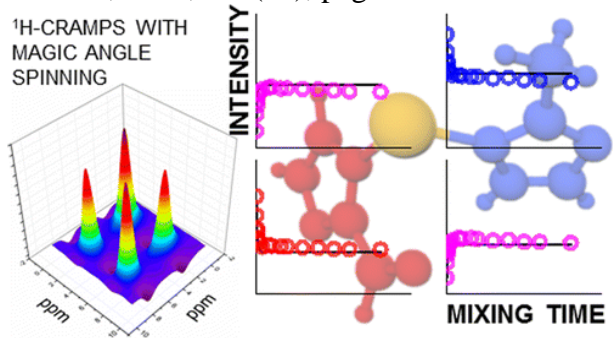
**Figure E.3** Ideal n-butane/isobutane diffusion selectivity as a function of mIm linker in SALEM-2/ZIF-8 hybrids with a SRO  $\alpha=0$  (red circles) at 308 K and 1.01 bar. The ideal diffusion selectivities measured by Zhang and Koros at the same conditions are shown as solid black circles.<sup>370</sup> Lines are guides for the eye.



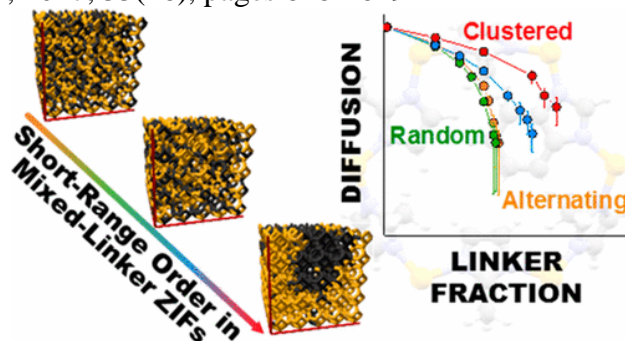
**Figure E.4** Predicted ideal diffusion selectivities of combinations of benzene, isobutane, and SF<sub>6</sub> in SALEM-2/ZIF-8 hybrids at 308 K and 1.01 bar. The dashed line indicates a selectivity of 1. Lines are guides for the eye.

## APPENDIX F

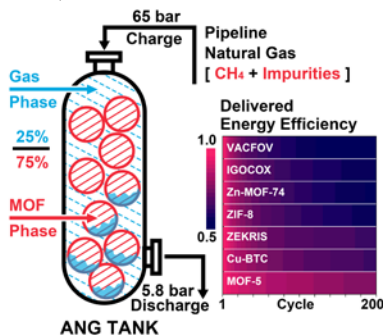
### PUBLISHED WORK

<b>Title</b>	Temperature and Loading-Dependent Diffusion of Light Hydrocarbons in ZIF-8 as Predicted Through Fully Flexible Molecular Simulations
<b>Authors</b>	<b>Ross J. Verploegh</b> , Sankar Nair, and David S. Sholl
<b>Source</b>	<i>J. Am. Chem. Soc.</i> , 2015, 137(50), pages 15760-15771
 <p>HYDROCARBON-LOADED ZIF-8 MODELS, FLEXIBILITY INCLUDED</p>	
<b>Title</b>	Structure Elucidation Mixed-Linker Zeolitic Imidazolate Frameworks by Solid-State <sup>1</sup> H CRAMPS NMR Spectroscopy and Computational Modeling
<b>Authors</b>	Krishna C. Jayachandrababu*, <b>Ross J. Verploegh</b> *, Johannes Leisenen, Ryan C. Nieuwendaal, David S. Sholl, and Sankar Nair (*co-first authors)
<b>Source</b>	<i>J. Am. Chem. Soc.</i> , 2016, 138(23), pages 7325-7336
	

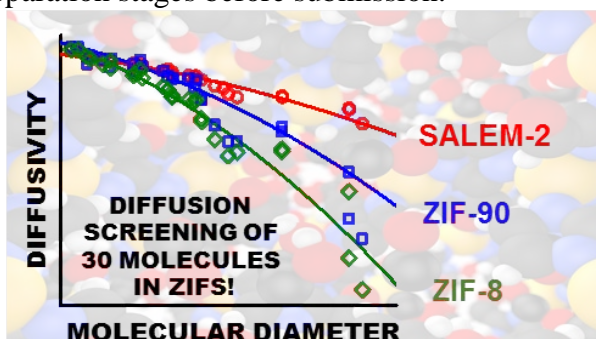
Title	Lattice-Gas Modeling of Adsorbate Diffusion in Mixed-Linker Zeolitic Imidazolate Frameworks: Effect of Local Ordering (ACS Editor's Choice)
Authors	<b>Ross J. Verploegh*</b> , Ying Wu*, and David S. Sholl (*co-first authors)
Source	<i>Langmuir</i> , 2017, 33(26), pages 6481-6491



Title	Impacts of Gas Impurities From Pipeline Natural Gas on Methane Storage in Metal-Organic Frameworks During Long Term Cycling
Authors	Ying Wu, Dai Tang, <b>Ross J. Verploegh</b> , Hongxia Xi, and David S. Sholl
Source	<i>J. Phys. Chem. C</i> , 2017, Article ASAP

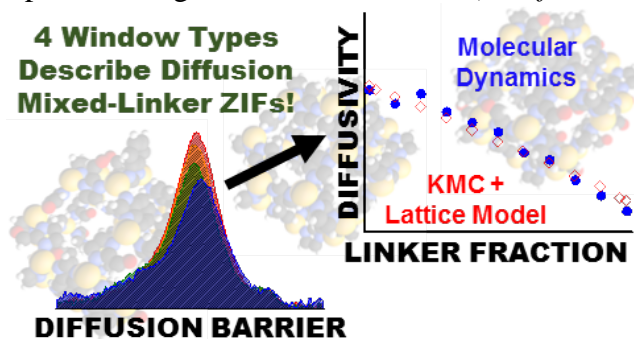


Title	Screening Diffusion of Small Molecules In Flexible Zeolitic Imidazolate Frameworks using a DFT Parameterized Force Field
Authors	<b>Ross J. Verploegh</b> , Ambarish Kulkarni, Salah Eddine Boulfelel, Jonathan C. Haydak, Dai Tang, and David S. Sholl
Source	In final preparation stages before submission.





Title	Predicting Diffusion in Binary Mixed-Linker Zeolitic Imidazolate Frameworks
Authors	<b>Ross J. Verploegh*</b> , Ying Wu*, Salah Eddine Boulfelfel, and David S. Sholl
Source	In final preparation stages before submission. (* <i>co-first authors</i> )



# APPENDIX G

## COPYRIGHT AGREEMENT LETTERS




[Home](#)
[Create Account](#)
[Help](#)




**Title:** Temperature and Loading-Dependent Diffusion of Light Hydrocarbons in ZIF-8 as Predicted Through Fully Flexible Molecular Simulations

**Author:** Ross J. Verploegh, Sankar Nair, David S. Sholl

**Publication:** Journal of the American Chemical Society

**Publisher:** American Chemical Society

**Date:** Dec 1, 2015

Copyright © 2015, American Chemical Society

**LOGIN**

If you're a [copyright.com](#) user, you can login to RightsLink using your [copyright.com](#) credentials. Already a [RightsLink user](#) or want to [learn more?](#)

### PERMISSION/LICENSE IS GRANTED FOR YOUR ORDER AT NO CHARGE

This type of permission/license, instead of the standard Terms & Conditions, is sent to you because no fee is being charged for your order. Please note the following:

- Permission is granted for your request in both print and electronic formats, and translations.
- If figures and/or tables were requested, they may be adapted or used in part.
- Please print this page for your records and send a copy of it to your publisher/graduate school.
- Appropriate credit for the requested material should be given as follows: "Reprinted (adapted) with permission from (COMPLETE REFERENCE CITATION). Copyright (YEAR) American Chemical Society." Insert appropriate information in place of the capitalized words.
- One-time permission is granted only for the use specified in your request. No additional uses are granted (such as derivative works or other editions). For any other uses, please submit a new request.

**Figure G.1** Copyright permission for Chapter 2 content.



RightsLink®

Home

Create Account

Help



ACS Publications  
Most Trusted. Most Cited. Most Read.

**Title:** Structure Elucidation of Mixed-Linker Zeolitic Imidazolate Frameworks by Solid-State 1H CRAMPS NMR Spectroscopy and Computational Modeling

**Author:** Krishna C. Jayachandrababu, Ross J. Verploegh, Johannes Leisen, et al

**Publication:** Journal of the American Chemical Society

**Publisher:** American Chemical Society

**Date:** Jun 1, 2016

Copyright © 2016, American Chemical Society

**LOGIN**  
If you're a copyright.com user, you can login to RightsLink using your copyright.com credentials. Already a RightsLink user or want to [learn more?](#)

#### PERMISSION/LICENSE IS GRANTED FOR YOUR ORDER AT NO CHARGE

This type of permission/license, instead of the standard Terms & Conditions, is sent to you because no fee is being charged for your order. Please note the following:

- Permission is granted for your request in both print and electronic formats, and translations.
- If figures and/or tables were requested, they may be adapted or used in part.
- Please print this page for your records and send a copy of it to your publisher/graduate school.
- Appropriate credit for the requested material should be given as follows: "Reprinted (adapted) with permission from (COMPLETE REFERENCE CITATION). Copyright (YEAR) American Chemical Society." Insert appropriate information in place of the capitalized words.
- One-time permission is granted only for the use specified in your request. No additional uses are granted (such as derivative works or other editions). For any other uses, please submit a new request.

**Figure G.2** Copyright permission for Chapter 4 content.

## REFERENCES

1. Ren, T.; Patel, M.; Blok, K. *Energy* **2006**, *31*, 425-451.
2. Sholl, D. S.; Lively, R. P. *Nature* **2016**, *532*, 435-437.
3. Boehme, U.; Barth, B.; Paula, C.; Kuhnt, A.; Schwieger, W.; Mundstock, A.; Caro, J.; Hartmann, M. *Langmuir* **2013**, *29*, 8592-8600.
4. van den Bergh, J.; Gucuyener, C.; Pidko, E. A.; Hensen, E. J.; Gascon, J.; Kapteijn, F. *Chemistry* **2011**, *17*, 8832-8840.
5. Van Miltenburg, A.; Zhu, W.; Kapteijn, F.; Moulijn, J. A. *Chem. Eng. Res. Des.* **2006**, *84*, 350-354.
6. U.S. Energy Information Administration **2017**; Vol. 2017.
7. Luo, Y.; Bernot, K.; Calvez, G.; Freslon, S.; Daiguebonne, C.; Guillou, O.; Kerbellec, N.; Roisnel, T. *Cryst. Eng.* **2013**, *15*, 1882-1896.
8. Adams, R.; Carson, C.; Ward, J.; Tannenbaum, R.; Koros, W. *Microporous Mesoporous Mater.* **2010**, *131*, 13-20.
9. Bae, T.-H.; Lee, J. S.; Qiu, W.; Koros, W. J.; Jones, C. W.; Nair, S. *Angew. Chem. Int. Ed.* **2010**, *49*, 9863-9866.
10. Bradshaw, D.; Garai, A.; Huo, J. *Chem. Soc. Rev.* **2012**, *41*, 2344-2381.
11. Brown, A. J.; Johnson, J. R.; Lydon, M. E.; Koros, W. J.; Jones, C. W.; Nair, S. *Angew. Chem. Int. Ed.* **2012**, *51*, 10615-10618.
12. Qiu, S.; Xue, M.; Zhu, G. *Chem. Soc. Rev.* **2014**.
13. Koros, W. J.; Fleming, G. K. *J. Membr. Sci.* **1993**, *83*, 1-80.
14. Koros, W. J. *AIChE J.* **2004**, *50*, 2326-2334.
15. Koros, W. J.; Zhang, C. *Nat. Mater.* **2017**, *16*, 289-297.
16. Brown, A. J.; Brunelli, N. A.; Eum, K.; Rashidi, F.; Johnson, J. R.; Koros, W. J.; Jones, C. W.; Nair, S. *Science* **2014**, *345*, 72-75.

17. Zhou, H.-C.; Long, J. R.; Yaghi, O. M. *Chem. Rev.* **2012**, *112*, 673-674.
18. Watanabe, T.; Sholl, D. S. *Langmuir* **2012**, *28*, 14114-14128.
19. Sarkisov, L.; Duren, T.; Snurr, R. Q. *Mol. Phys.* **2004**, *102*, 211-221.
20. Keskin, S.; Liu, J.; Rankin, R. B.; Johnson, J. K.; Sholl, D. S. *Ind. Eng. Chem. Res.* **2009**, *48*, 2355-2371.
21. Gubbins, K. E.; Liu, Y.-C.; Moore, J. D.; Palmer, J. C. *Physical Chemistry Chemical Physics* **2011**, *13*, 58-85.
22. Keskin, S.; van Heest, T. M.; Sholl, D. S. *ChemSusChem* **2010**, *3*, 879-891.
23. Lee, J.; Farha, O. K.; Roberts, J.; Scheidt, K. A.; Nguyen, S. T.; Hupp, J. T. *Chem. Soc. Rev.* **2009**, *38*, 1450-1459.
24. Kreno, L. E.; Leong, K.; Farha, O. K.; Allendorf, M.; Van Duyne, R. P.; Hupp, J. T. *Chem. Rev.* **2012**, *112*, 1105-1125.
25. Sarkisov, L. *J. Phys. Chem. C* **2012**, *116*, 3025-3033.
26. Zhuang, J.; Kuo, C.-H.; Chou, L.-Y.; Liu, D.-Y.; Weerapana, E.; Tsung, C.-K. *ACS Nano* **2014**, *8*, 2812-2819.
27. Li, J.-R.; Kuppler, R. J.; Zhou, H.-C. *Chem. Soc. Rev.* **2009**, *38*, 1477-1504.
28. Li, J.-R.; Sculley, J.; Zhou, H.-C. *Chem. Rev.* **2012**, *112*, 869-932.
29. Snurr, R. Q.; Hupp, J. T.; Nguyen, S. T. *AIChE J.* **2004**, *50*, 1090-1095.
30. Allen, F. *Acta Crystallogr. Sect. B: Struct. Sci.* **2002**, *58*, 380-388.
31. Kong, X.; Deng, H.; Yan, F.; Kim, J.; Swisher, J. A.; Smit, B.; Yaghi, O. M.; Reimer, J. A. *Science* **2013**, *341*, 882-885.
32. First, E. L.; Gounaris, C. E.; Floudas, C. A. *Langmuir* **2013**, *29*, 5599-5608.
33. Krishna, R. *Chem. Soc. Rev.* **2012**, *41*, 3099-3118.
34. Yilmaz, B.; Trukhan, N.; Mueller, U. *Chinese Journal of Catalysis* **2012**, *33*, 3-10.
35. Caro, J. *Current Opinion in Chemical Engineering* **2011**, *1*, 77-83.

36. Brown, A. J.; Brunelli, N. A.; Eum, K.; Rashidi, F.; Johnson, J. R.; Koros, W. J.; Jones, C. W.; Nair, S. *Science (New York, N.Y.)* **2014**, *345*, 72-75.
37. Kortunov, P.; Ni, Z.; Paur, C.; Reyes, S.; Zengel, J. In *MAGNETIC RESONANCE IN POROUS MEDIA: Proceedings of the 10th International Bologna Conference on Magnetic Resonance in Porous Media (MRPM10), including the 10th Colloquium on Mobile Magnetic Resonance (CMMR10)*; AIP Publishing: 2011; Vol. 1330, p 57-60.
38. Hara, N.; Yoshimune, M.; Negishi, H.; Haraya, K.; Hara, S.; Yamaguchi, T. *J. Membr. Sci.* **2014**, *450*, 215-223.
39. Pan, Y.; Li, T.; Lestari, G.; Lai, Z. *J. Membr. Sci.* **2012**, *390*, 93-98.
40. Pan, Y.; Lai, Z. *Chem. Commun.* **2011**, *47*, 10275-10277.
41. Park, K. S.; Ni, Z.; Côté, A. P.; Choi, J. Y.; Huang, R.; Uribe-Romo, F. J.; Chae, H. K.; O'Keeffe, M.; Yaghi, O. M. *Proc. Natl. Acad. Sci. U. S. A.* **2006**, *103*, 10186-10191.
42. Thompson, J. A.; Blad, C. R.; Brunelli, N. A.; Lydon, M. E.; Lively, R. P.; Jones, C. W.; Nair, S. *Chemistry of Materials* **2012**, *24*, 1930-1936.
43. Rashidi, F.; Blad, C. R.; Jones, C. W.; Nair, S. *AIChE J.* **2016**, *62*, 525-537.
44. Groom, C. R.; Bruno, I. J.; Lightfoot, M. P.; Ward, S. C. *Acta Crystallographica Section B: Structural Science, Crystal Engineering and Materials* **2016**, *72*, 171-179.
45. Chung, Y. G.; Camp, J.; Haranczyk, M.; Sikora, B. J.; Bury, W.; Krungleviciute, V.; Yildirim, T.; Farha, O. K.; Sholl, D. S.; Snurr, R. Q. *Chemistry of Materials* **2014**, *26*, 6185-6192.
46. Jayachandrababu, K. C.; Verploegh, R. J.; Leisen, J.; Nieuwendaal, R. C.; Sholl, D. S.; Nair, S. *J. Am. Chem. Soc.* **2016**, *138*, 7325-7336.
47. Coudert, F. X.; Boutin, A.; Jeffroy, M.; Mellot-Draznieks, C.; Fuchs, A. H. *ChemPhysChem* **2011**, *12*, 247-258.
48. Ruthven, D. M. *Chemie Ingenieur Technik* **2011**, *83*, 44-52.
49. Yashonath, S.; Ghorai, P. K. *J. Phys. Chem. B* **2008**, *112*, 665-686.
50. Krishna, R. *J. Phys. Chem. C* **2009**, *113*, 19756-19781.
51. Boulfelfel, S.; Ravikovitch, P. I.; Sholl, D. S. *J. Phys. Chem. C* **2015**, *119*, 15643-15653.

52. Gucuyener, C.; van den Bergh, J.; Gascon, J.; Kapteijn, F. *J. Am. Chem. Soc.* **2010**, *132*, 17704-17706.
53. Saint Remi, J. C.; Remy, T.; Van Hunskerken, V.; van de Perre, S.; Duerinck, T.; Maes, M.; De Vos, D.; Gobechiya, E.; Kirschhock, C. E. A.; Baron, G. V.; Denayer, J. F. M. *ChemSusChem* **2011**, *4*, 1074-1077.
54. Nalaparaju, A.; Zhao, X. S.; Jiang, J. W. *Energy & Environmental Science* **2011**, *4*, 2107-2116.
55. Liu, X.; Jin, H.; Li, Y.; Bux, H.; Hu, Z.; Ban, Y.; Yang, W. *J. Membr. Sci.* **2013**, *428*, 498-506.
56. Zhang, C.; Lively, R. P.; Zhang, K.; Johnson, J. R.; Karvan, O.; Koros, W. J. *J. Phys. Chem. Lett.* **2012**, *3*, 2130-2134.
57. Haldoupis, E.; Watanabe, T.; Nair, S.; Sholl, D. S. *ChemPhysChem* **2012**, *13*, 3449-3452.
58. Sitprasert, C.; Wang, F. Y.; Rudolph, V.; Zhu, Z. H. *Chem. Eng. Sci.* **2014**, *108*, 23-32.
59. Haldoupis, E.; Nair, S.; Sholl, D. S. *J. Am. Chem. Soc.* **2010**, *132*, 7528-7539.
60. Zhang, K.; Lively, R. P.; Zhang, C.; Chance, R. R.; Koros, W. J.; Sholl, D. S.; Nair, S. *J. Phys. Chem. Lett.* **2013**, *4*, 3618-3622.
61. Pera-Titus, M.; Farrusseng, D. *J. Phys. Chem. C* **2012**, *116*, 1638-1649.
62. Fairen-Jimenez, D.; Moggach, S. A.; Wharmby, M. T.; Wright, P. A.; Parsons, S.; Duren, T. *J. Am. Chem. Soc.* **2011**, *133*, 8900-8902.
63. Ania, C. O.; Garcia-Perez, E.; Haro, M.; Gutierrez-Sevillano, J. J.; Valdes-Solis, T.; Parra, J. B.; Calero, S. *J. Phys. Chem. Lett.* **2012**, *3*, 1159-1164.
64. Coudert, F.-X.; Jeffroy, M.; Fuchs, A. H.; Boutin, A.; Mellot-Draznieks, C. *J. Am. Chem. Soc.* **2008**, *130*, 14294-14302.
65. Coudert, F.-X.; Boutin, A.; Fuchs, A. H.; Neimark, A. V. *J. Phys. Chem. Lett.* **2013**, *4*, 3198-3205.
66. Salles, F.; Ghoufi, A.; Maurin, G.; Bell, R. G.; Mellot-Draznieks, C.; Ferey, G. *Angew. Chem. Int. Ed.* **2008**, *47*, 8487-8491.
67. Robeson, L. M. *J. Membr. Sci.* **2008**, *320*, 390-400.

68. Allen, F. H. *Acta Crystallographica Section B: Structural Science* **2002**, 58, 380-388.
69. Chung, Y. G.; Camp, J.; Haranczyk, M.; Sikora, B. J.; Bury, W.; Krungleviciute, V.; Yildirim, T.; Farha, O. K.; Sholl, D. S.; Snurr, R. Q. *Chemistry of Materials* **2014**, 26, 6185-6192.
70. Wilmer, C. E.; Leaf, M.; Lee, C. Y.; Farha, O. K.; Hauser, B. G.; Hupp, J. T.; Snurr, R. Q. *Nature Chemistry* **2012**, 4, 83-89.
71. Haldoupis, E.; Nair, S.; Sholl, D. S. *Journal of the American Chemical Society* **2010**, 132, 7528-7539.
72. Willems, T. F.; Rycroft, C. H.; Kazi, M.; Meza, J. C.; Haranczyk, M. *Microporous Mesoporous Mater.* **2012**, 149, 134-141.
73. Awati, R. V.; Ravikovitch, P. I.; Sholl, D. S. *J. Phys. Chem. C* **2015**, 119, 16596-16605.
74. Camp, J. S.; Sholl, D. S. *J. Phys. Chem. C* **2016**, 120, 1110-1120.
75. Gee, J. A.; Chung, J.; Nair, S.; Sholl, D. S. *J. Phys. Chem. C* **2013**, 117, 3169-3176.
76. Kim, K. C.; Yu, D.; Snurr, R. Q. *Langmuir* **2013**, 29, 1446-1456.
77. Frysali, M. G.; Klontzas, E.; Tylisanakis, E.; Froudakis, G. E. *Microporous and Mesoporous Materials* **2016**.
78. Nazarian, D.; Camp, J. S.; Sholl, D. S. *Chemistry of Materials* **2016**.
79. Wollmann, P.; Leistner, M.; Stoeck, U.; Grunker, R.; Gedrich, K.; Klein, N.; Throl, O.; Grahlert, W.; Senkovska, I.; Dreisbach, F.; Kaskel, S. *Chemical Communications* **2011**, 47, 5151-5153.
80. Frenkel, D.; Smit, B. *Understanding molecular simulation: from algorithms to applications*; Academic press, 2001; Vol. 1.
81. Duren, T.; Bae, Y.-S.; Snurr, R. Q. *Chemical Society Reviews* **2009**, 38, 1237-1247.
82. Walton, K. S.; Sholl, D. S. *AIChE Journal* **2015**, 61, 2757-2762.
83. Murthi, M.; Snurr, R. Q. *Langmuir* **2004**, 20, 2489-2497.
84. Fang, H.; Demir, H.; Kamakoti, P.; Sholl, D. S. *Journal of Materials Chemistry A* **2014**, 2, 274-291.



85. Fang, H.; Demir, H.; Kamakoti, P.; Sholl, D. S. *J. Mater. Chem. A* **2014**, *2*, 274-291.
86. Gee, J. A.; Sholl, D. S. *J. Phys. Chem. C* **2016**, *120*, 370-376.
87. Witman, M.; Ling, S.; Jawahery, S.; Boyd, P. G.; Haranczyk, M.; Slater, B.; Smit, B. *J. Am. Chem. Soc.* **2017**, *139*, 5547-5557.
88. Nazarian, D.; Camp, J. S.; Chung, Y. G.; Snurr, R. Q.; Sholl, D. S. *Chemistry of Materials* **2017**, *29*, 2521-2528.
89. Coudert, F.-X.; Jeffroy, M.; Fuchs, A. H.; Boutin, A.; Mellot-Draznieks, C. *Journal of the American Chemical Society* **2008**, *130*, 14294-14302.
90. Zhang, L.; Hu, Z.; Jiang, J. *Journal of the American Chemical Society* **2013**, *135*, 3722-3728.
91. Salles, F.; Ghoufi, A.; Maurin, G.; Bell, R. G.; Mellot-Draznieks, C.; Férey, G. *Angewandte Chemie International Edition* **2008**, *47*, 8487-8491.
92. Wu, H.; Gong, Q.; Olson, D. H.; Li, J. *Chemical Reviews* **2012**, *112*, 836-868.
93. Zhao, P.; Lampronti, G. I.; Lloyd, G. O.; Suard, E.; Redfern, S. A. T. *Journal of Materials Chemistry A* **2014**, *2*, 620-623.
94. Wu, H.; Zhou, W.; Yildirim, T. *Journal of Physical Chemistry C* **2009**, *113*, 3029-3035.
95. Keller, J. U.; Robens, E.; du Fresne von Hohenesche, C. In *Studies in Surface Science and Catalysis*; F. Rodriguez-Reinoso, B. M. J. R., Unger, K., Eds.; Elsevier: 2002; Vol. Volume 144, p 387-394.
96. Skoulidas, A. I.; Sholl, D. S. *The Journal of Physical Chemistry B* **2005**, *109*, 15760-15768.
97. Verploegh, R. J.; Nair, S.; Sholl, D. S. *Journal of the American Chemical Society* **2015**, *137*, 15760-15771.
98. Karger, J.; Binder, T.; Chmelik, C.; Hibbe, F.; Krautscheid, H.; Krishna, R.; Weitkamp, J. *Nature Materials* **2014**, *13*, 333-343.
99. Chmelik, C.; Kärger, J. *Microporous Mesoporous Mater.* **2016**, *225*, 128-132.
100. Skoulidas, A. I.; Sholl, D. S.; Krishna, R. *Langmuir* **2003**, *19*, 7977-7988.
101. Remi, J. C. S.; Lauerer, A.; Chmelik, C.; Vandendael, I.; Terryn, H.; Baron, G. V.; Denayer, J. F. M.; Karger, J. *Nat. Mater.* **2016**, *15*, 401-406.

102. Sholl, D. S.; Lively, R. P. *The Journal of Physical Chemistry Letters* **2015**, 6, 3437-3444.
103. Haldoupis, E.; Watanabe, T.; Nair, S.; Sholl, D. S. *ChemPhysChem* **2012**, 13, 3449-3452.
104. Crank, J. *The Mathematics of Diffusion*; 2 ed.; Oxford University Press: Oxford, 1975.
105. Kärger, J.; Ruthven, D. M.; Theodorou, D. N. *Diffusion in Nanoporous Materials*; Wiley, 2012.
106. Karger, J.; Caro, J.; Cool, P.; Coppens, M.-O.; Jones, D.; Kapteijn, F.; Rodriguez-Reinoso, F.; Stocker, M.; Theodorou, D.; Vansant, E. F.; Weitkamp, J. *Chem. Engg. Technol.* **2009**, 32, 1494-1511.
107. Jobic, H. *Physical Chemistry Chemical Physics* **2016**.
108. Karger, J.; Ruthven, D. M. *New Journal of Chemistry* **2016**.
109. Bux, H.; Chmelik, C.; Baten, J. v.; Krishna, R.; Caro, J. *Adv. Mater.* **2010**, 22, 4741-4743.
110. Krishna, R. *RSC Advances* **2015**, 5, 52269-52295.
111. Krishna, R.; Long, J. R. *Journal of Physical Chemistry C* **2011**, 115, 12941-12950.
112. Crank, J. *The Mathematics of Diffusion*; Oxford University Press: New York, 1979.
113. Keskin, S.; Sholl, D. S. *Energy & Environmental Science* **2010**, 3, 343-351.
114. Erucar, I.; Keskin, S. *Industrial & Engineering Chemistry Research* **2011**, 50, 12606-12616.
115. Keskin, S.; Sholl, D. S. *Langmuir* **2009**, 25, 11786-11795.
116. Thompson, J. A.; Vaughn, J. T.; Brunelli, N. A.; Koros, W. J.; Jones, C. W.; Nair, S. *Microporous and Mesoporous Materials* **2014**, 192, 43-51.
117. Li, Y.-S.; Liang, F.-Y.; Bux, H.; Feldhoff, A.; Yang, W.-S.; Caro, J. *Angewandte Chemie International Edition* **2010**, 49, 548-551.
118. Diestel, L.; Bux, H.; Wachsmuth, D.; Caro, J. *Microporous and Mesoporous Materials* **2012**, 164, 288-293.
119. Mueller, R.; Zhang, S.; Zhang, C.; Lively, R.; Vasenkov, S. *Journal of Membrane Science* **2015**, 477, 123-130.

120. Bux, H.; Chmelik, C.; Krishna, R.; Caro, J. *Journal of Membrane Science* **2011**, 369, 284-289.
121. Diestel, L.; Wang, N.; Schwiedland, B.; Steinbach, F.; Giese, U.; Caro, J. *Journal of Membrane Science* **2015**, 492, 181-186.
122. Sheng, L.; Wang, C.; Yang, F.; Xiang, L.; Huang, X.; Yu, J.; Zhang, L.; Pan, Y.; Li, Y. *Chem. Commun.* **2017**.
123. Zhang, L.; Hu, Z.; Jiang, J. *Journal of Physical Chemistry C* **2012**, 116, 19268-19277.
124. Singh, T.; Kang, D.-Y.; Nair, S. *Journal of Membrane Science* **2013**, 448, 160-169.
125. Semino, R.; Ramsahye, N. A.; Ghoufi, A.; Maurin, G. *ACS Applied Materials & Interfaces* **2016**, 8, 809-819.
126. Eldridge, R. B. *Ind. Eng. Chem. Res.* **1993**, 32, 2208-2212.
127. Gücüyener, C.; Gascon, J.; Kapteijn, F. In *Small-Scale Gas to Liquid Fuel Synthesis*; CRC Press: Boca Raton, FL, 2015, p 135-188.
128. Kwon, H. T.; Jeong, H.-K. *J. Am. Chem. Soc.* **2013**, 135, 10763-10768.
129. Liu, D.; Ma, X.; Xi, H.; Lin, Y. S. *J. Membr. Sci.* **2014**, 451, 85-93.
130. Bux, H.; Chmelik, C.; Krishna, R.; Caro, J. *J. Membr. Sci.* **2011**, 369, 284-289.
131. Hertäg, L.; Bux, H.; Caro, J.; Chmelik, C.; Remsungnen, T.; Knauth, M.; Fritzsche, S. *J. Membr. Sci.* **2011**, 377, 36-41.
132. Parkes, M. V.; Demir, H.; Teich-McGoldrick, S. L.; Sholl, D. S.; Greathouse, J. A.; Allendorf, M. D. *Microporous Mesoporous Mater.* **2014**, 194, 190-199.
133. Zheng, B.; Sant, M.; Demontis, P.; Suffritti, G. B. *J. Phys. Chem. C* **2012**, 116, 933-938.
134. Gee, J. A.; Chung, J.; Nair, S.; Sholl, D. S. *J. Phys. Chem. C* **2013**, 117, 3169-3176.
135. Sholl, D. S. *Acc. Chem. Res.* **2006**, 39, 403-411.
136. Zheng, B.; Pan, Y.; Lai, Z.; Huang, K.-W. *Langmuir* **2013**, 29, 8865-8872.
137. June, R. L.; Bell, A. T.; Theodorou, D. N. *J. Phys. Chem.* **1991**, 95, 8866-8878.

138. Snurr, R. Q.; Bell, A. T.; Theodorou, D. N. *J. Phys. Chem.* **1994**, *98*, 11948-11961.
139. Auerbach, S. M.; Henson, N. J.; Cheetham, A. K.; Metiu, H. I. *J. Phys. Chem.* **1995**, *99*, 10600-10608.
140. Mosell, T.; Schrimpf, G.; Brickmann, J. *J. Phys. Chem.* **1996**, *100*, 4582-4590.
141. Maginn, E. J.; Bell, A. T.; Theodorou, D. N. *J. Phys. Chem.* **1996**, *100*, 7155-7173.
142. Mosell, T.; Schrimpf, G.; Brickmann, J. *J. Phys. Chem. B* **1997**, *101*, 9476-9484.
143. Mosell, T.; Schrimpf, G.; Brickmann, J. *J. Phys. Chem. B* **1997**, *101*, 9485-9494.
144. R. Forester, T.; Smith, W. *J. Chem. Soc., Faraday Trans.* **1997**, *93*, 3249-3257.
145. Jousse, F.; Auerbach, S. M. *J. Chem. Phys.* **1997**, *107*, 9629-9639.
146. Vlugt, T. J. H.; Dellago, C.; Smit, B. *J. Chem. Phys.* **2000**, *113*, 8791-8799.
147. Auerbach, S. M. *Acta Chem. Scand., Ser. A* **2000**, *19*, 155-198.
148. Dubbeldam, D.; Beerdsen, E.; Vlugt, T. J. H.; Smit, B. *J. Chem. Phys.* **2005**, *122*, 224712.
149. Dubbeldam, D.; Beerdsen, E.; Calero, S.; Smit, B. *J. Phys. Chem. B* **2006**, *110*, 3164-3172.
150. Fairen-Jimenez, D.; Moggach, S. A.; Wharmby, M. T.; Wright, P. A.; Parsons, S.; Düren, T. *J. Am. Chem. Soc.* **2011**, *133*, 8900-8902.
151. Peralta, D.; Chaplais, G.; Paillaud, J.-L.; Simon-Masseron, A.; Barthelet, K.; Pirngruber, G. D. *Microporous Mesoporous Mater.* **2013**, *173*, 1-5.
152. Skoulidas, A. I.; Sholl, D. S. *J. Phys. Chem. B* **2005**, *109*, 15760-15768.
153. Karger, J.; Binder, T.; Chmelik, C.; Hibbe, F.; Krautscheid, H.; Krishna, R.; Weitkamp, J. *Nat. Mater.* **2014**, *13*, 333-343.
154. Frenkel, D.; Smit, B. *Understanding Molecular Simulation: From Algorithms to Applications*; 2nd ed.; Academic Press: New York, 2002.
155. Sholl, D. S.; Steckel, J. A. *Density Functional Theory: A Practical Introduction*; John Wiley & Sons, Inc.: Hoboken, NJ, 2009.
156. Henkelman, G.; Jonsson, H. *J. Chem. Phys.* **2000**, *113*, 9978-9985.

157. Torrie, G. M.; Valleau, J. P. *J. Comput. Phys.* **1977**, *23*, 187-199.
158. Kaestner, J. *Wiley Interdiscip. Rev. Comput. Mol. Sci.* **2011**, *1*, 932-942.
159. Voter, A. F.; Sørensen, M. R. In *MRS Proceedings: Symposium J – Multiscale Modelling of Materials*; Bulatov, V. V., Diazde la Rubia, T., Phillips, R., Kaxiras, E., Ghoniem, N., Eds. 1998; Vol. 538, p 427-439.
160. Izrailev, S.; Stepaniants, S.; Isralewitz, B.; Kosztin, D.; Lu, H.; Molnar, F.; Wriggers, W.; Schulten, K. In *Computational Molecular Dynamics: Challenges, Methods, Ideas*; Springer: New York, 1999, p 39-65.
161. Laio, A.; Parrinello, M. *Proc. Natl. Acad. Sci. U. S. A.* **2002**, *99*, 12562-12566.
162. Tunca, C.; Ford, D. M. *J. Chem. Phys.* **1999**, *111*, 2751-2760.
163. Dellago, C.; Bolhuis, P. G.; Csajka, F. S.; Chandler, D. *J. Chem. Phys.* **1998**, *108*, 1964-1977.
164. van Erp, T. S.; Bolhuis, P. G. *J. Comput. Phys.* **2005**, *205*, 157-181.
165. Kirkwood, J. G. *J. Chem. Phys.* **1935**, *3*, 300-313.
166. Abouelnasr, M. K. F.; Smit, B. *Physical Chemistry Chemical Physics* **2012**, *14*, 11600-11609.
167. Voter, A. F.; Doll, J. D. *J. Chem. Phys.* **1985**, *82*, 80-92.
168. Awati, R. V.; Ravikovitch, P. I.; Sholl, D. S. *J. Phys. Chem. C* **2013**, *117*, 13462-13473.
169. Tunca, C.; Ford, D. M. *Chem. Eng. Sci.* **2003**, *58*, 3373-3383.
170. Tunca, C.; Ford, D. M. *J. Phys. Chem. B* **2002**, *106*, 10982-10990.
171. Beerdsen, E.; Dubbeldam, D.; Smit, B. *J. Phys. Chem. B* **2006**, *110*, 22754-22772.
172. Jee, S. E.; Sholl, D. S. *J. Am. Chem. Soc.* **2009**, *131*, 7896-7904.
173. Kolokathis, P. D.; Pantatosaki, E.; Gatsiou, C.-A.; Jobic, H.; Papadopoulos, G. K.; Theodorou, D. N. *Mol. Simul.* **2014**, *40*, 80-100.
174. Zhang, L.; Hu, Z.; Jiang, J. *J. Am. Chem. Soc.* **2013**, *135*, 3722-3728.

175. Wu, H.; Zhou, W.; Yildirim, T. *J. Am. Chem. Soc.* **2007**, *129*, 5314-5315.
176. Martin, M. G.; Siepmann, J. I. *J. Phys. Chem. B* **1998**, *102*, 2569-2577.
177. Wick, C. D.; Martin, M. G.; Siepmann, J. I. *J. Phys. Chem. B* **2000**, *104*, 8008-8016.
178. Dubbeldam, D.; Calero, S.; Vlugt, T. J. H.; Krishna, R.; Maesen, T. L. M.; Smit, B. *J. Phys. Chem. B* **2004**, *108*, 12301-12313.
179. Talu, O.; Myers, A. L. *AIChE J.* **2001**, *47*, 1160-1168.
180. Clark, L. A.; Gupta, A.; Snurr, R. Q. *J. Phys. Chem. B* **1998**, *102*, 6720-6731.
181. Brand, S. K.; Colón, Y. J.; Getman, R. B.; Snurr, R. Q. *Microporous Mesoporous Mater.* **2013**, *171*, 103-109.
182. Potoff, J. J.; Siepmann, J. I. *AIChE J.* **2001**, *47*, 1676-1682.
183. Zhang, L.; Siepmann, J. I. *Theor Chem Acc* **2006**, *115*, 391-397.
184. Harris, J. G.; Yung, K. H. *J. Phys. Chem.* **1995**, *99*, 12021-12024.
185. Dubbeldam, D.; Calero, S.; Ellis, D. E.; Snurr, R. Q. *Mol. Simul.* **2015**, 1-21.
186. Plimpton, S. *J. Comput. Phys.* **1995**, *117*, 1-19.
187. Fiorin, G.; Klein, M. L.; Hénin, J. *Mol. Phys.* **2013**, *111*, 3345-3362.
188. Grossfield, A. *WHAM: the weighted histogram analysis method, version 2.0.9*, <http://membrane.urmc.rochester.edu/content/wham>; Department of Biochemistry and Biophysics, University of Rochester Medical Center: Rochester, NY, 2013.
189. Eum, K.; Jayachandrababu, K. C.; Rashidi, F.; Zhang, K.; Leisen, J.; Graham, S.; Lively, R. P.; Chance, R. R.; Sholl, D. S.; Jones, C. W.; Nair, S. *J. Am. Chem. Soc.* **2015**, *137*, 4191-4197.
190. Willems, T. F.; Rycroft, C. H.; Kazi, M.; Meza, J. C.; Haranczyk, M. *Microporous Mesoporous Mater.* **2012**, *149*, 134-141.
191. Corma, A.; Rey, F.; Rius, J.; Sabater, M. J.; Valencia, S. *Nature* **2004**, *431*, 287-290.
192. Newman, M. E. J.; Ziff, R. M. *Phys. Rev. E: Stat., Nonlinear, Soft Matter Phys.* **2001**, *64*, 016706.

193. Fairen-Jimenez, D.; Galvelis, R.; Torrisi, A.; Gellan, A. D.; Wharmby, M. T.; Wright, P. A.; Mellot-Draznieks, C.; Duren, T. *Dalton Trans.* **2012**, 41, 10752-10762.
194. Dubbeldam, D.; Ford, D. C.; Ellis, D. E.; Snurr, R. Q. *Mol. Simul.* **2009**, 35, 1084-1097.
195. Pusch, A.-K.; Splith, T.; Moschkowitz, L.; Karmakar, S.; Biniwale, R.; Sant, M.; Suffritti, G.; Demontis, P.; Cravillon, J.; Pantatosaki, E.; Stallmach, F. *Adsorption* **2012**, 18, 359-366.
196. Pantatosaki, E.; Megariotis, G.; Pusch, A.-K.; Chmelik, C.; Stallmach, F.; Papadopoulos, G. K. *J. Phys. Chem. C* **2012**, 116, 201-207.
197. Jobic, H.; Kolokolov, D. I.; Stepanov, A. G.; Koza, M. M.; Ollivier, J. *J. Phys. Chem. C* **2015**, 119, 16115-16120.
198. Zhang, L.; Wu, G.; Jiang, J. *J. Phys. Chem. C* **2014**, 118, 8788-8794.
199. Chmelik, C.; Bux, H.; Caro, J.; Heinke, L.; Hibbe, F.; Titze, T.; Kärger, J. *Phys. Rev. Lett.* **2010**, 104, 085902.
200. Chmelik, C.; Freude, D.; Bux, H.; Haase, J. *Microporous Mesoporous Mater.* **2012**, 147, 135-141.
201. Chmelik, C. *Microporous Mesoporous Mater.* **2015**, 216, 138-145.
202. Chmelik, C.; van Baten, J.; Krishna, R. *J. Membr. Sci.* **2012**, 397–398, 87-91.
203. Bux, H.; Chmelik, C.; van Baten, J. M.; Krishna, R.; Caro, J. *Adv. Mater.* **2010**, 22, 4741-4743.
204. Bux, H.; Liang, F.; Li, Y.; Cravillon, J.; Wiebcke, M.; Caro, J. *J. Am. Chem. Soc.* **2009**, 131, 16000-16001.
205. Pan, Y.; Wang, B.; Lai, Z. *J. Membr. Sci.* **2012**, 421–422, 292-298.
206. Sholl, D. S. *Nat. Chem.* **2011**, 3, 429-430.
207. Kulkarni, A.; Sholl, D. S. *Langmuir* **2015**, 31, 8453-8468.
208. Furukawa, H.; Cordova, K. E.; O’Keeffe, M.; Yaghi, O. M. *Science* **2013**, 341, 1230444.
209. Shah, M.; McCarthy, M. C.; Sachdeva, S.; Lee, A. K.; Jeong, H.-K. *Ind. Eng. Chem. Res.* **2012**, 51, 2179-2199.

210. Peng, Y.; Li, Y.; Ban, Y.; Jin, H.; Jiao, W.; Liu, X.; Yang, W. *Science* **2014**, *346*, 1356-1359.
211. Corma, A.; García, H.; Llabrés i Xamena, F. X. *Chem. Rev.* **2010**, *110*, 4606-4655.
212. Van de Voorde, B.; Bueken, B.; Denayer, J.; De Vos, D. *Chem. Soc. Rev.* **2014**, *43*, 5766-5788.
213. Li, B.; Wen, H.-M.; Zhou, W.; Chen, B. *J. Phys. Chem. Lett.* **2014**, *5*, 3468-3479.
214. Stavila, V.; Talin, A. A.; Allendorf, M. D. *Chem. Soc. Rev.* **2014**, *43*, 5994-6010.
215. Bennett, T. D.; H. Fuchs, A.; Cheetham, A. K.; Coudert, F.-X. *Dalton Transactions* **2016**, *45*, 4058-4059.
216. Pimentel, B. R.; Parulkar, A.; Zhou, E.-k.; Brunelli, N. A.; Lively, R. P. *ChemSusChem* **2014**, *7*, 3202-3240.
217. Wharmby, M. T.; Henke, S.; Bennett, T. D.; Bajpe, S. R.; Schwedler, I.; Thompson, S. P.; Gozzo, F.; Simoncic, P.; Mellot-Draznieks, C.; Tao, H.; Yue, Y.; Cheetham, A. K. *Angew. Chem.* **2015**, *127*, 6547-6551.
218. Du, Y.; Wooller, B.; Nines, M.; Kortunov, P.; Paur, C. S.; Zengel, J.; Weston, S. C.; Ravikovitch, P. I. *J. Am. Chem. Soc.* **2015**, *137*, 13603-13611.
219. Verploegh, R. J.; Nair, S.; Sholl, D. S. *J. Am. Chem. Soc.* **2015**, *137*, 15760-15771.
220. Haldoupis, E.; Nair, S.; Sholl, D. S. *Physical Chemistry Chemical Physics* **2011**, *13*, 5053-5060.
221. Greathouse, J. A.; Allendorf, M. D. *J. Am. Chem. Soc.* **2006**, *128*, 10678-10679.
222. Greathouse, J. A.; Allendorf, M. D. *J. Phys. Chem. C* **2008**, *112*, 5795-5802.
223. Dubbeldam, D.; Walton, K. S.; Ellis, D. E.; Snurr, R. Q. *Angew. Chem.* **2007**, *119*, 4580-4583.
224. Mayo, S. L.; Olafson, B. D.; Goddard, W. A. *J. Phys. Chem.* **1990**, *94*, 8897-8909.
225. Gee, J. A.; Sholl, D. S. *J. Phys. Chem. C* **2015**.
226. Li, P.; Merz, K. M. *Journal of Chemical Information and Modeling* **2016**, *56*, 599-604.



227. Rappe, A. K.; Casewit, C. J.; Colwell, K. S.; Goddard, W. A.; Skiff, W. M. *J. Am. Chem. Soc.* **1992**, *114*, 10024-10035.
228. Wang, J.; Wolf, R. M.; Caldwell, J. W.; Kollman, P. A.; Case, D. A. *Journal of computational chemistry* **2004**, *25*, 1157-1174.
229. Seminario, J. M. *Int. J. Quantum Chem* **1996**, *30*, 1271-1277.
230. Hagler, A. T. *Journal of Chemical Theory and Computation* **2015**, *11*, 5555-5572.
231. Wang, L.-P.; Martinez, T. J.; Pande, V. S. *J. Phys. Chem. Lett.* **2014**, *5*, 1885-1891.
232. Tafipolsky, M.; Amirjalayer, S.; Schmid, R. *Journal of Computational Chemistry* **2007**, *28*, 1169-1176.
233. Amirjalayer, S.; Tafipolsky, M.; Schmid, R. *Angew. Chem. Int. Ed.* **2007**, *46*, 463-466.
234. Bureekaew, S.; Amirjalayer, S.; Tafipolsky, M.; Spickermann, C.; Roy, T. K.; Schmid, R. *Physica Status Solidi B-Basic Solid State Physics* **2013**, *250*, 1128-1141.
235. Allinger, N. L.; Yuh, Y. H.; Lii, J. H. *J. Am. Chem. Soc.* **1989**, *111*, 8551-8566.
236. Bristow, J. K.; Tiana, D.; Walsh, A. *Journal of Chemical Theory and Computation* **2014**, *10*, 4644-4652.
237. Vanduyfhuys, L.; Vandenbrande, S.; Verstraelen, T.; Schmid, R.; Waroquier, M.; Van Speybroeck, V. *Journal of Computational Chemistry* **2015**, *36*, 1015-1027.
238. Rogge, S. M. J.; Wieme, J.; Vanduyfhuys, L.; Vandenbrande, S.; Maurin, G.; Verstraelen, T.; Waroquier, M.; Van Speybroeck, V. *Chemistry of Materials* **2016**, *28*, 5721-5732.
239. Battisti, A.; Taioli, S.; Garberoglio, G. *Microporous Mesoporous Mater.* **2011**, *143*, 46-53.
240. Thornton, A. W.; Dubbeldam, D.; Liu, M. S.; Ladewig, B. P.; Hill, A. J.; Hill, M. R. *Energy & Environmental Science* **2012**, *5*, 7637-7646.
241. Chokbunpiam, T.; Chanajaree, R.; Saengsawang, O.; Reimann, S.; Chmelik, C.; Fritzsche, S.; Caro, J.; Remsungnen, T.; Hannongbua, S. *Microporous Mesoporous Mater.* **2013**, *174*, 126-134.
242. Krokidas, P.; Castier, M.; Moncho, S.; Brothers, E.; Economou, I. G. *J. Phys. Chem. C* **2015**.

243. Krokidas, P.; Castier, M.; Moncho, S.; Sredojevic, D. N.; Brothers, E. N.; Kwon, H. T.; Jeong, H.-K.; Lee, J. S.; Economou, I. G. *J. Phys. Chem. C* **2016**, *120*, 8116-8124.
244. Phuong, V. T.; Chokbunpiam, T.; Fritzsche, S.; Remsungnen, T.; Rungrotmongkol, T.; Chmelik, C.; Caro, J.; Hannongbua, S. *Microporous Mesoporous Mater.* **2016**, *235*, 69-77.
245. Gao, M.; Misquitta, A. J.; H. N. Rimmer, L.; Dove, M. T. *Dalton Transactions* **2016**.
246. Wu, R.; Lu, Z.; Cao, Z.; Zhang, Y. *Journal of Chemical Theory and Computation* **2011**, *7*, 433-443.
247. Hoops, S. C.; Anderson, K. W.; Merz, K. M. *J. Am. Chem. Soc.* **1991**, *113*, 8262-8270.
248. Lin, F.; Wang, R. *Journal of Chemical Theory and Computation* **2010**, *6*, 1852-1870.
249. Hartsough, D. S.; Merz, K. M., Jr. *J. Phys. Chem.* **1995**, *99*, 11266-11275.
250. Peters, M. B.; Yang, Y.; Wang, B.; Füsti-Molnár, L. s.; Weaver, M. N.; Merz Jr, K. M. *Journal of chemical theory and computation* **2010**, *6*, 2935-2947.
251. Sakharov, D. V.; Lim, C. *Journal of Computational Chemistry* **2009**, *30*, 191-202.
252. Morris, W.; Doonan, C. J.; Furukawa, H.; Banerjee, R.; Yaghi, O. M. *J. Am. Chem. Soc.* **2008**, *130*, 12626-+.
253. Karagiari, O.; Lalonde, M. B.; Bury, W.; Sarjeant, A. A.; Farha, O. K.; Hupp, J. T. *J. Am. Chem. Soc.* **2012**, *134*, 18790-18796.
254. Kresse, G.; Furthmüller, J. *Physical Review B* **1996**, *54*, 11169-11186.
255. Perdew, J. P.; Burke, K.; Ernzerhof, M. *Phys. Rev. Lett.* **1996**, *77*, 3865-3868.
256. Perdew, J. P.; Burke, K.; Ernzerhof, M. *Phys. Rev. Lett.* **1997**, *78*, 1396-1396.
257. Grimme, S. *Journal of computational chemistry* **2006**, *27*, 1787-1799.
258. Grimme, S.; Ehrlich, S.; Goerigk, L. *Journal of Computational Chemistry* **2011**, *32*, 1456-1465.
259. Grimme, S.; Antony, J.; Ehrlich, S.; Krieg, H. *J. Chem. Phys.* **2010**, *132*, 154104.
260. Manz, T. A.; Sholl, D. S. *Journal of Chemical Theory and Computation* **2010**, *6*, 2455-2468.

261. Cornell, W. D.; Cieplak, P.; Bayly, C. I.; Gould, I. R.; Merz, K. M.; Ferguson, D. M.; Spellmeyer, D. C.; Fox, T.; Caldwell, J. W.; Kollman, P. A. *J. Am. Chem. Soc.* **1995**, *117*, 5179-5197.
262. Allinger, N. L.; Zhou, X.; Bergsma, J. *Journal of Molecular Structure: THEOCHEM* **1994**, *312*, 69-83.
263. Hutter, J.; Iannuzzi, M.; Schiffmann, F.; VandeVondele, J. *Wires Comput Mol Sci* **2014**, *4*, 15-25.
264. VandeVondele, J.; Krack, M.; Mohamed, F.; Parrinello, M.; Chassaing, T.; Hutter, J. *Comput Phys Commun* **2005**, *167*, 103-128.
265. VandeVondele, J.; Hutter, J. *J Chem Phys* **2003**, *118*, 4365-4369.
266. Krack, M.; Parrinello, M. *Phys Chem Chem Phys* **2000**, *2*, 2105-2112.
267. Lippert, G.; Hutter, J.; Parrinello, M. *Theor Chem Acc* **1999**, *103*, 124-140.
268. Goedecker, S.; Teter, M.; Hutter, J. *Phys Rev B* **1996**, *54*, 1703-1710.
269. Hartwigsen, C.; Goedecker, S.; Hutter, J. *Phys Rev B* **1998**, *58*, 3641-3662.
270. Frenkel, D.; Smit, B. *Understanding molecular simulation : from algorithms to applications*; 2nd ed.; Academic Press: San Diego, 2002.
271. Brown, W. M.; Wang, P.; Plimpton, S. J.; Tharrington, A. N. *Comput. Phys. Commun.* **2011**, *182*, 898-911.
272. Wang, L.-P.; Head-Gordon, T.; Ponder, J. W.; Ren, P.; Chodera, J. D.; Eastman, P. K.; Martinez, T. J.; Pande, V. S. *J. Phys. Chem. B* **2013**, *117*, 9956-9972.
273. Guvench, O.; MacKerell, A. D. *J. Mol. Model.* **2008**, *14*, 667-679.
274. Baburin, I. A.; Leoni, S. *J. Mater. Chem.* **2012**, *22*, 10152-10154.
275. Baburin, I. A.; Leoni, S.; Seifert, G. *J. Phys. Chem. B* **2008**, *112*, 9437-9443.
276. Gee, J. A.; Sholl, D. S. *J. Phys. Chem. C* **2013**, *117*, 20636-20642.
277. Han, R.; Sholl, D. S. *J. Phys. Chem. C* **2016**, *120*, 27380-27388.
278. Galvelis, R.; Slater, B.; Cheetham, A. K.; Mellot-Draznieks, C. *Cryst. Eng.* **2012**, *14*, 374-378.

279. Chapman, K. W.; Halder, G. J.; Chupas, P. J. *J. Am. Chem. Soc.* **2009**, *131*, 17546-17547.
280. Gabrieli, A.; Sant, M.; Demontis, P.; Suffritti, G. B. *Microporous Mesoporous Mater.* **2014**, *197*, 339-347.
281. Boulfelfel, S. E.; Ravikovitch, P. I.; Koziol, L.; Sholl, D. S. *J. Phys. Chem. C* **2016**, *120*, 14140-14148.
282. Coudert, F.-X. *ChemPhysChem*, n/a-n/a.
283. Karger, J.; Valiullin, R. *Chem. Soc. Rev.* **2013**, *42*, 4172-4197.
284. Hu, Z.; Zhang, L.; Jiang, J. *J. Chem. Phys.* **2012**, *136*, 244703.
285. Kolokolov, D. I.; Stepanov, A. G.; Jobic, H. *J. Phys. Chem. C* **2015**, *119*, 27512-27520.
286. Lee, L.-K.; Ruthven, D. M. *Journal of the Chemical Society, Faraday Transactions 1: Physical Chemistry in Condensed Phases* **1979**, *75*, 2406-2422.
287. Brandani, S. *Adsorption* **1998**, *4*, 17-24.
288. Tanaka, S.; Fujita, K.; Miyake, Y.; Miyamoto, M.; Hasegawa, Y.; Makino, T.; Van der Perre, S.; Cousin Saint Remi, J.; Van Assche, T.; Baron, G. V.; Denayer, J. F. M. *J. Phys. Chem. C* **2015**, *119*, 28430-28439.
289. Kolokathis, P. D.; Káli, G.; Jobic, H.; Theodorou, D. N. *J. Phys. Chem. C* **2016**, *120*, 21410-21426.
290. Liédana, N.; Galve, A.; Rubio, C.; Téllez, C.; Coronas, J. *ACS Applied Materials & Interfaces* **2012**, *4*, 5016-5021.
291. Sholl, D. S.; Lively, R. P. *J. Phys. Chem. Lett.* **2015**, *6*, 3437-3444.
292. Phan, A.; Doonan, C. J.; Uribe-Romo, F. J.; Knobler, C. B.; O'Keeffe, M.; Yaghi, O. M. *Acc. Chem. Res.* **2010**, *43*, 58-67.
293. Chokbunpiam, T.; Fritzsche, S.; Caro, J.; Chmelik, C.; Janke, W.; Hannongbua, S. *J. Phys. Chem. C* **2017**, *121*, 10455-10462.
294. Freeman, B. D. *Macromolecules* **1999**, *32*, 375-380.
295. Zhao, P.; Lampronti, G. I.; Lloyd, G. O.; Wharmby, M. T.; Facq, S.; Cheetham, A. K.; Redfern, S. A. T. *Chemistry of Materials* **2014**, *26*, 1767-1769.

296. Zhao, P.; Lampronti, G. I.; Lloyd, G. O.; Suard, E.; Redfern, S. A. T. *J. Mater. Chem. A* **2014**, *2*, 620-623.
297. Pilvar, P.; Fritzsche, S.; Caro, J.; Janke, W.
298. Wu, X.; Niknam Shahrak, M.; Yuan, B.; Deng, S. *Microporous Mesoporous Mater.* **2014**, *190*, 189-196.
299. Thornton, A. W.; Simon, C. M.; Kim, J.; Kwon, O.; Deeg, K. S.; Konstas, K.; Pas, S. J.; Hill, M. R.; Winkler, D. A.; Haranczyk, M.; Smit, B. *Chemistry of Materials* **2017**, *29*, 2844-2854.
300. Pophale, R.; Cheeseman, P. A.; Deem, M. W. *Physical Chemistry Chemical Physics* **2011**, *13*, 12407-12412.
301. Park, K. S.; Ni, Z.; Cote, A. P.; Choi, J. Y.; Huang, R.; Uribe-Romo, F. J.; Chae, H. K.; O'Keeffe, M.; Yaghi, O. M. *Proc. Natl. Acad. Sci. U. S. A.* **2006**, *103*, 10186-10191.
302. Banerjee, R.; Phan, A.; Wang, B.; Knobler, C. B.; Furukawa, H.; O'Keeffe, M.; Yaghi, O. M. *Science* **2008**, *319*, 939-943.
303. Phan, A.; Doonan, C. J.; Uribe-Romo, F. J.; Knobler, C. B.; O'Keeffe, M.; Yaghi, O. M. *Acc. Chem. Res.* **2009**, *43*, 58-67.
304. Li, Y.; Liang, F.; Bux, H.; Yang, W.; Caro, J. *J. Membr. Sci.* **2010**, *354*, 48-54.
305. Brown, A. J.; Johnson, J. R.; Lydon, M. E.; Koros, W. J.; Jones, C. W.; Nair, S. *Angew. Chem.* **2012**, *124*, 10767-10770.
306. Thornton, A. W.; Dubbeldam, D.; Liu, M. S.; Ladewig, B. P.; Hill, A. J.; Hill, M. R. *Energy Environ. Sci.* **2012**, *5*, 7637-7646.
307. Pimentel, B. R.; Parulkar, A.; Zhou, E.-k.; Brunelli, N. A.; Lively, R. P. *ChemSusChem* **2014**, *7*, 3202-3240.
308. Banerjee, R.; Furukawa, H.; Britt, D.; Knobler, C. B.; O'Keeffe, M.; Yaghi, O. M. *J. Am. Chem. Soc.* **2009**, *131*, 3875-3877.
309. Morris, W.; Leung, B.; Furukawa, H.; Yaghi, O. K.; He, N.; Hayashi, H.; Houndonougbo, Y.; Asta, M.; Laird, B. B.; Yaghi, O. M. *J. Am. Chem. Soc.* **2010**, *132*, 11006-11008.
310. Remi, J. C. S.; Remy, T.; Hunskerken, V. V.; Perre, S. v. d.; Duerinck, T.; Maes, M.; Vos, D. D.; Gobechiya, E.; Kirschhock, C. E. A.; Baron, G. V.; Denayer, J. F. M. *ChemSusChem* **2011**, *4*, 1074-1077.

311. Zhang, C.; Lively, R. P.; Zhang, K.; Johnson, J. R.; Karvan, O.; Koros, W. J. *J. Phys. Chem. Lett.* **2012**, *3*, 2130-2134.
312. Zhang, K.; Lively, R. P.; Zhang, C.; Koros, W. J.; Chance, R. R. *J. Phys. Chem. C* **2013**, *117*, 7214-7225.
313. Zhang, K.; Lively, R. P.; Dose, M. E.; Brown, A. J.; Zhang, C.; Chung, J.; Nair, S.; Koros, W. J.; Chance, R. R. *Chem. Commun.* **2013**, *49*, 3245.
314. Zhang, K.; Lively, R. P.; Zhang, C.; Chance, R. R.; Koros, W. J.; Sholl, D. S.; Nair, S. *J. Phys. Chem. Lett.* **2013**, *4*, 3618-3622.
315. Thompson, J. A.; Blad, C. R.; Brunelli, N. A.; Lydon, M. E.; Lively, R. P.; Jones, C. W.; Nair, S. *Chem. Mater.* **2012**, *24*, 1930-1936.
316. Thompson, J. A.; Brunelli, N. A.; Lively, R. P.; Johnson, J. R.; Jones, C. W.; Nair, S. *J. Phys. Chem. C* **2013**, *117*, 8198-8207.
317. Eum, K.; Jayachandrababu, K. C.; Rashidi, F.; Zhang, K.; Leisen, J.; Graham, S.; Lively, R. P.; Chance, R. R.; Sholl, D. S.; Jones, C. W.; Nair, S. *J. Am. Chem. Soc.* **2015**, *137*, 4191-4197.
318. Rashidi, F.; Blad, C. R.; Jones, C. W.; Nair, S. *AIChE J.* **2016**, *62*, 525-537.
319. Wu, Y.; Chen, H.; Liu, D.; Qian, Y.; Xi, H. *Chem. Eng. Sci.* **2015**, *124*, 144-153.
320. Thornton, A. W.; Dubbeldam, D.; Liu, M. S.; Ladewig, B. P.; Hill, A. J.; Hill, M. R. *Energy Environ. Sci.* **2012**, *5*, 7637-7646.
321. Liu, B.; Smit, B. *J. Phys. Chem. C* **2010**, *114*, 8515-8522.
322. Liu, J.; Keskin, S.; Sholl, D. S.; Johnson, J. K. *J. Phys. Chem. C* **2011**, *115*, 12560-12566.
323. Clauss, J.; Schmidt-Rohr, K.; Spiess, H. W. *Acta Polymer.* **1993**, *44*, 1-17.
324. Mellinger, F.; Wilhelm, M.; Spiess, H. W. *Macromolecules* **1999**, *32*, 4686-4691.
325. Jia, X.; Wolak, J.; Wang, X.; White, J. L. *Macromolecules* **2003**, *36*, 712-718.
326. Schmidt-Rohr, K.; Spiess, H. W. *Multidimensional solid-state NMR and polymers*; Academic Press, 1994.
327. Baias, M.; Lesage, A.; Aguado, S.; Canivet, J.; Moizan-Basle, V.; Audebrand, N.; Farrusseng, D.; Emsley, L. *Angew. Chem. Int. Ed* **2015**, *54*, 5971-5976.

328. Kong, X.; Deng, H.; Yan, F.; Kim, J.; Swisher, J. A.; Smith, B.; Yaghi, O. M.; Reimer, J. A. *Science* **2013**, *341*, 882-885.
329. Krajnc, A.; Kos, T.; Zabukovec Logar, N.; Mali, G. *Angew. Chem. Int. Ed* **2015**, *54*, 10535-10538.
330. Kamakoti, P.; Sholl, D. S. *Phys. Rev. B* **2005**, *71*, 014301 014301-014309.
331. Lee, M.; Goldberg, W. I. *Phys. Rev.* **1965**, *140*, A1261-A1271.
332. Leskes, M.; Madhu, P. K.; Vega, S. *Chem. Phys. Lett.* **2007**, *447*, 370-374.
333. Morris, W.; Doonan, C. J.; Furukawa, H.; Banerjee, R.; Yaghi, O. M. *J. Am. Chem. Soc.* **2008**, *130*, 12626-12627.
334. Kresse, G.; Furthmüller, J. *Phys. Rev. B* **1996**, *54*, 11169-11186.
335. Perdew, J. P.; Burke, K.; Ernzerhof, M. *Phys. Rev. Lett.* **1996**, *77*, 3865-3868.
336. Grimme, S. *J. Comput. Chem.* **2006**, *27*, 1787-1799.
337. Newman, M. E. J.; Ziff, R. M. *Phys. Rev. E.* **2001**, *64*, 016706.
338. Macrae, C. F.; Bruno, I. J.; Chisholm, J. A.; Edgington, P. R.; McCabe, P.; Pidcock, E.; Rodriguez-Monge, L.; Taylor, R.; van de Streek, J.; Wood, P. A. *J. Appl. Crystallogr.* **2008**, *41*, 466-470.
339. Macrae, C. F.; Edgington, P. R.; McCabe, P.; Pidcock, E.; Shields, G. P.; Taylor, R.; Towler, M.; van de Streek, J. *J. Appl. Crystallogr.* **2006**, *39*, 453-457.
340. Bruno, I. J.; Cole, J. C.; Edgington, P. R.; Kessler, M.; Macrae, C. F.; McCabe, P.; Pearson, J.; Taylor, R. *Acta Crystallographica Section B: Structural Science* **2002**, *58*, 389-397.
341. Taylor, R.; Macrae, C. F. *Acta Crystallographica Section B: Structural Science* **2001**, *57*, 815-827.
342. Perrin, C. L.; Dwyer, T. J. *Chem. Rev.* **1990**, *90*, 935-967.
343. Elena, B.; Emsley, L. *J. Am. Chem. Soc.* **2005**, *127*, 9140-9146.
344. Elena, B.; Pintacuda, G.; Mifsud, N.; Emsley, L. *J. Am. Chem. Soc.* **2006**, *128*, 9555-9560.
345. Suter, D.; Ernst, R. R. *Phys. Rev. B* **1985**, *32*, 5608-5627.

346. Henrichs, P. M.; Linder, M.; Hewitt, J. M. *J. Chem. Phys.* **1986**, *85*, 7077-7086.
347. Kubo, A.; McDowell, C. A. *J. Chem. Soc., Faraday Trans. 1* **1988**, *84*, 3713-3730.
348. VanderHart, D. L.; McFadden, G. B. *Solid State Nucl. Magn. Reson.* **1996**, *7*, 45-66.
349. Spiegel, S.; Schmidt-Rohr, K.; Boeffel, C.; Spiess, H. W. *Polymer* **1993**, *34*, 4566-4569.
350. Chen, Q.; Schmidt-Rohr, K. *Solid State Nucl. Magn. Reson.* **2006**, *29*, 142-152.
351. Kidron, A. *Phys. Lett.* **1967**, *25A*, 112-113.
352. Zhou, H.-C.; Long, J. R.; Yaghi, O. M. *Chemical Reviews* **2012**, *112*, 673-674.
353. Ma, S.; Zhou, H.-C. *Chem. Commun.* **2010**, *46*, 44-53.
354. Li, J.-R.; Sculley, J.; Zhou, H.-C. *Chem. Rev.* **2012**, *112*, 869-932.
355. Horcajada, P.; Chalati, T.; Serre, C.; Gillet, B.; Sebrie, C.; Baati, T.; Eubank, J. F.; Heurtaux, D.; Clayette, P.; Kreuz, C.; Chang, J.-S.; Hwang, Y. K.; Marsaud, V.; Bories, P.-N.; Cynober, L.; Gil, S.; Ferey, G.; Couvreur, P.; Gref, R. *Nat. Mater.* **2010**, *9*, 172-178.
356. Kreno, L. E.; Leong, K.; Farha, O. K.; Allendorf, M.; Van Duyne, R. P.; Hupp, J. T. *Chem. Rev.* **2012**, *112*, 1105-1125.
357. Deng, H.; Doonan, C. J.; Furukawa, H.; Ferreira, R. B.; Towne, J.; Knobler, C. B.; Wang, B.; Yaghi, O. M. *Science* **2010**, *327*, 846-850.
358. Furukawa, H.; Müller, U.; Yaghi, O. M. *Angew. Chem. Int. Ed.* **2015**, *54*, 3417-3430.
359. Qin, J.-S.; Yuan, S.; Wang, Q.; Alsalme, A.; Zhou, H.-C. *J. Mater. Chem. A* **2017**, *5*, 4280-4291.
360. Jasuja, H.; Burtch, N. C.; Huang, Y.-g.; Cai, Y.; Walton, K. S. *Langmuir* **2013**, *29*, 633-642.
361. Zhang, Y.-B.; Furukawa, H.; Ko, N.; Nie, W.; Park, H. J.; Okajima, S.; Cordova, K. E.; Deng, H.; Kim, J.; Yaghi, O. M. *J. Am. Chem. Soc.* **2015**, *137*, 2641-2650.
362. Marx, S.; Kleist, W.; Huang, J.; Maciejewski, M.; Baiker, A. *Dalton Transactions* **2010**, *39*, 3795-3798.



363. Goh, T. W.; Xiao, C.; Maligal-Ganesh, R. V.; Li, X.; Huang, W. *Chem. Eng. Sci.* **2015**, *124*, 45-51.
364. Krajnc, A.; Kos, T.; Zabukovec Logar, N.; Mali, G. *Angew. Chem. Int. Ed.* **2015**, *54*, 10535-10538.
365. Hong, H. L.; Wang, Q.; Dong, C.; Liaw, P. K. *Scientific Reports* **2014**, *4*, 7065.
366. Ice, G.; Sparks, C. *Annu. Rev. Mater. Sci.* **1999**, *29*, 25-52.
367. Thompson, J. A.; Vaughn, J. T.; Brunelli, N. A.; Koros, W. J.; Jones, C. W.; Nair, S. *Microporous Mesoporous Mater.* **2014**, *192*, 43-51.
368. Pimentel, B. R.; Lively, R. P. *Ind. Eng. Chem. Res.* **2016**, *55*, 12467-12476.
369. Pimentel, B. R.; Parulkar, A.; Zhou, E. k.; Brunelli, N. A.; Lively, R. P. *ChemSusChem* **2014**, *7*, 3202-3240.
370. Zhang, C.; Koros, W. J. *ACS Applied Materials & Interfaces* **2015**, *7*, 23407-23411.
371. Allen, F. *Acta Crystallogr., Sect. B: Struct. Sci.* **2002**, *58*, 380-388.
372. Cowley, J. M. *Physical Review* **1950**, *77*, 669-675.
373. Park, K. S.; Ni, Z.; Côté, A. P.; Choi, J. Y.; Huang, R.; Uribe-Romo, F. J.; Chae, H. K.; O’Keeffe, M.; Yaghi, O. M. *Proc. Natl. Acad. Sci. U.S.A.* **2006**, *103*, 10186-10191.
374. Morris, W.; Doonan, C. J.; Furukawa, H.; Banerjee, R.; Yaghi, O. M. *J. Am. Chem. Soc.* **2008**, *130*, 12626–12627.
375. Trout, B. L.; Chakraborty, A. K.; Bell, A. T. *Chem. Eng. Sci.* **1997**, *52*, 2265-2276.
376. Saravanan, C.; Auerbach, S. M. *J. Chem. Phys.* **1997**, *107*, 8132-8137.
377. Coppens, M.-O.; Bell, A. T.; Chakraborty, A. K. *Chem. Eng. Sci.* **1998**, *53*, 2053-2061.
378. Paschek, D.; Krishna, R. *Chem. Phys. Lett.* **2001**, *342*, 148-154.
379. Dubbeldam, D.; Snurr, R. Q. *Mol. Simul.* **2007**, *33*, 305-325.
380. Gabrieli, A.; Demontis, P.; Pazzona, F. G.; Suffritti, G. B. *Phys. Rev. E: Stat., Nonlinear, Soft Matter Phys.* **2011**, *83*, 056705.

381. Gillespie, D. T. *J. Comput. Phys.* **1976**, 22, 403-434.
382. Bortz, A. B.; Kalos, M. H.; Lebowitz, J. L. *J. Comput. Phys.* **1975**, 17, 10-18.
383. Chatterjee, A.; Vlachos, D. G. *J. Comput. Aided Mater. Des.* **2007**, 14, 253-308.
384. Stauffer, D.; Aharony, A. *Introduction to Percolation Theory*; 2nd ed.; Taylor and Francis: Philadelphia 1994.
385. Keffer, D.; McCormick, A. V.; Davis, H. T. *J. Phys. Chem.* **1996**, 100, 967-973.
386. Newman, M. E. J.; Ziff, R. M. *Phys. Rev. Lett.* **2000**, 85, 4104-4107.
387. Edvinsson, T.; Råsmark, P. J.; Elvingson, C. *Mol. Simul.* **1999**, 23, 169-190.
388. van Brakel, J.; Heertjes, P. M. *Int. J. Heat Mass Transfer* **1974**, 17, 1093-1103.
389. Shen, L.; Chen, Z. *Chem. Eng. Sci.* **2007**, 62, 3748-3755.
390. Lorenz, C. D.; Ziff, R. M. *Phys. Rev. E: Stat., Nonlinear, Soft Matter Phys.* **1998**, 57, 230-236.
391. Lorenz, C. D.; May, R.; Ziff, R. M. *Journal of Statistical Physics* **2000**, 98, 961-970.
392. van der Marck, S. C. *Phys. Rev. E: Stat., Nonlinear, Soft Matter Phys.* **1997**, 55, 1514-1517.
393. van der Marck, S. C. *Phys. Rev. E: Stat., Nonlinear, Soft Matter Phys.* **1997**, 55, 6593-6597.
394. Zhang, C.; Lively, R. P.; Zhang, K.; Johnson, J. R.; Karvan, O.; Koros, W. J. *J. Phys. Chem. Lett.* **2012**, 3, 2130-2134.
395. Maginn, E. J.; Bell, A. T.; Theodorou, D. N. *J. Phys. Chem.* **1996**, 100, 7155-7173.
396. Osborn Popp, T. M.; Yaghi, O. M. *Acc. Chem. Res.* **2017**, 50, 532-534.
397. Yuan, S.; Lu, W.; Chen, Y.-P.; Zhang, Q.; Liu, T.-F.; Feng, D.; Wang, X.; Qin, J.; Zhou, H.-C. *J. Am. Chem. Soc.* **2015**, 137, 3177-3180.
398. Yaghi, O. M. *J. Am. Chem. Soc.* **2016**, 138, 15507-15509.
399. *Nat Chem* **2016**, 8, 987-987.

400. Helal, A.; Yamani, Z. H.; Cordova, K. E.; Yaghi, O. M. *National Science Review* **2017**, nwx013.
401. Liu, L.; Konstas, K.; Hill, M. R.; Telfer, S. G. *J. Am. Chem. Soc.* **2013**, *135*, 17731-17734.
402. Yuan, S.; Lu, W.; Chen, Y.-P.; Zhang, Q.; Liu, T.-F.; Feng, D.; Wang, X.; Qin, J.; Zhou, H.-C. *J. Am. Chem. Soc.* **2015**, *137*, 3177-3180.
403. Krajnc, A.; Bueken, B.; De Vos, D.; Mali, G. *Journal of Magnetic Resonance* **2017**, *279*, 22-28.
404. Cacho-Bailo, F.; Catalán-Aguirre, S.; Etxeberria-Benavides, M.; Karvan, O.; Sebastian, V.; Téllez, C.; Coronas, J. *J. Membr. Sci.* **2015**, *476*, 277-285.
405. Banerjee, R.; Phan, A.; Wang, B.; Knobler, C.; Furukawa, H.; O'Keeffe, M.; Yaghi, O. M. *Science* **2008**, *319*, 939-943.
406. Jayachandrababu, K. C.; Sholl, D. S.; Nair, S. *J. Am. Chem. Soc.* **2017**, *139*, 5906-5915.
407. Thompson, J. A.; Brunelli, N. A.; Lively, R. P.; Johnson, J. R.; Jones, C. W.; Nair, S. *J. Phys. Chem. C* **2013**, *117*, 8198-8207.
408. Eum, K.; Jayachandrababu, K. C.; Rashidi, F.; Zhang, K.; Leisen, J.; Graham, S.; Lively, R. P.; Chance, R. R.; Sholl, D. S.; Jones, C. W.; Nair, S. *J. Am. Chem. Soc.* **2015**, *137*, 4191-4197.
409. Verploegh, R. J.; Wu, Y.; Sholl, D. S. *Langmuir* **2017**, *33*, 6481-6491.
410. Kamakoti, P.; Sholl, D. S. *Physical Review B* **2005**, *71*, 014301.
411. Saravanan, C.; Auerbach, S. M. *J. Chem. Phys.* **1997**, *107*, 8132-8137.
412. Hibbe, F.; Chmelik, C.; Heinke, L.; Pramanik, S.; Li, J.; Ruthven, D. M.; Tzoulaki, D.; Kärger, J. *J. Am. Chem. Soc.* **2011**, *133*, 2804-2807.
413. Karger, J.; Ruthven, D. M.; Theodorou, D. N. *Diffusion in Nanoporous Materials*; Wiley-VCH: Weinheim, Germany, 2012.
414. Zhang, K.; Lively, R. P.; Dose, M. E.; Brown, A. J.; Zhang, C.; Chung, J.; Nair, S.; Koros, W. J.; Chance, R. R. *Chem. Commun.* **2013**, *49*, 3245-3247.
415. Sarkisov, L.; Centineo, A.; Brandani, S. *Carbon* **2017**, *118*, 127-138.
416. Sholl, D. S.; Lee, C. K. *J. Chem. Phys.* **2000**, *112*, 817-824.

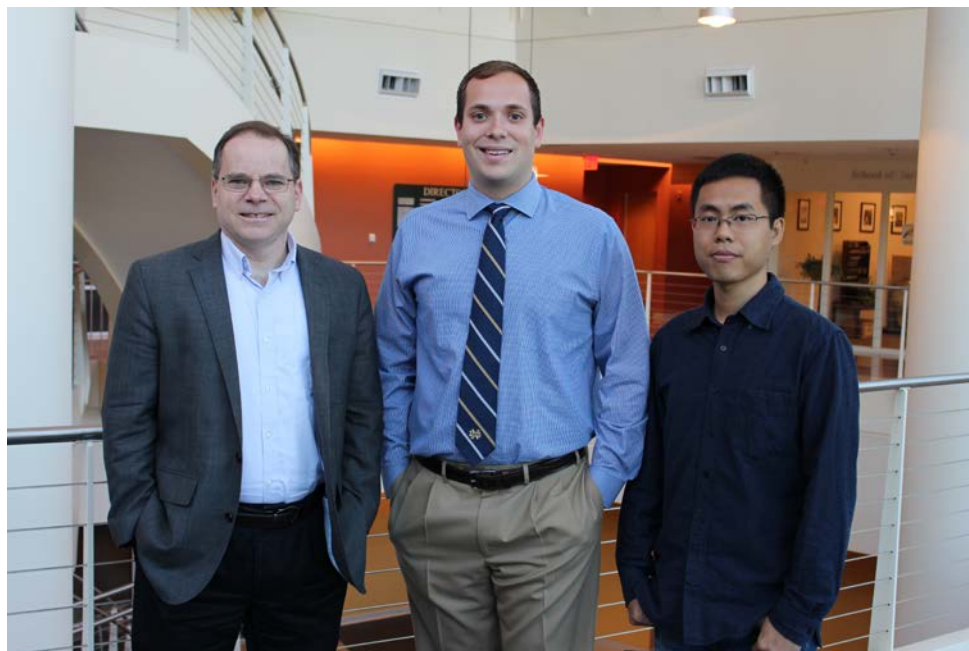
417. Vilhelmsen, L. B.; Walton, K. S.; Sholl, D. S. *J. Am. Chem. Soc.* **2012**, *134*, 12807-12816.
418. Dempsey, E.; Kühl, G.; Olson, D. H. *J. Phys. Chem.* **1969**, *73*, 387-390.
419. Herrero, C. P. *J. Phys. Chem.* **1991**, *95*, 3282-3288.
420. He, Y.; Lutz, T.; Ediger, M.; Ayyagari, C.; Bedrov, D.; Smith, G. D. *Macromolecules* **2004**, *37*, 5032-5039.
421. Case, D. A. *Acc. Chem. Res.* **2002**, *35*, 325-331.
422. Mueller, R.; Zhang, S.; Zhang, C.; Lively, R.; Vasenkov, S. *J. Membr. Sci.* **2015**, *477*, 123-130.
423. Ernst, S. *Advances in Nanoporous Materials*; Elsevier Science, 2009.
424. P.J. Linstrom and W.G. Mallard NIST Chemistry WebBook, N. S. R. D. N., National Institute of Standards and Technology, Gaithersburg MD, 20899, <http://webbook.nist.gov>, (retrieved April 21, 2015). Ed.
425. Boutin, A.; Springuel-Huet, M.-A.; Nossov, A.; Gédéon, A.; Loiseau, T.; Volkringer, C.; Férey, G.; Coudert, F.-X.; Fuchs, A. H. *Angew. Chem. Int. Ed.* **2009**, *48*, 8314-8317.
426. Zhang, C.; Gee, J. A.; Sholl, D. S.; Lively, R. P. *J. Phys. Chem. C* **2014**, *118*, 20727-20733.
427. Clark, L. A.; Gupta, A.; Snurr, R. Q. *J. Phys. Chem. B* **1998**, *102*, 6720.
428. Chen, B.; Potoff, J. J.; Siepmann, J. I. *J. Phys. Chem. B* **2001**, *105*, 3093-3104.
429. Stubbs, J. M.; Potoff, J. J.; Siepmann, J. I. *J. Phys. Chem. B* **2004**, *108*, 17596-17605.
430. Jorgensen, W. L.; Laird, E. R.; Nguyen, T. B.; Tirado-Rives, J. *Journal of Computational Chemistry* **1993**, *14*, 206-215.
431. Castillo, J. M.; Vlugt, T. J. H.; Calero, S. *J. Phys. Chem. C* **2009**, *113*, 20869-20874.
432. Berendsen, H. J. C.; Grigera, J. R.; Straatsma, T. P. *J. Phys. Chem.* **1987**, *91*, 6269-6271.
433. Orsi, M. *Mol. Phys.* **2014**, *112*, 1566-1576.
434. Chalaris, M.; Samios, J. *J. Chem. Phys.* **2000**, *112*, 8581-8594.

435. Rai, N.; Siepmann, J. I. *J. Phys. Chem. B* **2007**, *111*, 10790-10799.
436. Sanjeewa, R.; Weerasinghe, S. *Journal of Molecular Structure: THEOCHEM* **2010**, *944*, 116-123.
437. Wu, H.; Gong, Q.; Olson, D. H.; Li, J. *Chem. Rev.* **2012**, *112*, 836-868.
438. Perrin, C. L.; Dwyer, T. J. *Chem. Rev.* **1990**, *90*, 935-967.
439. Elena, B.; Emsley, L. *J. Am. Chem. Soc.* **2005**, *127*, 9140-9146.
440. Kolokolov, D. I.; Stepanov, A. G.; Jobic, H. *J. Phys. Chem. C* **2015**, *119*, 27512-27520.

## VITA

### ROSS J. VERPLOEGH

VERPLOEGH was born on September 12, 1990, to Diane Baum and James (Jim) Verploegh and spent his childhood years in Northville, Michigan, attending Detroit Catholic Central high school in Novi, MI. He became a member of the Fightin' Irish, attending the University of Notre Dame in South Bend, IN where he received a B.S. in Chemical Engineering (*cum laude*) in 2012. He was in the marching band for two years and worked as an undergraduate researcher in Dr. Joan Brennecke's ionic liquids laboratory. He came to Georgia Tech in the Fall 2012 to pursue a doctorate in Chemical Engineering under the guidance of Dr. David Sholl. Outside of research, he likes hiking, traveling, coding for fun, 3D design/printing, and spending time with his family.



*From left to right: Prof. David Sholl, Ross Verploegh, and Ying Wu in the atrium of the Ford ES&T Building at the Georgia Institute of Technology, Atlanta, GA, June 28<sup>th</sup>, 2017*